ELSEVIER
ACADEMIC
PRESS

DIAGNOSTIC ULTRASOUND IMAGING

INSIDE OUT

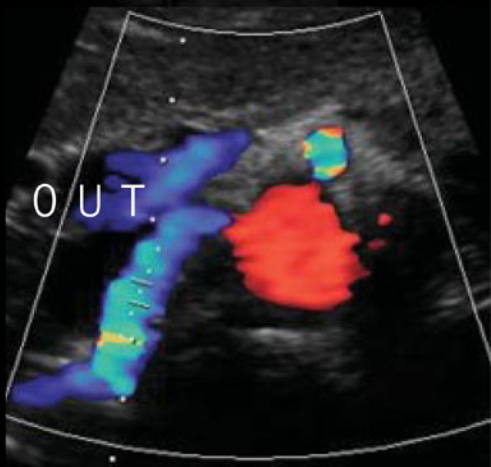

THOMAS L. SZABO

DIAGNOSTIC ULTRASOUND IMAGING: INSIDE OUT

This is a volume in the
ACADEMIC PRESS SERIES IN BIOMEDICAL ENGINEERING

Joseph Bronzino, Series Editor
Trinity College - Hartford, Connecticut

DIAGNOSTIC ULTRASOUND IMAGING: INSIDE OUT

Thomas L. Szabo

ELSEVIER
ACADEMIC
PRESS

Amsterdam Boston Heidelberg London New York Oxford
Paris San Diego San Francisco Singapore Sydney Tokyo

Elsevier Academic Press
200 Wheeler Road, 6th Floor, Burlington, MA 01803, USA
525 B Street, Suite 1900, San Diego, California 92101-4495, USA
84 Theobald's Road, London WC1X 8RR, UK

This book is printed on acid-free paper. ♾

Library of Congress Cataloging-in-Publication Data
Application submitted

British Library Cataloguing in Publication Data
A catalogue record for this book is available from the British Library

ISBN: 0-12-680145-2

For all information on all Academic Press publications
visit our Web site at www.books.elsevier.com

04 05 06 07 08 09 9 8 7 6 5 4 3 2 1

Printed in the United States of America

ACKNOWLEDGMENTS

This volume is based on the work of hundreds of people who contributed to advancing the science of diagnostic imaging. Your articles, books, conversations, presentations, and visits helped to inspire this book and shape my understanding.

I am thankful to my colleagues at Hewlett Packard, Agilent Technologies, and Philips for their advice, friendship, and help over the years. I gratefully acknowledge the suggestions, figures, and contributions of Michael Averkiou, Rob Entrekin, Rajesh Panda, Patrick Rafter, Gary A. Schwartz, and Karl Thiele of Philips Medical Systems.

Special thanks are due to Paul Barbone with whom I taught the first version of the material for an ultrasound course and whose encouragement was invaluable. We conceived of the block diagram for the imaging process at a table in a nearby café. I am also thankful for the forbearance and help of the Aerospace and Mechanical Engineering Department of Boston University during the writing of this book. Finally, I am grateful to my students, who helped clarify and correct the presentation of the material.

There are a number of people who supplied extra help for which I am particularly grateful. Thank you, Jack Reid, for your insights, articles, reviews, picture, and pioneering contributions. Special thanks to Robin Cleveland, Francis Duck, William O'Brien, Jr., Peder Pedersen, Patrick Rafter, and Karl Thiele for their wisdom and recommendations for improving the text. I extend my appreciation to the following people for their contributions to the book in the form of collaborations, advice, new

figures or many old ones, writings, and/or extremely useful web sites: Andrew Baker, Paul Dayton, Nico deJong, Kathy Ferrara, Barry Goldberg, Jim Greenleaf, Sverre Holm, Victor Humphrey, Jørgen Jensen, Jim Miller, Kevin J. Parker, Michael D. Sherar, Steve Smith, Gregg E. Trahey, Dan Turnbull, Bob Waag, Arthur Worthington, Junru Wu, and Marvin Ziskin.

I am indebted to Jim Brown and Mike Miller of Philips Medical Systems, whose patience and generosity did not waver under my many strange requests for images and imaging system illustrations; these superb figures have enhanced the book greatly. I acknowledge with gratitude figures contributed by David Bell of Precision Acoustics Ltd., Peter Chang of Teratech Corporation, Jackie Ferreira and Arun Tirumalai of Siemens Medical Solutions, Inc., Ultrasound Group, Lynda A. Hammond of ATS Laboratories, Inc., George Keilman of Sonic Concepts, Kai Thomenius and Richard Y. Chiao of GE Medical Systems, Jennifer Sabel of Sonosite, and Claudio I. Zanelli of Onda Incorporated. In addition, I appreciate those who gave me permission to reproduce their work.

Finally, I thank my children, Sam and Vivi, for their understanding and amusing diversions. My greatest debt is to Deborah, my wife, whose sacrifice, patience, good cheer, encouragement, and steady support made this marathon effort possible.

DEDICATION

To my wife, Deborah,
a continuous acoustic source of song and laughter, wisdom and understanding.

This page intentionally left blank

PREFACE

The purpose of this book is to provide both an introduction and a state-of-the-art review of the essential physics and signal processing principles of diagnostic ultrasound in a single reference volume with a unified approach. This book draws together many of the ideas from seminal papers, the author's research, and other sources in a single narrative and point of view. Unlike texts that present only the theory of acoustic fundamentals, this book relates topics to each other in the context of ultrasound imaging and practical application. It is the author's hope that this work will contribute to the overall development of ultrasound diagnostic imaging by serving as a focus for discussion, an information source for newcomers, and a foundation for further inquiry.

This text is intended for a graduate level course in diagnostic ultrasound imaging and as a reference for practicing engineers in the field, medical physicists, clinicians, researchers, design teams, and those who are beginning in medical ultrasound, as well as those who would like to learn more about a particular aspect of the imaging process. This book is an introduction to the basic physical processes and signal processing of imaging systems, and as a guide to corresponding literature and terminology. Parts of the book can be read on several levels, depending on the intent and background of the reader. While this book provides sufficient equations for a scientific foundation, there are also many parts of the book that go on for long stretches without any equations. Equations can be thought of as a more precise description of the variables involved and provide the means of simulation and deeper analysis. The

This page intentionally left blank

book are presented in both the time and frequency domains, Fourier transforms are used frequently to facilitate a more balanced and deeper understanding of the physical processes. For those who have not used Fourier transforms recently, a review is provided in Appendix A, along with information about digital Fourier transforms and fast Fourier transforms and step-by-step worked-out examples.

This work is based in part on my nearly 20 years of research and development experience at Hewlett Packard, later Agilent Technologies. Since my departure, the healthcare group where I worked for nearly 20 years has become, by acquisition, part of Philips Medical Ultrasound. I am indebted to my former colleagues for our many collaborations over the years and for providing many requested images and material for this book. Even though many of the images and system descriptions are from Philips, readers can take some of this material to represent typical imaging systems.

Diagnostic ultrasound has been in use for over 50 years, yet it continues to evolve at a surprisingly rapid rate. In this fragmented world of specialization, there is information in abundance, but it is difficult to assimilate without order and emphasis. This book strives to consolidate, organize, and communicate major ideas concisely, even though this has been a challenging process. In addition, many essential pieces of information and assumptions, known to those experienced in the field and not available in journals and books, are included.

Thomas L. Szabo
Newburyport, Massachusetts
May 2004

This page intentionally left blank

CONTENTS

1 INTRODUCTION

Chapter Contents

1.1 INTRODUCTION

The archetypal modern comic book superhero, Superman, has two superpowers of interest: x-ray vision (the ability to see into objects) and telescopic vision (the ability to see distant objects). Ordinary people now have these powers as well because of

medical ultrasound imaging and sonar (sound navigation and ranging) instruments. Ultrasound, a type of sound we cannot hear, has enabled us to see a world otherwise invisible to us.

The purpose of this chapter is to explore medical ultrasound from its antecedents and beginnings, relate it to sonar, describe the struggles and discoveries necessary for its development, and provide the basic principles and reasons for its success. The development of medical ultrasound was a great international effort involving thousands of people during the last half of the twentieth century, so it is not possible to include many of the outstanding contributors in the short space that follows. Only the fundamentals of medical ultrasound and representative snapshots of key turning points are given here, but additional references are provided. In addition, the critical relationship between the growth of the science of medical ultrasound and key enabling technologies is examined. Why these allied technologies will continue to shape the future of ultrasound is also described. Finally, the unique role of ultrasound imaging is compared to other diagnostic imaging modalities.

1.1.1 Early Beginnings

Robert Hooke (1635-1703), the eminent English scientist responsible for the theory of elasticity, pocket watches, compound microscopy, and the discovery of cells and fossils, foresaw the use of sound for diagnosis when he wrote (Tyndall, 1875):

> It may be possible to discover the motions of the internal parts of bodies, whether animal, vegetable, or mineral, by the sound they make; that one may discover the works performed in the several offices and shops of a man's body, and therby (sic) discover what instrument or engine is out of order, what works are going on at several times, and lie still at others, and the like. I could proceed further, but methinks I can hardly forbear to blush when I consider how the most part of men will look upon this: but, yet again, I have this encouragement, not to think all these things utterly impossible.

Many animals in the natural world, such as bats and dolphins, use echo-location, which is the key principle of diagnostic ultrasound imaging. The connection between echo-location and the medical application of sound, however, was not made until the science of underwater exploration matured. Echo-location is the use of reflections of sound to locate objects.

Humans have been fascinated with what lies below the murky depths of water for thousands of years. ''To sound'' means to measure the depth of water at sea, according to a naval terms dictionary. The ancient Greeks probed the depths of seas with a ''sounding machine,'' which was a long rope knotted at regular intervals with a lead weight on the end. American naturalist and philosopher Henry David Thoreau measured the depth profiles of Walden Pond near Concord, Mass., with this kind of device. Recalling his boat experiences as a young man, American author and humorist Samuel Clemens chose his pseudonym, Mark Twain, from the second mark or knot on a sounding lead line. While sound may or may not have been involved in a sounding

machine, except for the thud of a weight hitting the sea bottom, the words "to sound" set the stage for the later use of actual sound for the same purpose.

The sounding-machine method was in continuous use for thousands of years until it was replaced by ultrasound echo-ranging equipment in the twentieth century. Harold Edgerton (1986), famous for his invention of stroboscopic photography, related how his friend, Jacques-Yves Cousteau, and his crew found an ancient Greek lead sounder (250 B.C.) on the floor of the Mediterranean sea by using sound waves from a side scan sonar. After his many contributions to the field, Edgerton used sonar and stroboscopic imaging to search for the Loch Ness monster (Rines *et al*., 1976).

1.1.2 Sonar

The beginnings of sonar and ultrasound for medical imaging can be traced to the sinking of the Titanic. Within a month of the Titanic tragedy, British scientist L. F. Richardson (1913) filed patents to detect icebergs with underwater echo ranging. In 1913, there were no practical ways of implementing his ideas. However, the discovery of piezoelectricity (the property by which electrical charge is created by the mechanical deformation of a crystal) by the Curie brothers in 1880 and the invention of the triode amplifier tube by Lee De Forest in 1907 set the stage for further advances in pulse-echo range measurement. The Curie brothers also showed that the reverse piezoelectric effect (voltages applied to certain crystals cause them to deform) could be used to transform piezoelectric materials into resonating transducers. By the end of World War I, C. Chilowsky and P. Langevin (Biquard, 1972), a student of Pierre Curie, took advantage of the enabling technologies of piezoelectricity for transducers and vacuum tube amplifiers to realize practical echo ranging in water. Their high-power echo-ranging systems were used to detect submarines. During transmissions, they observed schools of dead fish that floated to the water surface. This shows that scientists were aware of the potential for ultrasound-induced bioeffects from the early days of ultrasound research (O'Brien, 1998).

The recognition that ultrasound could cause bioeffects began an intense period of experimentation and hopefulness. After World War I, researchers began to determine the conditions under which ultrasound was safe. They then applied ultrasound to therapy, surgery, and cancer treatment. The field of therapeutic ultrasound began and grew erratically until its present revival in the forms of lithotripsy (ultrasound applied to the breaking of kidney and gallstones) and high-intensity focused ultrasound (HIFU) for surgery. However, this branch of medical ultrasound, which is concerned mainly with ultrasound transmission, is distinct from the development of diagnostic applications, which is the focus of this chapter.

During World War II, pulse-echo ranging applied to electromagnetic waves became radar (radio detection and ranging). Important radar contributions included a sweeping of the pulse-echo direction in a 360-degree pattern and the circular display of target echoes on a plan position indicator (PPI) cathode-ray tube screen. Radar developments hastened the evolution of single-direction underwater ultrasound ranging devices into sonar with similar PPI-style displays.

1.2 ECHO RANGING OF THE BODY

After World War II, with sonar and radar as models, a few medical practitioners saw the possibilities of using pulse-echo techniques to probe the human body for medical purposes. In terms of ultrasound in those days, the body was vast and uncharted. In the same way that practical underwater echo ranging had to wait until the key enabling technologies were available, the application of echo ranging to the body had to wait for the right equipment. A lack of suitable devices for these applications inspired workers to do amazing things with surplus war equipment and to adapt other echo-ranging instruments.

Fortunately, the timing was right in this case because F. Firestone's (1945) invention of the supersonic reflectoscope in 1940 applied the pulse-echo ranging principle to the location of defects in metals in the form of a reasonably compact instrument. A diagram of a basic echo-ranging system of this type is shown in Figure 1.1 A transmitter excites a transducer, which sends a sequence of repetitive ultrasonic pulses into a material or a body. Echoes from different target objects and boundaries are received and amplified so they can be displayed as an amplitude versus time record on an oscilloscope. This type of display became known as the "A-line," (or "A-mode" or "A-scope"), with "A" representing amplitude.

When commercialized versions of the reflectoscope were applied to the human body in Japan, the United States, and Sweden in the late 1940s and early 1950s (Goldberg and Kimmelman, 1988), a new world of possibility for medical diagnosis was born. Rokoru Uchida in Japan was one of the first to use flaw detectors for medical A-line pulse-echo ranging. In Sweden in 1953, Dr. I. Edler (1991) and Professor C. H. Hertz detected heart motions with a flaw detector and began what later was called "echocardiography," the application of ultrasound to the characterization and imaging of the heart.

Medical ultrasound in the human body is quite different from many sonar applications that detect hard targets, such as metal ships in water. At the Naval Medical

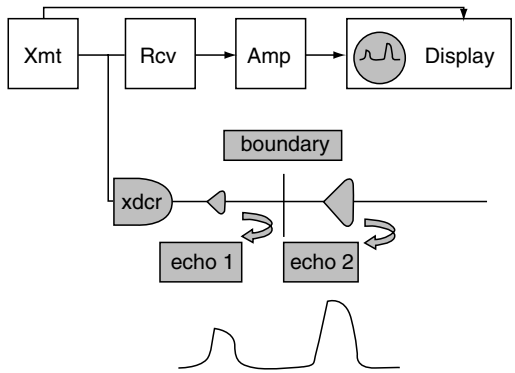

Figure 1.1 Basic echo-ranging system showing multiple reflections and an A-line trace at the bottom.

Research Institute, Dr. George Ludwig, who had underwater ranging experience during World War II, and F. W. Struthers embedded hard gallstones in canine muscles to determine the feasibility of detecting them ultrasonically. Later, Ludwig (1950) made a number of time-of-flight measurements of sound speed through arm, leg, and thigh muscles. He found the average to be $c_{av} = 1540\,m/s$, which is the standard value still used today. The sound speed, c, can be determined from the time, t, taken by sound to pass through a tissue of known thickness, d, from the equation, $c = d/t$. He found the sound speeds to be remarkably similar, varying in most soft tissues by only a few percent. Normalized speed of sound measurements taken more recently are displayed in Figure 1.2.

The remarkable consistency among sound speeds for the soft tissues of the human body enables a first-order estimation of tissue target depths from their round trip (pulse-echo) time delays, t_{rt}, and an average speed of sound, c_{av}, from $z = c_{av}t_{rt}/2$. This fact makes it possible for ultrasound images to be faithful representations of tissue geometry.

In the same study, Ludwig also measured the characteristic acoustic impedances of tissues. He found that the soft tissues and organs of the body have similar impedances because of their high water content. The characteristic acoustic impedance, Z, is defined as the product of density, ρ, and the speed of sound, c, or $Z = \rho c$. The amplitude reflection factor of acoustic plane waves normally incident at an interface of two tissues with impedances Z_1 and Z_2 can be determined from the relation, $RF = (Z_2 - Z_1)/(Z_2 + Z_1)$.

Fortunately, amplitude reflection coefficients for tissue are sensitive to slight differences in impedance values so that the reflection coefficients relative to blood (Figure 1.3) are quite different from each other as compared to small variations in the speed of sound values for the same tissues (see Figure 1.2). This fortuitous range of reflection coefficient values is why it is possible to distinguish between different tissue types for both echo ranging and imaging. Note that the reflection coefficients are

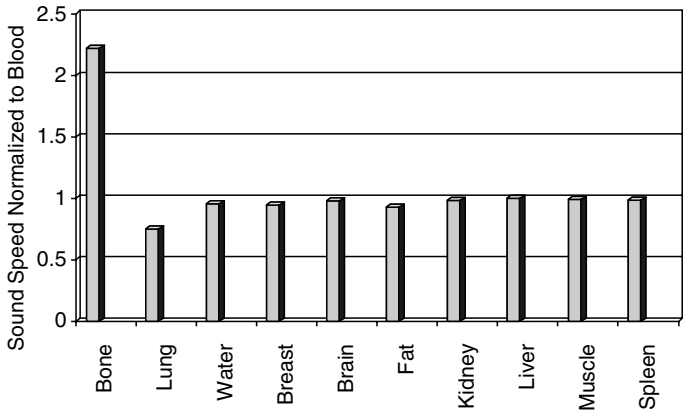

Figure 1.2 Acoustic speed of sound of tissues normalized to the speed of sound in blood.

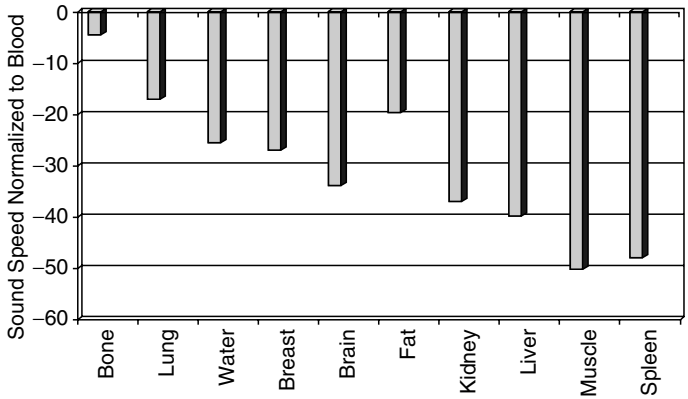

Figure 1.3 Amplitude reflection factor coefficients in dB for tissues relative to blood.

plotted on a dB, or logarithmic, scale (explained in Chapter 4). For example, each change of −10 dB means that the reflection coefficient value is a factor 3.2 less in amplitude or a factor 10 less in intensity.

Also in 1949, Dr. D. Howry of Denver, Colo., who was unaware of Ludwig's work, built a low-megahertz pulse-echo scanner in his basement from surplus radar equipment and an oscilloscope. Howry and other workers using A-line equipment found that the soft tissues and organs of the body, because of their small reflection coefficients and low absorption, allowed the penetration of elastic waves through multiple tissue interfaces (Erikson *et al*., 1974). This is illustrated in Figure 1.1. In Minnesota, Dr. John J. Wild, an English surgeon who also worked for some time in his basement, applied A-mode pulse echoes for medical diagnosis in 1949, and shortly thereafter, he developed imaging equipment with John M. Reid, an electrical engineer.

When identifying internal organs with ultrasound was still a novelty, Wild used a 15-MHz Navy radar trainer to investigate A-lines for medical diagnosis. He reported the results for cancer in the stomach wall in 1949. In 1952, Wild and Reid analyzed data from 15-MHz breast A-scans. They used the area underneath the echoes to differentiate malignant from benign tissue, as well as to provide the first identification of cysts. These early findings triggered enormous interest in diagnosis, which became the most important reason for the application of ultrasound to medicine. Later this topic split into two camps: diagnosis—findings directly observable from ultrasound images, and tissue characterization—findings about the health of tissue and organ function determined by parameterized inferences and calculations made from ultrasound data.

1.3 ULTRASOUND PORTRAIT PHOTOGRAPHERS

The A-mode work described in the previous section was a precursor to diagnostic ultrasound imaging just as echo ranging preceded sonar images. The imaginative leap

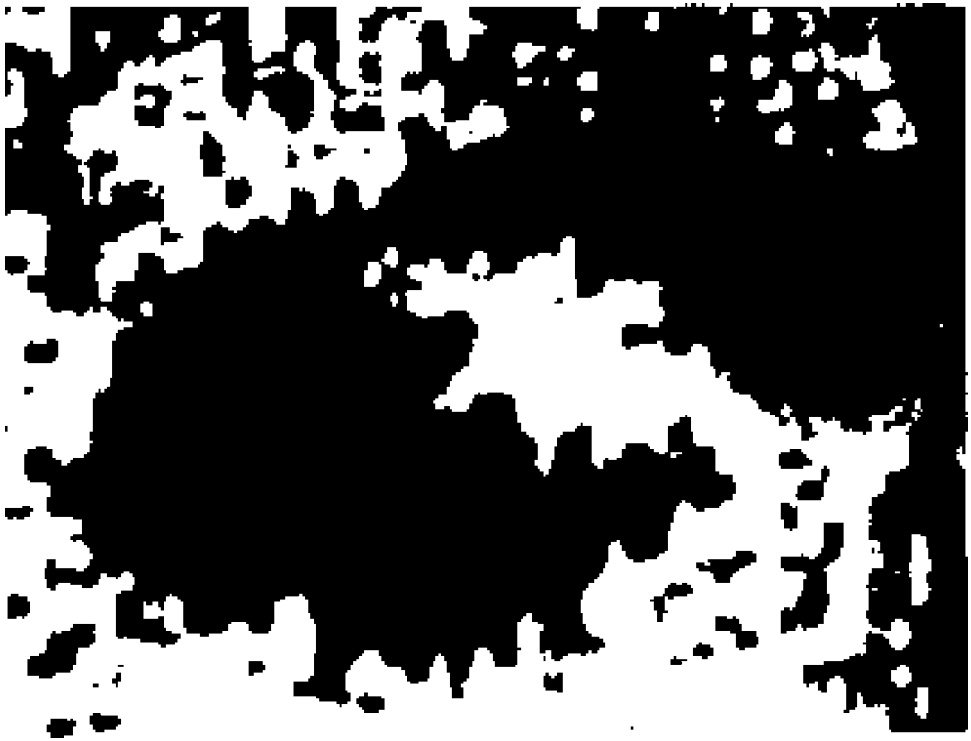

Figure 1.4 The Dussik transcranial image, which is one of the first ultrasonic images of the body ever made. Here white represents areas of signal strength and black represents complete attenuation (from Goldberg and Kimmelman, 1988; reprinted with permission of the AIUM).

to imaging came in 1942 in Austria when Dr. Karl Dussik and his brother published their through-transmission ultrasound attenuation image of the brain, which they called a "hyperphonogram." In their method, a light bulb connected to the receiving transducer glowed in proportion to the strength of the received signal, and the result was optically recorded (Figure 1.4). This transcranial method was not adopted widely because of difficult refraction and attenuation artifacts in the skull, but it inspired many others to work on imaging with ultrasound. Their work is even more remarkable because it preceded the widespread use of radar and sonar imaging.

Despite the problems caused by refraction through varying thicknesses of the skull, others continued to do ultrasound research on the brain. This work became known as "echoencephalography." Dr. Karl Dussik met with Dr. Richard Bolt, who was then inspired to attempt to image through the skull tomographically. Bolt tried this in 1950 with his group and Dr. George Ludwig at the MIT Acoustic Laboratory, but he later abandoned the project. In 1953, Dr. Lars Leksell, of Lund University in Sweden, used flaw detectors to detect midline shifts in the brain caused by disease or trauma. Leksell found an acoustic window through the temples. Equipment for detecting midline shifts and cardiac echoes became available in the 1960s.

The Dussiks' work, as well as war developments in pulse-echo imaging, motivated others to make acoustic images of the body. For example, Dr. D. Howry and his group were able to show that highly detailed pulse-echo tomographic images of cross sections of the body correlated well with known anatomical features (Holmes, 1980). Their intent was to demonstrate that ultrasound could show accurate pictures of soft tissues that could not be obtained with x-rays. Howry and his group transformed the parts of a World War II B-29 bomber gun turret into a water tank. A subject was immersed in this tank, and a transducer revolved around the subject on the turret ring gear. See Figure 1.5 for pictures of their apparatus and results.

The 1950s were a period of active experimentation with both imaging methods and ways of making contact with the body. Many versions of water bath scanners were in use. Dr. John J. Wild and John M. Reid, both affiliated with the University of Minnesota, made one of the earliest handheld contact scanners. It consisted of a transducer enclosed in a water column and sealed by a condom. Oils and eventually gels were applied to the ends of transducers to achieve adequate coupling to the body (Wells, 1969a).

The key element that differentiates a pulse-echo-imaging system (Figure 1.6) from an echo-ranging system is a means of either scanning the transducer in a freehand form with the detection of the transducer position in space or by controlling the motion of the transducer. As shown, the position controller or position sensor is triggered by the periodic timing of the transmit pulses. The display consists of time traces running vertically (top to bottom) to indicate depth. Because the brightness along each trace is proportional to the echo amplitude, this display presentation came to be known as "B-mode," with "B" meaning brightness. However, it was first used by Wild and Reid, who called it a "B-scan." In an alternative (b) in Figure 1.6, a single transducer is scanned mechanically at intervals across an elliptically shaped object. At each controlled mechanical stopping point, sound (shown as a line) is sent across an object and echoes are received. For the object being scanned linearly upward in the figure, the bright dots in each trace on the display indicate the front and back wall echoes of the object. By scanning across the object, multiple lines produce an "image" of the object on the display.

Various scanning methods are shown in Figure 1.7. A straightforward method is linear scanning, or translation of a transducer along a flat surface or straight line. Angular rotation, or sector scanning, involves moving the transducer in an angular arc without translation. Two combinations of the translation and angular motions are compound (both motions are combined in a rocking, sliding motion) and contiguous (angular motion switches to translation and back to angular). An added twist is that the scanning surface may not be flat but may be curved or circular instead. Dr. Howry's team, along with Dr. Ian Donald and his group at the University of Glasgow, developed methods to display each scan line in its correct geometric attitude. For example, the first line in an angular scan at −45 degrees would appear on the scope display as a brightness-modulated line at that angle with the depth increasing from top to bottom.

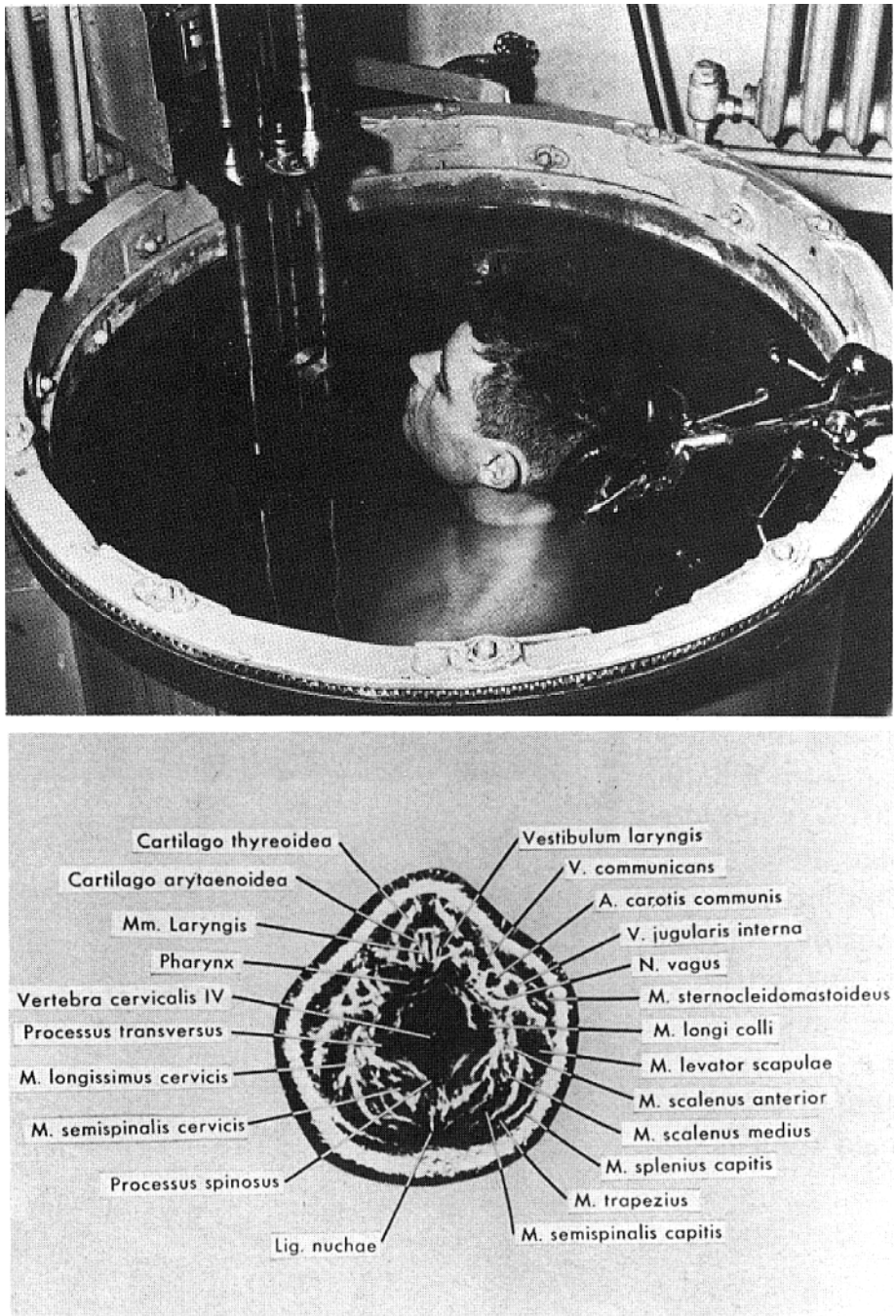

Figure 1.5 Howry's B-29 gun turret ultrasonic tomographic system and resulting annotated image of neck (from Goldberg and Kimmelman, 1988; reprinted with permission of the AIUM).

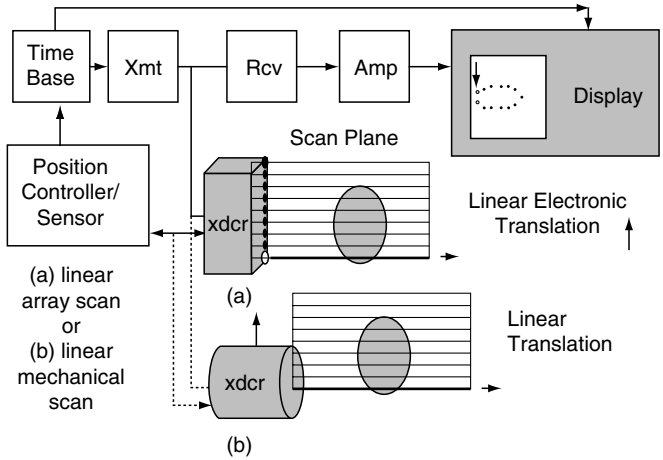

Figure 1.6 Basic elements of a pulse echo-imaging system shown with linear scanning of two types: (a) electronic linear array scanning, which involved switching from one element to another, and (b) mechanical scanning, which involved controlled translation of a single transducer.

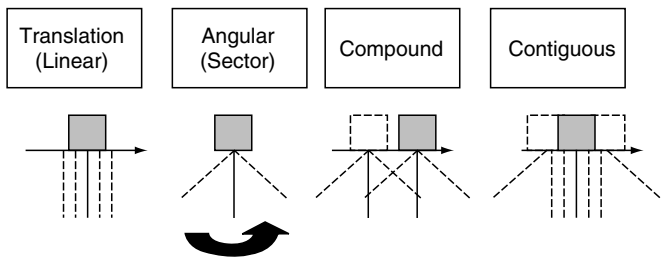

Figure 1.7 Scanning methods: translation, angular rotation, compound (translation and rotation), and contiguous (rotation, translation, and rotation).

The most popular imaging method from the 1950s to the 1970s became freehand compound scanning, which involved both translation and rocking. Usually transducers were attached to large articulated arms that both sensed the position and attitude of the transducer in space and also communicated this information to the display. In this way, different views (scan lines) contributed to a more richly detailed image because small curved interfaces were better defined by several transducer positions rather than one.

Sonography in this time period was like portrait photography. Different patterns of freehand scanning were developed to achieve the "best picture." For each position of the transducer, a corresponding time line was traced on a cathode-ray tube (CRT) screen. The image was not seen until scanning was completed or later because the

picture was usually in the form of either a storage scope image or a long-exposure photograph (Devey and Wells, 1978; Goldberg and Kimmelman, 1988). Of course, the "subject" being imaged was not to move during scanning. In 1959, the situation was improved by the introduction of the Polaroid scope camera, which provided prints in minutes.

During the same time, seemingly unrelated technologies (*EE Times*, 1997) were being developed that would revolutionize ultrasound imaging. The inventions of the transistor and the digital computer in the late 1940s set profound changes in motion. In 1958, Jack Kilby's invention of an integrated circuit accelerated the pace by combining several transistors and circuit elements into one unit.

In 1964, Gordon Moore predicted that the density of integrated circuits would grow exponentially (double every 12 months), as illustrated in Figure 1.8 (Santo and Wollard, 1978; Brenner, 2001). By 1971, 2300 transistors on a single chip had as much computational power as the ENIAC (Electronic Numerical Integrator and Computer) computer that, 25 years before, was as big as a boxcar and weighed 60,000 lb. Hand calculators, such as the Hewlett Packard scientific calculator HP-35, speeded up chip miniaturization. Digital memories and programmable chips were also produced.

By the early 1960s, the first commercialized contact B-mode static scanners became available. These consisted of a transducer mounted on a long moveable articulated arm with spatial position encoders, a display, and electronics (Goldberg and Kimmelman, 1988). An early scanner of this type, called the "Diasonograph" and designed by Dr. Ian Donald and engineer Tom G. Brown (1968) of Scotland, achieved commercial success. For stable imaging, the overall instrument weighed 1 ton and was sometimes called the "Dinosaurograph." Soon other instruments, such as the Picker unit, became available, and widespread use of ultrasound followed.

These instruments, which began to incorporate transistors (Wells, 1969b), employed the freehand compound scanning method and produced still (static) pictures. The biphasic images were black and white. Whereas A-mode displays had a

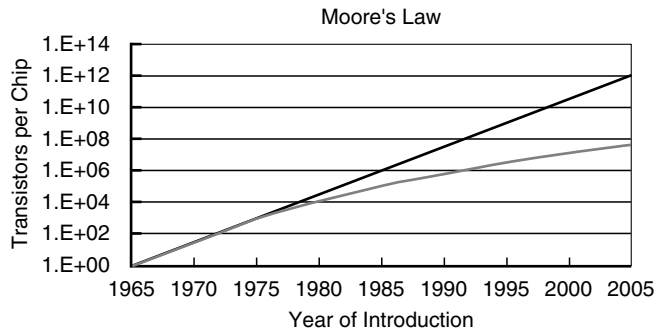

Figure 1.8 Moore's law predicts exponential growth of microprocessor density (indicated as a solid black line). Actual growth is shown as a gray line.

dynamic range of 40 dB, B-mode storage scopes had only a 10-dB range (a capability to display 1-10X in intensity), and regular scopes had a 20-dB (1-100X) range (Wells, 1977). Storage scopes and film had blooming and exposure variations, which made consistent results difficult to obtain.

At the time of biphasic imaging, interest was focused on tissue interfaces and boundaries. During an extended stay at W. J. Fry's focused ultrasound surgery laboratory at the University of Illinois, George Kossoff observed that the pulse echoes from boundaries were strongly dependent on the angle of insonification. Because the transducer had a large focal gain and power, Kossoff also noticed that the lower amplitude scattering from tissue was much less sensitive to angular variation. These insights led to his methods to image the soft tissues more directly. By emphasizing the region of dynamic range for soft tissue scattering and implementing logarithmic amplifiers to better display the range of information, Kossoff (1974) and his coworkers at the Commonwealth Acoustic Laboratory in Australia published work on implementing gray-scale imaging though analog methods. Gray-scale became widespread because of the availability of digital electronic programmable read-only memories (EPROMs), random-access memories (RAMs), microprocessors, and analog/digital (A/D) converters. These allowed the ultrasound image to be stored and scan-converted to the rectangular format of cathode-ray tubes (CRTs) at video rates. By 1976, commercial gray-scale scan converters revolutionized ultrasound imaging by introducing subtle features and an increased dynamic range for better differentiation and resolution of tissue structures.

One of the most important applications of ultrasound diagnosis is obstetrics. A study by Alice Stewart of England in 1956 linked deaths from cancer in children to their prenatal exposure to x-rays (Kevles, 1997). Dr. Ian Donald foresaw the benefit of applying ultrasound to obstetrics and gynecology, and his Diasonograph became successful in this area. Eventually ultrasound imaging completely replaced x-rays in this application and provided much more diagnostic information. An estimated 70% of pregnant women in the United States had prenatal ultrasounds (Kevles, 1997).

Ultrasound was shown to be a safe noninvasive methodology for the diagnosis of diseased tissue, the location of cysts, fetal abnormalities, and heart irregularities. By the late seventies, millions of clinical exams had been performed by diagnostic ultrasound imaging (Devey and Wells, 1978).

1.4 ULTRASOUND CINEMATOGRAPHERS

Gray-scale was not enough to save the static B-scanner (the still portrait camera of ultrasound) because the stage was set for movies, or ultrasound cinematography. In the early 1950s, Dr. John J. Wild and John Reid worked on an alternative method: a real-time handheld array-like scanner, in which they used mechanically scanned (controlled position) transducers (Figure 1.9). In this figure, the rectangular B-scan image format is a departure from the plan position indication (PPI) format of sonar

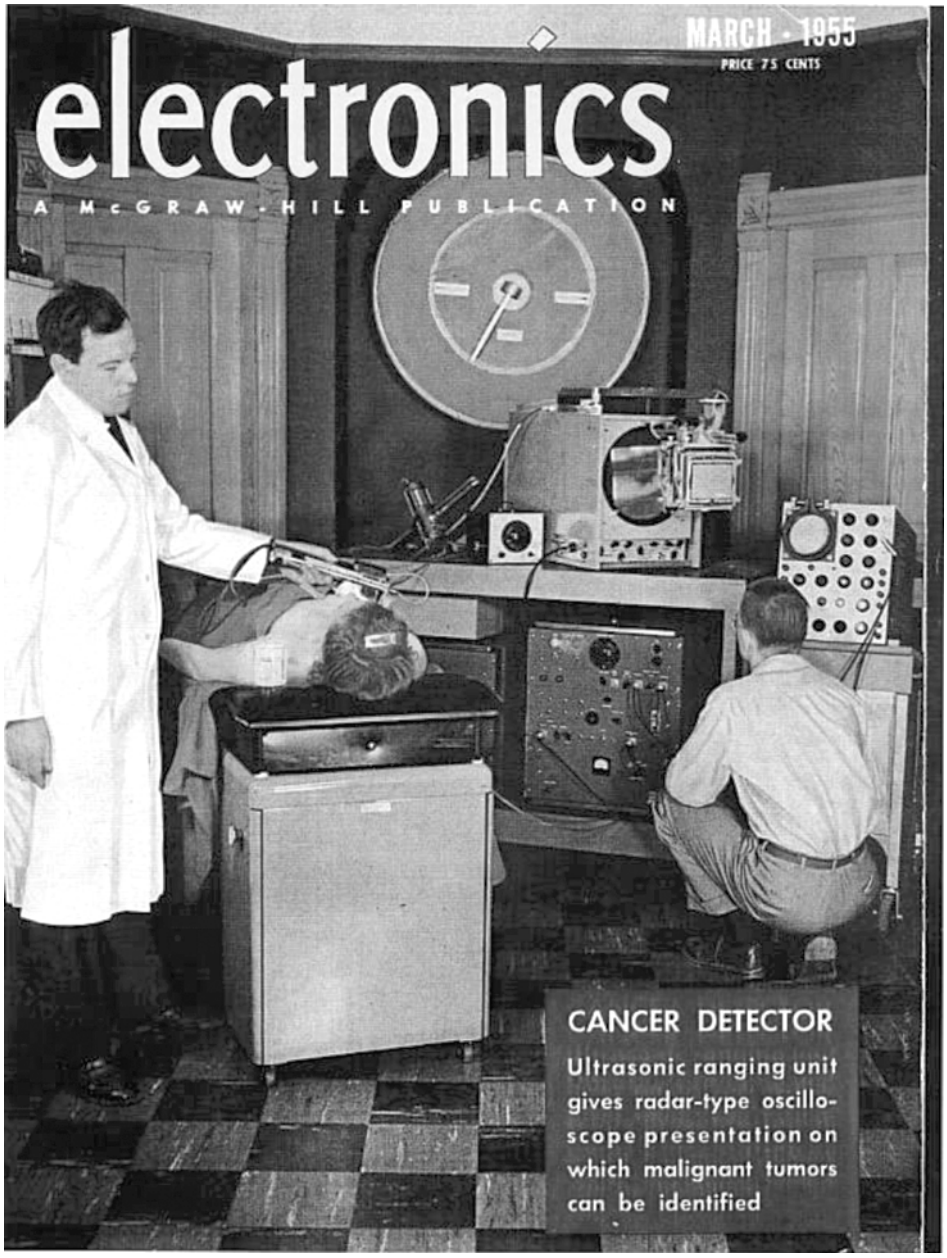

Figure 1.9 Dr. John J. Wild scans a patient with a handheld, linearly scanned 15-MHz contact transducer. John Reid (later Professor Reid) adjusts modified radar equipment to produce a B-scan image on a large-diameter scope display with a recording camera (courtesy of J. Reid; reprinted with permission of VNU Business Publications) (see also color insert).

B-mode images and earlier tomographic (circular) images. Wild and Reid's vision of real-time scanning was a few years ahead of its time.

The year 1965 marked the appearance of Vidoson from Siemens, the first real-time mechanical commercial scanner. Designed by Richard Soldner, the Vidoson consisted of a revolving transducer and a parabolic mirror. By the early 1970s, real-time contact mechanical scanners with good resolution were beginning to replace the static B-scanners.

Radar and sonar images, and eventually ultrasonic images, benefited from the maturing of electronically scanned and focused phased array technology for electromagnetic applications in the late 1950s and 1960s. In 1971, Professor N. Bom's group in Rotterdam, Netherlands built linear arrays for real-time imaging (Bom *et al.*, 1973). An example of an early linear array imaging system was illustrated in Figure 1.6. The position controller takes the form of a multiplexer, which is an electronic switch that routes the input/output channel to different transducer array elements sequentially. As each transducer element is fired in turn, a pulse-echo image line is created. These efforts produced the Minivisor (Ligtvoet *et al.*, 1978; Roelandt *et al.*, 1978), which was the first portable ultrasound system including a built-in linear array, electronics, display, and a $1\frac{1}{2}$ hr battery, with a total weight of 1.5 kg (shown in Figure 1.13).

J. C. Somer (1968) of the Netherlands reported his results for a sector (angular) scanning phased array for medical ultrasound imaging. Shown in Figure 1.10 are two views of different steering angles from the same array. On the left are Schlieren measurements (an acousto-optic means of visualizing sound beams) of beams steered at different angles. They are depicted as acoustic lines on the oscilloscope images on the right. By 1974, Professor Thurstone and Dr. von Ramm (1975) of Duke University obtained live images of the heart with their 16-channel phased array imaging system called the "Thaumascan."

The appearance of real-time systems with good image quality marked the end of the static B-scanners (Klein, 1981). Parallel work on mechanically scanned transducers resulted in real-time commercial systems by 1978. By 1980, commercial real-time phased array imaging systems were made possible by recent developments in video, microprocessors, digital memory, small delay lines, and the miniaturization offered by programmable integrated circuits. In 1981, the Hewlett Packard 70020A phased array system became a forerunner of future systems, which had wheels, modular architectures, microprocessors, programmable capabilities, and their upgradeability (*HP Journal*, 1983).

During the 1980s, array systems became the dominant imaging modality. Several electronic advancements (*EE Times*, 1997) rapidly improved imaging during this decade: application-specific integrated circuits (ASICs), digital signal processing chips (DSPs), and the computer-aided design (CAD) of very large scale integration (VLSI) circuits.

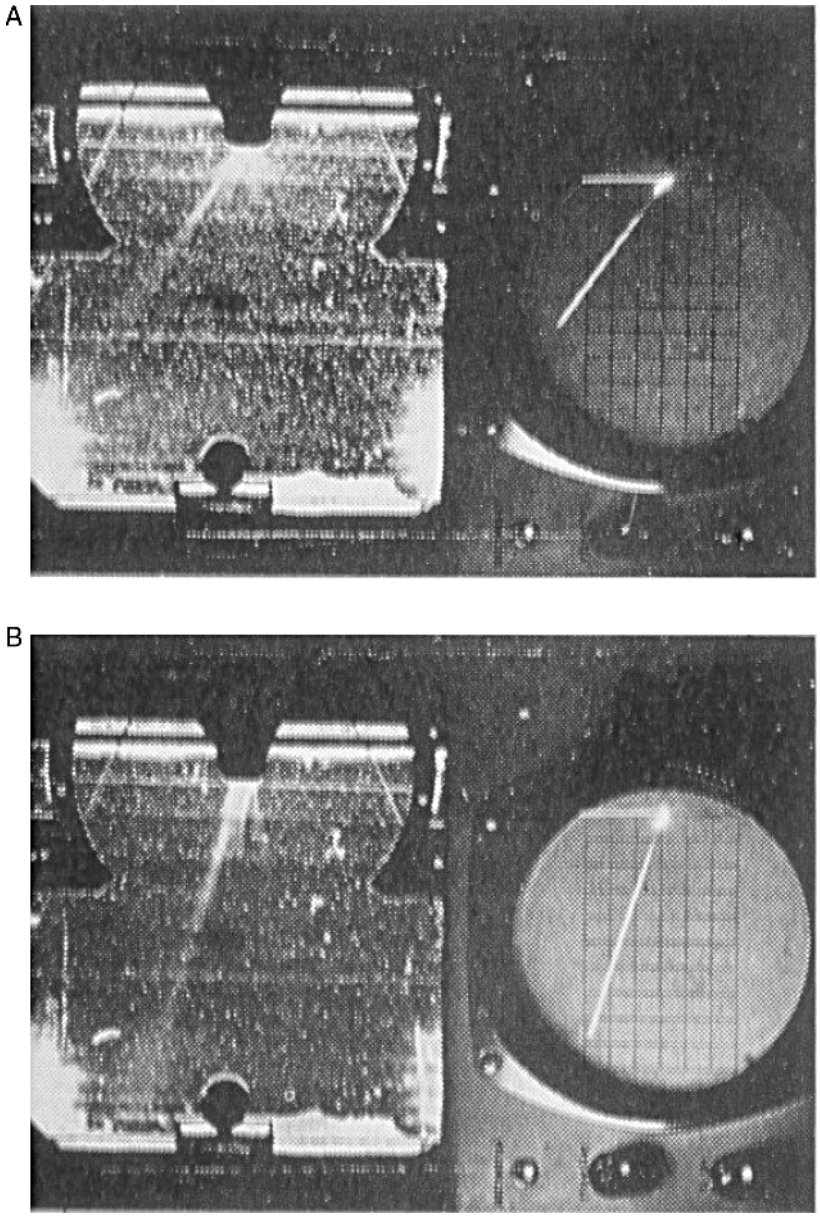

Figure 1.10 (A) Pulse-echo acoustic lines at two different angles on an oscilloscope from a phased array designed by J. C. Somer (1968). (B) Schlieren pictures of the corresponding acoustic beams as measured in water tank (courtesy of N. Bom).

Figure 1.11 The first Hewlett Packard phased array system, the 70020A (courtesy of Philips Medical Systems).

1.5 MODERN ULTRASOUND IMAGING DEVELOPMENTS

The concept of deriving real-time parameters other than direct pulse-echo data by signal processing or by displaying data in different ways was not obvious at the very beginning of medical ultrasound. M-mode, or a time–motion display, presented new

time-varying information about heart motion at a fixed location when I. Elder and C. H. Hertz introduced it in 1954. In 1955, S. Satomura, Y. Nimura, and T. Yoshida reported experiments with Doppler-shifted ultrasound signals produced by heart motion. Doppler signals shifted by blood movement fall in the audio range and can be heard as well as seen on a display. By 1966, D. Baker and V. Simmons had shown that pulsed spectral Doppler was possible (Goldberg and Kimmelman, 1988). P. N. T. Wells (1969b) invented a range-gated Doppler to isolate different targets.

In the early 1980s, Eyer *et al*. (1981) and Namekawa *et al*. (1982) described color flow imaging techniques for visualizing the flow of blood in real time. During the late 1980s, many other signal processing methods for imaging and calculations began to appear on imaging systems. Concurrently, sonar systems evolved to such a point that Dr. Robert Ballard was able to discover the Titanic at the bottom of the sea with sonar and video equipment in 1986 (Murphy, 1986).

Also during the 1980s, transducer technology underwent tremendous growth. Based on the Mason equivalent circuit model and waveguide, as well as the matching-layer design technology and high coupling piezoelectric materials developed during and after World War II, ultrasonic phased array design evolved rapidly. Specialized phased and linear arrays were developed for specific clinical applications: cardiogy; radiology (noncardiac internal organs); obstetrics/gynecology and transvaginal; endoscopic (transducer manipulated on the tip of an endoscope); transesophageal (transducer down the esophagus) and transrectal; surgical, intraoperative (transducer placed in body during surgery), laparoscopic, and neurosurgical; vascular, intravascular, and small parts. With improved materials and piezoelectric composites, arrays with several hundred elements and higher frequencies became available. Wider transducer bandwidths allowed the imaging and operation of other modes within the same transducer at several frequencies selectable by the user.

By the 1990s, developments in more powerful microprocessors, high-density gate arrays, and surface mount technology, as well as the availability of low-cost analog/digital (A/D) chips, made greater computation and faster processing in smaller volumes available at lower costs. Imaging systems incorporating these advances evolved into digital architectures and beamformers. Broadband communication enabled the live transfer of images for telemedicine. Transducers appeared with even wider bandwidths and in 1.5D (segmented arrays with limited elevation electronic focusing capabilities) and matrix array configurations.

By the late 1990s, near–real-time three-dimensional (3D) imaging became possible. Commercial systems mechanically scanned entire electronically scanned arrays in ways similar to those used for single-element mechanical scanners. Translating, angular fanning, or spinning an array about an axis created a spatially sampled volume. Special image-processing techniques developed for movies such as John Cameron's *Titanic* enabled nearly real-time three-dimensional imaging, including surface-rendered images of fetuses. Figure 1.12 shows a survey of fetal images that begins with a black-and-white image from the 1960s and ends with a surface-rendered fetal face from 2002.

True real-time three-dimensional imaging is much more challenging because it involves two-dimensional (2D) arrays with thousands of elements, as well as an

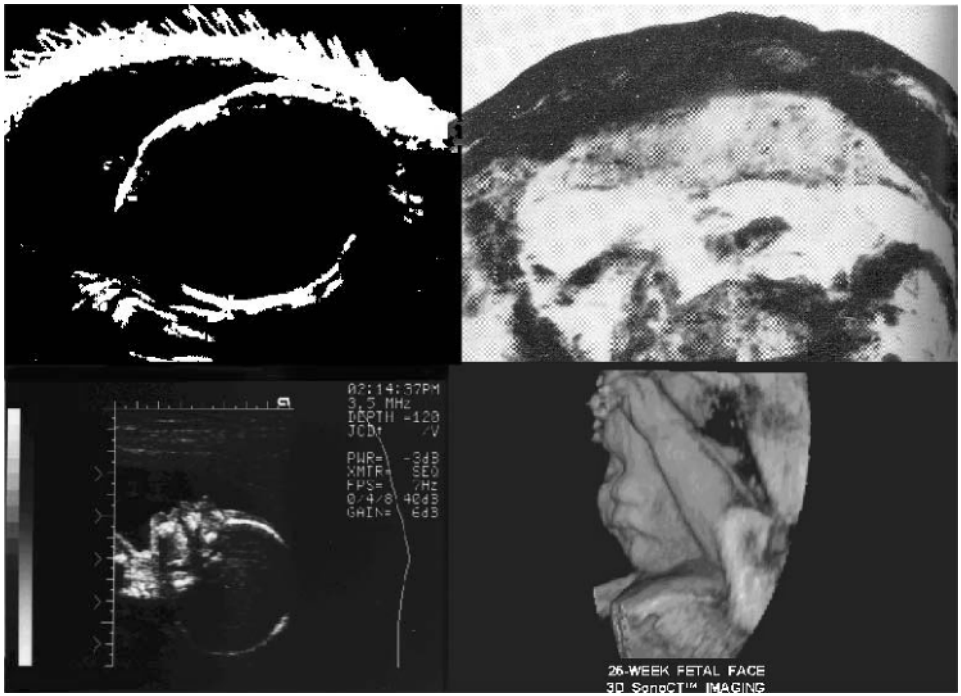

Figure 1.12 The evolution of diagnostic imaging as shown in fetal images. (Upper left) Fetal head black-and-white image (I. Donald, 1960). (Upper right) Early gray-scale negative image of fetus from the 1970s. (Lower left) High-resolution fetal profile from the 1980s. (Lower right) Surface-rendered fetal face and hand from 2002 (Goldberg and Kimmelman, 1988, reprinted with permission of AIVM. Courtesy of B. Goldberg, Siemens Medical Solutions, Inc., Ultrasound Group and Philips Medical Systems).

adequate number of channels to process and beamform the data. An early 2D array, 3D real-time imaging system with 289 elements and 4992 scanlines was developed at Duke University in 1987 (Smith *et al*., 1991; von Ramm, 1991). A non–real-time, 3600 two-dimensional element array was used for aberration studies at the University of Rochester (Lacefield and Waag, 2001). In 2003, Philips introduced a real-time three-dimensional imaging system that utilized fully sampled two-dimensional 2900-element array technology with beamforming electronics in the transducer handle.

To extend the capabilities of ultrasound imaging, contrast agents were designed to enhance the visibility of blood flow. In 1968, Gramiak and Shah discovered that microbubbles from indocyanine green dye injected in blood could act as an ultrasound contrast agent. By the late 1980s, several manufacturers were developing contrast agents to enhance the visualization of and ultrasound sensitivity to blood flow. To emphasize the detection of blood flow, investigators imaged contrast agents at harmonic frequencies generated by the microbubbles. As imaging system manufacturers became involved in imaging contrast agents at second harmonic frequencies, they discovered that tissues could also be seen. Signals sent into the body at a

fundamental frequency returned from tissue at harmonic frequencies. Tissues talked back. P. N. T. Wells (1969*a*) mentioned indications that tissues had nonlinear properties. Some work on imaging the nonlinear coefficient of tissues directly (called their "B/A" value) was done in the 1980s but did not result in manufactured devices. By the late 1990s, the clinical value of tissue harmonic imaging was recognized and commercialized. Tissue harmonic images have proved to be very useful in imaging otherwise difficult-to-image people, and in many cases, they provide superior contrast resolution and detail compared with images made at the fundamental frequency.

In the more than 60 years since the first ultrasound image of the head, comparatively less progress has been made in imaging through the skull. Valuable Doppler data have been obtained through transcranial windows. By the late 1980s, methods for visualizing blood flow to and within certain regions of the brain were commercialized in the form of transcranial color flow imaging. The difficult problems of producing undistorted images through other parts of the skull have been solved at research laboratories but not in real time (Aarnio *et al*., 2001; Aubry *et al*., 2001).

1.6 ENABLING TECHNOLOGIES FOR ULTRASOUND IMAGING

Attention is usually focused on ultrasound developments in isolation. However, continuing improvements in electronics, seemingly unrelated, are shaping the future of medical ultrasound. The accelerated miniaturization of electronics, especially ASICs, made possible truly portable imaging systems for arrays with full high-quality imaging capabilities. When phased array systems first appeared in 1980, they weighed about 800 lbs. The prediction of the increase in transistor density, according to Moore's original law, is a factor of 1,000,000 in area-size reduction from 1980 to 2000. Over the years, Moore's law has slowed down a bit, as shown by the more realistic Moore's law (shown in Figure 1.8 as a gray line). This shows an actual reduction of 1290. This actual Moore's law reflects the physical limits of complementary metal oxide semiconductor (CMOS) technology and the increased costs required for extreme miniaturization (Brenner, 2001). While a straightforward calculation in the change of size of an imaging system cannot be made, several imaging systems that were available in 2003 have more features than some of the first-phased array systems and yet weigh only a few pounds (shown in Figure 1.13). Another modern achievement is handheld two-dimensional array with built-in beamforming.

Portable systems, because of their affordability, can be used as screening devices in smaller clinics, as well as in many places in the world where the cost of an ultrasound imaging system is prohibitive. Figure 1.13 shows four examples of portable systems that appeared on the cover of a special issue of the *Thoraxcentre Journal* on portable cardiac imaging systems (2001). The first portable system, the Minivisor, was self-contained with a battery, but its performance was relatively primitive (this was consistent with the state of the art in 1978). The OptiGo owes its small size to custom-designed ASICs, as well as automated and simplified controls. The Titan, a newer version of the original Sonosite system and one of the first modern portables, has a keyboard and trackball, and it is also miniaturized by several ASICs. The Terason

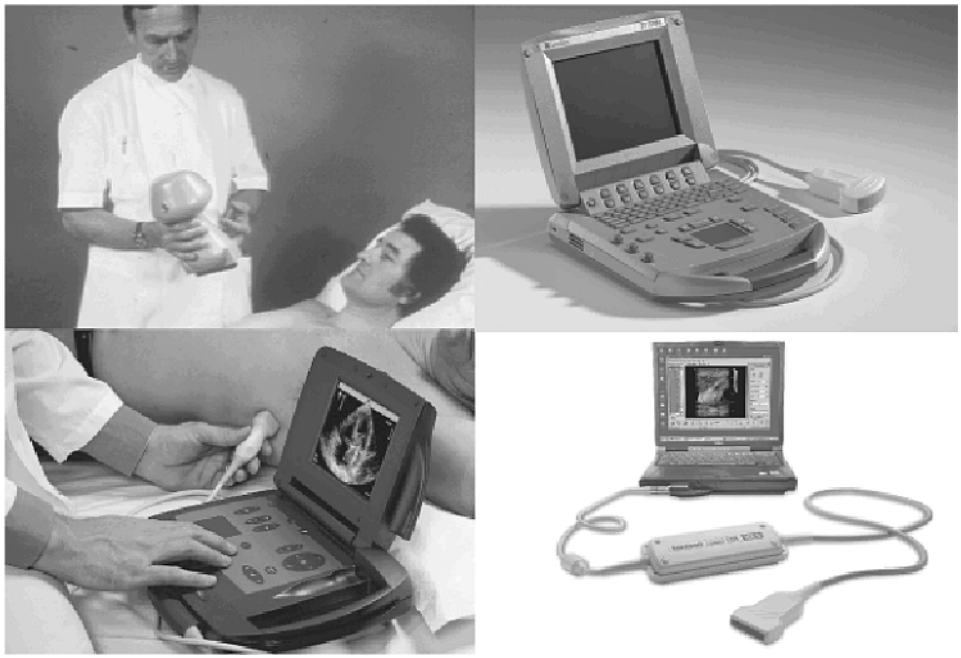

Figure 1.13 (Upper left) Minivisor, the self-contained truly portable ultrasound imaging system. (Upper right) A newer version of the Sonosite, the first modern handheld ultrasound portable. (Lower left) OptiGo, a cardiac portable with automated controls. (Lower right) Terason, 2000 laptop-based ultrasound system with a proprietary beamformer box (courtesy of N. Bom, Philips Medical Systems, Sonosite, Inc., and P.P. Charg, Terason, Teratech Corp.).

system has a charge-coupled device (CCD)-base proprietary 128-channel beamformer, and much of its functionality is software-based in a powerful laptop. More information on these portables can be found in the December 2001 issue of the *Thoraxcentre Journal*.

Change is in the direction of higher complexity at reduced costs. Modern full-sized imaging systems have a much higher density of components and far more computing power than their predecessors. The enabling technologies and key turning points in ultrasound are summarized in Table 1.1.

1.7 ULTRASOUND IMAGING SAFETY

Diagnostic ultrasound has had an impressive safety record since the 1950s. In fact, no substantiated cases of harm from imaging have been found (O'Brien, 1998). Several factors have contributed to this record. First, a vigilant worldwide community of investigators is looking continuously for possible ultrasound-induced bioeffects.

TABLE 1.1 Chronology of Ultrasound Imaging Developments and Enabling Technologies

Time	Ultrasound	Enablers
Pre-WWII	Echo ranging	Piezoelectricity Vacuum tube amplifiers
1940s	Dussik image of brain PPI images Therapy and surgery	Radar, sonar Supersonic reflectoscope Colossus and ENIAC computers Transistor
1950s	A-line Compound scanning Doppler ultrasound M-mode	Integrated circuits Phased-array antennas
1960s	Contact static B-scanner Real-time mechanical scanner Echoencephalography	Moore's law Microprocessors VLSI Handheld calculators
1970s	Real-time imaging Scan-conversion Gray-scale Linear and phased arrays	RAM EPROM ASIC Scientific calculators Altair, first PC
1980s	Commercial array systems Pulsed wave Doppler Color flow imaging Wideband and specialized transducers	Gate arrays Digital signal processing chips Surface mount components Computer-aided design of VLSI circuits
1990s	Digital systems 1.5D and matrix arrays Harmonic imaging Commercialized 3D imaging	Low-cost A/D converters Powerful PCs 3D image processing 0.1 μm fabrication of linewidths for electronics
2000s	Handheld 2D array for real-time 3D imaging	Continued miniaturization

Second, the two main bioeffects (cavitation and thermal heating) are well enough understood so that acoustic output can be controlled to limit these effects. The Output Display Standard provides imaging system users with direct on-screen estimates of relative indices related to these two bioeffects for each imaging mode selected. Third, a factor may be the limits imposed on acoustic output of U. S. systems by the Food and Drug Administration (FDA). All U. S. manufacturers measure acoustic output levels of their systems with wide-bandwidth–calibrated hydrophones, force balances, and report their data to the FDA.

1.8 ULTRASOUND AND OTHER DIAGNOSTIC IMAGING MODALITIES

1.8.1 Imaging Modalities Compared

Ultrasound, because of its efficacy and low cost, is often the preferred imaging modality. Millions of people have been spared painful exploratory surgery by noninvasive imaging. Their lives have been saved by ultrasound diagnosis and timely intervention, their hearts have been evaluated and repaired, their children have been found in need of medical help by ultrasound imaging, and their surgeries have been guided and checked by ultrasound. Many more people have breathed a sigh of relief after a brief ultrasound exam found no disease or confirmed the health of their future child. In 2000, an estimated 5 million ultrasound exams were given weekly worldwide (Cote, 2001).

How does ultrasound compare to other imaging modalities? Each major diagnostic imaging method is examined in the following sections, and the overall results are tallied in Table 1.2 and compared in Figure 1.14.

1.8.2 Ultrasound

Ultrasound imaging has a spatially variant resolution that depends on the size of the active aperture of the transducer, the center frequency and bandwidth of the transducer, and the selected transmit focal depth. A commonly used focal-depth-to-aperture ratio is five, so that the half power beam-width is approximately two wavelengths at the center frequency. Therefore, the transmit lateral spatial resolution in millimeters is $\lambda(mm) = 2c_{av}/f_c = 3/f_c(MHz)$, where f_c is center frequency in megahertz. For typical frequencies in use ranging from 1 to 15 MHz, lateral resolution corresponds to 3 mm to 0.3 mm. This resolution is best at the focal length distance and widens away from this distance in a nonuniform way because of diffraction effects

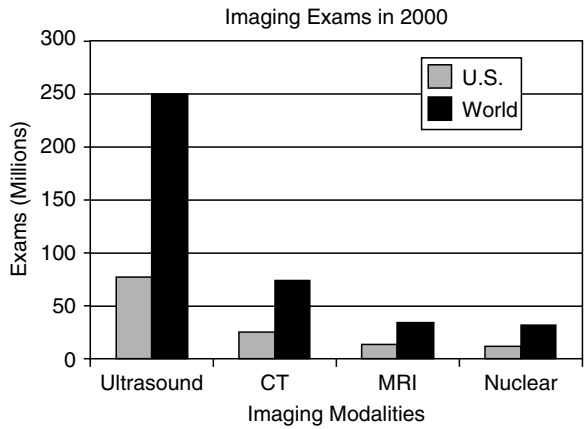

Figure 1.14 Estimated number of imaging exams given worldwide and in the United States for the year 2000.

TABLE 1.2 Comparison of Imaging Modalities

Modality	Ultrasound	X-ray	CT	MRI
What is imaged	Mechanical properties	Mean tissue absorption	Tissue absorption	Biochemistry (T_1 and T_2)
Access	Small windows adequate	2 sides needed	Circumferential Around body	Circumferential Around body
Spatial resolution	Frequency and axially dependent 0.3–3 mm	~1 mm	~1 mm	~1 mm
Penetration	Frequency dependent 3–25 cm	Excellent	Excellent	Excellent
Safety	Very good	Ionizing radiation	Ionizing radiation	Very good
Speed	100 frames/sec	Minutes	½ minute to minutes	10 frames/sec
Cost	$	$	$$$$	$$$$$$$$
Portability	Excellent	Good	Poor	Poor

caused by apertures on the order of a few to tens of wavelengths. The best axial resolution is approximately two periods of a short pulse or the reciprocal of the center frequency, which also works out to be two wavelengths in distance since $z = 2c_{av}T = 2c_{av}/f_c = 2\lambda$.

Another major factor in determining resolution is attenuation, which limits penetration. Attenuation steals energy from the ultrasound field as it propagates and, in the process, effectively lowers the center frequency of the remaining signals, another factor that reduces resolution further. Attenuation also increases with higher center frequencies and depth; therefore, penetration decreases correspondingly so that fine resolution is difficult to achieve at deeper depths. This limitation is offset by specialized probes such as transesophageal (down the throat) and intracardiac (inside the heart) transducers that provide access to regions inside the body. Otherwise, access to the body is made externally through many possible ''acoustic windows,'' where a transducer is coupled to the body with a water-based gel. Except for regions containing bones, air, or gas, which are opaque to imaging transducers, even small windows can be enough to visualize large interior regions.

Ultrasound images are highly detailed and geometrically correct to the first order. These maps of the mechanical structures of the body, (according to their ''acoustic properties,'' such as differences in characteristic impedance) depend on density and stiffness or elasticity. The dynamic motion of organs such as the heart can be revealed by ultrasound operating up to hundreds of frames per second.

Diagnostic ultrasound is noninvasive (unless you count the ''trans'' and ''intra'' families of transducers, which are somewhat annoying to the patient but otherwise very effective). Ultrasound is also safe and does not have any cumulative biological side effects. Two other strengths of ultrasound imaging are its relatively low cost and portability. With the widespread availability of miniature portable ultrasound systems for screening and imaging, these two factors will continue to improve.

A high skill level is needed to obtain good images with ultrasound. This expertise is necessary because of the number of access windows, the differences in anatomy, and

the many possible planes of view. Experience is required to find relevant planes and targets of diagnostic significance and to optimize instrumentation. Furthermore, a great deal of experience is required to recognize, interpret, and measure images for diagnosis.

1.8.3 X-rays

Conventional x-ray imaging is more straightforward than ultrasound. Because x-rays travel at the speed of light with a wavelength of less than 1 Å (0.0001 mm), they do so in straight ray paths without diffraction effects. As a result of the ray paths, highly accurate images are obtained in a geometric sense. As the x-rays pass through the body, they are absorbed by tissue so that a overall ''mean attenuation'' image results along the ray path. Three-dimensional structures of the body are superimposed as a two-dimensional projection onto film or a digital sensor array. The depth information of structures is lost as it is compressed into one image plane. Spatial resolution is not determined by wavelength but by focal spot size of the x-ray tube and scatter from tissue. The state of the art is about 1 mm as of this writing. X-rays cannot differentiate among soft tissues but can detect air (as in lungs) and bones (as in fractures). Radioactive contrast agents can be ingested or injected to improve visualization of vessels. Still x-ray images require patients not to move during exposure. Because these are through transmission images, parts of the body that can be imaged are limited to those that are accessible on two sides.

Most conventional x-ray systems in common use are dedicated systems (fixed in location) even though portable units are commercially available for special applications. Systems tend to be stationary so that safety precautions can be taken more easily. Though exposures are short, x-rays are a form of ionizing radiation, so dosage effects can be cumulative. Extra precautions are needed for sensitive organs such as eyes and for pregnancies.

The taking of x-ray images is relatively straightforward after some training. Interpretation of the images varies with the application, from broken bones to lungs, and in general requires a high level of skill and experience to interpret.

1.8.4 Computed Tomography Imaging

Computed tomography (CT), which is also known as computed axial tomography (CAT), scanning also involves x-rays. Actually, the attenuation of x-rays in different tissues varies, so tomographic ways of mathematically reconstructing the interior values of attenuation from those obtained outside the body, have been devised. In order to solve the reconstruction problem uniquely, enough data have to be taken to provide several views of each spatial position in the object.

This task is accomplished by an x-ray fan-beam source on a large ring radiating through the subject's body to an array of detectors working in parallel on the opposite side of the ring. The ring is rotated mechanically in increments until complete coverage is obtained. Rapid reconstruction algorithms create the final image of a

cross-section of a body. The latest multislice equipment utilizes a cone beam and a two-dimensional array of sensors. The result has over two orders of magnitude more dynamic range than a conventional x-ray, so subtle shades of the attenuation variations through different tissue structures are seen. The overall dose is much higher than that of a conventional x-ray, but the same safety precautions as those of conventional x-rays apply. CT equipment is large and stationary in order to fit a person inside, and as a result, it is relatively expensive to operate. Consecutive pictures of a moving heart are now achievable through synchronization to electrocardiogram (ECG) signals.

The resolution of CT images is typically 1 mm. CT scanning creates superb images of the brain, bone, lung, and soft tissue, so it is complementary to ultrasound.

While the taking of CT images requires training, it is not difficult. Interpretation of CT cross-sectional images demands considerable experience for definitive diagnosis.

1.8.5 Magnetic Resonance Imaging

Magnetic resonance has been applied successfully to medical imaging of the body because of its high water content. The hydrogen atoms in water (H_2O) and fat make up 63% of the body by weight. Because there is a proton in the nucleus of each hydrogen atom, a small magnetic field or moment is created as the nucleus spins. When hydrogen is placed in a large static magnetic field, the magnetic moment of the atom spins around it like a tiny gyroscope at the Larmor frequency, which is a unique property of the material. For imaging, a radiofrequency rotating field in a plane perpendicular to the static field is needed. The frequency of this field is identical to the Larmor frequency. Once the atom is excited, the applied field is shut off and the original magnetic moment decays to equilibrium and emits a signal. This voltage signal is detected by coils, and two relaxation constants are sensed. The longitudinal magnetization constant, T_1, is more sensitive to the thrermal properties of tissue. The transversal magnetization relaxation constant, T_2, is affected by the local field inhomogeneities. These constants are used to discriminate among different types of tissue and for image formation.

For imaging, the subject is placed in a strong static magnetic field created by a large enclosing electromagnet. The resolution is mainly determined by the gradient or shape of the magnetic field, and it is typically 1 mm. Images are calculated by reconstruction algorithms based on the sensed voltages proportional to the relaxation times. Tomographic images of cross-sectional slices of the body are computed. The imaging process is fast and safe because no ionizing radiation is used. Because the equipment needed to make the images is expensive, exams are costly.

Magnetic resonance imaging (MRI) equipment has several degrees of freedom, such as the timing, orientation, and frequency of auxiliary fields; therefore, a high level of skill is necessary to acquire diagnostically useful images. Diagnostic interpretation of images involves both a thorough knowledge of the settings of the system, as well a great deal of experience.

1.9 CONCLUSION

With the exception of standard x-ray exams, ultrasound is the leading imaging modality worldwide and in the United States. Over the years, ultrasound has adapted to new applications through new arrays suited to specific clinical purposes and to signal processing, measurement, and visualization packages. Key strengths of ultrasound are its abilities to reveal anatomy, the dynamic movement of organs, and details of blood flow in real time. Diagnostic ultrasound continues to evolve by improving in diagnostic capability, image quality, convenience, ease of use, image transfer and management, and portability.

From the tables chronicling ultrasound imaging developments and enabling technologies, it is evident that there is often a time lag between the appearance of a technology and its effect. The most dramatic changes have been through the continual miniaturization of electronics in accordance with a modified Moore's law. Smaller-sized components led to the first commercially available phased array imaging systems as well as to new, portable imaging systems, which weigh only a few pounds. Moore's first law is apparently approaching physical limits, and a second Moore's law predicts rapidly increasing production costs with reduced chip size (Bimbaum and Williams, 2000). Because of the time lag of technology implementation, the latest developments have not had their full impact on ultrasound imaging.

The potential in diagnostic ultrasound imaging seen by early pioneers in the field has been more than fulfilled. The combination of continual improvements in electronics and a better understanding of the interaction of ultrasound with tissues will lead to imaging systems of increased complexity. In the future, it is likely that the simple principles on which much of ultrasound imaging is based will be replaced by more sophisticated signal processing algorithms.

BIBLIOGRAPHY

Electronic Engineering Times. (Dec. 30, 1996).

Proceedings of the IEEE on Acoustical Imaging. (April, 1979). State-of-the-art review of acoustic imagining and holography.

Wells, P. N. T. (1979). Historical reviews of C. T. Lancee, and M. Nijhoff (eds.). The Hague, Netherlands. This book, as well as Wells' other books in the References, provide an overview of evolving ultrasound imaging technology.

Woo, J. D. http://www.ob-ultrasound.net. An excellent web site for the history of medical ultrasound imaging technology and a description of how it works.

Gouldberg, B. B., Wells, P. N. T., Claudon, M., and Kondratas, R. History of Medical Ultrasound, A CD-ROM compiled by WFUMB History/Archives Committee, WFUMB, 2003, 10th Congress, Montreal. A compilation of seminal papers, historical reviews, and retrospectives.

References

Aarnio, J., Clement, G. T., and Hynynen, K. (2001). Investigation of ultrasound phase shifts caused by the skull bone using low-frequency relection data. *IEEE Ultrasonics Symp. Proc*. 1503–1506.

Aubry, J. F., Tanter, M., Thomas, J. L., and Fink, M. (2001). Pulse echo imaging through a human skull: In vitro experiments. *IEEE Ultrasonics Symp. Proc*. 1499–1502.

Biquard, P., (1972). Paul Langevin. *Ultrasonics* **10**, 213–214.

Bom, N., Lancee, C. T., van Zwieten, G., Kloster, F. E., and Roelandt, J. (1973). Multiscan echocardiography. *Circulation* **XLVIII**, 1066–1074.

Brenner, A. E. (2001). More on Moore's law. *Physics Today* **54**, 84.

Brown, T. G. (1968). Design of medical ultrasonic equipment. *Ultrasonics* **6**, 107–111.

Cote, Daniel. (2001). Personal Communication.

Devey, G. B. and Wells, P. N. T. (1978). Ultrasound in medical diagnosis. *Sci. Am*. **238**, 98–106.

Edler, I. (1991). Early echocardiography. *Ultrasound in Med. & Biol*. **17**, 425–431.

Edgerton, H. G. (1986). *Sonar Images*. Prentice Hall, Englewood Cliffs, NJ.

Electronic Engineering Times. (Oct. 30, 1997).

Erikson, K. R., Fry, F. J., and Jones, J. P. (1974). Ultrasound in medicine: A review. *IEEE Trans. Sonics Ultrasonics* **SU-21**, 144–170.

Eyer M. K., Brandestini, M. A., Philips, D. J., and Baker, D. W. (1981). Color digital echo/Doppler presentation. *Ultrasound in Med. & Biol*. **7**, 21.

Firestone, F. A. (1945). The supersonic reflectoscope for interior inspection. *Metal Prog*. **48**, 505–512.

Goldberg, B. B. and Kimmelman, B. A. (1988). *Medical Diagnostic Ultrasound: A Retrospective on its 40th Anniversary*. Eastman Kodak Company, New York.

Hewlett Packard Journal **34**, 3–40. (1983).

Holmes, J. H. (1980). Diagnostic ultrasound during the early years of the AIUM. *J. Clin. Ultrasound* **8**, 299–308.

Kevles, B. H. (1997). *Naked to the Bone*. Rutgers University Press, New Brunswick, NJ.

Klein, H. G. (1981). Are B-scanners' days numbered in abdominal diagnosis? *Diagnostic Imaging* **3**, 10–11.

Kossoff, G. (1974). Display techniques in ultrasound pulse echo investigations: A review. *J. Clin. Ultrasound* **2**, 61–72.

Lacefield, J. C. and Waag, R. C. (2001). Time-shift estimation and focusing through distributed aberration using multirow arrays. *IEEE Trans. UFFC* **48**, 1606–1624.

Ligtvoet C., Rijsterborgh, H., Kappen, L., and Bom, N. (1978). Real time ultrasonic imaging with a hand-held scanner: Part I, Technical description. *Ultrasound in Med. & Biol*. **4**, 91–92.

Ludwig, G. D. (1950). The velocity of sound through tissues and the acoustic impedance of tissues. *J. Acoust. Soc. Am*. **22**, 862–866.

Murphy, J. (1986). Down into the deep. *Time* **128**, 48–54.

Namekawa, K., Kasai, C., Tsukamoto, M., and Koyano, A. (1982). Imaging of blood flow using autocorrelation. *Ultrasound in Med. & Biol*. **8**, 138.

O'Brien. (1998). Assessing the risks for modern diagnostic ultrasound imaging. *Japanese J. of Applied Physics* **37**, 2781–2788.

Richardson, L. F. (Filed May 10, 1912, issued March 27, 1913). *British Patent No. 12*.
Rines, R. H., Wycofff, C. W., Edgerton, H. E., and Klein, M. (1976). Search for the Loch Ness Monster. *Technology Rw* **78**, 25–40.
Roelandt, J., Wladimiroff, J. W., and Bars, A. M. (1978). Ultrasonic real time imaging with a hand-held scanner: Part II, Initial clinical experience. *Ultrasound in Med. & Biol*. **4**, 93–97.
Santo, B. and Wollard, K. (1978). The world of silicon: It's dog eat dog. *IEEE Spectrum* **25**, 30–39.
Smith, S. W. *et al*. (1991). High speed ultrasound volumetric imaging system 1: Transducer design and beam steering. *IEEE Trans. UFFC* **37**, 100–108.
Somer, J. C. (1968). Electronic sector scanning for ultrasonic diagnosis. *Ultrasonics*. 153–159.
The Thoraxcentre Journal **13**, No. 4, cover. (2001).
Tyndall, J. (1875). *Sound* **3**, 41. Longmans, Green and Co., London.
von Ramm, O. T. *et al*. (1991). High speed ultrasound volumetric imaging system II: Parallel processing and image display. *IEEE Trans. UFFC* **38**, 109–115.
von Ramm, O. T. and Thurstone, F. L. (1975). Thaumascan: Design considerations and performance characteristics. *Ultrasound in Med* **1**, 373–378.
Wells, P. N. T. (1969a). *Physical Principles of Ultrasonic Diagnosis*. Academic Press, London.
Wells, P. N. T. (1969b). A range-gated ultrasonic Doppler system. *Med. Biol. Eng*. **7**, 641–652.
Wells, P. N. T. (1977). *Biomedical Ultrasonics*. Academic Press, London.

2 OVERVIEW

Chapter Contents

2.1 INTRODUCTION

Ultrasound imaging is a complicated interplay between physical principles and signal processing methods, so it provides many opportunities to apply acoustic and signal processing principles to relevant and interesting problems. In order to better explain the workings of the overall imaging process, this book uses a block diagram approach to organize various parts, their functions, and their physical processes. Building blocks reduce a complex structure to understandable pieces. This chapter introduces the overall organization that links upcoming chapters, each of which describe the principles of blocks in more detail. The next sections identify the principles used to relate the building blocks to each other and apply MATLAB programs to illustrate concepts.

2.2 FOURIER TRANSFORM

2.2.1 Introduction to the Fourier Transform

Signals such as the Gaussian pulse in Figure 2.1a can be represented as either a time waveform or as a complex spectrum that has both magnitude and phase. These forms are alternate but completely equivalent ways of describing the same pulse. Some problems are more easily solved in the frequency domain, while others are better done in the time domain. Consequently, it will be necessary to use a method to switch from one domain to another. Joseph Fourier (Bracewell, 2000), a nineteenth century French mathematician, had an important insight that a waveform repeating in time could be synthesized from a sum of simple *sines* and *cosines* of different frequencies and phases. These frequencies are harmonically related by integers: a fundamental frequency (f_0) and its harmonics, which are integral multiples ($2f_0$, $3f_0$, etc.). This sum forms the famous Fourier series.

While the Fourier series is interesting from a historical point of view and its applicabilty to certain types of problems, there is a much more convenient way of doing Fourier analysis. A continuous spectrum can be obtained from a time waveform through a single mathematical operation called the "Fourier transform." The minus i Fourier transform, also known as the Fourier integral, is defined as

$$H(f) = \Im_{-i}[h(t)] = \int_{-\infty}^{\infty} h(t)e^{-i2\pi ft}dt \tag{2.1}$$

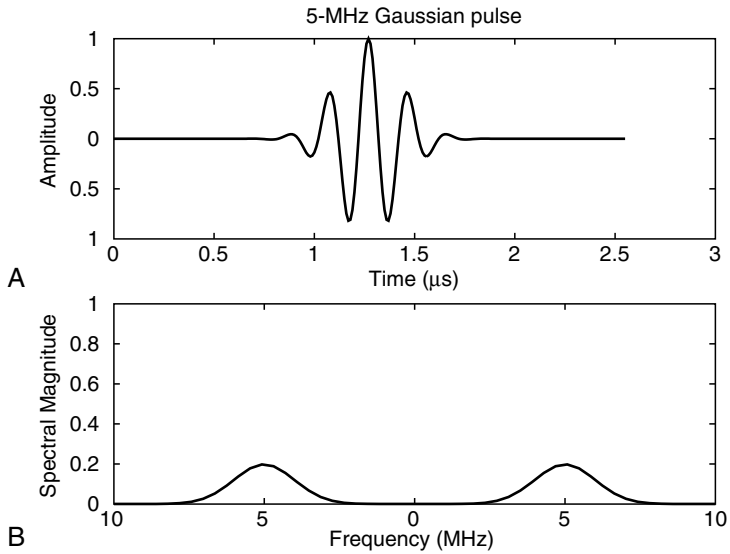

Figure 2.1 (A) Short 5-MHz time pulse and its (B) spectrum magnitude and phase.

in which $H(f)$ (with an upper-case letter convention for the transform) is the minus i Fourier transform of $h(t)$ (lower-case letter for the function), "i" is $\sqrt{-1}$, and $\mathfrak{I}_{-i}$ symbolizes the minus i Fourier transform operator. Note that, in general, both $h(t)$ and $H(f)$ may be complex with both real and imaginary parts. Another operation, the minus i inverse Fourier transform, can be used to recover $h(t)$ from $H(f)$ as follows:

$$h(t) = \mathfrak{I}_{-i}^{-1}[H(f)] = \int_{-\infty}^{\infty} H(f)e^{i2\pi ft}df \tag{2.2}$$

In this equation, $\mathfrak{I}_{-i}^{-1}$ is the symbol for the inverse minus i Fourier transform. A sufficient but not necessary condition for a Fourier transform is the existence of the absolute value of the function over the same infinite limits; another condition is a finite number of discontinuities in the function to be transformed. If a function is physically realizable, it most likely will have a transform. Certain generalized functions that exist in a limiting sense and that may represent measurement extremes (such as an impulse in time or a pure tone) are convenient and useful abstractions. The Fourier transform also provides an elegant and powerful way of calculating a sequence of operations represented by a series of building blocks, as shown shortly.

For applications involving a sequence of numbers or data, a more appropriate form of the Fourier transform, the discrete Fourier transform (DFT), has been devised. The DFT consists of a discrete sum of N-weighted complex exponents, $exp(-i2\pi mn/N)$, in which m and n are integers. J. W. Cooley and J. W. Tukey (1965) introduced an efficient way of calculating the DFT called the fast Fourier transform (FFT). The DFT and its inverse are now routine mathematical algorithms and have been implemented directly into signal processing chips.

2.2.2 Fourier Transform Relationships

The most important relationships for the Fourier transform, the DFT, and their application are reviewed in Appendix A. This section emphasizes only key features of the Fourier transform, but additional references are provided for more background and details.

A key Fourier transform relationship is that time lengths and frequency lengths are related reciprocally. A short time pulse has a wide extent in frequency, or a broad bandwidth. Similarly, a long pulse, such as a tone burst of n cycles, has a narrow band spectrum. These pulses are illustrated in Figures 2.2 and 2.3. If, for example, a tone burst of 10 cycles in Figure 2.2 is halved to 5 cycles in Figure 2.3, its spectrum is doubled in width. All of these effects can be explained mathematically by the Fourier transform scaling theorem:

$$\mathfrak{I}_{-i}[g(at)] = \frac{1}{|a|}G(f/a) \tag{2.3}$$

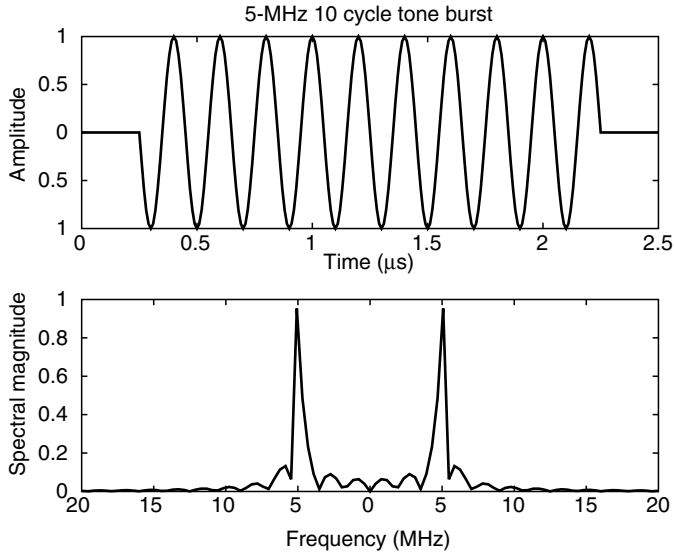

Figure 2.2 A 5-MHz center frequency tone burst of 10 cycles and its spectral magnitude.

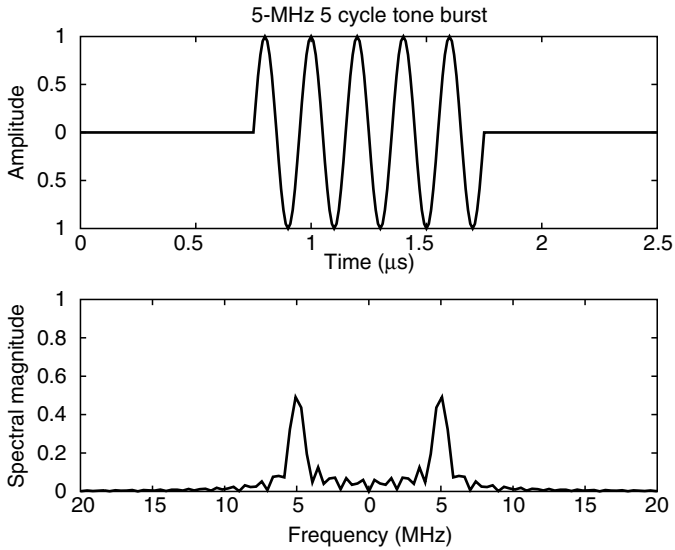

Figure 2.3 A 5-MHz center frequency tone burst of 5 cycles and its spectral magnitude.

For this example, if $a = 0.5$, then the spectrum is doubled in amplitude and its width is stretched by a factor of two in its frequency extent. Many other Fourier transform theorems are listed in Table A.1 of Appendix A.

Consider the Fourier transform pair from this table for a Gaussian function,

$$\Im_{-i}[exp(-\pi t^2)] = exp(-\pi f^2) \tag{2.4}$$

To find the minus i Fourier transform of a following given time domain Gaussian analytically, for example,

$$g(t) = exp(-wt^2) \tag{2.5a}$$

first put it into a form appropriate for the scaling theorem, Eq. (2.3),

$$g(t) = exp\left[-\pi\left(t\sqrt{w/\pi}\right)^2\right] \tag{2.5b}$$

so that $a = \sqrt{w/\pi}$. Then by the scaling theorem, the transform is

$$G(f) = exp\left[-\pi(f/\sqrt{w/\pi})^2\right]/\sqrt{w/\pi} = \sqrt{\pi/w}\ exp[-(\pi^2/w)f^2] \tag{2.6}$$

The Gaussian is well-behaved and has smooth time and frequency transitions. Fast-time transitions have a wide spectral extent. An extreme example of this characteristic is the impulse in Figure 2.4. This pulse is so short in time that, in practical terms, it appears as a spike or as a signal amplitude occurring only at the smallest measurable time increment. The ideal impulse would have a flat spectrum (or an extremely wide one in realistic terms). The converse of the impulse in time is a tone burst so long that it would mimic a *sine* wave in Figure 2.5. The spectrum of this nearly pure tone would appear on a spectrum analyzer (an instrument for measuring the spectra of signals) as either an amplitude at a single frequency in the smallest resolvable frequency resolution cell or as a spectral impulse. Note that instead of a pair of spectral lines

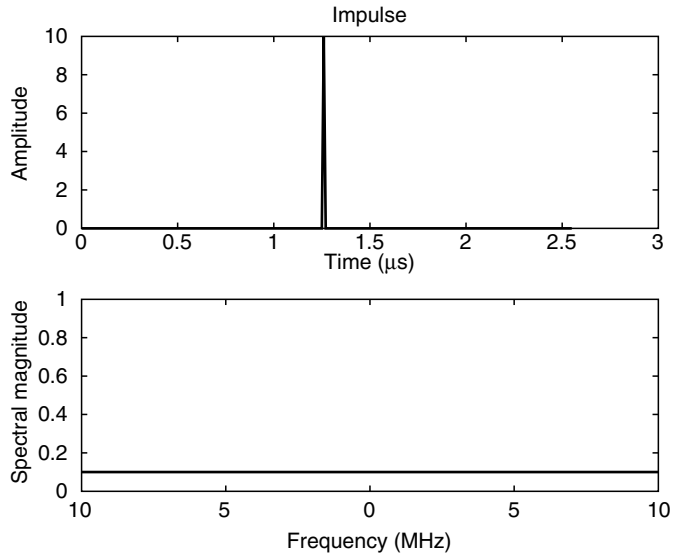

Figure 2.4 A time impulse and its spectral magnitude.

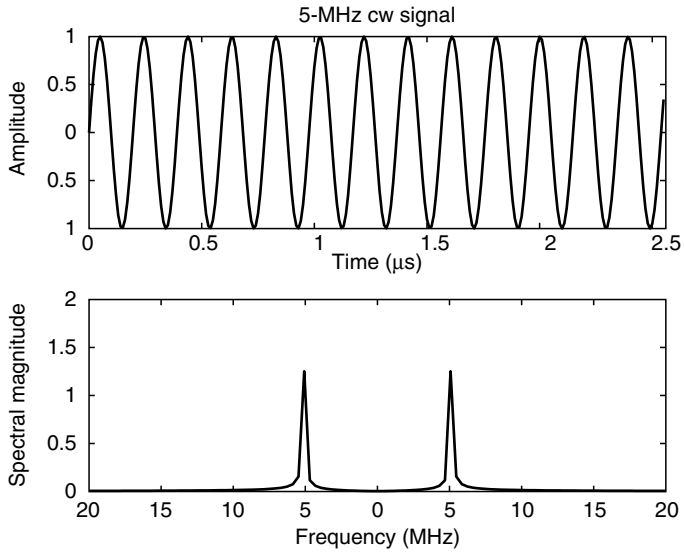

Figure 2.5 A 5-MHz pure tone and its spectral magnitude.

representing impulse functions in Figure 2.5, finite width spectra are shown as a consequence of the finite length time waveform used for this calculation by a digital Fourier transform. All of these effects can be demonstrated beautifully by the Fourier transform. The Fourier transform operation for Figures 2.1–2.5 were implemented by MATLAB program chap2figs.m.

2.3 BUILDING BLOCKS

2.3.1 Time and Frequency Building Blocks

One of the motivations for using the Fourier transform is that it can describe how a signal changes its form as it propagates or when it is sent through a device or filter. Both of these changes can be represented by a building block. Assume there is a filter that has a time response, $q(t)$, and a frequency response, $Q(f)$. Each of these responses can be represented by a building block, as given by Figure 2.6. A signal, $p(t)$, sent into the filter, $q(t)$, with the result, $r(t)$, can be symbolized by the building blocks of Figure 2.6.

As a general example of a building block, a short Gaussian pulse is sent into a filter with a longer Gaussian impulse response (from Figure 2.1). This filtering operation is illustrated in both domains by Figure 2.7. In this case, the output pulse is longer than the original, and its spectrum is similar in shape to the original but slightly narrower. For the same filter in Figure 2.8, the time impulse input of Figure 2.4 results in a replication of the time response of the filter as an output response (also known as "impulse response"). Because the impulse has a flat frequency response, Figure 2.8 also replicates the frequency response of the filter as an output response. In Figure 2.9, a single-

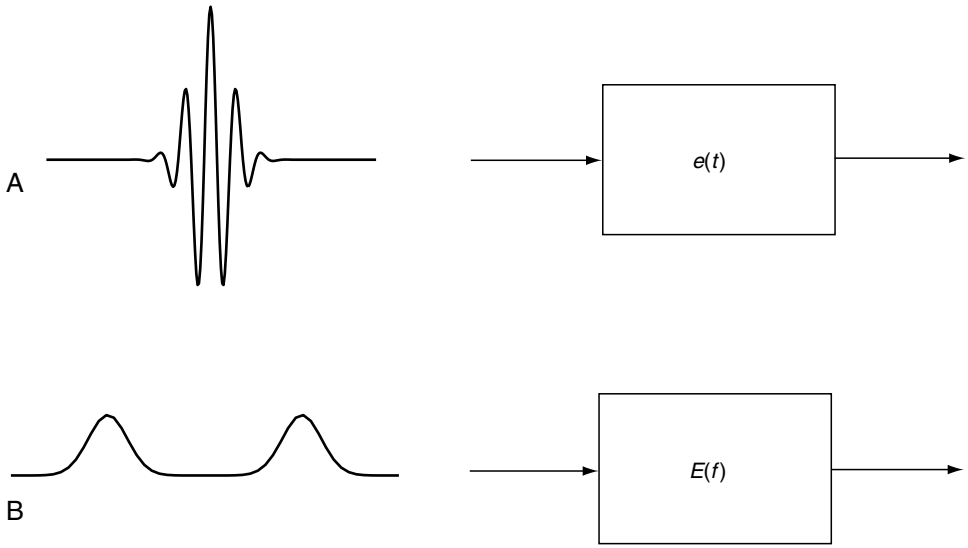

Figure 2.6 (A) A time domain building block and (B) its frequency domain equivalent.

frequency input signal of unity amplitude from Figure 2.5 results in a single-frequency output weighted with amplitude and phase of the filter at the same frequency.

The operations illustrated in Figures 2.7–2.9 can be generalized by two simple equations. In the frequency domain, the operation is just a multiplication,

$$R(f) = P(f)\ Q(f). \tag{2.7a}$$

The three frequency domain examples in these figures show how the products of $P(f)$ and $Q(f)$ result in $R(f)$.

In the time domain, a different mathematical operation called "convolution" is at work. Time domain convolution, briefly stated, is the mathematical operation that consists of flipping one waveform around left to right in time, sliding it past the other waveform, and summing the amplitudes at each time point. The details of how this is done are covered in Appendix A. Again, this is a commonplace computation that is represented by the symbol $*_t$ meaning time domain convolution. Therefore, the corresponding general relation for the time domain operations of these figures is written mathematically as

$$r(t) = p(t) *_t q(t) \tag{2.7b}$$

It does not take much imagination to know what would happen if a signal went through a series of filters, $W(f)$, $S(f)$, and $Q(f)$. The end result is

$$R(f) = P(f)\ Q(f)\ S(f)\ W(f) \tag{2.8a}$$

and the corresponding time domain version is

$$r(t) = p(t) *_t q(t) *_t s(t) *_t w(t) \tag{2.8b}$$

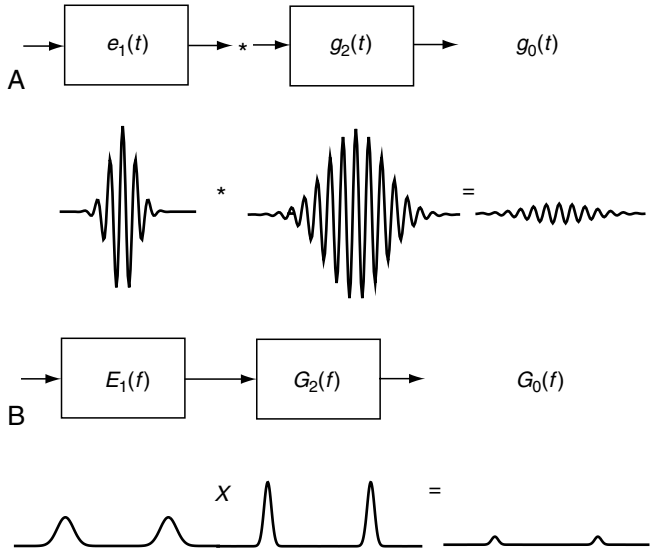

Figure 2.7 (A) Time waveforms for input, filter, and output result represent filter with a time domain convolution operation. (B) Corresponding frequency domain representation includes a multiplication. Both the filter and input have the same 5-MHz center frequency but different bandwidths.

We are close to being able to construct a series of blocks for an imaging system, but first we have to discuss spatial dimensions.

2.3.2 Space Wave Number Building Block

A Fourier transform approach can also be applied to the problems of describing acoustic fields in three dimensions. Until now, the discussion has been limited to what might be called "one-dimensional" operations. In the one-dimensional sense, a signal was just a variation of amplitude in time. For three dimensions, a source such as a transducer occupies a volume of space and can radiate in many directions simultaneously. Again, a disturbance in time is involved, but now the wave has a three-dimensional spatial extent that propagates through a medium but does not change the structure permanently as it travels.

2.3.2.1 Spatial transforms

In the one-dimensional world there are signals (pulses or sine waves). In the three-dimensional world, waves must have a direction also. For sine waves (the primitive elements used to synthesize complicated time waveforms), the period T is the fundamental unit, and it is associated with a specific frequency by the relation $T = 1/f$. The period is a measure in time of the length of a sine wave from any point to another point where the sine wave repeats itself. For a wave in three dimensions, the primitive

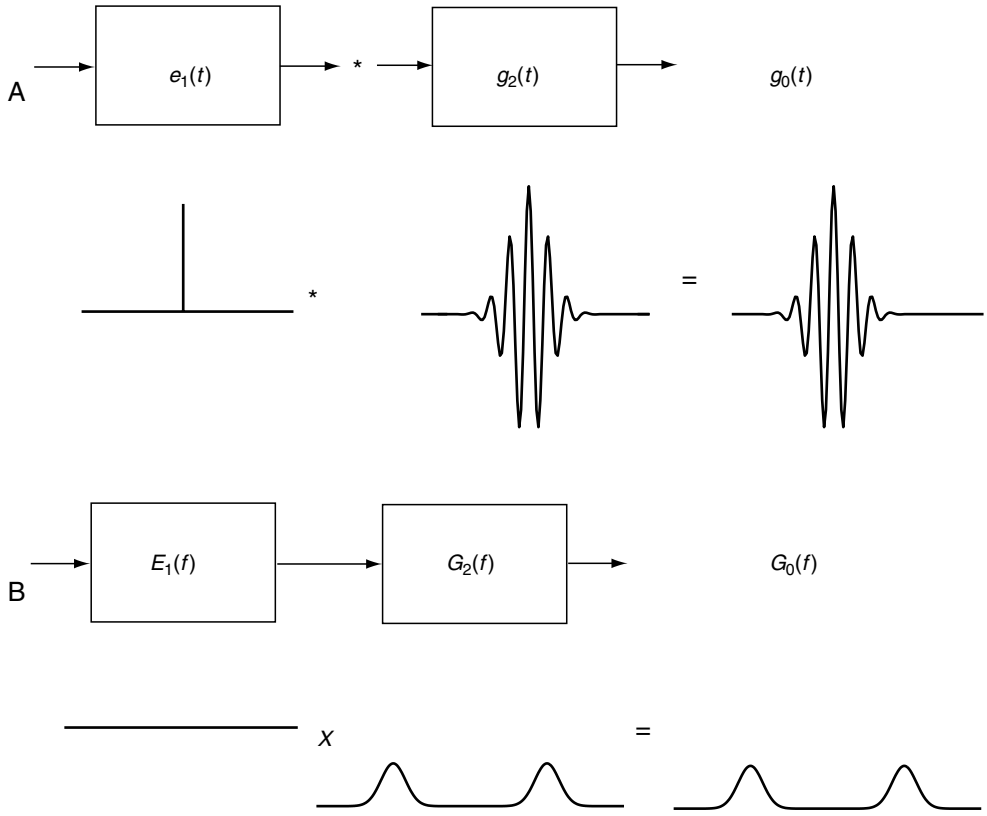

Figure 2.8 (A) Time domain filter output, or impulse response, for a time domain impulse input. (B) Spectrum magnitude of filter output.

element is a plane wave with a wavelength λ, which is also a measure of the distance in which a sinusoidal plane wave repeats itself. A special wavevector (**k**) is used for this purpose; it has a direction and a magnitude equal to the wavenumber, $k = 2\pi f/c = 2\pi/\lambda$, in which ($c$) is the sound speed of the medium. Just as there is frequency (f) and angular frequency ($\omega = 2\pi f$), an analogous relationship exists between spatial frequency ($\tilde{f}$) and the wavenumber (k) so that $k = 2\pi\tilde{f}$. Spatial frequency can also be thought of as a normalized wavenumber or the reciprocal of wavelength, $\tilde{f} = k/2\pi = 1/\lambda$.

Before starting three dimensions, consider a simple single-frequency plane wave that is traveling along the positive z axis and that can be represented by the exponential, $exp[i(\omega t - kz)] = exp[i2\pi(ft - \tilde{f}z)]$. Note that the phase of the wave has two parts: the first is associated with frequency and time, and the second, opposite in sign, is associated with inverse wavelength and space. In order to account for the difference in sign of the second term, a different Fourier transform operation is needed for (k) or spatial frequency and space. For this purpose, the plus i Fourier transform is appropriate:

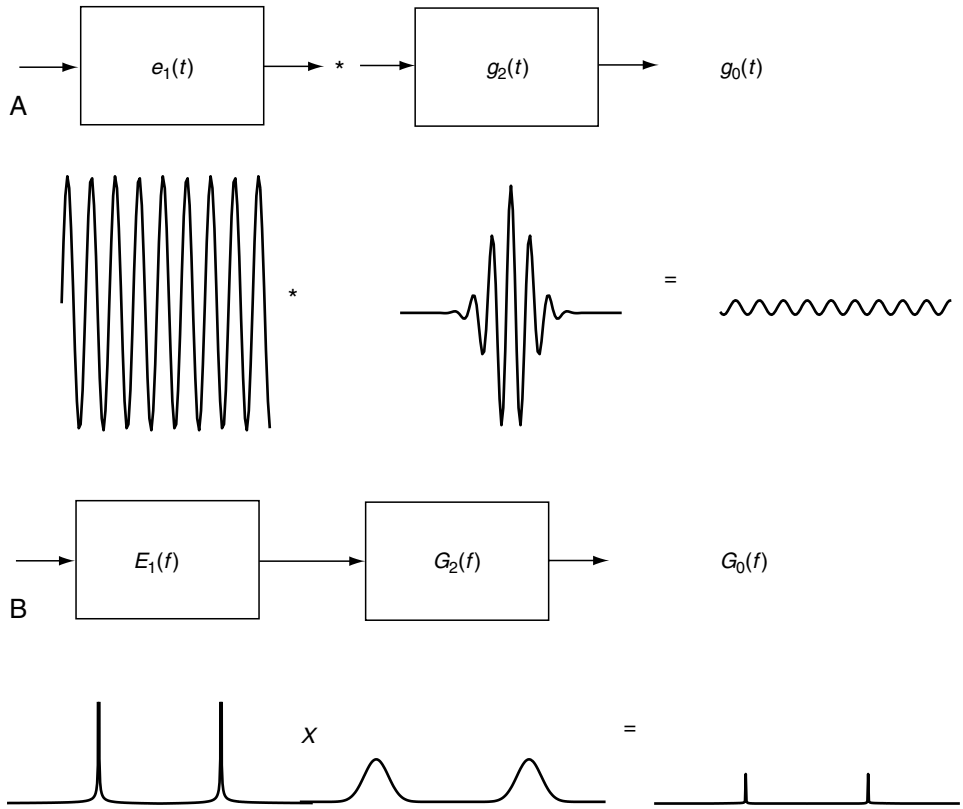

Figure 2.9 (A) Time domain filter output, to a 4.5-MHz tone input. (B) Spectrum magnitude of filter output is also at the input frequency but changed in amplitude and phase. The filter is centered at 5 MHz.

$$G(\tilde{f}) = \Im_{+i}[g(x)] = \int_{-\infty}^{\infty} g(x)e^{i2\pi\tilde{f}x}dx \tag{2.9a}$$

Of course, there is an inverse plus i Fourier transform to recover $g(x)$:

$$g(x) = \Im_i^{-1}\left[G(\tilde{f})\right] = \int_{-\infty}^{\infty} G(\tilde{f})e^{i2\pi\tilde{f}x}d\tilde{f} \tag{2.9b}$$

One way to remember the two types of transforms is to associate the conventional $-i$ Fourier transform with frequency and time. You can also remember to distinguish the plus i transform for wavenumber (spatial frequency) and space as "Kontrary" to the normal convention because it has an opposite phase or sign in the exponential argument. More information on these transforms is given in Appendix A. To simplify these transform distinctions in general, a Fourier transform will be assumed to be a

minus i Fourier transform unless specifically named, in which case it will be called a plus i Fourier transform.

In three dimensions, a point in an acoustic field can be described in rectangular coordinates in terms of a position vector r (Figure 2.10a). In the corresponding three-dimensional world of k-space, projections of the k wavevector corresponding to the x, y, and z axes are k_1, k_2, and k_3 (depicted in Figure 2.10b). Each projection of $\mathbf{k}$ has a corresponding spatial frequency ($\tilde{f}_1 = k_1/2\pi$, etc). See Table 2.1 for a comparison of the variables for both types of Fourier transforms. To extend calculations to dimensions higher than one, Fourier transforms can be nested within each other as explained in Chapter 6.

2.3.2.2 Spatial transform of a line source

As an example of how plane waves can be used to synthesize the field of a simple source, consider the two-dimensional case for the xz plane with propagation along z. The xz plane in Figure 2.11a has a one-dimensional line source that lies along the x

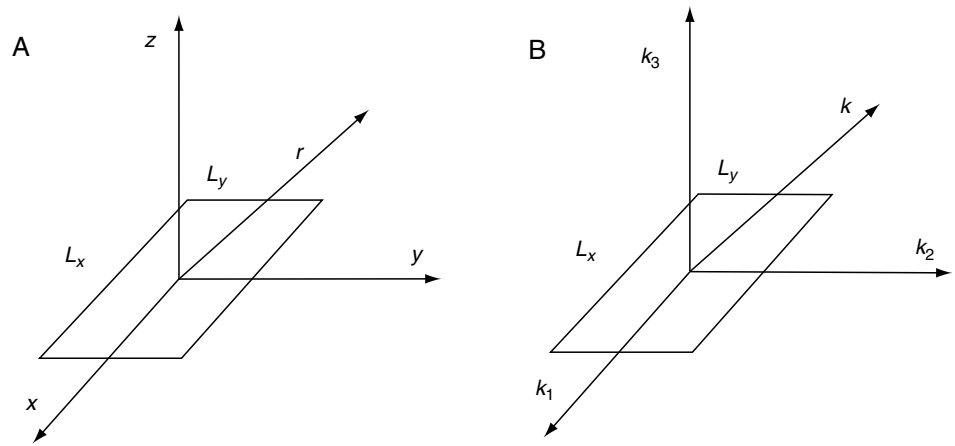

Figure 2.10 (A) Normal space with rectangular coordinates and a position vector r to a field point and (B) corresponding k-space coordinates and vector $\mathbf{k}$.

TABLE 2.1 Fourier Transform Acoustic Variable Pairs

Variable	Transform Variable	Type
Time	Frequency	
t	f	i
Space	Spatial Frequency	
x	$\tilde{f}_1$	$+i$
y	$\tilde{f}_2$	$+i$
z	$\tilde{f}_3$	$+i$

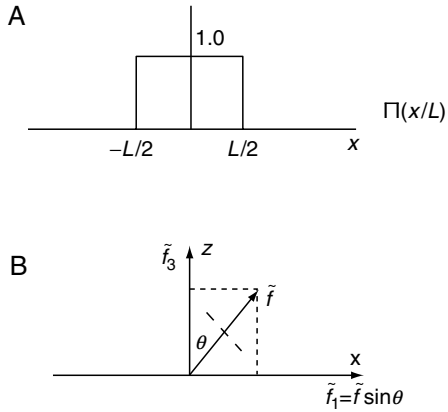

Figure 2.11 (A) Line source of length (*L*) and amplitude one lying along the *x* axis in the *xz* plane. (B) The plane wave wavevector at an angle θ to the k_3 axis and its projections. A plane wavefront is shown as a dashed line.

axis and has a length (L) and an amplitude of one. This shape can be described by the rect function (Bracewell, 2000) shown in Figure 2.11a and is defined as follows:

$$\prod(x/L) = \left\{ \begin{array}{ll} 0 & |x| > L/2 \\ 1/2 & |x| = L/2 \\ 1 & |x| < L/2 \end{array} \right\} \tag{2.10}$$

As the source radiates, plane waves are sprayed in different directions. For each plane wave, there is a corresponding wavevector that has a known magnitude, $k = \omega/c$, and lies at an angle θ to the k_3 axis, which corresponds to the z-axis direction. In Figure 2.11b, each k vector has a projection $k_1 = k\sin\theta$ along x and a value $k_3 = \sqrt{k^2 - k_1^2}$ along the z axis. This vector symbolizes the direction and magnitude of a plane wave with a flat wavefront perpendicular to it, as illustrated by the dashed line in Figure 2.11b.

In a manner analogous to a time domain waveform having a spectrum composed of many frequencies, the complicated acoustic field of a transducer can be synthesized from a set of weighted plane waves from all angles (θ), called the "angular spectrum of plane waves" (Goodman, 1968). Correspondingly, there is a Fourier transform relation between the source amplitude and spatial angular spectrum or spatial frequency (proportional to wavenumber) distribution as a function of $\tilde{f}_1 = \tilde{f}\sin\theta$ in the *xz* plane. For a rectangular coordinate system, it is easier mathematically to deal with projection $\tilde{f}_1$ rather than θ directly. To find the continuous distribution of plane waves with angle, the $+i$ Fourier transform of the rectangular source function depicted in Figure 2.11a is taken at the distance $z = 0$,

$$G(\hat{f}_1) = \Im_{+i}[g(x)] = \int_{-\infty}^{\infty} \prod (x/L) e^{i2\pi \tilde{f}_1 x} dz = L sin\, c(L\tilde{f}_1) = L sin\, c(L\hat{f}\, sin\theta) \tag{2.11}$$

in which the *sin c* function (Bracewell, 2000), also listed in Appendix A, is defined as

$$sin\, c(a\hat{f}) = \frac{sin(\pi a\hat{f})}{(\pi a\hat{f})} \tag{2.12a}$$

with the properties,

$$\begin{aligned} &sin\, c\ 0 = 1 \\ &sin\, c\ n = 0\ (n = \text{nonzero integer}) \\ &\int_{-\infty}^{\infty} sin\, c\ x\ dx = 1 \end{aligned} \tag{2.12b}$$

The simplest case would be one in which a single plane wave came straight out of the transducer with the $\tilde{f}$ vector oriented along the z axis ($\theta = 0$). Figure 2.12b reveals this is not the case. While the amplitude is a maximum for the plane wave in that

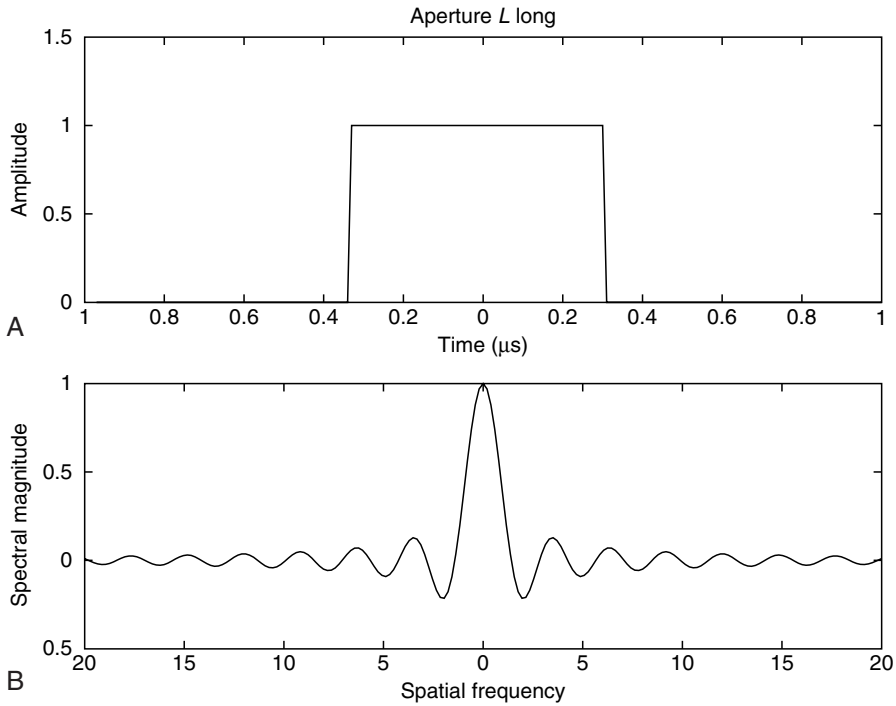

Figure 2.12 (A) A source function of length (L) and amplitude one along the x axis. (B) The corresponding spatial frequency distribution from the Fourier transform of the source as a function of $\tilde{f}_1$.

direction, and most of the highest amplitudes are concentrated around a small angle near the $\tilde{f}_3$ axis, the rest are plane waves diminishing in amplitude at larger angles. Based on our previous experience with transform pairs with steep transitions, such as the vertical edges of the source function of Figure 2.3a, we would expect a broad angular spectrum weighted in amplitude from all directions or angles. The sinc function, which applies to cases with the steep transitions, as well as to the present one, has infinite spectral extent. If the source is halved to $L/2$, for example, the main lobe of the sinc function is broadened by a factor of two, as is predicted by the Fourier transform scaling theorem and as was shown for the one-dimensional cases earlier. More information about the calculation of an acoustic field amplitude in two and three dimensions can be found in Chapter 6.

2.3.2.3 Spatial frequency building blocks

Building blocks can be constructed from spatial frequency transforms (Figure 2.13). Because these represent three-dimensional quantities, it is helpful to visualize a block as representing a specific spatial location. For example, planes for specific values of z, such as a source plane ($z = 0$) and an image plane ($z \neq 0$), are in common use. Functions of spatial frequency can be multiplied in a manner similar to functions of frequency, as is done in the field of Fourier optics (Goodman, 1968). Functions in the space (xyz) domain are convolved, and the symbols for convolution have identifying subscripts: $*_x$ for the xz plane and $*_y$ for the yz plane. A simplifying assumption for most of these calculations is that the medium of propagation is not moving, or is "time invariant."

Recall that the scalar wavenumber k is also a function of frequency (here $k = 2\pi f/c$). In general, building blocks associated with acoustic fields are functions of both frequency (f) and wavenumber (k), so they can be connected and multiplied. Conceptually, a time domain pulse has a spectrum with many frequencies. Each of

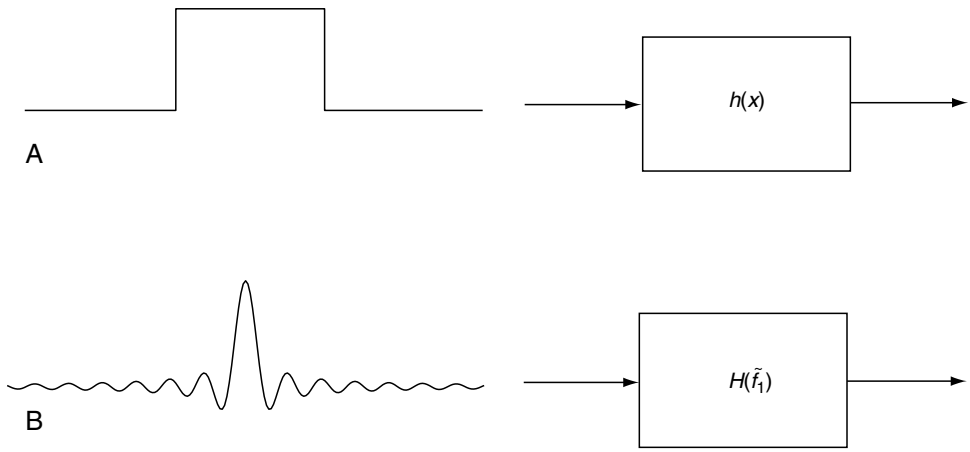

Figure 2.13 (A) An angular spatial frequency domain building block and (B) its spatial domain equivalent.

these frequencies could interact with an angular frequency block to describe an acoustic field. All frequencies are to be calculated in parallel and involve many parallel blocks (mathematically represented by a sum operation); this process can be messy. Fortunately, a simpler numerical method is to use convolution. Just as there is a time pulse, a time domain equivalent of calculating acoustic fields has been invented, called the spatial impulse response (to be explained in Chapter 7).

2.4 CENTRAL DIAGRAM

Building blocks are assembled into a diagram in Figure 2.14. This diagram is not that of an imaging system but of a picture of the major processes that occur when an ultrasound image is made. Shaded blocks such as the first one, $E(f)$, or the transmit waveform generator, are related to electrical signals. The other (unshaded) blocks represent acoustic or electro-acoustic events.

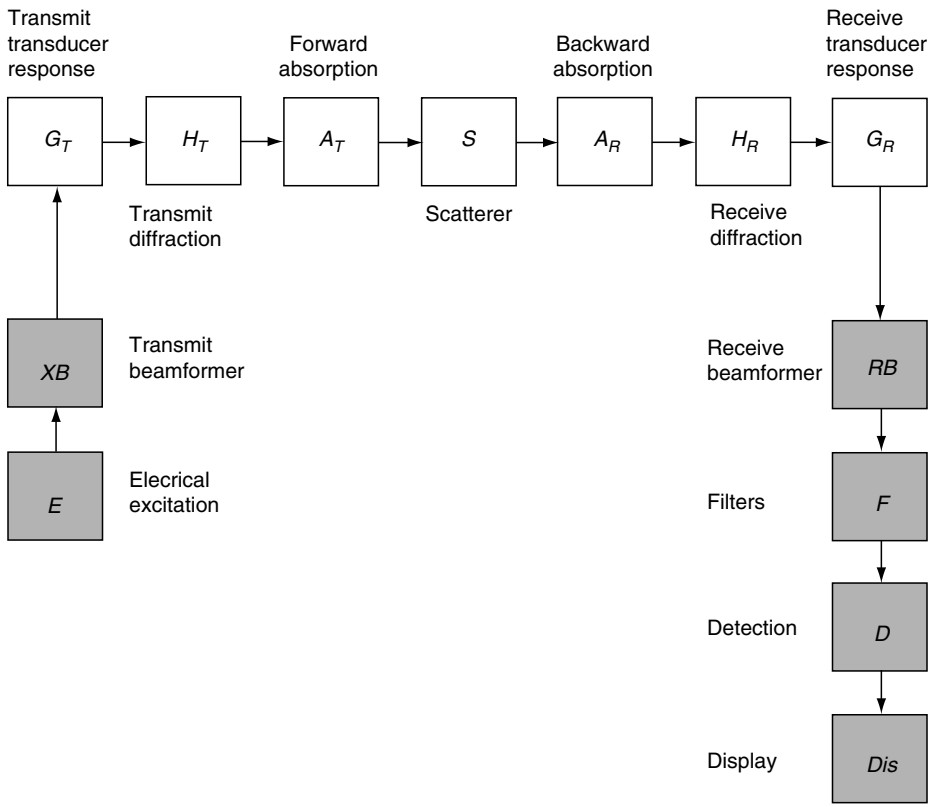

Figure 2.14 The central diagram, including the major signal and acoustic processes as a series of frequency domain blocks.

This central diagram provides a structure that organizes the different aspects of the imaging process. Future chapters explain each of the frequency domain blocks in more detail. Note that a similar and equivalent time-domain block diagram can be constructed with convolution operations rather than the multipliers used here. The list below identifies each block with appropriate chapters, starting with $E(f)$ at the left and proceeding left to right. Finally, there are topics that deal with several blocks together.

$E(f)$ is the transmit waveform generator explained in Chapter 10: *Imaging Systems and Applications*. Signals from $E(f)$ are sent to $XB(f)$, the transmit beamformer found in Chapter 7: *Array Beamforming*.

From the beamformer, appropriately timed pulses arrive at the elements of the transducer array. More about how these elements work and are designed can be found in Chapter 5: *Transducers*. These elements transform electrical signals from the beamformer, $XB(f)$, to pressure or stress waves through their responses, $G_T(f)$.

Acoustic (stress or pressure) waves obey basic rules of behavior that are described in review form in Chapter 3: *Acoustic Wave Propagation*. Waves radiate from the faces of the transducer elements and form complicated fields, or they diffract as described by transmit diffraction block $H_T(f)$ and Chapter 6: *Beamforming*. How the fields of individual array elements combine to focus and steer a beam is taken up in more detail in Chapter 7: *Array Beamforming*.

While diffracting and propagating, these waves undergo loss. This is called attenuation or forward absorption and is explained by $A_T(f)$ in Chapter 4: *Attenuation*. Also, along the way, these waves encounter obstacles large and small that are represented by $S(f)$ and described in Chapters 8 and 9: *Wave Scattering and Imaging* and *Scattering from Tissue and Tissue Characterization*.

Portions of the wave fields that are scattered find their way back toward the transducer array. These echoes become more attenuated on their return through factor $A_R(f)$, backward absorption, as is also covered in Chapter 4: *Attenuation*. The fields are picked by the elements according to principles of diffraction $H_R(f)$, as noted in Chapter 6: *Beamforming*. These acoustic waves pass back through array elements and are converted back to electrical signals through $G_R(f)$, as is explained in Chapter 5: *Transducers*. The converted signals are shaped into coherent beams by the receive beamformer, $RB(f)$, as is described in Chapter 7: *Array Beamforming*.

Electrical signals carrying pulse–echo information undergo filtering, $Q(f)$, and detection, $DF(f)$, processes, which are included in Chapter 10: *Imaging Systems and Applications*. This chapter also includes the diagram of a generic digital imaging system. In addition, it covers different types of arrays and major clinical applications. Alternate imaging modes are discussed in Chapter 11: *Doppler Modes*.

In most of the chapters, linear principles apply. Harmonic imaging, based on the science of nonlinear acoustics, is explained in Chapter 12: *Nonlinear Acoustics and Imaging*. The use of contrast agents, which are also highly nonlinear acoustically, is described in Chapter 14: *Ultrasound Contrast Agents*. Topics in both these chapters involve beam formation, scattering attenuation, beamforming, and filtering in interrelated ways.

Chapter 13: *Ultrasonic Exposimetry and Acoustic Measurements* applies to measurements of transducers, acoustic output and fields, and related effects. Safety issues related to ultrasound are covered in Chapter 15: *Ultrasound-Induced Bioeffects*.

Appendices supplement the main text. Appendix A shows how the Fourier transform and digital Fourier transform (DFT) are related in a review format. It also lists important theorems and functions in tabular form. In addition, it covers the Hilbert transform and quadrature signals. Appendix B lists tissue and transducer material properties. Appendix C derives a transducer model from simple 2-by-2 matrices and serves as the basis for a MATLAB transducer program. Numerous MATLAB programs, such as program chap2figs.m used to generate Figures 2.1–2.5, also supplement the text and serve as models for homework problems that are listed by chapter on the main web site, www.books.elsevier.com.

References

Bracewell, R. (2000). *The Fourier Transform and Its Applications*. McGraw-Hill, New York.

Cooley, J. W. and Tukey, J. W. (1965). An algorithm for the machine computation of complex Fourier series. *Math. Comp.* **19**, 297–301.

Goodman, J. W. (1968). *Introduction to Fourier Optics*. Mc Graw-Hill, New York.

This page intentionally left blank

3 ACOUSTIC WAVE PROPAGATION

Chapter Contents

3.1 INTRODUCTION TO WAVES

Waves in diagnostic ultrasound carry the information about the body back to the imaging system. Both elastic and electromagnetic waves can be found in imaging systems. How waves propagate through and interact with tissue will be discussed in several chapters, beginning with this one. This chapter also introduces powerful matrix methods for describing the complicated transmission and reflection of plane waves through several layers of homogeneous tissue. It first examines the properties of

plane waves of a single frequency along one axis. This type of wave is the basic element that can be applied later to build more complicated wave fields through Fourier synthesis and the angular spectrum of waves method. Second, this chapter compares types of waves in liquids and solids. Third, matrix tools will be created to simplify the understanding and analysis of wave propagation, as well as reflections at boundaries. Fourth, this chapter presents methods of solving two- and three-dimensional wave problems of mode conversion and refraction at the boundaries of different media, such as liquids and solids.

Because tissues have a high water content, the simplifying approximation that waves in the body are like waves propagating in liquids is often made. Many ultrasound measurements are made in water also, so modeling waves in liquids is a useful starting point. In reality, tissues are elastic solids with complicated structures that support many different types of waves. Later in this chapter, elastic waves will be treated with the attention they deserve.

Another convenient simplification is that the waves obey the principles of linearity. Linearity means that waves and signals keep the same shape as they change amplitude and that different scaled versions of waves or signals at the same location can be combined to form or synthesize more complicated waves or signals. This important principle of superposition is at the heart of Fourier analysis and the designs of all ultrasound imaging systems. You may have heard that tissue is actually nonlinear, as is much of the world around you. This fact need not bother us at this time because linearity will allow us to build an excellent foundation for learning not only about how a real imaging system works, but also about how nonlinear acoustics (described in Chapter 12) alters the linear situation.

Finally, in this chapter, materials that support sound waves are assumed to be lossless. Of course, both tissue and water have loss (a topic saved for Chapter 4).

3.2 PLANE WAVES IN LIQUIDS AND SOLIDS

3.2.1 Introduction

Three simple but important types of wave shapes are plane, cylindrical, and spherical (Figure 3.1). A plane wave travels in one direction. Stages in the changing pattern of the wave can be marked by a periodic sequence of parallel planes that have infinite lateral extent and are all perpendicular to the direction of propagation. When a stone is thrown into water, a widening circular wave is created. In a similar way, a cylindrical wave has a cross section that is an expanding circular wave that has an infinite extent along its axial direction. A spherical wave radiates a growing ball-like wave rather than a cylindrical one. In general, however, the shape of a wave will change in a more complicated way than these simple idealized shapes, which is why Fourier synthesis is needed to describe a journey of a wave.

In order to describe these basic wave surfaces, some mathematics is necessary. The next section presents the essential wave equations for basic waves propagating in an unbounded fluid medium. In order to characterize simple echoes, following sections

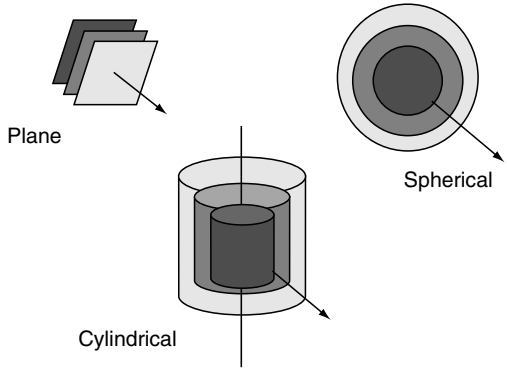

Figure 3.1 Plane, cylindrical, and spherical waves showing surfaces of constant phase.

will introduce equations and powerful matrix methods for describing waves hitting and reflecting from boundaries.

3.2.2 Wave Equations for Fluids

In keeping with the common application of a fluid model for the propagation of ultrasound waves, note that fluid waves are of a longitudinal type. A longitudinal wave creates a sinusoidal back-and-forth motion of particles as it travels along in its direction of propagation. The particles are displaced from their original equilibrium state by a distance or displacement amplitude (u) and at a rate or particle velocity (v) as the wave disturbance passes through the medium. This change also corresponds to a local pressure disturbance (p). The positive half cycles are called "compressional," and the negative ones, "rarefactional." If the direction of this disturbance or wave is along the z axis, the time required to travel from one position to another is determined by the longitudinal speed of sound c_L, or $t = z/c_L$. This wave has a wavenumber defined as $k_L = \omega/c_L$ where $\omega = 2\pi f$ is the angular frequency.

In an idealized inviscid (incompressible) fluid, the particle velocity is related to the displacement as

$$v = \partial u/\partial t \tag{3.1a}$$

or for a time harmonic or steady-state particle velocity (where capitals represent frequency dependent variables), as follows:

$$V(\omega) = i\omega U(\omega) \tag{3.1b}$$

For convenience, a velocity potential (ϕ) is defined such that

$$v = \nabla\phi \tag{3.2}$$

Pressure is then defined as

$$p = -\rho \partial\phi/\partial t \tag{3.3a}$$

or for a harmonic wave,

$$P(\omega) = -i\omega\rho\Phi(\omega) \tag{3.3b}$$

where ρ is the density of the fluid at rest. Overall, wave travel in one dimension is governed by the wave equation in rectangular coordinates,

$$\frac{\partial^2\phi}{\partial z^2} - \frac{1}{c_L^2}\frac{\partial^2\phi}{\partial t^2} = 0 \tag{3.4}$$

in which the longitudinal speed of sound is

$$c_L = \sqrt{\frac{\gamma B_T}{\rho_0}} \tag{3.5}$$

where γ is the ratio of specific heats, ρ_0 is density, and B_T is the isothermal bulk modulus. The ratio of a forward traveling pressure wave to the particle velocity of the fluid is called the specific acoustic or characteristic impedance, as follows:

$$Z_L = p/v_L = \rho_0 c_L \tag{3.6}$$

and this has units of Rayls (Rayl = kilogram/meter^2. second).

Note Z_L is negative for backward traveling waves. For fresh water at 20°C, $c_L = 1481$ m/s, $Z_L = 1.48$ MegaRayls (10^6kg/m^{2}sec), $\rho_0 = 998$ kg/m^3, $B_T = 2.18 \times 10^9$ newtons/m^2, and $\gamma = 1.004$.

The instantaneous intensity is

$$I_L = pp^*/Z_L = vv^*Z_L \tag{3.7}$$

The plane wave solution to Eq. (3.4) is

$$\phi(z, t) = g(t - z/c_L) + h(t + z/c_L) \tag{3.8}$$

in which the first term represents waves traveling along the positive z axis, and the second represents them along the $-z$ axis. One important specific solution is the time harmonic,

$$\phi = \phi_0(exp[i(\omega t - k_L z)] + exp[i(\omega t + k_L z)]) \tag{3.9}$$

In a practical situation, the actual variable would be the real part of the exponential; for example, the instantaneous pressure of a positive-going wave is

$$p = p_0 RE\{exp[i(\omega t - k_L z)]\} = p_0 \cos(\omega t - k_L z) \tag{3.10}$$

Note that the phase can also be expressed as $i(\omega t \pm k_L z) = i\omega(t \pm z/c_L)$ in which the ratio can be recognized as the travel time due to the speed of sound.

The plane wave Eq. (3.4) can be generalized to three dimensions as

$$\nabla^2\phi - \frac{1}{c^2}\phi_{tt} = 0 \tag{3.11}$$

in which the abbreviated notation $\phi_{tt} = \frac{\partial^2 \phi}{\partial t^2}$ is introduced. Basic wave equations for other geometries include the spherical,

$$\phi_{rr} + \frac{2}{r}\phi_r - \frac{1}{c_2}\phi_{tt} = 0 \tag{3.12}$$

where r is the radial distance, and the cylindrical case, where

$$\phi_{rr} + \frac{1}{r}\phi_r - \frac{1}{c^2}\phi_{tt} = 0 \tag{3.13}$$

The solution for Eq. (3.11) is

$$\phi = \phi_0(exp[i(\omega t - k \cdot r)] + \exp[i(\omega t + k \cdot r)]) \tag{3.14}$$

where k can be broken down into its projections (k_1, k_2, and k_3) along the x, y, and z axes, respectively, and r is the direction of the plane wave and

$$k^2 = k_1^2 + k_2^2 + k_3^2 \tag{3.15}$$

Note Eq. (3.11) can be expressed in the frequency domain as the Helmholtz equation,

$$\nabla^2 \Phi + k^2 \Phi = 0 \tag{3.16}$$

where Φ is the Fourier transform of ϕ.

The general solution for the spherical wave equation (Blackstock, 2000) is

$$\phi(z,t) = \frac{g(t - r/c_L)}{r} + \frac{h(t + r/c_L)}{r} \tag{3.17}$$

Unfortunately, there is no simple solution for the cylindrical wave equation except for great distances r,

$$\phi(z,t) \approx \frac{g(t - r/c_L)}{\sqrt{r}} + \frac{h(t + r/c_L)}{\sqrt{r}} \tag{3.18}$$

Finally, it is worth noting that the same wave equations hold if p or v is substituted for ϕ.

Most often the characteristics of ultrasound materials, such as the sound speed (c) and impedance (Z), are given in tabular form in Appendix B, so calculations of these values are often unnecessary. The practice of applying a fluid model to tissues involves using tabular measured values of acoustic longitudinal wave characteristics in the previous equations.

The main difference between waves in fluids and solids is that only longitudinal waves exist in fluids; many other types of waves are possible in solids, such as shear waves. These waves can be understood through electrical analogies. The main analogs are stress for voltage and particle velocity for current. The relationships between acoustic variables and similar electrical terms are summarized in Table 3.1. Correspondence between electrical variables for a transmission line and those for sound waves along one dimension in both fluids and solids enables the borrowing of electrical models for the solution of acoustics problems, as is explained in the rest

TABLE 3.1 Similar Wave Terminology

Sound			**Sound**			**Electrical**		
Liquid			Solid					
Variable	Symbol	Units	Variable	Symbol	Units	Variable	Symbol	Units
Pressure	p	MPa	Stress	T	Newton	Voltage	V	Volts
Particle velocity	v	m/s	Particle velocity	v	m/s	Current	I	Amps
Particle displacement	u	m	Particle displacement	u	m	Charge	Q	Coulombs
Density	ρ	kg/m^3	Density	ρ	kg/m^3			
Longitudinal speed of sound	c_L	m/s	Longitudinal speed of sound	c_L	m/s	Wave speed	$1/\sqrt{LC}$	m/s
Longitudinal impedance	$Z_L(\rho c_L)$	Mega Rayls	Longitudinal impedance	$Z_L(\rho c_L)$	Mega Rayls	Impedance	$\sqrt{L/C}$	Ohms
Longitudinal wave number	k_L	m^{-1}	Longitudinal wave number	k_L	m^{-1}			
			Shear vertical speed of sound	c_S	m/s			
			Shear vertical impedance	$Z_S(\rho c_S)$	Mega Rayls			
			Shear vertical wave number	k_S	m^{-1}			

of this chapter. Note that for solids, stress replaces pressure, but otherwise all the basic relationships of Eqs. (3.1–3.4) carry over. Another major difference for elastic waves in solids in Table 3.1 is the inclusion of shear waves. Waves in solids will be covered in more detail in Section 3.3.

3.2.3 One-Dimensional Wave Hitting a Boundary

An important solution to the wave equation can be constructed from exponentials like those of Eq. 3.9. Consider the problem of a single-frequency acoustic plane wave propagating in an ideal fluid medium with the characteristics k_1 and Z_1 and bouncing off a boundary of different impedance (Z_2), as shown in Figure 3.2. Assume a solution of the form,

$$p = p_0 exp(i[\omega t - k_L z]) + RF p_0 exp(i[\omega t + k_L z]) \tag{3.19}$$

which satisfies the previous wave equation. *RF* is a reflection factor for the amplitude of the negative-going wave. An electrical transmission line analog for this problem, described in more detail shortly, is symbolized by the right-hand side of Figure 3.2. The transmission line has a characteristic impedance (Z_1), a wavenumber (k_1), and a length (d). The second medium is represented by a real load of impedance (Z_2) located at $z = 0$ and a wavenumber (k_2). By the analogy presented in Table 3.1, the pressure at $z = 0$ is like a voltage drop across Z_2,

$$p_2 = p_0(1 + RF) \tag{3.20a}$$

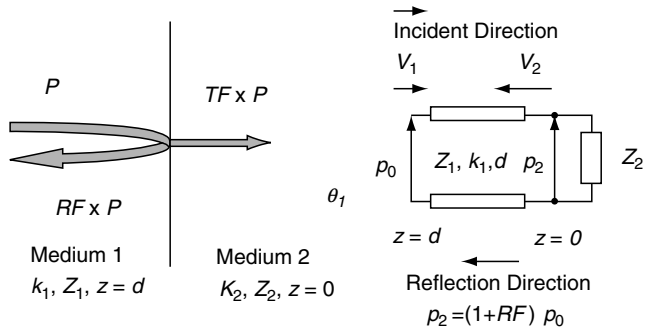

Figure 3.2 One-dimensional model of wave propagation at a boundary.

and the particle velocity there is like the sum of currents flowing in the transmission line in opposite directions, corresponding to the two wave components,

$$v_2 = (1 - RF)p_0/Z_1 \tag{3.20b}$$

The impedance (Z_2) can be found from

$$Z_2 = \frac{p_2}{v_2} = \frac{(1 + RF)Z_1}{1 - RF} \tag{3.21}$$

Finally, solve the right-hand side of Eq. (3.21) to obtain

$$RF = \frac{Z_2 - Z_1}{Z_2 + Z_1} \tag{3.22a}$$

A transmission factor (TF) can be determined from $TF = 1 + RF$,

$$TF = \frac{2Z_2}{Z_1 + Z_2} \tag{3.22b}$$

Eq. (3.22a) tells us that there will be a reflection if $Z_2 \neq Z_1$, but not if $Z_2 = Z_1$. If $Z_2 = 0$, an open circuit or air-type boundary, there will be a 180-degree inversion of the incident wave, or $RF = -1$. Here the reflected wave cancels the incident, so $TF = 0$. If $Z_2 = \infty$, corresponding to a short circuit condition or a stress-free boundary, the incident wave will be reflected back, or $RF = +1$. In this case, $TF = 2$ because the incident and reflected waves add in phase; however, no power or intensity (see Eq. (3.7)) is transferred to medium 2 because $v_2 = p_2/Z_2 = 0$.

3.2.4 ABCD Matrices

Extremely useful tools for describing both acoustic and electromagnetic waves in terms of building blocks are matrices (Matthaei *et al.*, 1980). In particular, the ABCD matrix form (Sittig, 1967) is shown in Figure 3.3 for the electrical case and is given by the following equations:

$$\begin{bmatrix} V_1 \\ I_1 \end{bmatrix} = \begin{pmatrix} A & B \\ C & D \end{pmatrix} \begin{bmatrix} V_2 \\ I_2 \end{bmatrix}$$

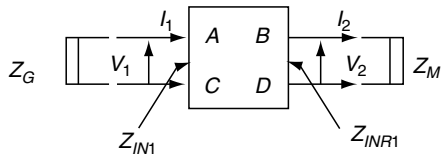

Figure 3.3 General ABCD matrix form.

$$V_1 = AV_2 + BI_2 \tag{3.23a}$$

$$I_1 = CV_2 + DI_2 \tag{3.23b}$$

where V is voltage and I is current. The analogous acoustic case is

$$p_1 = Ap_2 + Bv_2 \tag{3.24a}$$

$$v_1 = Cp_2 + Dv_2 \tag{3.24b}$$

The comparisons for these analogies are given in Table 3.1. The variables on the left (subscript 1) are given in terms of those on the right because usually the impedance on the right (Z_M) is known. The input impedance looking in from the left is given by

$$Z_{IN1} = \frac{AZ_M + B}{CZ_M + D} \tag{3.25a}$$

and the ratio of output to input voltages or pressures is

$$\frac{V_2}{V_1} = \frac{Z_M}{AZ_M + B} \tag{3.25b}$$

There are also equations that can be used for looking from right to left,

$$Z_{INR1} = \frac{DZ_G + B}{CZ_G + A} \tag{3.26a}$$

and input to output ratios are of the form,

$$\frac{V_1}{V_2} = \frac{Z_G}{DZ_G + B} \tag{3.26b}$$

What are A, B, C, and D? Figure 3.4 shows specific forms of ABCD matrices (Matthaei *et al.*, 1980). With only these four basic matrix types, more complicated configurations can be built up. From these types, a complete transducer model will be constructed in Chapter 5. Figure 3.4c is the ABCD matrix for a transmission line

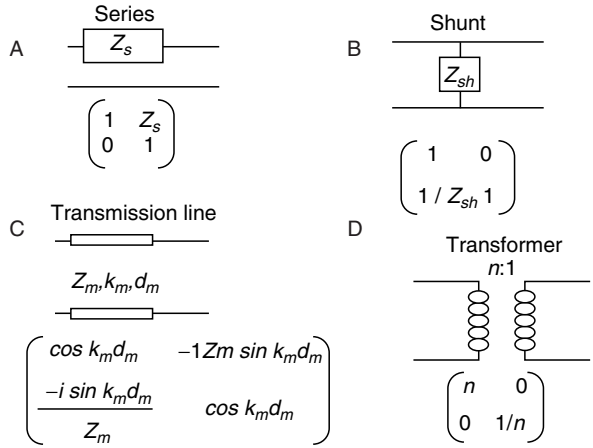

Figure 3.4 Specific forms of ABCD matrices. (A) Series. (B) Shunt. (C) Transmission line. (D) Transformer.

(acoustic or electric) with a wavenumber (k_1), impedance (Z_1), and length (d_1) for a medium designated by "1." This important matrix can model continuous wave, one-dimensional wave propagation and scattering. A transmission line that is a quarter of a wavelength long and loaded by Z_M, the input impedance, $Z_{IN1} = Z_1^2/Z_M$ is an impedance transformer. A half-wavelength line is also curious, $Z_{IN1} = Z_M$; the transmission line does not appear to be there. Reflection factors similar to Eq. (3.22a) can also be determined at the load end of the transmission line, designated by "R," for either voltage or pressure (stress),

$$RF_R = \frac{Z_M - Z_{IN2}}{Z_M + Z_{IN2}} \tag{3.27}$$

A transmission factor can also be written at the load,

$$TF_R = \frac{2Z_M}{Z_M + Z_{IN2}} \tag{3.28}$$

Another set of equations are appropriate for current (electrical model) or particle velocity (acoustical model) reflection and transmission at the left (input) end,

$$RF_i = \frac{1/Z_M - 1/Z_{IN2}}{1/Z_M + 1/Z_{IN2}} \tag{3.29}$$

and

$$TF_i = \frac{2/Z_M}{1/Z_M + 1/Z_{IN2}} \tag{3.30}$$

A similar set of equations for the other end of the transmission line (looking to the left) mimic those above: Eqs. (3.27–3.30) with Z_{IN1} replacing Z_{IN2} and Z_G replacing Z_M.

These transmission lines (shown in Figure 3.4) can be cascaded and combined with circuit elements. Primitive ABCD circuit elements can be joined to form more complicated circuits and loads. In Figure 3.4a is a series element, Z_S, and as an example, this matrix leads to the equations (Fig. 3.3),

$$V_1 = V_2 + Z_S I_2 \tag{3.31}$$

$$I_1 = I_2 \tag{3.32}$$

Figure 3.4b is a shunt element. A transformer with a turns ratio n:1 is depicted in Figure 3.4d. Different types of loads include the short circuit (electrical, $V = 0$) or vacuum load (acoustical, $p = -T_{ZZ} = 0$) and the open circuit (electrical, $I = 0$) or clamped load (acoustical, $v = 0$). In general, $AD - BC = 1$ if the matrix is reciprocal. If the matrix is symmetrical, then $A = D$.

Individual matrices can be cascaded together (illustrated in Figure 3.5). For example, the input impedance to the rightmost matrix loaded by Z_R is given by

$$Z_{IN1} = \frac{A_1 Z_R + B_1}{C_1 Z_R + D_1} \tag{3.33}$$

and for the impedance of the leftmost matrix,

$$Z_{IN2} = \frac{A_2 Z_{IN1} + B_2}{C_2 Z_{IN1} + D_2} \tag{3.34}$$

As an example of cascading, consider the matrices for the case shown in Figure 3.6. Individually, the matrices are

$$\begin{bmatrix} A_1 & B_1 \\ C_1 & D_1 \end{bmatrix} = \begin{bmatrix} 1 & 0 \\ i\omega C & 1 \end{bmatrix} \tag{3.35a}$$

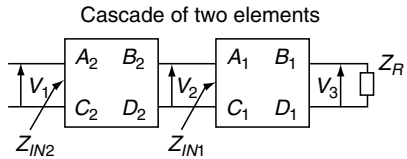

Figure 3.5 ABCD matrices in cascade.

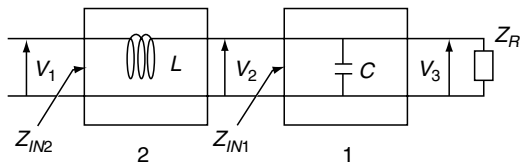

Figure 3.6 An example of two ABCD matrices in cascade terminated by a load (Z_R).

$$\begin{bmatrix} A_2 & B_2 \\ C_2 & D_2 \end{bmatrix} = \begin{bmatrix} 1 & i\omega L \\ 0 & 1 \end{bmatrix} \tag{3.35b}$$

The problem could be solved by multiplying the matrices together and by substituting the overall product matrix elements in Eq. (3.33) for those of the first matrix. Instead, the problem can be solved in two steps: Substituting matrix elements from Eq. (3.35a) into Eq. (3.33) yields

$$Z_{IN1} = \frac{Z_R}{i\omega C Z_R + 1} \tag{3.35c}$$

which, when inserted as the load impedance for Eq. (3.34), provides

$$Z_{IN2} = \frac{Z_R - \omega^2 L C Z_R + i\omega L}{i\omega C Z_R + 1} \tag{3.35d}$$

Another important calculation is the overall complex voltage ratio, which, for this case, is

$$\frac{V_3}{V_1} = \frac{V_2}{V_1}\frac{V_3}{V_2} \tag{3.35e}$$

From Eq. (3.25b), the individual ratios are

$$\frac{V_3}{V_2} = \frac{Z_R}{A_2 Z_R + B_2} = \frac{Z_R}{1 \times Z_R + i\omega L} \tag{3.35f}$$

and

$$\frac{V_2}{V_1} = \frac{Z_{IN1}}{A_1 Z_{IN1} + B_1} = \frac{Z_R/(1 + i\omega C Z_R)}{1 \times Z_R/(1 + i\omega C Z_R) + 0} = 1 \tag{3.35g}$$

so that from Eq. (3.35e), $V_3/V_1 = V_3/V_2$ for this example.

3.2.5 Oblique Waves at a Liquid–Liquid Boundary

Because of the common practice of modeling tissues as liquids, next examine what happens to a single-frequency longitudinal wave incident at an angle to a boundary with a different liquid medium 2 in the plane x–z (depicted in Figure 3.7). At the boundary, stress (or pressure) and particle velocity are continuous. The tangential components of wavenumbers must also match, so along the boundary,

$$k_{1x} = k_1 \sin\theta_i = k_2 \sin\theta_T = k_1 \sin\theta_R \tag{3.36a}$$

where k_1 and k_2 are the wavenumbers for mediums 1 and 2, respectively. The reflected angle (θ_R) is equal to the incident angle (θ_I), and an acoustic Snell's law is a result of this equation,

$$\frac{\sin\theta_i}{\sin\theta_T} = \frac{c_1}{c_2} \tag{3.36b}$$

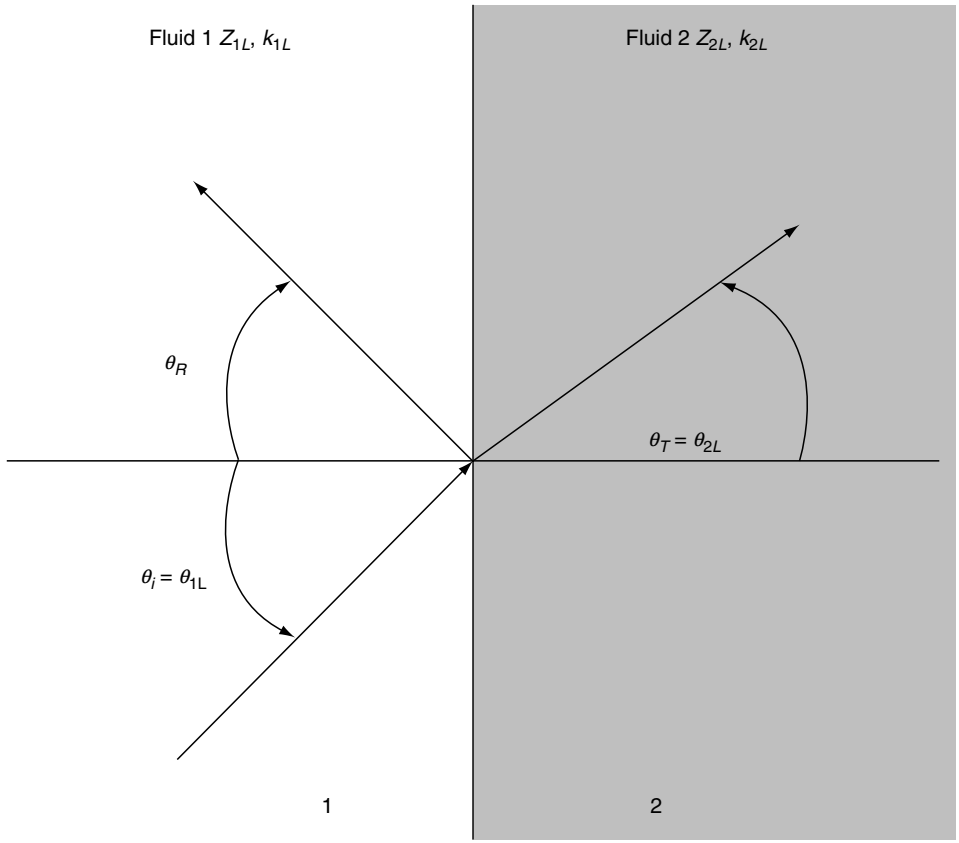

Figure 3.7 Oblique waves at a liquid–liquid interface.

which can be used to find the angle θ_T. Equation (3.36a) can also be used to determine θ_R. The wavenumber components along z are the following:

$$\text{Incident} \quad k_{Iz} = k_1 \cos\theta_i \tag{3.37a}$$

$$\text{Reflected} \quad k_{Rz} = k_1 \cos\theta_R \tag{3.37b}$$

$$\text{Transmitted} \quad k_{Tz} = k_2 \cos\theta_T \tag{3.37c}$$

which indicate that the effective impedances at different angles are the following:

$$Z_{1\theta} = \frac{\rho_1 c_1}{\cos\theta_i} = \frac{Z_1}{\cos\theta_i} \tag{3.38a}$$

and

$$Z_{2\theta} = \frac{\rho_2 c_2}{\cos\theta_T} = \frac{Z_2}{\cos\theta_T} \tag{3.38b}$$

Note that impedance is a function of the angle, reduces to familiar values at normal incidence, and otherwise grows with the angle. The incident wave changes direction as it passes into medium 2; this bending of the wave is called refraction. Since we are dealing at the moment with semi-infinite fluid media joined at a boundary, each medium is represented by its characteristic impedance, given by Eq. (3.38). Then just before the boundary, the impedance looking towards medium 2 is given by Eq. (3.38b). The reflection coefficient there is given by Eq. (3.22a),

$$RF = \frac{Z_{2\theta} - Z_{1\theta}}{Z_{2\theta} + Z_{1\theta}} = \frac{Z_2 \cos\theta_i - Z_1 \cos\theta_T}{Z_2 \cos\theta_i + Z_1 \cos\theta_T} \tag{3.39a}$$

where the direction of the reflected wave along θ_R and the transmission factor along θ_T is

$$TF = \frac{2Z_{2\theta}}{Z_{1\theta} + Z_{2\theta}} = \frac{2Z_2 \cos\theta_i}{Z_2 \cos\theta_i + Z_1 \cos\theta_T} \tag{3.39b}$$

Note that in order to solve these equations, θ_T is found from Eq. (3.36).

3.3 ELASTIC WAVES IN SOLIDS

3.3.1 Types of Waves

Stresses (force/unit area) and particle velocities tend to be used for describing elastic waves in solids. If we imagine a force applied to the top of a cube, the dimension in the direction of the force is compressed and the sides are pushed out (exaggerated in Figure 3.8). Not only does the vertical force on the top face get converted to lateral forces, but it is also related to the forces on the bulging sides. This complicated interrelation of stresses in different directions results in a stress field that can be described by naming conventions. For example, the stress on the *xz* face has three orthogonal components: T_{zy} along *z*, T_{xy} along *x*, and T_{yy} along *y*. The first subscript denotes the direction of the component, and the second denotes the normal to the face. Thanks to symmetry, these nine stress components for three orthogonal faces reduce to six unique values in what is called the "reduced form" notation, T_I (Auld, 1990). This notation is given in Table 3.2 and will be explained shortly.

In general, a displacement due to the vibration of an elastic wave is described by a vector (u) having three orthogonal components. Stress along one direction can be described as a vector,

$$T_y = \hat{\boldsymbol{x}} T_{xy} + \hat{\boldsymbol{y}} T_{yy} + \hat{\boldsymbol{z}} T_{zy} \tag{3.40a}$$

First-order strain is defined as an average change in relative length in two directions, such as

$$S_{ij} = \frac{1}{2}\left(\frac{\partial u_i}{\partial x_j} + \frac{\partial u_j}{\partial x_i}\right) \tag{3.40b}$$

For example,

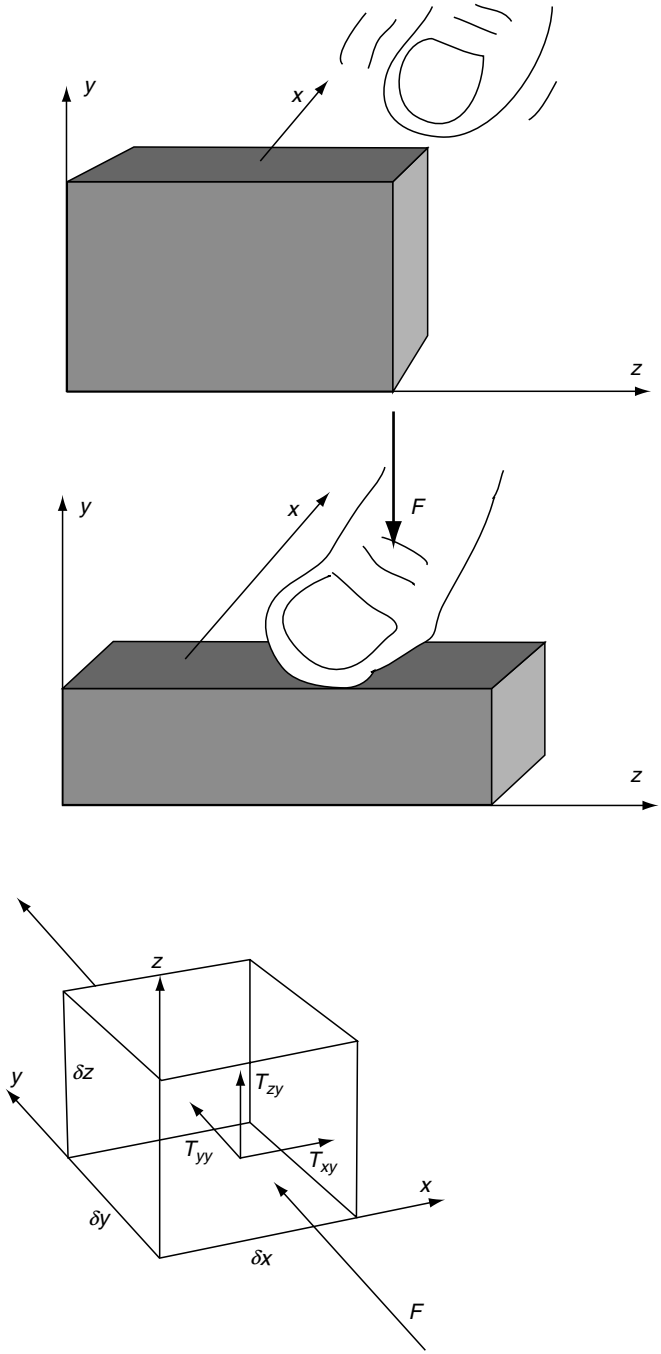

Figure 3.8 Stress conventions.

TABLE 3.2 Reduced Forms for Stress and Strain (From Kino, 1987)

T_I Reduced	T_{ij} Equivalent	S_I Reduced	S_{ij} Equivalent	Type of Stress or Strain
T_1	T_{xx}	S_1	S_{xx}	Longitudinal along x axis
T_2	T_{yy}	S_2	S_{yy}	Longitudinal along y axis
T_3	T_{zz}	S_3	S_{zz}	Longitudinal along z axis
T_4	T_{yz}	$S_4/2$	S_{yz}	Shear about x axis
T_5	T_{zx}	$S_5/2$	S_{zx}	Shear about y axis
T_6	T_{xy}	$S_6/2$	S_{xy}	Shear about z axis

$$S_{xy} = \frac{1}{2}\left(\frac{\partial u_x}{\partial y} + \frac{\partial u_y}{\partial x}\right) \tag{3.40c}$$

Sometimes the directions coincide:

$$S_{xx} = \frac{1}{2}\left(\frac{\partial u_x}{\partial x} + \frac{\partial u_x}{\partial x}\right) = \frac{\partial u_x}{\partial x} \tag{3.40d}$$

Reduced-form notation for strain is given in Table 3.2. For example,

$$S_{xy} = S_{yx} = \frac{S_6}{2} \tag{3.40e}$$

Overall, the strain relation can be described in reduced notation as follows (Kino, 1987):

$$\begin{bmatrix} S_1 \\ S_2 \\ S_3 \\ S_4 \\ S_5 \\ S_6 \end{bmatrix} = \begin{bmatrix} \frac{\partial}{\partial x} & 0 & 0 \\ 0 & \frac{\partial}{\partial y} & 0 \\ 0 & 0 & \frac{\partial}{\partial z} \\ 0 & \frac{\partial}{\partial z} & \frac{\partial}{\partial y} \\ \frac{\partial}{\partial z} & 0 & \frac{\partial}{\partial x} \\ \frac{\partial}{\partial y} & \frac{\partial}{\partial x} & 0 \end{bmatrix} \begin{bmatrix} u_x \\ u_y \\ u_z \end{bmatrix} \tag{3.40f}$$

An equivalent way of expressing strain as a six-element column vector, Eq. (3.40f), is in an abbreviated dyadic notation,

$$S = \nabla_S u \tag{3.40g}$$

in which each term is given by Eq. (3.40f). Stress and strain are related through Hooke's law, which can be written in matrix form,

$$\begin{bmatrix} T_1 \\ T_2 \\ T_3 \\ T_4 \\ T_5 \\ T_6 \end{bmatrix} = [C] \begin{bmatrix} S_1 \\ S_2 \\ S_3 \\ S_4 \\ S_5 \\ S_6 \end{bmatrix} \tag{3.41a}$$

where symmetry $C_{IJ} = C_{JI}$ has reduced the number of independent terms. Depending on additional symmetry constraints, the number is significantly less. Equation (3.41a) can be written in a type of symbolic shorthand called dyadic notation for vectors,

$$T = C : S \tag{3.41b}$$

As an example of how these relations might be used, consider the case of a longitudinal wave traveling along the z axis

$$u = \hat{z}\cos(\omega t - kz) \tag{3.42}$$

in which the displacement direction denoted by the unit vector ($\hat{z}$) and the direction of propagation (z) coincide, and $k = \omega/(C_{11}/\rho)^{1/2}$. Then the strain is

$$S_3 = S_{zz} = \hat{z}\,ksin(\omega t\text{-}kz) \tag{3.43}$$

The corresponding stress for an isotropic medium (one in which k or sound speed, c, is the same in all directions for a given acoustic mode) is given by the isotropic elastic constant matrix,

$$\begin{aligned}\begin{bmatrix} T_1 \\ T_2 \\ T_3 \\ T_4 \\ T_5 \\ T_6 \end{bmatrix} &= \begin{bmatrix} C_{11} & C_{12} & C_{13} & C_{14} & C_{15} & C_{16} \\ C_{21} & C_{22} & C_{23} & C_{24} & C_{25} & C_{26} \\ C_{31} & C_{32} & C_{33} & C_{34} & C_{35} & C_{36} \\ C_{41} & C_{42} & C_{43} & C_{44} & C_{45} & C_{46} \\ C_{51} & C_{52} & C_{53} & C_{54} & C_{55} & C_{56} \\ C_{61} & C_{62} & C_{63} & C_{64} & C_{65} & C_{66} \end{bmatrix} \begin{bmatrix} 0 \\ 0 \\ S_3 \\ 0 \\ 0 \\ 0 \end{bmatrix} \\ &= \begin{bmatrix} C_{11} & C_{12} & C_{12} & 0 & 0 & 0 \\ C_{12} & C_{11} & C_{12} & 0 & 0 & 0 \\ C_{12} & C_{12} & C_{11} & 0 & 0 & 0 \\ 0 & 0 & 0 & C_{44} & 0 & 0 \\ 0 & 0 & 0 & 0 & C_{44} & 0 \\ 0 & 0 & 0 & 0 & 0 & C_{44} \end{bmatrix} \begin{bmatrix} 0 \\ 0 \\ S_3 \\ 0 \\ 0 \\ 0 \end{bmatrix}\end{aligned} \tag{3.44}$$

which results in the following nonzero values:

$$T_1 = C_{12}S_3 = \hat{x}C_{12}ksin(\omega t\text{-}kz) \tag{3.45a}$$

$$T_2 = C_{12}S_3 = \hat{y}C_{12}ksin(\omega t\text{-}kz) \tag{3.45b}$$

$$T_3 = C_{11}S_3 = \hat{z}C_{11}ksin(\omega t\text{-}kz) \tag{3.45c}$$

For an isotropic medium, the elastic constants are related:

$$C_{44} = \frac{1}{2}(C_{11} - C_{12}) \tag{3.46}$$

Other often-used constants are Lame's constants, $\bar{\lambda}$ and μ,

$$C_{11} = \bar{\lambda} + 2\mu \tag{3.47a}$$

$$C_{12} = \bar{\lambda} \tag{3.47b}$$

$$C_{44} = \mu \tag{3.47c}$$

where $\bar{\lambda}$ is an elastic constant (not wavelength). Another is Poisson's ratio,

$$\sigma = \frac{C_{12}}{C_{11} + C_{12}} \tag{3.48}$$

This is the ratio of transverse compression to longitudinal expansion when a static longitudinal axial stress is applied to a thin rod. Poisson's ratio is between 0 and 0.5 for solids, and it is 0.5 for liquids (Kino, 1987). The ratio of axial stress to strain in a thin rod is Young's modulus,

$$E = C_{11} - \frac{2C_{12}^2}{C_{11} + C_{12}} \tag{3.49}$$

Though there are many types of waves other than longitudinal waves that propagate along the surface between media or in certain geometries, the other two most important wave types are shear. Earlier Eq. (3.42) described a longitudinal wave along z in the x–z plane with a sound speed,

$$c_L = \left(\frac{C_{11}}{\rho}\right)^{1/2} \tag{3.50a}$$

Now consider a shear vertical (*SV*) wave in an isotropic medium with a sound speed,

$$c_S = \left(\frac{C_{44}}{\rho}\right)^{1/2} \tag{3.50b}$$

with a transverse displacement along x and a propagation direction along z,

$$u_{SV} = \hat{x}u_{SV0}\cos(\omega t - k_S z) \tag{3.51}$$

as depicted in Figure 3.9. When these *SV* waves travel at an angle θ to the z axis, they can be described more generally by

$$u_{SV} = (\hat{x}u_{SVX} + \hat{z}u_{SVZ})\cos(\omega t - k_S \cdot r) = (\hat{x}u_{SVX} + \hat{z}u_{SVZ})\cos(\omega t - k_S z\cos\theta + k_S x\sin\theta) \tag{3.52}$$

A shear horizontal (*SH*) wave, on the other hand, would have a transverse displacement along y perpendicular to the xz plane and a propagation along z,

$$u_{SH} = \hat{y}u_{SH0}\cos(\omega t - k_S z) \tag{3.53}$$

How are these three types of waves interrelated when a longitudinal wave strikes the surface of a solid? Stay tuned to the next section to find out.

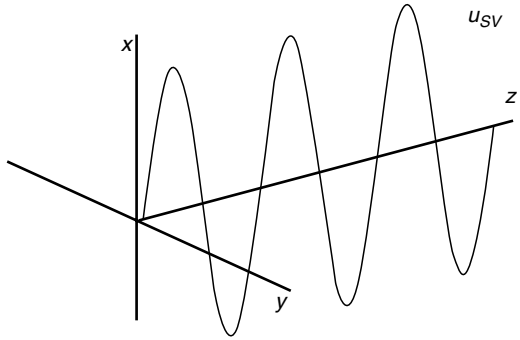

A

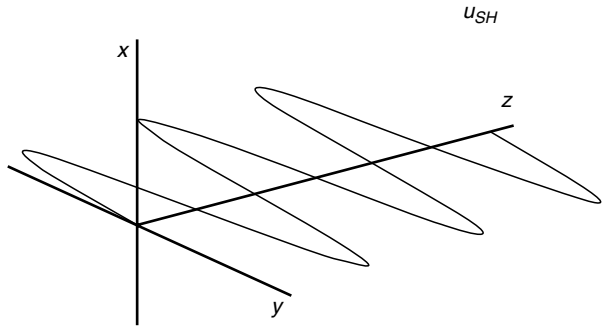

B

Figure 3.9 Types of basic shear waves. (A) Shear vertical (*SV*) and (B) shear horizontal (*SH*).

3.3.2 Equivalent Networks for Waves

Oliner (1969, 1972a, 1972b) developed a powerful methodology for modeling acoustic waves with transmission lines and circuit elements, and it is translated here into ABCD matrix form. This approach can be applied to many different types of elastic waves in solids and fluids, as well as to infinite media and stacks of layers of finite thickness. Rather than rederiving applicable equations for each case, this method

offers a simple solution in terms of the reapplication and combination of already derived equivalent circuits. At the heart of most of these circuits is one or more transmission lines, each with a characteristic impedance, wave number, and length.

As an example, we will re-examine an oblique wave at a fluid-to-fluid boundary. From Section 3.2.4, we can construct a transmission line of length (d) for the first medium by using the appropriate relations for the incident wave from Eqs. (3.37a and 3.38a). Figure 3.10 shows two diagrams: the top diagram shows a general representation of each medium with its own transmission line, and the bottom drawing indicates the second medium as being semi-infinite and as represented by an impedance, $Z_{2\theta}$. Note that different directions are associated with the incident, reflected, and transmitted waves even though the equivalent circuit appears to look one-dimensional; this approach follows that outlined in Section 3.2.5. At normal incidence to the boundary, previous results are obtained. Connecting the load to the transmission line automatically satisfies appropriate boundary conditions.

Applications of different boundary conditions are straightforward, as is illustrated for fluids by transmission lines shown for normal incidence in Figure 3.11. In this figure, the notation is the following: k_f is wavenumber, V_f corresponds to pressure, and I_f corresponds to particle velocity (v). In Figure 3.11a, for an air/vacuum boundary (called a pressure-release boundary), a short circuit for T_{zz} is applied ($T_{zz} = -p$). For a rigid solid or clamped condition, given by Figure 3.11b, an open circuit load is appropriate. When there is an infinitesimally thin interface between two fluids, the coupling of different transmission lines corresponding to the characteristics of the fluids ensures that the stress and particle velocity are continuous across the boundary (Figure 3.11c). If the waves are at an angle, impedances of the forms given by Eq. (3.38) are assumed.

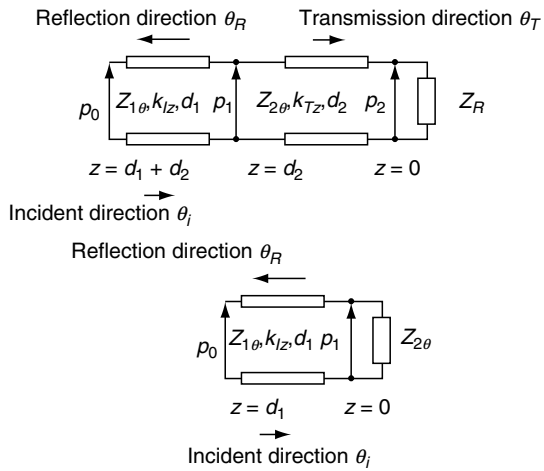

Figure 3.10 Equivalent circuits for acoustic waves in fluids. (Top) Two-transmission line representation of fluid boundaries. (Bottom) Transmission line for fluid and semi-infinite fluid boundary.

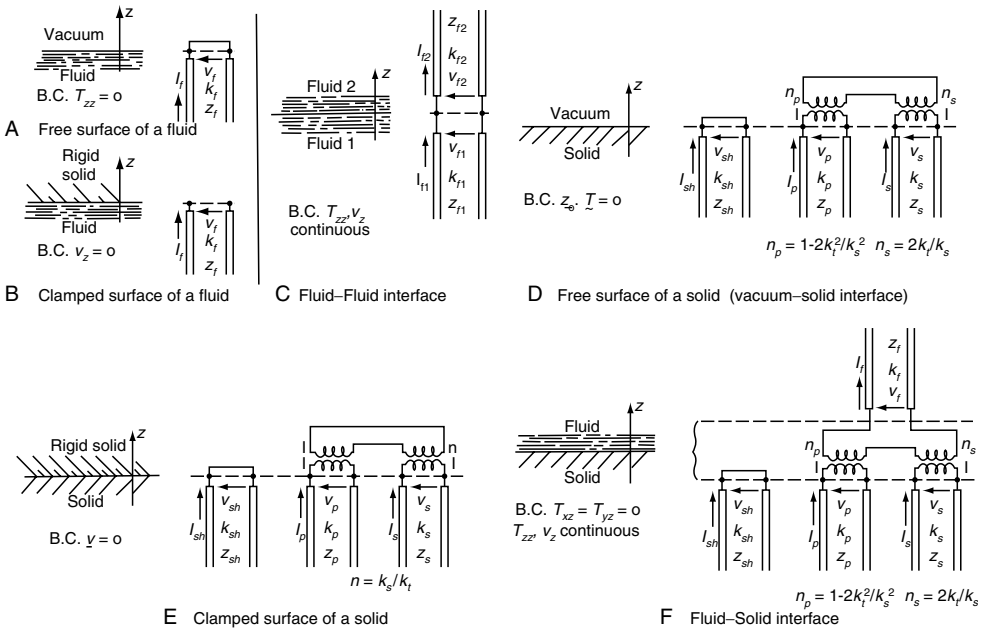

Figure 3.11 Equivalent circuits for acoustic waves at boundaries of solids. (A) Free surface of a fluid. (B) Clamped surface of a fluid. (C) Fluid–fluid interface. (D) Free surface of a solid. (E) Clamped surface of a solid. (F) Fluid–solid interface (from Oliner, 1972b, 1972 *IEEE).*

3.3.3 Waves at a Fluid–Solid Boundary

A longitudinal wave incident on the surface of a solid creates, in general, a longitudinal and shear wave as shown in Figure 3.12. A reflected shear wave is not generated because it is not supported in liquids; however, one would be reflected at the interface between two solids. The fluid pressure at the boundary is continuous ($p = -T_3$), as are the particle velocities.

Circuits applicable to three types of loading for solids (shown in Figure 3.11) anticipate the discussion of this section. In this figure the notation is slightly different and corresponds to the following: "*p*" designates a longitudinal wave, "*s*" a shear vertical wave, and "*sh*" a shear horizontal wave. Note that in Figure 3.11f, a wave from a fluid is in general related to three types of waves in the solid. In these cases, transformers represent the mode conversion processes. In Figure 3.11d is the circuit for the pressure release (air) boundary, and in Figure 3.11e is the clamped boundary condition, both for waves traveling upward in the solid. In all three cases, the shear horizontal wave does not couple to other modes. In the more general case of all three types of waves coupling from one solid to another (not shown), a complicated interplay among all the modes exists. This problem, as well as the circuits for many others, are found in Oliner (1972a and 1972b). Derivations and more physical insights for these equivalent circuits are in Oliner (1969, 1972a, 1972b).

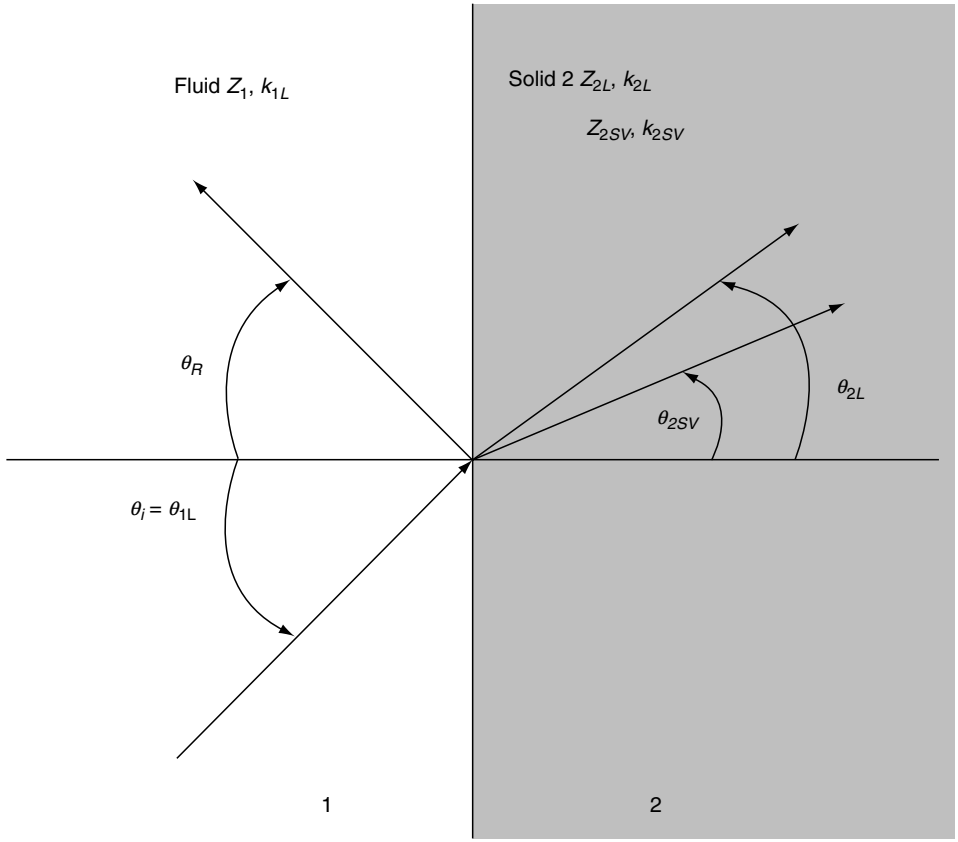

Figure 3.12 Wavevectors in the x–z plane for fluid–solid interface problem.

The case of wave in a fluid incident on a solid (Figure 3.12) is now treated in more detail in terms of an equivalent circuit. This problem is translated into the equivalent circuit representation of Figure 3.13a, which shows mode conversion from the incoming longitudinal wave into a longitudinal wave and a vertical shear wave in the solid. Since the motions of these waves all lie in the *xz* plane, they do not couple into a horizontally polarized shear wave with motion orthogonal to that plane. Also, because an ideal nonviscous fluid does not support transverse motion, none of the shear modes in the solid couple into shear motion in the fluid. Here the solid and fluid are semi-infinite in extent, so characteristic impedances replace the transmission lines. Because the input impedances of the converted waves are transformed via Eq. (3.33) and the ABCD matrix for a transformer, the input impedance at position (*a*), looking to the right in Figure 3.13b, is

$$Z_{INA} = n_L^2 Z_{2L\theta} + n_{SV}^2 Z_{2SV\theta} \tag{3.54}$$

Where the angular impedances used for the fluid–fluid problem are used,

$$Z_{2L\theta} = \frac{\rho_2 c_{2L}}{\cos\theta_{2L}} = \frac{Z_{2L}}{\cos\theta_{2L}} \tag{3.55a}$$

$$Z_{2SV\theta} = \frac{\rho_2 c_{2S}}{\cos\theta_{2SV}} = \frac{Z_{2SV}}{\cos\theta_{2SV}} \tag{3.55b}$$

in which these angles can be determined from the Snell's law for this boundary,

$$k_{1x} = k_1 \sin\theta_{1L} = k_{2SV} \sin\theta_{2SV} = k_{2L} \sin\theta_{2L} \tag{3.56}$$

The stress reflection factor at (*a*) is simply

$$RF_a = \frac{Z_{INA} - Z_{1L\theta}}{Z_{INA} + Z_{1L\theta}} \tag{3.57a}$$

where

$$Z_{1L\theta} = \frac{\rho_1 c_{1L}}{\cos\theta_i} \tag{3.57b}$$

The transmission stress factors for each of the two waves in the solids can be found from Eq. (3.28) and impedance at each location. First at (*b*) in Figure 3.13b:

$$TF_L = \frac{2n_L^2 Z_{2L\theta}}{Z_{1L\theta} + Z_{INA}} \tag{3.58}$$

second at (*c*),

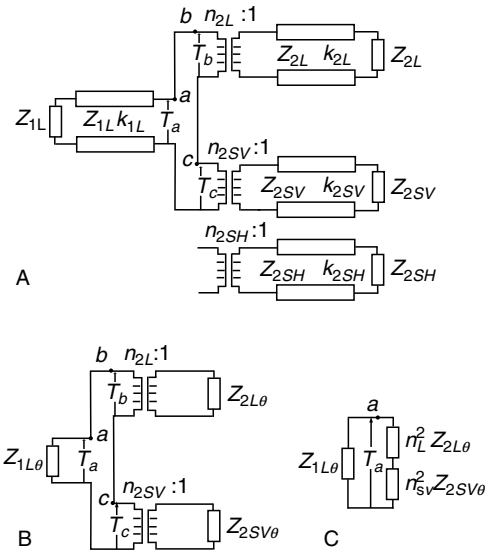

Figure 3.13 Equivalent circuit for fluid–solid interface problem. (A) Overall equivalent circuit diagram. (B) Reduction of circuit to transformed loads. (C) Simplified circuit.

$$TF_{SV} = \frac{2n_{SV}^2 Z_{2SV\theta}}{Z_{1L\theta} + Z_{INA}} \tag{3.59}$$

Here these factors represent the ratios of amplitudes arriving at different loads over the amplitude arriving at both loads, position (*a*) in Figure 3.13b. Usually, it is most desirable to know the intensity rather than the stress arriving at different locations (e.g., the relative intensities being converted into shear and longitudinal waves). From the early definitions of time average intensity (Eq. 3.7) and the three previous factors, it is possible to arrive at the following intensity ratios relative to the input intensity: first the intensity reflection ratio,

$$r = (RF_a)^2 = \frac{(Z_{INA} - Z_{1L\theta})^2}{(Z_{INA} + Z_{1L\theta})^2} \tag{3.60}$$

and the intensity ratio for the longitudinal waves

$$\tau_L = (TF_L)^2 \frac{Z_{1L\theta}}{n_L^2 Z_{2L\theta}} = \frac{4Z_{1L\theta} n_L^2 Z_{2L\theta}}{(Z_{1L\theta} + Z_{INA})^2} \tag{3.61}$$

and the intensity ratio for the shear waves

$$\tau_{SV} = (TF_{SV})^2 \frac{Z_{1L\theta}}{n_{SV}^2 Z_{2SV\theta}} = \frac{4Z_{1L\theta} n_{SV}^2 Z_{2SV\theta}}{(Z_{1L\theta} + Z_{INA})^2} \tag{3.62}$$

An example of an intensity calculation is shown in Figure 3.14.

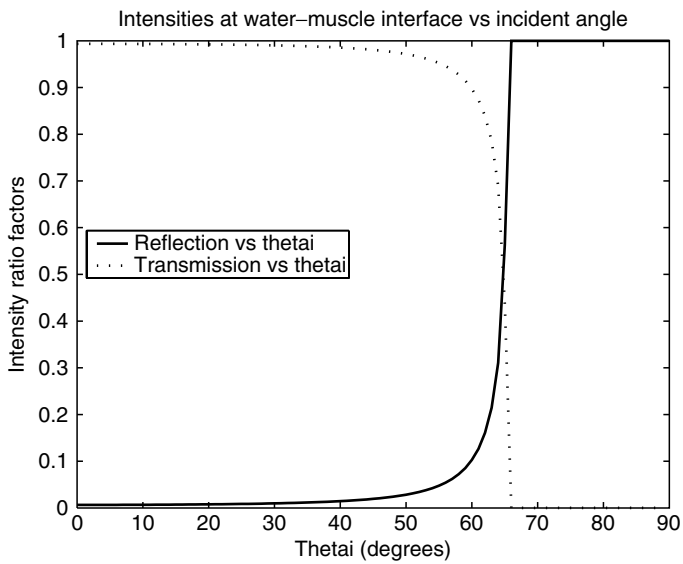

Figure 3.14 Intensity transmission and reflection graphs for water–muscle boundary as an example of a fluid–solid interface.

3.4 CONCLUSION

In this chapter, wave equations describe three basic wave shapes. When waves strike a boundary, they are transmitted and reflected. For the one-dimensional case, solutions consist of positive- and negative-going waves. Through the application of ABCD matrices, solutions for complicated cases consisting of several layers can be constructed from cascaded matrices rather than by rederiving the equations needed to satisfy boundary conditions at each interface. This approach will be used extensively in developing a transducer model in Chapter 5 and Appendix C. Matrix methodology has been extended to oblique waves at an interface between different media.

Even though tissues are most often represented as fluid media, they are, in reality, elastic. An important case is the heart, which has muscular fibers running in preferential directions (to be described in Chapter 9). In addition, elastic waves are necessary to describe transducer arrays and piezoelectric materials (to be discussed in Chapters 5 and 6). An extra level of complexity is introduced by elasticity, namely, the existence of shear and other forms of waves created from both boundary conditions and geometry. Reflection and mode conversions among different elastic modes can be handled in a direct manner with the equivalent approach introduced by A. A. Oliner. His methodology is well suited to the ABCD matrix approach developed here. It also has the capability of handling mode conversions to other elastic modes, such as Lamb waves and Rayleigh waves (as described in his publications).

Bibliography

For more information on elastic waves, see Kino (1987), now available on a CD-ROM archive from the IEEE Ultrasonics, Ferroelectrics, and Frequency Control Group and Auld (1990).

References

Auld, B. A. (1990). *Acoustic Waves and Fields in Solids*. Vol. 1, Chap. 8. Krieger Publishing, Malabar, FL.

Blackstock, D. T. (2000). *Fundamentals of Physical Acoustics*. John Wiley & Sons, New York.

Duck, F. A. (1990). *Physical Properties of Tissue: A Comprehensive Reference Book*. Academic Press, London.

Kino, G. S. (1987). *Acoustic Waves: Devices, Imaging, and Analog Signal Processing*. Prentice-Hall, Englewood Cliffs, NJ.

Matthaei, G. L., Young, L., and Jones, E. M. T. (1980). *Microwave Filters, Impedance-Matching Networks, and Coupling Structures*. Chap. 6, pp. 255–354. Artech House, Dedham, MA.

Oliner, A. A. (1969). Microwave network methods for guided elastic waves. *IEEE Trans. Microwave Theory Tech*. **MTT-17**, 812–826.

Oliner, A. A., Bertoni, H. L., and Li, R. C. M. (1972a). A microwave network formalism for acoustic waves in isotropic media. *Proc. IEEE* **60**, 1503–1512.

Oliner, A. A., Bertoni, H. L., and Li, R. C. M. (1972b). Catalog of acoustic equivalent networks for planar interfaces. *Proc. IEEE* **60**, 1513–1518.

Sittig, E. K. (1967). Transmission parameters of thickness-driven piezoelectric transducers arranged in multilayer configurations. *IEEE Trans. Sonics Ultrasonics* **SU-14**, 167–174.

4 ATTENUATION

Chapter Contents

4.1 LOSSES IN TISSUES

Waves in actual media encounter losses. Real tissue data indicate that absorption has a power law dependence on frequency. As a result of this frequency dependence, acoustic pulses not only become smaller in amplitude as they propagate, but they also change shape. Absorption in the body is a major effect; it limits the detectable penetration of sound waves in the body or the maximum depth at which tissues can be imaged. In order to compensate for absorption, all imaging systems have a way of increasing amplification with depth. These methods will be discussed at the end of this chapter.

Usually absorption is treated in the frequency domain. Because imaging is done with pulse echoes, it is important to understand the effect of absorption on waveforms. This chapter introduces model suitable for the kind of losses in tissues that can work equally well in the domains of both time and frequency. When absorption is present, phase velocity usually changes with frequency as well (an effect known as dispersion). The loss model can predict how both absorption and phase-velocity dispersion affect pulse shape during propagation. Absorption and dispersion are related through the principle of causality. Tissues are viscoelastic media, meaning they have both elastic properties and losses. The model can also be extended to cover these characteristics. In addition, appropriate wave equations and stress–strain relations (Hooke's law for lossy media) complete the simulation of acoustic waves propagating in tissue with losses.

4.1.1 Losses in Exponential Terms and in Decibels

When waves propagate in real media, losses are involved. Just as forces encounter friction, pressure and stress waves lose energy to the medium of propagation and result in weak local heating. These small losses are called "attenuation" and can be described by an exponential law with distance. For a single-frequency (f_c) plane wave, a multiplicative amplitude loss term can be added,

$$A(z, t) = A_0 \, exp(i(\omega_c t - kz)) \, exp(-\alpha z) \tag{4.1}$$

The attenuation factor (α) is usually expressed in terms of nepers per centimeter in this form. Another frequently used measure of amplitude is the decibel (dB), which is most often given as the ratio of two amplitudes (A and A_0) on a logarithmic scale,

$$Ratio(\text{dB}) = 20 \log_{10} (A/A_0) \tag{4.2}$$

or in those cases where intensity is simply proportional to amplitude squared ($I_0 \propto A_0^2$),

$$Ratio(\text{dB}) = 10 \log_{10} (I/I_0) = 10 \log_{10} (A/A_0)^2 \tag{4.3}$$

Most often, α is given in dB/cm,

$$\alpha_{\text{dB}} = 1/z\{20 \times \log_{10} [\, exp(-\alpha_{\text{nepers}} z)]\} = 8.6886(\alpha_{\text{nepers}}) \tag{4.4}$$

Graphs for a loss constant α equivalent to 1 dB/cm are given in Figure 4.1 on several scales.

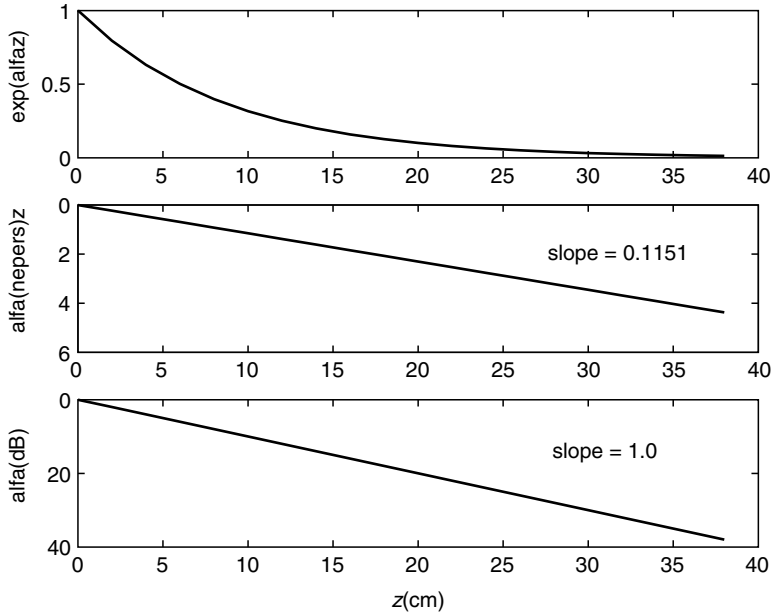

Figure 4.1 Constant absorption as a function of depth on a (top) linear scale, (middle) dB scale, and (bottom) neper scale.

A plane wave multiplied by a loss factor that increases with travel distance (z) was shown in Eq. (4.1). This equation for a single-frequency (f_c) plane wave can be rewritten as

$$A(z, t) = A_0 \, exp(-\alpha z) \, exp[i\omega_c(t - z/c_0)] \tag{4.5a}$$

in which c_0 is a constant speed of sound and $\alpha = \alpha_0$ is a constant. Also, the second exponential argument can be recognized as a time delay. The Fourier transform of this equation is

$$A(z, f) = A_0 \, exp([-\alpha_0 z - i\omega_c z/c])\delta(f - f_c) \tag{4.5b}$$

This result indicates that the exponential term is frequency independent and acts as a complex weighting amplitude for this spectral frequency.

The actual loss per wavenumber is very small, or $\alpha/k << 1$, a fact that will be useful later. Even though the loss per wavelength is small, absorption has a strong cumulative effect over many wavelengths. Absorption for a round-trip echo path usually determines the allowable tissue penetration for imaging.

4.1.2 Tissue Data

These simple loss and delay factors are not observed in real materials and tissues. Data indicate that the absorption is a function of frequency. Many of these losses obey a frequency power law, defined as

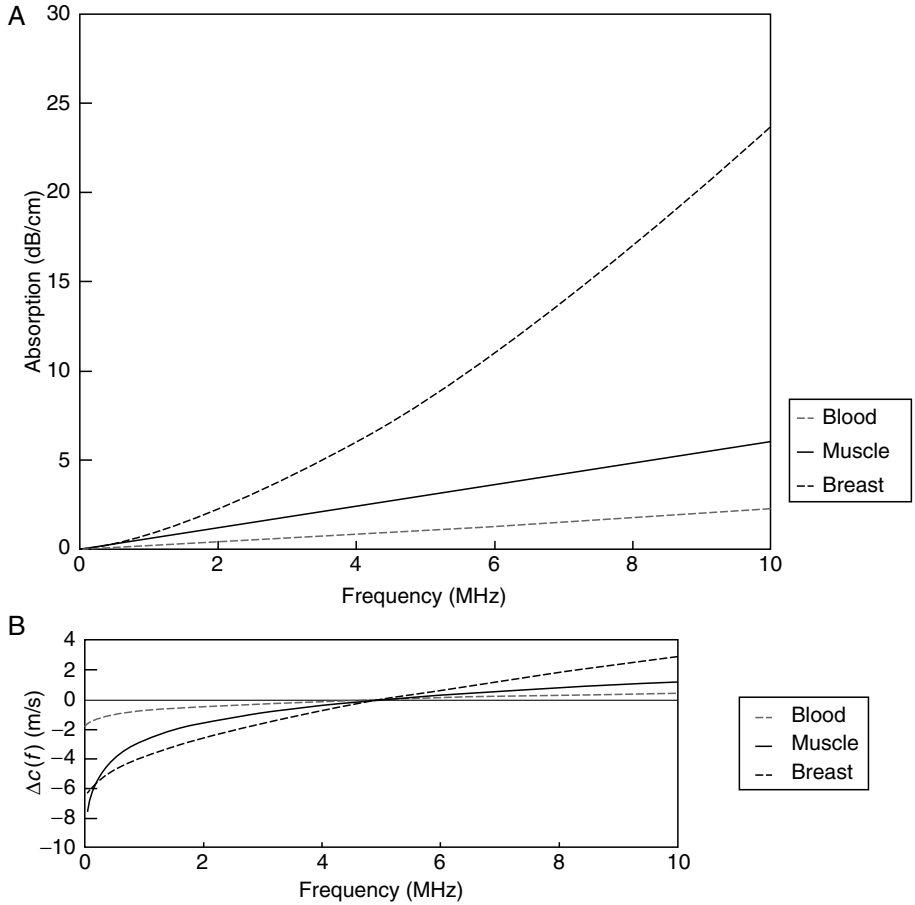

Figure 4.2 (A) Absorption as a function of frequency for muscle, fat, and blood. (B) Phase velocity dispersion difference minus a midband (5 MHz) sound speed value for the same tissues.

$$\alpha(f) = \alpha_0 + \alpha_1 |f|^y \tag{4.6a}$$

in which α_0 is often zero and y is a power law exponent. A graph for the measured absorption of common tissues as a function of frequency is given in Figure 4.2a. In addition to absorption loss, the phase velocity of tissue also varies with frequency,

$$c(f) = c_0 + \Delta c(f) \tag{4.6b}$$

where $\Delta c(f)$ is a small change in sound speed with frequency. What is plotted in Figure 4.2b is the change in sound speed with the constant term subtracted out for convenience,

$$\Delta c(f) = c(f) - c_0 \tag{4.6c}$$

This change of phase velocity with frequency is required by causality, as will be shown shortly. Although this velocity dispersion is considered by many to be a small effect, the consequences of neglecting it can be significant, especially for broad bandwidth pulses.

As pointed out in Chapter 1, soft tissues are mostly (60%) composed of water; therefore, values for average velocity are similar, varying only about ±10% from a mean value (see Figure 1.2). Lists of common tissue average absorption, average phase velocity values, and characteristic impedances are in Appendix B, and a more complete list is in Duck (1990). Tissue attenuation has two parts: absorption and scattering. At low-MHz frequencies, scattering is typically 10–15% of the total value of attenuation (Bamber,1986, 1998). The tissue structure causes the scattering to vary with angle. Both absorption and scattering are frequency dependent because the wavelength changes in relation to the scale of tissue structure. This scaling implies that as the imaging frequency is lowered, greater averaging over the structure occurs. The topic of scattering will be treated in more depth in Chapters 8 and 9; for now, we neglect scattering and assume that each type of tissue has characteristics that are uniform everywhere (homogeneous).

4.2 LOSSES IN BOTH FREQUENCY AND TIME DOMAINS

4.2.1 The Material Transfer Function

The combined effects of absorption and dispersion on pulse propagation can be described by a material transfer function (MTF) in the frequency domain,

$$MTF(f, z) = exp[\gamma_T(f)z] \tag{4.7a}$$

in which

$$\gamma_T(f) = -\alpha(f) - i\beta(f) = -\alpha(f) - i[k_0(f) + \beta_E(f)] \tag{4.7b}$$

where $k_0 = \omega/c_0$, a baseline wavenumber (where c_0 is a sound speed value usually taken to be at the center frequency of the spectrum of a pulse), and $\beta_E(f)$ is an excess dispersion term required by causality (to be presented later). In Eq. (4.7), a frequency-dependent amplitude term is associated with $\alpha(f)$, and an effective frequency-dependent phase velocity is determined by

$$1/c(\omega) = \beta/\omega = k_0/\omega + \beta_E/\omega = 1/c_0 + \beta_E/\omega \tag{4.8}$$

in which, because the second term is very small relative to the first, can be approximated by

$$c(\omega) - c_0 = -c_0^2\beta_E/\omega \tag{4.9}$$

like Eq. (4.6c).

4.2.2 The Material Impulse Response Function

The material transfer function (MTF) has its time domain counterpart, called the material impulse response function, *mirf*(*t*):

$$mirf(t, z) = \Im^{-1}\{exp[\gamma_T(f)z]\} \tag{4.10}$$

For an initial pulse described by p_0(t) having a spectrum P_0(f), the pulse at a distance z can be described simply by either

$$p(t, z) = p_0(t) *_t mirf(t, z) \tag{4.11a}$$

or, equivalently, in the frequency domain as

$$P(f, z) = P_0(f)MTF(f, z) \tag{4.11b}$$

Equation (4.11a) was used to calculate pulses at increasing distances (z) in Figure 4.3 for a medium with loss. An initial starting pulse of a Gaussian modulated sinusoid was used. A series of *mirfs* that were used for Figure 4.3 are shown in Figure 4.4 for the case of a frequency dependence for absorption, with $y = 1.5$ (based on the time causal model, which will be introduced shortly). Note that the *mirfs* follow a delay time that is approximately z/c_0, where $c_0 = 1.5$ mm/μs.

From these figures, we can see that the *mirf* function has some very interesting properties. Its amplitude diminishes with increasing distance. As the delay time approaches zero, *mirf* must become impulse-like. For short distances, *mirf*(*t*) has a steep leading edge, as required by causality, so that its left edge does not extend into negative time.

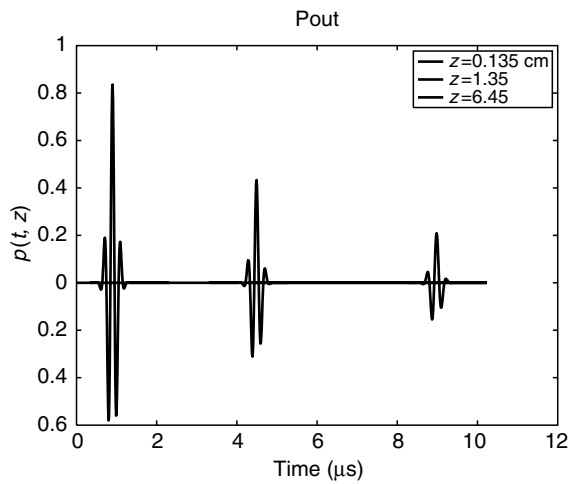

Figure 4.3 Changes in pressure-pulse shape of an initially Gaussian pulse propagating in a medium with a 1dB/MHz$^{1.5}$-cm absorption $y = 1.5$ for three different increasing propagation distances (z).

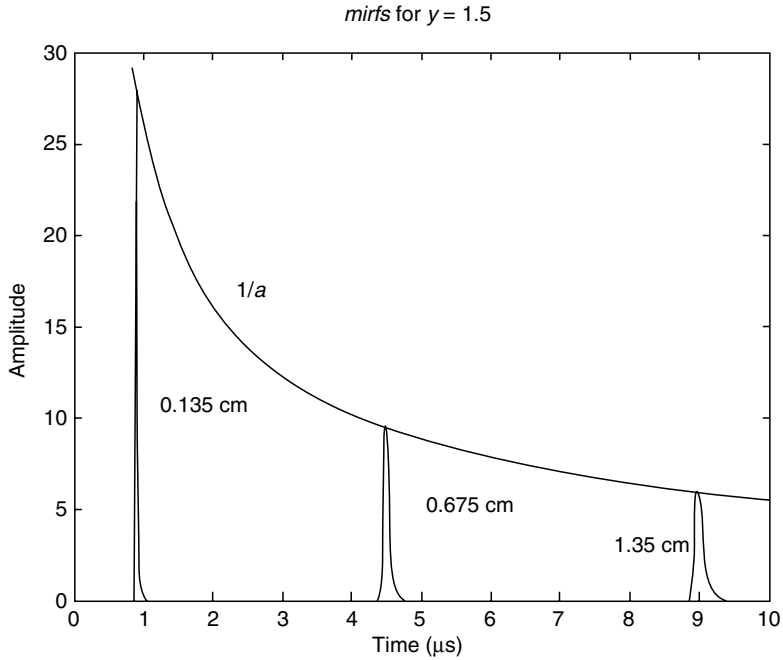

Figure 4.4 Material impulse response functions for a medium with a 1dB/MHz$^{1.5}$-cm absorption for different propagation distances (z). Note that peaks follow a $1/a$ characteristic. Here, $a = (a_1 z)^{1/y}$ from section 4.4.1.

What is causality? It is natural law that does not allow a response to precede its cause. In order for the pulse response to be zero for $t < 0$, the complex Fourier spectral components must add up to produce an effect in the time domain, which is the equivalent of canceling out the pulse response for times less than zero. This mathematical operation is similar to multiplying the time response by $H(t)$, the step function that is zero for $t < 0$.

4.3 TISSUE MODELS

4.3.1 Introduction

In order to calculate the material transfer function and the material impulse response, a model must be selected. The models available describe both absorption and dispersion as a function of frequency and differ in terms of their convenience and accuracy. These models are not very satisfying in terms of an explanation based on first principles, but they can describe adequately, in an empirical way, the way absorption affects acoustic propagation.

The choices for models are the classic relaxation model, the time causal model, and the Kramers–Krönig relation. The relaxation model (Kinsler *et al*., 2000) is the most well known; however, it has its own absorption function that is not exactly the power law dependence observed for tissues (to be described shortly). An often–used approach is to fit the one or more relaxation–absorption functions to match the power law absorption characteristic over a limited frequency range. While this procedure is suitable for valid band or a band-limited starting spectrum (P_0), the responses at very low and high frequencies (which are important in Fourier inversion) must be watched carefully.

The time causal model (Szabo, 1994, 1995) is based on the observed power law absorption characteristic and provides a more direct implementation. A third approach, the application of the Kramers–Krönig relation (Krönig, 1926), is more challenging for an absorption power law type characteristic, which increases exponentially as frequency approaches an infinite limit. This difficult problem has been solved by the method of subtractions and has been found to be equivalent to the time causal method (Waters *et al*., 2000a, 2000b). These last two methods (really the same result solved in different domains), though more recent, have had extensive experimental validation. All of these models satisfy the laws of causality.

4.3.2 Thermoviscous Model

In the classic thermoviscous model (Blackstock, 2000), the medium is composed of noninteracting molecules that all have an associated sound speed and relaxation constant (τ). For this model, the absorption divided by frequency (α/ω) has the form shown in Figure 4.5a. Also, the excess dispersion divided by frequency (β_E/ω) is plotted in Figure 4.5b, with (τ) as a relaxation constant. The equations used for calculating the absorption and dispersion in Figure 4.5 are the following:

$$\alpha(\omega) = \alpha_1 \omega \left(\frac{1}{\sqrt{1 + (\omega\tau)^2}} - \frac{1}{1 + (\omega\tau)^2} \right) \tag{4.12}$$

$$\beta_E(\omega) = \alpha_1 \omega \left(\frac{1}{\sqrt{1 + (\omega\tau)^2}} + \frac{1}{1 + (\omega\tau)^2} \right) \tag{4.13}$$

In the time domain, the *mirf* can be found from Eq. (4.10) with substitutions from Eqs. (4.12–4.13).

The graphs for absorption loss for tissues in Figure 4.2 show characteristics that are monotonically increasing because they follow a power law; therefore, they do not have inflection points and negative slopes like those for the relaxation model depicted in Figure 4.5. Because of this fact and the smallness of the loss per wavenumber, $(\alpha/k_0)^2 << 1$, a low-frequency approximation of the relaxation model is applied more often to model loss in tissues and other materials. Note that in this region where $\omega\tau < 1$, the absorption depends on the frequency squared and the phase velocity is nearly constant.

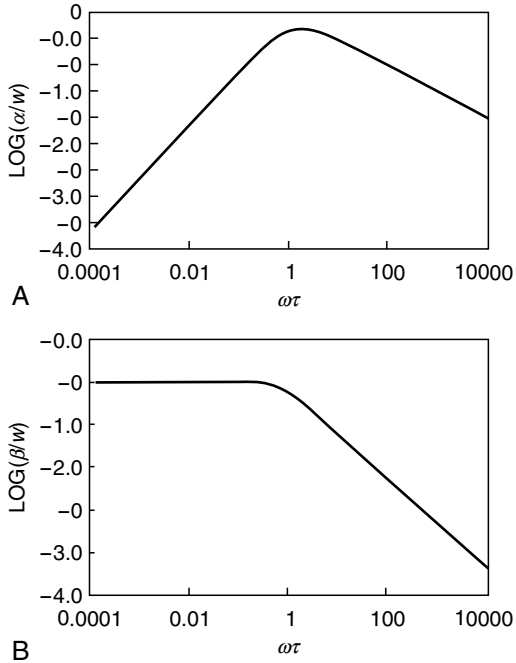

Figure 4.5 (A) Absorption (α) divided by angular frequency (ω) versus angular frequency (ω) times (τ) for the thermoviscous model. Loss peak at $\omega_p = 1/\tau$, where τ is relaxation time. (B) Excess dispersion (β_E) divided by angular frequency (ω) versus angular frequency (ω) times τ (from Szabo and Wu, 2000, Acoustical Society of America).

4.3.3 Multiple Relaxation Model

One way of overcoming the discrepancy between the thermoviscous model and observed power law absorption characteristics of tissues is to use a fitting procedure to Eq. (4.6a), involving either a superposition or distribution of several relaxation time constants (Bamber, 1986; Nachman *et al.*, 1990; Wojcik *et al.*, 1999). This multiple relaxation model corresponds to a tissue model with different, independent, noninteracting molecules, each with its own relaxation constant and associated speed of sound. Typically, two to three relaxation constants are used to fit a measured absorption frequency characteristic for a prescribed frequency range.

4.3.4 The Time Causal Model

The time casual model is based on a power law that includes macromolecular effects. The relaxation models are causal, which means that an effect cannot precede its cause. Traditionally, the effects of causality have been determined by use of the Kramers–

Krönig relation, which relates the excess dispersion characteristic to a convolution integral operator on absorption over all frequencies,

$$\beta_E(f) = \frac{-1}{\pi f} * [-\alpha(f) + \alpha_0] \tag{4.14}$$

In other words, β_E is the Hilbert transform of $\alpha(f) - \alpha_0$. This approach poses numerical evaluation problems for the Hilbert transform integral of power law absorption because, unlike the characteristics of the thermoviscous model in Figure 4.6, which decrease with very high frequencies, power law characteristics increase monotonically

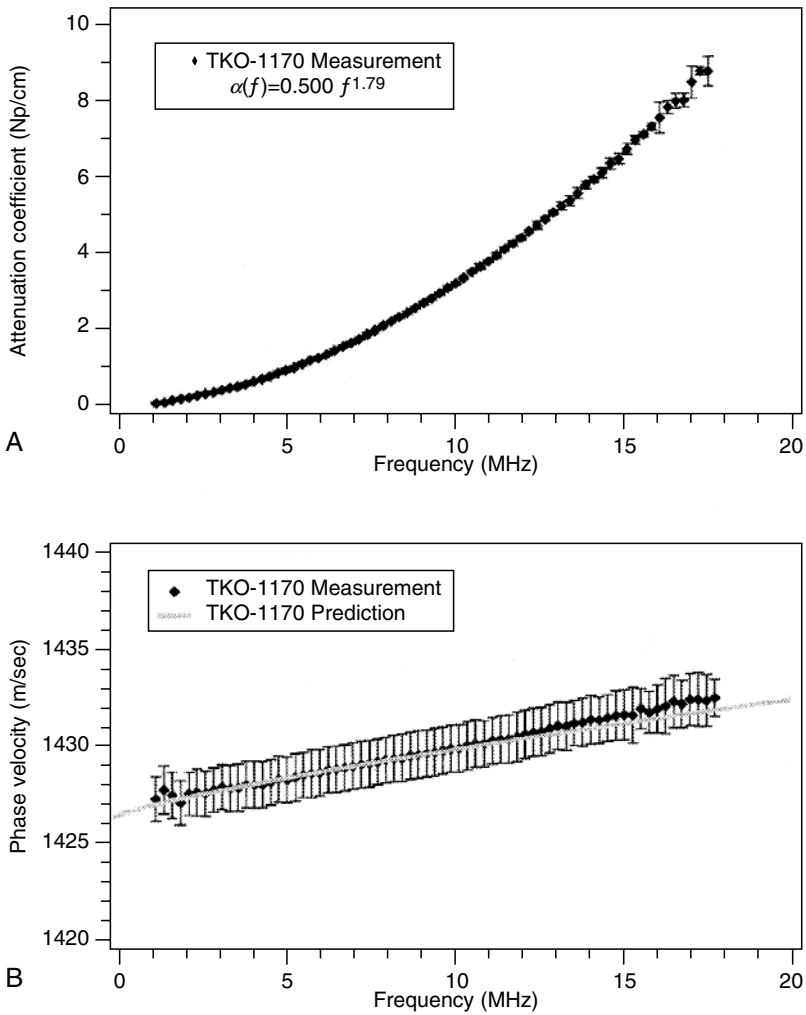

Figure 4.6 (A) Measured absorption data as a function of frequency for TKO-1170 (high-viscosity hydrocarbon oil) with power law fit. (B) Measured relative velocity dispersion with error bars compared to prediction from Eq. (4.19a) using the measured absorption data power law fit (from Waters *et al.*, 2000a, Acoustical Society of America).

with frequency. One solution to this problem is to use a time causal relation. Another way to solve the numerical difficulties is to apply a method of subtractions to the Kramers–Krönig method (Waters *et al*., 2000a, 2000b). These two approaches give the same results and can be considered to be complementary statements of causality.

For the time causal method, causality can be expressed directly in the time domain (Szabo, 1994, 1995; Szabo and Wu, 2000) through the use of generalized functions, as

$$L_{\beta_E}(t) = -i\ sgn(t) * L_\alpha(t) \tag{4.15}$$

where $sgn(t)$ is a signum function (Bracewell, 2000),

$$\begin{aligned} sgn(t) &= 1 \quad t > 0 \\ sgn(t) &= 1 \quad t < 0 \end{aligned} \tag{4.16}$$

and L_{β_E} as well as L_α are Fourier transform pairs of $\beta_E(f)$ and $\alpha 0 - \alpha(f)$, respectively. These transforms involve the application of generalized functions (these details need not concern us here and can be found in the references above). The overall propagation operator can be written as

$$L_\gamma(t) = L_\alpha(t) + iL_{\beta_E}(t) = [1 + sgn(t)]L_\alpha(t) = 2H(t)L_\alpha(t) \tag{4.17}$$

where $H(t)$ is the step function (Bracewell, 2000).

Note that because the Hilbert transform is involved, there is a similarity between this operation and that for creating an analytic signal (described in section A.2.7 of Appendix A). In this case, the time absorption operator is multiplied by $2H(t)$, ensuring causality, whereas for the analytic signal, the negative frequency components were dropped by a similar operation in the frequency domain (as described in Appendix A). From the time causal relation, an imaginary signal $iL_{\beta_E}(t)$ is created from the real one, $L_\alpha(t)$, just as for the analytic signal, an imaginary quadrature signal was derived from the original real signal. From the power law, the time causal relation, and the Fourier transform relation between these time operators and α_1 and β_E, the excess dispersion has been found to depend on the kind of power law type of exponent y. The steps in the process are the following:

1. Find $L_\alpha(t)$ from the inverse Fourier transform of $\alpha(f) - \alpha_0$ through the use of generalized functions.
2. Obtain $L_{\beta_E}(t)$ from Eq. (4.15), the time causal relation.
3. Find $\beta_E(f)$ from the Fourier transform of $L_{\beta_E}(t)$ through the use of generalized functions.

The results for $\beta_E(f)$ indicate that various functions are necessary for different forms of y. For y as an even integer or noninteger,

$$\beta_E(f) = \alpha_1\, tan(\pi y/2) f|f|^{y-1} \tag{4.18a}$$

and for y as an odd integer,

$$\beta_E(f) = -(2/\pi)\alpha_1 f^y \ell n|f| \tag{4.18b}$$

Versions of these equations that are more appropriate for phase velocity data follow. For y as an even integer or noninteger,

$$1/c(f) = 1/c(f_0) + \alpha_1\, tan(\pi y/2)\left[|f|^{y-1} - |f_0|^{y-1}\right] \tag{4.19a}$$

in which $c(f_0)$ is the speed of sound at a reference frequency (f_0), usually a midband value. For y as an odd integer,

$$1/c(f) = 1/c(f_0) - (2\alpha_1 f^{y-1}/\pi)(\ell n|f| - \ell n|f_0|) \tag{4.19b}$$

Dispersion is maximum for $y = 1$ or equal to an odd integer, given equivalent absorption loss coefficients. Note that if y is zero or an even constant, $\beta_E = 0$. The

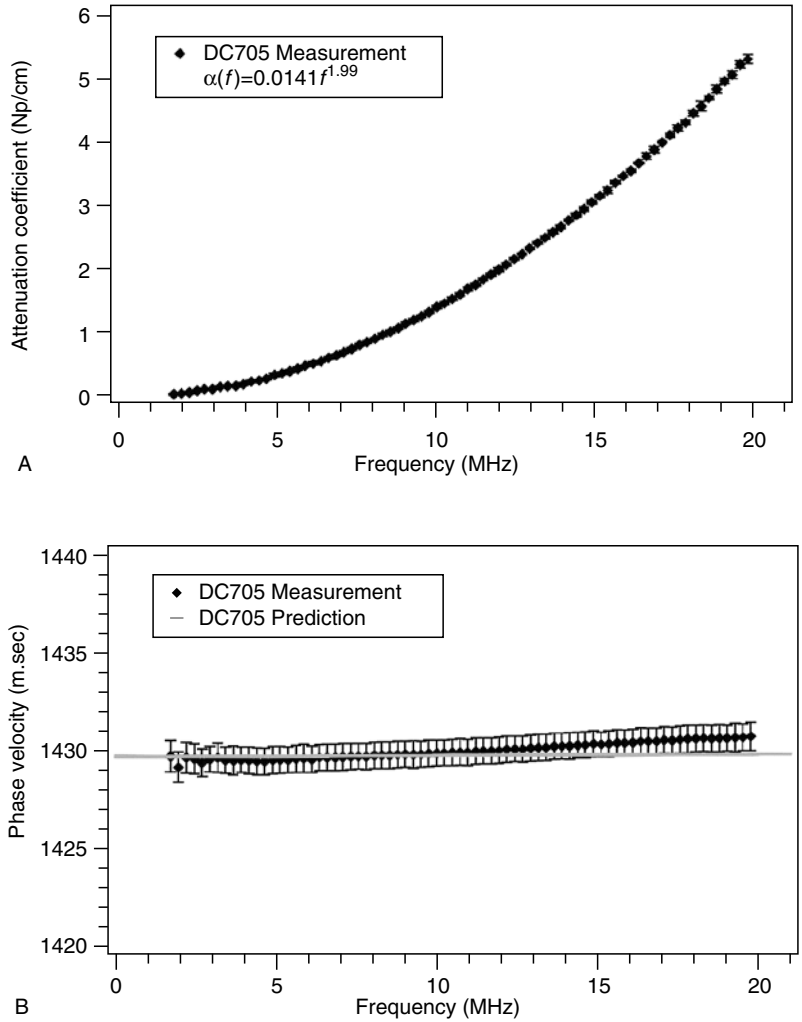

Figure 4.7 (A) Measured absorption data as a function of frequency for DC 705 (silicone fluid) with power law fit of $y \approx 2$. (B) Measured relative velocity dispersion with error bars compared to prediction from Eq. (4.19a) using the measured absorption data power law fit. Note that dispersion is nearly zero for this quadratic loss case (from Waters *et al.*, 2000a, Acoustical Society of America).

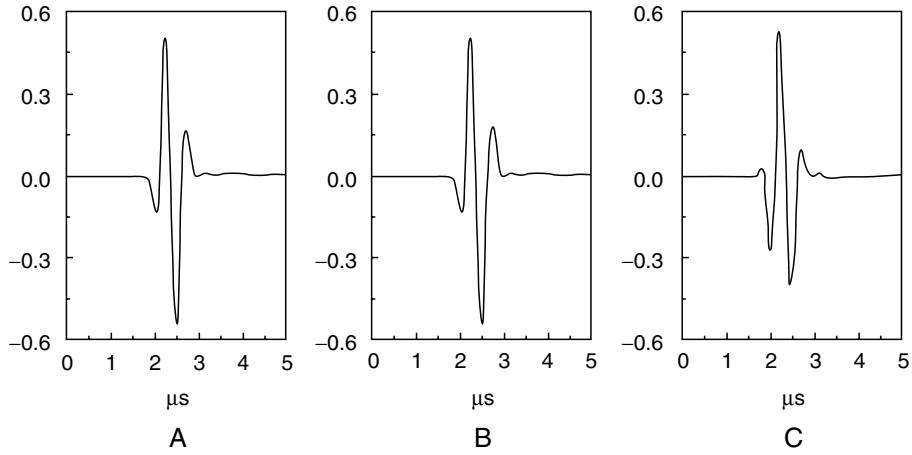

Figure 4.8 Comparison of simulations to data for a broadband pulse passing through an ATS Laboratories, I. tissue mimicking phantom with $\alpha\,(f_{MHz}) = 0.21 + 0.20\, f^{1.98}$ dB/cm. (A) Pulse data. (B) Time causal model. (C) Nearly local Kramers–Krönig model (from He, 1998a, IEEE).

validity of these results has been verified by independent analysis and confirmed by experiments at several laboratories (Szabo, 1995; He, 1998a, 1998b, 1999; Waters *et al*., 2000a; Szabo and Wu, 2000; Trousil *et al*., 2001). Examples of data comparisons are given in Figures 4.7–4.8. In Figure 4.6, the attenuation follows a power law with an exponent $y = 1.79$, and the phase velocity increases with frequency. For the second case (Figure 4.7), $y \approx 2$, so very little dispersion is expected (in excellent agreement with data).

The time causal analysis, though it uses a low-frequency approximation, holds for the entire ultrasound imaging range and is valid to very high frequencies, including multiple harmonic frequencies. A very conservative estimate of the upper frequency limit is given by

$$f_{LIM} = 0.1/[\alpha_1 C_0/(2\pi)] \tag{4.20}$$

For the cases where y is equal to one and a noninteger, the Kramers–Krönig approach with the method of subtractions (Waters *et al*., 2000a) has shown these dispersion results to be valid without a high-frequency limit.

4.4 PULSES IN LOSSY MEDIA

4.4.1 Scaling of the Material Impulse Response Function

Even though losses are evaluated most often in the frequency domain, it is also possible to examine the combined effects of loss and dispersion in the time domain directly through the material impulse response function. At each depth (z), the *mirf* from Eq. (4.10) encodes all the frequency loss and dispersion into a time waveform.

This waveform can be determined from the inverse Fourier transform of the material transfer function, which can be calculated from Eqs. (4.6), (4.7), and (4.18). In general, the material impulse response has to be evaluated numerically. When a fast Fourier transform (FFT) of a digital Fourier transform (DFT) is used, enough frequency points need to be taken to ensure that the nearly vertical leading edge of the response is captured accurately.

Because the velocity dispersion is often small, about $\pm 2x10^{-3}$ of c_0 in Figure 4.6, for example, most people assume its effect is negligible. In Figure 4.8, simulations of broadband pulse propagation with and without dispersion are compared to experiment. In this case, the power exponent is the same as that for Figure 4.7 ($y \approx 2$), so no dispersion is expected from the time causal model (in agreement with data). The third comparison is to an older, nearly local Kramers–Krönig model that predicts dispersion for this case. This older model is more accurate near $y \approx 1$ and has been replaced by Eq. (4.19) (Szabo, 1995; Waters *et al.*, 2000a). The differences in the pulse predictions are noticeable and show the need for correctly accounting for dispersion, especially for wider bandwidth pulses.

As indicated in the last section, dispersion is maximum for $y = 1$. In Figure 4.9, corresponding time domain calculations for $y = 1$ are shown for a material impulse response for propagation of 1 cm in a tissue with absorption equal to 1 dB/MHz-cm (0.1151 neper/MHz-cm) and a reference phase velocity of $c_0 = 0.15$ cm/μs with and without dispersion calculated from causality. Two striking differences are that the acausal response is symmetrical ($\beta_{EM} = 0$) while the causal one is not, and the causal waveform peaks at $0.972z/c_0$. A simple explanation of the earlier arrival of the causal response is that for most of its frequency range, the phase velocity increases

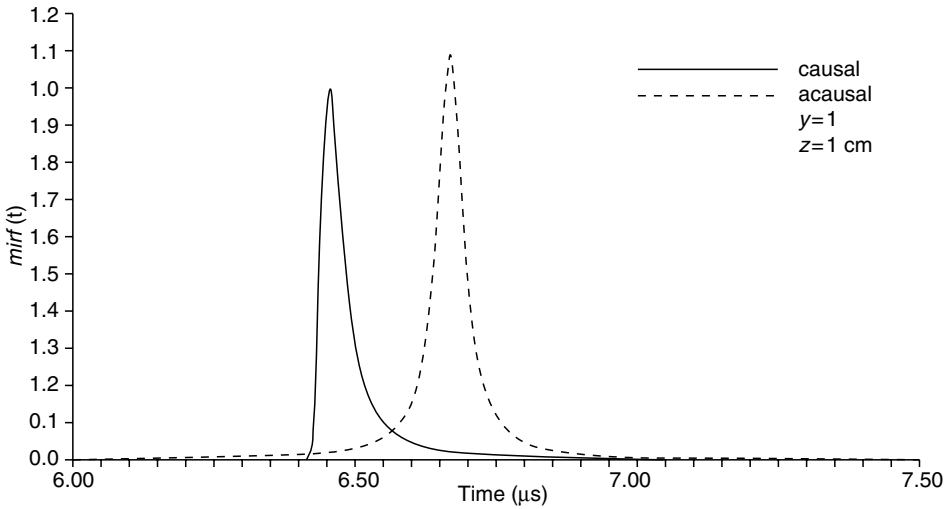

Figure 4.9 Comparison of causal time *mirf* and an acausal nondispersive *mirf* for linear loss ($y=1$), for a propagation distance of 1 cm and an absorption coefficient of 0.1151 neper/MHz-cm (1 dB/MHz-cm) (from Szabo, 1993).

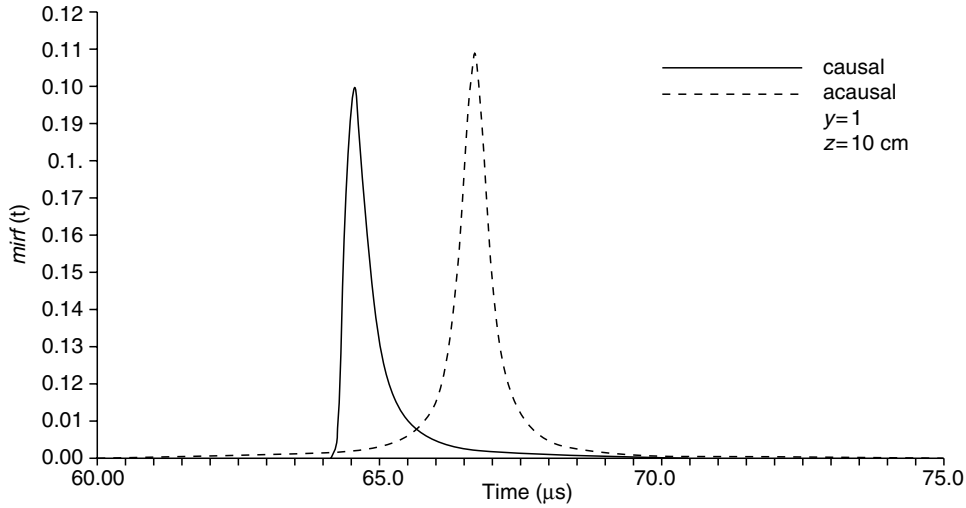

Figure 4.10 Comparison of causal time *mirf* and an acausal nondispersive *mirf* for linear loss (y = 1) for a propagation distance of 10 cm and an absorption coefficient of 0.1151 neper/MHz-cm (1 dB/MHz-cm) (from Szabo, 1993).

and is greater than its value at zero frequency, whereas in the acausal case, the phase velocity is constant.

A second calculation, for propagation in the same material to a depth of 10 cm, is shown in Figure 4.10. Note that the amplitude has dropped by a factor of 10 and the timescale has been expanded by a factor of 10. Careful observation shows that the time delays for the causal model at the 1-cm distance are slightly earlier (about 1% of the total delay) than the *mirf* for the 10-cm distance because more high frequencies get through the shorter distance.

It is possible to generalize these results through the scaling theorem. Rewriting the material transfer function (*MTF*) into an equivalent scaled function,

$$MTF(f) = M(af) \tag{4.21a}$$

in which

$$a = (\alpha_1 z)^{1/y} \tag{4.21b}$$

leads to a material impulse response function (*mirf*) through the scaling theorem,

$$mirf(t) = \Im^{-1}[MTF(f)] = \Im^{-1}[M(af)] = (1/a)m(t/a) \tag{4.22}$$

This time relationship, Eq. (4.22), provides a more direct and intuitive understanding of how loss changes with distance than the more often-used MTF. For $y = 1$, this relation shows that the amplitude of the *mirf* drops by $1/z$ and expands in length by z. Figures 4.9 and 4.10 show, to first order, how the amplitude drops by a factor of 10 and the response elongates by a factor of 10 in accordance with Eq. (4.22). Interest-

ingly, the *mirf* waveform shape and area are nearly maintained! In another example for $y = 2$, Eq. (4.22) shows that amplitude falls off more gradually with distance as $1/\sqrt{z}$. Figure 4.4 shows how amplitude falls as $1/a$ for $y = 1.5$.

More formally, the *MTF* scaling relation, Eq. (4.21a), can be rewritten in the following way:

$$M(af) = exp\left\{\left[-(\alpha_1 z)^{1/y}|f|\right]^y\right\} exp\left\{-i\left[2\pi(\alpha_1 z)^{1/y} f/\left[(\alpha_1 z)^{1/y} c_0\right] + \hat{\beta}_E\left[(\alpha_1 z)^{1/y} f\right]\right]\right\} \tag{4.23a}$$

$$M(af) = exp\{-[a|f|]^y\} exp\left\{-i\left[2\pi af/(ac_0) + \hat{\beta}_E(af)\right]\right\}$$

where

$$\hat{\beta}_E\left[(\alpha_1 z)^{1/y} f\right] = \beta_E(f) \tag{4.23b}$$

so that the material impulse response is found from the inverse Fourier transform,

$$\mathfrak{I}_{-i}^{-1}\{MTF[f]\} = \mathfrak{I}^{-1}\{M[af]\} = \mathfrak{I}^{-1}\left\{M\left[(\alpha_1 z)^{1/y} f\right]\right\} = \left[1/(\alpha_1 z)^{1/y}\right] m\left[t/(\alpha_1 z)^{1/y}\right] \tag{4.24}$$

Equations (4.23) and (4.24) are exact formulations of the scaling relations and include the effects of dispersion. To first order, the shapes of the *mirf* functions at different distances are nearly the same except for scaling, and if we assume the slight differences in delay are negligible (they will be small when applied to finite bandwidth pulses), then losses can be explained through the scaling of the material impulse response functions with distance. In summary, Eq. (4.24) provides an intuitively satisfying picture of loss in the time domain through the *mirf*. The amplitude of the *mirf* falls by $1/a$, and the *mirf* widens by a factor of a with distance.

4.4.2 Pulse Propagation: Interactive Effects in Time and Frequency

In order to apply this scaling principle to the propagation of pulses in lossy media, the interaction of the pulse characteristics, with the constantly changing *mirf* with distance, must be taken into account. For example, the *mirfs* in Figure 4.4 obey the scaling law, but the corresponding pulses in Figure 4.3 undergo changes in shape and a slightly different drop in amplitude with distance.

A perspective that includes both the time and frequency domain viewpoints is helpful in explaining the changes in pulse propagation in a lossy medium. The bandwidth of a pulse can have a considerable effect on pulse shape during propagation. The Fourier theory, Eq. (4.11), can be applied to predict the shape of a pulse at some point in the medium, if its initial shape at $z = 0$ is known in either the frequency or time domain (illustrated by Figure 4.3). Beginning with Eq. (4.11), we can examine the effects of loss on the spectral magnitude for an initial pulse, which is a sine wave amplitude modulated by a Gaussian envelope, that propagates into a medium that has an absorption with linear frequency dependence, as follows:

$$|P(f, z)| = |P_0(f) MTF(f, z)| \tag{4.25a}$$

$$|P(f, z)| = |\, exp[-b(f - f_c)^2]\, exp(-\alpha_1 |f| z - i\beta z)| \tag{4.25b}$$

The $\neq$ dispersion has a magnitude equal to one, so

$$|P(f, z)| = exp[-b(f - f_c)^2]\, exp(-\alpha_1 |f| z) \tag{4.25c}$$

By differentiating this magnitude with respect to frequency and setting the result to zero, we obtain the position of the spectral peak as a function of propagation distance,

$$\partial |P(f, z)| / \partial z = [-2b(f - f_c) - \alpha_1 |f| z] |P(f, z)| = 0 \tag{4.26a}$$

and solving for f gives

$$f_{peak} = f_c - \frac{\alpha_1 z}{2b} \tag{4.26b}$$

This result indicates a downshift in peak frequency as depth z is increased. Since a smaller value of b indicates a broader original bandwidth, Eq. (4.26b) shows a greater downshift for wider bandwidths, as shown in Figure 4.11.

Recall from Eq. (4.11a) that the overall spectrum at a depth is the product of the *MTF* for that depth multiplied by the spectrum of the initial pulse. To explore these effects in more detail, we plot the magnitude of spectra for 10-MHz center frequency

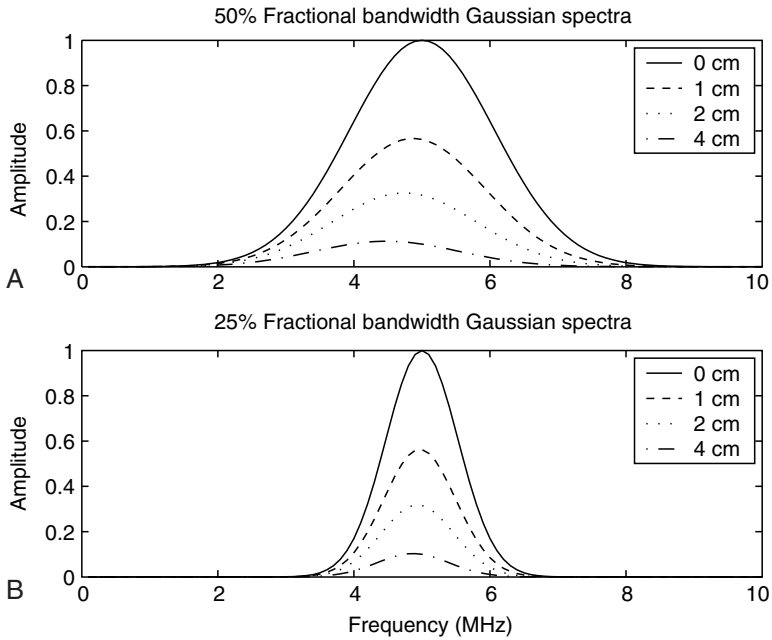

Figure 4.11 (A) Downshift in peak frequency of spectra for a Gaussian-pulse input pulse with a 50% fractional bandwidth as a function of increasing depth in a medium with 1 dB/MHz-cm linear frequency loss dependence. (B) Spectra for a Gaussian pulse with 25% fractional bandwidth.

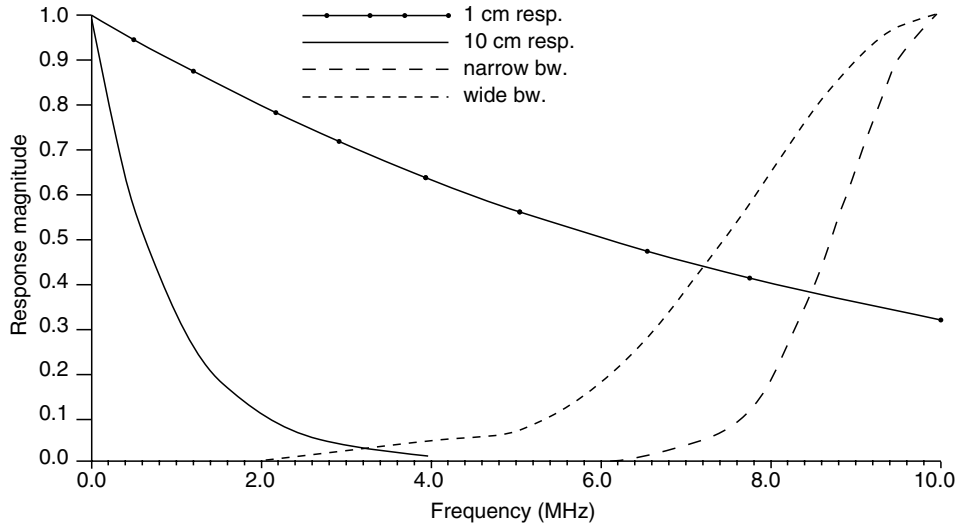

Figure 4.12 On the left are curves for material transfer functions for $y = 1$, $z = 1$, and $z = 10$ cm, and an absorption coefficient of 0.1151 neper/MHz-cm (1 dB/MHz-cm). On the right are curves for the spectral magnitudes of a narrowband Gaussian (long dashes, 25% fractional bandwidth) and wideband Gaussian (short dashes, 50% fractional bandwidth). Both spectra have a center frequency of 10 MHz (from Szabo, 1993).

Gaussian starting pulses with fractional bandwidths of 25% and 50% (on the right side of Figure 4.12). On the left side of this figure are *MTFs* for distances of 1 and 10 cm, for a medium with linear frequency absorption ($y = 1$) and a coefficient of 1dB/MHz-cm (0.1151 neper/MHz-cm). The underlying causes for spectral downshift are evident in this figure. For the *MTF* for a 1-cm depth, the considerable overlap of spectra shows that the product of spectra will result in a high peak frequency. In contrast, there is little interaction between the *MTF* for 10 cm and the Gaussian spectra. The overlap, and consequently, the resulting peak frequency, is lower for the broader bandwidth.

The effects of bandwidth on pulses can be seen by comparing pulse envelopes with the *mirfs* corresponding to the same propagation distances. This perspective on loss mechanisms is found in Figures 4.13 and 4.14 for the time domain plots of the analytic envelopes of propagated pulses that are compared with the corresponding *mirfs* used for the calculations in Figures 4.9 and 4.10. For the 1-cm distance (Figure 4.13), the *mirf* is narrow, the delays of the peaks remain grouped together, and the original pulse envelopes are relatively unchanged. At a larger distance ($z = 10$ cm), the effects of dispersion alter both the delays of the peaks and the shapes of the envelopes in Figure 4.14.

4.4.3 Pulse Echo Propagation

In order to cover the effects of absorption to pulse echoes, both the effect of reflections and the return path must be included. For a round-trip path, the *MTF* for each

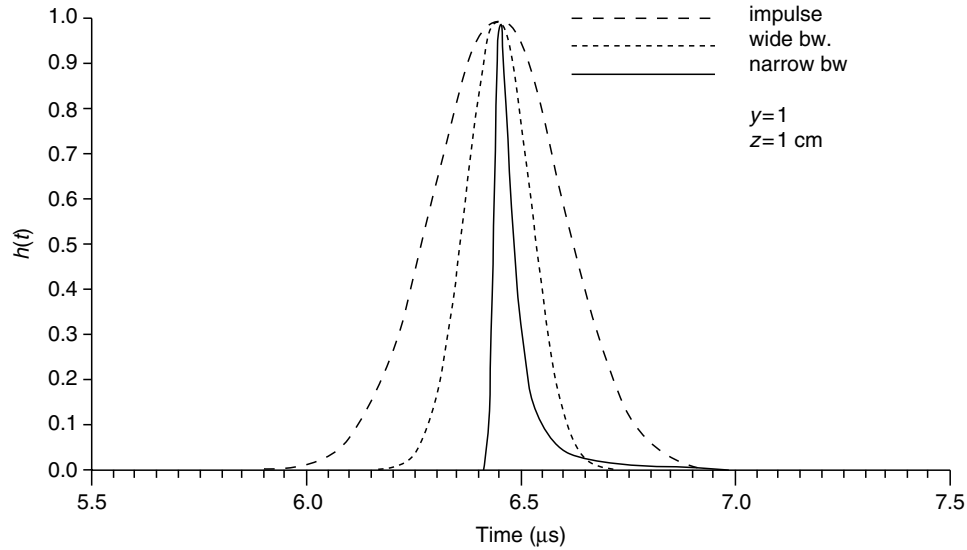

Figure 4.13 (Solid curve) Material impulse response function (*mirf*) for $y = 1$, $z = 1$ cm, and an absorption coefficient of 0.1151 neper/MHz-cm (1 dB/MHz-cm). (Long dashes) Pulse envelope of a mirf convolved with narrowband Gaussian (25% fractional bandwidth) input pulse. (Short dashes) Pulse envelope of a *mirf* convolved with wideband Gaussian (50% fractional bandwidth) input pulse curves normalized to one (from Szabo, 1993).

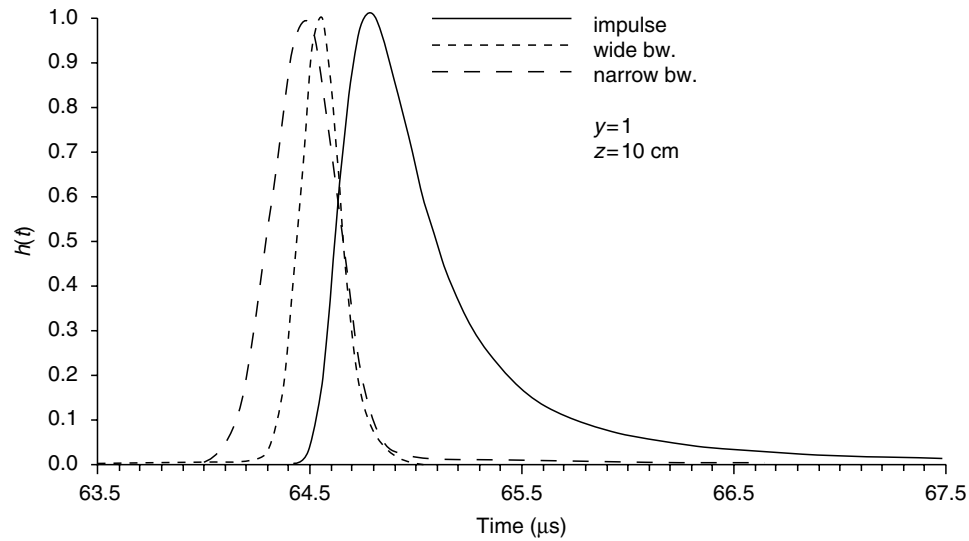

Figure 4.14 (Solid curve) *Mirf* for $y = 1$, $z = 10$ cm, and an absorption coefficient of 0.1151 neper/MHz-cm (1 dB/MHz-cm). (Long dashes) Pulse envelope of a *mirf* convolved with narrowband Gaussian (25% fractional bandwidth) input pulse. (Short dashes) Pulse envelope of a *mirf* convolved with wideband Gaussian (50% fractional bandwidth) input pulse curves normalized to one (from Szabo, 1993).

part of the propagation path is accounted for by multiplying the individual *MTF*s. In general, for paths z_1 and z_2, the exponential nature of the *MTF*s result in an overall *MTF* of $MTF(f, z) = exp[\gamma_T(f)(z_1 + z_2)]$. The corresponding time domain equivalent is the convolution of a *mirf* for z_1 and one for z_2.

To add reflections to a lossy medium, the analysis of the last chapter on reflections and wave propagation can be extended. A simple modification of the ABCD transmission line matrix can be made. For the transmission line matrix for a path length (d), hyperbolic functions replace the trigonometric ones, and γ replaces k in the arguments. Then the matrix elements are

$$\begin{pmatrix} cosh(\gamma d) & Z_M\, sinh(\gamma d) \\ sinh(\gamma d)/Z_M & cosh(\gamma d) \end{pmatrix} \tag{4.27}$$

where *sin h* and *cos h* are the hyperbolic *sine* and *cosine* functions of complex argument. With these changes, the matrix approaches for reflections and mode conversion can be combined with losses.

4.5 PENETRATION AND TIME GAIN COMPENSATION

In order to compensate for the effects of absorption and focusing, imaging systems have a method called time gain compensation built in as a set of controls. The depth dimension of the image is divided into horizontal (linear format) or radial (sector format or curved linear array format) strips, each of which is connected to a separate amplifier stage with a variable gain. These gain controls can be adjusted manually to boost the gain independently in each strip zone. The net effect of these gains is that they provide a means to increase gain with depth in a stepwise manner in order to offset the effects of absorption. Adjustments in time gain compensation (TGC) are made to approximate a uniform background level throughout the field of view (illustrated in Figure 4.15). For this example, the overall absorption as a function of depth (z) is divided into four zones, each of which has an amplification gain adjusted to offset the average loss in the zone.

The penetration depth of an imaging system can be determined from a knowledge of the effective dynamic range of the system and the loss in a phantom or body, as well as from the fact that round-trip absorption decays as $exp(-\alpha 2z)$. For example, if the dynamic range (*DR*) of the system was 100 dB, and the one-way loss was 5 dB/cm at 5 MHz, then if $DR = \alpha_{dB} 2z$, the penetration depth is $z = 10$ cm.

4.6 HOOKE'S LAW FOR VISCOELASTIC MEDIA

Hooke's law, which shows that the proportionality of stress to strain holds only for purely elastic media, was described in Chapter 3. A modified Hooke's law for viscoelastic media (elastic media with losses) is (Auld, 1990):

$$T = C{:}\, S + \eta{:}\frac{\partial S}{\partial t} \tag{4.28a}$$

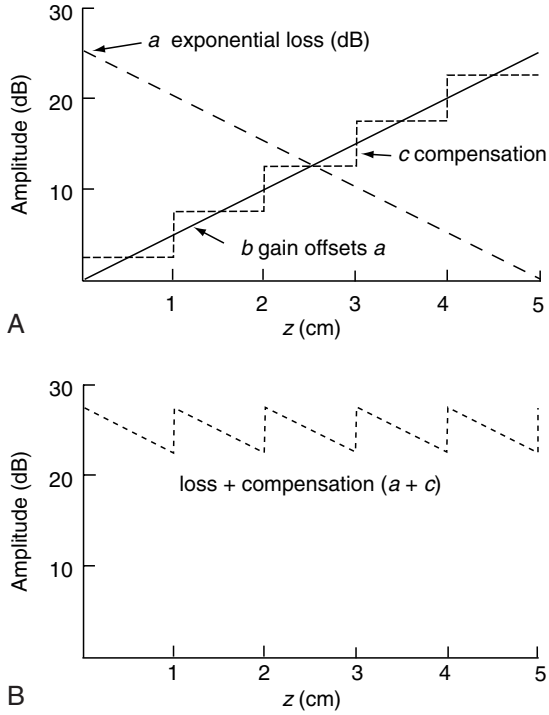

Figure 4.15 (A) Exponential decay of round-trip loss with depth in dB and (*b*) gain to offset loss in dB. Gain is approximated by (*c*) stepwise five TGC zones with depth for compensation. (B) Net effect of compensation (*c*) and absorption (*a*) on background level in image.

where C is an elastic stiffness constant matrix and η is a viscosity stiffness constant matrix of the same size. The Voigt dashpot, or low-frequency version of a thermoviscous model for a single cell, corresponding to this equation is given by Figure 4.16a. The spring on the left of Figure 4.16a represents the first elastic term of Eq. (4.28a). The dashpot on the right of this figure introduces loss and symbolizes the second term of Eq. (4.28a). The Fourier transform of this modified Hooke's law is

$$T(f) = C{:}S(f) + i\omega\eta{:}S(f) \tag{4.28b}$$

For single-frequency cases, Eq. (4.28b), has led to the concept of Hooke's law with a complex elastic constant, $C + i\omega\eta$ (Auld, 1990).

An alternative approach is depicted in Figure 4.16b, in which the dashpot is replaced by a more general response function, $r(t)$. In this case, the counterpart to Eq. (4.28a) is

$$T = C{:}S + \eta{:}r(t) *_t S \tag{4.29a}$$

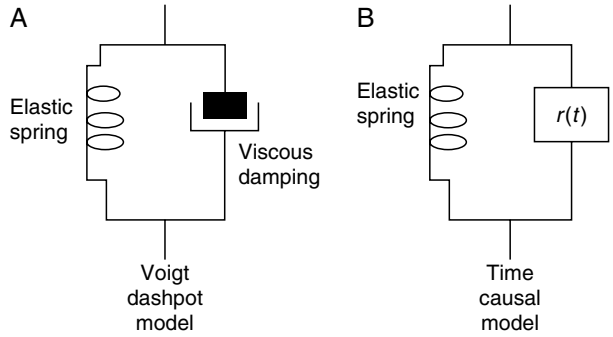

Figure 4.16 Models for loss in viscoelastic materials. (A) Relaxation or Voigt dashpot model. (B) Time causal model (from Szabo and Wu, 2000, Acoustical Society of America).

and its Fourier transform is

$$T(f) = C{:}\,S(f) + i\eta{:}\,R(f)S(f) \tag{4.29b}$$

so that the concept of a complex elastic constant no longer holds except at a single frequency. Eq. (4.29b) shows that the imaginary term changes in a more complicated way than that of Eq. (4.28b) as a function of frequency. This second model is the time causal model, which has more general applicability, and Eq. (4.29) reduces to Eq. (4.28) for the case of $y = 2$. Expressions for $r(t)$ can be found in Szabo and Wu (2000).

4.7 WAVE EQUATIONS FOR TISSUES

4.7.1 Voigt Model Wave Equation

If Eq. (4.28a) for the thermoviscous model is applied to the derivation of a wave equation for this type of solid (Auld, 1990), the following equations can be obtained for a plane wave propagating along the z axis of an isotropic solid:

$$\frac{\partial^2 v}{\partial z^2} - \frac{1}{c_0^2}\rho\frac{\partial^2 v}{\partial t^2} + \frac{\eta_{ii}}{C_{ii}}\frac{\partial^3 v}{\partial z^2 \partial t} = 0 \tag{4.30a}$$

where $v = v_m$ is the particle velocity in the direction m such as z, and the speed of sound is

$$c_0 = \sqrt{C_{ii}/\rho} \tag{4.30b}$$

Note the addition of a third loss term at the end of the usual wave equation. Here this type of equation applies equally well to simple cases of elastic longitudinal wave and shear wave propagation in an isotropic medium through the use of the appropriate elastic constants, C_{11} and C_{44}, respectively, or for fluids by the appropriate constants (Szabo, 1994; Szabo and Wu, 2000).

When this equation is converted to the frequency domain and a solution for the particle velocity of the form and direction associated with a specific mode,

$$v(z, \omega) = v_0(0, \omega)\, exp(i\omega t + \gamma z) \tag{4.31}$$

is substituted in Eq. (4.30a), γ can be obtained. Equations (4.12) and (4.13) are the result of this operation. Here $\alpha_1 = \sqrt{\rho/2C_{ii}}$ and $\tau = \eta_{ii}/C_{ii}$.

In order to derive a useful low-frequency approximation to this model, substitute the plane wave approximation,

$$\frac{\partial v}{\partial z} = \frac{1}{c_0}\frac{\partial v}{\partial t} \tag{4.32}$$

into Eq. (4.30a). The result is

$$\frac{\partial^2 v}{\partial z^2} - \frac{1}{c_0^2}\frac{\partial^2 v}{\partial t^2} + L_0\frac{\partial^3 v}{\partial t^3} = 0 \tag{4.33a}$$

where

$$L_0 = \frac{\eta_{ii}}{C_{ii}c_0^2} \tag{4.33b}$$

This approach results in a quadratic frequency dependence for loss ($\alpha = \alpha_1 f^2$) and a nearly constant sound speed with frequency to first order; therefore, it is quite limited in mimicking the observed behavior of tissue listed in Appendix B and illustrated by Figure 4.2.

4.7.2 Multiple Relaxation Model Wave Equation

One way of overcoming the discrepancy between the thermoviscous model and observed power law absorption characteristics of tissues is to apply a fitting procedure to Eq. (4.6a) involving a superposition of several time constants. As described by Nachman *et al*. (1990), the multiple relaxation wave equation results in quite complicated expressions for attenuation and phase velocity. At low frequencies, these equations are approximately as follows:

$$\alpha(\omega) \cong \frac{\rho c \omega^2}{2}\sum_n \kappa_n \tau_n \tag{4.34a}$$

$$c(\omega) \cong c \tag{4.34b}$$

where constants κ_n and time constants τ_n are associated with each relaxation mode (n). This multiple relaxation model corresponds to the tissue model with different molecules, each with its own relaxation constant and sound speed.

4.7.3 Time Causal Model Wave Equations

Are there wave equations with losses that correspond more directly with the frequency power law behavior of absorption for many types of materials? Szabo (1994)

and Szabo and Wu (2000) have shown that, in general, the wave equation can be written as

$$\nabla^2 v - \frac{1}{c_0^2}\frac{\partial^2 v}{\partial t^2} - L_\gamma * v = 0 \tag{4.35}$$

where L_γ is a time convolution propagation operator determined by the constraints of causality in the time domain (explained in Section 4.3.4). Specifically, the form of L_γ depends on whether y is an even or odd integer or a noninteger, so we denote it as $L_\gamma = L_{\alpha,\, y,\, t}$. It is helpful to express higher order derivatives in the abbreviated notation, $v_{z^n} = \partial^n v/\partial z^n$. For example, if $n = 2$, $v_{zz} = \partial^2 v/\partial z^2$. For the even integer case, Eq. (4.35) becomes

$$\nabla^2 v - \frac{1}{c_0^2} v_{tt} - (-1)^{y/2}\frac{2\alpha_0}{c_0} v_{t^{y+1}} = 0 \tag{4.36}$$

The form of L_γ in this instance of even integers has the specific form,

$$L_{\alpha,\, y,\, t} * v = (-1)^{y/2}\frac{2\alpha_0}{c_0} v_{t^{y+1}} = (-1)^{y/2}\frac{2\alpha_0}{c_0}\delta^{y+1}(t) * v \tag{4.37a}$$

For the y as an odd integer case,

$$L_{\alpha,\, y,\, t} * v = \frac{4h_0}{c_0}\int_{-\infty}^{t} \frac{v(t')}{(t-t')^{y+2}}dt' = \frac{4h_0}{c_0}\frac{H(t)}{t^{y+2}} * v \tag{4.37b}$$

in which

$$h_0 = -\alpha_1(y+1)!(-1)^{(y+1)/2}/\pi \tag{4.37c}$$

and

$$\alpha_1 = \frac{\eta_{ii}}{2c_0 C_{ii}} \tag{4.37d}$$

Similarly, for y as a noninteger,

$$L_{\alpha,\, y,\, t} * v = \frac{4h_{ni}}{c_0}\int_{-\infty}^{t} \frac{v(t')}{|t-t'|^{y+2}}dt' = \frac{4h_{ni}}{c_0}\frac{H(t)}{|t|^{y+2}} * v \tag{4.37e}$$

where

$$h_{ni} = \alpha_0 \Gamma(y+2)\sin(\pi y/2)/\pi \tag{4.37f}$$

More details about the derivation of a wave equation for a viscoelastic solid can be found from equations of the previous forms (Szabo and Wu, 2000). An implementation of the version of these equations for fluids (Szabo, 1994) can be found in Norton and Novarini (2003). They demonstrate that absorption and dispersion can be calculated by these operators directly in the time domain.

References

Auld, B. A. (1990). *Acoustic Fields and Waves in Solids*. **2**, Vol. 1, Krieger Publishing, Malabar, FL.

Bamber, J. C. (1986). *Physical Principles of Medical Ultrasonics*. C. R. Hill (ed.). John Wiley & Sons, Chichester, UK, pp. 118–199.

Bamber, J. C. (1998). Ultrasonic properties of tissue. *Ultrasound in Medicine* F. A. Duck, A. C. Baker, H. C. Starritt (eds.). Institute of Physics Publishing, Bristol, UK.

Blackstock, D. T. (2000). *Fundamentals of Physical Acoustics*. John Wiley & Sons, New York.

Bracewell, R. (2000). *The Fourier Transform and its Applications*. McGraw-Hill, New York.

Duck, F. A. (1990). *Physical Properties of Tissue*. Academic Press, New York.

He, P. (1998a). Simulation of ultrasound pulse propagation in lossy media obeying a frequency power law. *IEEE Trans. Ultrason. Ferroelectr. Freq. Control* **45**, 114–125.

He, P. (1998b). Determination of ultrasonic parameters based on attenuation and dispersion measurements. *Ultrason. Imaging* **20**, 275–287.

He, P. (1999). Experimental verification of models for determining dispersion from attenuation. *IEEE Trans. Ultrason. Ferroelectr. Freq. Control* **46**, 706–714.

Kinsler, L. E., Frey, A. R., Coppens, A. B., & Sanders, J. V. (2000). *Fundamentals of Acoustics*. John Wiley & Sons, New York.

Krönig, R. D. L. (1926). On the theory of dispersion of x-rays. *J. Opt. Soc. Am.* **12**, 547–557.

Nachman, A. I., Smith, J. F. III, and Waag, R. C. (1990). An equation for acoustic propagation in inhomogeneous media with relaxation losses. *J. Acoust. Soc. Am.* **88**, 1584–1595.

Norton, G. V. and Novarini, J. G. (2003). Including dispersion and attenuation directly in the time domain for wave propagation in isotropic media. *J. Acoust. Soc. Am.* **113**, 3024–3031.

Szabo, T. L. (1993). *Linear and Nonlinear Acoustic Propagation in Lossy Media*, Ph.D. thesis. University of Bath, Bath, UK.

Szabo, T. L. (1994). Time domain wave equations for lossy media obeying a frequency power law. *J. Acoust. Soc. Am.* **96**, 491–500.

Szabo, T. L. (1995). Causal theories and data for acoustic attenuation obeying a frequency power law. *J. Acoust. Soc. Am.* **97**, 14–24.

Szabo, T. L. and Wu, J. (2000). A model for longitudinal and shear wave propagation in viscoelastic media. *J. Acoust. Soc. Am.* **107**, 2437–2446.

Trousil, R. L., Waters, K. R., and Miller, J. G. (2001). Experimental validation of the use of Kramers–Krönig relations to eliminate the phase sheet ambiguity in broadband phase spectroscopy. *J. Acoust. Soc. Am.* **109**, 2236–2244.

Waters, K. R., Hughes, M. S., Mobley, J., Brandenburger, G. H., and Miller, J. G. (2000a). On the applicability of Kramers–Krönig relations for ultrasonic attenuation obeying a frequency power law. *J. Acoust. Soc. Am.* **108**, 556–563.

Waters, K. R., Hughes, M. S., Brandenburger, G. H., and Miller, J. G. (2000b). On a time-domain representation of the Kramers–Krönig dispersion relations. *J. Acoust. Soc. Am.* **108**, 2114–2119.

Wojcik, G. L., Mould Jr. J. C., Ayter, S., and Carcione, L. M. (1998). A study of second harmonic generation by focused medical transducer pulses. *Proc IEEE Ultrason Symp*, 1583–1588.

This page intentionally left blank

5 TRANSDUCERS

Chapter Contents

5.1 INTRODUCTION TO TRANSDUCERS

The one indispensible part of a diagnostic imaging system is the transducer. Transducers come in many shapes, frequencies, and sizes. Specific forms of transducers for different clinical applications and scanning methods will be covered in Chapter 10. This chapter concentrates on the essential questions: How do transducers work? What are they made of? How can piezoelectric materials for transducers be compared? What are the characteristics of transducers? How can transducers be modeled and designed? How are they constructed? What are promising new developments for transducers of the future?

5.1.1 Transducer Basics

This section presents a basic intuitive model of a piezoelectric transducer to describe its essential acoustic and electrical characteristics. The simplest transducer is a piece of piezoelectric material with electrodes on the top and bottom (depicted in Figure 5.1). Unlike the drawing at the top of this figure, the top has a cross-sectional area (A) and sides that are much longer (>10X) than the thickness (d). Piezoelectric material is dielectric; therefore, it has a clamped capacitance,

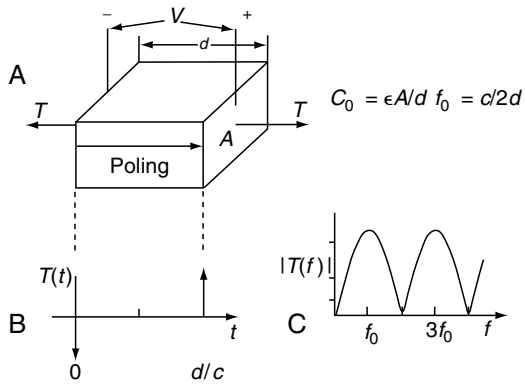

Figure 5.1 (A) Diagram for a thickness expander piezoelectric crystal radiating into a medium matched to its impedance. (B) Stress time response. (C) Stress frequency response.

$$C_0 = \varepsilon^S A/d \tag{5.1}$$

in which ε^S is a clamped dielectric constant under the condition of zero strain. Because of piezoelectricity, the Hooke's law for this capacitor has an extra term,

$$T = C^D S - hD \tag{5.2}$$

in which (h) is a piezoelectric constant. The elastic stiffness constant (C^D) is obtained under a constant dielectric displacement (D), and (E) is the electric field,

$$D = \varepsilon^S E = \frac{\varepsilon^S AV}{dA} = C_0 V/A \tag{5.3}$$

If a voltage impulse is applied across the electrodes, the piezoelectric effect creates forces at the top and bottom of the transducer, given by

$$F(t) = TA = (hC_0V/2)[-\delta(t) + \delta(t - d/c)] \tag{5.4}$$

for which we have assumed that the media outside the electrodes has the same acoustic impedance as the transducer (see Figure 5.1a). To obtain the spectrum of this response, take the Fourier transform of Eq. (5.4),

$$F(f) = -i(hC_0V)e^{-i\pi fd/c} sin[\pi(2n+1)f/2f_0] \tag{5.5}$$

an expression with maxima at odd harmonics (note that $n = 1, 2, 3$, etc.) of the fundamental resonance $f_0 = c/2d$ (shown in Figure 5.1c). The speed of sound between the electrodes is given by $c = \sqrt{C^D/\rho}$.

5.1.2 Transducer Electrical Impedance

Because of the forces generated by the transducer, the electrical impedance looking through the voltage terminals is affected. A radiation impedance, (Z_A) is added to the capacitive reactance so that an equivalent circuit (see Figure 5.2a) for the overall electrical impedance is

$$Z_T = Z_A - i(1/\omega C_0) = R_A(f) + i[X_A(f) - 1/\omega C_0] \tag{5.6}$$

Here Z_A is radiation impedance, of which R_A and X_A are its real and imaginary parts.

What is R_A? To first order, it can be found from the total real electrical power flowing into the transducer for an applied voltage (V) and current (I)

$$W_E = II^* R_A/2 = |I^2|R_A/2 \tag{5.7a}$$

where current is $I = i\omega Q = i\omega C_0 V$. The total power radiated from both sides of the transducer into a surrounding medium of specific acoustic impedance, $Z_C = \rho cA$ (equal to that of the crystal) is

$$W_A = ATT^*/(2Z_C/A) = A^2|F(f)/A|^2/2Z_C = |hC_0V\, sin(\pi f/2f_0)|^2/2Z_C \tag{5.7b}$$

Setting the powers of Eqs. (5.7a) and (5.7b) equal, we can solve for R_A,

$$R_A(f) = R_{AC}\, sinc^2(f/2f_0) \tag{5.8a}$$

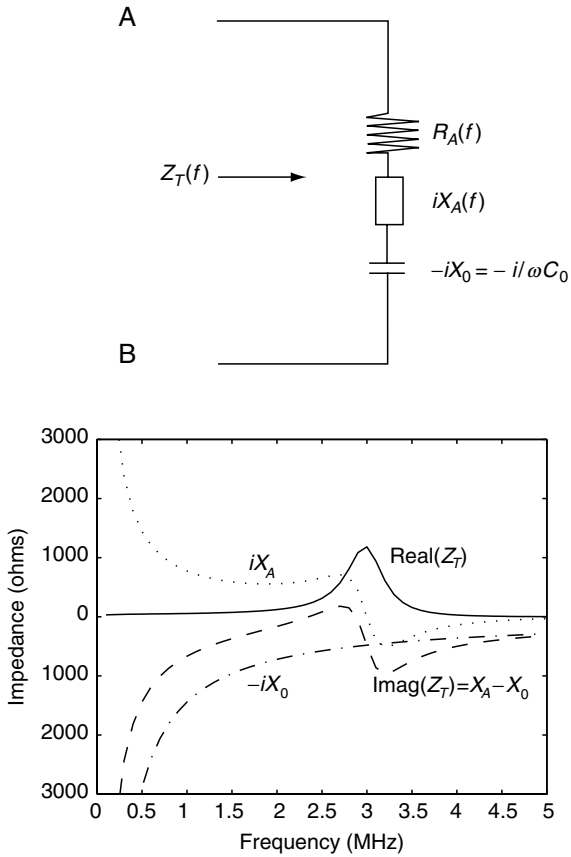

Figure 5.2 (A) Transducer equivalent circuit. (B) Transducer impedance as a function of frequency.

where $sin\,c(x) = sin(\pi x)/(\pi x)$ and

$$R_{AC} = \frac{k_T^2}{4f_0C_0} = \frac{d^2k_T^2}{2A\varepsilon^S} \tag{5.8b}$$

The electroacoustic coupling constant is k_T, and $k_T = h/\sqrt{C^D/\varepsilon^S}$. Interesting properties of R_{AC} include an inverse proportionality to the capacitance and area of the transducer and a direct dependence on the square of the thickness (d). Note that at resonance,

$$R_A(f_0) = \frac{k_T^2}{\pi^2 f_0 C_0} \tag{5.8c}$$

Network theory requires that the imaginary part of an impedance be related to the real part through a Hilbert transform (Nalamwar and Epstein, 1972) (Appendix A), so the radiation reactance can be found as

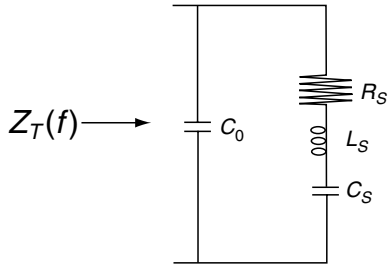

Figure 5.3 Electrical lumped element circuit mimicking basic electrical–transducer impedance.

$$X_A(f) = \Im_{Hi}[R_A(f)] = R_{AC}\frac{[sin(\pi f/f_0) - \pi f/f_0]}{2(\pi f/2f_0)^2} \tag{5.8d}$$

The transducer impedance is plotted as a function of frequency in Figure 5.2b. Here R_A is maximum at the center frequency, where X_A is zero.

Because both R_A and X_A are complicated functions of frequency, it is useful to understand them in terms of a purely electrical lumped element equivalent circuit (Mason, 1964; Kino, 1987). This circuit mimics the electrical impedance characteristic of a simple transducer with acoustic loads Z_1 and Z_2 on the electroded faces of the piezoelectric material. The lumped element circuit with a series resonance (ω_1) and a parallel antiresonance (ω_0) is shown in Figure 5.3. The values of these parameters are given as follows:

$$R_S = \frac{\pi(Z_1 + Z_2)}{4k_T^2\omega_1 C_0 Z_C} \tag{5.9a}$$

$$L_S = \frac{1}{\omega_1^2 C_S} \tag{5.9b}$$

$$C_S = \frac{8C_0k_T^2/\pi^2}{1 - 8k_T^2/\pi^2} \tag{5.9c}$$

This type of representation is limited to the simplest kinds of transducer configurations, but it is useful for explaining and simulating the electrical characteristics of a transducer impedance. In other words, this circuit simulates the real and imaginary parts of the electrical transducer impedance for these simple acoustic loads (shown in Figure 5.2). However, because this circuit is just electrical, it does not describe the acoustic response. Therefore, it is not a replacement for a more complete model.

5.1.3 Summary

In summary, the piezoelectric element sends out two acoustic signals for each electrical excitation in this simple model. When transducers resonate, they have a distinctive electrical impedance signature that can be measured electrically. The spectral

response of a transducer peaks at odd multiples of the fundamental frequency. Most piezoelectric transducers are reciprocal, so they act as receivers equally well.

If the acoustic impedances on either side of the crystal differ from that of the crystal, then multiple reflections occur at the interfaces as described by Redwood (1963). A pair of oppositely signed stress pulses are created at each crystal boundary in this case. In order to develop a more complete transducer equivalent circuit model that accounts for these effects in both the time and frequency domains, it is necessary to discuss transducer geometry, construction, and piezoelectric materials.

5.2 RESONANT MODES OF TRANSDUCERS

5.2.1 Resonant Crystal Geometries

Key factors in determining transducer parameters are the geometry or shape of the piezoelectric material, the crystallographic orientation of the piezoelectric crystal with respect to the electrical–poling direction, and the placement of the electrodes. Piezoelectric materials are anisotropic, meaning that their properties vary with angle. In other words, depending on which direction the crystal is poled (a process in which a high voltage is applied to opposite sides of a crystal to align domains), the piezoelectric coupling and sound speed can vary. Piezoelectric materials are explained in more detail in Section 5.8.

An important factor in determining transducer performance is the shape or geometry of the piezoelectric material in the transducer. From the simple model of a transducer (explained in Section 5.1.1), the fundamental resonance and odd frequency harmonics, $f_m = (2m + 1)f_0$, correspond to odd multiples of half wavelengths, $(2m + 1)\lambda_0/2$. A practical implementation of this simple resonance idea is the "thickness–expander mode" geometry (see Figure 5.4a), where the lateral dimensions are much greater than the thickness dimension, and *poling* is oriented perpendicular

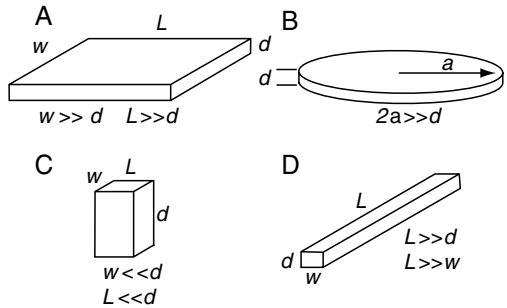

Figure 5.4 Resonator geometries for longitudinal vibration modes along the *z* axis. (A) Thickness-expander rectangular plate. (B) Thickness-expander circular plate disk. (C) Length-expander bar. (D) Width-extensional bar or beam plate.

to the electrodes. In other words, the vibrations are dominated by the thickness direction (z) so that resonances in the lateral directions are so low in frequency that they are negligible (shown in Figures 5.4a and 5.4b for rectangular and circular plates). The appropriate piezoelectric coupling constant for this geometry is the thickness coupling constant (K_T) and the speed of sound (c_T). Electrical polarization is along the z or 001 axis shown as the depth axis (d) for all four geometries in Figure 5.4.

In the early days of ultrasound imaging, transducers were of the thickness–expander type, were usually circular in cross section, and were used in mechanical scanning; however, most of the transducers in use today are arrays. Among the earliest arrays was the annular type (Reid and Wild, 1958; Melton and Thurstone, 1978), with circular concentric rings on the same disk, phased to focus electronically (Foster *et al*., 1989).

The two geometries most relevant to one-dimensional (1D) and two-dimensional (2D) arrays are the length-expander bar and the beam or width-extensional mode (shown in Figures 5.4c and 5.4d). In each case, two dimensions are either much smaller or larger than the third so that only one resonance mode is represented by each picture. In reality, these rectangular geometries are limiting cases of a rectangular parallelepiped, in which three orthogonal coupled resonances are possible; each is determined by the appropriate half-wavelength thickness (d, w, or L). In the cases shown in Figure 5.4, the relative disparity in the lateral resonance dimensions compared with the thickness dimension allow them to be neglected relative to a dominant thickness resonance determined by geometry.

The bar geometry (Figure 5.4c) has an antiresonant frequency determined by length, which is the dominant dimension. This shape is the one used as piezoelectric pillars in 1–3 composites (to be described in Section 5.8.7) and is also helpful for two-dimensional arrays. Important constants for design are summarized for different piezoeletric materials and geometries in Table B2 in Appendix B. From Figure 5.4.c, the appropriate coupling constant for this geometry is k_{33} and the speed of sound is c_{33}.

The geometry most applicable to elements of one dimensional arrays is the beam mode, in which the length (L), corresponding to an elevation direction, is much greater than the lateral dimensions (Souquet *et al*., 1979; deJong *et al*., 1985). For this representation to be applicable, the width to thickness ratio (w/d) must be less than 0.7. Other w/d ratios will be discussed shortly. One lucky break for transducer designers was that, in general, the coupling constant for this geometry (k_{33}) is significantly greater than k_T (e.g., for PZT-5H, $k_{33} = 0.7$ and $k_T = 0.5$).

The beam mode represents a limiting case. Imagine a steamroller running over a tall piezoelectric element of the beam shape (Figure 5.4d) and changing it into a thickness-expander shape (Figure 5.4a), which is the other extreme. For the cases in between, calculations are necessary to predict characteristics as a function of the ratio w/d (shown in Figure 5.5), in which two sound speed dispersion curves are indicated for different aspect ratios and vibrational modes. For more precise design for w/d ratios of less than 0.7, sound speed dispersion and coupling characteristics must be calculated or measured (Selfridge *et al*., 1980; Szabo, 1982). For w/d ratios of greater than 0.7, spurious multiple resonant modes can degrade transducer performance

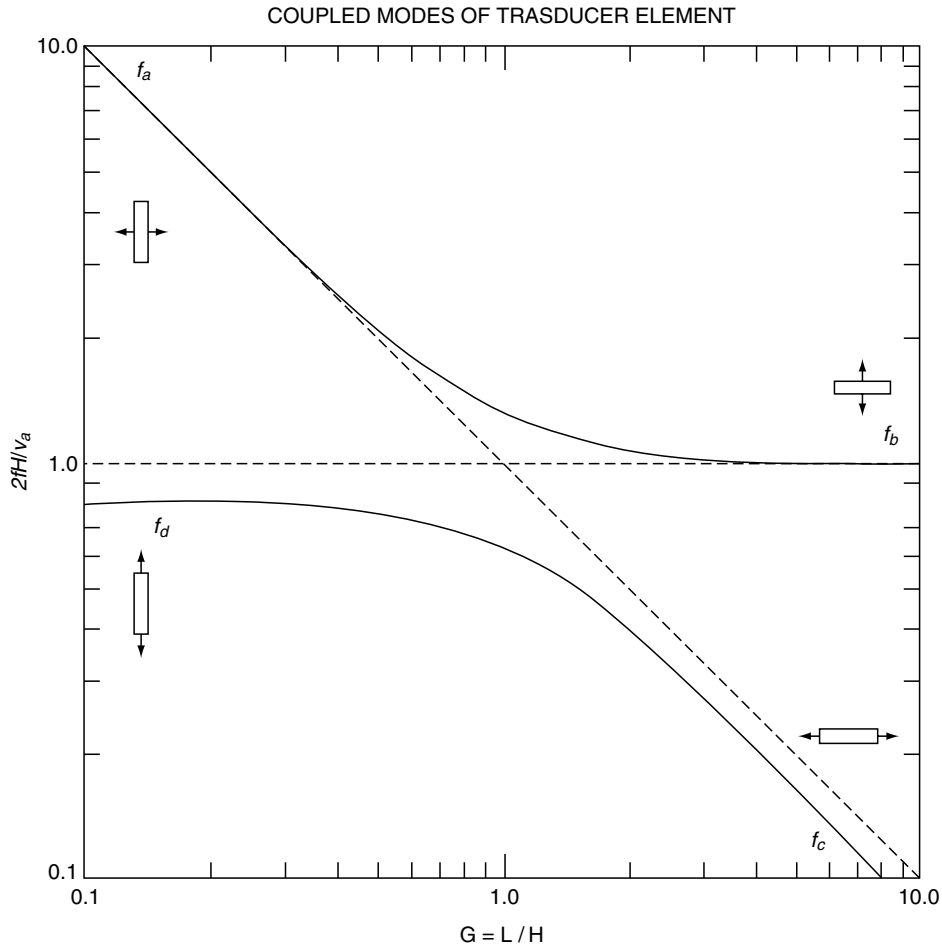

Figure 5.5 Sound speed dispersion (v_a) for a piezoelectric element as a function of aspect ratio ($G = w/d$) (from Selfridge *et al.*, 1980, *IEEE*.).

(de Jong *et al*., 1985). In general, the coupling constant and speed of sound vary with this ratio (Onoe and Tiersten, 1963; Sato *et al*., 1979), as shown in Figure 5.5.

5.2.2 Determination of Electroacoustic Coupling Constants

The relevant equations are given in Selfridge *et al*. (1980).When the input electrical impedance of a crystal of this thickness-expander geometry is measured in air, it has a unique spectral signature. As discussed earlier, the electrical characteristics of a simply loaded crystal are like the circuit of Figure 5.3, which has a resonant and an anti-resonant frequency. These frequencies are related to the coupling constant and sound speed through the following equations:

$$f_a = c_T/2d \tag{5.10a}$$

also known as the antiresonant frequency. The resonant frequency (f_r), can be found from the solution of the transcendental equation,

$$K_T^2 = \frac{\pi f_r}{2f_a}\ cot\ \left(\frac{\pi f_r}{2f_a}\right) \tag{5.10b}$$

where K_T can be calculated from fundamental constants. Alternatively, a resonant and an antiresonant frequency can be measured and used to find the coupling constant experimentally through Eq. (5.10b). Both the electromechanical coupling constant (k_T) and speed of sound (c_T) equations are also given for different geometries in Selfridge *et al*. (1980) and Kino (1987).

5.2.3 Array Construction

How does a single piezoelectric crystal plate fit into the structure of an array? The array begins as a series of stacked layers with a relatively large area or footprint (e.g., 3×1 cm). The crystal and matching layers are bonded together and onto a backing pedestal. This sandwich of materials is cut into rows by a saw or by other means (as Figure 5.6 illustrates). The cut space between the elements is called a "kerf," and the remaining material has a width (w), repeated with a periodicity or pitch (p). Only after the cutting process does an individual crystal element resemble the beam mode shape with a *long* elevation length (L), width (w), and thickness (d). After the elements are cut, they are covered by a cylindrical lens for elevation focusing

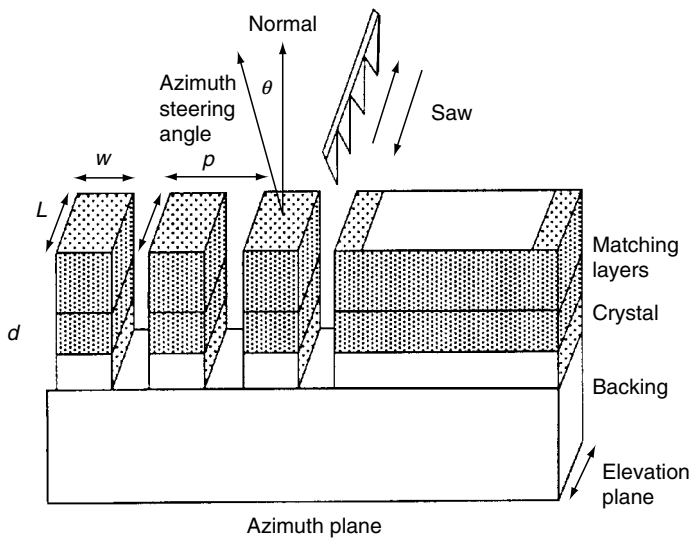

Figure 5.6 A multilayer structure diced by a saw into one-dimensional array elements (from Szabo, 1998, IOP Publishing Limited).

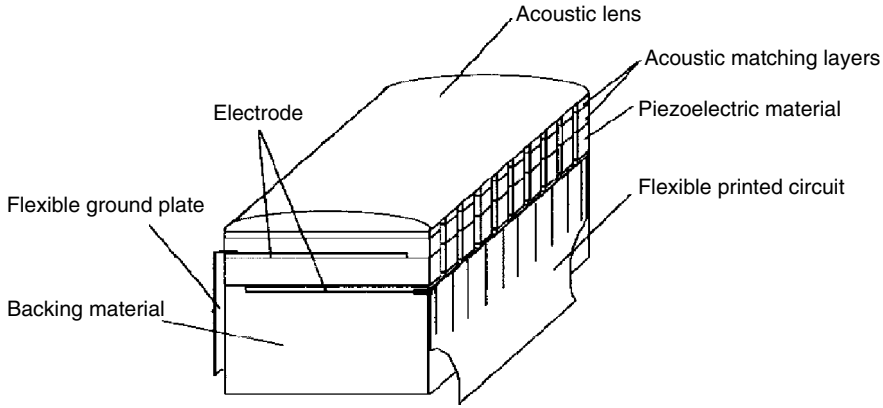

Figure 5.7 Construction of a one-dimensional array with an elevation plane lens (from Saitoh *et al.*, 1999, *IEEE*).

and are connected electrically to the imaging system through a cable. Figure 5.7 shows the overall look of the array before placement into a handle.

A typical design constraint for phased arrays is that the pitch (p) between elements be approximately one-half a wavelength in water. The thickness dimension of the element is also close to one-half a wavelength along the depth direction in beam mode in the crystal material, which has a considerably different speed of sound than water. These constraints often determine the allowable w/d ratio. For two-dimensional arrays, elements have small sides. This is a difficult design problem in which strong coupling can exist among all three dimensions. Models are available for these cases (Hutchens and Morris, 1985; Hutchens, 1986;), and there are materials designed to couple less energy into unwanted modes (Takeuchi *et al.*, 1982). Finite element modeling (FEM) of these geometries is another alternative that can include other aspects of array construction for accurate simulations (McKeighen, 2001; Mills and Smith, 2002).

5.3 EQUIVALENT CIRCUIT TRANSDUCER MODEL

5.3.1 KLM Equivalent Circuit Model

To first order, the characteristics of a transducer can be well described by a one-dimensional equivalent circuit model when there is one dominant resonant mode. To implement a model for a particular geometry, the same equivalent circuit model can be applied, but with the appropriate constants for the geometry selected. This complete model includes all impedances, both acoustic and electrical, as well as signal amplitudes in both forward and backward directions as a function of frequency. By looping through this single-frequency model a number of times, a complex spectrum can be generated, from which a time waveform can be calculated by an inverse Fourier transform.

To connect acoustic and electrical parameters, use will be made of acoustical–electrical analogs (described in Chapter 3). Warren P. Mason (1964) utilized these analogs to derive several models for different piezoelectric transducer geometries. The most applicable model for medical transducers is the thickness-expander model. Based on exactly the same wave equations, a newer model was introduced by Leedom, Krimholtz, and Matthaei (1978). This "KLM model," named after the initials of the authors, gives exactly the same numerical results as the Mason model but has several advantages for design (shown in Figure 5.8).

One of the main advantages of the KLM model is a separation of the acoustical and electrical parts of the transduction process. Three major sections can be seen in Figure 5.8: an electrical group extending from port 3, and two acoustic groups extending to the left and right from a center junction with the electrical group. This partitioning will allow us to analyze these ports separately to improve the design of the transducer. Port 1 will be used to represent forward transmission into water or the body, whereas port 2 will be for the acoustic backing, a load added to modify the bandwidth, and sensitivity of the transducer. Derivations for the physical basis of the KLM model can be found in Leedom *et al*. (1978) and Kino (1987). As shown in Figure 5.8b, the entire model can be collapsed into a single ABCD matrix between the electrical port and the forward acoustic load. The derivation of this matrix from the basic 2×2 ABCD forms introduced in Chapter 3 is explained thoroughly in Appendix C.

The piezoelectric element, described by the KLM model in Figure 5.8, is part of the overall representation of a transducer or an array element. The complete model can be represented by a series of simple ABCD matrices cascaded together

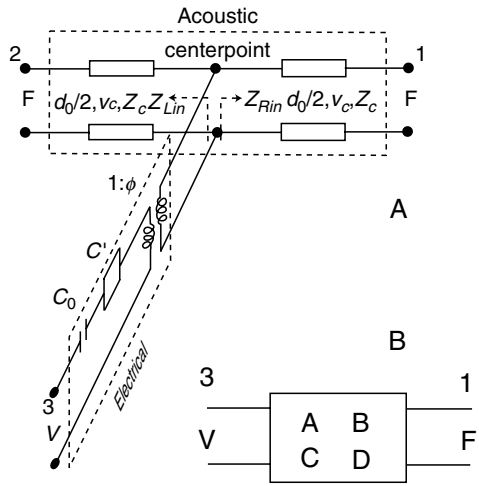

Figure 5.8 (A) Schematic representation of the KLM transducer three-port equivalent circuit model. (B) ABCD representation of the KLM model by an ABCD matrix between the electrical port 3 and acoustic port 1.

(Sittig, 1967; van Kervel and Thijssen, 1983; Selfridge and Gehlbach, 1985) as derived in detail in Appendix C. This derivation forms the basis for a numerical ABCD matrix implementation in the form of MATLAB program xdcr.m.

5.3.2 Organization of Overall Transducer Model

The organization of the model as a whole is illustrated by Figure 5.9. Physically, this model mimics the layers in an element of an array (see Figure 5.7), in which the layers on top of the piezoelectric element are represented by those on the right side of the piezoelectric element in the model (Figure 5.9). The piece from Figure 5.8 for the piezoelectric element is connected through port 3 to an electrical source. These parameters are needed for the piezoelectric element: a crystal that has a thickness (d_0), a speed of sound (c), an area (A), resonant frequency ($f_0 = c/2d_0$), a clamped capacitance ($C_0 = \varepsilon_R^S \varepsilon_0 A/d_0$), an electromechanical coupling constant (k_T), and a specific acoustic impedance ($Z_C = \rho cA$). In the KLM model, an artificial acoustic center is created by splitting the crystal into halves, each with a thickness of $d_0/2$ (refer to Figure 5.8). Each of these halves, as well as all layers, are represented by an acoustic transmission line. The right end load, usually to tissue or water, is represented by a real load impedance, Z_R.

Each layer numbered "n," which can be a matching layer, bond layer, electrode, or lens, is represented by the following acoustic transmission line parameters: an area (A), an impedance (Z_{nR}), a sound speed (c_{nR}), a propagation factor (γ_{nR}), and physical

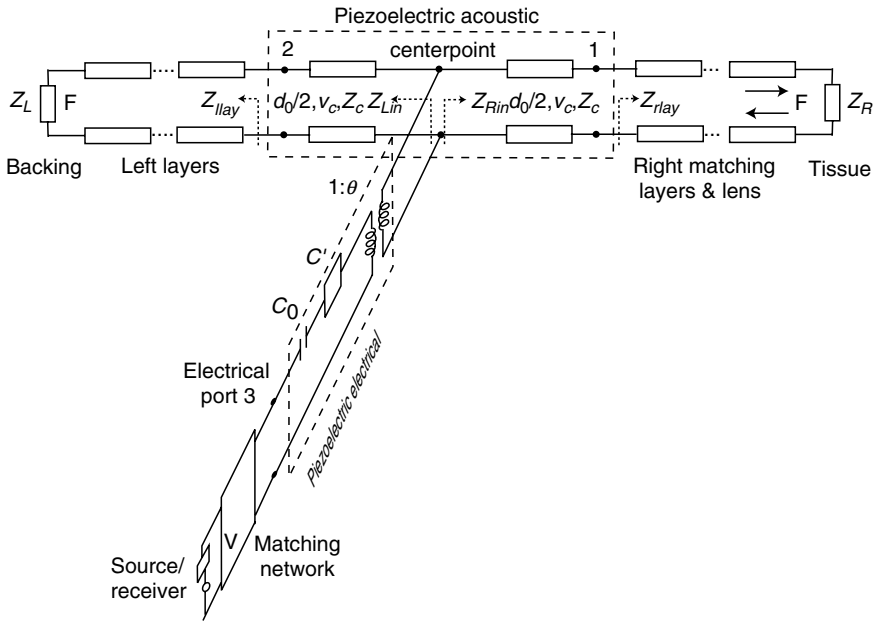

Figure 5.9 Overall equivalent circuit transducer model.

length (d_{nR}). The acoustic impedance looking from port 1 into the series of layers is called Z_{rlay}. Port 2 is usually connected to a backing, represented by a simple load (Z_B), or the acoustic impedance looking to the left is $Z_{llay} = Z_B$. If layers need to be added to the left side of the crystal, the same layer approach can be followed with indices such as d_{nL}. However, there is usually not a design incentive for doing so. Because force, rather than stress, is a key acoustic variable, all acoustic impedances are multiplied by the area (A), as is done for the definition of Z_C. More details can be found in Appendix C.

5.3.3 Transducer at Resonance

Now that all the pieces are accounted for in the model, they can be used to predict the characteristics of the transducer. This section starts with a more general description of the electrical impedance of the transducer. The key part of the model that connects the electrical and acoustic realms is the electroacoustic transformer. As shown in Figure 5.8.a, this transformer has a turns ratio (ϕ) defined as

$$\phi = k_T \left(\frac{1}{2f_0 C_0 Z_C} \right)^{\frac{1}{2}} sinc\left(\frac{f}{2f_0} \right) \tag{5.11a}$$

that converts electrical signals to acoustic waves and vice versa. The *sinc* function is related to the Fourier transform of the dielectric displacement field between the electrodes, which has a rectangular shape. The KLM model also accommodates multiple piezoelectric layers, which can be represented by a single-turns ratio related to the transform of the complete field through all the piezoelectric layers together (Leedom *et al.*, 1978).

Other electrical elements of the model includes block C′, a strange negative capacitance-like component:

$$C' = -C_0 / [K_T^2 \, sinc(f/f_0)] \tag{5.11b}$$

that has to do with the acoustoelectric feedback and the Hilbert transform of the dielectric displacement. Finally, there is the ordinary clamped capacitance C_0.

The electrical characteristics of a transducer can be reduced to the simple equivalent circuit (shown earlier in Figure 5.2a). A complex acoustic radiation impedance (Z_A) can be found by looking through the KLM transformer at the combined acoustic impedance found at the center point of the model, $Z_{in}(f)$, as

$$Z_A(f) = \phi^2 Z_{in}(f) \tag{5.12}$$

where Z_A is purely electrical. Recall that at the center point, the acoustic impedance to the right is Z_{Rin}, and to the left, it is Z_{Lin}. By throwing in other components in the electrical leg of the KLM model, we arrive at the overall electrical transducer impedance,

$$Z_T(f) = \phi^2 \mathrm{Real}(Z_{in}) + i \left[\phi^2 \mathrm{Imag}(Z_{in}) - \frac{k_T^2}{\omega_0 C_0} \, sinc(f/f_0) - 1/\omega C_0 \right] \tag{5.13a}$$

$$Z_T(f) = R_A(f) + i[X_A(f) - 1/\omega C_0] = Z_A(f) - i/\omega C_0 \tag{5.13b}$$

A typical plot of Z_T was given in Figure 5.2b.

At resonance, the radiation reactance, $X_A(f_0)$, is zero. The radiation resistance, R_A, is

$$R_A(f) = \left[\frac{k_T^2}{2f_0 C_0 Z_c}\, sinc^2(f/2f_0)\right]\left[\frac{Z_{Lin} Z_{Rin}}{Z_{Lin} + Z_{Rin}}\right] \tag{5.14}$$

and at f_0, it becomes

$$R_A(f_0) = R_{A0} = \left[\frac{k_T^2}{2f_0 C_0 Z_c}\, sinc^2(f_0/2f_0)\right]\left[\frac{Z_c^2}{Z_{llay} + Z_{rlay}}\right] = \frac{2k_T^2}{\pi^2 f_0 C_0}\left(\frac{Z_c}{Z_{llay} + Z_{rlay}}\right) \tag{5.15a}$$

where the resonant half crystals have become quarter-wave transformers ($Z_{Rin} = Z_c^2/Z_{rlay}$). The impedance looking from the right face of the crystal to the right is Z_{rlay}, and that looking from the left face of the crystal is Z_{lray}. If there are no other layers, then a medical transducer (typically $Z_{lray} = Z_B$, the backing impedance, and $Z_{rlay} = Z_w$, the impedance of water or tissue) the radiation resistance at resonance is

$$R_A(f_0) = R_{A0} = \frac{2k_T^2}{\pi^2 f_0 C_0}\left(\frac{Z_c}{Z_B + Z_w}\right) \tag{5.15b}$$

Note that as a sanity check, if the loads are instead made equal to Z_c, Eq. (5.15b) reduces to the simple model result of Eq. (5.8c).

To complete the electrical part of the transducer model, a source and matching network are added as in Figure 5.10. A convenient way to add electrical matching is a series inductor. A voltage source (V_g) with an internal resistance (R_g) is shown with a series tuning inductance. These components can be represented in a series ABCD matrix (see Chapter 3). A more complicated tuning network can be used instead with the more general matrix elements A_{ET}, B_{ET}, C_{ET}, and D_{ET}, as Figure 5.10 implies.

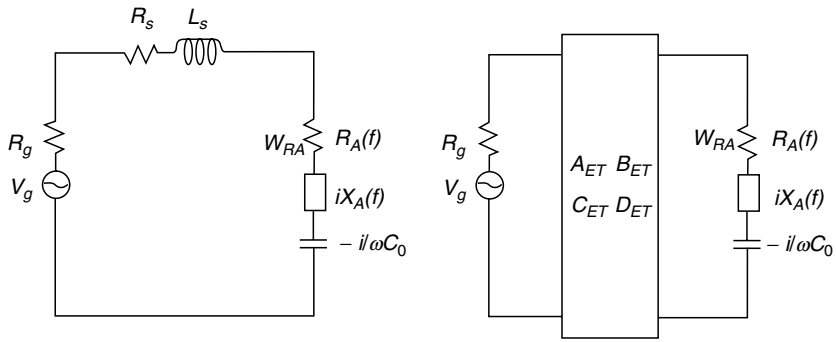

Figure 5.10 Electrical voltage source and electrical matching network. (Left) Simple series inductor and resistor. (Right) ABCD representation of a more general network.

5.4 TRANSDUCER DESIGN CONSIDERATIONS

5.4.1 Introduction

In order to design a transducer, we need criteria to guide us. To make a transducer sensitive, some measure of efficiency is required. For a pulse–echo configuration, two different transducers can be used for transmission and reception (indicated in Figure 5.11). In general, there may be two different matching networks: E_T, for transmit, and E_R (each represented by its ABCD matrix). If the transducers, matching networks, and loads R_g and R_f are the same, the transducer efficiencies are identical and reciprocal (Sittig, 1967; Sittig, 1971; Saitoh *et al*., 1999).

In this situation, if the transmit transducer has an ABCD matrix relating the electrical and acoustic variables, then the receiver will have a DCBA matrix. From repeated calculations of this model for a range of frequencies, pulses can be calculated using an inverse Fourier transform from the spectrum. If the round-trip pulse length is shorter than the transit time between the transducers, then the models can be decoupled or calculated independently; however, for a longer pulse or a continuous wave transmit situation, the individual transducer models are connected by a transmission line between the transmit and receive sections of the model.

5.4.2 Insertion Loss and Transducer Loss

One measure of overall round-trip efficiency is "insertion loss." As illustrated in Figure 5.12, efficiency is measured by comparing the power in load resistor R_f with the transducer in place to the power there without the transducer. Insertion loss is defined as the ratio of the power in R_f over that available from the source generator,

$$IL(f) = \frac{W_f}{W_g} = \left[\left|\frac{V_f}{V_g}\right|^2 \left(\frac{R_f + R_g}{R_f}\right)\right] \tag{5.16a}$$

and in dB, it is

$$IL_{dB}(f) = 10 \log_{10} IL(f) \tag{5.16b}$$

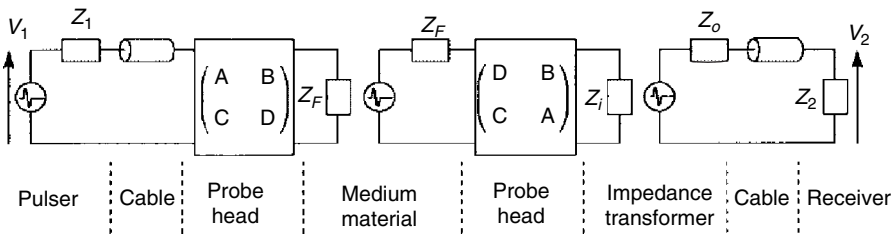

Figure 5.11 Equivalent circuit for the round-trip response of a transducer with a cable and lens (from Saitoh *et al.*, 1999, *IEEE*).

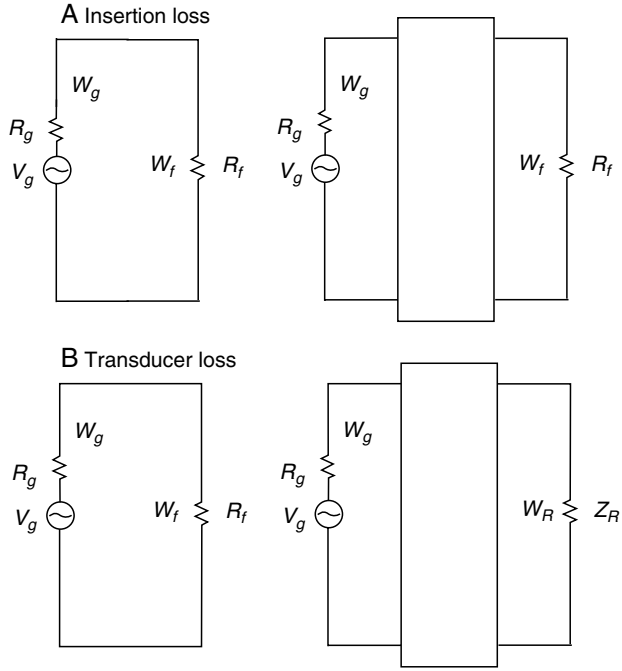

Figure 5.12 (A) Transducer insertion loss shown as a comparison of the source and load with and without a device in between. (B) Similar transducer loss definition for one-way transducer loss.

where W_f is the power in R_f, and W_g is that available from the source V_g. The maximum power available is for $R_f = R_g$. In Figure 5.11, $R_f = Z_2$.

Likewise, it is possible to define a one-way loss, called a "transducer loss" (Sittig, 1971), that is a measure of how much acoustic power arrives in right acoustic load Z_R from a source V_g. Transducer loss (as shown in Figure 5.12b) is

$$TL(f) = \frac{W_R}{W_g} = \left[\left| \frac{F_{AR}}{V_g} \right|^2 \left(\frac{4R_g}{Z_R} \right) \right] \tag{5.17a}$$

and defined in dB as

$$TL_{dB}(f) = 10 \log_{10} TL(f) \tag{5.17b}$$

where W_R is the power in Z_R, and F_{AR} is the acoustic force across load Z_R. Note that for identical transducers,

$$TL = \sqrt{IL}(\text{linear}) \tag{5.18a}$$

$$TL_{dB} = IL_{dB}/2(dB) \tag{5.18b}$$

5.4.3 Electrical Loss

For highest transducer sensitivity, we would like transducer and insertion losses to be as small as possible. With the KLM model, it is possible to partition the transducer loss into electrical loss (*EL*) and acoustic loss, (*AL*),

$$TL(f) = EL(f)AL(f) \tag{5.19}$$

as symbolized by Figure 5.13. By looking at each loss factor individually, we can determine how to minimize the loss of each contribution. From Figure 5.10, the voltage transfer ratio for the specific case in which the matching network (E_T) is a series tuning inductor, $Z_s = R_z + i\omega L_s$, with matrix elements, A_{ET}, B_{ET}, C_{ET}, and D_{ET},

$$\frac{V_T}{V_g} = \frac{Z_T}{A_{ET}Z_T + B_{ET}} = \frac{Z_T}{Z_T + Z_S + R_g} \tag{5.20}$$

Now electrical loss is defined as the power reaching R_A divided by the maximum power available from the source,

$$EL = \frac{W_{RA}}{W_g} = \frac{I^2R_A/2}{V_g^2/8R_g} = \frac{\left|\frac{V_T}{Z_T}\right|^2 R_A/2}{V_g^2/8R_g} = \left|\frac{V_T}{V_g}\right|^2 \frac{4R_AR_g}{|Z_T|^2} \tag{5.21}$$

Combining Eqs. (5.20) and (5.21),

$$EL = \frac{4R_AR_g}{|A_{ET}Z_T + B_{ET}|^2} \tag{5.22a}$$

$$EL = \frac{4R_AR_g}{(R_A + R_g + R_s)^2 + (X_A - 1/\omega C_0 + \omega L_S)^2} \tag{5.22b}$$

If the capacitance is tuned out by a series inductor, $L_S = 1/\left(\omega_0^2 C_0\right)$, then at resonance,

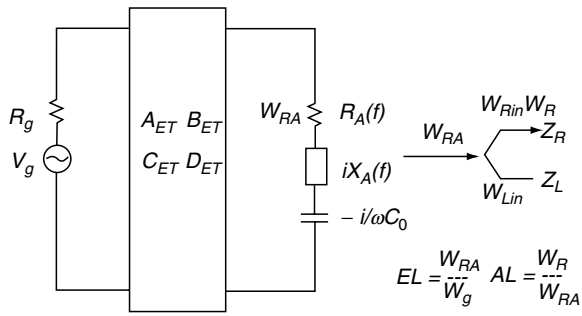

Figure 5.13 Diagram of electrical loss as the power reaching the radiation resistance, divided by source power and acoustical loss as the power reaching the right acoustic load, divided by the power reaching the radiation resistance.

$$EL(f_0) = \frac{4R_A R_g}{(R_A + R_g + R_s)^2} \tag{5.22c}$$

Furthermore, if $R_A = R_g$, and $R_s \ll R_g$, then $EL(f_0) \sim 1$.

An example of the effect of electrical tuning is given by Figure 5.14a. In this case, a 3-MHz center frequency transducer is tuned with an inductor at 3 MHz. These curves were generated by the MATLAB program xdcr.m. The effect of tuning is strong and alters both the shape of the transducer loss response and its absolute sensitivity.

5.4.4 Acoustical Loss

Acoustical loss is the ratio of the acoustic power reaching the front load (Z_R), over the total acoustic power converted. In order to determine acoustical loss, we begin with the real electrical power reaching R_A, which, after being converted to acoustical power at the acoustic center of the KLM model, splits into the left and right directions,

$$W_{RA} = W_{Lin} + W_{Rin} \tag{5.23a}$$

Refer to Figure 5.13. If the equivalent acoustic voltage or force at the center is F_c, then the power (W_{Rin}) to the right side is

$$W_{Rin} = \frac{1}{2}\left|\frac{F_c}{Z_{Rin}}\right|^2 REAL(Z_{Rin}) \tag{5.23b}$$

and the power to the left is

$$W_{Lin} = \frac{1}{2}\left|\frac{F_c}{Z_{Lin}}\right|^2 REAL(Z_{Lin}) \tag{5.23c}$$

If there is absorption loss along the acoustic path, then the power to the right is instead

$$W_R = vv^* \text{REAL}(Z_R)/2 = \left|\frac{F_R}{Z_R}\right|^2 REAL(Z_R)/2 \tag{5.24}$$

where F_R is the force across load Z_R. The acoustical loss is simply the power to the right divided by the total incoming acoustic power,

$$AL(f) = \frac{W_R}{W_{RA}} = \frac{W_R}{W_{Lin} + W_{Rin}} \tag{5.25}$$

If there is no absorption loss along the right path, then $W_R = W_{Rin}$. At resonance with no loss, this expression can be shown to be (see Figure 5.9)

$$AL(f_0) = \frac{Z_{rlay}}{Z_{rlay} + Z_{llay}} \tag{5.26}$$

where these are the acoustic impedances to the right and left of the center. For no layers,

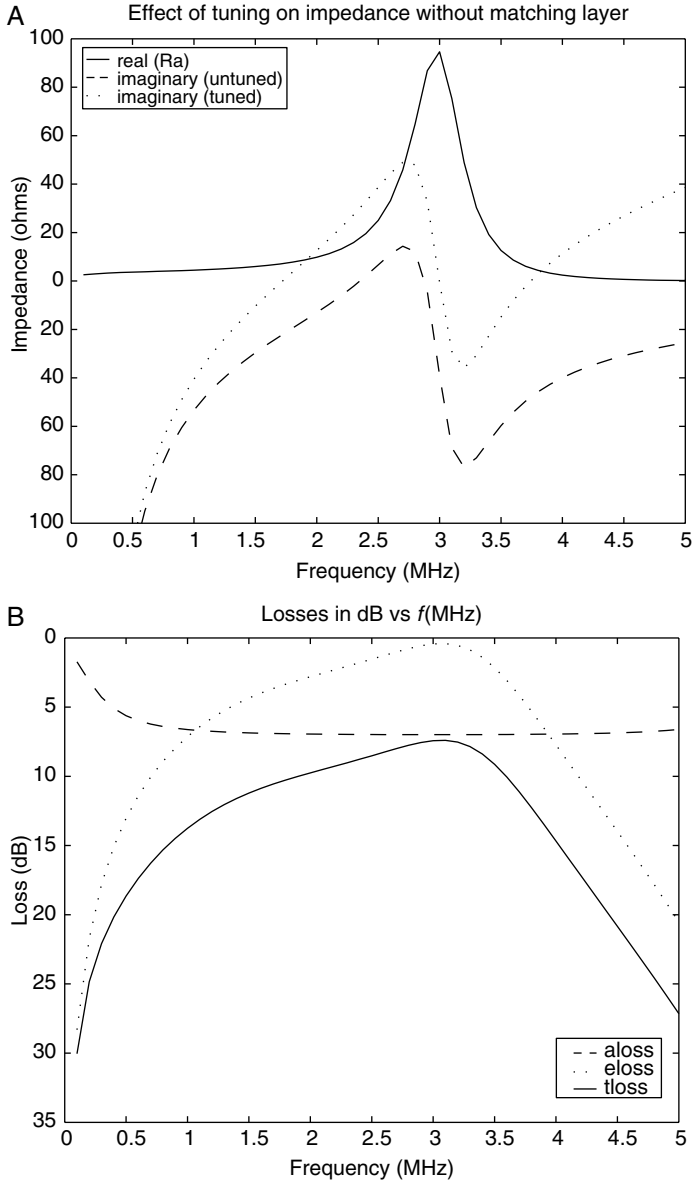

Figure 5.14 Transducer operating into a water load in a beam mode with a crystal of PZT-5H, having an area of 5.6 mm^2 and a backing impedance of 6 megaRayls. (A) Transducer impedance untuned and tuned with a series inductor. (B) Two pairs of curves of electrical loss and transducer loss with and without tuning.

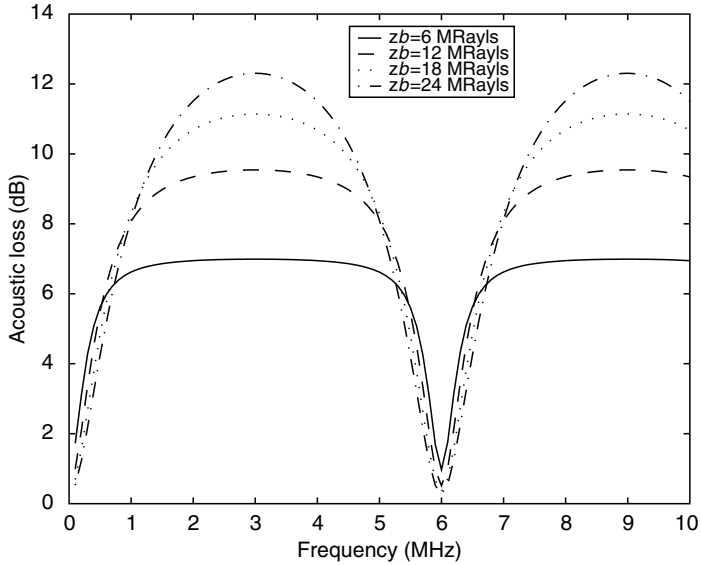

Figure 5.15 Acoustical loss versus frequency for a water load and several backing (z_b) values for a transducer with a 3-MHz center frequency.

$$AL(f_0) = \frac{Z_R}{Z_R + Z_L} = \frac{Z_W}{Z_B + Z_W} \tag{5.27}$$

For an air backing, $AL(f_0) = 1$. For a backing matched to the crystal-specific impedance, $Z_B \approx 30A$ (recall A is area), and for a water load, $Z_R = Z_w = 1.5A$, $AL(f_0) = 0.05$. Acoustic loss curves for several back acoustic loads at port 2 are plotted for a 3.5-MHz center frequency in Figure 5.15.

5.4.5 Matching Layers

To improve the transfer of energy to the forward load, quarter-wave matching layers are used. The simplest matching is the mean of the impedances to be matched,

$$Z_{ml} = \sqrt{Z_1 Z_2} \tag{5.28}$$

If we interpose this quarter-wave matching layer on the right side for the last case of a matched backing, then since $Z_1 = Z_c = 30A$, $Z_2 = Z_w = 1.5A$, $Z_{ml} = 6.7A$, and $Z_{rlay} = 30A$, so then $AL(f_0) = 0.5$. At the resonant frequency, recall that the value of acoustic loss can be found from the simple formula in Eq. (5.26). The dramatic effect matching layers can have in lowering loss over a wide bandwidth will be demonstrated with examples in section 5.4.6. The increase in fractional bandwidth as a function of the number of matching layers is shown in Figure 5.16. Note that for a single matching layer, the −3-dB fractional bandwidth is about 60%. More matching layers can be used to increase bandwidth. Philosophies differ as to how the values for

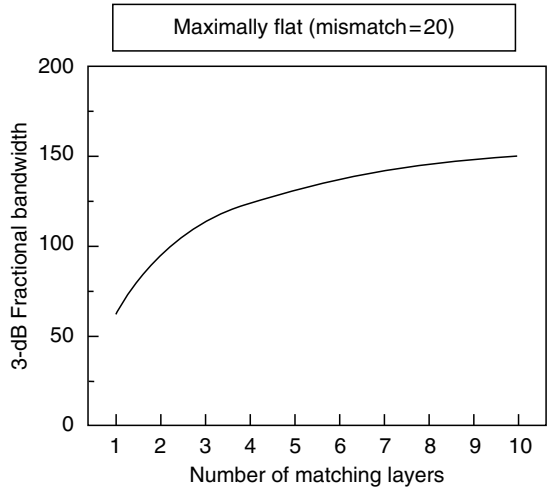

Figure 5.16 The −3-dB fractional bandwidths versus the number of matching layers determined from the maximally flat criteria for an overall mismatch ratio of $20 = Z_c/Z_w$ (from Szabo, 1998, IOP Publishing Limited).

matching layer impedances are selected (Goll and Auld, 1975; Desilets *et al*., 1978); however, a good starting point is the maximally flat approach borrowed from microwave design (Matthaei *et al*., 1980). For two matching layers, for example, the values are $z_1 = z_c^{4/7} z_w^{3/7}$ and $z_2 = z_c^{1/3} z_w^{2/3}$. This approach was used to estimate one-way −3-dB fractional acoustic bandwidths in percent for the right side as a function of the number of matching layers (shown in Figure 5.16).

5.4.6 Design Examples

We are now ready to look at two examples. The first case is a transducer element made of PZT-5H with a 3-MHz resonant frequency desired. From Table B2 (in Appendix B), the coupling constant and parameters for the beam mode for this material can be selected. From the crystal sound speed, the crystal thickness is 662 μm ($c/2f_0$). The given area is $A = 7e - 6\,m^2$, and the backing impedance is $Z_b = 6$ megaRayls. The crystal acoustic impedance is 29.8 megaRayls. This case is the default for the transducer simulation program xdcr.m. The values of these variables can be found by typing the following variable names, one at a time, at the MATLAB prompt: edi, area, zbi, and zoi. Finally, the clamped capacitance can be found from Eq. (5.1) to be $C_0 = 1380\ pf (pf = picofarad = e - 12 farad)$, with the variable name *c*0. The value of reactance at f_0 is tuned out by a series inductor (matching oppositely signed reactances) as $L_s = 1/(\omega_0^2 C_0) = 2.04 \mu H$ (symbol for microHenry), with the variable name ls0. Putting all of these input variables into the program gives a tuned impedance similar in shape to that shown in Figure 5.14a. Transducer, electrical, and acoustical loss curves are given in Figure 5.17.

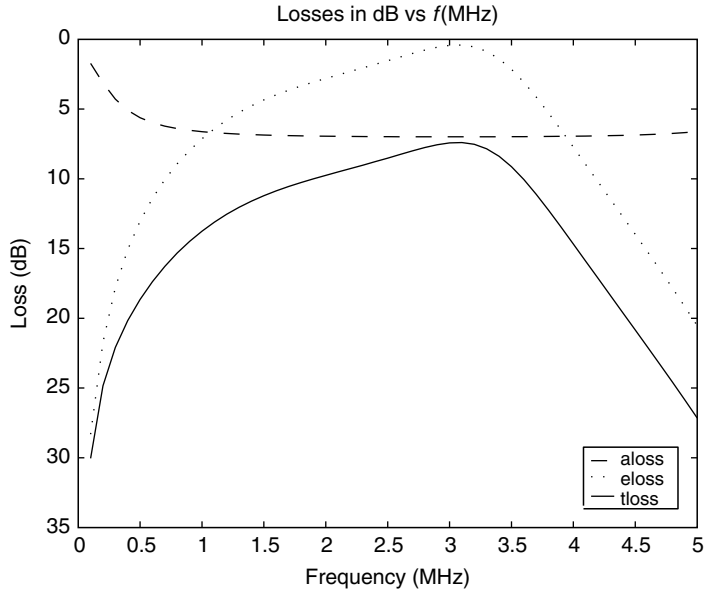

Figure 5.17 Transducer, acoustical, and electrical loss curves for 3-MHz tuned design.

In all cases, the values of the loss curves at resonance (predictable by simple formulas) provide a sanity check. From Eq. (5.27),

$$AL(f_0) = \frac{1.5}{6 + 1.5} = 0.2 \tag{5.29a}$$

or –7 dB. This checks with the program variable alossdb(30), where index 30 corresponds to 3 MHz. From Eq. (5.15b), $R_{A0} = 94.6$ ohms, variable real ($zt(30)$). Then from the definition of electrical loss at resonance, Eq. (5.22c), since $R_s = 0$, and $R_g = 50$ ohms,

$$EL(f_0) = \frac{4x94.62x50}{(94.62 + 50)^2} = 0.9048 \tag{5.29b}$$

or –0.43 dB, for a total one-way transducer loss of –7.43 dB at the resonant frequency. The points at resonance serve as sanity anchors for the curves in Figure 5.17. Note that the losses in dB can be simply added. Though both the acoustical and electrical losses are interrelated, it is apparent that the acoustical loss has a much wider bandwidth.

Now a matching layer will be used for the forward side. From Eq. (5.28), $Z_{ml} = 6.68$ megaRayls. Assume that a matching layer material with the correct impedance and a sound speed of 3.0 mm/μs can be applied. For a quarter wave at the resonant frequency, the layer thickness is $d = c_{ml}/(4f_0) = 250$ μm. This information can be turned on in the program by setting the parameter $ml = 1$ rather than $ml = 0$ (default). Note that even with a matching layer, the tuning inductor is unchanged. The resulting impedance has a different appearance (shown in Figure 5.18a). The

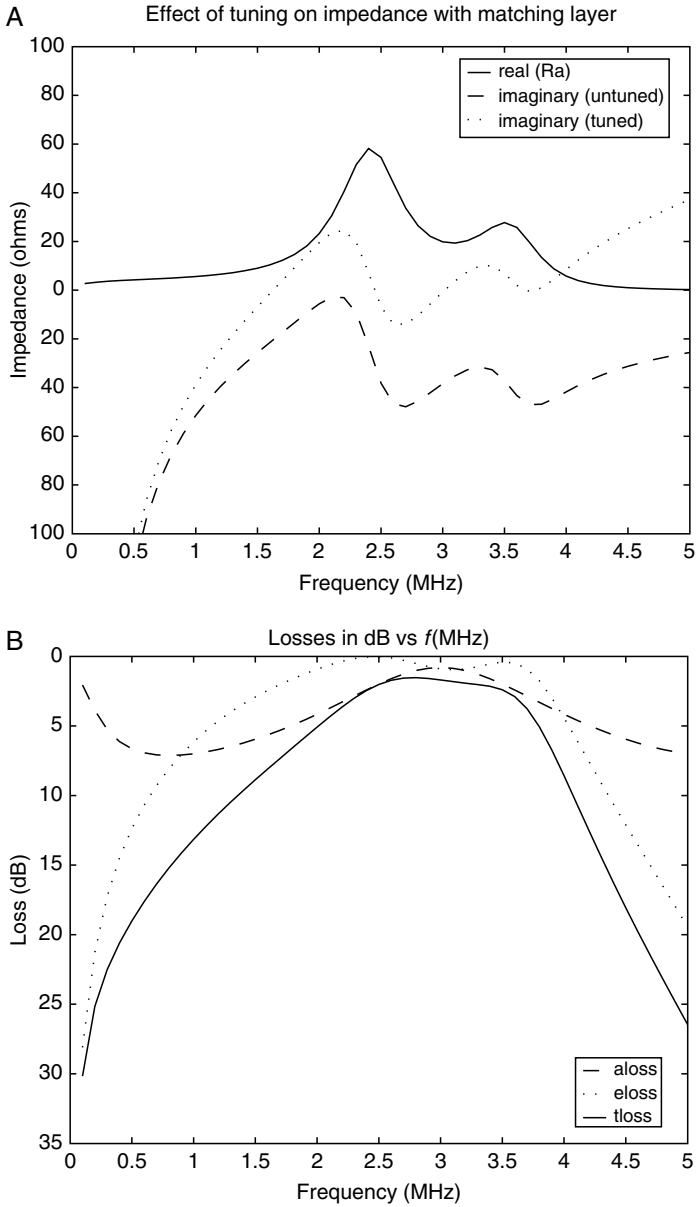

Figure 5.18 (A) Electrical impedance for design with matching layer, with and without tuning. (B) Corresponding transducer loss, acoustical loss, and electrical loss curves for 3 MHz-tuned design with a matching layer.

corresponding losses are shown in Figure 5.18b. This time, the acoustical loss is found from Eq. (5.26), in which the acoustic impedance at the right crystal face looking toward the matching layer is $Z_{Rlay} = 29.8A$ megaRayls, so that

$$AL(f_0) = \frac{29.8}{6 + 29.8} = 0.832 \tag{5.30a}$$

or 0.798 dB. In this case, $R_{A0} = 19.85$ ohms, so from Eq. (5.22c),

$$EL(f_0) = \frac{4x19.85x50}{(19.85 + 50)^2} = 0.8137 \tag{5.30b}$$

or 0.895 dB, for a total one-way transducer loss of −1.69 dB at the resonant frequency.

Comparison of the two cases shows considerable improvement in sensitivity and bandwidth from the inclusion of a matching layer. The overall shape of the transducer loss could be improved because it is related to the pulse shape.

In order to refine the design, the resonant frequencies of the crystal and matching layer can be adjusted, or more matching layers can be added. Because of constraints beyond the designer's control, transducer design requires adaptability, creativity, and patience. For a typical array element design, nonlinear electronic circuitry and a coaxial cable are added to the electrical port. In addition, a lens with absorption loss as a function of frequency is thrown into the mix to make the design a little more interesting. More information on design can be found in the following references: Sittig (1967); Goll and Auld (1975); Desilets *et al.* (1978); Souquet *et al.* (1979); Van Kervel and Thijssen (1983); Szabo (1984); Persson and Hertz (1985); Kino (1987); Rhyne (1996).

5.5 TRANSDUCER PULSES

Because the primary purpose of a medical transducer is to produce excellent images, an ideal pulse shape is the ultimate design goal. Agreement has been reached that the pulse should be as short as possible and with a high-amplitude peak (good sensitivity). Some would argue that the ideal shape is Gaussian because this shape is maintained during propagation in absorbing tissue. Unfortunately, because of causality, a Gaussian shape is not achieved by transducers; instead, the leading edge of a pulse is usually much steeper than its tail.

To get beyond the "looks nice" stage requires quantitative measures of a spectrum and its corresponding pulse. Spectral bandwidths are measured from a certain number of decibels down from the spectral maximum. Typical values are −6-dB, −10-dB, and −20-dB bandwidths. The center frequency of a round-trip spectrum is defined as

$$f_c = (f_{low} + f_{high})/2 \tag{5.31}$$

where f_{low} and f_{high} are the −6 (or other number) dB low and high round-trip frequencies, respectively. For the pulse, the pulse widths, as measured in dB levels down from the peak of the analytical envelope (see Appendix A), are usually at the

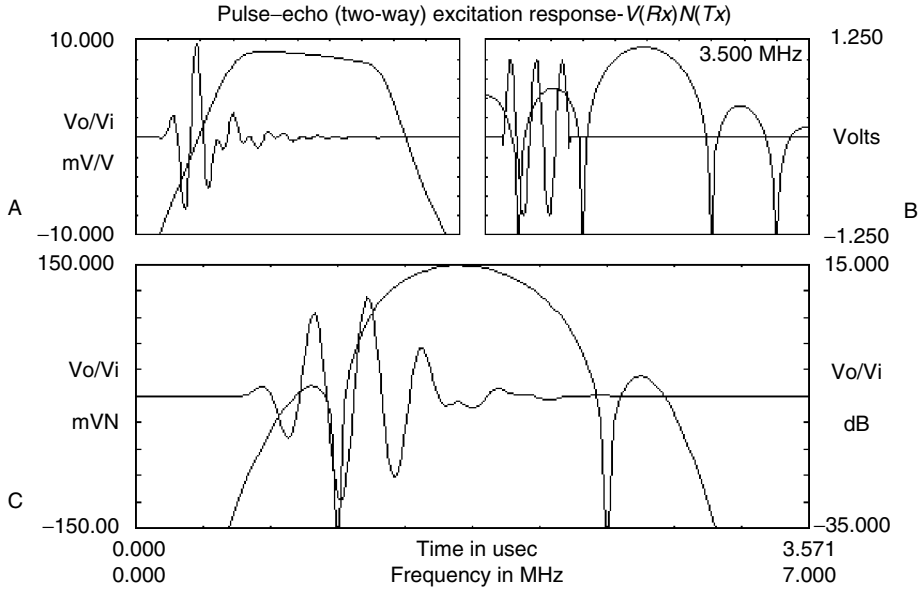

Figure 5.19 (A) Pulse–echo impulse response and spectrum for a 3.5-MHz linear array design. (B) A 3.5-MHz, 2½ cycle sinusoid excitation pulse and spectrum. (C) Resultant output pulse and spectrum. All calculations by PiezoCAD transducer design program (courtesy of G. Keilman, Sonic Concepts, Inc).

−6-dB, −20-dB, and −40-dB levels. These widths measure pulse "ringdown" and quantify the axial spatial resolution of the transducer.

Another consideration in pulse shaping is the excitation pulse. The overall pulse is the convolution of the excitation pulse and the impulse response of the transducer. Figure 5.19 shows plots for these pulses from a 3.5-MHz linear array design with two matching layers and a PZT-5H crystal operating in the beam mode. They were calculated by a commercially available transducer simulation/design program called PiezoCAD. Here the excitation pulse is 3.5 MHz, 2½ cycle sinusoid.

This program calculates the spectral and pulse envelope widths as given by Table 5.1. It has many features that make it convenient for design and has examples and tables of piezoelectric and other materials.

TABLE 5.1 Linear Array Design Width Measurements from Figure 5.19

	−6 dB	**−20 dB**	**−40 dB**
Center frequency (CF) (MHz)	3.404	3.472	3.513
Bandwidth (BW) (MHz)	1.649	2.494	4.704
Fractional BW of CF (%)	48.44	71.83	133.90
Pulse length (μs)	0.511	1.072	1.932

The design problem is to create pulses that are short in the sense that the tail is short and the so-called time sidelobes in the tail section after the main lobe are at very low levels. If these time sidelobes are high, a single actual target may appear as a series of targets or an elongated target under image compression, a process that elevates lower image signals for visualization. From the Fourier transform theory of Chapter 2, these restrictions require that the spectrum not contain sharp transitions or corners at the band edges. In other words, a wideband (for short temporal extent) rounded spectrum will do. This requirement presents another design constraint—shaping the spectrum so as to achieve short pulses. Various solutions have been proposed. One of the most widely known solutions is that of Selfridge *et al*. (1981). They developed a computer-aided design program that varies acoustic and electric parameters so as to achieve a pleasing pulse shape. Lockwood and Foster (1994) based their computer-aided design algorithm on a generalized ABCD matrix representation of the transducer. Rhyne (1996) developed an optimization program that is based on spectral shaping and the physical limitations of the transducer.

Finally, it is important to remember that pulse design is usually done with the system in mind. The overall shaping of the round-trip pulse after the transducer has been excited by a certain-shaped drive pulse and has passed through receive filters is a primary design goal (McKeighen, 1997). For better inclusion of the effects of electronics, SPICE transducer models (Hutchens and Morris, 1984; Morris and Hutchens, 1986; Puttmer *et al*., 1997) have been developed that marry the transducer more directly to the driver and to receive electronics. Nonlinearities of switching and noise figures can be handled by this approach.

5.6 EQUATIONS FOR PIEZOELECTRIC MEDIA

What are the effects of piezoelectricity on material constants? As shown earlier in Section 5.1.1, Hooke's law is different for piezoelectric materials than for purely elastic (see Chapter 3) or viscoelastic (see Chapter 4) materials and is stated more generally below (Auld, 1990):

$$T = C^{D}{:}S - h{:}D \tag{5.32a}$$

where C^D is a 6-by-6 tensor matrix of elastic constants taken under conditions of constant D, h is a 6-by-3 tensor matrix, and D is a 1-by-3 tensor vector. This type of equation can be calculated by the same type of matrix approach used for elastic media in Chapter 3. The companion constitutive relation is

$$E = -h{:}S + \beta^{S}{:}D \tag{5.32b}$$

where β^S is dielectric impermeability under constant or zero strain. Pairs of constitutive relations appear in various forms suitable for the problem at hand or the preference of the user, and they are given in Auld (1990).

Alternatively, stress can be put in the following form:

$$T = C^{E}{:}S - e{:}E \tag{5.33}$$

in which C^E is a set of elastic constants measured under constant or zero electric field and e is another piezoelectric constant. A companion constitutive equation to Eq. (5.33) is

$$D = \varepsilon^S : E + eS \tag{5.34}$$

where ε^S is permittivity determined under constant or zero strain. If $D = 0$ in this equation, and E is found for the one-dimensional case, then $E = -eS/\varepsilon^S$. With E substituted in Eq. (5.33) (Kino, 1987),

$$T = C^E\left(1 + \frac{e^2}{C^E\varepsilon^S}\right)S = C^D S \tag{5.35}$$

which is an abbreviated Hooke's law version of Eq. (5.33) with $D = 0$. C^D is called a stiffened elastic constant, with

$$C^D = C^E(1 + K^2) \tag{5.36}$$

in which K is not wave number but the piezoelectric coupling constant,

$$K = \frac{e^2}{C^E\varepsilon^S} \tag{5.37}$$

The consequence of a larger stiffened elastic constant is an apparent increase in sound speed caused by the piezoelectric coupling. The net effect of piezoelectric coupling seen from the perspective of Eq. (5.35) is an increased stress over the nonpiezoelectric case for the same strain. Various forms of K exist for specific geometries and crystal orientations 0 (to be covered in the next section). The term K^2 is often interpreted as the ratio of mutual coupling energy to the stored energy.

For the case of a stress-free condition ($T = 0$) in Eq. (5.33), the value of strain S can be substituted in Eq. (5.34) to yield

$$D = \varepsilon^T E = \varepsilon^S(1 + K^2)E \tag{5.38}$$

in which the stress-free dielectric constant ε^T is bigger than the often-used strain-free or clamped dielectric constant ε^S.

5.7 PIEZOELECTRIC MATERIALS

5.7.1 Introduction

How does piezoelectricity work? What are some of the values for the constants just described, and how can they be compared for different materials?

In 1880, the Curie brothers discovered piezoelectricity, which is the unusual ability of certain materials to develop an electrical charge in response to a mechanical stress on the material. This relation can be expressed for small signal levels as the following:

$$D = d : T + \varepsilon^T : E \tag{5.39}$$

There is a converse effect in which strain is created from an applied electric field, given by the companion equation,

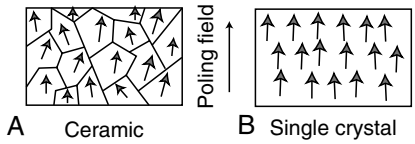

Figure 5.20 (A) Aligned electric dipoles in domains of a poled polycrystalline ferroelectric. (B) Highly aligned dipoles in domain-engineered, poled single crystal ferroelectric.

$$S = s^E : T + eS + d : E \tag{5.40}$$

where $s = C^{-1}$ is determined under a constant electric field condition. All piezoelectric materials are ferroelectric. This kind of material contains ferroelectric domains with electric dipoles, as depicted for a ceramic in Figure 5.20a. If an electric field is applied, the direction of spontaneous polarization (the alignment of the domains shown in Figure 5.20b) can be switched by the direction of the field. Furthermore, if an appropriately strong field is applied under the right conditions (usually at elevated temperature), the polarization remains even after the polarizing field is removed.

The major types of piezoelectric media are described as follows. Some of these materials can be found in Table B2 of Appendix B.

5.7.2 Normal Polycrystalline Piezoelectric Ceramics

For polarization to be possible, the material must be anisotropic. A phase diagram for the piezoelectric ceramic lead-zirconate-titanate (*PZT*[1]) is given by Figure 5.21. This plot indicates that the type of anisotropic symmetry depends on both composition and temperature. Note that in Figure 5.21, coupling and dielectric permittivity increase rapidly near the phase boundary. These ceramics are poled close to this boundary to get high values. All ferroelectric materials have a Curie temperature (T_C), above which the material no longer exhibits ferroelectric properties. Properties of the ceramic are more stable at temperatures farther from the Curie temperature.

Ceramics such as the polycrystalline PZT family are called normal ferroelectrics and are the most popular materials for medical transducers. Combining high coupling and large permittivity with low cost, physical durability, and stability, they are currently the material of choice for most array applications.

5.7.3 Relaxor Piezoelectric Ceramics

Relaxor ferroelectrics have many strange characteristics, as well as more diffuse phase boundaries and lower Curie temperatures (Shrout and Fielding, 1990) than normal

[1]Trademark, Vernitron Piezoelectric Division.

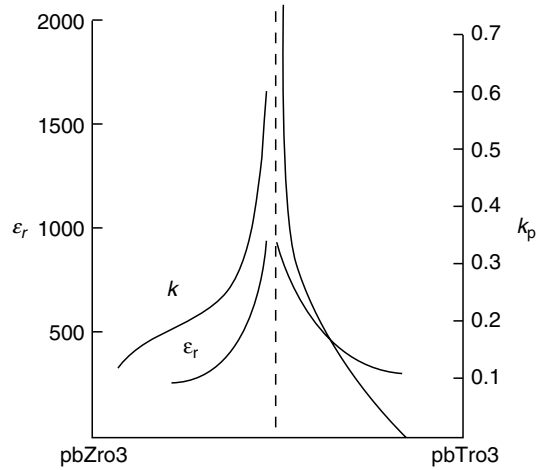

Figure 5.21 PZT phase diagram. On the left scale is the dielectric constant, and on the right scale is electromechanical coupling as a function of chemical composition. Dashed line is phase boundary (from Safari *et al.*, 1996).

ferroelectrics. Their permittivities are usually strongly frequency dependent. While crystals can function as normal piezoelectrics, they can also be electrostrictive under certain conditions. Electrostrictive materials have strains that change with the square of the applied electric fields (a different mechanism from piezoelectricity). This property leads to some unusual possibilities in which the piezoelectric characteristics of a device can be altered or switched on or off via a bias voltage (Takeuchi *et al.*, 1990; Chen and Gururaja, 1997). All dielectrics can be electrostrictors; however, the relaxor piezoelectrics have large coupling constants because they can be highly polarized.

The Maxwell stress tensor for dielectrics (Stratton, 1941) shows that the stress is proportional to the applied electric field squared:

$$T_{33} = \left(\frac{\varepsilon - a_3}{2}\right)E^2 \tag{5.41}$$

where a_3 is a deformation constant. If the thickness of the dielectric is d and a DC bias voltage (V_{DC}) is applied to electrodes in combination with an A.C. signal of amplitude A_0, then

$$T_{33} = \left(\frac{\varepsilon - a_3}{2d^2}\right)(V_{DC} + V_0 \sin \omega_1 t)^2 \tag{5.42a}$$

$$T_{33} = \left(\frac{\varepsilon - a_3}{2d^2}\right)\left(V_{DC}^2 + V_0^2/2 + 2V_{DC}V_0 \sin \omega_1 t - \frac{V_0^2 \cos 2\omega_1 t}{2}\right) \tag{5.42b}$$

in which the third term in the second parentheses indicates how the bias can control the amplitude of the original sinusoid at frequency ω_1, and the last term is at the second harmonic of this frequency.

5.7.4 Single Crystal Ferroelectrics

A number of ferroelectrics are termed single crystal because of their highly ordered domains, symmetrical structure, very low losses, and moderate coupling. These hard, brittle materials require optical grade cutting methods, and therefore, they tend not to be used for medical devices, but rather for high-frequency surface and bulk acoustic wave transducers, as well as for optical devices. This group of materials includes lithium niobate, lithium tantalate, and bismuth germanium oxide.

5.7.5 Piezoelectric Organic Polymers

Some polymers with a crystalline phase have been found to be ferroelectric and piezoelectric. Poling is achieved through a combination of stretching, elevating temperature, and applying a high electric field. Two popular piezopolymers are polyvinylidene fluoride, or PVDF (Kawai, 1969) and copolymer PVDF with trifluoroethylene (Ohigashi *et al*., 1984). Advantages of these materials are their conformability and low acoustic impedance. The low impedance is not as strong an advantage because matching layers can be utilized with higher-impedance crystals. Drawbacks are a relatively low coupling constant (compared to PZT), a small relative dielectric constant (5–10, which is a big drawback for small array element sizes), a high dielectric loss tangent (0.15–0.25 compared to 0.02 for PZT), and a low Curie temperature (70−100°C). These materials are better as receivers such as hydrophones and are less efficient as transmitters (Callerame *et al*., 1978). A special issue of the *IEEE Transactions on Ultrasonics, Ferroelectrics and Frequency Control* has been devoted to many applications of these polymers (2000).

5.7.6 Domain Engineered Ferroelectric Single Crystals

A relatively recent development is the growing of domain-engineered single crystals. Unlike other ferroelectric relaxor-based ceramics, in which domains are randomly oriented with most of them polarized, these materials are grown to have a nearly perfect alignment of domains (shown in Fig. 5.20b). Considerable investments in materials research and special manufacturing techniques were necessary to achieve extremely high coupling constants (Park and Shrout, 1997; Saitoh *et al*., 1999) and other desirable properties in crystals such as PZN-4.5% PT and 0.67 PMN-0.33 PT (Yin *et al*., 2000 and Zhang *et al*., 2001). Because both sensitivity and bandwidth are proportional to the coupling constant squared, significant improvements are possible (as discussed in Section 5.8).

5.7.7 Composite Materials

Another successful attempt at optimizing transducer materials for applications like medical ultrasound is the work on piezoelectric composites (Newnham *et al*., 1978; Gururaja *et al*., 1985). PZT, which has the drawback that its acoustic impedance is about 30 megaRayls, is mismatched to tissue impedances of about 1.5 megaRayls.

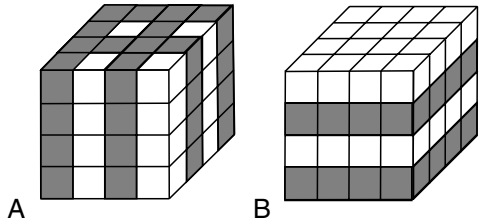

Figure 5.22 (A) 1–3 composite structure. (B) 2–2 composite structure (from Safari *et al.*, 1996).

By imbedding pieces of PZT in a low-impedance polymer material, a composite with both high coupling and lower impedance is achieved. Two of the most common composite structures are illustrated in Figure 5.22. In a 1–3 composite, posts of a piezoelectric material are organized in a grid and backfilled with a polymer such as epoxy. A 2–2 composite consists of alternating sheets of piezoelectric and polymer material. For design purposes, a composite can be described by ''effective parameters'' as if it was a homogeneous solid structure (Smith *et al.*, 1984). Effective parameters for two 1–3 composites, one with PZT-5H and another with single-crystal PMN (Ritter *et al.*, 2000), are listed in Table B2 in Appendix B.

5.8 COMPARISON OF PIEZOELECTRIC MATERIALS

Because of the many factors involved in transducer design (Sato *et al.*, 1980), it is difficult to select a single back-of-the-envelope criterium for comparing the most important material characteristics. The following are simplifications, but they provide a relative means that agrees with observations. Usually impedances of transducer elements are high because of their small size; therefore, $R_{A0} \gg R_g$. From the electrical side, the -3 dB bandwidth is given approximately by the electrical Q_e,

$$BW = 1/Q_e = \omega_0 C_0 R_{A0} = \frac{4k^2}{\pi} \tag{5.43}$$

in which matching layers are assumed as well as $Z_B \ll Z_C$ and $K = K_{33}$ for most materials except the composites $BaTiO_3$, and PVDF, for which K_T is used. Furthermore, the electrical bandwidth is assumed to be much smaller than the acoustical bandwidth from the acoustical loss factor, and therefore, it dominates. Another important factor in determining acoustic impedance, which is inversely proportional to clamped capacitance, is the relative dielectric constant (ε^s). These two figures of merit are plotted in Figure 5.23 for materials with the constants appropriate for a geometry in common use. Ideally, materials in the upper right of the graph would be best for array applications.

As a specific example, consider the spectrum of a design optimized for a 5-MHz array transducer on PZT-5H compared to that of a design optimized for PZN-M

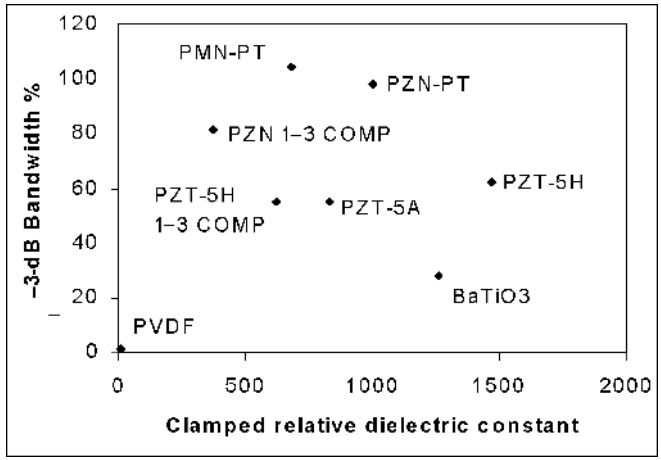

Figure 5.23 Comparison of piezoelectric materials, −3-dB bandwidth versus relative dielectric constant.

domain-engineered single-crystal material, which is shown in Figure 5.24. The coupling constants and calculated −6-dB round-trip bandwidths for the two cases are 0.66% and 66% and 0.83% and 90%, which are in good agreement with the bandwidth estimates of 56% and 86%, respectively (note a one-way −3-dB bandwidth is equivalent to a −6-dB round-trip bandwidth). A simple estimate of the relative spectral peak sensitivities is in proportion to their coupling constants to the fourth power [see Eqs. (5.15b) and (5.22c)]. In this case, the estimate for the relative −6-dB round-trip spectral peaks is + 4 dB compared to the calculated value of 3–5 dB.

5.9 TRANSDUCER ADVANCED TOPICS

Two other effects that often affect transducer performance are losses and connecting cables. Two major types of losses are internal mechanical losses within the crystal element and absorption losses in the materials used. The usually small crystal mechanical loss can be modeled by placing a loss resistance in parallel with the transducer C_0. Piezoelectric material manufacturers provide information about this loss through mechanical Q data. As we found from Chapter 4, all acoustic materials have absorption loss and dispersion. Loss can be easily included in an *ABCD* matrix notation by replacing the lossless transmission line matrix in Figure 3.4 by its lossy replacement,

$$\begin{pmatrix} A & B \\ C & D \end{pmatrix} = \begin{pmatrix} \cosh(\gamma d) & Z_0 \sinh(\gamma d) \\ \sinh(\gamma d)/Z_0 & \cosh(\gamma d) \end{pmatrix} \tag{5.44}$$

in which γ is the complex propagation factor from Chapter 4, d is the length of the transmission line, and Z_0 is its characteristic impedance. Finally, array elements are

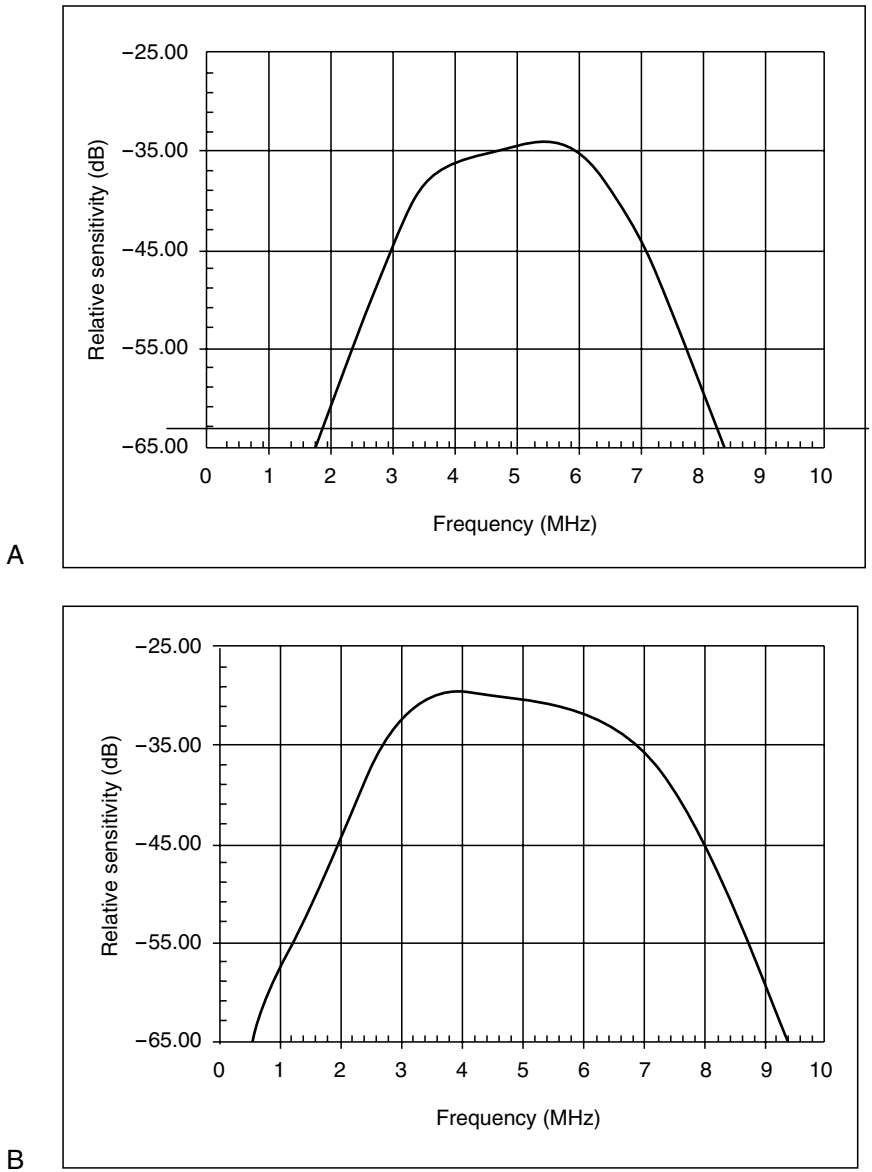

Figure 5.24 Comparison of round trip spectra for 2.5-MHz center frequency designs for (A) PZT-5H and (B) single-crystal PZN-M transducers (from Gururaja *et al.*, 1997, *IEEE*).

most often connected to a system through a coaxial cable, which can also be modeled by the same lossy transmission line matrix with appropriate electromagnetic parameters. Signal-to-noise ratios can also be calculated by a modified KLM model (Oakley, 1997). Methods of incorporating the switching directly in the transducer have been accomplished (Busse *et al.*, 1997).

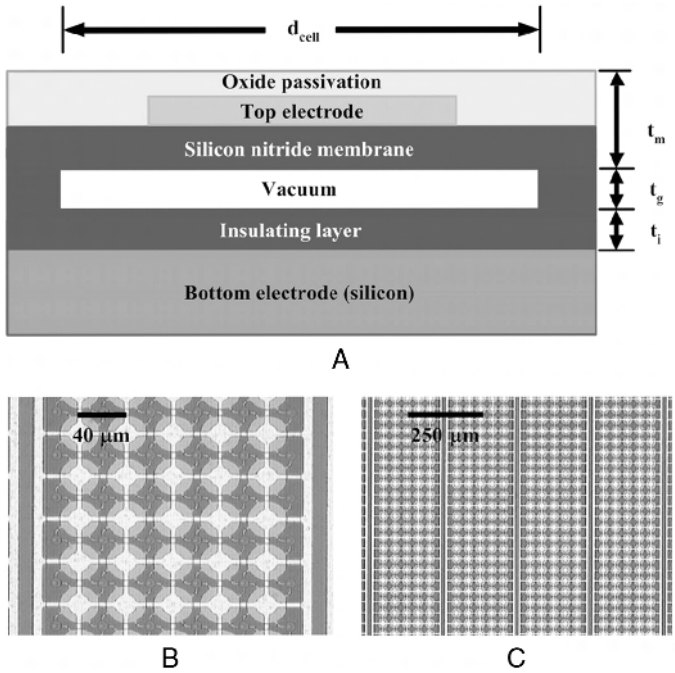

Figure 5.25 ID CMUT array. (A) Schematic cross section of a CMUT cell. (B) Magnified view of a single 5-cell wide, ID array element. (C) A portion of four elements of the ID CMUT array (from Oralkan *et al.*, 2002, *IEEE*).

The one-dimensional transducer model is a surprisingly useful and accurate design tool. Array architectures are not really composed of individual isolated elements because they are close to each other, and as a result, mechanical and electrical cross-coupling effects occur (to be discussed in Chapter 7). In addition to the dispersion of the elements, these effects can be predicted by more realistic finite element modeling (FEM) (Lerch, 1990). A three-dimensional depiction of the complicated vibrational mode of array elements can be predicted by a commercially available FEM program, PZFLEX (Wojcik *et al.*, 1996). To be accurate, a precise knowledge of all the material parameters is required, as discussed by McKeighen (2001).

FEM modeling is especially helpful in predicting the behavior of advanced arrays. These arrays include 1.5D (Wildes *et al.*, 1997 and 2D (Kojima, 1986) arrays.

Several major problems for two-dimensional arrays are electrically matching and connecting to large numbers of small elements, as well as spurious coupled vibrational modes. One solution is to integrate the electronics and switch into the transducer structure through the use of multilayer chip fabrication techniques (Erikson *et al.*, 1997). A 16,384-element two-dimensional array has been made by this method for C-scan imaging. Other alternatives are reviewed by von Ramm (2000). Philips medical systems introduced a fully populated, two-dimensional array with micro-beamformers built into the handle for a real-time 3D imaging system in 2003.

Another approach to the large array fabrication issue is an alternative transduction technology, called capacitive micromachined ultrasonic transducers (CMUTS), which is based on existing silicon fabrication methods (Ladabaum *et al*., 1996). To first order, the CMUT is a tiny, sealed, air-filled capacitor. When a bias voltage is applied to these miniature membrane transducers, a stress is developed proportional to the voltage applied squared, and the top electrode membrane deflects. Like the Maxwell stress tensor equations, Eqs. (5.41) and (5.42), if the DC bias includes an AC signal, the pressure or deflection can carry AC signal information. The voltage applied is

$$V = V_{DC} + V_{AC} \tag{5.45a}$$

resulting in a vertical deflection,

$$x = x_{DC} + x_{AC} \tag{5.45b}$$

To first order, the pressure on the membrane is

$$p_E = \frac{\varepsilon_0 V_{DC}}{d_0^2(r)} V_{AC} + \frac{\varepsilon_0 V_{DC}^2}{d_0^2(r)} x_{AC} \tag{5.45c}$$

where $d_0(r)$ is a radial displacement. Note the similarity to Eq. (5.42). A model more appropriate for two-dimensional arrays can be found in Bralkan *et al*. (1997) and Caronti *et al*. (1986). This equivalent circuit model is a combination of electrostatics and the acoustics of a miniature drum, and it predicts the radiation impedance and other characteristics of the CMUT. The attractiveness of CMUT technology for imaging is its simpler and more flexible fabrication as well as its high sensitivity and broad bandwidth. Imaging with CMUT arrays has been demonstrated (Oralkan *et al*., 2002; Panda *et al*., 2003).

An important trend is the development of transducers at higher frequencies. Commercially available intravascular ultrasound (IVUS) imaging systems operate in the 20–40 MHz range. Either a miniature, mechanical single-element transducer is rotated or phased or synthetic array elements are electronically scanned on the end of a catheter to obtain circumferential, highly detailed pictures of the interior of vessels of the human body. Ultrasound biomicroscopy (Foster *et al*., 2000; Saijo and Chubachi, 2000) provides extremely high-resolution images, as well as new information about the mechanical functioning and structure of living tissue. One of the main initiatives of the National Center for Transducers at Pennsylvania State University is the development of high-frequency transducers (Ritter *et al*., 2002) and arrays and materials.

BIBLIOGRAPHY

Overview treatments of transducers can be found in the following: Mason (1964); Sachse and Hsu (1979); Hunt *et al*. (1983); Kino (1987); Szabo (1998); Foster (2000); Reid and Lewin (1999).

References

Auld, B. A. (1990). *Acoustic Waves and Fields in Solids*, Vol. 1. Krieger Publishing, Malabar, FL.

Busse, L. J., Oakley, C. G., Fife, M. J., Ranalletta, J. V., Morgan, R. D., and Dietz, D. R. (1997). The acoustic and thermal effects of using multiplexers in small invasive probes. *IEEE Ultrason. Symp. Proc*., 1721–1724.

Callerame, J. D., Tancrell, R. H., and Wilson, D. T. (1978). Comparison of ceramic and polymer transducers for medical imaging. *IEEE Ultrason. Symp. Proc*., 117–121.

Caronti, A., Caliano, G., Iula, A., and Pappalardo, M. (1986). An accurate model for capacitive micromachined ultrasonic transducers. *IEEE Trans. Ultrason. Ferroelectr. Freq. Control* **33**, 295–298.

Chen, J. and Gururaja, T. R. (1997). DC-biased electrostrictive materials and transducers for medical imaging. *IEEE Ultrason. Symp. Proc*., 1651–1658.

Desilets, C. S., Fraser, J. D., and Kino, G. S. (1978). The design of efficient broad-band piezoelectric transducers. *IEEE Trans. Sonics Ultrason*. **SU-25**, 115–125.

de Jong, N., Souquet, J., and Bom, N. (July 1985). Vibration modes, matching layers, and grating lobes. *Ultrasonics*, 176–182.

Erikson, K., Hairston, A., Nicoli, A., Stockwell, J., and White, T. A. (1997). 128 X 128K (16 k) ultrasonic transducer hybrid array. *Acoust. Imaging* **23**, 485–494.

Foster, F. S. (2000). Transducer materials and probe construction. *Ultrasound in Med. & Biol*. **26**, Supplement 1, S2–S5.

Foster, F. S., Larson, J. D., Masom, M. K., Shoup, T. S., Nelson, G., and Yoshida, H. (1989). Development of a 12 element annular array transducer for real-time ultrasound imaging. *Ultrasound in Med. & Biol*. **15**, 649–659.

Foster, F. S., Pavlin, C. J., Harasiewicz, K. A., Christopher, D. A., and Turnbull, D. H. (2000). Advances in ultrasound biomicroscopy. *Ultrasound in Med. & Biol*. **26**, 1–27.

Goll, J. and Auld, B. A. (1975). Multilayer impedance matching schemes for broadbanding of water loaded piezoelectric transducers and high Q resonators. *IEEE Trans. Sonics Ultrason*. **SU-22**, 53–55.

Gururaja, T. R., Schulze, W. A., Cross, L. E., and Newnham, R. E. (1985). Piezoelectric composite materials for ultrasonic transducer applications, Part 11: Evaluation of ultrasonic medical applications. *IEEE Trans. Sonics Ultrason*. **SU-32**, 499–513.

Gururaja, T. R., Panda, R. K., Chen, J., and Beck, H. (1997). Single crystal transducers for medical imaging applictions. *IEEE Ultrason. Symp. Proc*., 969–972.

Hunt, J. W., Arditi, M., and Foster, F. S. (1983). Ultrasound transducers for pulse-echo medical imaging. *IEEE Trans. Biomed Engr.* **BME-30**, 452–481.

Hutchens, C. G. (1986). A three diemensional equivalent circuit for tall parallelpiped piezoelectric. *IEEE UFFC Symp. Proc*., 321–325.

Hutchens, C. G. and Morris, S. A. (1984). A three port model for thickness mode transducers using SPICE II. *IEEE Ultrason. Symp. Proc*., 897–902.

Hutchens, C. G. and Morris, S. A. (1985). A two dimensional equivalent circuit for the tall thin piezoelectric bar. *IEEE Ultrason. Symp. Proc*., 671–676.

IEEE Trans. on Ultrason. Ferroelec. and Freq. Control. (Nov. 2000). Special issue on the 30th anniversary of piezoelectric PVDF.

Kawai, H. (1969). The piezoelectricity of poly(vinylidene fluoride). *Jpn. J. Appl. Phys*. **8**, 975–976.

Kino, G. S. (1987). *Acoustic Waves: Devices, Imaging, and Analog Signal Processing*. Prentice-Hall, Englewood Cliffs, NJ.

Kojima, T. (1986). Matrix array transducer and flexible matrix array transducer. *IEEE Ultrason. Symp. Proc*., 335–338.

Ladabaum, I., Jin, X., Soh, H. T., Pierre, F., Atalar, A., and Khuri-Yakub, B. T. (1996). Microfabricated ultrasonic transducers: Towards robust models and immersion devices. *IEEE Ultrason. Symp. Proc*., 335–338.

Leedom, D. A., Krimholtz, R., and Matthaei, G. L. (1978). Equivalent circuits for transducers having arbitrary even- or odd-symmetry piezoelectric excitation. *IEEE Trans. Sonics Ultrason*. **SU-25**, 115–125.

Lerch, R. (1990). Simulation of piezuelectric devices by two- and three-dimensional finite elements. *IEEE Trans. Ultrason. Ferroelectr. Freq. Control* **37**, 233–247.

Lockwood, G. R. and Foster, S. F. (1994). Modeling and optimization of high frequency ultrasound transducers. *IEEE Trans. Ultrason. Ferroelectr. Freq. Control* **41**, 225–230.

Mason, W. P. (ed.). (1964). *Physical Acoustics*, Vol. 1A, Chap. 3. Academic Press, New York.

Matthaei, G. L., Young, L., and Jones, E. M. T. (1980). *Microwave Filters, Impedance-Matching networks, and Coupling Structures*, Chap. 6. Artech House, Dedham, MA, pp. 255–354.

McKeighen, R. (2001). Finite element simulation and modeling of 2D arrays for 3D ultrasonic imaging. *IEEE Trans. Ultrason. Ferroelectr. Freq. Control* **48**, 1395–1405.

McKeighen, (1997). Influence of pulse drive shape and tuning on the broadband response of a transducer, *IEEE Ultrasonics Symp Proc*., 1637–1642.

Melton, H. E. and Thurstone, F. L. (1978). Annular array design and logarithmic processing for ultrasonic imaging. *Ultrasound in Med. & Biol*. **4**, 1–12.

Mills, D. M. and Smith, S. W. (2002). Finite element comparison of single crystal vs. multi-layer composite arrays for medical ultrasound. *IEEE Trans. Ultrason. Ferroelectr. Freq. Control* **49**, 1015–1020.

Morris, S. A. and Hutchens, C. G. (1986). Implementation of Mason's model on circuit analysis programs. *IEEE Trans. Ultrason. Ferroelectr. Freq. Control* **33**, 295–298.

Nalamwar, A. L. and Epstein, M. (1972). Immitance characterization of acoustic surface-wave transducers. *Proc. IEEE* **60**, 336–337.

Newnham, R. E., Skinner, D. P., and Cross, L. E. (1978). Connectivity and piezoelectric-pyroelectric composites. *Mat. Res. Bull*. **13**, 525–536.

Oakley, C. G. (1997). Calculation of ultrasonic transducer signal-to-noise ratios using the KLM model. *IEEE Trans. Ultrason. Ferroelectr. Freq. Control* **44**, 1018–1026.

Ohigashi, H., Koga, K., Suzuki, M., Nakanishi, T., Kimura, K., and Hashimoto, N. (1984). Piezoelectric and ferroelectric properties of P (VDF-TrFE) copolymers and their application to ultrasonic transducers. *Ferroelectrics* **60**, 264–276.

Onoe, M. and Tiersten, H. F. (1963). Resonant frequencies of finite piezoelectric ceramic vibrators with high electromechanical coupling. *IEEE Trans. Ultrason. Eng*. **10**, 32–39.

Oralkan, O., Ergun, A. S., Johnson, J. A., Karaman, M., Demirci, U., Kaviani, K., Lee, T. H., and Khuri-Yakub, B. T. (2002). Capacitive micromachined ultrasonic transducers: Next-generation arrays for acoustic imaging? *IEEE Trans. Ultrason. Ferroelectr. Freq. Control* **49**, 1596–1610.

Oralkan, O., Jin, X. C., Degertekin, F. L., and Khuri-Yakub, B. T. (1997). Simulation and experimental characterization of a 2D, 3-MHz capacitive micromachined ultrasonic transducer (CMUT) array element. *IEEE Ultrason. Symp. Proc*., 1141–1144.

Panda, S., Daft, C., and Wagner, C. (2003). Microfabricated ultrasound transducer (CMUT) probes: Imaging advantages over piezoelectric probes. *Ultrasound in Med. & Biol*. **29**, (5S):S69.

Park, S. E. and Shrout, T. R. (1997). Characteristics of relaxor-based piezoelectric single crystals for ultrasonic transducers. *IEEE Trans. Ultrason. Ferroelectr. Freq. Control* **44**, 1140–1147.

Persson, H. W., and Hertz, C. H. (1985). Acoustic impedance matching of medical ultrasound transducers. *Ultrasonics*, 83–89.

Puttmer, A., Hauptmann, P., Lucklum, R., Krause, O., and Henning, B. (1997). SPICE model for lossy piezoceramic transducers. *IEEE Trans. Ultrason. Ferroelectr. Freq. Control* **44**, 60–67.

Redwood, M. (1963). A study of waveforms in the generation and detection of short ultrasonic pulses. *Applied Materials Research* **2**, 76–84.

Reid, J. M., and Lewin, P. A. (Dec. 17, 1999). Ultrasonic transducers, imaging. *Wiley Encyclopedia of Electrical and Electronics Engineering Online*, http://www.mrw.interscience.wiley.com/eeee.

Reid, J. M., and Wild, J. J. (1958). Current developments in ultrasonic equipment for medical diagnosis. *Proc. Nat. Electron. Conf.* **12**, 1002–1015.

Rhyne, T. L. (1996). Computer optimization of transducer transfer functions using constraints on bandwidth, ripple and loss. *IEEE Trans. Ultrason. Ferroelectr. Freq. Control* **43**, 136–149.

Ritter, T., Geng, X., Shung, K. K., Lopath, P. D., Park, S. E., and Shrout, T. R. (2000). Single crystal PZN/PT-polymer composites for ultrasound transducer applications. *IEEE Trans. Ultrason. Ferroelectr. Freq. Control* **47**, 792–800.

Ritter, T. A., Shrout, T. R., Tutwiler, R., and Shung, K.K. (2002). A 30-MHz piezo-composite ultrasound array for medical imaging applications. *IEEE Trans. Ultrason. Ferroelectr. Freq. Control* **49**, 217–230.

Sachse, W. and Hsu, N. N. (1979). Ultrasonic transducers for materials testing and their characterization. *Physical Acoustics*, Vol. XIV, Chap. 4. W. P. Mason and R. N. Thurston (eds.). Academic Press, New York.

Safari, A., Panda, R. K., and Janas, V. F. (1996). Ferroelectricity: Materials, characteristics and applications. *Key Engineering Materials*, 35–70, 122–124.

Saijo, Y. and Chubachi, N. (2000). Microscopy. *Ultrasound in Med. & Biol.* **26**, Supplement 1, S30–S32.

Saitoh, S., Takeuchi, T., Kobayashi, T., Harada, K., Shimanuki, S., and Yamashita, Y. A. (1999). 3.7 MHz phased array probe using 0.91Pb $(Zn_{1/3}Nb_{2/3})O_3 - 0.09\,PbTi\,O_3$ Single Crystal. *IEEE Trans. Ultrason. Ferroelectr. Freq. Control* **46**, 414–421.

Sato, J-I., Kawabuchi, M., and Fukumoto, A. (1979). Dependence of the electromechanical coupling coefficient on width-to-thickness ratio of plank-shaped piezoelectric transducers used for electronically scanned ultrasound diagnostic systems. *J. Acoust. Soc. Am.* **66**, 1609–1611.

Sato, J-I., Kawabuchi, M., and Fukumoto, A. (1980). Performance of ultrasound transducer and material constants of piezoelectric ceramics. *Acoust. Imaging* **10**, 717–729.

Selfridge, A. R., Baer, R., Khuri-Yakub, B. T., and Kino, G. S. (1981). Computer-optimized design of quarter-wave acoustic matching and electrical networks for acoustic transducers. *IEEE Ultrason. Symp. Proc.*, 644–648.

Selfridge, A. R. and Gehlbach, S. (1985). KLM transducer model implementation using transfer matrices. *IEEE Ultrason. Symp. Proc.*, 875–877.

Selfridge, A. R., Kino, G. S., and Khuri-Yakub, R. (1980). Fundamental concepts in acoustic transducer array design. *IEEE Ultrason. Symp. Proc.*, 989–993.

Shrout, T. R. and Fielding Jr., J. (1990). Relaxor ferroelectric materials. *IEEE Ultrason. Symp. Proc.*, 711–720.

Sittig, E. K. (1967). Transmission parameters of thickness-driven piezoelectric transducers arranged in multilayer configurations. *IEEE Trans. Sonics Ultrason.* **SU-14**, 167–174.

Sittig, E. K. (1971). Definitions relating to conversion losses in piezoelectric transducers. *IEEE Trans. Sonics Ultrason.* **SU-18**, 231–234.

Smith, W. A., Shaulov, A. A., and Singer, B. M. (1984). Properties of composite piezoelectric material for ultrasonic transducers. *IEEE Ultrason. Symp. Proc*., 539–544.

Souquet, J., Defranould, P., and Desbois, J. (1979). Design of low-loss wide-band ultrasonic transducers for noninvasive medical application. *IEEE Trans. Sonics Ultrason*. **SU-26**, 75–81.

Stratton, J. A. (1941). *Electromagnetic Theory.* McGraw Hill, New York, pp. 97–103.

Szabo, T. L. (1982). Miniature phased-array transducer modeling and design. *IEEE Ultrason. Symp. Proc*., 810–814.

Szabo, T. L. (1984). Principles of nonresonant transducer design. *IEEE Ultrason. Symp. Proc*., 804–808.

Szabo, T. L. (1998). Transducer arrays for medical ultrasound imaging, Chap. 5. *Ultrasound in Medicine*, Medical Science Series, F. A. Duck, A. C. Baker, and H. C. Starritt (eds.). Institute of Physics Publishing, Bristol, UK.

Takeuchi, H., Jyomura, S., Ishikawa, Y., and Yamamoto, E. (1982). A 7.5 MHz linear array ultrasonic probe using modified $PbTiO_3$. *IEEE Ultrason. Symp. Proc*., 849–853.

Takeuchi, H., Masuzawa, H., Nakaya, C., and Ito, Y. (1990). Relaxor ferroelectric transducers. *IEEE Ultrason. Symp. Proc*., 697–705.

van Kervel, S. J. H. and Thijssen, J. M. (1983). A calculation scheme for the optimum design of ultrasonic transducers. *Ultrasonics*, 134–140.

von Ramm, O. T. (2000). 2D arrays. *Ultrasound in Med. & Biol*. **26**, Supplement 1, S10–S12.

Wildes, D. G., Chiao, R. Y., Daft, C. M. W., Rigby, K. W., Smith, L. S., and Thomenius, K. E. (1997). Elevation performance of 1.25D and 1.5D transducer arrays. *IEEE Trans. Ultrason. Ferroelectr. Freq. Control* **44**, 1027–1036.

Wojcik, G., DeSilets, C., Nikodym, L.,Vaughan, D., Abboud, N., and Mould. Jr., J. (1996). Computer modeling of diced matching layers. *IEEE Ultrason. Symp. Proc*., 1503–1508.

Yin, J., Jiang, B., and Cao, W. (2000). Elastic, piezoelectric, and dielectric properties of 0.995Pb $(Zn_{1/3}Nb_{2/3})O_3 -)0.45\,PbTiO_3$ single crystal with designed multidomains. *IEEE Trans. Ultrason. Ferroelectr. Freq. Control* **47**, 285–291.

Zhang, R., Jiang, B., and Cao, W. (2001). Elastic, piezoelectric, and dielectric properties of multidomain $0.67\,Pb\,(Mg_{1/3}\,Nb_{2/3})O_3 -)0.33\,PbTiO_3$ single crystals. *J. Appl. Phys*. **90**, 3471–3475.

This page intentionally left blank

6 BEAMFORMING

Chapter Contents

6.1 WHAT IS DIFFRACTION?

Chapter 3 explained that radiation from a line source consists of not just one plane wave but many plane waves being sprayed in different directions. This phenomenon is called diffraction (a wave phenomenon in which radiating sources on the scale of wavelengths create a field from the mutual interference of waves generated along the source boundary). A similar effect occurs when an ultrasound wave is

scattered from an object with a size on the order of wavelengths (to be described in Chapter 8).

Acoustic diffraction is similar to what occurs in optics. When the wavelength is comparable to the size of the objects, light does not create a geometric shadow of the object but a more complicated shadow region with fringes around the object. Light from a distant source incident on an opening (aperture) on the scale of wavelengths in an opaque plane will cause a complicated pattern to appear on a screen plane behind it.

The same thing happens with sound waves as is shown in Figure 6.1, which is an intensity plot of an ultrasound field in the *xz* plane. In the front is the line aperture radiating along the beam axis *z*. Here the scale of the *z* axis is compressed and represents about 1920 wavelengths, whereas the lateral length of the aperture is 40 wavelengths. Figure 6.2 gives a top view of the same field with the aperture on the left. Sound spills out beyond the width of the original aperture. Diffraction, in this case, gives the appearance of bending around objects! This phenomenum can be explained by the sound entering an aperture (opening) and reradiating secondary waves along the aperture beyond the region defined by straight geometric projection.

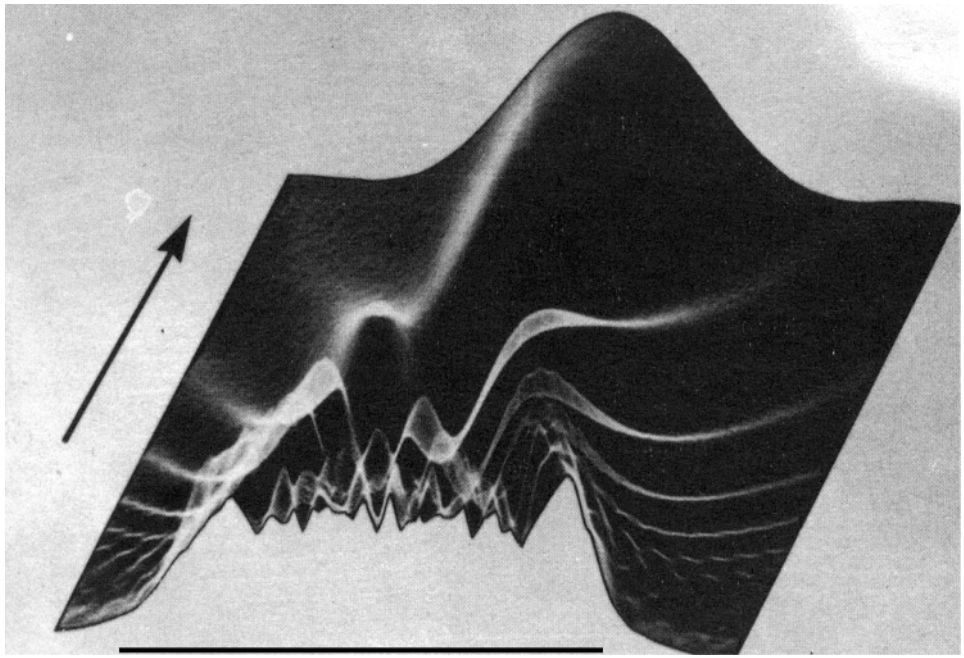

Figure 6.1 Diffracted field of a 40-wavelength-wide line aperture depicted as a black horizontal line. The vertical axis is intensity and shown as a gray scale (maximum equals full white), the beam axis is compressed relative to the lateral dimension, and 1920 wavelengths are shown (from Szabo and Slobodnik, 1973).

Figure 6.2 Top view of a diffracted field from a 40-wavelength-wide line aperture on the left. The same field from Figure 6.1 is shown in gray scale. The beam axis is compressed relative to the lateral dimension (from Szabo and Slobodnik, 1973).

Diffraction is the phenomenon that describes beams from transducers. This chapter emphasizes frequency domain methods of predicting the characteristics of the ultrasound fields radiated by transducer apertures. It examines two major approaches: One involves spatial frequencies (the angular spectrum of plane waves), and the other employs spherical waves. This chapter also covers both circular and rectangular apertures, as well as the important topics of focusing and aperture weighting (apodization). In Chapter 7, complementary time domain methods (spatial impulse response) are applied to simulate focused and steered beams from arrays.

6.2 FRESNEL APPROXIMATION OF SPATIAL DIFFRACTION INTEGRAL

Christian Huygens visualized the diffracting process as the interference from many infinitesimal spherical radiators on the surface of the aperture rather than many plane waves, an approach described in Section 2.3.2.2. His perspective gives an equally valid mathematical description of a diffracted field in terms of spherical radiators, as was shown in Eq. (3.17). Revisiting Figure 6.2, notice the many peaks and valleys near the aperture where the field could be interpreted as full of interference from many tiny sources crowded together. Also, far from the aperture, the spheres of influence have spread out, and the resulting field is smoother and more expansive. The Rayleigh–Sommerfeld integral (Goodman, 1968) is a mathematical way of describing Huygen's diffracting process as a velocity potential produced by an ideal radiating piston set in an (inflexible) hard baffle,

$$\phi(r, \omega) = \frac{-1}{2\pi} \int_s \frac{e^{i[\omega t - k\cdot(r-r_0)]} (\partial v(r_0)/\partial n) dS}{|r - r_0|} \tag{6.1a}$$

where $v_n = \partial v(r_0)/\partial n$ is the component of particle velocity normal to the element dS. Within the integrand, the frequency domain solution of a spherical radiator can be recognized from Chapter 3. In terms of the field pressure amplitude shown in Eq. (3.3b), this model can be described as a spatial integral of the particle velocity over the source S,

$$p(r, \omega) = \frac{i\rho_0 ck v_0}{2\pi} \int_s \frac{e^{i[\omega t - k\cdot(r-r_0)]} A(r_0) dS}{|r - r_0|} \tag{6.1b}$$

where $v_n = v_0 A(r_0)$ is the normal particle velocity and $A(r_0)$ is its distribution across the aperture S (shown in Figure 6.3). For a rectangular coordinate system, the Fresnel or paraxial approximation of this integral is an expansion of the vector $|r - r_0|$ as a small-term binomial series,

$$|r - r_0| = \sqrt{z^2 + (x - x_0)^2 + (y - y_0)^2} \tag{6.2a}$$

$$|r - r_0| \approx z \left[1 + \frac{1}{2} \left(\frac{x - x_0}{z} \right)^2 + \frac{1}{2} \left(\frac{y - y_0}{z} \right)^2 \right] \tag{6.2b}$$

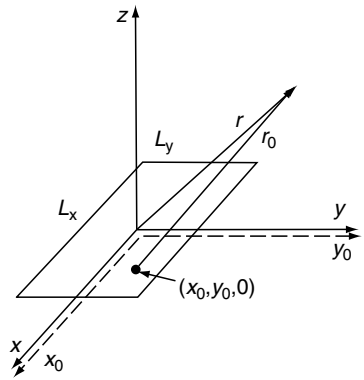

Figure 6.3 Coordinate system of an aperture in the *xy* plane and radiating along the *z* axis. Source coordinates in the aperture plane are denoted by the subscript (0). The rectangular aperture has sides L_x. and L_y. Radial arrows end in a spatial field point.

where the terms in Eq. (6.2b) are small compared to one and a replacement of $|r - r_0|$ in the denominator by z results in

$$p(r, \omega) = \frac{i\rho_0 ck v_0}{2\pi z} e^{i(\omega t - kz)} e^{-ik(x^2+y^2)/2z} \int\int_s [e^{-ik(x_0^2+y_0^2)/2z} A(x_0, y_0)] e^{ik(xx_0+yy_0)/z} dx_0 dy_0 \tag{6.3}$$

If the aperture has a rectangular shape (shown in Figure 6.4), it has sharp transitions along its boundary, and it can be represented by an aperture function,

$$A(x_0, y_0, 0) = A_x(x_0) A_y(y_0) \tag{6.4a}$$

should be $x_0 + y_0$ rather than $x + y$
$+L_x \quad L_y$ rather than $L_x \quad L_y$

$$A(x_0, y_0, 0) = \prod(x_0/L_x) \prod(y_0/L_y) \tag{6.4b}$$

If the aperture distribution function is separable, as in Eq. (6.4a), then the integration can be performed individually for each plane. As an example, if the plane-wave exponent is neglected, and

$$A_0 = \frac{\rho_0 ck v_0}{2\pi z} = \frac{p_0 k}{2\pi z} = \frac{p_0}{\lambda z} \tag{6.5a}$$

The overall integral can be factored as $p(x, y, z, w) = p_x(x, z, w)\ p_y(y, z, w)$ so that each integral is of the form,

$$p_x(x, \omega) = \sqrt{A_0}\ e^{i\pi/4} e^{-ikx^2/2z} \int_{-\infty}^{\infty} [e^{-ikx_0^2/2z} A(x_0)] e^{ik(xx_0)/z} dx_0 \tag{6.5b}$$

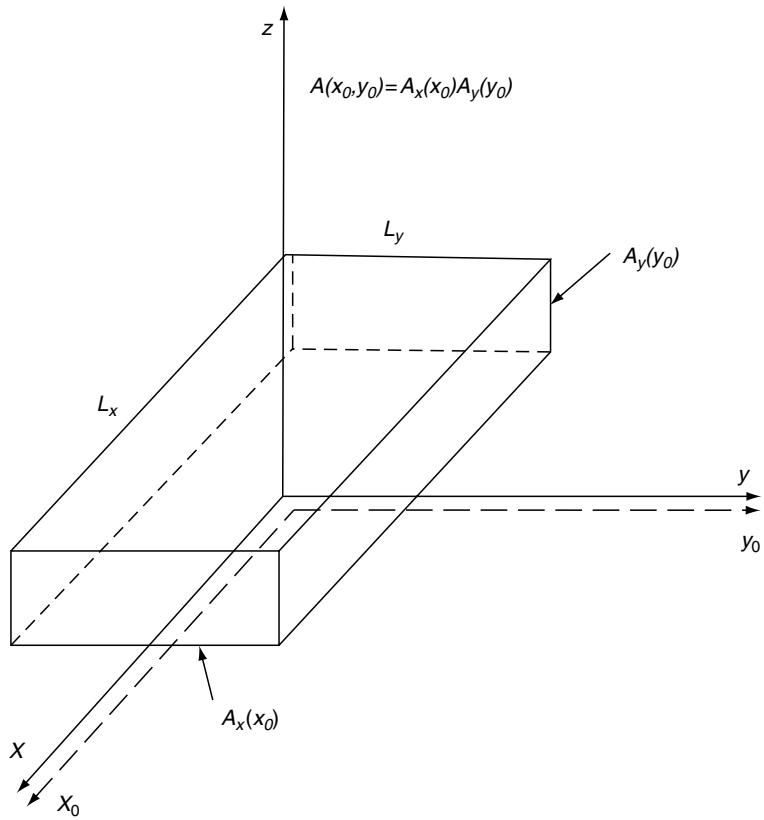

Figure 6.4 A constant amplitude aperture function for a rectangular aperture consists of two orthogonal rect functions multiplied together.

If we define $\Gamma = 1/(\lambda z)$, and $\varsigma = \Gamma x_0$, then this integral can be recognized as plus-i Fourier transform of the argument in the brackets (Szabo, 1977; Szabo, 1978),

$$p_x(x, \Gamma, \omega) = \frac{\sqrt{A_0}}{\Gamma} e^{i\pi/4} e^{-i\pi\Gamma x^2} \int_{-\infty}^{\infty} [e^{-i\pi\varsigma^2/\Gamma} A(\varsigma/\Gamma)] e^{i2\pi\varsigma x} d\varsigma \tag{6.5c}$$

which can be evaluated by a standard inverse Fast Fourier transform (FFT) algorithm.

6.3 RECTANGULAR APERTURE

The previous analysis can be applied to the prediction of a field from a solid rectangular aperture, which is the same outer shape as most linear and phased array transducers. These aperture shapes will be helpful in anticipating the fields of arrays. Predictions will be only for a single frequency, yet they will provide insights into the characteristics

of beams from any rectangular aperture radiating straight ahead along the beam axis. Here relations for fields from line sources are derived to clarify the main features of an ultrasound field. For example, a line source can be used to simulate the field in an azimuth or *xz* imaging plane. Two orthogonal line apertures can be applied to simulate a rectangular aperture, as is given by Eq. (6.4a) and Figure 6.4.

For many cases, simple analytic solutions can be found (Szabo, 1978). For example, for the case of a constant normal velocity on the aperture, with A as the rectangular function of Eq. (6.4b), an exact expression for the pressure field under the Fresnel approximation can be found from Eq. (6.5c),

$$p_x(x, z, \omega) = \frac{\sqrt{p_0}}{\sqrt{2}} e^{i\pi/4} \left[F\left(\frac{x + L_x/2}{\sqrt{\lambda z/2}} \right) - F\left(\frac{x - L_x/2}{\sqrt{\lambda z/2}} \right) \right] \tag{6.6}$$

where

$$F(z) = \int_0^z e^{-i\pi t^2/2} dt \tag{6.7a}$$

and $F(z)$ is the Fresnel integral of negative argument (Abramowitz and Stegun, 1968),

Far from the aperture, the quadratic phase terms in Eq. (6.5c) are negligible, and the pressure at a field point is simply the plus-i Fourier transform of the aperture distribution, as

$$p_x(x, \Gamma, \omega) = \frac{\sqrt{A_0}}{\Gamma} e^{i\pi/4} \int_{-\infty}^{\infty} [A(\varsigma/\Gamma)] e^{i2\pi\varsigma x} d\varsigma \tag{6.8}$$

which, for a constant amplitude aperture distribution is

$$p_x(x, \Gamma, \omega) = \frac{L_x}{\lambda z} \left(\frac{\sqrt{A_0}}{\Gamma} \right) e^{i\pi/4} \, sinc\left(\frac{L_x x}{\lambda z} \right) = \frac{L_x \sqrt{\rho_0}}{\sqrt{\lambda z}} e^{i\pi/4} \, sinc\left(\frac{L_x x}{\lambda z} \right) \tag{6.9a}$$

The field from a 28-wavelength-wide aperture, is presented as a contour plot in Figure 6.5a. The contours represent points in the field that are −3 dB, −6 dB, −10 dB, and −20 dB below the maximum axial value at each depth (z) in the field. This plot was generated by a public beam simulation program developed by Professor S. Holm and his group at the University of Oslo, Norway (see Section 7.8 for more information). The far-field beam profile pattern is given by Eq. (6.9a) and shown in Figure 6.11. To determine the −6-dB beam halfwidth far from the aperture, solve for the value of x in the argument of the *sinc* function of Eq. (6.9a) that gives a pressure amplitude value of 0.5 of the maximum value,

$$x_{-6} = 0.603 \lambda z / L \tag{6.9b}$$

and the full width half maximum (FWHM) is twice the −6-dB half beamwidth,

$$FWHM = 1.206 \lambda z / L \tag{6.9c}$$

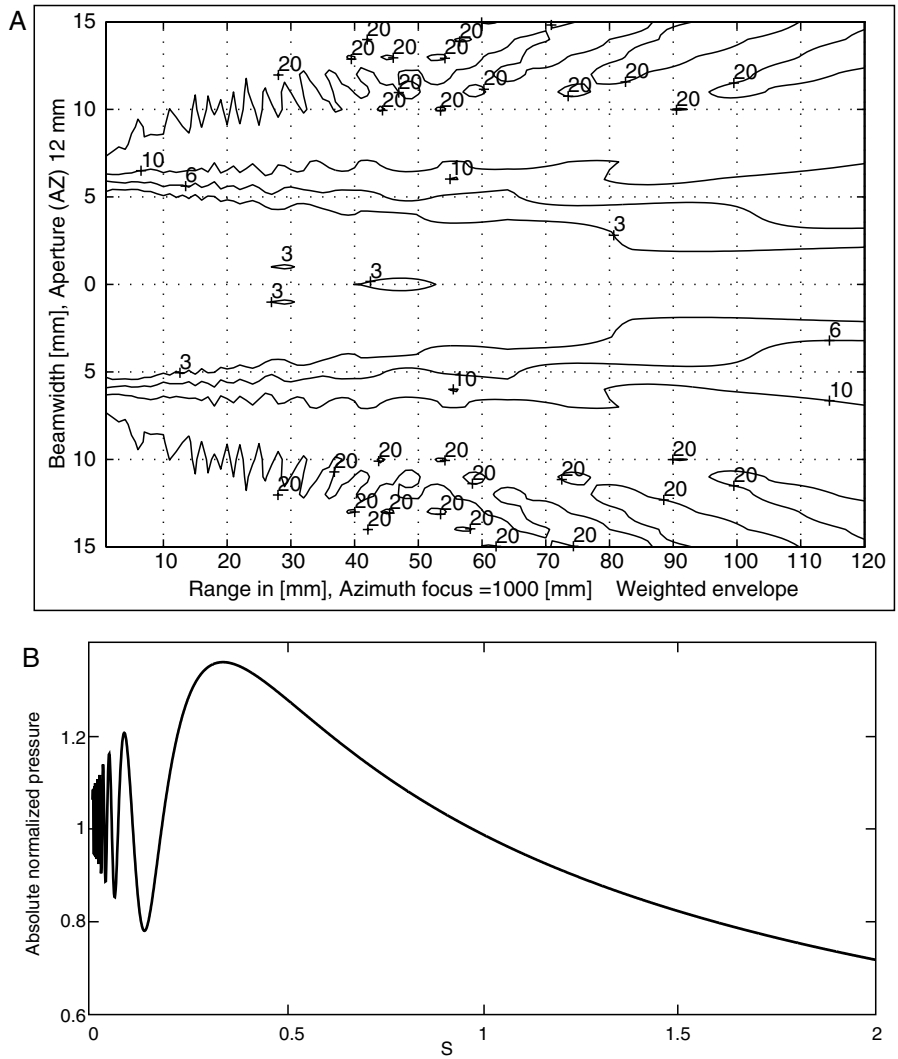

Figure 6.5 (A) Contour beam plot for a 12-mm (28 wavelength), 3.5-MHz line aperture with −3-dB, −6-dB, −10-dB, and −20-dB contours normalized to axial values at each depth. Nonfocusing aperture approximated by setting deep focal depth to 1000 mm ($S = 3$) (Plot generated using Ultrasim software developed by Professor S. Holm of the University of Oslo.) (B) Axial plot of normalized absolute pressure versus S from Eq. (6.10a) with $S = 0.36$ corresponding to $Z = 120$ mm.

The −6-dB beamwidth just calculated can be compared to the actual −6-dB contour in Figure 6.5a to illustrate the good match at longer distances from the aperture. Other beamwidths, such as the -20 dB, can be determined by this approach as well. A decibel plot of the half-beam (symmetry applies) over a larger range is shown in the top right of Figure 6.6. Section 6.4 will explain the effect of changing the amplitude profile of the source on the beam shape.

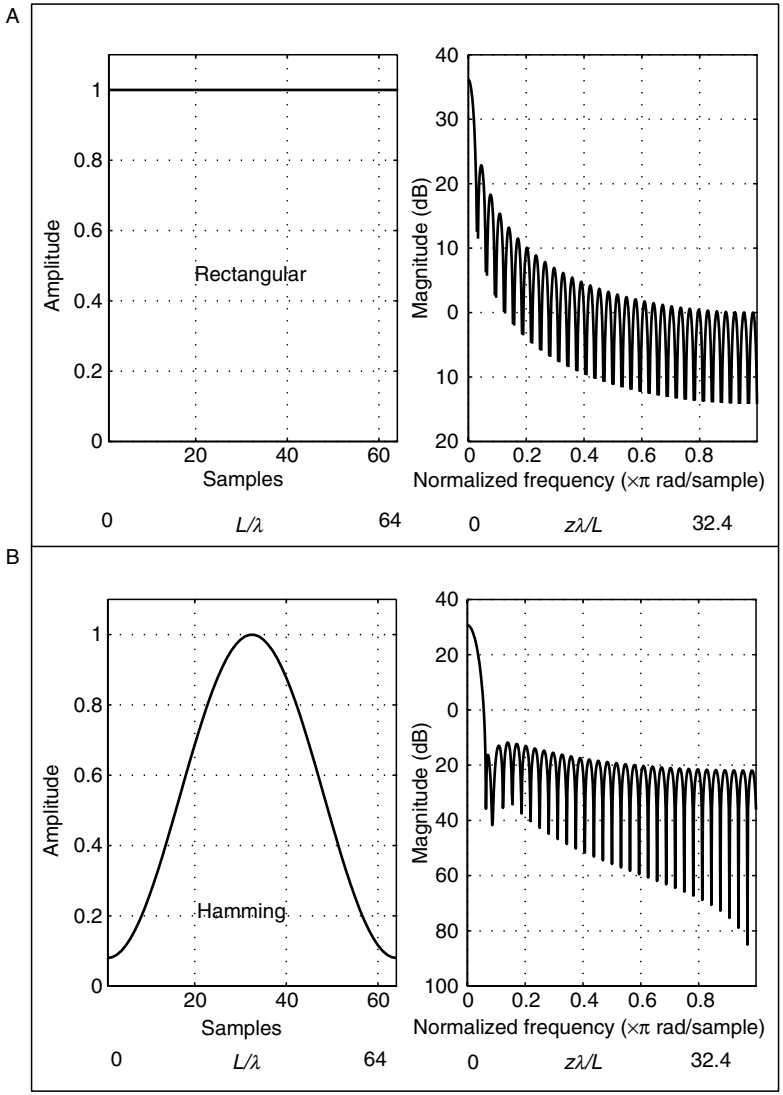

Figure 6.6 Far-field beam cross sections or beam profile on a scale for a (A) rectangular constant amplitude function source and (B) truncated Gaussian source.

The beam along the z axis can be found by setting $x = 0$ in Eq. (6.6),

$$p(0, z, \omega) = e^{i\pi/4}\sqrt{2p_0}\left[F\left(\frac{L_x/2}{\sqrt{\lambda z/2}}\right)\right] = e^{i\pi/4}\sqrt{2\rho_0}\left[F\left(\frac{1}{\sqrt{2S}}\right)\right] \tag{6.10a}$$

An axial cross section of the beam that was calculated from this equation is plotted in Figure 6.5b. Note that for any combination of parameters L_x, z, and λ that have the

same argument in F of Eq. (6.10a), identical results will be obtained. This argument leads to a universal parameter (S),

$$S = \lambda z/L^2 = \hat{z}/\hat{L}^2 \tag{6.10b}$$

where wavelength-scaled parameters are useful, $\hat{z} = z/\lambda$, and $\hat{L} = L/\lambda$. The universal parameter S can be expressed equally well in wavelength-scaled variables, as can previous equations such as Eqs. (6.6), (6.9a), and (6.10a). The mathematical substitution of wavelength-scaled variables shows that what matters are the aperture and distance in wavelengths. For example, a 40-wavelength wide aperture will have the same beam-shape irrespective of frequency.

A second observation is that nearly identical beam-shapes will occur for the same value of S, as shown for beam profiles in Figure 6.7. A definite progression of beam patterns occurs as a function of z, but if these profiles are replotted as a function of the universal parameter S, this same sequence of profile shapes can apply to all apertures and distances except very near the aperture. For the same value of S, the same shapes occur for different combinations of z and L. Look at Figure 6.8, in which different apertures and distances combine to give the same value of $S = 0.3$. For example, if $\lambda = 1\,\text{mm}$, and $L_1 = 40\,\text{mm}$, $z_1 = 480\,\text{mm}$; if $L_2 = 40\,\text{mm}$, then $z_2 = 1920\,\text{mm}$ to give the same value of S. This scaling result can be shown by reformulating the arguments of Eq. (6.6) in terms of wavelength-scaled parameters and S,

$$\left(\frac{\hat{x} + \hat{L}_x/2}{\sqrt{\hat{z}/2}}\right) = \left(\frac{\hat{x}/\hat{L}_x \pm 1/2}{\sqrt{S/2}}\right) \tag{6.10c}$$

From this relation, it is evident that for two combinations of z and L values having the same value of S, the argument will have exactly the same numerical value when $\hat{x}_2 = (\hat{L}_2/\hat{L}_1)\hat{x}_1$. In the previous example, this result shows that for the larger aperture, the profile is stretched by a scaling factor of two over the profile for the smaller aperture (shown in Figure 6.8). Remember that a limitation to this approach is that the distance and aperture combinations must satisfy the Fresnel approximation, Eq. (6.2b), on which this result depends.

A third realization is that the last axial maximum, shown in Figure 6.5, occurs at a transition distance, $z_t \approx L_x^2/(\pi\lambda)$, or when the argument in Eq. (6.10a) is equal to $\sqrt{\pi/2}$. This distance separates the "near" and "far" fields and is called the "natural focus." More exactly, Figure 6.5b shows $z_{\max} = 0.339\,L_x^2/\lambda$. The location of minimum -6-dB beamwidth is $z_{\min} = 0.4L_x^2/\lambda$. Eq. (6.6) describes the whole field along the axis (except perhaps very close to the aperture). A program rectax.m, based on Eq. (6.10a), was used to calculate Figure 6.5b. In the far field, given by Eq. (6.9a), the pressure along the axis falls off as $(\lambda z)^{-1/2}$. The shape of the far field is only approximately given by Eq. (6.9a) because, in reality, the transition to a final far-field shape (in this example, a *sinc* function) occurs gradually with distance from the aperture. For a rectangular array, the contributions from both apertures to the field can be written as

$$p(x, y, z, \lambda) = \frac{p_0}{2} e^{i\pi/2} \left[F\left(\frac{x + L_x/2}{\sqrt{\lambda z/2}}\right) - F\left(\frac{x - L_x/2}{\sqrt{\lambda z/2}}\right)\right] \left[F\left(\frac{y + L_y/2}{\sqrt{\lambda z/2}}\right) - F\left(\frac{y - L_y/2}{\sqrt{\lambda z/2}}\right)\right] \tag{6.11a}$$

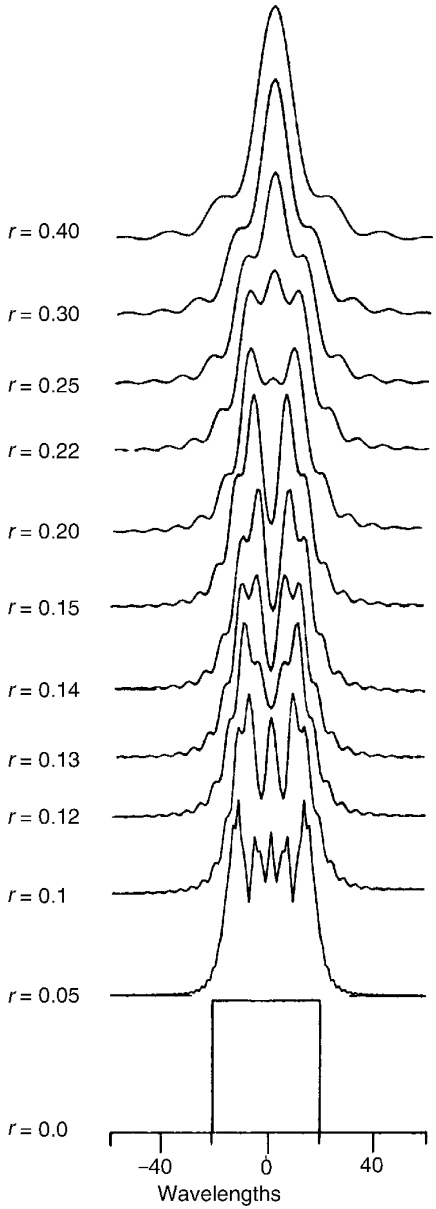

Figure 6.7 Diffraction beam profiles for different values of $S = r$ with $\hat{L} = 40(\lambda)$. Profiles for other values of L can be found by scaling the profile at the appropriate value of S (from Szabo and Slobodnik, 1973).

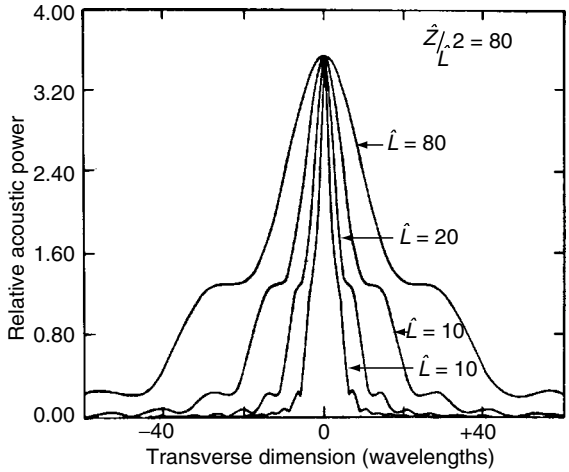

Figure 6.8 Diffraction beam profiles versus transverse wavelength-scaled distance ($\hat{x}$) for different values of wavelength-scaled apertures $\hat{L}$ and the same value of $S = 0.3$ (from Szabo and Slobodnik, 1973).

and the on-axis pressure is

$$p(0,\ 0,\ z,\ \lambda) = e^{i\pi/2} 2p_0 \left[F\left(\frac{L_x/2}{\sqrt{\lambda z/2}} \right) F\left(\frac{L_y/2}{\sqrt{\lambda z/2}} \right) \right] \tag{6.11b}$$

and there can be two on-axis peaks if $L_x \neq L_y$ (one from the natural focus in the xz plane and another from the natural focus in the yz plane). Experimental verification of these equations for rectangular apertures can be found in Sahin and Baker (1994).

6.4 APODIZATION

Apodization is amplitude weighting of the normal velocity across the aperture. In a single transducer, apodization can be achieved in many ways, such as by tapering the electric field along the aperture, by attenuating the beam on the face of the aperture, by changing the physical structure or geometry, or by altering the phase in different regions of the aperture. In arrays, apodization is accomplished by simply exciting individual elements in the array with different voltage amplitudes.

One of the main reasons for apodization is to lower the sidelobes on either side of the main beam. Just as time sidelobes in a pulse can appear to be false echoes, strong reflectors in a beam profile sidelobe region can interfere with the interpretation of on-axis targets. Unfortunately, for a rectangular aperture, the far-field beam pattern is a *sinc* function with near-in sidelobes only −13 dB down from the maximum on-axis value (shown in Figure 6.6a). A strong reflector positioned in the first sidelobe could be misinterpreted as a weak (−13 dB) reflector on-axis. Shaping is also important

because, as we shall discuss later, the beam-shape at the focal length of a transducer has the same shape as that in the far field of a nonfocusing aperture.

A key relationship for apodization for a rectangular aperture is that in each plane, the far-field pattern is the plus-i Fourier transform of the aperture function, according to Eq. (6.8). Aperture functions need to have rounded edges that taper toward zero at the ends of the aperture to create low sidelobe levels. Functions commonly used for antennas and transversal filters are *cosine*, Hamming, Hanning, Gaussian, Blackman, and Dolph–Chebycheff (Harris, 1978; Szabo, 1978; Kino, 1987). There is a trade-off in selecting these functions: The main lobe of the beam broadens as the sidelobes lower (illustrated by Figure 6.6b). A number of window functions can be explored conveniently and interactively through the wintool graphical user interface in the MATLAB signal processing toolbox; this interface was used to create Figure 6.6, which compares Hamming apodization to no apodization. The effect of apodization on the overall field is given by Figure 6.9, which compares the field from the same truncated Gaussian apodization with that from an unapodized aperture. Here not only is the apodized beamshape more consistent, but also the axial variation is less. Note that for any apodization, universal scaling can be still applied even though the beam evolution is different.

6.5 CIRCULAR APERTURES

6.5.1 Near and Far Fields for Circular Apertures

Many transducers are not rectangular in shape but are circularly symmetric; expressions for their fields can be described by a single integral. The spatial diffraction integral, Eq. (6.3), can be rewritten in polar coordinates for apertures with a circular geometry, neglecting the plane wave factor (Goodman, 1968; Szabo, 1981), as

$$p(\bar{\rho}, z,) = \frac{i2\pi p_0}{\lambda z} e^{-i\pi\bar{\rho}^2/\lambda z} \int_0^\infty A(\bar{\rho}_0) e^{-i\pi\bar{\rho}_0^2/\lambda z} J_0\left(\frac{2\pi\overline{\rho\rho}_0}{\lambda z}\right) \bar{\rho}_0 d\bar{\rho}_0 \tag{6.12a}$$

in which $\bar{\rho}$ and $\bar{\rho}_0$ are the cylindrical coordinate radii of the field and source (as distinct from ρ_0 used for density),

$$\bar{\rho}^2 = x^2 + y^2 \tag{6.12b}$$

$$\bar{\rho}_0^2 = x_0^2 + y_0^2 \tag{6.12c}$$

for a field point $(\bar{\rho}, z)$ (given in Figure 6.10), and J_0 is a zero-order Bessel function. By letting $\Upsilon = 2\pi\bar{\rho}/(\lambda z)$, we can transform the integral above through a change in variables,

$$p(\bar{\rho}, z,) = \frac{i2\pi p_0}{\lambda z} e^{-i\Upsilon\bar{\rho}/2} \int_0^\infty [A(\bar{\rho}_0) e^{-i\pi\bar{\rho}_0^2/\lambda z}] J_0(\Upsilon\bar{\rho}_0) \bar{\rho}_0 d\bar{\rho}_0 \tag{6.13}$$

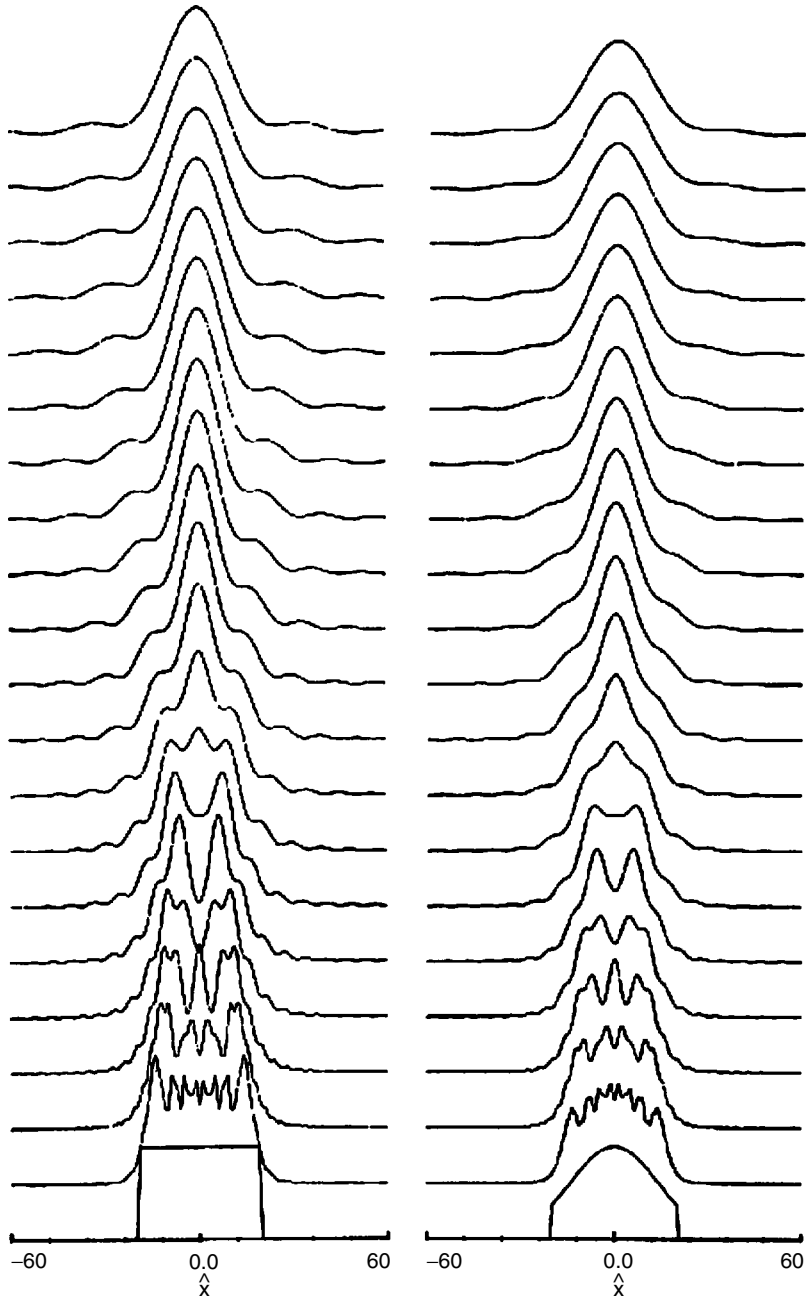

Figure 6.9 Diffraction beam profiles for an unapodized aperture (on the left) compared to a truncated Gaussian aperture (on the right), both with an overall aperture of 40 wavelengths (from Szabo, 1978).

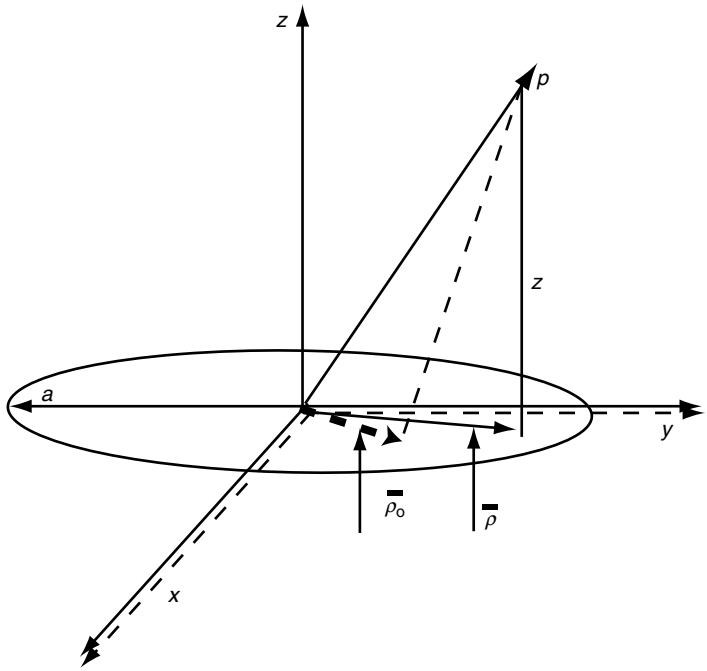

Figure 6.10 Cylindrical coordinate system for circularly symmetric apertures.

This equation is a zero-order Hankel transform, defined with its inverse as the following:

$$\mathbf{A}(q) = H[\mathbf{U}(r)] = \int_0^\infty U(r)J_0(qr)rdr \tag{6.14a}$$

$$U(q) = H^{-1}[\mathbf{A}(q)] = \int_0^\infty \mathbf{A}(q)J_0(qr)qdq \tag{6.14b}$$

Equations (6.12a) and (6.13) are valid for both the near and far fields. In the far field, as $\bar{\rho}/z$ and $\bar{\rho}_0/z$ become very small, then

$$p(\bar{\rho}, z, \lambda) \approx \frac{i2\pi p_0}{\lambda z} \int_0^\infty A(\bar{\rho}_0)J_0(\Upsilon\bar{\rho}_0)\bar{\rho}_0 d\bar{\rho}_0 \tag{6.15}$$

Therefore, the pressure beam pattern in the far field is the Hankel transform of the aperture function. For a constant normal velocity across the aperture of radius a,

$$A(\bar{\rho}_0) = \prod\left(\frac{\bar{\rho}_0/2}{a}\right) \tag{6.16}$$

$$p(\bar{\rho}, z, \lambda) \approx \frac{i2\pi p_0}{\lambda z} H\left[\prod\left(\frac{\bar{\rho}_0/2}{a}\right)\right] \tag{6.17a}$$

$$p(\bar{\rho}, z, \lambda) \approx \frac{ip_0\pi a^2}{\lambda z}\frac{2J_1(2\pi pa/(\lambda z))}{2\pi pa/(\lambda z)} = ip_0 c u_0\left(\frac{\pi a^2}{\lambda z}\right) jinc\left(\frac{\rho a}{\lambda z}\right) \tag{6.17b}$$

where

$$jinc(x) = 2J_1(2\pi x)/(2\pi x) \tag{6.18a}$$

and J_1 is a first order Bessel function. The far-field beam cross section is shown in Figure 6.11. The FWHM for this aperture is

$$FWHM = 0.7047\lambda z/a \tag{6.18b}$$

An exact expression without approximation can be obtained for on-axis pressure,

$$|p(0, z, \lambda)| = 2p_0 \sin\left\{\frac{kz}{2}\left[\sqrt{1 + (a/z)^2} - 1\right]\right\} \tag{6.19a}$$

which under the Fresnel approximation, $z^2 \gg a^2$, is

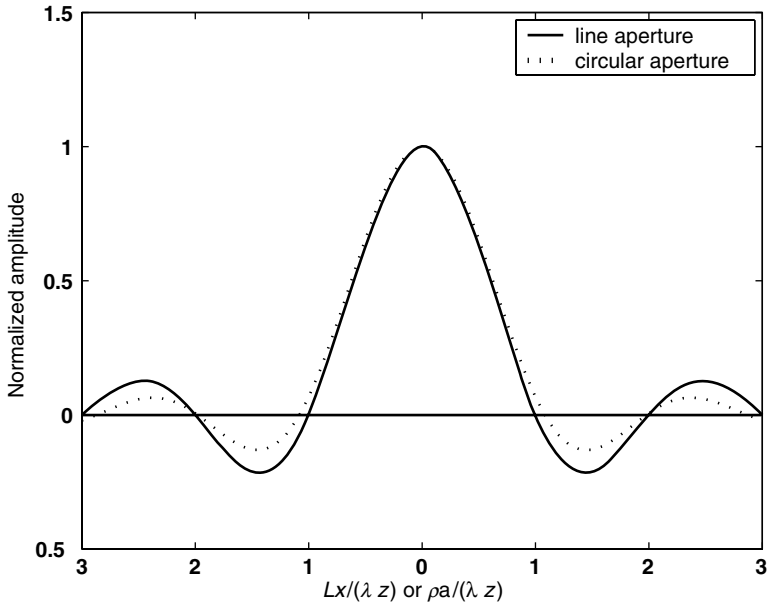

Figure 6.11 Far-field *jinc* beam-shape from a circular aperture (dashed line) normalized to a far-field *sinc* function from a line aperture (solid line) with the same aperture area.

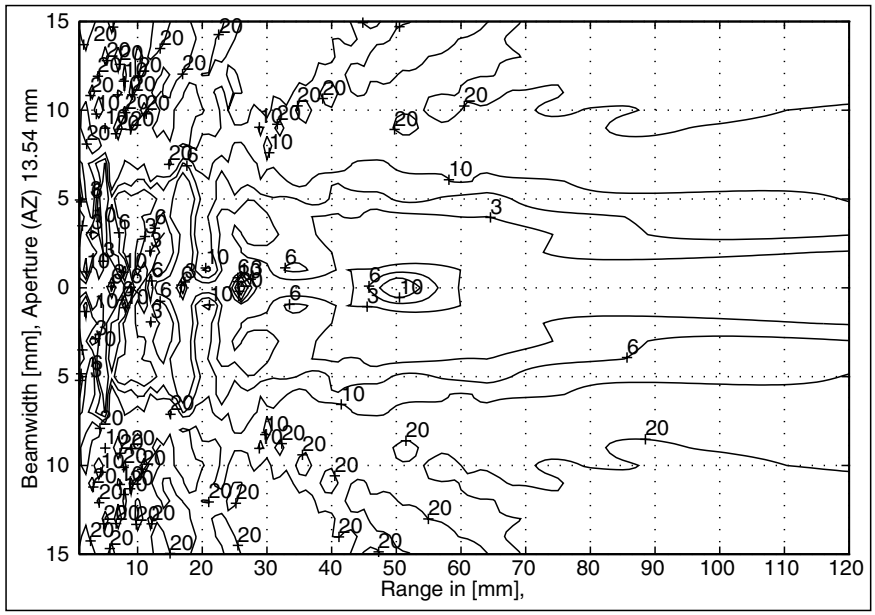

Figure 6.12 Contour beam plot for a 13.54-mm-diameter, 3.5-MHz circular aperture with −3-dB, −6-dB, −10-dB, and −20-dB contours normalized to axial values at each depth. (Plot generated using Ultrasim software developed by Professor S. Holm of the University of Oslo.)

$$p(0,\, z,\, \lambda) \approx i2p_0 e^{-ikz} e^{-i\pi a^2/2\lambda z} \sin\left(\frac{\pi a^2}{2\lambda z}\right) \tag{6.19b}$$

Note that for large values of z, the phase from the beginning factor of Eq. (6.19b) goes to $\pi/2$ as in Eq. (6.11b). A contour plot for a 13.54-mm-diameter aperture is given in Figure 6.12.

6.5.2 Universal Relations for Circular Apertures

The argument of the *sine* function in Eq. (6.19b) has a familiar look. If we define a diffraction parameter for circular apertures as $S_c = z\lambda/a^2$, then (6.19b) becomes

$$|p(0,\, z,\, \lambda)| \approx 2p_0 \sin\left(\frac{\pi}{2S_c}\right) \tag{6.19c}$$

We can see that the last axial maximum occurs when $S_c = 1$ (the argument $= \pi/2$) or equivalently, when $z_{\max} = z_t = a^2/\lambda$, the transition point is between near and far fields. Note the similarity to the transition distance for a line source, which occurs when the argument of Eq. (6.10a) is equal to $\sqrt{\pi/2}$.

As we would expect from linearity and transform scaling, similar beam-shapes occur for the same values of the S_c parameter. Apodization can be applied to circular apertures using Hankel transforms of window functions.

The aperture area also plays a role in determining the axial far-field falloff in amplitude. If the circular aperture area is set equal to a square aperture, then

$\pi a^2 = L^2$, or $a = L/\sqrt{\pi}$. Beam profiles of different shapes can be compared on an equivalent area basis as done in Figure 6.11. Figures 6.5a and 6.12 were generated on an equivalent area basis for a square aperture and a circular one. Substitute this equivalent value of a in

$$z_{\max} = a^2/\lambda \approx L^2/(\pi\lambda) \tag{6.20a}$$

where the distance to the maximum for a line aperture is given approximately. Recall that a more accurate value for the line aperture is $z_{\max} = 0.339L^2/\lambda$. In general, approximately

$$z_{\max} = AREA/(\pi\lambda) \tag{6.20b}$$

For large values of z, the replacement of *sine* by its argument in Eq. (6.19b) leads to a far-field falloff of

$$|p(0, z, \lambda)| \approx p_0(\pi a^2)/(z\lambda) = p_0 AREA/(z\lambda) \tag{6.21a}$$

and a similar far-field approximation for Eq. (6.11b) for a rectangular aperture gives

$$|p(0, z)| \approx \sqrt{p_0(L^2)/(z\lambda)} = \sqrt{p_0 AREA/(z\lambda)} \tag{6.21b}$$

6.6 FOCUSING

6.6.1 Derivation of Focusing Relations

Focusing is usually accomplished by a lens on the outer surface of a transducer, by the curvature of the transducer itself, or by electronic means in which a sequence of

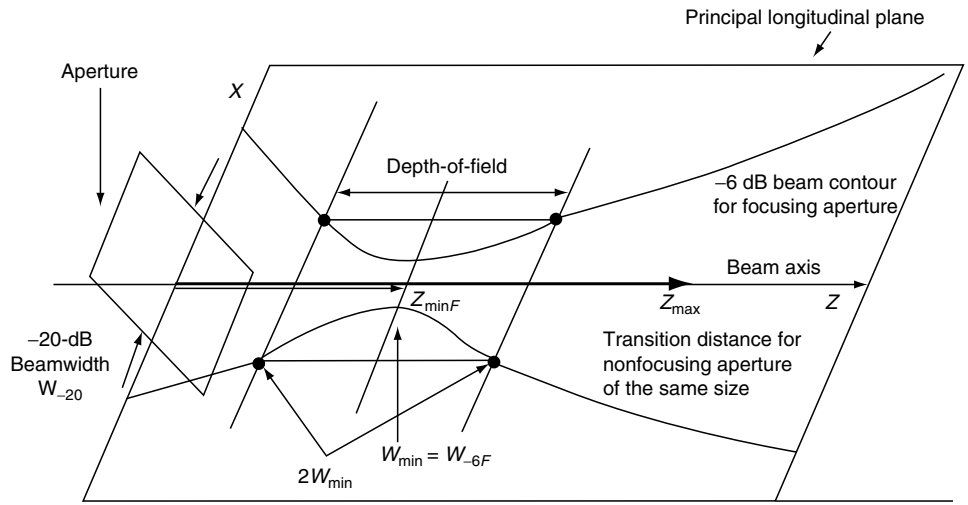

Figure 6.13 Focusing as defined by the narrowness of a beam in a specified plane (from IEC 61828, 2001).

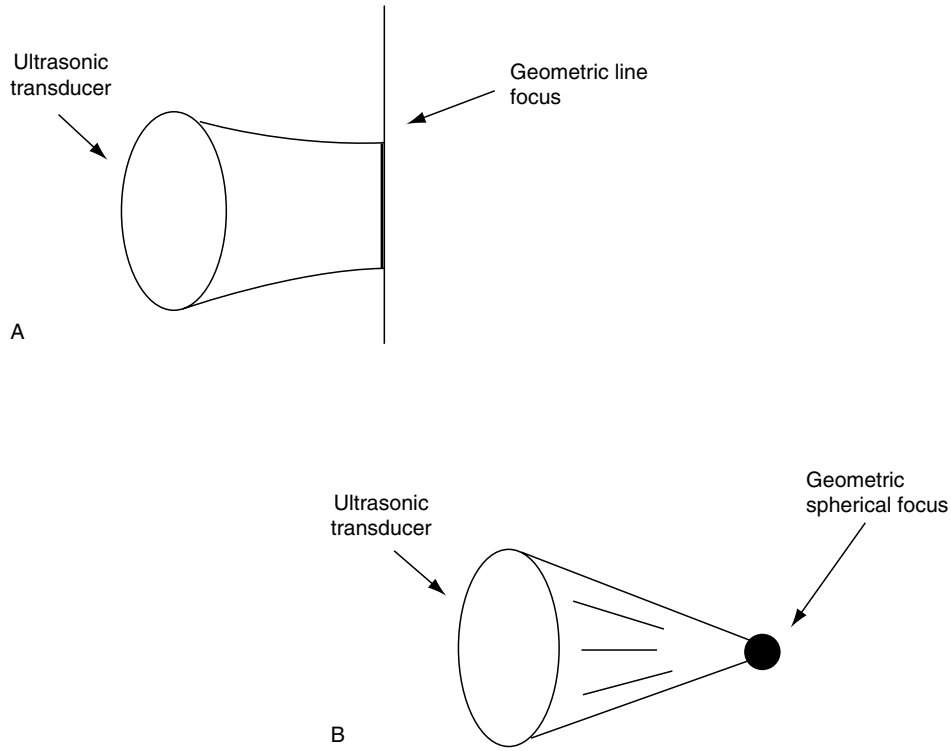

Figure 6.14 (A) Line focusing for a cylindrical lens. (B) Point focusing by a spherical lens (from IEC 61828, 2001).

delayed pulses produce the equivalent of a lens. We shall focus our attention on the thin lens. Lenses can be cylindrical (curvature in one plane only) for a geometric line focus or spherical (curvature the same in all planes around an axis) for a geometric focus at a point (shown in Figure 6.14).

By a convention similar to but opposite in sign to that of optics, a thin lens is made of a material with an index of refraction, n, and a thickness, $\Delta(x, y)$, as shown in Figure 6.15. This lens has a phase factor,

$$T_L(x, y) = \exp(ik\Delta_0)\exp(ik(n-1)\Delta(x, y)) \tag{6.22}$$

where k is for the medium of propagation (usually water or tissue) and Δ_0 is a constant. For a paraxial approximation (Goodman, 1968),

$$\Delta(x, y) \approx \Delta_0 - \frac{(x^2 + y^2)}{2}\left(\frac{1}{R_2} - \frac{1}{R_1}\right) \tag{6.23}$$

where R_1 and R_2 are the lens radii (shown in Figure 6.15). A geometric focal length is defined (Goodman, 1968) as

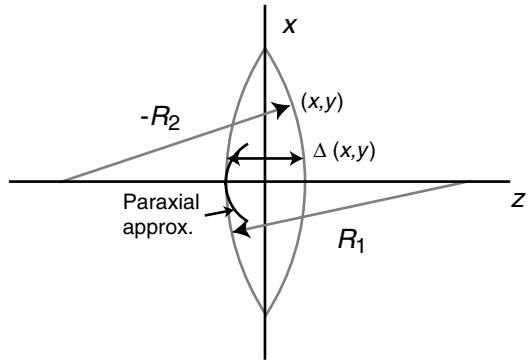

Figure 6.15 Thin lens geometry and definitions.

$$\frac{1}{F} \triangleq (n-1)\left(\frac{1}{R_1} - \frac{1}{R_2}\right) \tag{6.24}$$

so that the phase factor for a thin lens is

$$T_L(x, y) = \exp(ikn\Delta_0)\exp(ik(x^2 + y^2)/2F) \tag{6.25}$$

and the first factor, $\exp(ikn\Delta_0)$, a constant, is dropped or set to equal one.

Unlike optics, ultrasonic lenses can have an index of refraction of less than one (shown in Figure 6.16). Here common lens shapes are plano-convex or plano-concave, where one side is flat and the corresponding R is infinite. For example, for the plano-concave lens and the convention (opposite of that used in optics) shown in Figure 6.16, the focal length becomes

$$\frac{1}{F} \triangleq (n-1)\left(\frac{1}{\infty} - \frac{1}{R_{LENS}}\right) \tag{6.26a}$$

or

$$F = \frac{-R_{LENS}}{n-1} = \left|\frac{R_{LENS}}{n-1}\right| \tag{6.26b}$$

which numerically is a positive number because n is less than one (the case in Figure 6.16b). By similar reasoning, in the case in Figure 6.16c, which has a positive radius of curvature by convention and a positive index of refraction, the focal length also ends up being a positive number,

$$F = \frac{R_{LENS}}{n-1} = \left|\frac{R_{LENS}}{n-1}\right| \tag{6.26c}$$

If the phase factor, Eq. (6.25), with the understanding of the numerical value of the geometric focal length,

$$T_L(x, y) = \exp(ik(x^2 + y^2)/2F) \tag{6.27a}$$

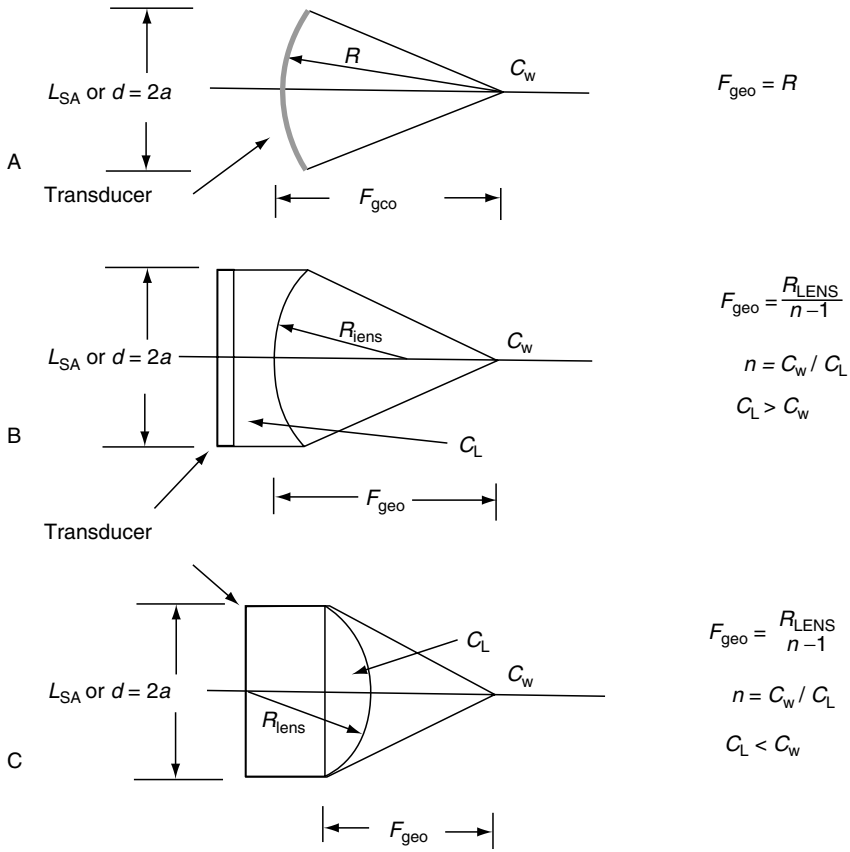

Key

R	radius of curvature
F_{geo}	geometric focal length
c	speed of sound
n	index of refraction
C_L	speed of sound in lens
C_w	speed of sound in water

Figure 6.16 Methods of focusing. (A) Transducer with a radius of curvature R so that the focal length is equal to R. (B) Transducer with a plano-concave lens. (C) Transducer with a plano-convex lens (from IEC 61828, 2001).

is put in the diffraction integral, Eq. (6.3) under the Fresnel approximation, the following results:

$$p(r, \omega) = \frac{ip_0 k}{2\pi z} e^{i(\omega t - kz)} e^{-ik(x^2+y^2)/2z} \iint_s [e^{-ik(x_0^2+y_0^2)/2z} e^{ik(x_0^2+y_0^2)/2F} A(x_0, y_0)] e^{ik(xx_0+yy_0)/z} dx_0 dy_0 \tag{6.27b}$$

The net effect is replacing the $-1/z$ term in the quadratic term in the integrand by $-(1/z - 1/F)$, or

$$1/z_e = 1/z - 1/F \tag{6.28a}$$

This relation can be thought of as replacing the original z in Eq. (6.3) by an equivalent z_e,

$$z_e = z/(1 - z/F) \tag{6.28b}$$

Recall that without focusing, a prescribed sequence of beam patterns occurs along the beam axis z (shown in Figure 6.7). With focusing, the same shapes occur but at an accelerated rate at distances given by z_e. Thus, the whole beam evolution that would normally take place for a nonfocusing aperture from near field to extreme far field occurs for a focusing transducer within the geometric focal length F! At the focal distance, $z = F$, the quadratic term in the integrand of Eq. (6.27b) is zero, and the beam-shape is the double $+i$ Fourier transform of the aperture function in rectangular coordinates. Note, as before, that the aperture can be factored into two functions, so a single Fourier transform is required for each plane (xz or yz). Similarly, for a spherically focusing transducer, Eq. (6.28) also holds; the Hankel transform of the aperture function occurs at $z = F$.

6.6.2 Zones for Focusing Transducers

To understand the different regions of focusing, we return to an approximate expression for the on-axis pressure, Eq. (6.19b) from a circularly symmetric transducer, but this time with spherical focusing and for $z \neq F$,

$$p(0, z,) \approx \frac{i2p_0 e^{-ikz} e^{-i\pi a^2/2\lambda z_e}}{(z/z_e)} \sin\left(\frac{\pi a^2}{2\lambda z_e}\right) \tag{6.29a}$$

and for $z = F$ (note the similarity to Eq. (6.21a)),

$$p(0, z,) \approx i2p_0 e^{-ikF} \left(\frac{\pi a^2}{2\lambda F}\right) \tag{6.29b}$$

Recall that the transition distance z_t for the nonfocusing case, when substituted in the on-axis pressure equation, gave an overall phase of $\pi/2$ in the argument of the *sine* function. To obtain this same equivalent phase for the focusing aperture, we set the argument of the *sine* in Eq. (6.29a) to $\pm\pi/2$ and solve for z_e,

$$z_e = \pm a^2/\lambda \tag{6.30}$$

For a positive value of z_e and the definition of z_e in Eq. (6.28a), as well as the definition, $z_e = z_t = a^2/\lambda$, Eq. (6.30) can be applied to the determination of the near-transition distance, $z = z_{t1}$, for a focusing transducer, which separates the near Fresnel zone from the focal Fraunhofer zone depicted in Figure 6.17,

$$1/z_{t1} = 1/z_t + 1/F \tag{6.31a}$$

or,

$$z_{t1} = z_t F/(z_t + F) \tag{6.31b}$$

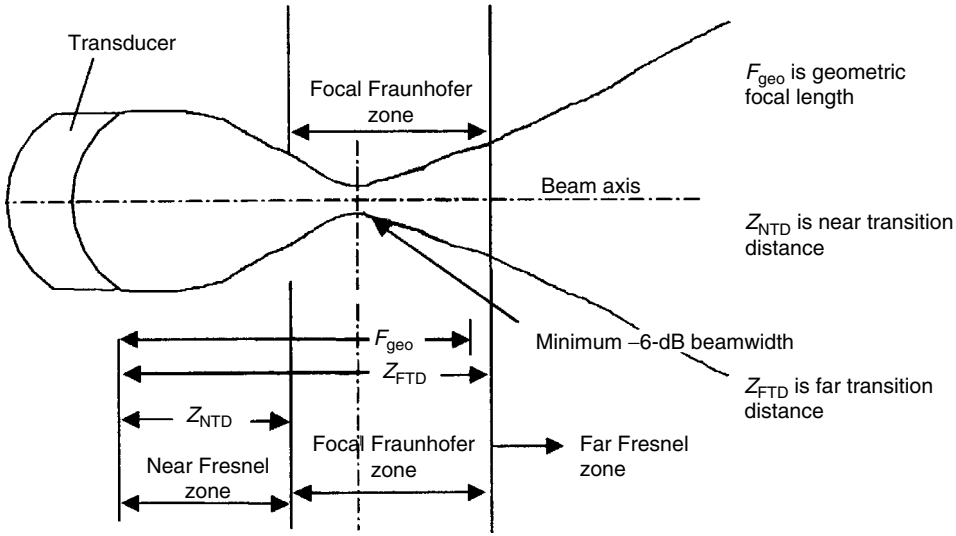

Figure 6.17 Beamwidth diagram in a plane showing the three zones of a focused field separated by transition distances one and two (from IEC 61828, 2001).

Similarly, through the use of the negative value of z_e in Eq. (6.30), the far transition distance between the far end of the focal Fraunhofer zone and the far Fresnel zone,

$$1/z_{t2} = 1/z_t + 1/F \tag{6.31c}$$

$$z_{t2} = z_t F/(z_t - F) \tag{6.31d}$$

Another way of interpreting Eq. (6.31a) is that the location of the maximum amplitude is reciprocally related to the combined effects of natural focusing and geometric focusing. Note that these comments and Eqs. (6.31a–6.31d) apply equally well to the focusing of rectangular transducers in a plane with the appropriate value of $z_t \approx L_x^2/(\pi\lambda)$ for the plane considered.

From the equivalent distance relation, Eq. (6.28b), it is possible to compare the beam profiles of a focusing aperture to that of a nonfocusing aperture. The beam of a focusing aperture undergoes the equivalent of the complete evolution from near to far field of a nonfocusing aperture within the geometric focal length because as z approaches F in value, z_e increases to infinity. At the focal length, previous far-field Eqs. (6.8), (6.9a), and (6.17) can be used with $z = F$. For $z > F$, the phase becomes negative. A curious result is that the near-transition distance is the location of the highest amplitude in the focused field, which does not occur at the focal length. The location of this peak can be found from Eq. (6.31b), which can be rewritten as

$$z_{t1} = F/(1 + S_{cF}) \tag{6.31e}$$

where

$$S_{cF} = F\lambda/a^2 = F/z_t, \tag{6.31f}$$

where Z_t is the transition distance for the same aperture without focusing. Another odd consequence of focusing is that for strongly focused apertures, significant peaks and valleys may be generated beyond the focal length in the far Fresnel zone. Because these Fresnel interference effects happen much farther from the aperture, they are generally less severe and may not occur at all, depending on the strength of the focusing. These interesting features are shown in the beam contour plot of Figure 6.18 for a spherically focusing aperture.

This section now examines several examples of these remarkable scaling laws for focusing. Recall that in the far field, the −6-dB half-beamwidth is proportional to the distance divided by the line aperture in wavelengths, as in Eq. 6.9b. This equation can actually be generalized to any distance in terms of wavelength-scaled parameters,

$$\hat{x}_{-6} = b\hat{z}/\hat{L} \tag{6.32a}$$

where away from the far-field region, the constant b must be determined numerically. The angle from the origin to this width can be shown to be inversely proportional to the aperture in wavelengths,

$$\tan\theta_{-6} = \hat{x}_{-6}/\hat{z} = b/\hat{L} \tag{6.32b}$$

These equations can be applied to any beamwidths (such as −20 dB), provided the appropriate constant b is determined.

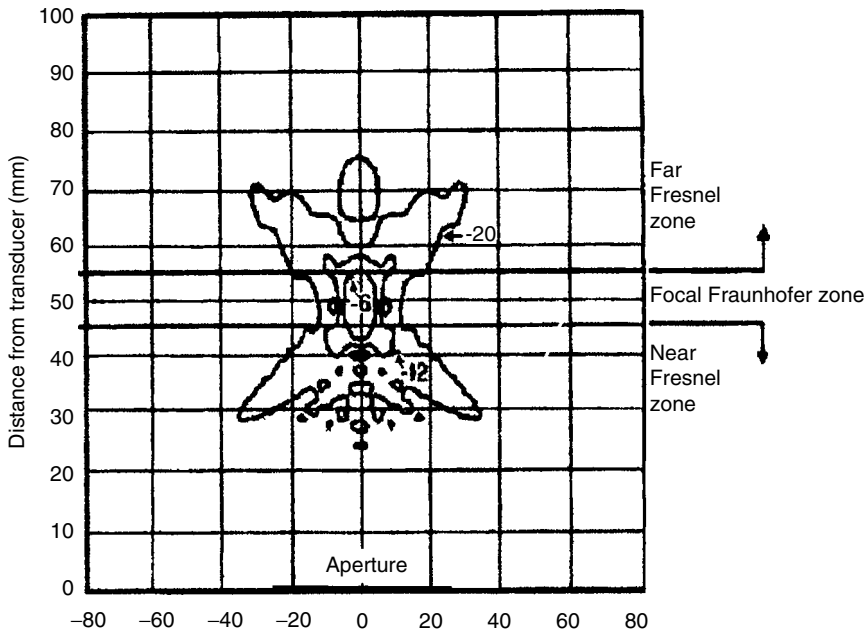

Figure 6.18 Beam contours (−6 dB, −12 dB, and −20 dB) for a 5-MHz spherically centered aperture at location (0,0) (shown at the bottom center of graph) with a diameter of 25 mm and a radius of curvature of 50 mm. The near Fresnel zone, focal Fraunhofer zone, and far Fresnel zone are marked (from IEC 61828, 2001).

This series of examples for an aperture of 32 wavelengths will demonstrate how equivalent beam cross-sections can be obtained for a variety of condition. Beamplots as a function of angle are calculated by the MATLAB focusing program beamplt.m, which uses a numerical FFT calculation of Eq. (6.27b) for a one-dimensional unapodized line aperture. The first example is a nonfocusing aperture, and since this is a focusing program, the nonfocusing case can be approximated well by setting the focal distance to a large number (approximating infinity), $\hat{F} = 50,000$. Using the location of the transition distance in wavelengths (see Section 6.3), we obtain $\hat{z}_t = \hat{L}^2/\pi = 326$. The corresponding beamplot and half-beamwidth angles are in Figure 6.19a.

The next example is for a focusing aperture with $\hat{F} = 100$. The first transition distance can be found from Eq. (6.31b) to be $\hat{z}_{t1} = 76.5$. The corresponding beamplot is shown in Figure 6.19b, where the beam-shape is that of the nonfocusing case with half-beamwidth angles agreeing within quantization and round-off errors. Similarly, from Eq. (6.31d), the second transition distance is $\hat{z}_{t2} = 144.3$, and the corresponding

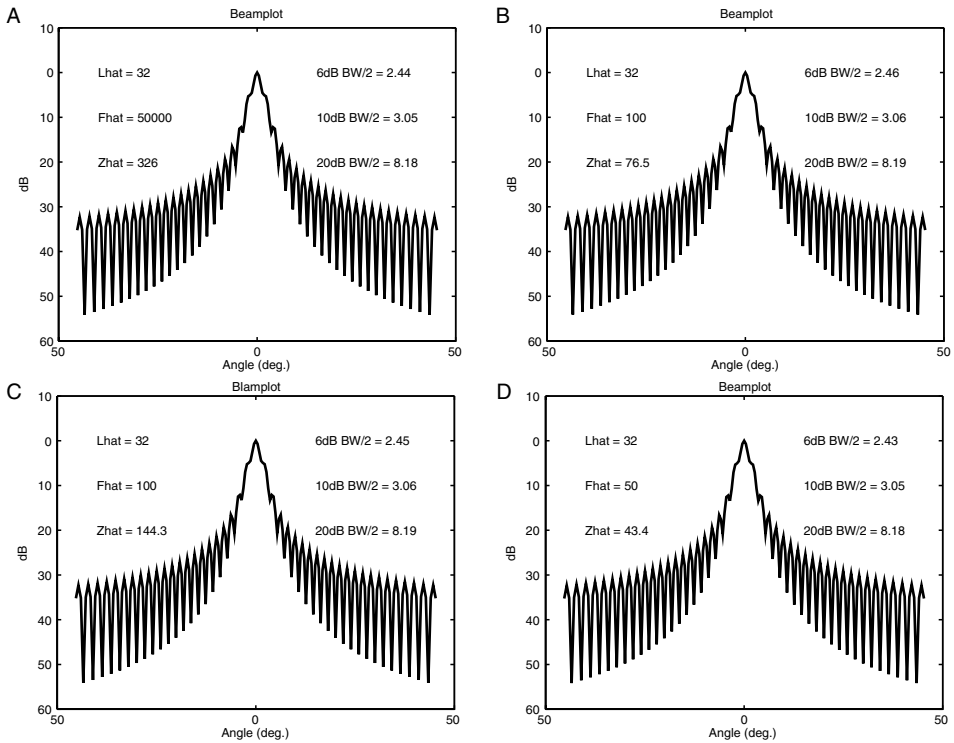

Figure 6.19 (A) Beamplot in dB versus angle from the beam axis for a nonfocusing line aperture of 32 wavelengths ($\hat{L} = 32$) at the transition distance $z_t = 326$ with the half-beamwidth angles shown. (B) Beamplot at the first transition distance, $\hat{z}_{t1} = 76.5$, for the same aperture with a focal distance of $\hat{F} = 100$. (C) Beamplot for the same case but at the second transition distance, $\hat{z}_{t2} = 144.3$. (D) Beamplot at the first transition distance, $\hat{z}_{t1} = 43.4$, for the same aperture with a focal distance of $\hat{F} = 50$.

plot is Figure 6.19c. Finally, if we keep the aperture the same but switch the focal length to $\hat{F} = 50$, the first transition distance falls to $\hat{z}_{t1} = 43.4$, but the shape is essentially the same. Note that the beam-shapes for all of these cases are the same, but, because of the different axial distances involved for each case, the linear lateral beamwidths along x differ. Another striking illustration of the similarities in scaling can be found in Figures 12.19a and 12.19c, where complete two-dimensional contour plots for focusing beams are compared at one frequency and also at twice the same frequency. Similar relations to Eq. (6.32) hold for circular transducers as indicated by Eq. (6.18b).

One measure of the strength of focusing is focusing gain, which is defined as the ratio of the pressure amplitude at the focal length to the pressure amplitude on the face of the aperture. For a circularly symmetric unapodized aperture, the focal gain is

$$G_{focal} = \pi a^2/(\lambda F) \tag{6.33a}$$

as can be seen from the on-axis pressure equation for a circularly symmetric focusing transducer, Eq. (6.29b). For an unapodized line aperture, the gain in a focal plane is

$$G_{focalx} = \sqrt{L^2/\lambda F} \tag{6.33b}$$

Focal gain for a rectangular aperture is trickier to define here because noncoincident foci can interfere; nonetheless, it can be found from the product of the gains for the line apertures. For the case in which the focal lengths are coincident,

$$G_{focal} = L_x L_y/\lambda F \tag{6.33c}$$

In general, the gain for coincident foci is

$$G_{focal} = ApertureArea/\lambda F \tag{6.33d}$$

This result is a consequence of a Fourier transform principle, which states that the center value of a transform is equal to the area of the corresponding function in the other domain. In other words, the axial (center) value in the focal plane is proportional to the area of the aperture. Associated with focal gain is the all-important improvement in resolution. The $-$dB-beamwidth can still be found in the FWHM equations, such as Eqs. (6.9c) and (6.18b), but with $z = F$ (the focal length). Since F is much closer to the aperture than a far-field distance for a nonfocusing aperture, an improvement in resolution is obtained.

A measure of the quality of focusing is a quantity called depth of field (DOF). From optics, this term has been taken to mean a falloff in axial intensity around the focal length for a spherically focusing aperture. For example, the difference between locations of the -3-dB points below the last axial peak has been approximated by Kino (1987) as

$$DOF3dB = 1.8S_{cF}F \tag{6.34}$$

A more general approach to defining DOF is to use the lateral changes in the beam. A definition of DOF more appropriate to rectangular geometries as well as to circular ones, is the difference between distances where the lateral -6-dB beamwidth has doubled over its minimum value as illustrated by Fig 6.13.

Kossoff (1979) has shown that for spherically focusing apertures, the −6-dB beamwidths, W_{-6}, can be approximated from the axial intensity. The premise for this approach is that the energy in a beam is approximately constant in each plane where z is constant. The steps are the following:

(1) Find the absolute pressure amplitude A_F (A) and beamwidth, W_{-6F}, in the focal plane. For example, A_F can be found from Eq. (6.29a), and the beamwidth can be found from Eq. (6.17b). Specifically, for the −6-dB beamwidth, use the FWHM value from Eq. (6.18b), or $w_{-6F} = FWHM$.
(2) The intensity beamwidth-squared product is constant in any plane, so the unknown product is set equal to that easily calculated in the focal plane,

$$A^2 w_{-6}^2 = A_F^2 w_{-6F}^2 \tag{6.35}$$

(3) The unknown beamwidth at a depth (z) can be found by solving Eq. (6.35) for w_{-6}, since A and A_F (A in the focal plane) can be found from Eqs. (6.29a) and (6.29b), and the focal beamwidth can be found from Eq. (6.18b).

This approximate method is attractive because the calculation of beam profiles at planes other than the focal plane can be computationally involved for spherically focusing apertures. There is no benefit of applying this approach to the rectangular case because calculations involve either straightforward Fresnel integrals or FFTs.

To summarize, focusing compresses the whole beam evolution, normally expected for a nonfocusing aperture, into the geometric focal length. The universal scaling relationships derived previously for nonfocusing apertures can be combined with the focusing equivalent z relation, Eq. (6.28), to quickly determine beam patterns for a particular case of interest. The same beam-shapes occur as in the nonfocusing cases, but they are compressed laterally and shifted to different axial distances. Focused fields can be divided into three regions: the near Fresnel zone, the focal Fraunhofer zone, and the far Fresnel zone. The terms near field and far field are only appropriate for nonfocusing apertures. Focusing has been defined in terms of beamwidth in a plane so that the contributions from different focusing mechanisms can be separated. Focusing creates a beamwidth that is narrower than what would be obtained for the natural focusing of a nonfocusing aperture.

6.7 ANGULAR SPECTRUM OF WAVES

For completeness, we will now review an alternative way of calculating beam patterns called the angular spectrum of plane waves. This approach, which is an exact solution to the wave equation, is a powerful numerical method and can be applied to anisotropic media and mode conversion. A drawback to this method is that it cannot provide as much analytical insight as the spatial diffraction methods can.

By extending the results for the angular spectrum of a single line aperture given in Chapter 3, we take the double $+i$ Fourier transform of Eq. (6.4b), which, in this case, is just two one-dimensional transforms multiplied, since Eq. (6.4b) is separable,

$$G(\tilde{f}_1, \tilde{f}_2) = \int_{-\infty}^{\infty} \prod (x/L_x) e^{i2\pi \tilde{f}_1 x} d\tilde{f}_1 \int_{-\infty}^{\infty} \prod (y/L_y) e^{i2\pi \tilde{f}_2 y} d\hat{f}_2 \tag{6.36a}$$

$$G(\tilde{f}_1, \tilde{f}_2) = L_x L_y \, sinc(L_x \tilde{f}_1) \, sinc(L_y \tilde{f}_2) \tag{6.36b}$$

in which $\tilde{f}_1$ is a spatial frequency along axis 1 (the x axis, here), $k_1 = 2\pi\tilde{f}_1$, and so forth. Recall that this result from Chapter 3 meant that these apertures radiate plane waves of different amplitudes dependent on their direction. Each of these plane waves can be represented as $exp\ (i(\mathbf{k}\cdot\mathbf{r}\text{-}\omega t)$. Now if this propagation factor is broken down into Cartesian coordinates and weighted by the directivity of the aperture, all the contributions from the aperture source can be allowed to propagate so that at any field point, the pressure amplitude can be represented by the following integral:

$$p(x, y, z) = p_0 \int\int\int_{-\infty}^{\infty} G(\tilde{f}_1, \tilde{f}_2, 0) e^{i2\pi(\tilde{f}_1 x + \tilde{f}_2 y + \tilde{f}_3 z)} d\tilde{f}_1 d\tilde{f}_2 d\tilde{f}_3 \tag{6.37a}$$

where

$$p_0 = -4\pi\omega\rho_0 L_x L_y v_{30} \tag{6.37b}$$

in which the normal particle velocity (along axis 3) is v_{30}. Fortunately, the spatial frequencies are related by

$$\tilde{f}_1^2 + \tilde{f}_2^2 + \tilde{f}_3^2 = \frac{k^2}{4\pi^2} = \frac{f^2}{c^2} = \frac{1}{\lambda^2} \tag{6.38a}$$

$$\tilde{f}_3^2 = \pm(\tilde{f}^2 - \tilde{f}_1^2 - \tilde{f}_2^2)^{1/2} \quad \text{if} \quad \tilde{f}^2 > \tilde{f}_1^2 + \tilde{f}_2^2 \tag{6.38b}$$

$$\tilde{f}_3^2 = i(\tilde{f}_1^2 + \tilde{f}_2^2 - \tilde{f}^2)^{1/2} \quad \text{if} \quad \tilde{f}^2 < \tilde{f}_1^2 + \tilde{f}_2^2 \tag{6.38c}$$

so that Eq. (6.37a) can be reduced to two dimensions,

$$p(x, y, z) = p_0 \int_{-\infty}^{\infty} [G(\tilde{f}_1, \tilde{f}_2) e^{2\pi \tilde{f}_3(\tilde{f}_1, \tilde{f}_2)z}] e^{i2\pi(\tilde{f}_1 x + \tilde{f}_2 y)} d\tilde{f}_1 d\tilde{f}_2 \tag{6.39}$$

Values of $\tilde{f}_3$, which are imaginary in Eq. (6.38c), represent evanescent waves that die out quickly or attenuate. Note that this integral can be evaluated as a double plus-i Fourier transform with FFTs. For a one-dimensional calculation in the xz plane, only one FFT is needed with $\tilde{f}_3 = +\sqrt{\tilde{f}^2 - \tilde{f}_1^2}$ for propagation in the positive half-plane. An alternate version of Eq. (6.39) is applicable to circular apertures and cylindrical coordinates (Kino, 1987; Christopher and Parker, 1991).

6.8 DIFFRACTION LOSS

When two transducers act as a transmitter–receiver pair, only a part of the spreading radiated beam is intercepted by the receiver, and this loss of power is called "diffraction loss." A mathematically identical problem is that of a single transducer acting as a

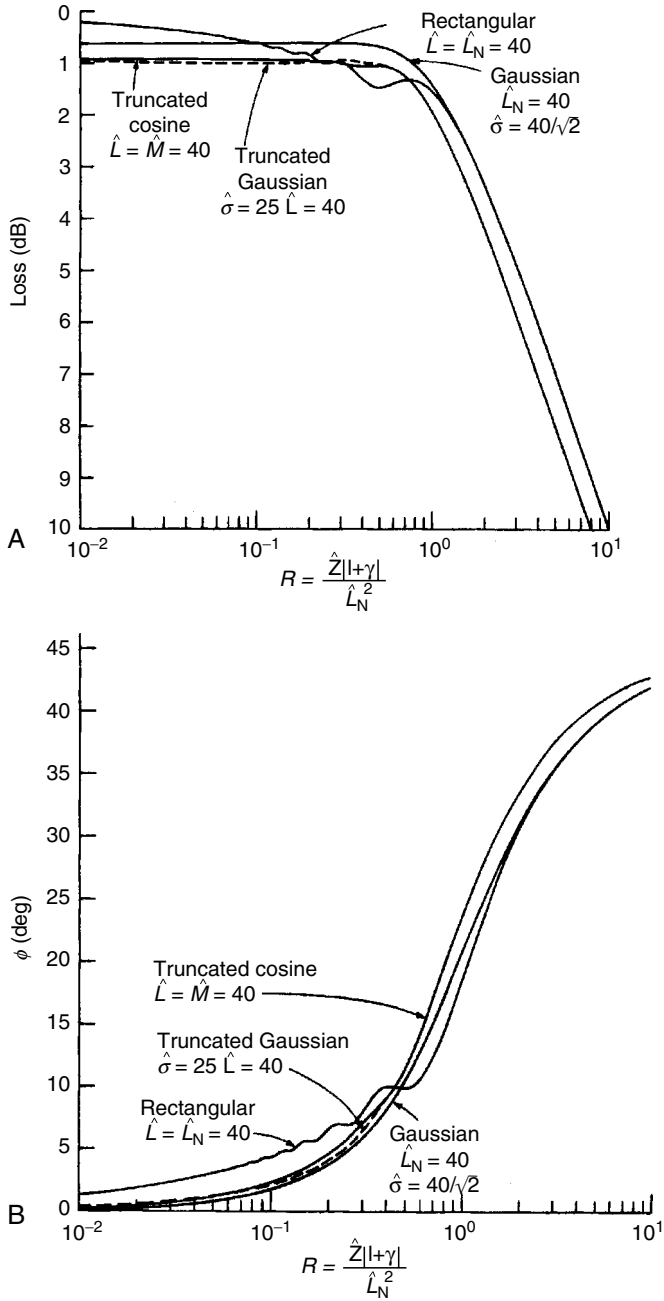

Figure 6.20 (A) Diffraction loss curves as a function of S for several different apodized transmit line source apertures and unapodized receivers. (B) Corresponding phase advances (from Szabo, 1978, Acoustical Society of America).

transceiver radiating at an infinitely wide, perfect reflector plane. In the first case, the transmitter and receiver are separated by a distance z; in the second, they are separated by a distance $2z$, where z is the distance to the reflector. The simplest definition of diffraction loss is the ratio of the received acoustic power to that emitted at the face of the transducer (Szabo, 1978):

$$DL(z) = \frac{\int_{\sigma_R} p(x, y, z)p^*(x, y, z)dxdy}{\int_{\sigma_T} p(x, y, 0)p^*(x, y, 0)dxdy} \tag{6.40a}$$

and in dB,

$$DL_{dB}(z) = 10\log_{10}|DL(z)| \tag{6.40b}$$

and the phase advance is

$$\phi_{DL} = \arctan[imag(DL)/real(DL)] \tag{6.40c}$$

where σ_T and σ_R are the areas of the transmitter and receiver, respectively. The pressure is that calculated by diffraction integrals and integrated over the face of the receiving transducer. The transmitted power can be obtained from the known aperture function. For separable functions such as those for rectangular transducers, the integration can be carried out in each plane (xz and yz) separately as line sources, and the results can be multiplied. Calculations for several apodized line sources and unapodized receivers are given in Figure 6.20. Note that the results can be plotted as a function of the universal parameter S, and they are reciprocal (transmitters and

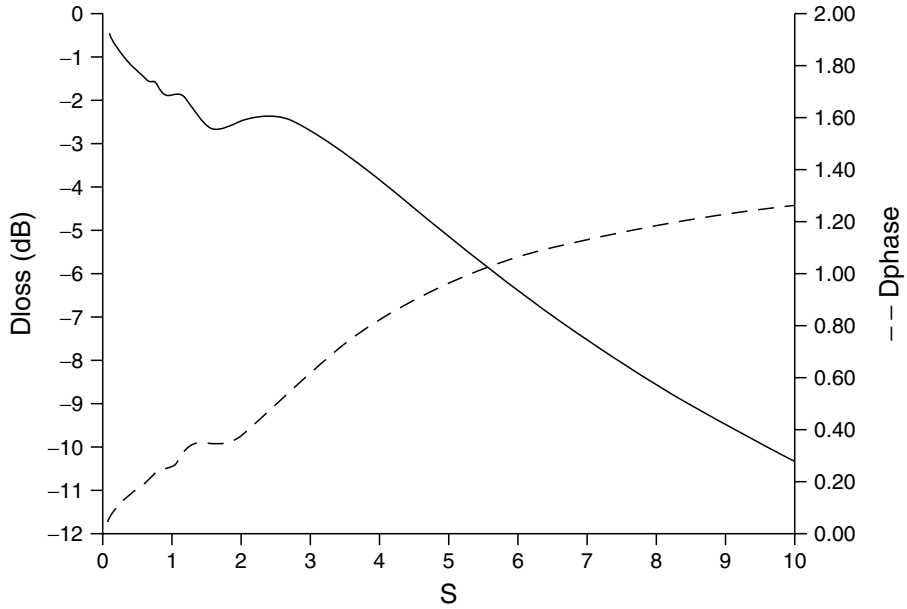

Figure 6.21 Diffraction loss (dB) and phase curves (radians) as a function of S_c for an unapodized circular transmitter and receiver of radius a (from Szabo, 1993).

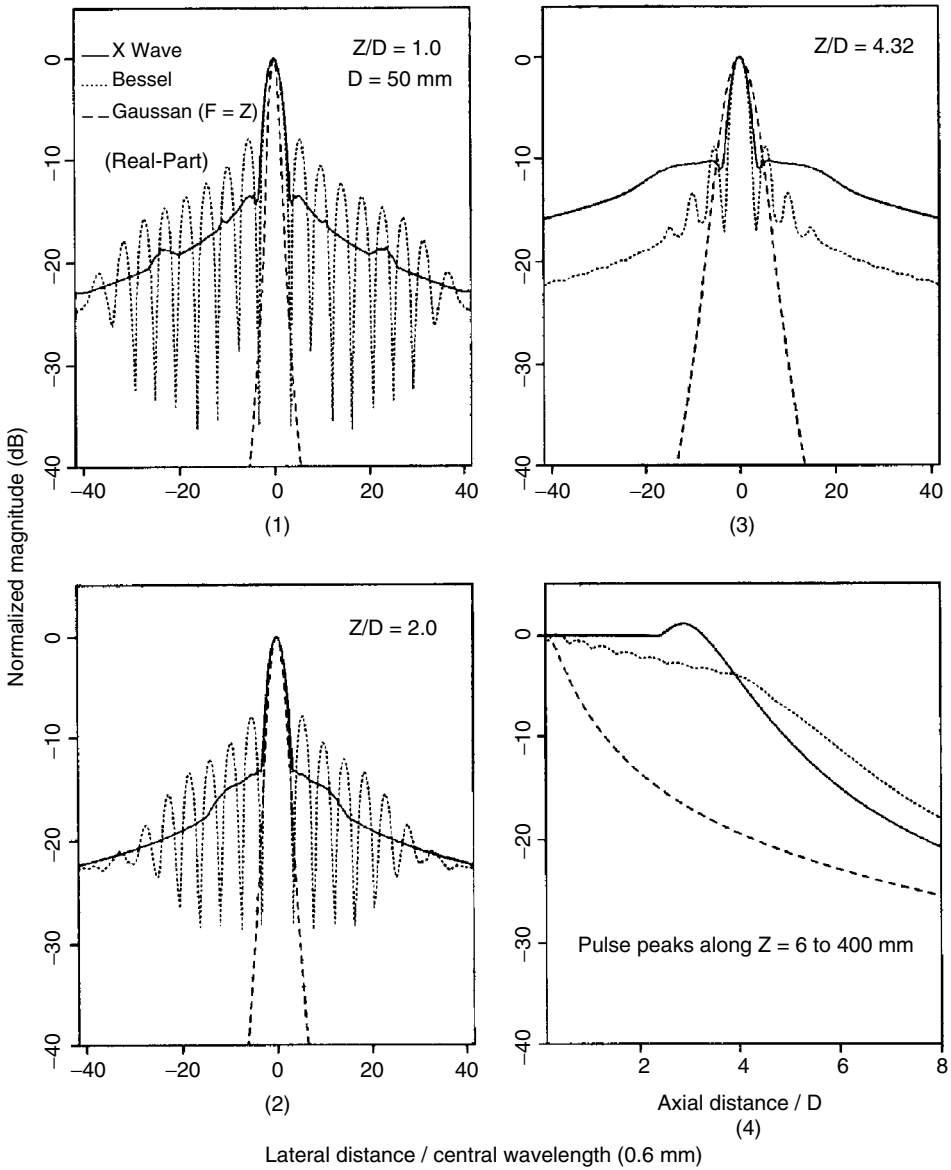

Figure 6.22 Three types of beams compared to a zeroth-order X wave (full lines), J_0 Bessel beam (dotted lines), and dynamically focused ($F = z$) Gaussian beam (dashed lines), all for an aperture diameter of 50 mm and a center frequency of 2.5 MHz. The real part of complex beams are plotted as lateral beam profiles for three depths: (1) 50 mm, (2) 100 mm, and (3) 216 mm. The peaks of pulses are plotted as pulses propagate from 6 to 400 mm in (4) (from Lu *et al.*, 1994, with permission from the World Federation of Ultrasound in Medicine and Biology).

receivers can be interchanged to give identical curves). The loss consists of an absolute power loss and a phase advance, which for one plane goes to $\pi/4$ in the extreme far field. The contribution from both planes for a rectangular aperture provides a total phase shift of $\pi/2$ for large distances (z).

For circularly symmetric transducers, the same definition applies in a cylindrical coordinate system and results in a single radial integration (Seki *et al*., 1956). Loss is plotted in Figure 6.21 against S_c, and phase advance rises asymptotically to a value $\pi/2$ for large z.

6.9 LIMITED DIFFRACTION BEAMS

The curves in the last section show that the variations in the near field of the beam can be smoothed out by apodization. In the far field, even apodized nonfocused beams spread out. Focusing also has a limited effect over a predictable DOF. A way to offset these changes and reduce diffraction loss is by a type of complex apodization that involves both amplitude and phase weighting over the aperture. A class of functions with this type of weighting can produce "limited diffraction beams." These beams have unusual characteristics: They maintain their narrow beamwidths for considerable distances, and they maintain axial amplitudes better than normal beams.

Two examples of limited diffraction beams are the zeroth-order Bessel beam and "X beam" shown in Figure 6.22. While the details of these beams are beyond the scope of this chapter, they are reviewed by Lu *et al*. (1994).

Bibliography

Goodman, J. W. (1968). *Introduction to Fourier Optics*. McGraw-Hill, New York. A resource for classic treatments of optical diffraction.

IEC 61828 (2001). *Ultrasonics: Focusing Transducers Definitions and Measurement Methods for the Transmitted Fields*. International Electrotechnical Commission, Geneva, Switzerland. An international standard on focusing terms, principles and related measurements.

Kino, G. S. (1987). *Acoustic Waves: Devices, Imaging, and Analog Signal Processing*. Prentice Hall, Englewood Cliffs, NJ. Sections 3.1 to 3.3 introduce diffraction and diffraction loss related to imaging.

Krautkramer, J. and Krautkramer, H. (1975). *Ultrasonic Testing of Materials*. Springer Verlag, New York. Thorough treatment of diffraction, focusing, and apodization related to scattering.

Lu, J.-Y., Zou, H., and Greenleaf, J. F. (1994). Biomedical beam forming. *Ultrasound in Med. & Biol*. **20**, 403–428. An excellent review of diffraction and focusing, including limited diffraction beams.

References

Abramowitz, M. and Stegun, I. (1968). *Handbook of Mathematical Functions*, Chap. 7, 7th printing. U. S. Government Printing Office, Washington, D.C.

Bracewell, R. (2000). *The Fourier Transform and its Applications*. McGraw-Hill, New York.

Christopher, P. T., and Parker, K. J. (1991). New approaches to the linear propagation of acoustic fields. *J. Acoust. Soc. Am.* **90**, 507–521.

Goodman, J. W. (1968). *Introduction to Fourier Optics*. McGraw-Hill, New York.

Harris, F. J. (1978). On the use of windows for harmonic analysis with the discrete Fourier transform. *Proc. IEEE* **66**.

IEC 61828. Ed. 1.0 English (2001). *Ultrasonics: Focusing Transducers Definitions and Measurement Methods for the Transmitted Fields*. International Electrotechnical Commission, Geneva, Switzerland.

Kino, G. S. (1987). *Acoustic Waves: Devices, Imaging, and Analog Signal Processing*. Prentice-Hall, Englewood Cliffs, NJ.

Kossoff, G. (1979). Analysis of focusing action of spherically curved transducers. *Ultrasound in Med. & Biol.* **5**, 359–365.

Lu, J.-Y., Zou, H., and Greenleaf, J. F. (1994). Biomedical ultrasound beam forming. *Ultrasound in Med. & Biol.* **20**, 403–428.

Sahin, A. and Baker, A. C. (1994) Ultrasonic pressure fields due to rectangular apertures. *J. Acoust. Soc. Am.* **96**, 552–556.

Seki, H., Granato, A., and Truell, R. (1956). Diffraction effects in the ultrasonic field of a piston source and their importance in the accurate measurement of attenuation. *J. Acoust. Soc. Am.* **28**, 230–238.

Szabo, T. L. (1977). Anisotropic surface acoustic wave diffraction, Chap. 4. *Physical Acoustics*, Vol XIII, W. P. Mason and R. N. Thurston (eds.). Academic Press, New York, pp. 79–113.

Szabo, T. L. (1978). A generalized Fourier transform diffraction theory for parabolically anisotropic media. *J. Acoust. Soc. Am.* **63**, 28–34.

Szabo, T. L. (1981). Hankel transform diffraction theory for circularly symmetric sources radiating into parabolically anisotropic (or isotopic) media. *J. Acoust. Soc. Am.* **70**, 892–894.

Szabo, T. L. (1993). *Linear and Nonlinear Acoustic Propagation in Lossy Media*. Ph.D. thesis. University of Bath, Bath, UK.

Szabo, T. L. and Slobodnik Jr., A. J. (1973). *Acoustic Surface Wave Diffraction and Beam Steering*. AFCRL-TR-73-0302, AF Cambridge Research Laboratories, Bedford, MA.

This page intentionally left blank

7 ARRAY BEAMFORMING

Chapter Contents

7.1 WHY ARRAYS?

If, to first order, the beam pattern of an array is similar to that of a solid aperture of the same size, why bother with arrays? Arrays provide flexibility not possible with solid apertures. By the control of the delay and weighting of each element of an array, beams can be focused electronically at different depths and steered or shifted automatically. Lateral resolution and beam-shaping can also be changed through adjustment of the length and apodization of the active aperture (elements turned on in the array.) Dynamic focusing on receive provides nearly perfect focusing throughout the scan depth instead of the fixed focal length available with solid apertures. Finally, electronically scanned arrays do not have any moving parts compared to mechanically scanned solid apertures, which require maintenance. Somer (1968) demonstrated that phased array antenna methods could be implemented at low MHz frequencies for medical ultrasound imaging (illustrated by Figure 1.10). An early phased array imaging system, the Thaumascan, was built at Duke University (Thurstone and von Ramm, 1975; von Ramm and Thurstone, 1975). The technology to make compact delay lines and phase shifters for focusing and steering enabled the first reasonably sized clinical phased array ultrasound imaging systems to be made in the early 1980s.

Because images are formed from pulse echoes, this chapter introduces time domain diffraction approaches that are suited to short pulses. The benefit of the time domain approach is that it involves a single convolution calculation with a pulse instead of the many repeated frequency domain calculations necessary to synthesize a pulse using the frequency domain methods of Chapter 6. Both approaches will be helpful in describing arrays that can be thought of as continuous apertures sampled along spatial coordinates.

As a warm-up, this chapter first applies time domain approaches to the previous results for circular apertures. Next it describes arrays in detail, including how they differ from solid radiating apertures. The chapter also discusses pulse-echo beamforming and focusing, as well as the principles and implementations of two-dimensional (2D) arrays. Finally, it examines factors that prevent arrays from realizing ideal performance.

7.2 DIFFRACTION IN THE TIME DOMAIN

The Rayleigh–Sommerfeld diffraction integral from Eq. (6.1a) can be rewritten in a frequency domain form,

$$\Phi(r, f) = \int_A \frac{V_n(r_0, f)X(z, r_0)\exp(-i2\pi f(r - r_0)/c]}{2\pi(r - r_0)} dA_0 \tag{7.1a}$$

An inverse $-i$ Fourier transform leads to its equivalent time domain form,

$$\phi(r, t) = \int_A \frac{\chi(z, t)v_n[r_0, t - (r - r_0)/c]}{2\pi(r - r_0)} dA_0 = v_n(t) *_t h(r_0, t) \tag{7.1b}$$

in which ϕ is the velocity potential, v_n is particle velocity normal to the rigid source plane at $z = 0$, dA_0 is an infinitesimal surface area element, A is the surface area of the source, and χ or X is an obliquity factor (see Section 7.5) set equal to one for now. If we factor v_n into a time and aperture distribution function, $v_n(r_0, t) = v_n(t)v_n(r_0)$, and let $v_n(r_0)$ be constant over the aperture for the remainder of the chapter, then we can express Eq. (7.1b) in a convolution form later.

The geometry for a circularly symmetric radiator is given in Figure 7.1. Here h is the spatial impulse response function defined as

$$h(r, t) = \chi(z, t) \int_A \frac{\delta[t - (r - r_0)/c_0]}{2\pi(r - r_0)} dA_0 \tag{7.2}$$

Recall that the instantaneous particle velocity (v) and pressure (p) at a position (r) in a fluid can be found from

$$v(r, t) = -\nabla\phi(r, t) \tag{7.3}$$

$$p(r, t) = \rho_0 \partial\phi(r, t)/\partial t \tag{7.4}$$

Just as in the diffraction integrals of the previous chapter, these time domain field expressions are geometry specific. The previous integrals will first be applied to the familiar circular piston radiator and then to array elements with a rectangular shape.

7.3 CIRCULAR RADIATORS IN THE TIME DOMAIN

Fortunately, time domain diffraction integrals have been worked out for simple geometries (Oberhettinger, 1961; Tupholme, 1969; Stephanishen, 1971; Harris, 1981a). For the geometry given in Figure 7.1 for a circular aperture of radius a, the following delay variables are convenient:

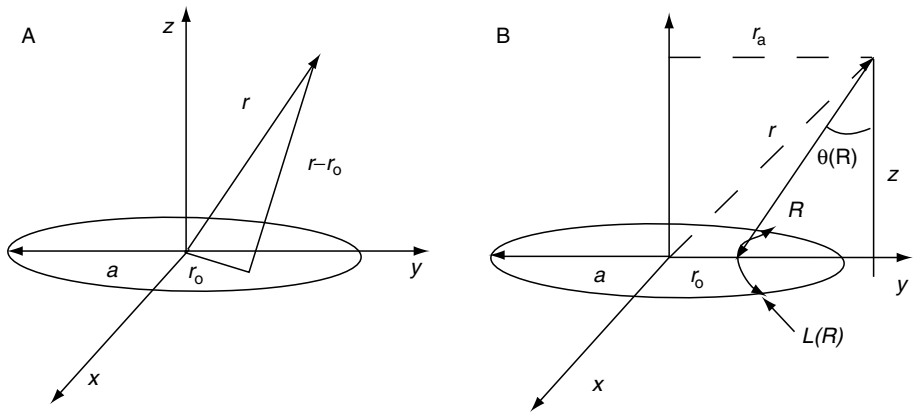

Figure 7.1 Geometries for circularly symmetric radiating elements. (A) Conventional geometry. (B) Field-point–centered coordinates.

$$\eta_1 = z/c_0 \tag{7.5a}$$

$$\eta_2 = \sqrt{(z^2 + a^2)}/c_0 \tag{7.5b}$$

The local observer approach advocated by Stepanishen (1971) is based on time domain spatial impulse responses that have finite start and stop times defined by the intersections of lines from the field point to the closest and farthest points on the aperture (Figure 7.1). For example, for field points on-axis, the spatial impulse response is a rect function (Stepanishen, 1971; Kramer *et al.*, 1988),

$$h(r, t) = -c_0 \prod \left[\frac{t - (\eta_1 + \eta_2)/2}{\eta_2 - \eta_1} \right] \tag{7.6}$$

where η_1 is the delay from the closest point from the center of the aperture, and η_2 is that from the farthest points on the edges. This response, along with Eqs. (7.1.b) and (7.4), lead to an on-axis pressure,

$$p(z, t) = \rho_0 [v_n(t) *_t \partial h(z, t)/\partial t] = \rho_0 c_0 v_n(t) *_t [\delta(t - \eta_1) - \delta(t - \eta_2)] \tag{7.7a}$$

The Fourier transform of Eq. (7.7a) can be shown to be

$$p(z, f) = i2\rho_0 c_0 v_n \exp\left[ikz(1 + \sqrt{1 + (a/z)^2})\right] \sin\left[\frac{kz}{2}\left(\sqrt{1 + (a/z)^2} - 1\right)\right] \tag{7.7b}$$

in agreement with the earlier exact result of Eq. (6.19a). In Eq. (7.7a), the on-axis pressure has a pulse from the center of the transducer, $\delta(t - \eta_1)$, and an inverted pulse from the edges of the aperture, $\delta(t - \eta_2)$. These contributions, called the "plane wave" and the "edge wave," merge eventually and interfere at half-wavelength intervals on-axis, depending on the pulse shape and length, $v_n(t)$. For broadband excitation, the on-axis pressure can differ remarkably from the continuous wave (cw) case, as illustrated by Figure 7.2.

Off-axis, expressions for the spatial impulse response are

$$h(r, r_0, z, t) = \begin{cases} 0, & ct < z \text{ for } a > r_a,\ ct < R_1 \text{ for } a \le r, \\ c, & r_a \le r \le R_1 \\ \dfrac{c}{\pi}\cos^{-1} & \left[\dfrac{r_0^2 + c^2t^2 - z^2 - a^2}{2r_a(c^2t^2 - z^2)^{1/2}}\right],\ R_1 < ct \le R_2 \\ 0, & ct > R_2 \end{cases} \tag{7.8a}$$

in which

$$R_1 = \sqrt{z^2 + (a - r_a)^2} \tag{7.8b}$$

$$R_2 = \sqrt{z^2 + (a + r_a)^2} \tag{7.8c}$$

and r_a is the radius from the z axis to the field point so that the field point is at (r_a, z). This expression is far simpler to evaluate numerically than the Hankel transform from Eq. (6.19).

Expressions (Arditi *et al.*, 1981) for a concave spherical focusing radiator are similar in form to those above. The geometry for a spherically focusing aperture is

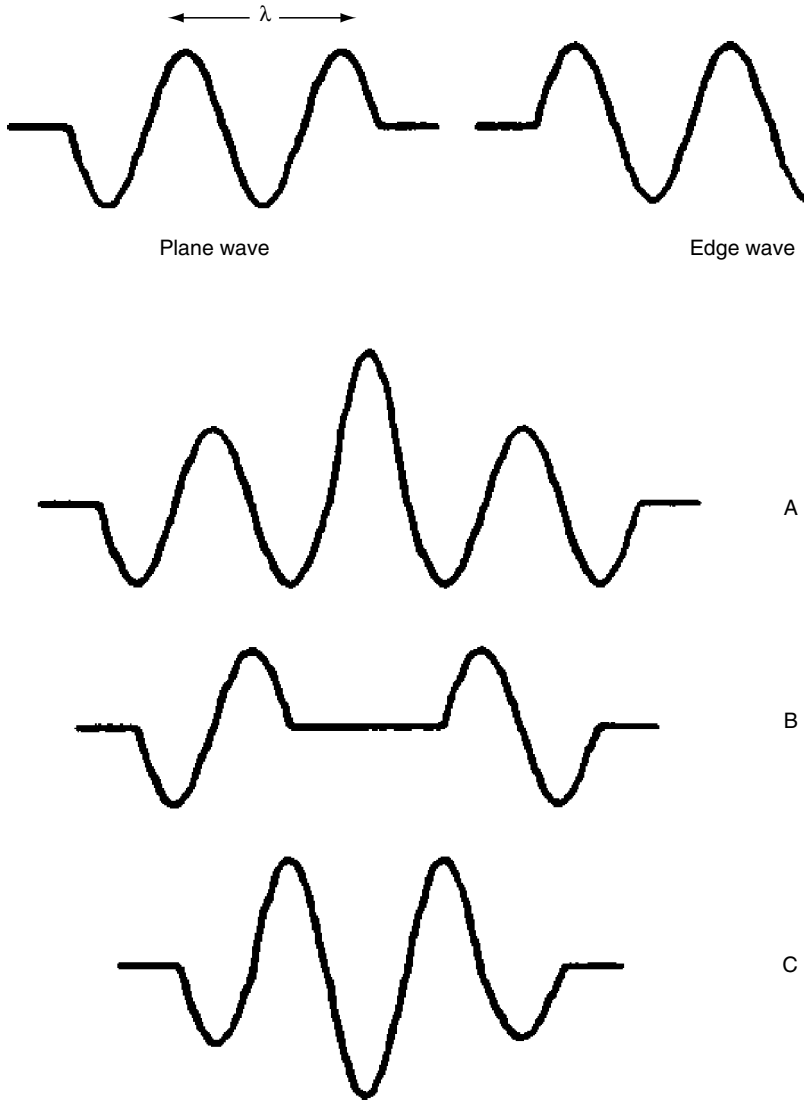

Figure 7.2 Plane and edge wave interference at three axial positions for an excitation function of two sinusoidal cycles: (A) $ct = 3\lambda/2$, (B) $ct = \lambda$, (C) $ct = \lambda/2$. (from Kramer *et al.*, 1988, *IEEE*).

given by Figure 7.3. Note the two regions: Region I is within the geometric cone of the aperture, and Region II lies outside it. Cylindrical symmetry is implied. Key variables are the following:

$$x = r\cos\theta,\ y = r\sin\theta \tag{7.9a}$$

The depth (d) of the concave radiator is:

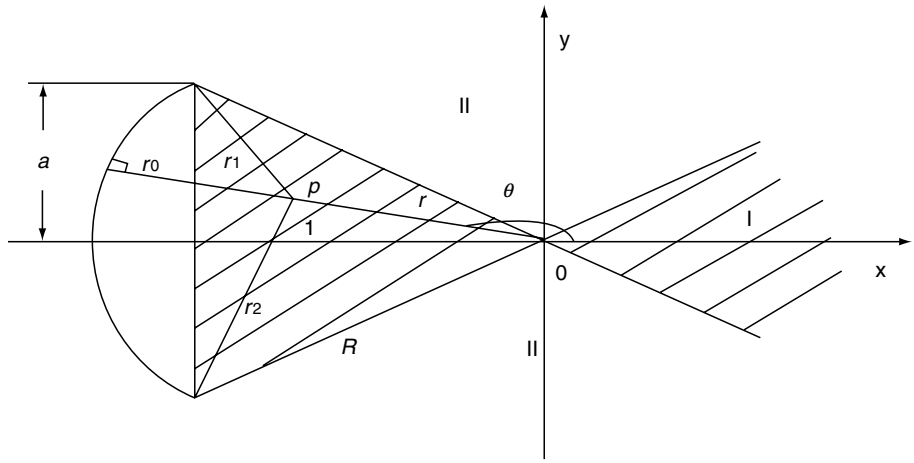

Figure 7.3 Nomenclature for spatial impulse response geometry for spherical focusing transducer (from Arditi *et al.*, 1981, with permission of Dynamedia, Inc.).

$$d = R\left[1 - \left(1 - \frac{a^2}{R^2}\right)^{1/2}\right] \tag{7.9b}$$

where R is the radius of curvature of the radiator, and a is the radius of the radiator.

For a field point P in Region I, r_0 is defined as the shortest (for $z < 0$) or longest (for $z > 0$) distance between P and the source, and it is the line that passes through the origin and P and intersects the surface of the source at normal incidence. Furthermore, r_0 can be expressed as:

$$r_0 = \begin{cases} R - r & for\ z < 0 \\ R + r & for\ z > 0 \end{cases} \tag{7.9c}$$

where r_1 and r_2 represent the distances from P to the closest and farthest edges of the radiator for both Regions I and II:

$$r_1 = [(a - y)^2 + (R - d + z)^2]^{1/2} \tag{7.9d}$$

$$r_2 = [(a + y)^2 + (R - d + z)^2]^{1/2} \tag{7.9e}$$

The spatial impulse response of a concave radiator is:

$$h(\vec{r}, t) = \begin{cases} 0 & \left| \begin{array}{l} c_0 t < r_0 \\ r_0 < c_0 t < r_1 \end{array} \right. \left| \begin{array}{l} c_0 t < r_1 \\ r_2 < c_0 t < r_0 \end{array} \right. \left| \begin{array}{l} c_0 t < r_1 \\ - - - - \end{array} \right. \\ \dfrac{c_0 R}{r} & \left| \begin{array}{l} \\ \end{array} \right. \left| \begin{array}{l} \\ \end{array} \right. \left| \begin{array}{l} \\ \end{array} \right. \\ \dfrac{c_0 R}{r}\dfrac{1}{\pi}\cos^{-1}\left[\dfrac{\eta(t)}{\sigma(t)}\right] & \left| \begin{array}{l} r_1 < c_0 t < r_2 \\ r_2 < c_0 t \end{array} \right. \left| \begin{array}{l} r_1 < c_0 t < r_2 \\ r_0 < c_0 t \end{array} \right. \left| \begin{array}{l} r_1 < c_0 t < r_2 \\ r_2 < c_0 t \end{array} \right. \\ 0 & \end{cases} \tag{7.9f}$$

Region I $z < 0$ Region II $z > 0$

in which,

$$\eta(t) = R\left[\frac{1 - d/R}{\sin\theta} + \frac{1}{\tan\theta}\left(\frac{R^2 + r^2 - c_0^2 t^2}{2rR}\right)\right] \tag{7.9g}$$

$$\sigma(t) = R\left[1 - \left(\frac{R^2 + r^2 - c_0^2 t^2}{2rR}\right)^2\right]^{1/2} \tag{7.9h}$$

On the beam axis, the spatial impulse response is:

$$h(z, t) = \frac{c_0 R}{|z|} \prod\left(\frac{c_0 t - M}{\Delta(z)}\right) \tag{7.10a}$$

where

$$M = (r_0 + r_1)/2,\ \Delta(z) = r_1 - r_0 \tag{7.10b}$$

At the geometric focal point, the solution is a δ function multiplied by d,

$$h(0, t) = d\delta(t - R/c_0) \tag{7.10c}$$

Therefore, the pressure waveform at the focal point is a delayed replica of the time derivative of the normal velocity at the face of the aperture from Eqs. (7.1b) and (7.4).

7.4 ARRAYS

As opposed to large continuous apertures, arrays consist of many small elements that are excited by signals phased to steer and focus beams electronically (shown in Figure 7.4). The elements scan a beam electronically in the azimuth or xz plane. A molded cylindrical lens provides a fixed focal length in the elevation or yz plane. The nominal

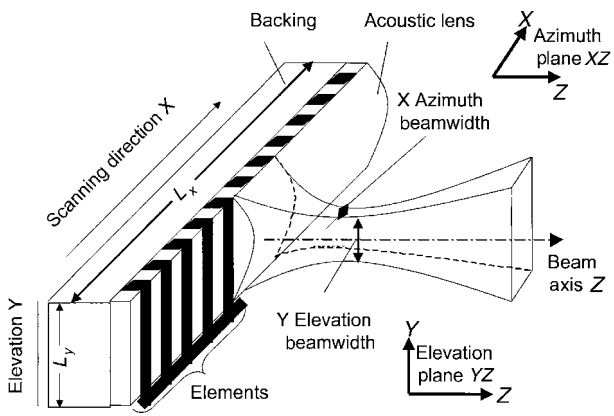

Figure 7.4 Relation of phased array to azimuth (imaging) and elevation planes (adapted from Panda, 1998).

beam axis is the z axis (the means of steering the beam in the azimuth plane will be discussed later).

A layout of array element dimensions and steering angle notation are given by Figure 5.6. Here the pitch or element periodicity is p, the element width is w, and the space between elements, or kerf width, is p-w. Two-dimensional and other array geometries will be discussed later.

7.4.1 The Array Element

This section first examines the directivity of an individual element. These elements are most often rectangular in shape, such as the one depicted in Figure 7.5. For small elements with apertures on the order of a wavelength, the far-field beam pattern can be found from the $+i$ Fourier transforms of the aperture functions,

$$H_e(x, y, z, \lambda) = \frac{c_0}{2\pi z} \int_{-\infty}^{\infty} A_x(x_0) e^{i2\pi x_0 (x/\lambda z)} dx_0 \int_{-\infty}^{\infty} A_y(y_0) e^{i2\pi y_0 (y/\lambda z)} dy_0 \qquad (7.11a)$$

which, for line sources of lengths describing a rectangular aperture with sides L_x and L_y, gives

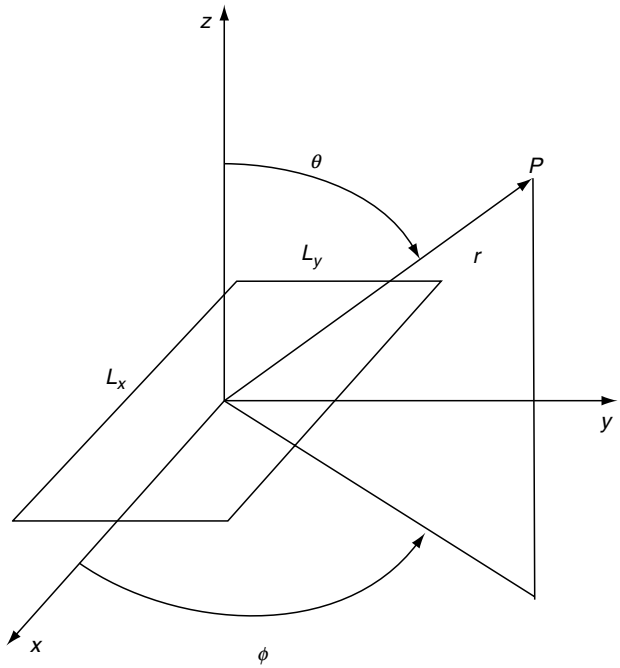

Figure 7.5 Simplified geometry for a rectangular array element in the xz plane.

$$H_e(x,y,z,\lambda) = H_x\ H_y = \frac{c_0}{2\pi z} L_x\, sinc\left(\frac{L_x x}{\lambda z}\right) L_y\, sinc\left(\frac{L_y y}{\lambda z}\right) \tag{7.11b}$$

Recall in the original diffraction integral that the Fresnel approximation was made by a binomial approximation of the difference vector $|r - r_0|$ and the substitution of z for r, so that this approximation was valid only for the xz and yz planes. A more exact result for any field point in the far field can be derived by accounting for the total rectangular shape of the aperture. The direction *cosines* to the field point are introduced from the spherical coordinate geometry given by Figure 7.5:

$$u = \sin\theta\cos\phi \tag{7.12a}$$

$$v = \sin\theta\sin\phi \tag{7.12b}$$

where θ is the angle between r and the z axis, and ϕ is the angle between r and the x axis.

Stepanishen (1971) has shown that the far-field response for this geometry is

$$H_e(x,y,z,\lambda) = H_x H_y = \frac{c_0}{2\pi r} L_x\, \mathrm{sinc}\left(\frac{L_x u}{\lambda}\right) L_y\, \mathrm{sinc}\left(\frac{L_y v}{\lambda}\right) \tag{7.13}$$

which reduces to the previous expression in the xz plane, ($\phi = 0$) and the yz plane, ($\theta = 0$), and z is replaced by r. The time domain equivalent of this expression can be found from the inverse Fourier transform of Eq. (7.13) with $\lambda = c/f$,

$$h_e(u,v,r,t) = \frac{c_0}{2\pi r} L_x \left(\frac{c}{L_x u}\right) \prod\left(\frac{t}{L_x u/c}\right) * L_x\left(\frac{c}{L_y v}\right) \prod\left(\frac{t}{L_y v/c}\right) \tag{7.14}$$

This convolution of two rectangles has the trapezoidal shape illustrated by Figure 7.6. For equal aperture sides, a triangle results. For on-axis values, the rect functions reduce to impulse functions, so that

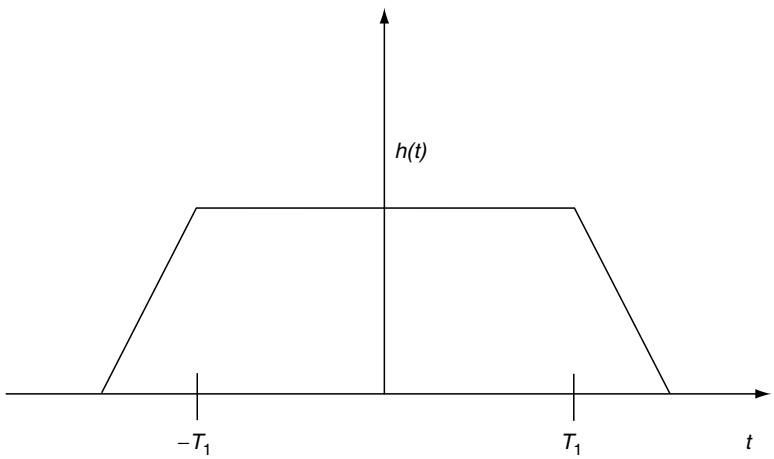

Figure 7.6 Trapezoidal far-field spatial impulse response for a rectangular array element.

$$h_e(0, 0, r, t) = \frac{c_0}{2\pi r} L_x L_x \delta(t) \tag{7.15}$$

This equation, in combination with Eqs. (7.1b and 7.4), indicates that on-axis pressure in the far-field is the derivative of the normal velocity, is proportional to the area of the aperture, and falls off inversely with r.

For two-dimensional beam scanning in the xz plane, a one-dimensional array will extend along the x-axis (two-dimensional arrays are covered later in Section 7.6). For this plane, H_x can be expressed as a function of frequency from Eq. (7.13) with $1/\lambda = f/c$ and the convenient substitution $h_{ox} = \sqrt{c_0/2\pi r}$ as

$$H_x(\theta, r, f) = h_{0x} L_x \, sinc\left(\frac{L_x f \, sin\theta}{c}\right) \tag{7.16}$$

where on-axis as $\theta \to 0$, the $H_x \to h_{0x} L_x$ (as shown in Figure 7.7). Note that this function has zeros when u is integral multiples of λ/L_x. This element directivity has been examined (Smith *et al.*, 1979; Sato *et al.*, 1980), and it is discussed in more detail in Section 7.5. The far-field time response is the inverse Fourier transform of Eq. (7.7),

$$h_x(\theta, r, t) = h_{0x} L_x \left(\frac{c}{L_x \sin\theta}\right) \prod\left(\frac{t}{L_x \sin\theta / c}\right) \tag{7.17a}$$

which is illustrated by Figure 7.8. The limiting value of this expression on-axis is

$$h_x(0, r, t) = h_{0x} L_x \delta(t) \tag{7.17b}$$

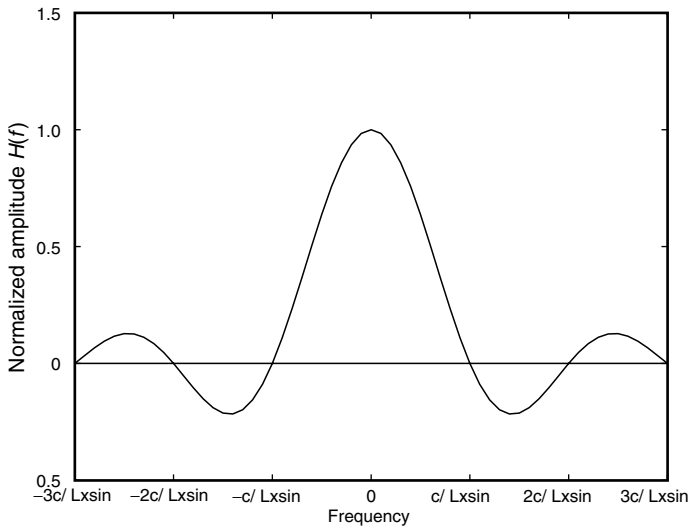

Figure 7.7 Far-field element directivity as a function of frequency for an element length L_x.

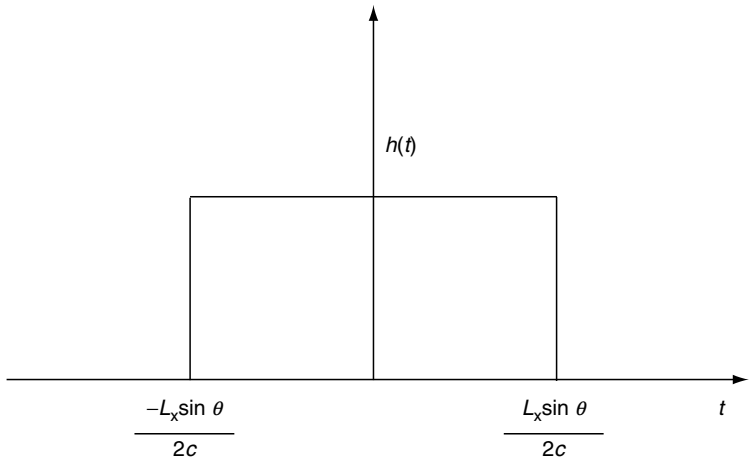

Figure 7.8 Spatial impulse response h_x along the z axis for an element of length L_x oriented along the x axis.

7.4.2 Pulsed Excitation of an Element

To find the pressure pulse in the far field of an element in the scan (xz) plane for a pulse excitation $g(t)$, we convolve the input pulse that we assume is in the form of the normal velocity, $g(t) = \partial v_n/\partial t$, with the time derivative of ψ_x, as given by Eq. (7.2a),

$$p(r, t) = \rho_0 \partial\psi/\partial t = \rho_0 \partial v_n/\partial t *_t h(r, t) = \rho_0 g *_t h(r, t) \tag{7.18}$$

As an example (Bardsley and Christensen, 1981), let $g(t)$ have the decaying exponential form shown in Figure 7.9,

$$g(t) = v_{0x} e^{-at} H(t) \cos(\omega_c t) \tag{7.19}$$

in which $H(t)$ is the step function and v_{0x} is the normal particle velocity on the aperture. Then the pressure can be found from

$$p(r, t) = \rho_0 g(t) *_t h_{0x} L_x \left(\frac{c}{L_x \sin\theta}\right) \prod\left(\frac{t}{L_x \sin\theta/c}\right) \tag{7.20a}$$

off-axis and from

$$p(r, t) = \rho_0 g *_t h = \rho_0 g(t) *_t h_{0x}\delta(t) = \rho_0 h_{x0} g(t) \tag{7.20b}$$

for the on-axis value. The pressure response calculated from Eq. (7.20b) is plotted in Figure 7.10 over a small angular range.

An equivalent frequency domain expression for pressure at a field point, from Eq. (7.20a), is

$$P(r, f, \theta) = G(f) H_x(r, f, \theta) \tag{7.21}$$

where $r = \sqrt{x^2 + z^2}$.

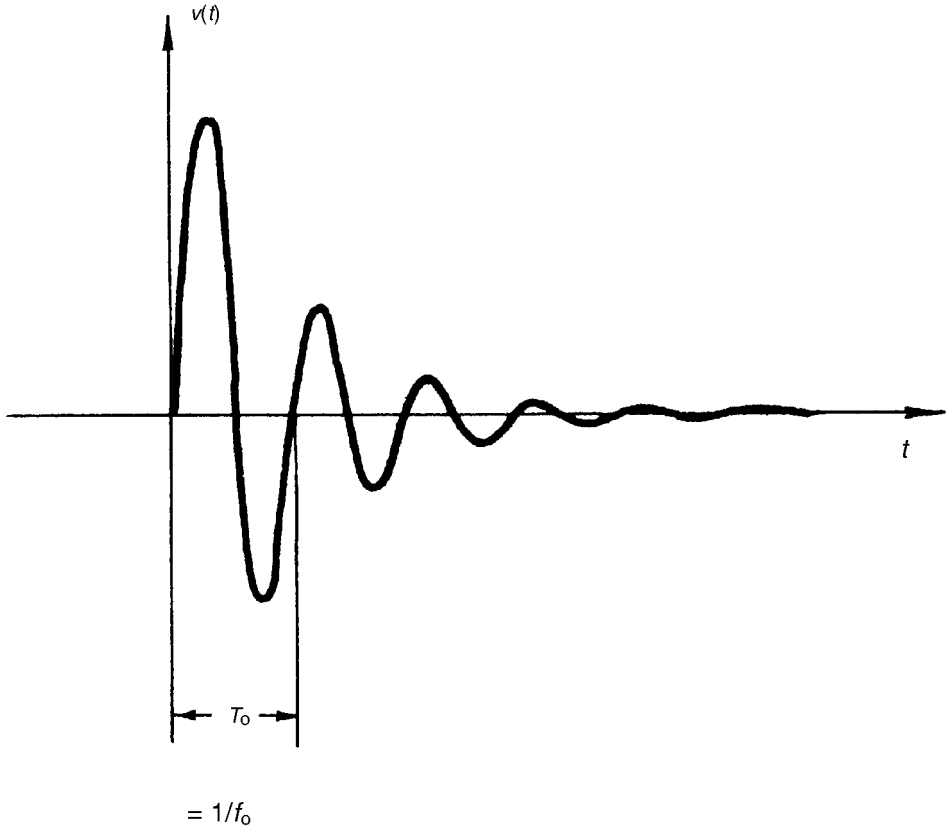

Figure 7.9 Typical short acoustic pulse waveform with Q = 3.1 and center frequency of 2.2.5 MHz used for array calculations for examples (from Bardsley and Christensen, 1981, Acoustical Society of America).

7.4.3 Array Sampling and Grating Lobes

In order to find out how an element functions as part of an array, a good starting point is a perfect ideal array made up of spatial point samplers. An infinitely long array of these samples (shown in Figure 7.11a) can be represented by a shah function with a periodicity or pitch (p). Since the pressure at a field point is related to a Fourier transform of the aperture or array, the result is another shah function with a periodicity (λ/p), as given by this expression, Figure 7.11b, and (see Section A.2.4 of Appendix A):

$$\Im_i\left[\text{III}\left(\frac{x}{p}\right)\right] = p\text{III}\left(\frac{puf}{c_0}\right) = p\text{III}\left(\frac{u}{\lambda/p}\right) \tag{7.22}$$

For an aperture of finite length L_x, the infinite sum of the shah function is reduced to a finite one in the spatial x domain, as is given in Figure 7.12 and as follows:

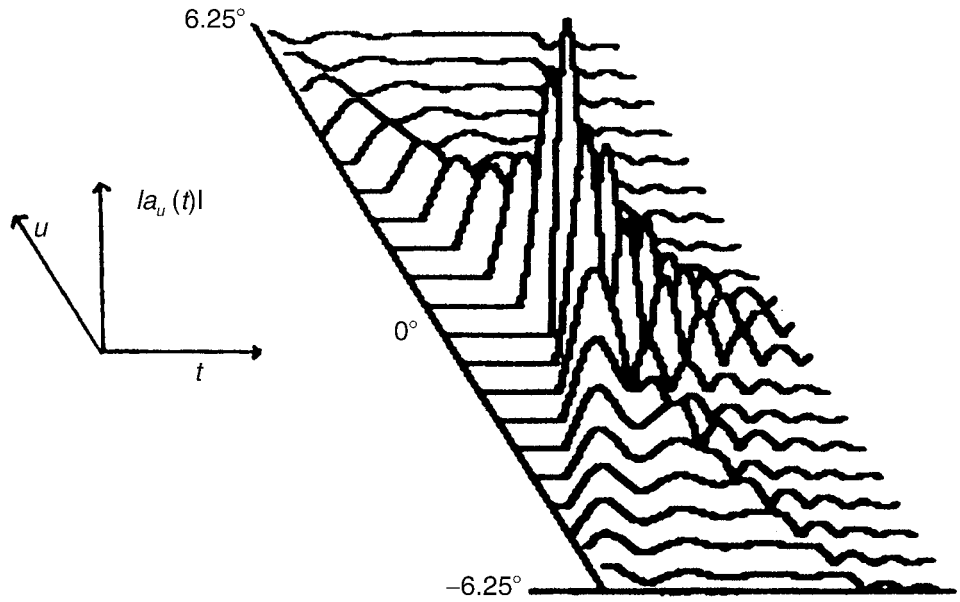

Figure 7.10 Absolute values of pressure waveforms as a function of angular direction (u) and time (t) plotted in an isometric presentation over a small angular range: -6.25° to 6.25° in 0.625° angular increments for the pulse of Figure 7.9 and a 2.56-cm-long aperture (from Bardsley and Christensen, 1981, Acoustical Society of America).

$$\Im_i\left[\prod\left(\frac{x}{L_x}\right)\mathrm{III}\left(\frac{x}{p}\right)\right] = pL_x\sum_{-\infty}^{\infty} sinc\left[\frac{L_x}{\lambda}(u - m\lambda/p)\right] = L_x sinc\left[\frac{L_x u}{\lambda}\right] *_u p\mathrm{III}\left(\frac{u}{\lambda/p}\right) \tag{7.23}$$

In this figure, the main lobe is centered at $u = 0$, and the other modes for which $m \neq 0$ are called grating lobes. Grating lobes are centered on direction *cosines* u_g at angles

$$\theta_g = \pm \arcsin(m\lambda/p) \tag{7.24}$$

The first grating lobe is the most important, or $m = \pm 1$. If the periodicity is set equal to half-wavelength spacing, which is the Nyquist sampling rate, there are no grating lobes (the usual spacing for phased arrays). If the spacing is larger in terms of wavelengths, then instead of one beam transmitted, three or more are sent. For example, for a two-wavelength spacing, beams appear at 0° and $\pm 30^\circ$. For linear arrays, spacing is often one or two wavelengths because steering requirements are minimal, but for phased arrays that create sector scans, grating lobe minimization is important (described in Section 7.4.5).

For the cw case, grating lobes can be as large as the main lobe, but for pulses, grating lobes can be reduced by shortening the pulse. The effect of the transducer bandwidth on the grating lobe can be seen from Eq. (7.21) and Figure 7.13. Shown are the main lobe and grating lobe centered on the center frequency f_0 and with a -3-dB bandwidth, given approximately by $\frac{0.88c}{Npu_g}$. The fractional bandwidth

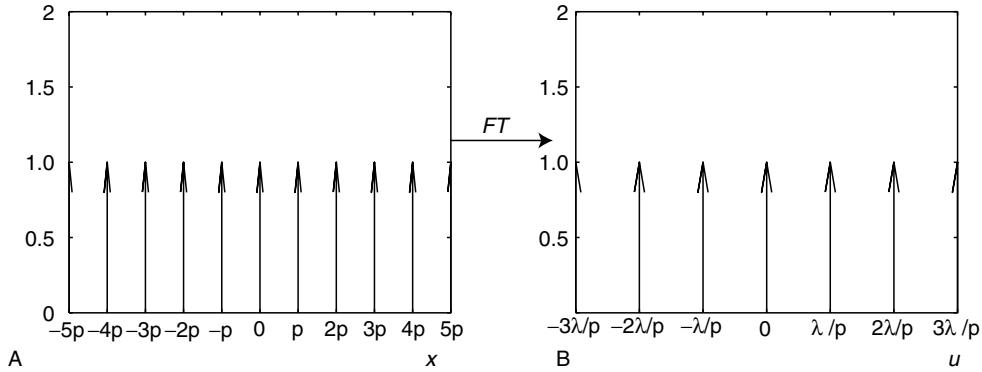

Figure 7.11 (A) A shah function of ideal samplers spaced along the x axis with a periodicity of p. (B) Normalized Fourier transform of a shah function is another shah function with samplers situated at intervals of u equal to integral multiples of λ/p. The amplitude of the transformed shah function is p.

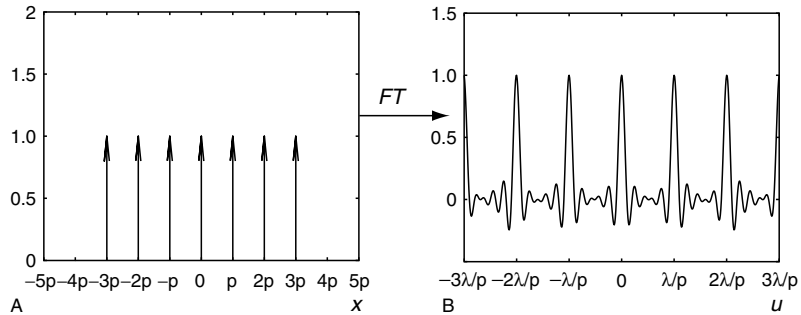

Figure 7.12 (A) An array of $2n_L + 1$ point samples along the x axis with a periodicity of p. (B) Normalized Fourier transform of a finite length array of point samplers is an infinitely long array of *sinc* functions situated at intervals of u equal to integral multiples of λ/p with an actual amplitude of $L_x p$.

of $G(f)$ is approximately $0.88f_0/n$, where n is the number of periods (cycles) in the pulse (corresponding to a $Q = 1.1.2n$). Recall the overall response is given by the product of $H(f)$ and $G(f)$ from Eq. (7.21) and that amplitude of the grating lobe will be proportional to the overlap area of these functions from their Fourier transform relation. As a consequence of these factors, the wider the bandwidth of $G(f)$ (the shorter the pulse), the smaller the overlap and the lower the amplitude of the grating lobe in the time domain. An approximate expression for the grating lobe is Q/N, where N is the number of elements (Schwartz and Steinberg, 1998).

Another perspective on grating lobe effects is the time domain for finite length pulses through the convolution operation. The on-axis main lobe pulse contributions add coherently, and, at grating lobe locations, pulses add sequentially to form a long, lower-level pulse. The overall impact of a grating lobe can be seen over a small angular

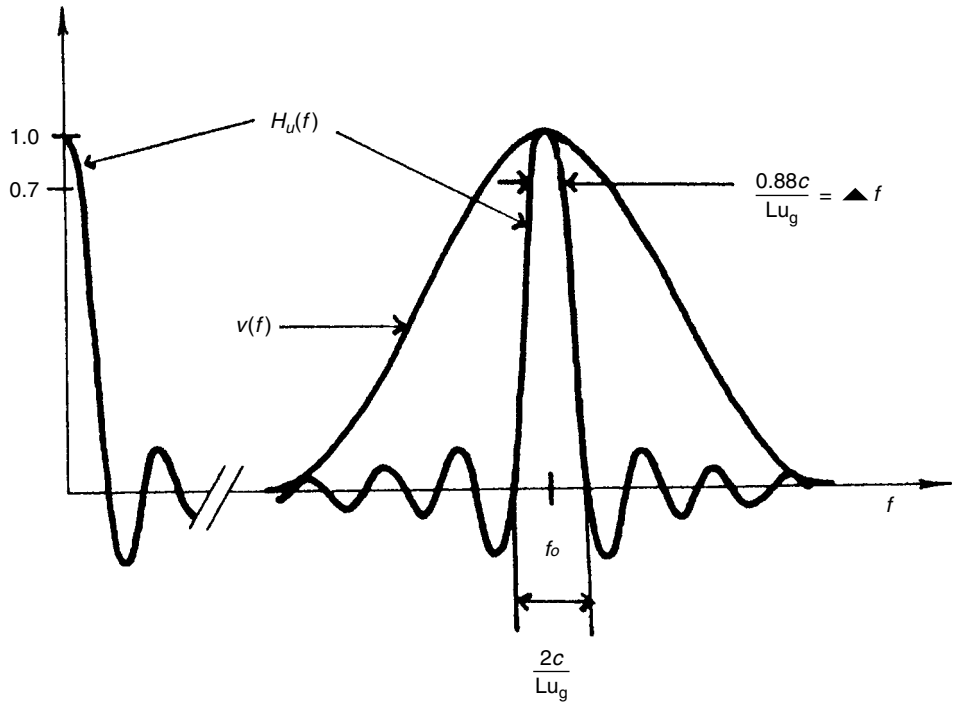

Figure 7.13 The spatial transfer function *H(f,u)*, showing a first-order grating lobe $u_g = \lambda/p = 1/2.4$ at 24.6° with a bandwidth of $\frac{0.88c}{N_p u_g} = 0.124$ MHz as well as the pulse spectrum $G(f) = V(f)$ with a bandwidth of 0.726 MHz (from Bardsley and Christensen, 1981, Acoustical Society of America.).

range in Figure 7.14, in which the long grating lobe pulse builds at larger angles. From this viewpoint, it is evident that the shorter the pulse, the less pulses will overlap and build in amplitude to create a significant grating lobe.

7.4.4 Element Factors

Until now, the array was treated as having point sources. To include the imperfect sampling effects of rectangular elements described in Section 7.4, we replace the point samplers by elements of width w, as shown in Figure 7.15 and by the following:

$$H_0(u, \lambda) = h_{0x}\Im_i\left[\prod\left(\frac{x}{w}\right) * \sum_{-n_L}^{n_L}\delta(x - np)\right] = \sum_m h_{0x}L_x pw\, sinc\left(\frac{\mathrm{wu}}{\lambda}\right) sinc\left[\frac{L_x}{\lambda}(u - m\lambda/(p))\right] \tag{7.25}$$

Here the first *sinc* term is called the element factor. In the angle or frequency domain, the small element size translates into a broad directivity modulating the sequence of grating lobes as shown in Figure 7.15. The −3-dB directivity width is approximately $0.88\lambda/w$ as opposed to the width of a main or grating lobe, which is about $0.88\lambda/L$.

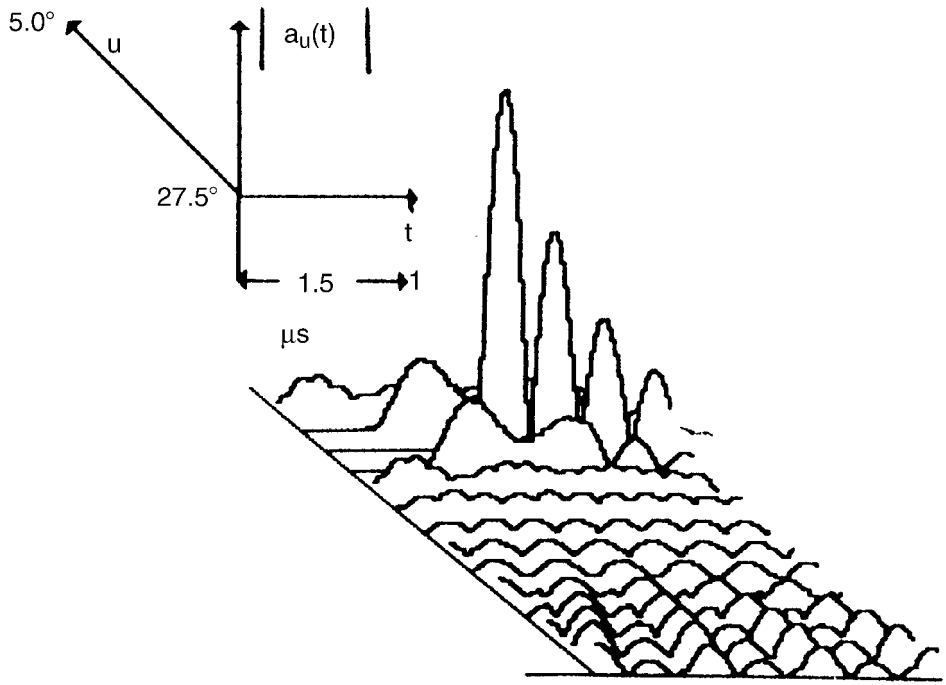

Figure 7.14 An isometric presentation of pulse on-axis and the long pulse at the grating lobe. The angular range of $-5^\circ - 27.5^\circ$ in increments of 2.5° for the parameters given in Figures 7.12–7.13. At 0°, the pulses add coherently to give an amplitude N. Near the grating lobe angle of 24.6°, pulses overlap sequentially to create a long pulse with an amplitude approximately equal to *Q* (from Bardsley and Christensen, 1981, Acoustical Society of America).

7.4.5 Beam Steering

If a linear phase is placed across the array elements, corresponding to a wave front at an angle θ_s from the z axis, the result is a beam steered at an angle θ_s (shown in Figure 7.16). This phase (τ_{sn}) is applied, one element at a time, as a linear phase factor with $u_s = \sin\theta_s$,

$$\exp(-i\omega_c\tau_{sn}) = \exp(-i2\pi f_c(npu_s)/c) = \exp(-i2\pi npu_s/\lambda_c) \tag{7.26}$$

to unsteered array response, Eq. (7.25), then the beams are steered at u_s,

$$\begin{aligned} H_s(u, u_s, \lambda_c) &= \Im_i\left[\Pi\left(\frac{x}{w}\right)\sum_{-n_L}^{n_L} a_n\delta(x-np)\exp(-i2\pi(npu_s)/\lambda_c)\right] \\ &= L_x pw \sin c\left(\frac{wu}{\lambda_c}\right)\sin c\left[\frac{L_x}{\lambda_c}(u - m\lambda_c/p - u_s)\right] \end{aligned} \tag{7.27}$$

and the amplitude weights (a_n) are equal to one. Figure 7.17 shows the effects of element directivity on the steered beam and grating lobes. In sector or angular scanning, the location of the grating lobe is related to the steering angle,

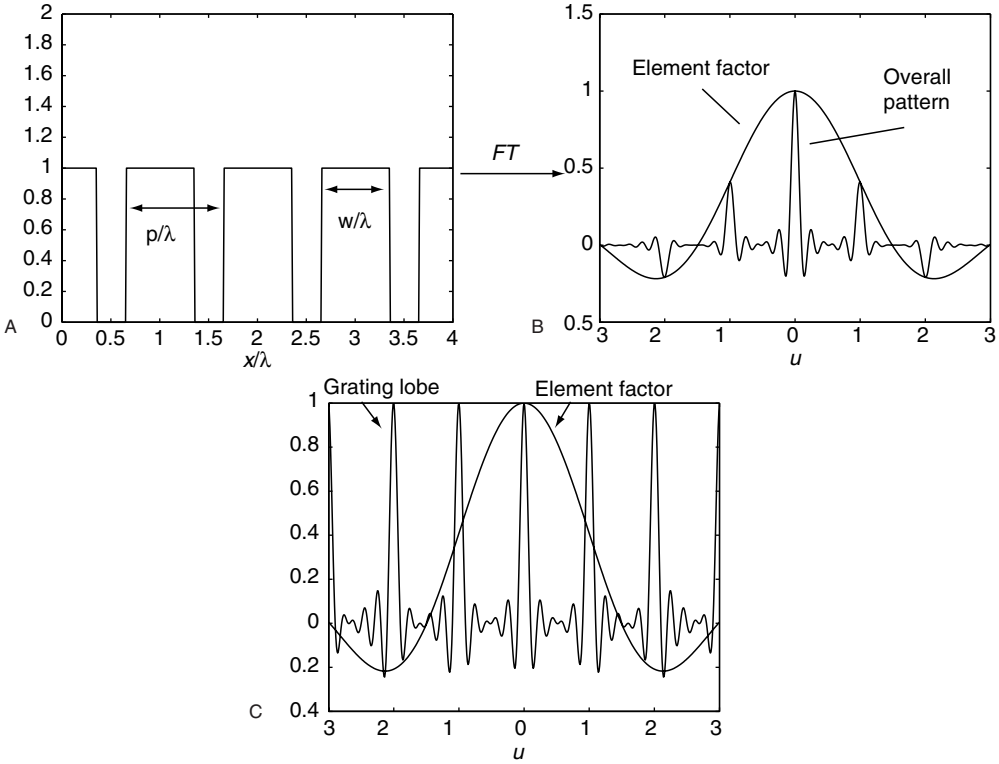

Figure 7.15 (A) A finite length array of elements of width *w* and periodicity *p*. (B) Fourier transform of spatial element amplitude results in modulation of grating lobes by broad angular directivity of element factor. (C) Factors contributing to overall transform.

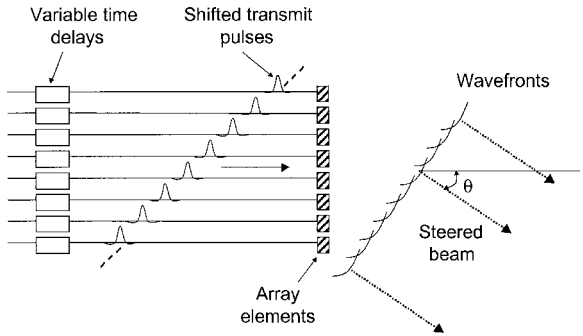

Figure 7.16 Delays for steering an array (from Panda, 1998).

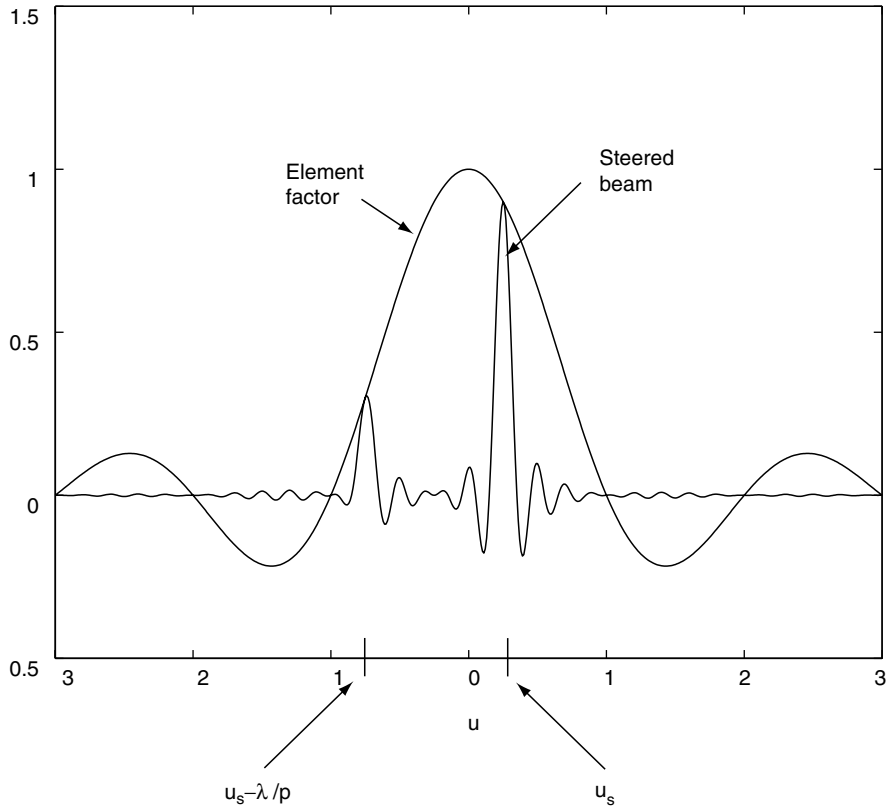

Figure 7.17 Array angular response when steered at θ_s.

$$\theta_g = \pm \arcsin\left(m\lambda/p + u_s\right) \tag{7.28}$$

where $m = \pm 1$ are the indices of the first grating lobes. As an example, consider a period of one wavelength and a steering angle of -45°, then the first grating lobe will be at

$$\theta_g = \arcsin\left(1 - 0.707\right) = 17^\circ$$

This result would not be appropriate for a phased array, but it would do for a linear array. What periodicity would be necessary to place the grating lobe at 45° for a steering angle of -45°?

7.4.6 Focusing and Steering

Until now, a far-field condition was assumed; however, this is not true in general. For an array aperture of several or many wavelengths in length, a near-field pattern will emerge. Just as lenses were used to focus (as explained in Section 6.6), arrays can be focused by adding time-delayed pulses that simulate the effect of a lens to compensate

for the quadratic diffraction phase term. The time delays to focus each element (n) are:

$$\tau_n = \left[r - \sqrt{(x_r - x_n)^2 + z_r^2} \right] / c + t_0 \tag{7.29a}$$

where r is the distance from the origin to the focal point, $r = \sqrt{x_r^2 + z_r^2}$, x_n is the distance from the origin to the center of an element indexed as "n" ($x = np$), and t_0 is a constant delay added to avoid negative (physically unrealizable) delays. The application of a paraxial approximation under the assumption that lateral variations are smaller than the axial distance leads to

$$\tau_n \approx (x_n u_s - x_n^2/2z_r)/c + t_0 = [npu_s - (np)^2/2z_r] + t_0 \tag{7.29b}$$

From this approximate expression, the first term is recognizable as the steering delay, Eq. (7.26), and the second is recognizable as the quadratic phase term needed to cancel the similar term caused by beam diffraction, as shown for a lens in Eq. (6.27b). In practice, usually the exact Eq. (7.29a) is used for arrays rather than its approximation. Putting all this together, we start with a modification of Eq. (7.17a) for the spatial impulse response of a single element located at position $x_n = np$,

$$h_n(u, r, t) = a_n h_{0x} w\left(\frac{c}{wu}\right) \prod\left(\frac{t}{wu/c}\right) \tag{7.30a}$$

where u is defined in Eq. (7.12a), and then the one-way transmit spatial impulse response for an element with focusing is of the form,

$$h_n\left(t - \frac{1}{c}\sqrt{(x - x_n)^2 + z^2} - \tau_n\right) = h\left(t - \frac{\sqrt{(x - x_n)^2 + z^2}}{c} - r/c + \sqrt{\frac{(x_r - x_n)^2 + z_r^2}{c}}\right) \tag{7.30b}$$

and when $x = x_r$, and $z = z_r$ at the focus,

$$h_n\left(t - \frac{1}{c}\sqrt{(x - x_n)^2 + z^2} - \tau_n\right) = h(t - r/c) \tag{7.30c}$$

The overall array response (h_a) is simply the sum of the elements,

$$h_a(t) = \sum_{-n_L}^{n_L} a_n h_n\left(t - \frac{1}{c}\sqrt{(x - x_n)^2 + z^2} - \tau_n\right) \tag{7.30d}$$

The pressure can be found from the convolution of the excitation pulse and array response as in Eq. (7.18). Here a perfect focus is achieved when the field point at (x, z) is coincident with the focal point (x_r, z_r). However, at all other points, zones corresponding to those described in Section 6.6.2 (a near Fresnel zone, focal Fraunhofer zone, and far Fresnel zone) will be created. Figure 7.18 illustrates the delays needed for focusing. The same type of delay equations can be used for receive or transmit.

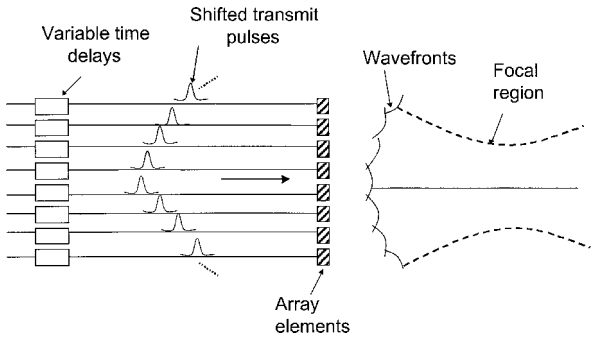

Figure 7.18 Array delays for focusing a beam (from Panda, 1998).

7.5 PULSE-ECHO BEAMFORMING

7.5.1 Introduction

Several factors are involved in the ultrasound imaging of the body, as was symbolized by the block diagram in Figure 2.14. In Chapter 5, the response of the transducer to a pulse excitation in a pulse-echo mode was discussed. These are covered by the electrical excitation and are also represented by the electrical excitation block (E), the transmit transducer response (G_T), and the receive response (G_R). A more practical description includes the effects of the transmit pulse, e_T(t). The electroacoustic conversion impulse response of the transducer from voltage to the time derivative of the particle velocity, g_T(t), the derivative operation, and the corresponding receive functions (denoted by R), can all be lumped together as

$$e_{RT}(t) = e_T(t) *_t g_T(t) *_t g_R(t) \tag{7.31a}$$

or in the frequency domain as

$$E_{RT}(f) = E_T(f)G_T(f)G_R(f) \tag{7.31b}$$

The overall voltage output, including focusing on transmit and receive, can be described by the product of the array transmit and receive spatial responses (shown by Figure 7.16),

$$V_0(r, f, \theta) = H_T(r_T, f, \theta_T)H_R(r_R, f, \theta_R)E_{RT}(f) \tag{7.32a}$$

The equivalent time domain formulation of the pulse-echo signal is

$$v_o(z, r, t) = h_t *_t h_r *_t e_{RT} \tag{7.32b}$$

Implicit in the spatial impulse responses are the beamformers, which organize the appropriate sequence of transmit pulses and the necessary sum and delay operations for reception. The beamforming operations, represented by blocks XB (transmit) and RB (receive), reside in the imaging system (to be explained in Chapter 10).

Attenuation effects, symbolized by blocks A_T (forward path) and A_R (return path), will be discussed in Section 7.9.4. Chapters 8–9 describe the scattering block (S), as well as the scattering of sound from real tissue and how it affects the imaging process.

The ability of a beamformer to resolve a point target is determined by the spatial impulse response of the transmit and receive beams intercepting the target. A measure of how well an imaging system can resolve a target is called the "point spread function," which is another name for the function given by Eq. (7.32). This equation shows that the beam-shape is related to the type of pulse applied. For example, the effect of bandwidth on the beam profile can be seen in Figure 7.19. For very short pulses or wider bandwidths, sidelobe levels can rise; this suggests that a moderate fractional bandwidth in the 60–80% is a better compromise between resolution and sidelobe suppression. The shaping of the pulse is also important in achieving a compact point spread function with low-time and spatial sidelobes (Wright, 1985).

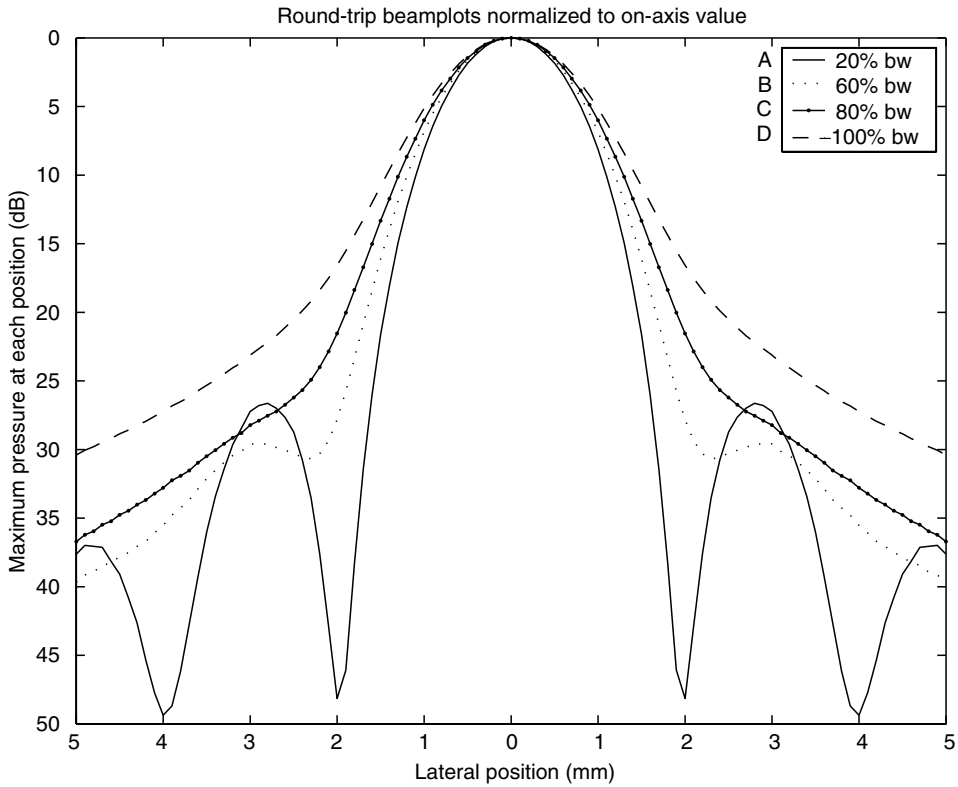

Figure 7.19 Normalized full Hamming apodized beams in focal plane for three round-trip Gaussian pulses of differing fractional bandwidths. (A) 20%. (B) 60%. (C) 80%. (D) 100% (created with Graphical User interface (GUI) for Field 2 from the Duke University virtual imaging lab).

7.5.2 Beam-Shaping

From Eq. (7.32a), the overall beam-shape is the product of the transmit and receive beams, each of which can be altered in shape by apodization ('t Hoen, 1982). So far, each element had an amplitude weight of one that led to a sinc-shaped directivity in the focal plane. By altering the weight of each element (a_n), see Eq. (7.27), through a means such as changing the voltage applied to each element, other weighting functions can be obtained, such as those discussed in Section 6.4 to lower sidelobes (Harris, 1978). Individual transmit and receive aperture lengths and apodizations can be combined to complement each other to achieve narrow beams with low sidelobes. The apodization can also increase the depth of field. Two drawbacks of apodization are an increased mainlobe width and a reduction in amplitude proportional to the area of the apodization function.

Two ways of measuring the effectiveness of a beam-shape are its detail resolution and its contrast resolution. Detail resolution, commonly taken as the −6-dB beamwidth, is the ability of the beam to resolve small structures. Point scatterers end up being imaged as blobs. The size of a blob is determined by the point spread function and can be estimated by a −6-dB ellipsoid, which has axes that are the axial resolution (pulse envelope) and lateral resolutions in x and y at −6 dB below the peak value in each dimension (Figure 7.20).

The contrast resolution of a beam (Maslak, 1985; Wright, 1985) is a measure of its ability to resolve objects that have different reflection coefficients and is typically taken to be the −40-dB (or −50-dB) round-trip beamwidth. Pulse-echo imaging is dependent on the backscattering properties of tissue. To first order, the possibility of distinguishing different tissues in an image is related to the reflection coefficients of tissues relative to each other (such as those shown in Figure 1.3). These often subtle differences occur at the −20- to −50-dB level. Consider three scatterers at reflectivity levels of 0, −20, and −40 dB. If the main beam is clear of sidelobes down to the -50 dB level, then these three scatterers can be cleanly distinguished. If, however, the beam has high sidelobes at the −13-dB level, then both weak scatterers would be lost

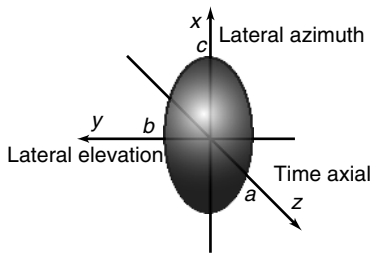

Figure 7.20 A −6-dB resolution ellipsoid. The axes represent −6-dB resolution in the lateral directions x and y and the axial pulse resolution along z.

in the sidelobes. The level of the sidelobes sets a range between the strongest scatterers and the weakest ones discernible. In other words, the sidelobe level sets an acoustic clutter floor in the image.

As an example of the effect of apodization, Figure 7.21 compares an image without apodization to one with receive Hanning apodization, both at the same amplitude settings. The amplitude apodization functions are graphed above each image (recall that the overall beam pattern is the product of the transmit and receive beam patterns). What is being imaged is a tissue-mimicking phantom with small wirelike objects (slightly smaller than the resolution capability of the imaging system) seen in cross section against a background of tissuelike material full of tiny unresolvable scatterers. The appearance of the wire objects is bloblike and varies with the detail resolution, as expected, through the field of view. Near the transmit focal length, the blobs are smaller. Careful observation of the wire targets in the image with apodization indicates that they are slightly dimmer and wider, results of less area under the apodization curve and a wider −6-dB beamwidth; therefore, the penetration (the maximum depth at which the background can be observed) is less.

In the image made without apodization, the resolvable objects appear to have more noticeable sidelobe ''wings'' (a smearing effect caused by high sidelobe levels). Another difference in the image made with apodization is contrast: The wire targets stand out more against a darker background. For extended diffuse targets, such as the tissue-mimicking material, the sidelobes have an integrating effect. For a beam with high sidelobes, the overall level in a background region results in a higher signal level; however, for a beam with low sidelobes, the overall integration produces a lower signal level that gives the appearance of a darker background in the image. The net

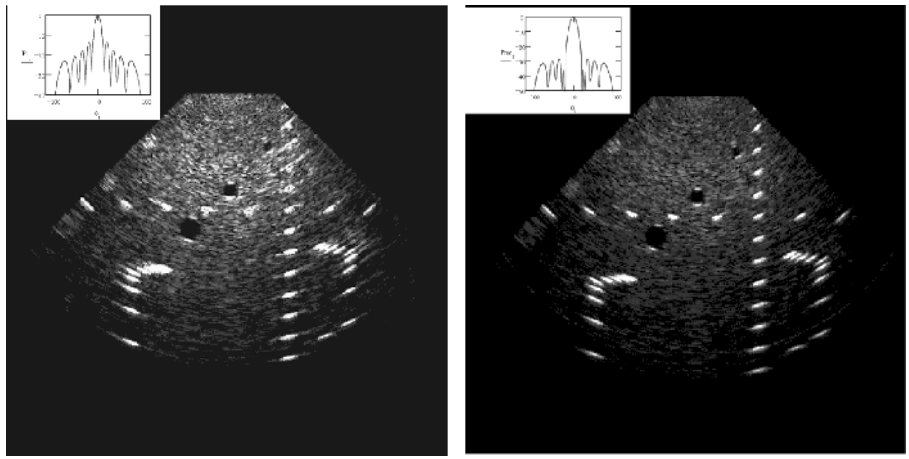

A B

Figure 7.21 (A) Unapodized beam plot insert and corresponding image of phantom with point targets. (B) Hanning apodization on receive beam shown in insert and corresponding image of phantom (courtesy of P. Chang, Terasun, Teratech Corporation).

result is that the difference in gray levels of a bright (wire) target and its background (tissue-mimicking material) is less for the first case than the second, so that the apparent contrast is greater for the second case.

7.5.3 Pulse-Echo Focusing

On transmit, only a single focal length can be selected. However, if the region of interest is not moving too fast, the scan depth can be divided into smaller ranges close to the focal zones of multiple transmit foci. These multiple transmit ranges can then be "spliced" together to form a composite image that has better resolution over the region of interest (see Figure 10.7 for an example). The transmit aperture length can be adjusted to hold a constant F number, ($F = F/L$) to keep the resolution constant over an extended depth (Maslak, 1985). For example, from Eq. (6.9c), the one-way, -6-dB FWHM beamwidth for an unapodized aperture is $2x_{-6} = 0.384\lambda F\#$. This approach has the disadvantage of slowing the frame rate by a factor equal to the number of transmit foci used.

One way to increase frame rate is to employ "parallel focusing"(Shattuck *et al*., 1984; von Ramm *et al*., 1991; Davidsen and Smith, 1993; Thomenius, 1996). In this method, a smaller number of broad transmit beams are sent so that two or more narrower receive beams can fit within each one. On reception, multiple beams are offset in steering angle to fit within the width of each transmit beam (Figure 7.22). In this way, the frame rate, which is normally limited by the round-trip time of the selected scan depth, can be increased by a factor equal to the number of receive beams.

On receive, however, a method called "dynamic focusing" (Vogel *et al*., 1979) provides nearly perfect focusing throughout the entire scan depth. In this case, the

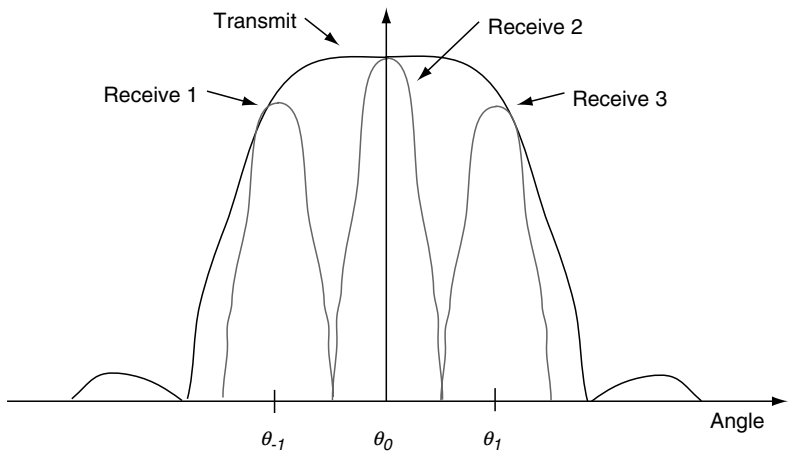

Figure 7.22 Parallel receive beamforming in which the transmit beam is broadened so that two or more receive beams can be extracted. Frame rate is increased by reducing the number of transmit beams.

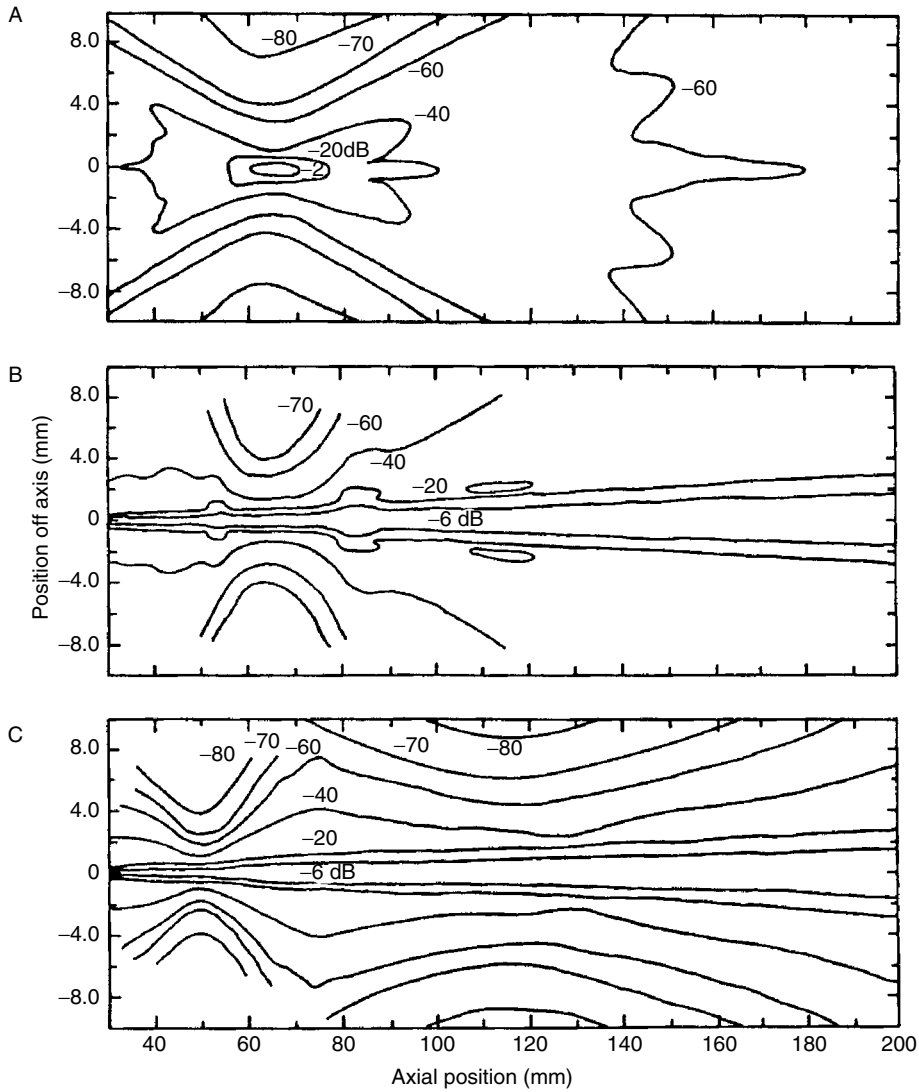

Figure 7.23 Beam contour plots for a 12-element, 4.5-MHz annular array. (A) Fixed transmit focus = 65 mm and fixed receive focus = 65 mm. (B) Fixed transmit focus = 65 mm and dynamic receive focusing. (C) First fixed transmit focus = 50 mm and second fixed focus = 130 mm, both with dynamic focusing and spliced together at 76 mm.

scan depth is divided into many zones, each one of which is assigned a receive focal length. In modern digital scanners, the number of zones can be increased so that the transitions between zones are indistinguishable and focusing tracks the received echo depth. In addition, the receive aperture can be changed and/or apodized with depth to maintain consistent resolution. Finally, the overall scan depth can be divided into N

sections, each one with a separate transmit focus, and the individual sections can be spliced together; however, this approach reduces frame rate by 1/N. Examples of the resolution improvements attainable are shown in Figure 7.23 for a 12-element, 4.5-MHz annular array with an outer diameter of 30 mm (Foster *et al*., 1989a, 1989b). The top of the figure shows the highly localized short depth of field for a fixed focus on receive, the middle demonstrates the benefits of receive dynamic focusing, and the bottom illustrates the effects of a two-transmit–zone splice with dynamic focusing.

7.6 TWO-DIMENSIONAL ARRAYS

One-dimensional (1D) arrays (Figure 7.24) typically have 32 to 300 elements and come in many forms (to be described in more detail in Chapter 10). These arrays scan in the azimuth plane, and a mechanical cylindrical lens produces a fixed focal length in the elevation plane. Two-dimensional (2D) arrays (refer to Figure 7.24) are needed to achieve completely arbitrary focusing and steering in any direction. While a typical phased array may have 64 elements, a 2D array might have 64^2 or 4096 elements. Because of their large number of elements, 2D arrays present challenges for their physical realization (see Section 7.9.2) as well as for efficient simulation of their fields. 1.5 dimensional (1.5D) arrays, intermediate between 1D and 2D arrays are described in Section 7.9.3.

The geometry for a 2D array of point sources of period p is shown in Figure 7.25 The diffraction impulse response for this array is

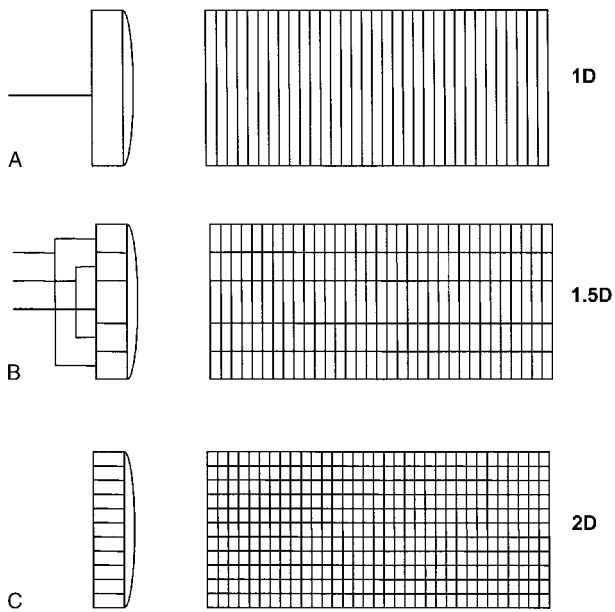

Figure 7.24 Types of arrays in profile and azimuth plane views. (A) 1D array. (B) 1.5D array. (C) 2D array.

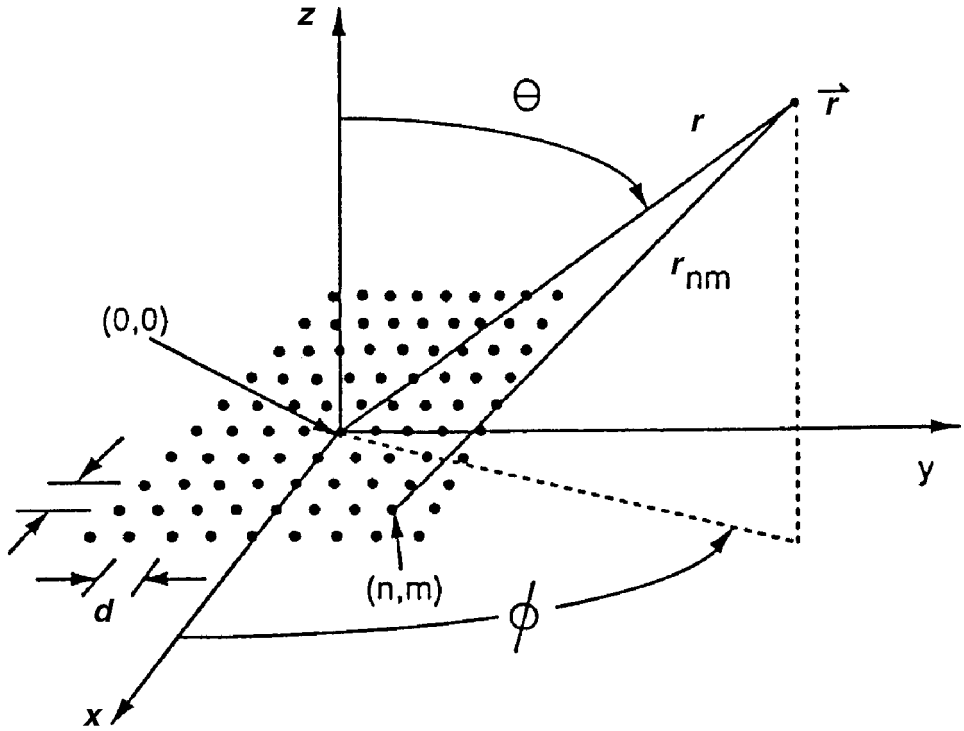

Figure 7.25 Geometry for a square 2D array of point sources with 2N + 1 elements on a side with *d* corresponding to p in the text (from Turnbull, 1991).

$$H_s(r,\theta,\phi,\lambda) = \frac{L_x L_y p^2}{2\pi r} \sum_{n=-\infty}^{\infty} sinc\left[\frac{L_x}{\lambda}(u - n\lambda/p - u_s)\right] \sum_{m=-\infty}^{\infty} sinc\left[\frac{L_y}{\lambda}(v - m\lambda/p - v_s)\right] \tag{7.33a}$$

in which the directions to the field point are u and v and the steering directions are

$$u_s = \sin\theta_0 \cos\phi_0 \tag{7.33b}$$

$$v_s = \sin\theta_s \sin\phi_s \tag{7.33c}$$

and the overall apertures are the following:

$$L_x = (2N+1)p \tag{7.33d}$$

$$L_y = (2M+1)p \tag{7.33e}$$

For a 2D array, grating lobes occur at the following locations:

$$u_g = u_s \pm n\lambda/p \tag{7.34a}$$

$$v_g = v_s \pm m\lambda/p \tag{7.34b}$$

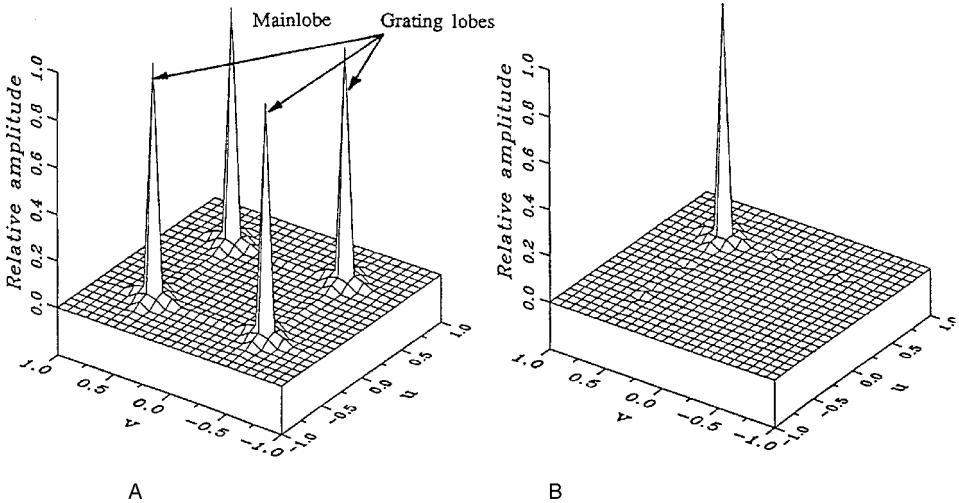

Figure 7.26 Far-field continuous wave pressure fields for an array of 101-by-101 point sources with array steered to $\theta = \phi = 45^{\circ}$. (A) $p = \lambda$. (B) $p = \lambda/2$ (from Turnbull, 1991).

For examples of the effect of spacing, refer to Figure 7.26. For a square array with 101 point sources on a side, first-order grating lobes appear when the periodicity is 1 wavelength according to steering at $(u_0, v_0) = (0.5, 0.5)$ for the main lobe and $(u, v) = (0.5, -0.5)$, $(-0.5, 0.5)$ and $(-0.5, -0.5)$ for the grating lobes.

The first-phased arrays were narrowband, so a CW model was adequate. With the arrival of digital systems, true-time delays for both steering and focusing became practical. For this approach, time domain models are more appropriate for broadband arrays. The method presented here is for 2D and 1D arrays; however, it can be extended to other cases in Section 7.9.3.

A general geometry is given by Figure 7.27, where small square elements with sides w and corresponding period p make up the array. Field positions are assumed to be in the far field of any individual element or $r >> p^2/(\pi\lambda)$. To determine field pressure, the effects of element directivity can be added to Eq. (7.33) through element factors,

$$P(r, \theta, \phi, f) = E_T(f)H_s(r, \theta, \phi, \lambda)w^2 \, sinc\left(\frac{wu}{\lambda}\right) sinc\left(\frac{wv}{\lambda}\right) \times \text{Obliquity Factor} \quad (7.34)$$

For pulses, Eq. (7.34) must be repeated for many frequencies (a computationally intensive process). An alternative is to develop a spatial impulse response for the array. From the far-field spatial impulse response of a rectangular element in Eq. (7.14), the overall time response of a rectangular element will be the convolution of two rect functions in time, or in general, the trapezoidal time function given by Figure 7.6. Therefore, the spatial impulse response of the central element at the origin to field point position (x, y, z) can be determined by the time delays to the corners given by Figure 7.27. Details can be found in Lockwood and Willette (1973) or Jensen and Svendsen (1992). Focusing and steering for the beams can be added by introducing the relative delays in Figure 7.27 to the spatial impulse response functions for each element,

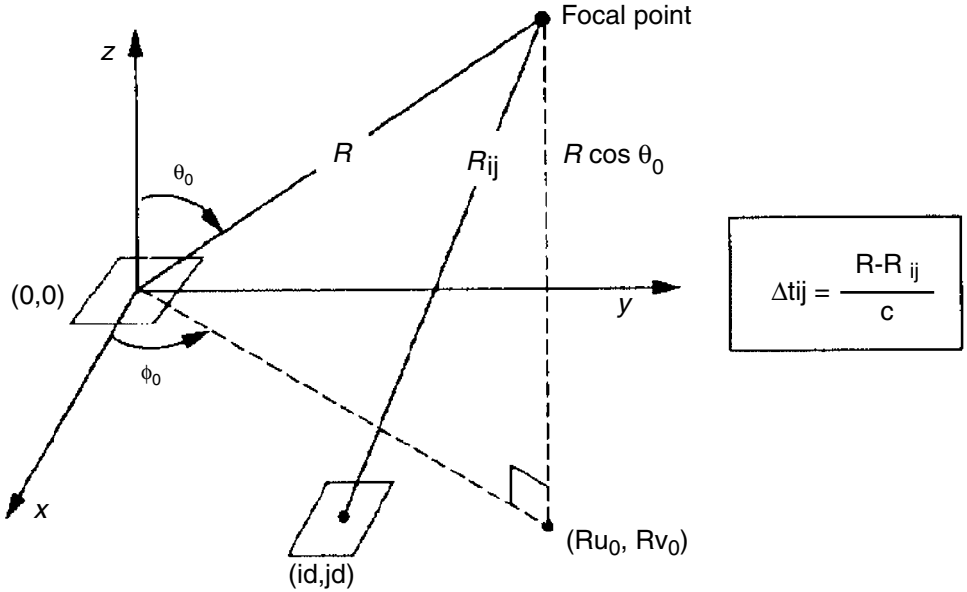

Figure 7.27 Time delay between central element at origin and element mn of a 2D array with indices *i, j* corresponding to indices m, n in the text and $d = p$ (adapted from Turnbull and Foster, 1991, *IEEE*).

$$t_{mn} = (r - r_{mn})/c = \frac{r}{c}\left\{1 - \sqrt{\left[(u_0 - mp_x/r)^2 + (v_0 - np_y/r)^2 + \cos^2\theta_0\right]}\right\} - t_0 \quad (7.35)$$

in which the focal point is defined by r and the direction *cosines* (u_0 and v_0). The one-way spatial impulse response is therefore

$$h_a(\bar{r}, t) = \sum_{n=-N}^{N} \sum_{m=-M}^{M} h_{m,n}(\bar{r}, t - t_{mn}) \quad (7.36)$$

For $\phi = 0$ and $n = 0$, this equation reduces to the 1D array result of Eq. (7.30). For r coincident with the focal point, Eq. (7.36) becomes $h(t - 2r/c + t_0)$. The pulse-echo overall response can be constructed from the transmit and receive array responses, as in Eq. (7.32b),

$$v_0(\bar{r}, t) = h_a^T(\bar{r}, t)^*{}_t \; h_a^R(\bar{r}, t)^*{}_t \; e_{RT}(t), \quad (7.37)$$

where superscripts T and R indicate transmit and receive, respectively.

7.7 BAFFLED

Recall that the element factor has a wide directivity and is an important effect for steered beams; consequently, this topic has received much attention beyond the studies previously mentioned. The directivity of an element is strongly influenced

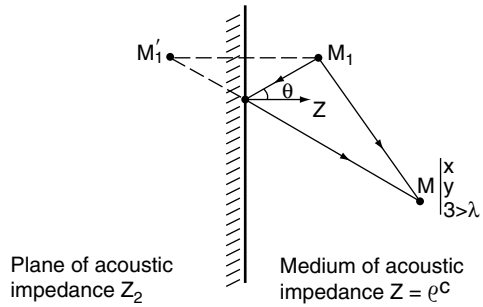

Figure 7.28 Geometry for an aperture, embedded in a medium of impedance Z_2, that radiates in medium Z. A point M_1 and its image M_1 are shown. (From Pesque' and Fink, 1984, IEEE).

by its surroundings. In Figure 7.28 is an illustration of a radiating element or active aperture embedded in a material called a baffle that has an impedance Z_2. This baffle determines the boundary conditions for aperture radiation into a medium with a wave number k and an impedance Z and modifies the directivity of the aperture by an obliquity factor that we shall now determine. Even more important is to find out what kind of baffle is most appropriate for medical ultrasound.

The radiation problem has the solution in the form of the Helmholtz–Kirchoff diffraction integral,

$$\psi(r, k) = \int_S \left[G \frac{\partial \psi(r_0)}{\partial n} - \psi \frac{\partial G(r_0)}{\partial n} \right] dS_0 \tag{7.38}$$

in which the Green's function consists of two parts associated with the field point r and its mirror image r',

$$G(k, r, r', k) = \frac{\exp(-ik|r - r_0|}{4\pi|r - r_0|} + R\frac{\exp(-ik|r' - r_0|}{4\pi|r' - r_0|} \tag{7.39}$$

where R is to be determined and the derivatives above are taken to be normal to the aperture.

Three commonly accepted cases have been studied and experimentally verified by measuring the directivity of a single slotted array element in the appropriate surrounding baffle (Delannoy *et al.*, 1979). All of these can be reduced to the form,

$$\Psi(r, k) = \int_S \frac{X(z, r, r_0) V_n(r_0, k) \exp(-i2\pi k(r - r_0))}{2\pi(r - r_0)} dS_0 \tag{7.40}$$

like Eq. (7.1a), where X is an obliquity factor. It is useful to define a direction *cosine* as

$$\cos\theta = \frac{z}{|r - r_0|} = \frac{z}{\sqrt{(x - x_0)^2 + (y - y_0)^2 + z^2}} \tag{7.41a}$$

The first case is when the element is dangling in free space and might be appropriate for an element completely surrounded by water. Here, $Z_2 = Z$, so in Eq. (7.40),

$$X = (1 + \cos\theta)/2 \tag{7.41b}$$

The second case is the hard baffle, for which $Z_2 \gg Z$ and

$$X = 1 \tag{7.41c}$$

so Eq. (7.40) becomes the Rayleigh integral (Strutt, 1896), which we have been using so far in this chapter and is the most common diffraction integral. The third case is the soft baffle, for which $Z_2 \ll Z$ and

$$X = \cos\theta \tag{7.41d}$$

and Eq. (7.40) becomes the Sommerfeld integral used in optics. Delannoy *et al.* (1979) obtained good experimental agreement with each of these cases and argued that the soft baffle situation might be the most appropriate of the three to represent a transducer held in air against a tissue boundary.

Each of these cases, however, are extreme ones. In general, we would expect the impedances Z_2 and Z to be different and to be within a reasonable range of known materials. Pesque' *et al.* (1983) found a solution for this practical intermediate case. They let the factor in Eq. (7.39) be the reflection factor,

$$R = RF = \frac{Z_2 \cos\theta - Z}{Z_2 \cos\theta + Z} \tag{7.42}$$

Their approach leads to the following obliquity factor:

$$X = \frac{Z_2 \cos\theta}{Z_2 \cos\theta + Z} \tag{7.43}$$

They (Pesque' *et al.*, 1983; Pesque' and Fink, 1984) show that their more general result reduces to the preceding soft and hard baffle cases. Their calculations for the directivity of an element in an array are compared to data in Figure 7.29. Note that this figure demonstrates that it is the impedance in contact with water (tissue) that determines what value of Z_2 to apply. They found that by accounting for the actual impedance at the interface with the body, which normally is a soft mechanical lens, good agreement could be obtained with data. The counterpart of this general result in the time domain is

$$\psi(r, t) = \int_S \frac{v_n[r_0, t - (r - r_0)/c]Z_2 \cos\theta}{2\pi(r - r_0)(Z_2 \cos\theta + Z)} dS_0 \tag{7.44}$$

As explained in Section 5.4, an array element vibrates in a mode dictated by its geometry, so it does not always act like a perfect piston. Smith *et al.* (1979) realized the nonuniform radiation problem and devised an approximate model. A more exact model was derived by Selfridge *et al.* (1980), who found that for elements typical in arrays, the element radiated nonuniformly. Delannoy *et al.* (1980) examined the problem from the viewpoint of Lamb-like waves generated along elements more than a water wavelength wide. They demonstrated that by subdicing the element, this effect was minimized. Finally, spurious modes and radiation patterns can be created through the architecture of the array, which provides possibilities for different

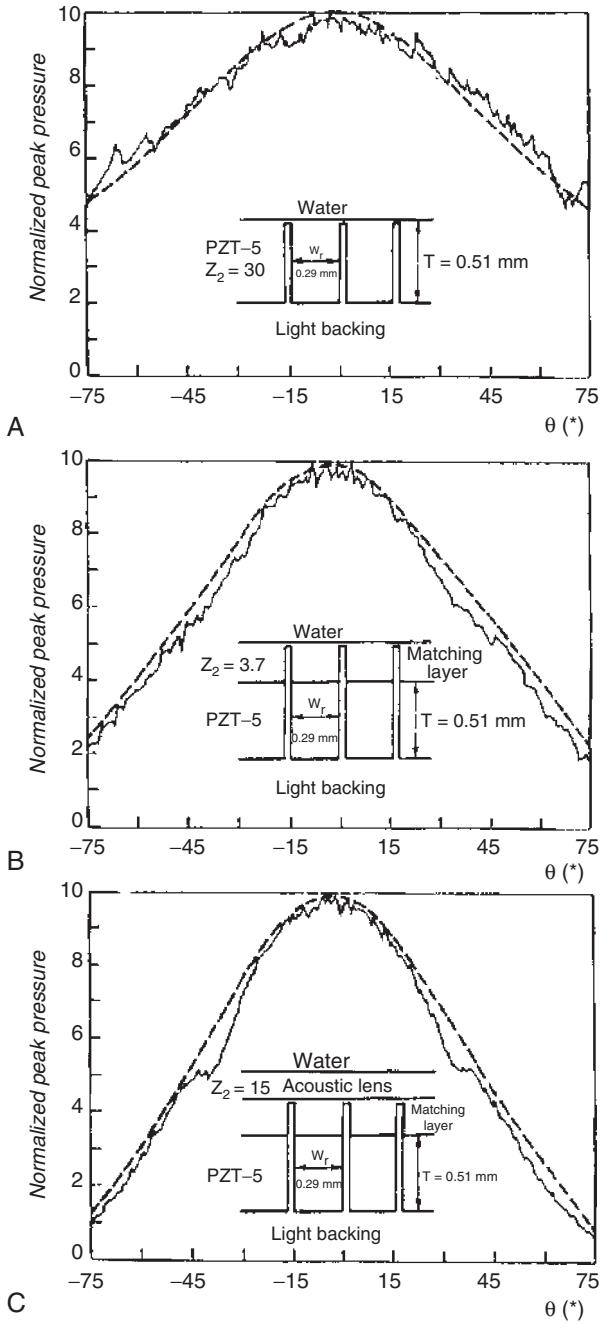

Figure 7.29 Simulations (solid lines) of the angular radiation pattern of a phased array element (directivity pattern) of width $w = 0.29$ mm excited at 3 MHz and radiating into water as a function for three different baffle impedances (Z_2) compared with data (dashed lines) (from Pesque' and Fink, 1984, *IEEE*).

waves to be generated simultaneously with the intended ones. In these cases, finite element modeling (FEM) (Lerch and Friedrich, 1986) is useful.

7.8 GENERAL APPROACHES

Because only a few geometries have been solved for time domain diffraction calculations, more general approaches have been devised. These methods apply to solid transducers of arbitrary shape and apodization, as well as arrays with larger elements. The first approach, used by Jensen (Jensen and Svendsen, 1992) in the Field 2 simulation program, breaks the aperture down into a mosaic of small squares (or triangles) like those used in a 2D array just described (Jensen, 1996). Each square is assigned an amplitude corresponding to an apodization weighting at that spatial location. Assumptions are that the radius of curvature is large compared to a wavelength and that each rectangular tile is small enough so that the field points are in its far field at the highest frequency in the pulse spectrum used. A second approach used by Holm (1995) in the diffraction simulation program Ultrasim is to perform a numerical integration of Eq. (7.1b) by breaking the surface velocity in the integrand into a product of spatial and time functions. Other methods have also been developed (Harris, 1981a; Harris, 1981b; Verhoef *et al*., 1984; Piwakowski and Delannoy, 1989; Hossack and Hayward, 1993), including an exact time domain solution for the rectangular element in both the near and far field (San Emeterio and Ullate, 1992).

Fortunately, two powerful programs with MATLAB interfaces for beamforming simulations are available to the general public. Jensen's program, Field II, is not only for beam calculations but also can simulate an entire ultrasound imaging system, including the creation of artificial phantoms to be imaged. Trahey and co-workers at Duke University have created a useful Graphical User interface (GUI) for Field 2 on their virtual imaging lab web site. Holm and his team at the University of Oslo have created Ultrasim, an interactive beam simulation program that includes 1D, annular, 1.5D, and 2D arrays. These can be found by doing a web search.

7.9 NONIDEAL ARRAY PERFORMANCE

7.9.1 Quantization and Defective Elements

Fields of arrays approach the shape of beams obtained by solid apertures that have the same outer dimensions if Nyquist sampling is achieved. For this case, to first order, array performance can be estimated by a solid aperture with appropriate delay and steering applied. A subtle difference between solid apertures and arrays of the same outer dimensions is that the active area of an array is slightly smaller because of the kerf cuts that isolate each element ($N(p\text{-}w)$ smaller for a 1D array). Because of the discrete nature of an array, however, performance is also dependent on the quantization of delay and amplitude that is possible in the imaging system (Thomenius, 1996), as well as individual variations in element-to-element performance and cross-coupling effects.

The first concern about quantization is the spacing of the array itself: Does it meet the Nyquist criteria ($\lambda/2$ spacing) at the highest frequency in the pulses used? In a digital system, phase quantization error is set by the sampling frequency of the system. The effects of phase quantization error (Magnin *et al*., 1981) increase as the number of samples per period near the center frequency decrease and result in a growth in the width and level of sidelobe structure in the beam (Bates, 1979). Amplitude quantization errors also bring similar effects in beam structure, but they are less severe, in general (Bates, 1979). These effects are caused by round-off errors at the highest number of bits available in the analog-to-digital (A/D) and digital-to-analog (D/A) converters in an imaging system.

While these sorts of errors are straightforward to analyze, second-order effects within the array itself are more troublesome. Unlike an ideal piston source that vibrates in a single longitudinal mode, the vibration of an array element consists of a more complicated combination of longitudinal and transverse modes (described in Section 5.4). Because the element may be physically connected to a backing pedestal, matching layers, and protective foils, other interrelated modes, such as Lamb and Rayleigh waves, can be generated (Larson, 1981). This strange dance of elements causes beam narrowing, ring-down, and other artifacts that can affect the image. Cross-coupling can also be caused by electromagnetic coupling from element to element and through the cable connecting elements to the system. Design solutions to these problems often involve experimental detective work and FEM modeling. An overview of the kinds of problems encountered in the design of a practical digital annular array system can be found in Foster *et al*. (1989a; 1989b).

Elements can also be defective; they can be completely inoperative or partially so. An element is called "dead" either because of depolarization of the crystal or an electrical disconnect (open) or an unexpected connection (short). Partial element functioning can be due to a number of possible flaws in construction, such as a debonding of a layer. The effect of inoperative elements is straightforward to analyze (Bates, 1979). In Eq. (7.18), for example, the amplitude coefficient of a dead or missing element is set to zero; therefore, the beam pattern is no longer a *sinc* or the intended function but a variation of it with higher sidelobes.

7.9.2 Sparse and Thinned Arrays

This topic leads us to the subject of deliberately stolen elements. Can the same beam pattern be achieved with fewer elements? Because channels are expensive, the challenge to do more with less is there for extremely low-cost portable systems, as well as for 2D arrays. What are the issues? Methods for linear arrays will be evaluated and then extended to 2D arrays.

Three main methods are used to decrease the number of elements in an array: periodic, deterministic aperiodic, and random (Schwartz and Steinberg, 1998). The simplest method is to make the elements fewer by increasing the period in terms of wavelengths with the consequence of creating grating lobes. There are also ways of "thinning" an array that usually start with a full half-wavelength spaced array, from which elements are removed by a prescribed method (deterministic aperiodic) (Skolnik,

1969). A fundamental transform law can be applied to the CW Fourier transform relation between the aperture function and its beam pattern in the focal plane or far field: The gain or on-axis value of the beam is equal to the area of the aperture function. As a result of this law, removing elements decreases the gain of the array and the missing energy reappears as higher sidelobes. If the fraction of elements remaining is P in a normally fully populated array with N elements, then the relative one-way reduced gain to an average far-out sidelobe level is $PN/(1\text{-}P)$. For example, if 70% of 64 elements remain, this relative gain drops from an ideal N squared (4096) to 149 or -22 dB.

The behavior of near-in sidelobes and the main beam are governed by the cumulative area of the thinned array (Skolnik, 1969). An algorithm can be developed to selectively remove elements of unity amplitude to simulate a desired apodization function in a least-squares sense. This method has been automated and extended to arbitrary weighted elements (Laker *et al*., 1977, 1978). The success of this approach improves as N increases, but the sidelobe level grows away from the main beam. This disadvantage can be compensated for by selecting a complementary (receive or transmit) beam with sidelobes that decrease away from the main beam.

Other approaches also have a similar sidelobe problem. A random method in which the periodicity is deliberately broken up to eliminate sidelobes and to simulate an apodization function statistically results in an average sidelobe level inversely proportional to the number of elements used (Skolnik, 1969; Steinberg, 1976).

One perspective is that the shape of the round-trip beamplot is the primary goal. For fully sampled arrays, the product of the transmit and receive CW beamshapes provides the desired result. Because of the Fourier transform relation between the aperture function and focal plane beamplot, an equivalent alternative is to tailor the aperture functions so that their convolution yields an effective aperture that gives the desired beamshape. With this approach, apertures with a few elements can simulate the shape of a fully sampled effective aperture with apodization. A minimum number of elements occurs when each array has the square root of the effective aperture of the final populated array to be simulated. Therefore, for a 64-element array, two differently arranged arrays of eight elements could provide the selected beam-shape.

Images generated by this approach were compared to those made by fully sampled arrays (Lockwood *et al*., 1996). While the expected resolution was obtained near the focal zone, grating lobes were seen away from this region. Penetration was also less than a normal array, as would be expected based on arguments described earlier for missing elements. In a follow-up work, Lockwood *et al*. (1998) estimated the effect of a decreased signal from a 1D sparse array by a signal-to-noise ratio (SNR) equal to $N_t (N_r)^{1/2}$, where transmit gain (N_t) is proportional to the number of elements, and receive gain (N_r) is related to the square root of elements due to receiver noise. This estimate gives a relative decrease of SNR of -54.9 dB for the 128-element full array, compared to the effective aperture method with only 31 total elements and with different halves (16) used on transmit and receive.

The need for decreasing channel count is even more urgent for 2D arrays for real-time 3D imaging (Thomenius, 1996). At Duke University (Davidsen and Smith, 1993), early 2D array work was done with a Mills cross and parallel processing to achieve high-speed imaging. Later work included a random array employing 192

transmit elements and 64 receive elements with a average sidelobe level of $1/\sqrt{N_t N_r}$ of −41 dB. Other work there (Smith *et al*., 1995) on a 484-element, 2D array and at the University of Toronto (Turnbull and Foster, 1991) showed that the principal difficulties were the requirement for many hundreds of active channels, severe difficulties in electrical connection, and the extremely low transducer SNR because of small element size. Alternative methods of 2D array construction also look promising. Kojima (1986) described a 2560-element matrix (2D) array. Greenstein *et al*. (1996) reported the construction of a 2.5-MHz, 2500-element array. Erikson *et al*. (1997) employed standard integrated circuit packaging to simplify the interconnection of a 30,000-element array for a real-time C-scan imaging system. Smith *et al*. (1995) discussed the challenges of 2D array construction and presented results for random sparse implementation.

In addition to random 2D arrays, other alternatives have been proposed. Lockwood and Foster (1994, 1996) simulated a radially symmetric array with 517 elements (one sixth the number of a fully populated 65-by-65 array) using the effective aperture approach and found it to be better than a random design. While most array designs are based on CW theory, Schwartz and Steinberg (1998) found that by accounting for pulse shape, ultrasparse, ultra-wideband can be designed with very low sidelobe levels on the order of N^{-2} one way. As pointed out in Section 7.4.3, grating lobes can be reduced by shortening the exciting pulse. In a similar way, very short pulses in this design do not interfere in certain regions, which leads to very low sidelobes. Inevitably, 2D arrays will be compared to the performance of conventional 1D arrays in terms of SNR. Schwartz and Steinberg (1998) showed that if the acoustic output of a conventional 1D array of area A is limited in terms of acoustic output by federal regulation, then a 2D array with elements of area (a) would have to have $N = A/a$ elements to achieve the same output and equivalent SNR. This conclusion returns us back to the concept of the gain in a beam on-axis as determined by the area of the active aperture, as given by Eq. (6.33d), $G_{focal} = ApertureArea/\lambda F$.

In 2003, Philips Medical Systems introduced a fully populated 2D array with 2900 elements with an active area comparable to conventional arrays. Highly integrated electronics in the transducer handle accomplish micro-beamforming to provide a true interactive, real-time 3D imaging capability. An image from this array is shown in Figure 10.25. More on 3D and 4D imaging can be found in Section 10.11.6.

7.9.3 1.5-Dimensional Arrays

Intermediate between 1D and 2D arrays are 1.5-dimensional (1.5D) arrays (Tournois *et al*., 1995; Wildes *et al*., 1997). This poor man's 2D array splits the elevation aperture into a number of horizontal strips, as shown in Figure 7.24 (middle). Elements in each strip can now be assigned at different delays for focusing, and each strip can become an element in a coarsely sampled array along the y-axis. Because of symmetry (focusing and no steering), the same delays can be applied to similarly symmetrically positioned strips, so they can be joined together, as shown in side view in the figure, in order to reduce connections. Note that the two central strips

merge into a wider combined strip. The individually addressable joined groups are referred to as "Y" groups.

To compare the three types of arrays in Figure 7.24, we start with a 1D array of 64 elements as an example. For the 1.5D array in the figure, there are three "Y" groups, corresponding to 6 horizontal strips or an overall element count of $6 \times 64 = 384$ effective elements. However, because of their joined grouping, only $3 \times 64 = 192$ connections are required. These numbers contrast the 64 elements and connections for the 1D array example and the 4096 (n^2) elements and connections for the 2D example. Note that a 1.5D array can combine electronic focusing with the focusing of an attached fixed lens to reduce absolute focusing delay requirements.

Other variants that permit primitive steering are possible (Wildes *et al*., 1997). Despite their coarse delay quantization in elevation, 1.5D arrays bring improved image quality because the elevation focusing can track the azimuth focusing electronically. Also, 1.5D arrays provide a cost-effective improvement over 1D arrays. A variant of the 1.5D array is an expanding aperture array, which can switch in different numbers of y groups with or without electronic elevation focusing to alter the F# in the elevation plane.

7.9.4 Diffraction in Absorbing Media

A major effect on array performance is attenuation (Foster and Hunt, 1979). Conceptually, the inclusion of attenuation seems straightforward: Replace the exponential argument in the diffraction integral, Eq. (7.1a), $-i2\pi k(r - r_0)$, with the complex propagation factor, $\gamma_T(r - r_0)$ from Eq. (4.7b). While this change can be done numerically (Goodsitt and Madsen, 1982; Lerch and Friedrich, 1986; Berkhoff *et al*., 1996), many of the computational advantages of the spatial impulse response approach no longer apply.

Fortunately, Nyborg and Steele (1985) found that by multiplying the Rayleigh integral by an external attenuation factor in the frequency domain for a circular transducer, they were able to obtain good correspondence with a straightforward numerical integration of the Rayleigh integral with attenuation included in the integrand. They improved their agreement when they used a mean distance equal to the maximum and minimum distances from points on the the aperture to the field point. Jensen *et al*. (1993) explored a time domain alternative, in which a factor containing attenuation and dispersion was convolved with the spatial impulse response and compared to a numerically integrated version of Eq. (7.1b) that was modified to include losses. Their findings were similar: Very good agreement was obtained, overall, and even better results were found using a mean distance for field points close to the transducer.

In summary, the findings of Nyborg and Steele (1985) and Jensen *et al*. (1993) can be generalized by separating out the effects of attenuation into an operation external to the diffraction process. In the frequency domain, this simplification is a multiplication by the material transfer function [MTF(r, f)] where r is the distance from the transducer to the field point on either the forward or return path. In the time domain, the material impulse response [mirf (r,t)], from Chapter 4 can be convolved with the

pulse or spatial impulse response. Slightly better results are possible by using the mean distance for short distances.

Overall, the *MTF* for the forward path is represented by block A_T, and that for the return path is represented by $A_R = MTF(r_R, f)$. Then Eq. (7.32a) can be extended to include attenuation,

$$V_o(r, f, \theta) = H_T(r_T, f, \theta_T)A_T(r_T, f)H_R(r_R, f, \theta_R)A_R(r_R, f)E_{RT}(f) \tag{7.45a}$$

Similarly, the corresponding time domain operations are $a_T(r_T, t) = mirf(r_T, t)$ and $a_R(r_R, t) = mirf(r_R, t)$, so that Eq. (7.32b) becomes

$$v_o(r, t) = h_t {}^*{}_t \; h_r {}^*{}_t \; a_T {}^*{}_t \; a_R {}^*{}_t \; e_{RT} \tag{7.45b}$$

7.9.5 Body Effects

Finally, the biggest detractor from ideal array performance is the body itself. The gain of an array is based on the coherent summation of identical waveforms. The fact that the paths from elements to the focal point can include different combinations of tissues leads to aberration effects that weaken focusing (to be explained in Chapter 9). Under real imaging circumstances, unexpected off-axis scatterers do occur. Grating lobes can be sensitive to low-level scatterers (Pesque' and Blanc, 1987). While sparse or thinned arrays appear attractive in simulations or water tank tests, they rely on fewer elements that mean a reduced figure of merit (discussed in Section 7.9.2) and the introduction of grating lobes that can bounce off strong scatterers not included in modeling. Body effects and their influence on imaging will be discussed in detail in Chapters 8, 9, and 12.

Bibliography

Collin, R. E. and Zucker, F. J. (eds). (1969). *Antenna Theory*, Part 1. McGraw Hill, New York. A general reference for more information on arrays.

Fink, M. A. and Cardoso, J. F. (1984). Diffraction effects in pulse-echo measurement. *IEEE Trans. Sonics Ultrason.* **SU-31**, 313–329. A helpful review article on arrays and time domain diffraction.

Jensen, J. A. (1996). *Estimation of Blood Velocities Using Ultrasound*. Cambridge, UK, Cambridge University Press. A book providing a brief introduction to ultrasound imaging, diffraction, and scattering.

Macovski, A. (1983). *Medical Imaging Systems*. Prentice-Hall, Englewood Cliffs, NJ. A general reference on arrays and medical imaging.

Sternberg, B. D. (1976). *Principles of Aperture and Array Design*. John Wiley & Sons, New York. A general engineering reference on arrays.

't Hoen, P. J. (1983). Design of ultrasonographic linear arrays. *Acta Electronica* **25**, 301–310. A helpful review article on array design, construction, diffraction, and simulation.

Thomenius, K. E. (1996). Evolution of ultrasound beamformers. *IEEE Ultrason. Symp. Proc.*, 1615–1622. A review article on beamforming methods.

von Ramm, O. and Smith, S. W. (1983). Beam steering with linear arrays. *IEEE Trans. Bromed. Engr.* **BME-30**, 438–452. A informative article on phased arrays.

Wright, J. N. (1985). Resolution issues in medical ultrasound. *IEEE Ultrason. Symp. Proc.*, 793–799. Article on design tradeoffs for beamforming.

References

Arditi, M., Foster, F. S., and Hunt, J. W. (1981). Transient fields of concave annular arrays. *Ultrason. Imag.* **3**, 37–61.

Bardsley, B. G. and Christensen, D. A. (1981). Beam patterns from pulsed ultrasonic transducers using linear systems theory. *J. Acoust. Soc. Am.* **69**, 25–30.

Bates, K. N. (1979). Tolerance analysis for phased arrays. *Acoustical Imaging*, Vol. **9**. Plenum Press, New York, pp. 239–262.

Berkhoff, A. P., Thijssen, J. M., and Homan, R. J. F. (1996). Simulation of ultrasonic imaging with linear arrays in causal absorptive media. *Ultrasound in Med & Biol*. **22**, 245–259.

Davidsen, R. E. and Smith, S. W. (1993). Sparse geometries for two-dimensional array transducers in volumetric imaging. *IEEE Ultrason. Symp. Proc.*, 1091–1094.

Delannoy, B., Bruneel, C., Haine, F., and Torguet, R. (1980). Anomalous behavior in the radiation pattern of piezoelectric transducers induced by parasitic Lamb wave generation. *J. Appl. Phys.* **51**, 3942–3948.

Delannoy, B., Lasota, H., Bruneel, C., Torguet, R., and Bridoux, E. (1979). The infinite planar baffles problem in acoustic radiation and its experimental verification. *J. Appl. Phys.* **50**, 5189–5195.

Erikson, K., Hairston, A., Nicoli, A., Stockwell, J., and White, T. A. (1997). 128 × 128 K (16 k) ultrasonic transducer hybrid array. *Acoust. Imaging*. Vol. **23**. Plenum Press, New York, pp. 485–494.

Foster, F. S. and Hunt, J. W. (1979). Transmission of ultrasound beams through human tissue: Focusing and attenuation studies. *Ultrasound in Med. & Biol.* **5**, 257–268.

Foster, F. S., Larson, J. D., Mason, M. K., Shoup, T. S., Nelson, G., and Yoshida, H. (1989a). Development of a 12 element annular array transducer for realtime ultrasound imaging. *Ultrasound in Med. & Biol.* **15**, 649–659.

Foster, F. S., Larson, J. D., Pittaro, R. J., Corl, P. D., Greenstein, A. P., and Lum, P. K. (1989b). A digital annular array prototye scanner for realtime ultrasound imaging. *Ultrasound in Med & Biol*. **15**, 661–672.

Goodsitt, M. M. and Madsen, E. L. (1982). Field patterns of pulsed, focused, ultrasonic radiators in attenuating and nonattenuating media. *J. Acoust. Soc. Am.* **71**, 318–329.

Greenstein, M., Lum, P., Yoshida, H., and Seyed-Bolorforosh, M. S. (1996). A 2.5 MHz 2D array with z-axis backing. *IEEE Ultrason. Symp. Proc.*, 1513–1516.

Harris, F. J. (1978). On the use of windows for harmonic analysis with the discrete Fourier transform. *Proc. IEEE* **66**.

Harris, G. R. (1981a). Review of transient field theory for a baffled planar piston. *J. Acoust. Soc. Am.* **70**, 10–20.

Harris, G. R. (1981b). Transient field of a baffled planar piston having an arbitrary vibration amplitude distribution. *J. Acoust. Soc. Am.* **70**, 186–204.

Holm, S. (Jan. 1995). Simulation of acoustic fields from medical ultrasound transducers of arbitrary shape. *Proc. Nordic Symposium in Physical Acoustics*. Ustaoset, Norway.

Hossack, J. A. and Hayward, G. (1993). Efficient calculation of the acoustic radiation from transiently excited uniform and apodised rectangular apertures. *IEEE Ultrason. Symp. Proc.*, 1071–1075.

Jensen, J. A. (1996). Field: A program for simulating ultrasound systems. Paper presented at the 10th Nordic-Baltic Conference on Biomedical Imaging. Published in *Medical & Biological Engineering & Computing*, Vol. 34, Supp. 1, Part 1, pp. 351–353.

Jensen, J. A., Ghandi, D., and O'Brien Jr., W. O. (1993). Ultrasound fields in an attenuating medium. *IEEE Ultrason. Symp. Proc*., 943–946.

Jensen, J. A. and Svendsen, N. B. (1992). Calculation of pressure fields from arbitrarily shaped, apodized, and excited ultrasound transducers. *IEEE Trans. Ultrason. Ferroelectr. Freq. Control* **39**, 262–267.

Kojima, T. (1986). Matrix array transducer and flexible matrix array transducer. *IEEE Ultrason. Symp. Proc*., 649–654.

Kramer, S. M., McBride, S. L., Mair, H. D., and Hutchins, D. A. (1988). Characteristics of wide-band planar ultrasonic transducers using plane and edge wave contributions. *IEEE Trans. Ultrason. Ferroelectr. Freq. Control* **35**, 253–263.

Laker, K. R., Cohen, E., Szabo, T. L., and Pustaver, J. A., (1977). Computer-aided design of withdrawal weighted SAW bandpass transversal filters. *IEEE International Symp. on Circuits and Systems*, Cat. CH1188-2CAS, pp. 126–130.

Laker, K. R., Cohen, E., Szabo, T. L., and Pustaver, J. A. (1978). Computer-aided design of withdrawal weighted SAW bandpass filters. *IEEE Trans., Circuits & Systems*, **CAS-25**, 241–251.

Larson, J. D. (1981). Non-ideal radiators in phased array transducers. *IEEE Ultrason. Symp. Proc*., 673–683.

Lerch, R. and Friedrich, W. (1986). Ultrasound fields in attenuating media. *J. Acoust. Soc. Am*. **80**, 1140–1147.

Lockwood, G. R. and Foster, F. S. (1994). Optimizing sparse two-dimensional transducer arrays using an effective aperture approach. *IEEE Ultrason. Symp. Proc*. 1497–1501.

Lockwood, G. R., Li, P-C., O'Donnell, M., and Foster, F. S. (1996). Optimizing the radiation pattern of sparse periodic linear arrays. *IEEE Trans. Ultrason. Ferroelectr. Freq. Control* **43**, 7–13.

Lockwood, G. R. and Foster, F. S. (1996). Optimizing the radiation pattern of sparse periodic two-dimensional arrays. *IEEE Trans. Ultrason. Ferroelectr. Freq. Control* **43**, 15–19.

Lockwood, G. R., Talman, J. R., and Brunke, S. S. (1998). Real-time 3-D ultrasound imaging using sparse synthetic aperture beamforming. *IEEE Trans. Ultrason. Ferroelectr. Freq. Control* **45**, 980–988.

Lockwood, J. C. and Willette, J. G. (1973). High-speed method for computing the exact solution for the pressure variations in the nearfield of a baffled piston. *J. Acoust. Soc. Am*. **53**, 735–741.

Magnin, P., von Ramm, O. T., and Thurstone, F. (1981). Delay quantization error in phased array images. *IEEE Trans. Sonics Ultrason*. **SU-28**, 305–310.

Maslak, S. M. (1985). Computed sonography. *Ultrasound Annual 1985*, R. C. Sanders and M. C. Hill (eds.). Raven Press, New York.

Nyborg, W. L., and Steele, R. B. (1985). Nearfield of a piston source of ultrasound in an absorbing medium. *J. Acoust. Soc. Am*. **78**, 1882–1891.

Oberhettinger, F. (1961). On transient solutions of the baffled piston problem. *J. Res. Nat. Bur. Stand*. **65B**, 1–6.

Panda, R. K. (1998). *Development of Novel Piezoelectric Composites by Solid Freeform Fabrication Techniques*, Dissertation. Rutgers University, New Brunswick, NJ.

Pesque', P. and Blanc, C. (1987). Increasing of the grating lobe effect in multiscatterers medium. *IEEE Ultrason. Symp. Proc*., 849–852.

Pesque', P., Coursant, R. H., and Me'quio, C. (1983). Methodology for the characterization and design of linear arrays of ultrasonic transducers. *Acta Electronica* **25**, 325–340.

Pesque', P., and Fink, M. (1984). Effect of the planar baffle impedance in acoustic radiation of a phased array element theory and experimentation. *IEEE Ultrason. Symp. Proc*., 1034–1038.

Piwakowski, B. and Delannoy, B. (1989). Method for computing spatial pulse response: Time domain approach. *J. Acoust. Soc. Am*. **86**, 2422–2432.

San Emeterio, J. L. and Ullate, L. G. (1992). Diffraction impulse response of rectangular transducers. *J. Acoust. Soc. Am*. **92**, 651–662.

Sato, J., Fukukita, H., Kawabuchi, M., and Fukumoto, A. (1980). Farfield angular radiation pattern generated from arrayed piezoelectric transducers. *J. Acoust. Soc. Am*. **67**, 333–335.

Schwartz, J. L. and Steinberg, B. D. (1998). Ultrasparse, ultrawideband arrays. *IEEE Trans. Ultrason. Ferroelectr. Freq. Control* **45**, 376–393.

Selfridge, A. R., Kino, G. S., and Khuri-Yakub, B. T. (1980). A theory for the radiation pattern of a narrow-strip transducer. *Appl. Phys. Lett*. **37**, 35–36.

Shattuck, D. P., Weinshenker, M. D., Smith, S. W., and von Ramm, O. T. (1984). Explososcan: A parallel processing technique for high speed ultrasound imaging with linear phased arrays. *J. Acoust. Soc. Am*. **75**, 1273–1282.

Skolnik, M. I. (1969). Nonuniform arrays. *Antenna Theory*, Part 1. R. E. Collin and F. J. Zucker (eds.). McGraw Hill, New York, pp. 207–234.

Smith, S. W., Davidsen, R. E., Emery, C. D., Goldberg, R. L., and Light, E. D. (1995). Update on 2-D array transducers for medical ultrasound. *IEEE Ultrason. Symp. Proc*., 1273–1278.

Smith, S. W., von Ramm, O. T., Haran, M. E., and Thurstone, F. I. (1979). Angular response of piezoelectric elements in phased array ultrasound scanners. *IEEE Trans. Sonics Ultrason*. **SU-26**, 186–191.

Somer, J. C. (1968). Electronic sector scanning for ultrasonic diagnosis. *Ultrasonics* **6**, 153–159.

Steinberg, B. D. (1976). *Principles of Aperture and Array Design*. John Wiley & Sons, New York.

Stephanishen, P. R. (1971). Transient radiation from pistons in an infinite planar baffle. *J. Acoust. Soc. Am*. **49**, 1629–1638.

Strutt, J. W., Lord Rayleigh. (1945 reprint of 1896 ed.). *Theory of Sound*, Vol. 2, Chap. 14. Dover, New York.

't Hoen, P. J. (1982). Aperture apodization to reduce the off-axis intensity of the pulsed-mode directivity function of linear arrays. *Ultrasonics* 231–236.

Thomenius, K. E. (1996). Evolution of ultrasound beamformers. *IEEE Ultrason. Symp. Proc*., 1615–1622.

Thurstone, F. L. and von Ramm, O. T. (1975). A new ultrasound imaging technique employing two-dimensional electronic beam steering. *Acoustical Holography and Imaging*, Vol. 5. Plenum Press, New York, pp. 249–259.

Tournois, P., Calisti, S., Doisy, Y., Bureau, J. M., and Bernard, F. (1995). A 128*4 channels 1.5D curved linear array for medical imaging. *IEEE Ultrason. Symp. Proc*., 1331–1335.

Tupholme, G. E. (1969). Generation of acoustic pulses by baffled plane pistons. *Mathematika* **16**, 209–224.

Turnbull, D. H. (1991). *Two-Dimensional Transducer Arrays for Medical Ultrasound Imaging*, PhD thesis, Department of Medical Biophysics, University of Toronto, Toronto, Canada.

Turnbull, D. H. and Foster, S. F. (1991). Beam steering with pulsed two-dimensional transducer arrays. *IEEE Trans. Ultrason. Ferroelectr. Freq. Control* **38**, 320–333.

Verhoef, W. A., Clostermans, M. J. T. M., and Thijssen, J. M. (1984). The impulse response of a focused source with an arbitrary axisymmetric surface velocity distribution. *J. Acoust. Soc. Am*. **75**, 1716–1721.

Vogel, J., Bom, N., Ridder, J., and Lance', C. (1979). Transducer design considerations in dynamic focusing. *Ultrasound in Med. Biol. & Biol.* **5**, 187–193.

von Ramm, O. T., and Thurstone, F. L. (1975). Thaumascan: Design considerations and performance characteristics. *Ultrasound in Med. & Biol.* **1**, 373–378.

von Ramm, O. T., Smith, S. W., and Pavey Jr., H. G. (1991). High speed ultrasound volumetric imaging system II: Parallel processing and image display. *IEEE Trans. UFFC* **38**, 109–115.

Wildes, D. G., Chiao, R. Y., Daft, C. M. W., Rigby, K. W., Smith, L. S., and Thomenius, K. E. (1997). Elevation performance of 1.25 D and 1.5 D transducer arrays. *IEEE Trans. Ultrason. Ferroelectr. Freq. Control* **44**, 1027–1036.

Wright, J. N. (1985). Resolution issues in medical ultrasound. *IEEE Ultrason. Symp. Proc.*, 793–799.

8 WAVE SCATTERING AND IMAGING

Chapter Contents

8.1 INTRODUCTION

What is it we see in an ultrasound image? To answer this question, several aspects of the overall imaging process must be understood in a comprehensive way. First, how does sound scatter from an object at typical ultrasound frequencies (Section 8.2)?

Second, what is the role of the spatial impulse response of the transducer (Section 8.3)? Third, how does the way the image is organized into multiple acoustic beams affect what is seen (Section 8.4)? The answers to these questions are about how an ultrasound imaging system senses and portrays tissue objects. The actual nature, structure, and acoustic characteristics of tissue are discussed in Chapter 9.

The array acts as an intermediary between the actual tissue and the created image. With ultrasound, the field is spatially variant, so the appearance of the same object depends on its location in the sound beam. In addition, the physical organization of tissue presents scatterers on several length scales so that their backscatter changes according to their shape and size relative to the insonifying wavelength.

These effects are apparent in an image of a tissue-mimicking phantom (Figure 8.1), in which three types of scattering objects are seen. Figure 8.2 illustrates the arrangement of scatterers in the phantom. Note the vertical column of nylon filament point targets that appear as dots in the cross section. To their right are columns of anechoic

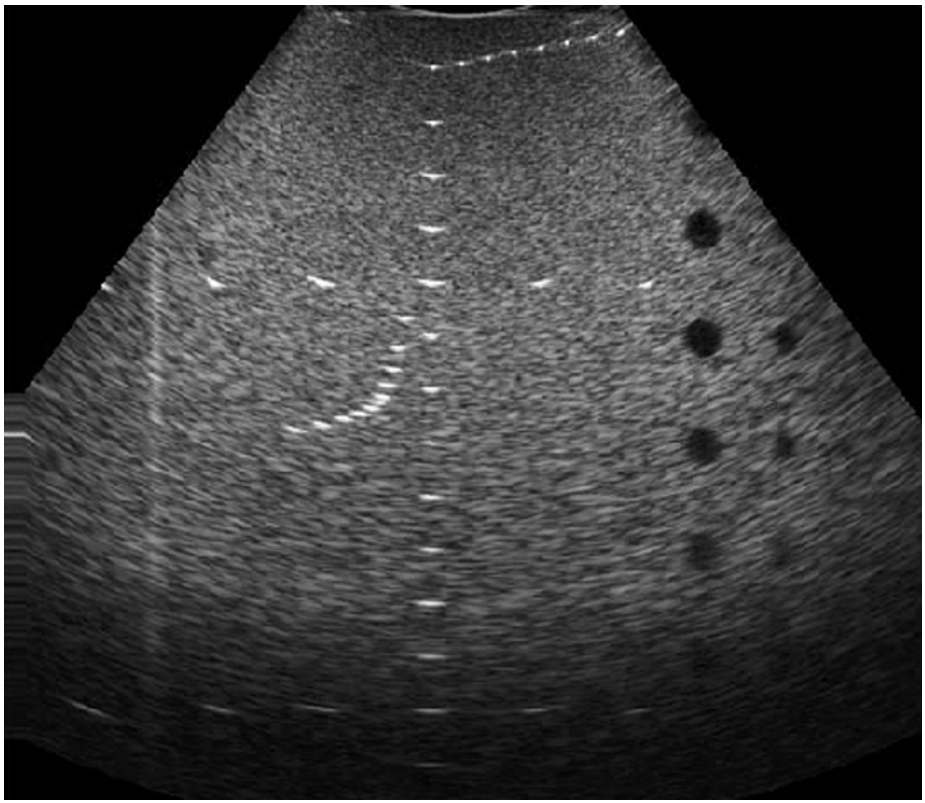

Figure 8.1 Two-dimensional ultrasound image of the same tissue-mimicking phantom with wire (point) targets and cyst targets. For this image, the transmit focal length of the 5-MHz convex array is positioned at 6 cm, which is the level of the horizontal wire target group (Image made with Analogic AN2800 imaging system).

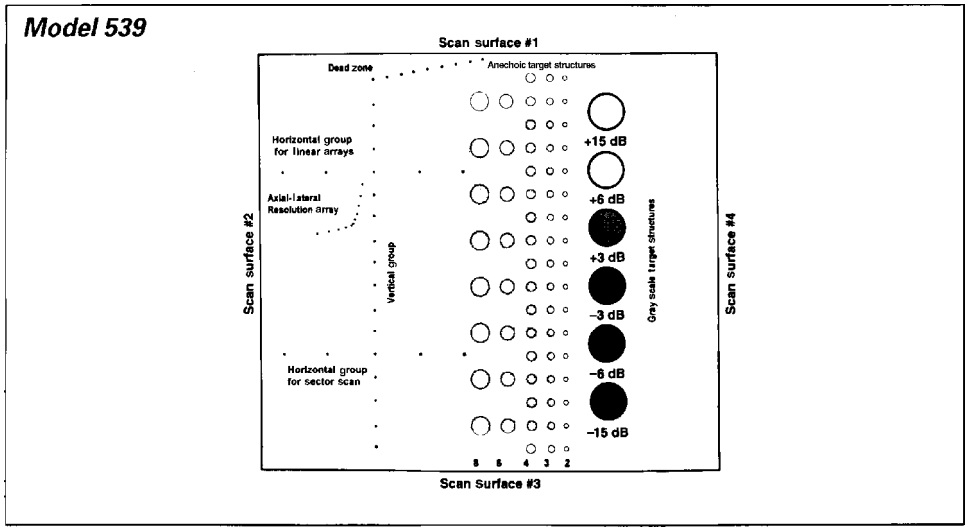

Figure 8.2 Illustration of arrangement of scattering objects in a tissue-mimicking phantom (courtesy of ATS Laboratories).

cylinders of varying diameters that appear as circles in the cross section. In Figure 8.1, on the left, images of nylon filament targets with a diameter much smaller than the wavelength at a frequency of 5 MHz, because of the transducer point spread function (see Section 7.4.1), appear larger than their physical size and vary in appearance away from the focal point. On the right are images of columns of cysts (seen as cross sections of cylinders) of varying diameters on the order of several wavelengths. These cysts have approximately the same impedance as the host matrix material surrounding it, but they have fewer subwavelength scatterers within them and appear black. Note that in the image, the smaller diameter cysts are more difficult to recognize and resolve. This problem is due in part to the resolving power of the transducer array used, as well as to the interfering effect of the background material, which has its own texture. The targets are suspended in a tissue-mimicking material composed of many subwavelength scatterers per unit volume. The imaging of this matrix material appears as speckle, a grainy texture. Speckle, described in more detail later, arises from the constructive and destructive interference of these tiny scatterers, and it appears as a light and dark mottled grainy pattern. This varying background interferes with the delineation of the shapes of the smaller cysts.

Note the vertical column of nylon filament point targets that appear as dots in cross section. To their right are columns of anechoic cylinders of varying diameters that appear as circles in cross section.

In general, there are three categories of scatterers based on length scales: *specular* for reflections from objects whose shapes are much bigger than a wavelength (large-diameter cysts in Figure 8.1); *diffractive* for objects slightly less than a wavelength to hundreds of wavelengths (smaller-diameter cysts); and *diffusive* for scatterers much smaller than a wavelength (background matrix material).

8.2 SCATTERING OF OBJECTS

8.2.1 Specular Scattering

Before examining the complexity of tissue structure, we shall find it easier to deal with the scattering process itself. The type of ultrasound scattering that occurs depends on the relation of the shape or roughness of the object to the insonifying sound wavelength. Objects fall roughly into three groups: those with dimensions either much larger or much smaller than a wavelength, and the rest that fall in between these extremes. Our discussion of backscattering will show how the scattering from a sphere will change its appearance depending on its size relative to the wavelength of the incident wave.

These categories are related to the smoothness of the object relative to a wavelength. If a wavelength is much smaller than any of the object's dimensions, the reflection process can be approximated by rays incident on the object so that the scattered wavefront is approximately a replica of the shape of the object. In the case of a plane wave of radius b illuminating a sphere of radius a much greater than a wavelength, as illustrated in Figure 8.3a, the intercepted sound sees a cross-sectional area of πb^2 and it is reflected by a reflection factor (RF) due to the impedance mismatch between the propagating medium and sphere. As the reflected wavefront is backscattered, it grows spherically so that the ratio of overall backscattered intensity (I_r) to the incident intensity (I_i); can be described by (Kino, 1987),

$$\frac{I_r}{I_i} = \frac{\pi b^2}{4\pi r^2}|RF|^2 = |RF|^2\frac{b^2}{4r^2} \tag{8.1a}$$

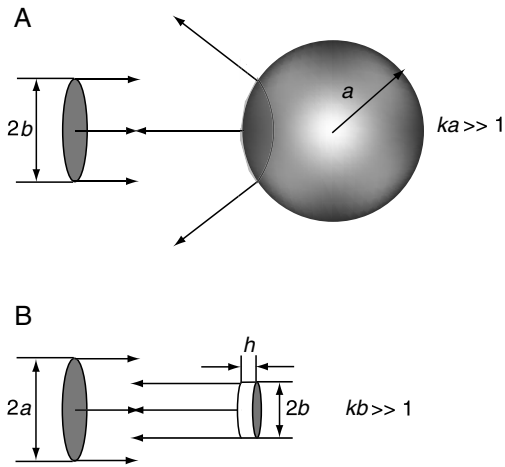

Figure 8.3 (A) Reflections from a rigid sphere of radius a in the $ka \gg 1$ regime. (B) Scattering from a rigid disk of radius b for $kb \gg 1$.

in which RF is from Eq. (3.22a) (Z_2 is the impedance of the sphere, and Z_1 is the impedance of the surrounding fluid). Note that this result does not depend on the wavelength. In this regime, ray theory holds. The importance of the angle of incidence was apparent for plane waves reflected from and mode converting into a smooth flat boundary in Chapter 3. The consequences of a nearly oblique plane wave striking a boundary are that the returning wave may be reflected away from the source and that the nearly normal components of the wave front are reflected more strongly, according to the impedance *cosine* variation described in Chapter 3. In the simple case presented here, the sphere is assumed to be rigid so that mode conversion is neglected.

Now consider a disk-shaped object of radius b illuminated by a cylindrical beam of radius a (shown by Figure 8.3.b). In this case, the ratio of backscattered intensities is

$$\frac{I_r}{I_i} = \frac{\pi b^2}{\pi a^2}|RF|^2 = |RF|^2 \frac{b^2}{a^2} \tag{8.1b}$$

Note that for a transducer positioned at one distance from a target, it would be difficult to tell these objects apart or determine their size only from their backscattered reflections.

8.2.2 Diffusive Scattering

At the other extreme, when the wavelength is large compared to a scattering object, individual reflections from roughness features on the surface of the object fail to cause any noticeable interference effects. In other words, the phase differences between reflections from high and low points on the surface are insignificant.

Lord Rayleigh discovered that for this type of scattering, intensity varies as the fourth power of frequency. Amazingly enough, for all the millions of humans who looked up at the sky, he was the first person determined enough to find out why it was blue. In his landmark paper, *On the Light from the Sky, Its Polarization and Colour* (1871), and in a later paper, he showed that the blueness of the sky was due to the predominant scattering of higher-frequency (blue) light by particles much smaller than a wavelength (Strutt, 1871).

Scattering in this regime has important implications in medical imaging. Tissue is often modeled as an aggregate of small subwavelength point scatterers like the one depicted in Figure 8.4. Blood flow, as measured by Doppler methods, is dependent on scattering by many small spatially unresolved blood cells. Also, most ultrasound contrast agents are tiny gas-filled resonant spheres used as tracers to enhance the scattering of ultrasound from blood pools and vessels. These topics will be covered in more detail in Chapters 11 and 14.

Lord Rayleigh (Strutt, 1871) and Morse and Ingard (1968) derived an expression for the scattering of pressure from a sphere much smaller than a wavelength with different elastic properties in density and compressibility from an exact solution for $ka \ll 1$,

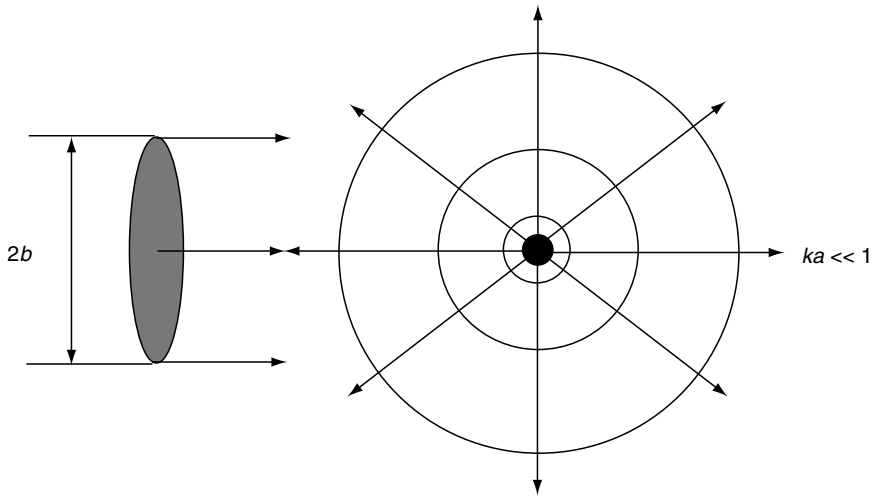

Figure 8.4 Reflections from a rigid sphere of radius a in the $ka \ll 1$ regime.

$$\frac{p_s}{p_i} = \frac{-k^2 a^3}{3r}\left[\frac{3(1-\rho_2/\rho_1)\cos\theta}{1+2\rho_2/\rho_1} + \left(1-\frac{\kappa_1}{\kappa_2}\right)\right] \tag{8.2a}$$

$$\frac{I_s}{I_i} = \frac{k^4 a^6}{9r^2}\left[\frac{3(1-\rho_2/\rho_1)\cos\theta}{1+2\rho_2/\rho_1} + \left(1-\frac{\kappa_1}{\kappa_2}\right)\right]^2 \tag{8.2b}$$

in which subscript 2 indicates the object density ρ and object compressibility κ, and $\theta = 0$ is along the axis of forward propagation (Figure 8.5). For a rigid sphere, $\rho_2/\rho_1 \to \infty$ and $\kappa_2/\kappa_1 \to \infty$, Eq. (8.2b) becomes

$$\frac{I_s}{I_i} = \frac{k^4 a^6}{9r^2}\left[1-\frac{3\cos\theta}{2}\right]^2 \tag{8.2c}$$

Lord Rayleigh (Strutt, 1871) showed that a small rigid sphere acts like a dipole (two main lobes at 0 and π) in its directivity. Therefore, the intensity backscattered along $\theta = \pi$ is

$$\frac{I_s}{I_i} = \frac{25k^4 a^6}{36r^2} \tag{8.2d}$$

a result that is frequency dependent (through k), unlike Eq. (8.1). Kino (1987) has pointed out that in this case, the total scattering cross section is the ratio of the total power scattered divided by the incident intensity,

$$\sigma(total) = \frac{7\pi k^4 a^6}{9} \tag{8.3}$$

which compares with the specular reflector cross section of $2\pi a^2$, since the sphere radiates equally in the forward and backward directions. In the specular case, the forward-scattered part of the wave cancels out the incident wave behind the sphere to create a geometric shadow.

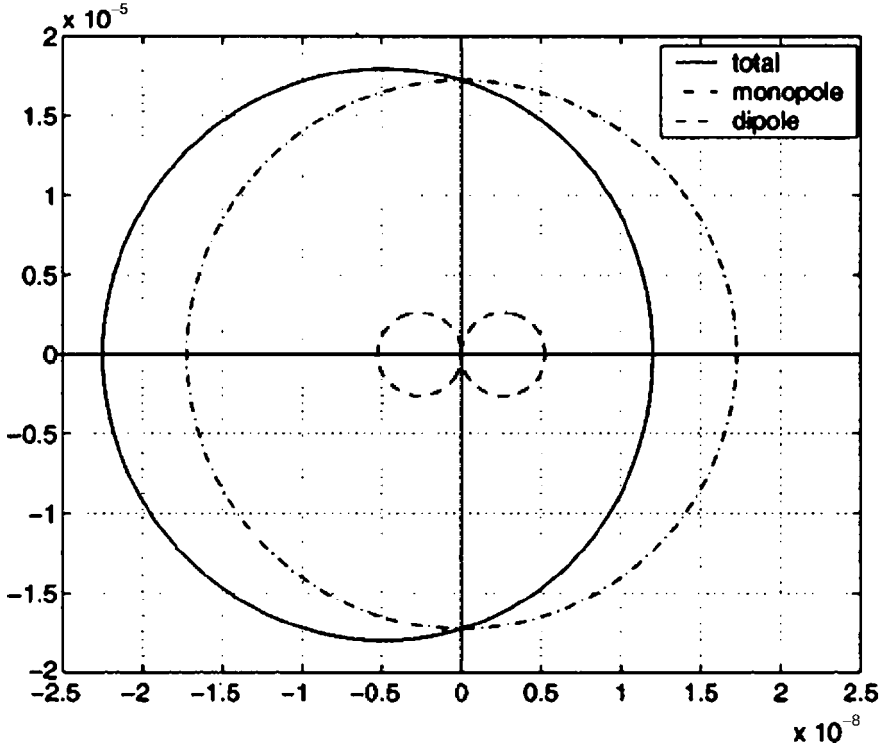

Figure 8.5 Contribution of the monopole (···) and dipole (----) terms of Eq. (8.2a) to the directivity pattern of the scattered field (—|—) produced by a red blood cell in water modeled as a fluid sphere for an incident plane wave coming in from the left (from Coussios, 2002, Acoustical Society of America).

Of interest is how the scattered intensity (related to pressure squared) is proportional to the frequency to the fourth power and to the sixth power of the radius in Eqs. (8.2b–8.2d). Note that just by changing frequency, the same scatterer will appear to have stronger or weaker reflections. As a result, the intensity reflected from this small sphere radiates outward as an expanding sphere whose intensity is proportional to the difference in compressibility and/or density and the fourth power of frequency. Later we shall return to the subject of how groups of these small scatterers can have a cumulative effect on imaging.

8.2.3 Diffractive Scattering

The last and largest category of scattering objects are those in between the extremes described earlier. Scattering for these objects is governed by the same Helmholtz–Kirchoff integral, Eq. (7.37), applied to the problem of diffraction of waves from transducer apertures. To first order, the scattered waves can be considered to be originating from the surfaces of the illuminated objects, which act as secondary

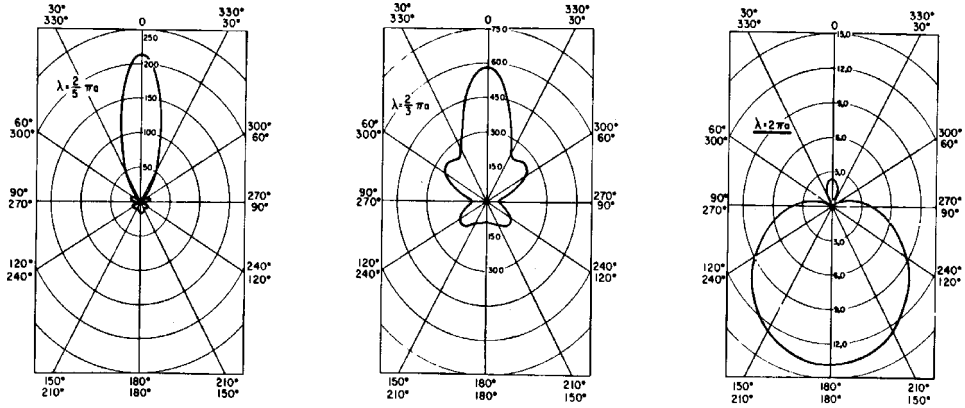

Figure 8.6 Polar scattering diagrams for a rigid sphere for different ka numbers (from Jafari, *et al.*, 1981, with permission from the World Federation of Ultrasound in Medicine and Biology).

sources. Actually, the scattering from elastic objects is far more involved, and only solutions for simply shaped objects have been solved analytically. Note that in this regime, scattered waves can be different in shape from the object and they can have maxima and minima that vary with angle and *ka* number. This conclusion is evident in Figure 8.6, in which the scattering of a rigid sphere for different values of *ka* and different directions show vastly different results for the same physical object (Jafari *et al.*, 1981). In these polar diagrams, 0° is the incident direction and 180° is the backscattered direction back toward the source. Exact solutions for elastic scattering from solid spheres and cylinders can be found in Faran (1951) and Hickling (1962).

8.2.3.1 Frequency domain Born approximation

An often-used estimate of scattering in this intermediate wavelength to object range is the Born approximation. The starting point is the Helmholtz–Kirchoff integral. The key assumption in this first-order approach is weak scattering so that the pressure on the surface of the scatterer is approximated by the incident pressure. Elastic mode conversion, multiple scattering, and resonance are neglected. The total pressure is taken to be the sum of the incident (p_i) and scattered fields (p_s)

$$p(r, t) = p_i(r, t) + p_s(r, t) \tag{8.4}$$

If we consider either an object slightly different from its surroundings, such as a piece of tissue suspended in water, or local mild fluctuations from a homogeneous region within tissue, the Born approximation is appropriate. These small fluctuations (f) from the local average of the host material (a) are usually expressed as the following for density and compressibility perturbations:

$$\rho(r) = \rho_a + \rho_f(r) \tag{8.5a}$$

$$\kappa(r) = \kappa_a + \kappa_f(r) \tag{8.5b}$$

which are rewritten in the more convenient form,

$$\gamma_\kappa = (\kappa_f - \kappa_a)/\kappa_a \tag{8.6a}$$

$$\gamma_\rho = (\rho_f - \rho_a)/\rho_f \tag{8.6b}$$

For an incident plane wave and with primed coordinates representing the scattering surface, an expression for the scattered pressure in spherical coordinates (Morse and Ingard, 1968) is

$$p_s(r) = \int_{V_0} \left\{ k^2 \gamma_\kappa(r_0) p(r_0) - div\left[\gamma_\rho(r_0) \cdot \nabla_0 p(r_0)\right] \right\} G(r/r_0) dV_0 \tag{8.7a}$$

in which standard r_0 coordinates are used for the scatterer, k is the local average wave number, θ is the angle between the incident plane wave direction and the vector r to the receiving point, and G is the usual Green's function,

$$G(r/r_0) = \exp(ik|r - r_0|)/4\pi|r - r_0| \tag{8.7b}$$

Here the Fourier transform of the object function is recognizable in Eq. (8.7a) with the exponent of the Green's function helping out. This relationship indicates that objects with sharp edges or corners will be strong scattering centers.

Nassiri and Hill (1986) have derived results from this integral under the Born approximation for a sphere of radius a and a disk of radius a and thickness h respectively,

$$p_{ss}(r) = \frac{e^{ikr}}{r} \frac{k^2}{k_s^3} \left(\gamma_\kappa + \gamma_\rho \cos\theta\right) (\sin k_s a - k_s a \cos k_s a) \tag{8.8a}$$

$$p_{sd}(r) = \frac{e^{ikr}}{r} \frac{hk^2 a^2}{2} \left(\gamma_\kappa + \gamma_\rho \cos\theta\right) \frac{J_1(k_s a)}{k_s a} \tag{8.8b}$$

where $k_s = 2k \sin(\theta/2)$. An often-used term for scattering is the differential scattering cross section, $\sigma_d(\theta)$, defined as "the fraction of power of a plane progressive wave disturbance incident on the scatterer that is scattered per unit angle." Nassiri and Hill (1986) provide cross sections for the sphere and disk,

$$\sigma_s(\theta) = \left[\frac{k^2}{k_s^3} \left(\gamma_\kappa + \gamma_\rho \cos\theta\right) (\sin k_s a - k_s a \cos k_s a) \right]^2 \tag{8.9a}$$

$$\sigma_d(\theta) = \left[\frac{hk^2 a^2}{2} \left(\gamma_\kappa + \gamma_\rho \cos\theta\right) \frac{J_1(k_s a)}{k_s a} \right]^2 \tag{8.9b}$$

8.2.4 Scattering Summary

In summary, specular reflectors have a reflected pressure that does not vary with frequency. At the other extreme, diffusive scatterers much smaller than a wavelength have a parabolic pressure dependence on frequency, according to Eq. (8.2a) in the small ka range ($ka < 0.35$). In between these extremes, the exact solution (Hickling, 1962) for a rigid sphere and the Born approximation are backscattered pressures what rise from a value of zero at $ka = 0$, and undulate with a periodicity related to the interference between the front and back surfaces of the sphere, and asymptotically approach the specular reflection value.

8.3 ROLE OF TRANSDUCER DIFFRACTION AND FOCUSING

The previous chapter stressed that the point-spread function (the ability of the excited transducer to resolve an ideal point scatterer) varies with position and orientation. The discussion in the last section on scattering objects presented results for incident plane waves. In reality, a complicated field pattern from a transducer is incident on a scattering object, not a plane wave. This pattern is then reradiated as a secondary source and scattered in a way dependent on the object's shape and size related to its wave number. In the simplest case, such as an object in the focal plane of a narrow-band transducer, where a *jinc* or *sinc* type beam cross section function might occur, the amplitude varies across the object and the phase changes sign at each spatial sidelobe. Inclusion of these kinds of effects is necessary in a more accurate model.

A simple approach to include these effects is to build on the model given in Section 7.4.1 by adding a scattering term (s). In the time domain, the overall response can be written as

$$v_0(z, r, t) = e_{RT}(t)^*{}_t\, h_t(z, r, t)^*{}_t\, h_r(z, r, t)^*{}_r\, s(r, t) \tag{8.10a}$$

where $e_{RT}(t)$ is the round-trip signal of the transducer from Section 7.4.1, and the h's are the diffraction impulse responses for the transmitter and receiver. The frequency counterpart of this equation is

$$V_0(z, r, f) = E_{RT}(f)H_t(z, r, f)H_r(z, r, f)S(z, r, f) \tag{8.10b}$$

These descriptions, which are reasonably accurate simplifications of the actual process in that it is broken down into identifiable factors, are already becoming rather complicated. For this reason, for simulation purposes, the models of scattering objects are often represented by many ideal rigid point scatterers with different reflection amplitudes organized in the shape of desired scattering objects or tissue. Using the scattered pressure for a rigid sphere, from Eq. (8.2), S can be expressed as an ensemble of ideal point targets each positioned at r_n,

$$S(r, f) = \sum_n s_n \frac{k^2 a^3}{3|r - r_n|}\left[1 - \frac{3\cos\theta}{2}\right] e^{-ik(r - r_n)} \tag{8.11a}$$

where frequency is contained in k, S_n is a constant, and a corresponding time domain version is

$$s(r, t) = \sum_n S_n \frac{a^3}{3c_0^2|r - r_n|}\left[1 - \frac{3\cos\theta}{2}\right] \frac{\partial^2 \delta(t - |r - r_n|/c_0)}{\partial t^2} \tag{8.11b}$$

Another important pulse-echo case of interest is the plane or mirror scatterer at depth Z_m (Carpenter and Stepanishen, 1984). This pulse-echo configuration (illustrated in Figure 8.7a) is equivalent to an identical transmitter–receiver pair separated by $2Z_m$ with a reflection factor (RF) included for a partially reflecting flat mirror (Chen and Schwartz, 1994; Chen *et al.*, 1997). From Figure 8.7b, this RF becomes a transmission factor (TF) $TF = RF(2Z_m)$, for a partially transparent membrane for the equivalent two-transducer configuration. The overall transfer function can be recognized as a modified diffraction loss (see Section 6.4),

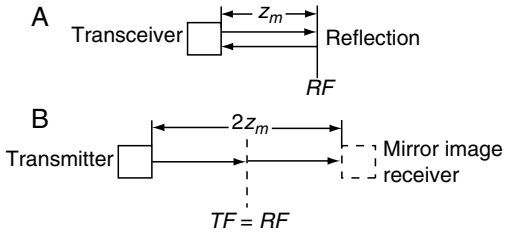

Figure 8.7 (A) Mirror or plane reflector configuration. (B) Equivalent transducer pair configuration.

$$DL_{eqiv}(2Z_m, f) = \exp(-ik2Z_m)RF_m DL(2Z_m, f) \tag{8.12}$$

A few cases have been worked out in the time domain. Rhyne (1977) derived a time domain equivalent for the circular piston and an ideal mirror. He called it the "impulse response of the radiation coupling filter."

8.3.1 Time Domain Born Approximation Including Diffraction

Jensen (1991) has reformulated the Born approximation in the time domain and has included the electromechanical and diffraction field effects of the transmitting and receiving transducers. Jensen points out that the scattered field can be expanded into higher-order terms that represent multiple scattering, but that a first-order approximation is usually sufficient. We can show that with a slight rearrangement of his results below, his formulation is similar in concept to the pulse-echo case of Eq. (8.10a).

$$v_0(t) = e_{RT}(t)^*{}_t f_m(r_c)^*{}_r h_{pe}(r_c, r, t) \tag{8.13a}$$

where v_0 is the round-trip pulse-echo voltage, r is the vector to the position on the scattering object, and r_c is the vector to the center of the receiving transducer,

$$h_{pe}(r_c, r, t) = \frac{1}{c_0^2}\frac{\partial^2 H_{pe}(r_c, r, t)}{\partial t^2} \tag{8.13b}$$

and $H_{pe}(t) = h_t(t)^*_t h_r(t)$, from Section 7.4.1. Also, an inhomogeneity scattering function is

$$f_m(r) = \Delta\rho(r_c)/\rho_0 - 2\Delta c(r_c)/c_0 \tag{8.13c}$$

that represents the small changes of density and the speed of sound from their nonperturbed average values,

$$\Delta\rho(r) = \rho(r) - \rho_0 \tag{8.14a}$$

$$\Delta c(r) = c(r) - c_0 \tag{8.14b}$$

Note that this definition of f_m is slightly different than the standard definitions of Eqs. (8.5–8.6). However, it can be recognized as the scattering function of Eq. (8.10a),

$$s(r, t) = \frac{f_m}{c_0^2}\frac{\partial^2 \delta(t - r/c_0)}{\partial t^2} \tag{8.15a}$$

and

$$S(r, f) = \frac{-\omega^2}{c_0^2} f_m \tag{8.15b}$$

if the double differential operator is shifted from Eq. (8.13b) to the scattering function. The function $f_m(r)$ represents the actual physical inhomogeneities or objects that are distorted by a time convolution and a spatial convolution, according to Eq. (8.13a) during the scattering process.

The overall scattering process can be rewritten as

$$V_o(t) = e_{RT}(t)^*{}_t H_{pe}(r_c, r, t)^*{}_r s(r, t) \tag{8.15c}$$

$$V_o(f) = E_{RT}(f) H_{pe}(r_c, r, f) S(r, f) \tag{8.15d}$$

As an example of how this approach may be used, consider a mirror placed at the focal plane of a circularly symmetric transducer where $z_m = F$. Chen *et al.* (1997) and Chen and Schwartz (1994) have shown that the response is a very weak function of frequency there, so that the round-trip response, $v_0(t)$, would correspond to the function $e_{RT}(t)$, as shown for a measurement in Figure 8.8. A point scatterer placed

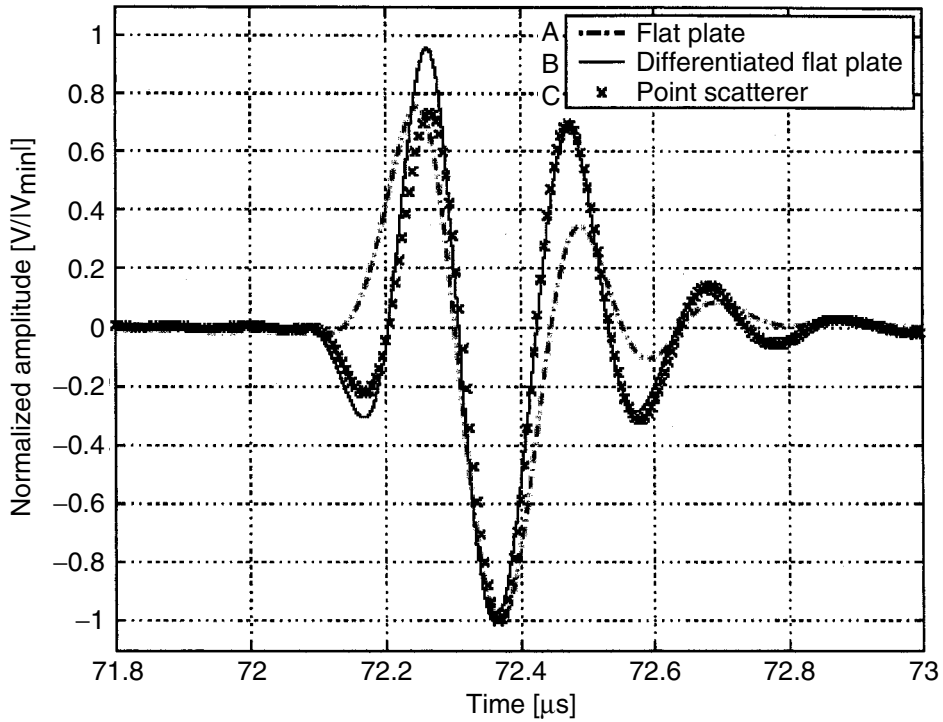

Figure 8.8 (A) Pulse-echo response ($v_0 = e_{RT}$) for a flat plate (---) placed at $Z_m = F$. (B) Doubly differentiated (——) ($\partial^2 e_{RT}/\partial t^2$). Normalized pulse-echo to (C). (C) A normalized measurement of a pulse-echo from the tip of an optical fiber also placed at the focal point of the same spherically focused 3.5-MHz transducer (from Szabo *et al.*, 2004, Acoustical Society of America).

also at the focus of this transducer would be expected to have the differential scattering characteristic of Eq. (8.15a). In this case, the overall response is proportional to $\partial^2 e_{RT}/\partial t^2$. This result is shown to be the case in Figure 8.8b and it is compared to data (Figure 8.8c) (Szabo *et al*., 2004).

Jensen (1996) has included a point scatterer approach for tissue representation with reflection strengths proportional to values obtained from the Born approximation in his Field II simulation program. The Field II program is based on Eq. (8.13a) and includes methods for implementing different array and transducer geometries with apodization, beamforming (including static and dynamic focusing), absorption effects, and the ability to create synthetic phantoms made from an organized set of point scatterers (Jensen and Munk, 1997). In Figure 8.9a, an organized set of weighted point scatterers represents an optical image of the right kidney and liver. In Figure 8.9b, an image is simulated as seen by a 128-element, 7-MHz phased array. Details can be found in Jensen and Nikolov (2000). In addition, the user interface for Field II is through a series of MATLAB scripts. This program is available for public use on the World Wide Web and can be found by searching for Field II or on J. A. Jensen's web site www.es.oerstd.dtu.dk/staffjag/field/index.html.

8.4 ROLE OF IMAGING

8.4.1 Imaging Process

A comprehensive viewpoint of imaging is necessary to include the major effects involved: beamforming and the spatially varying point spread function (p.s.f.) the extent of the scattering objects, angles of inclination of beams to these objects, image line sampling rate, interpolation, and presentation. The steps in the imaging process that include all these effects are shown schematically in Figure 8.10 and are listed below.

Images are constructed from a number of acoustic "lines" or vectors usually organized in a sequential pattern. Even though an acoustic vector appears as a thin line in an image after conversion by envelope detection into an image line, each line physically represents a time record of three-dimensional (3D) scattered waves from different depths. The process of image formation is explained by the following sequence of events with reference to letters denoting stages in Figure 8.10:

1. (a) A pulse packet, having 3D spatial extent, travels along the beam vector axis z and changes shape according to its p.s.f. field characteristics.
2. (b) After transmission along an acoustic vector direction, the traveling acoustic pulse is scattered over a broad angular range by a series of objects that are each located at a scattering depth z_i and correspond to time delays z_i/c.
3. (c) Angular portions of the series of reflections are intercepted by the receiving pulse-echo transducer. Each echo is at a time delay approximately equal to $2z_i/c$.
4. (d) These intercepted waves are integrated over the surface of the receiving transducer with appropriate weighting and time delays added for focusing and beamforming.

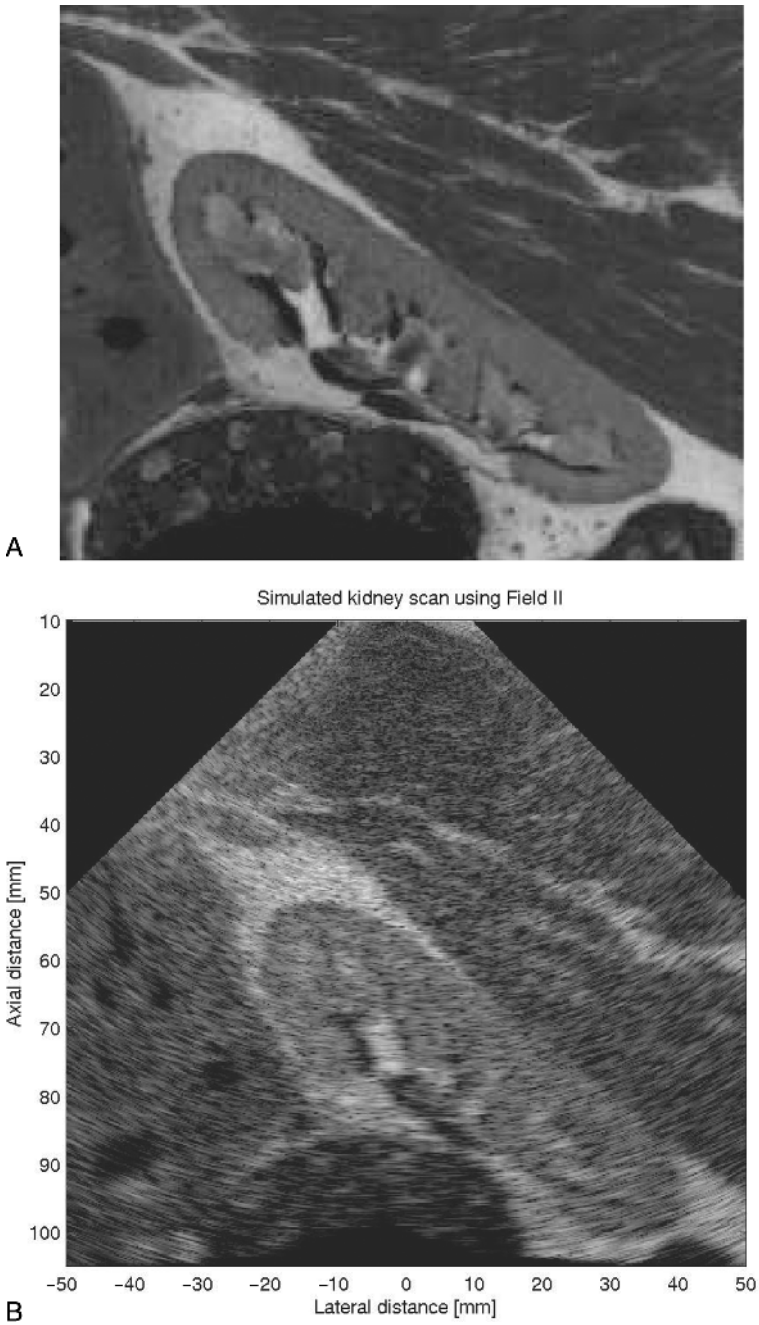

Figure 8.9 (A) Synthetic phantom scatter map of weighted point scatterers based on optical image of right kidney and liver, based on data from the Visible Human Project. (B) Gray-scale simulated B-mode image of the right kidney and liver created by Field II program (courtesy of J. A. Jensen, Technical University of Denmark).

5. (e) The integration of Step 4 has reduced the 3D scattered signals to a one-dimensional (1D) time record of length $2z_{max}/c$, where z_{max} corresponds to the maximum scan depth selected for the image.
6. (f) The time record is envelope detected.
7. (g) The amplitude of this envelope-detected time record is logarithmically compressed and processed nonlinearly so that a larger dynamic range of weak to strong echoes can be presented in the same image.
8. (h),(i) The next vector in a prescribed sequence of vector directions and spatial increments or directions repeats Steps 1–6.
9. (j) Once the line sequence is completed, all the lines are interpolated or "scan-converted" to form a filled-in pulse-echo image from a number of image lines arranged in their correct geometrical attitude.
10. (k) The image is converted to gray-scale mapping for final presentation.

8.4.2 A Different Attitude

As described in Chapter 1, early ultrasound images were formed by either mechanical translation or freehand with a mechanically sensed movement of a transducer. The vector direction coresponding to each transducer position was controlled or sensed and then displayed in its correct attitude (direction) on a cathode-ray tube (CRT) (see Figure 1.10). When the sequence of lines was completed, the image was created either from a long-term persistence of the phosphor on the CRT or through a long-term photographic exposure. As explained in Chapter 1, the two main movements were translational and rotational. The former is now associated with the rectangular format of linear arrays, and the latter is associated with the sector scans of phased arrays. Early on, workers found that the best images were those that combined a rotational (rocking) motion with translation, and this combination became known as compound imaging. Another combination in which rotational movements are added to the ends of translation movements is called contiguous imaging (see Figure 1.3).

As we have seen, in general, scattering from an object occurs over a wide angular extent, but only a portion may be intercepted by a receiving transducer. Furthermore, the direction of insonification is extremely important for determining in which direction sound will be scattered. For example, when sound is nearly parallel (large oblique angle) to the left ventricle wall, very little is reflected back toward the transducer. Figure 8.11 shows another example, in which a cylinder with a radius of curvature is large relative to a wavelength. The images strongly depend on its curvature and the angle of insonification, so that only the parts of the surface nearly perpendicular to the beam are effective at specularly backscattering sound to the transducer. Each image is a partial view that does not portray the cylinder as a complete circular object.

Perceived resolution in an image is dependent not only on the extent of the spatial impulse response for a specific beam, but also on the spacing and orientation of the vector lines themselves. To determine adequate sampling, consider a simple sector scan example. For an unapodized round-trip beam in the azimuth plane at the focal length, the beam-shape is approximately a $sinc^2$ function from Section 7.3. The first

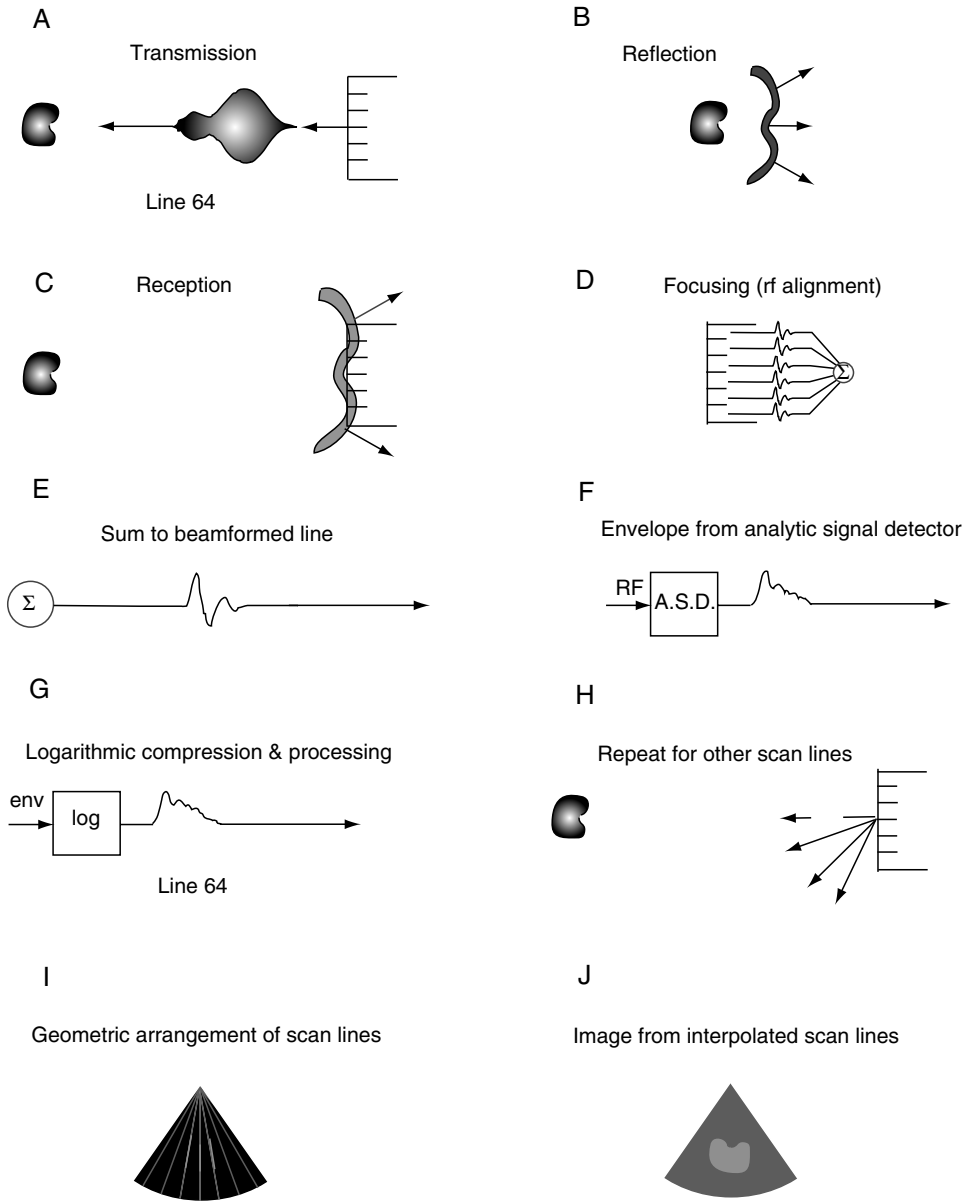

Figure 8.10 (A) Pulse packet (Step 1). (B) Pulse scattered by objects (Step 2). (C) Scattered wave fronts intercepted by receiving transducers (Step 3). (D) Receiving transducers integrate and focus signals (Step 4). (E) One-dimensional time record created (Step 5). (F) Envelope detection (Step 6). (G) Nonlinear processing of amplitude (Step 7). (H) Next line repeats previous steps until frame is complete (Step 8). (I) Scan lines arranged geometrically. (J) Interpolation and gray-scale mapping completes image (Step 9).

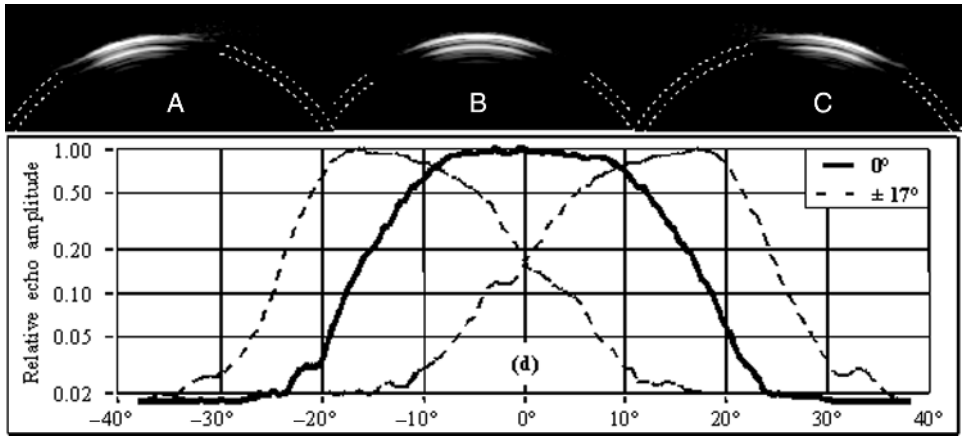

Figure 8.11 (Top) Three images of a cylindrical reflector insonified at steering angles of (A) 17°, (B) 0°, and (C) −17° by a 5–12 MHz linear array. (Bottom) Plots of the corresponding pulse-echo amplitudes for each angle (from Entrekin *et al.*, 2000, with permission of Kluwer Academic/Plenum Publishers).

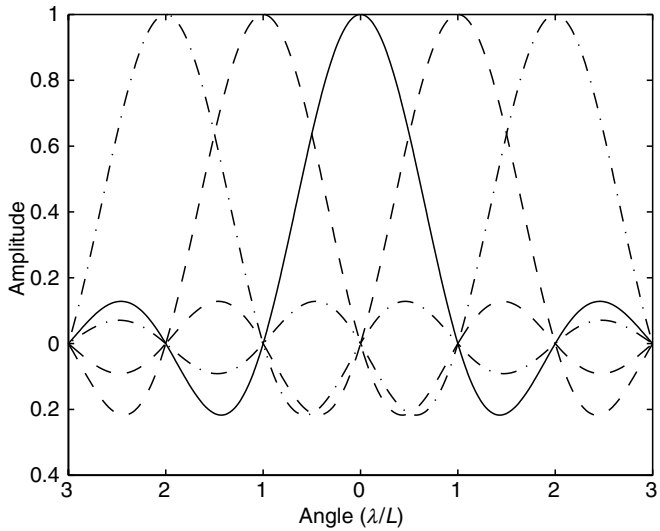

Figure 8.12 Adjacent point spread functions for a focal plane, centered at different angles, indicate that angular separation is achieved for $\Delta\theta \approx \lambda/L$.

nulls of this function occur when the argument is equal to π, or $\theta = arcsin\lambda/L \approx \lambda/L$, as illustrated in Figure 8.12. To achieve full system resolution, Nyquist sampling at $\theta/2$ should be applied (Steinberg, 1976; von Ramm and Smith, 1983). For example, for a 2.5-MHz transducer with $L = 30$ mm, $\theta = 0.02$ radian or 1.15°, for a scan angular sampling increment of 0.57° or about 157 lines in a 90° sector.

This approach is an oversimplification because it is based on targets that also have an angular variation; however, targets are better described in linear or rectangular coordinates. For example, an arc length s depends on depth r according to $s = r\Delta\theta$. Because resolution is spatially varying with depth, a linear target can be severely oversampled close to the transducer where many sector lines traverse it. At distances past the focal region, the target may not be resolved, not because of an adequate sampling rate but because the beamwidth may be too wide. This sampling criterion presented earlier is conservative and provides a reasonable estimate. Apodization produces broader beams that would result in a wider sampling rate requirement. For linear scanning, the same method can be applied with the argument in terms of x and z so that the lateral sampling increment becomes related to the F number (Section 7.4.3), $\Delta x = \lambda F\#/2$.

Unlike the optical cases, acoustic waves have a measurable phase. Sampling approaches based on both magnitude and phase can lead to an improvement in resolution. These methods preserve phase and include it in a different interpolation scheme than the one outlined previously. Phase itself can provide an alternative picture of backscattered signals. Also, phase can provide complimentary information about backscattering. Phase images for medical ultrasound have been proposed and implemented commercially (Ferrari *et al*., 1982).

Besides resolution, image contrast is important; it is the ability to identify objects against a background. This thought leads us to the concept of signal-to-noise in an image. The scan depth beyond which the image is lost to electronic noise is called the "penetration distance," as discussed in Chapter 4. This effect is mainly due to tissue absorption and the imaging system (front-end design), and it is somewhat dependent on the efficiency and size (focal gain) of the array. A different type of imaging noise occurs in an image even when there is enough signal; this interfering textural pattern leads us to the curious ultrasound imaging artifact of speckle.

8.4.3 Speckle

Apart from the larger tissue structures in an ultrasound image, there is a textural overlay on different types of tissue, as mentioned in connection with Figure 8.1. This granular texture is called "speckle" after a similar effect in laser optics, even though the physical mechanisms are somewhat different (Abbott and Thurstone, 1979). In optics, intensity plays a dominant role. In ultrasound, however, the phase and amplitude effects are important, as well as the way pulse envelope data are displayed on a gray scale (no amplitude is assigned to black and maximum amplitude is assigned to white). For many years, users of ultrasound systems assigned a diagnostic value to the appearance of speckle, and they assumed it was tissue microstructure. This discussion will examine the causes of speckle and show that speckle is an illusion more dependent on the measuring system than on the tissue itself (Wells and Halliwell, 1981; Thijssen and Oosterveld, 1986). Also, speckle is detrimental because it reduces both image contrast (the ability to see desired structure against a background) and the distinction of subtle gradations and boundaries in tissue structure. At the end of this section, methods to reduce speckle will be reviewed.

Even though a clinical image contains much more than speckle, in order to understand the effects of speckle in isolation, it is helpful to start with a medium filled with small weak scatterers and no other larger structures. In reality, tissue is filled with small inhomogeneities. Bamber and Dickinson (1980) created a scattering model in which tissue compressibility varied about a mean value. They found that the speckle was determined by the spatial impulse response and not the fluctuations.

A more common alternative is to view the scattering medium as homogeneous but filled with tiny rigid point scatterers that can be assigned some scattering strength value, as in Eq. (8.11b). The size of each of these ideal scatterers is beyond the resolution capability of the imaging system; nonetheless, these small scatterers can have a profound effect on the image. In a typical pulse-echo situation, a bundle of energy formed by the point-spread function is sent into tissue and is partially scattered along its path. At any instant of time, this energy bundle has a finite extent and weights the scatterers according to the spatial impulse response at that location (as discussed in Section 8.3.1). The extent of the influence of this 3D pulse is called the isochronous volume, which is depicted in two dimensions (2D) in Figure 8.13 (Foster *et al.*, 1983). Note that scatterers in the same isochronous volume produce a backscatter that corresponds to a specific time delay region over a wide angular range. Because

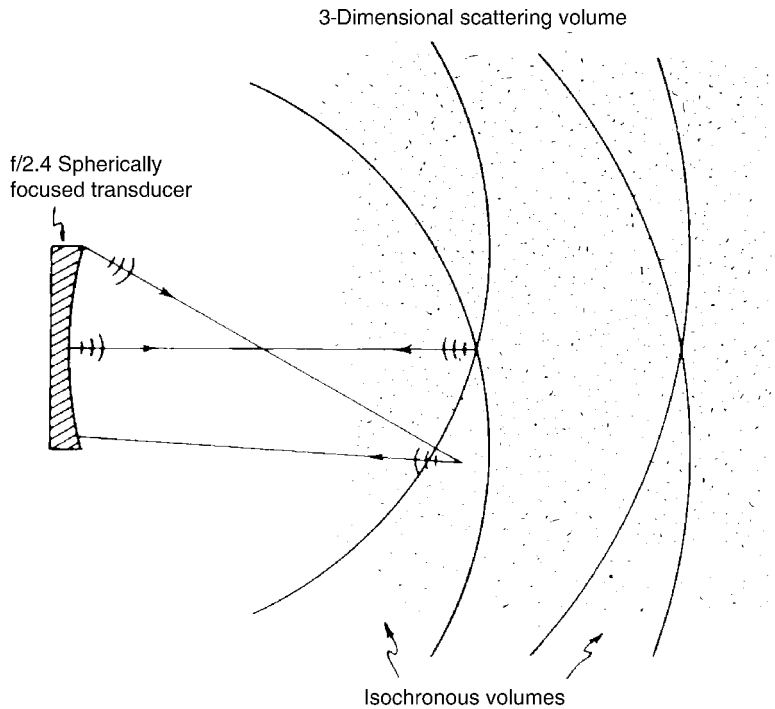

Figure 8.13 Transducers illuminating point scatterers in different 3D isochronous volumes (from Foster *et al.*, 1983, with permission of Dynamedia, Inc.).

individual scatterers in the same volume at different angles have the same time delay, there is an ambiguity in backscattering with angle.

For the simulation of speckle in the second or point scatterers model, the contributions of the spatial impulse responses at each scatterer are summed and added. The spacing between vector or image lines also plays a role. An arrangement of scatterers, along with related images, is illustrated by Figure 8.14. While an exact reproduction of speckle pattern is impossible without a knowledge of the actual positions of the

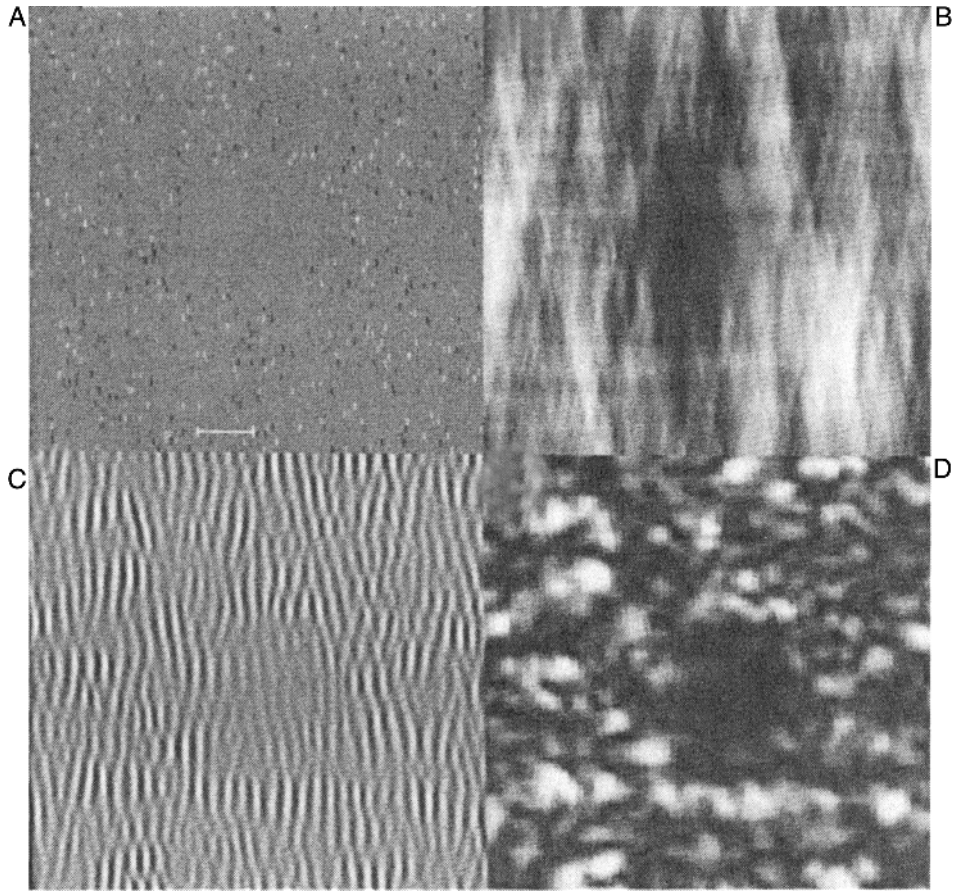

Figure 8.14 Stimulated images for random scatterers in a volume, including a simulated spherical 2.6-mm diameter void. (A) Randomly distributed point scatterers represented with amplitude weights shown as dark and light points against a homogeneous gray background 8 mm × 8 mm (line shown for scale = 1 mm). (B) Gray-scale representation of all the summed and weighted pulse-echo impulse response functions for all points lying in the 3D volume. (C) Simulated *rf* image of the random scattering medium. (D) Simulated B-scan image after envelope detection showing the formation of speckle and the presence of a cyst (from Foster *et al.*, 1983, with permission of Dynamedia, Inc.).

scatterers, simulations are remarkably effective in recreating the look of speckle (as seen in Figure 8.15). Here, Foster *et al.* (1983) compared simulated images of exactly the same arrangement of point scatterers with the corresponding images for three different transducer combinations at the University of Toronto. Speckle is an illusion despite its deceiving appearance as a tissue texture.

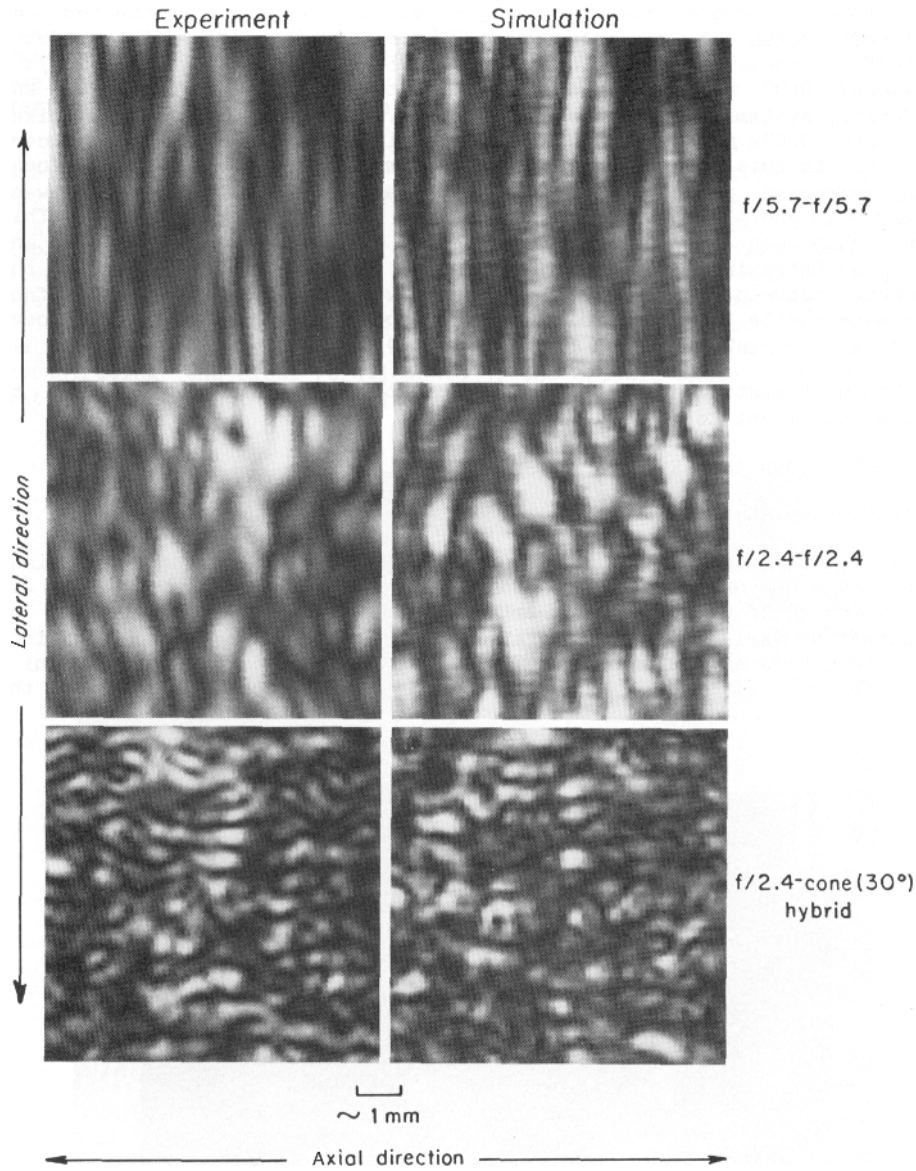

Figure 8.15 Comparison of simulated speckle and data for three different transducer combinations (from Foster *et al.*, 1983, with permission of Dynamedia, Inc.).

Speckle in simulation is the constructive and destructive interference of point-spread functions scattered at apparently random specific physical locations. Speckle in a clinical image is generated mainly by constructive and destructive interference of subresolution tissue scatterers at fixed spatial locations. The resulting images of these subresolution scatterers are not random but deterministic, and they can be reproduced exactly if the transducer is returned to the same position, as can be easily demonstrated with a tissue-mimicking phantom. This feature of speckle is used to track tissue movement and displacement, as well to correct for aberration (to be discussed in Chapter 9).

8.4.4 Contrast

The effect of speckle can be quantified by a "contrast ratio" (CR) and a signal-to-noise ratio (SNR). A classic imaging problem is quantifying the ability to define a cyst object against a speckle background. This contrast ratio is simply the average gray-scale brightness level in the cyst compared to its surround,

$$CR = \frac{\hat{A}_{out} - \hat{A}_{in}}{\hat{A}_{out} + \hat{A}_{in}} \tag{8.16}$$

where $\hat{A}_{in}$ is the average signal level in the cyst, and $\hat{A}_{out}$ is that in the surrounding material. Note that a value of ± 1 is for good contrast; values close to zero indicate poor contrast. For example, the contrast ratios for a 2.6-mm diameter cyst, of Figure 8.14), is 0.37 ± 0.04. For comparison, contrast ratios for a cyst for the transducer combinations, depicted (without a cyst) in the top, middle, and bottom of Figure 8.15 are 0.30 ± 0.04, and 0.37 ± 0.04, respectively. These ratios are governed by the first-order statistics of the speckle (Flax *et al*., 1981).

The probability density function (p.d.f.) for fully developed speckle can be approximated by a Rayleigh distribution based on a random walk assumption that the phase is randomly distributed between 0 and 2π. The Rayleigh probability density distribution, plotted in Figure 8.16, is given by

$$p(A) = \left(2A/\bar{A}^2\right) \exp\left(-A/\bar{A}^2\right) \tag{8.16}$$

in which A is brightness or amplitude and $\bar{A}^2$ is the mean of the squared amplitudes.

In general, the probability density function for the envelope amplitude in an image is governed by a K-distribution (Jakeman and Tough, 1987; Weng and Reid, 1991; Chen *et al*., 1994; Dutt and Greenleaf; 1995; Thijssen, 2000) that leads to a signal-to-noise ratio,

$$SNR = \frac{\sqrt{\pi}\Gamma(\eta + 1/2)}{\sqrt{4\Gamma(\eta + 1) - \pi\Gamma^2(\eta + 1/2)}} \tag{8.17}$$

where η is the effective number of scatterers within a resolution cell defined by the full width half maximum (FWHM) in axial and lateral dimensions of the point-spread function. This ratio approaches that of a Rayleigh p.d.f. when η is large ($\eta \geq 10$). For this case, the $SNR = 1.91$, as confirmed by many independent measurements. For

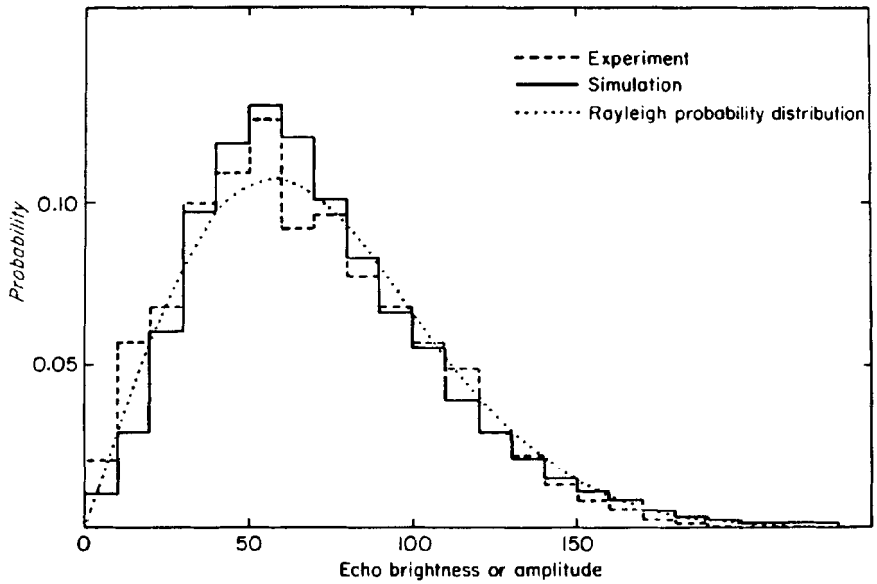

Figure 8.16 Rayleigh distribution compared to histograms of echo brightness or amplitude for an experimental image and a simulated one (from Foster *et al.*, 1983, with permission of Dynamedia, Inc.).

tissue with structure, a Rician is more appropriate (Insana *et al.*, 1986; Thijssen, 1992). It is important to realize that these statistics apply only to video data that have not undergone nonlinear processing. The use of the *SNR* belongs to first-order analysis of images.

Line-to-line aspects of images have been analyzed by second-order statistics. Wagner *et al.* (1983) and Smith *et al.* (1987) showed that the average size of speckle is related to an autocovariance function. Their conclusion can be summarized by the following steps. The relation between pressure at two different positions, X_1 and X_2, is conventionally described by an autocorrelation function defined for an incoherent source as (Wagner *et al.*, 1983; Mallart and Fink, 1991)

$$R_p(\mathbf{X}_1, \mathbf{X}_2, f) = \langle P(\mathbf{X}_1, f), P^*(\mathbf{X}_2, f)\rangle \tag{8.18}$$

in which P is pressure at positions X_1 and X_2, f is frequency, the brackets indicate an average over an ensemble of the scattering media, and * denotes complex conjugate. Another useful function is the covariance,

$$C_P(X_1, X_2) = R_P(X_1, X_2) - \langle P(X_1)\rangle\langle P^*(X_2)\rangle \tag{8.19a}$$

The second term is zero, so that the spatial autocovariance function is

$$C_P(\Delta X) = R_P(\Delta X) \tag{8.19b}$$

where $\Delta X = X_2 - X_1$ and the value used is often normalized to $C_P(0)$. Pressure must be related to the point-spread function, which for the simplest case, a square piston

source is proportional to a *sinc* function. In the focal plane of this transducer, $z = F$, if absorption is neglected. Then for the lateral direction,

$$C_{Px}(\Delta X) = B_x\, sinc^2(\tilde{f}_{0x}\Delta X)^*\, sinc^2(\tilde{f}_{0x}\Delta X) \tag{8.20}$$

in which the spatial frequency along the lateral x direction is $\tilde{f}_{0x} = L/(\lambda F)$, and B_x is a constant. Similarly, for a Gaussian spectrum varying as $\exp(-z^2/2\sigma_z^2)$ axial autocovariance is

$$C_{Pz}(\Delta X) = B_z \exp\left[-(\Delta z)^2/4\sigma_z^2\right] \tag{8.21}$$

These results can provide the average speckle size found from the correlation cell size,

$$S_c = \int_{-\infty}^{\infty} \frac{C_p(\Delta X)}{C_p(0)} d\Delta X \tag{8.22}$$

For the example of the rectangular transducer, the correlation lateral and axial cell sizes become

$$S_{cx} = 0.87\lambda F/L = 0.87/\tilde{f}_{0x} \tag{8.23a}$$

$$S_{cz} = 0.91c_0/\Delta f = 1.37/\Delta f \tag{8.23b}$$

where the last equation is in millimeters (mm) when the −6-dB bandwidth is in megahertz (MHz) and C_0 in ($mm/\mu s$).

For example, for a 2.5-MHz array that is 25 mm long and focused at 50 mm, the resolution from Chapter 6 is 0.46 mm, and the correlation cell size in the focal plane is 1.04 mm, from Eq. (8.23a). For a 60%, −6-dB fractional bandwidth, the axial correlation cell size is 0.91 mm. Other examples of autocovariance functions for lateral and axial ranges of the transducer combinations from Foster *et al*. (1983) (discussed in Section 8.4.3), are plotted in Figure 8.17.

Note that the results so far are for focal planes. Speckle size close to the transducer, for example, is much finer than that in the focal plane, yet the resolution is much poorer; this is an interesting counterintuitive result for those who associate speckle size with resolution or tissue microstructure. Later workers (Oosterveld *et al*., 1985; Huisman and Thijssen, 1998) found that lateral speckle size is strongly dependent on depth even after correction for diffraction and absorption effects.

8.4.5 van Cittert–Zernike Theorem

To complete the description of scattering objects, it is necessary to include the properties of random scattering media illuminated by the field of a focusing transducer. Somewhat surprisingly, the backscattered field from a random arrangement of small particles can be correlated. This interesting property can be formalized by the van Cittert–Zernike theorem. From Eq. (8.18), Mallart and Fink (1991) make a number of simplifications that include the Fresnel approximation and

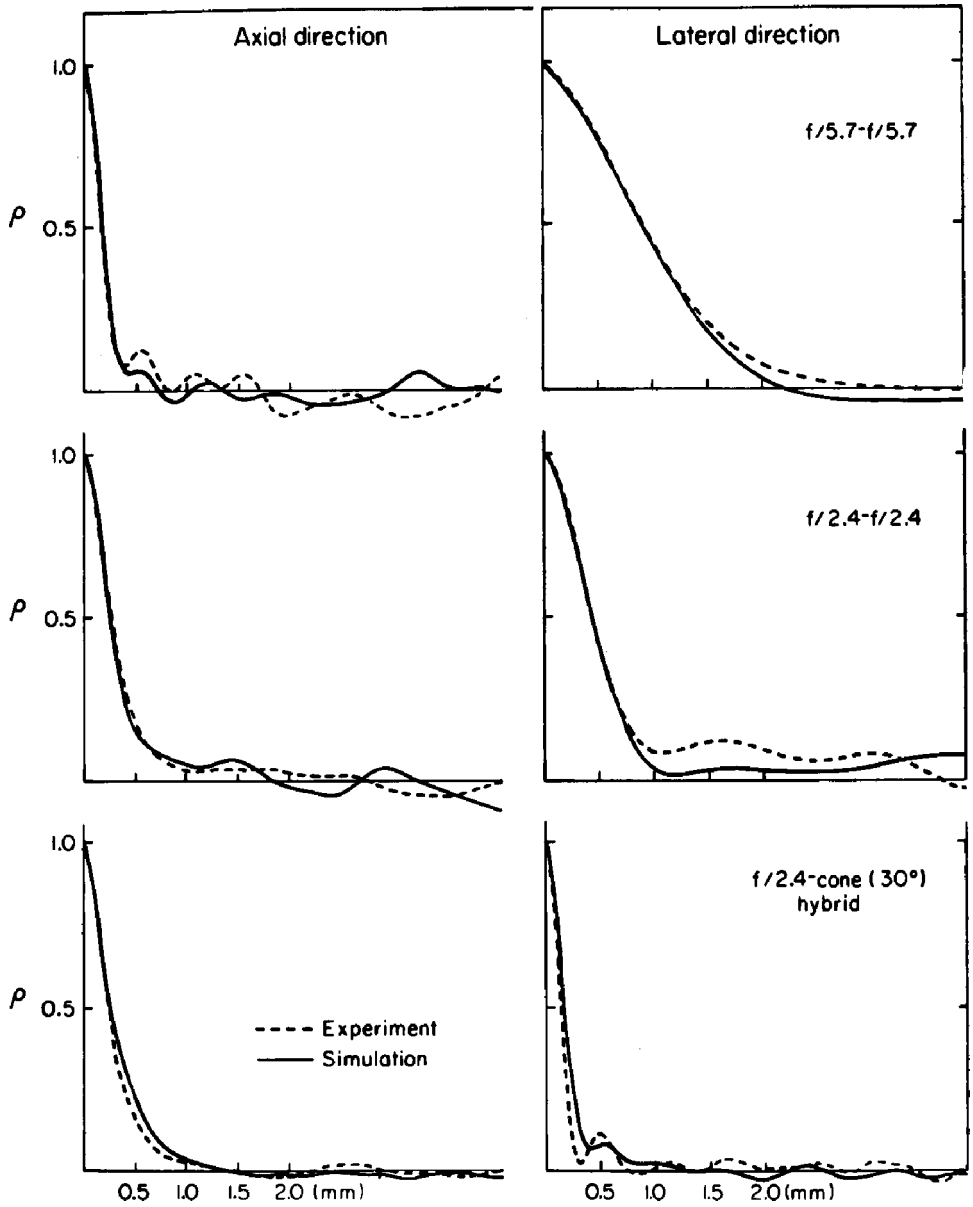

Figure 8.17 Plots of simulated and averaged-experimental lateral and axial covariance coefficients for the three transducer combinations used for Figure 8.15 (from Foster *et al.*, 1983, with permission of Dynamedia, Inc.).

$X_1 = (x_1, z)$, $X_2 = (x_2, z)$; the use of a narrow time window (short pulse); and a diffuse random scattering medium that is a separable function of frequency and space,

$$\langle \chi(X_1, f)\chi(X_2, f)\rangle = \chi_0(f)\delta(X_1 - X_2) \tag{8.24}$$

They show that

$$R_p(x_1, x_2, z, f) = \frac{\chi_0(f)}{z^4}\int\int \tilde{A}(x_1')\tilde{A}^*[x_1 - (x_1' - x_2')]d^2x_1' \tag{8.25a}$$

in which $\tilde{A}(x) = A(x)\exp\{[i2\pi/(z\lambda)]x \cdot x\}$ and A is the aperture weighting function, so

$$R_p(x_1, x_2, z, f) = \frac{\chi_0(f)}{z^4}R_{\tilde{A}}(x_1 - x_2) \tag{8.25b}$$

The van Cittert–Zernike theorem can be stated as follows for the ultrasound case (Mallart and Fink, 1991): "The spatial covariance of the field at points X_1 and X_2 of an observation plane is equal to the Fourier transform of the source aperture function $A(X)$ taken at spatial frequency $\tilde{f} = \Delta X/(\lambda z)$ where z is the distance between the source and the observation plane." Recall that the inverse Fourier transform of a power spectrum is the autocorrelation function,

$$\Im_{-i}[|G(f)|^2] = \int_{-\infty}^{\infty} G(f)G^*(f)e^{i2\pi ft}df = g(t) * g^*(-t) = g \otimes g^* \tag{8.26}$$

In practical terms, this theorem means that the spatial covariance function in the focal plane is proportional to the autocorrelation of the two-dimensional (2D) aperture function. As shown in Figure 8.18 for a 1D aperture with a weighting function $A(x, 0, 0)$, the field is backscattered by random tiny scatterers over a narrow time window as an energy pattern proportional to the autocorrelation of the aperture weighting, $A \otimes A^*$. For a uniformly weighted aperture, $A(x, 0, 0) = \prod(x/L)$, so R_p is proportional to the triangle function, $\Lambda(x/L)$. Here the physical explanation is as follows: The aperture radiates an energy pattern at its focal plane that is proportional to a *sinc* function squared. This energy pattern is reflected by random scatterers back to the transducer, where the spatial covariance at the aperture is the Fourier transform of this energy diagram. Because of the way Eq. (8.25b) was derived, wave fronts need to be brought into phase (time-aligned) before applying the theorem. Some of the surprising results of this theorem are that the spatial covariance pattern in a focal plane is independent of focal length, F number, and frequency and depends only on the autocorrelation function of the aperture (Trahey *et al.*, 1986b; Mallart and Fink, 1991). Thus, the longer the aperture, the wider the spatial covariance and the greater the region of spatial coherence of speckle. The signal-to-noise ratio (SNR) at a receiver varies inversely with spatial covariance, so to increase SNR, a wider receiver is needed. Away from the focal zone, decorrelation is more rapid (Trahey *et al.*, 1986b).This theorem is useful for locating regions where the speckle is well-correlated for speckle tracking applications (Bamber, 1993). In general, the applications of the van Cittert–Zernike theorem to real tissue needs further work because in tissue characterization, the exceptional deviation from normal tissue structure is of interest (Liu and Waag, 1995).

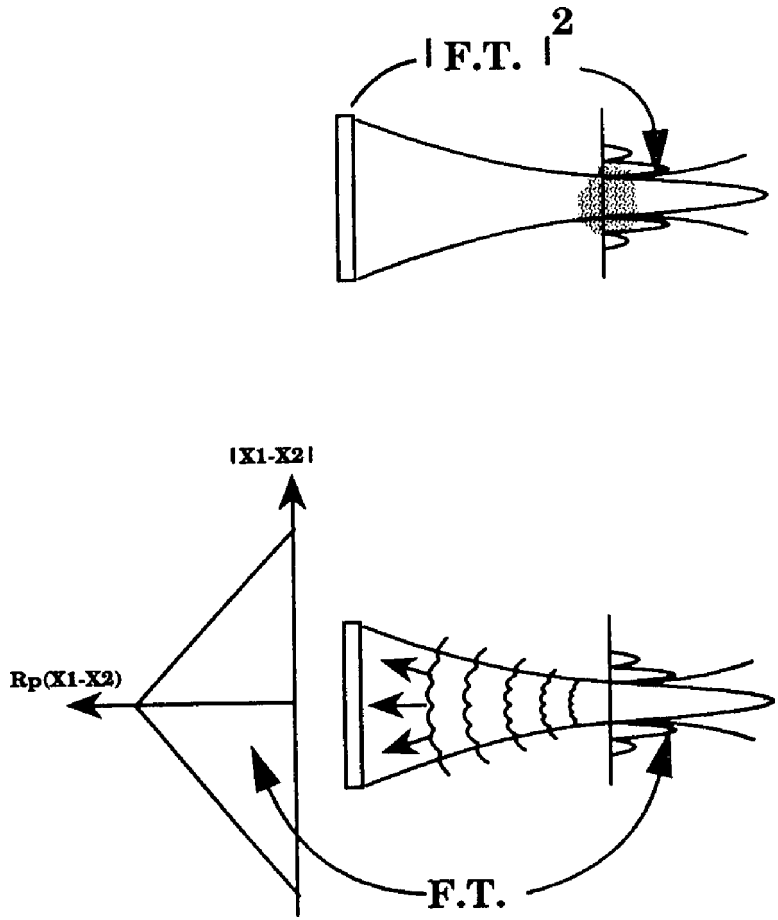

Figure 8.18 (Top) Energy pattern in focal plane is proportional to magnitude of Fourier transform (of aperture) squared. (Bottom) Energy pattern reflected by random scatterers back to the aperture, where the spatial covariance is the Fourier transform of this energy pattern, according to the van Cittert–Zernike theorem (from Mallart and Fink, 1991, Acoustical Society of America.)

Two transmit–receive systems can be compared by the correlation between received signals. Walker and Trahey (1995) have shown that correlation $\rho(f)$, as a function of frequency between a system denoted by subscript "0" and another called "1," is

$$\rho(f) = \frac{\int_{-\infty}^{\infty} [A_{T0}(X, f) * A_{R0}(X, f)][A_{T1}(X, f) * A_{R1}(X, f)]^* dX}{\sqrt{\int_{-\infty}^{\infty} |[A_{T0}(X, f) * A_{R0}(X, f)]|^2 dX \int_{-\infty}^{\infty} |[A_{T1}(X, f) * A_{R1}(X, f))]|^2 dX}} \tag{8.27}$$

where the convolution is in the direction $X = [x\ y]$ in the aperture planes, and "T" and "R" denote the transmitter and receiver in the focal plane, respectively.

8.4.6 Speckle Reduction

Many ways to reduce speckle have been proposed. Some of these have been reviewed by Bamber (1993). Most of these approaches involve a kind of diversity so that speckle effects can be averaged, minimized, or broken up. Several methods of compounding can be explored through Eq. (8.27). Trahey *et al*. (1986b) show that to reduce speckle effectively, N-independent speckle images are needed to reduce speckle by a factor $\sqrt{N}$. Breaking the overall aperture up into subapertures is a kind of spatial compounding that involves a trade-off between speckle reduction and resolution. For example, dividing the aperture in half and averaging images reduces speckle by $\sqrt{2}$ (Trahey *et al*., 1986b), but this arrangement also degrades resolution at the focus by a factor of two. Frequency compounding (Melton and Magnin, 1984; Trahey *et al*.,1986a) involves summing multiple images created from signals filtered at different center frequencies and bandwidths; this approach has enjoyed recent commercial success because of the availability of broad bandwidth transducers. Spatial compound imaging, which creates images from several angular views, was discussed in Chapter 1 and by Trahey *et al*., 1986b; and Entrekin *et al*., 2000. Examples of the implementation of real-time speckle reduction methods can be found in Chapter 10.

BIBLIOGRAPHY

Angelsen, B. A. J. (2000). *Ultrasound Imaging: Waves, Signals, and Signal Processing*. Emantec, Norway. An excellent and detailed mathematical explanation of scattering and many aspects of ultrasound imaging.

Bamber, J. C. and Dickinson, R. J. (1980). Ultrasonic B-scanning: A computer simulation. *Phys. Med. Biol*. **25**, 463. A review of speckle and speckle reduction methods.

Faran Jr., J. J. (1951). Sound scattering by solid cylinders and spheres. *J. Acoust. Soc. Am*. **23**, 405–418. Provides more information on scattering.

Kino, G. S. (1987). *Acoustic Waves: Devices, Imaging, and Signal Processing*. Prentice-Hall, Englewood Cliffs, NJ, pp. 300–357. A resource for more information on scattering transducers and imaging.

Morse, P. M. and Ingard, K. U. (1968). *Theoretical Acoustics*. Princeton University Press, Princeton, NJ, pp. 400–411. Provides more rigorous derivations for acoustic and elastic scattering.

Thijssen, J. M. (2000). Ultrasonic tissue characterization. *Acoustical Imaging*, Vol. **25**. Plenum Press, New York, pp. 9–25. A comprehensive review of speckle and texture analysis.

von Ramm, O. and Smith, S. W. (1983). Beam steering with linear arrays. *IEEE Trans. Biomed. Engr.* **BME-30**, 438–452. A useful resource for arrays related to imaging.

References

Abbot, J. G. and Thurstone, F. L. (1979). Acoustic speckle: Theory and experimental analysis. *Ultrason. Imag.* **1**, 303–324.

Bamber, J. C. (1993). Speckle reduction. *Advances on Ultrasound Techniques and Instrumentation*. P. N. T. Wells (ed.). Churchill Livingstone, New York, pp. 55–67.

Bamber, J. C., and Dickinson, R. J. (1980). Ultrasonic B-scanning: A computer simulation. *Phys. Med. Biol*. **25**, 463.

Carpenter, R. N. and Stepanishen, P. R. (1984). An improvement in the range resolution of ultrasonic pulse echo systems by deconvolution. *J. Acoust. Soc. Am*. **75**, 1084–1091.

Chen, J.-F., Zagzebski, J. A., and Madsen, E. L. (1994). Non-Gaussian versus non-Rayleigh statistical properties of ultrasound echo signals. *IEEE Trans. Ultrason. Ferroelectr. Freq. Control* **41**, 435–440.

Chen, X., Phillips, D., Schwarz, K. Q., Mottley, J. G., and Parker, K. J. (1997). The measurement of backscatter coefficient from a broadband pulse-echo system: A new formulation. *IEEE Trans. Ultrason. Ferroelectr. Freq. Control* **44**, 515–525.

Chen, X. and Schwarz, K. Q. (1994). Acoustic coupling from a focused transducer to a flat plate and back to the transducer. *J. Acoust. Soc. Am*. **95**, 3049–3054.

Coussios, C. C. (2002). The significance of shape and orientation in single-particle weak-scatterer models. *J. Acoust. Soc. Am*. **112**, 906–915.

Dutt, V. and Greenleaf, J. F. (1995). Speckle analysis using signal to noise ratios based on fractional order moments. *Ultrason. Imag*. **17**, 251–268.

Entrekin, R. R., Jago, J. R., and Kofoed, S. C. (2000). Real-time spatial compound imaging: Technical performance in vascular applications. *Acoustical Imaging*, Vol. **25**. Halliwell and Wells (eds.). Kluwer Academic/Plenum Publishers, New York, pp. 331–342.

Ferrari, L., Jones, J. P., Gonzalez, V., and Behrens, M. (1982). Acoustical imaging using the phase of echo waveforms. *Acoustical Imaging*, Vol. **12**. E. A. Ash and C. R. Hill (eds.). Plenum Press, New York, pp. 635–641.

Flax, S. W., Glover, G. H., and Pelc, N. J. (1981). Textural variations in B-mode ultrasonography: A stochastic model. *Ultrason. Imag*. **3**, 235–257.

Foster, D. R., Arditi, M., Foster, F. S., Patterson, M. S., and Hunt, J. W. (1983). Computer simulations of speckle in B-scan images, *Ultrason. Imag*. **5**, 308–330.

Hickling, R. (1962) Analysis of echoes from solid elastic sphere in water, *J. Acoust. Soc. Am*. **34**, 1582–1592.

Huisman, H. J. and Thijssen, J. M. (1998). An in vivo ultrasonic model of liver parenchyma. *IEEE Ultrason. Ferroelectr. Freq. Control* **45**, 739–750.

Insana, M. F., Wagner, R. F., Garra, B. S., Brown, D. G., and Shawker, T. H. (1986). Analysis of ultrasound image texture via generalized Rician statistics. *Opt. Eng*. **25**, 743–748.

Jakeman, E. and Tough, R. J. A. (1987). Generalized k-distribution: A statistical model for weak scattering. *J. Opt. Soc. Am*. **4**, 1764–1772.

Jafari, F., Madsen, E. L., Zagzebski, J. A., and Goodsitt, M. M. (1981). Exact evaluation of an ultrasonic scattering formula for a rigid immovable sphere. *Ultrasound in Med. & Biol*. **7**, 293–296.

Jensen, J. A. (1991). A model for the propagation and scattering of ultrasound in tissue. *J. Acoust. Soc. Am*. **89**, 182–190.

Jensen, J. A. (1996). Field: A program for simulating ultrasound systems. *Med. & Biol. Eng. and Comp*. **34**, Suppl. 1, Part 1, 351–353.

Jensen, J. A. and Munk, P. (1997). Computer phantoms for simulating ultrasound B-mode and CFM images. *Acoust. Imag.*, Vol. **23**, Plenum Press, New York, pp. 485–494.

Jensen, J. A. and Nikolov, S. (2000). Fast simulation of ultrasound images. *IEEE Ultrason. Symp. Proc.*

Kino, G. S. (1987). *Acoustic Waves: Devices, Imaging, and Analog Signal Processing*. Prentice-Hall, Englewood Cliffs, NJ, pp. 300–357.

Liu, D. -L. and Waag, R. C. (1995). About the application of the van Cittert-Zernike theorem in ultrasonic imaging. *IEEE Trans. Ultrason. Ferroelectr. Freq. Control* **42**, 590–601.

Mallart, R. and Fink, M. (1991). The van Cittert-Zernike theorem in pulse echo measurements. *J. Acoust. Soc. Am.* **90**, 2718–2727.

Melton, H. E. and Magnin, P. A. (1984). A-mode speckle reduction with compound frequencies and bandwidths. *Ultrason. Imag.* **6**, 159–173.

Morse, P. M. and Ingard, K. U. (1968). *Theoretical Acoustics*. Princeton University Press, Princeton, NJ, pp. 400–411.

Nassiri, D. K. and Hill, C. R. (1986). The use of angular acoustic scattering measurements to estimate structural parameters of human and animal tissues. *J. Acoust. Soc. Am.* **79**, 2048–2054.

Oostervald, B. J., Thijssen, J. M., and Verhoef, W. A. (1985). Texture in B-mode echograms: 3-D simulations and experiments of the effects of diffraction and scatter density. *Ultrason. Imag.* **7**, 142–160.

Rhyne, T. L. (1977). Radiation coupling of a disk to a plane and back or to a disk to disk: An exact solution. *J. Acoust. Soc. Am.* **61**, 318–324.

Smith, S. W., Sandrik, J. M., Wagner, R. F., and van Ramm, O. T. (1987). Measurements and analysis of speckle in ultrasound B-scans. *Acoust. Imag.* **10**, 195–211.

Steinberg, B. D. (1976). *Principles of Aperture and Array Design*. John Wiley & Sons, New York.

Strutt, J. W. (Lord Rayleigh). (1964 reprint of 1871). On the light from the sky, its polarization and colour. *Scientific Papers Lord Rayleigh*, Vol. 1. Dover Publications, New York.

Szabo, T. L., Karbeyaz, B. U., Miller, E., and Cleveland, R. (2004). Comparison of a flat plate and point targets for broadband determination of the pulse echo electromechanical characteristic of a transducer. *J. Acoust. Soc. Am.* **115**.

Thijssen, J. M. (1992). Echographic image processing. *Advances in Electronics and Electron Physics*, Vol. **84**. P. W. Hawkins (ed.), Academic Press, Boston, pp. 317–349.

Thijssen, J. M. and Oosterveld, B. J. (1986). Speckle and texture in echography: artifact or information? *IEEE Ultrason. Symp. Proc.* 803–809.

Trahey, G. E., Allison, J. W., Smith, S. W., and von Ramm, O. T. (1986a). Speckle pattern changes with varying acoustic frequency: Experimental measurements and implications for frequency compounding. *IEEE Ultrason. Symp. Proc.*, 815–818.

Trahey, G. E., Smith, S. W., and von Ramm, O. T. (1986b). Speckle pattern correlation with lateral aperture translation: Experimental results and implications for spatial compounding. *IEEE Trans. Ultrason. Ferroelectr. Freq. Control*. **32**, 257–264.

Wagner, R. F., Smith, S. W., Sandrik, J. M., and Lopez, H. (1983). Statistics of speckle in ultrasound B-scans. *IEEE Trans. Sonics Ultrason.* **SU-30**, 156–163.

Walker, W. F. and Trahey, G. E. (1995). The application of K-space in medical ultrasound. *IEEE Ultrason. Symp. Proc.*, 1379–1383.

Wells, P. N. T. and Halliwell, M. (1981) Speckle in ultrasonic imaging, Ultrasonics **19**, 225–229.

Weng, L. and Reid, J. M. (1991). Ultrasound speckle analysis based on the K distribution. *J. Acoust. Soc. Am.* **89**, 2992–2995.

9 SCATTERING FROM TISSUE AND TISSUE CHARACTERIZATION

Chapter Contents

9.1 INTRODUCTION

Until now, tissues have been treated as homogeneous elastic media with acoustic characteristics such as impedance, speed of sound, absorption and dispersion, and scattering. Tables of values of tissue characteristics are summarized in Appendix B, and many more can be found in Duck (1990). It is fair to say that at this point in time, there is much more that researchers do not know about the acoustic and elastic properties of tissues. This state of knowledge is in part due to simplified views of tissue as either uniform or random in structure.

Tissue is much more interesting than that! Living tissue is full of structure, movement, and organization on several length scales. It is nonlinear both elastically and dynamically. Tissue is continually adapting and self-regulating, growing and reproducing, becoming diseased, healing and repairing, altering metabolism, and interacting with other organs.

This chapter addresses some of the problems posed by the complexity of tissue. First, it reviews a method for classifying scattering from tissues on several length scales. Second, it presents actual measurements of heterogeneous tissue structure, as well as their impact on scattering. Third, this chapter examines recent developments in tissue characterization (the science of inferring tissue properties from ultrasound measurements), including dynamic as well as static methods. Fourth, it discusses adaptive means of measuring tissue characteristics and compensating for their undesirable effects, such as aberration. Finally, this chapter gives ways of simulating wave propagation in more realistic tissues.

9.2 SCATTERING FROM TISSUES

The similarity of the acoustic properties of tissues is primarily due to their high water content. The main constituents of the body are water (60%), protein (17%), and lipids (15%) (Greenleaf and Sehgal, 1992). In addition to blood, cells are bathed in fluid (interstitial) and have fluid within them (intracellular), as well as minerals and ions. Groups of similar cells (the basic building blocks) are organized into tissues. Different types of tissues are combined to perform specific functions as an organ, such as the heart or liver. Greenleaf and Sehgal (1992) provide more details of how tissues function and maintain homeostatis (equilibrium) in response to changing external factors (injury and disease).

They have also proposed a classification scheme for tissue scattering that is quite useful. In their terminology, Class 0 scattering is associated with molecular solvent effects on a length scale of 10^4 Å (10^{-10} m). This type of scattering is due to

macromolecular effects, which produce absorption and sound speed dispersion (discussed in Chapter 4). Class 1 scattering is caused by the concentrations of living cells being higher than 25 per resolution cell, and it is diffusive according to its length scale, $ka << 1$. Class 2, which is diffractive on a length scale, is scattering from the structure of tissue in concentrations lower than one per resolution cell. While Class 1 scatterers would result in speckle or measurable aggregate (combined) effects, Class 2 scatterers are independent and distinguishable through their unique space- and frequency-dependent characteristics. Class 3 scattering is specular on a length scale, $ka >> 1$, and is associated with organ and vessel boundaries. A fourth category, Class 4, applies to tissue in motion such as blood.

In a typical ultrasound image of the liver, as given by Figure 9.1, are examples of several scattering types. From the need to compensate for absorption, as indicated by the time gain compensation (TGC) profile not shown but disucssed (Section 4.5), we conclude that Class 0 scatterers are present. The speckle indicates Class 1 scatterers ($ka << 1$). Small vessels correspond to a Class 2 scatterer. Finally, the liver boundaries are Class 3 scatterers.

Figure 9.2 introduces frequently used terms for tissue. Tissue regions that can be represented by one value of a parameter at every spatial point are "homogeneous." Global values of parameters are assigned to each region that is homogeneous. Waves

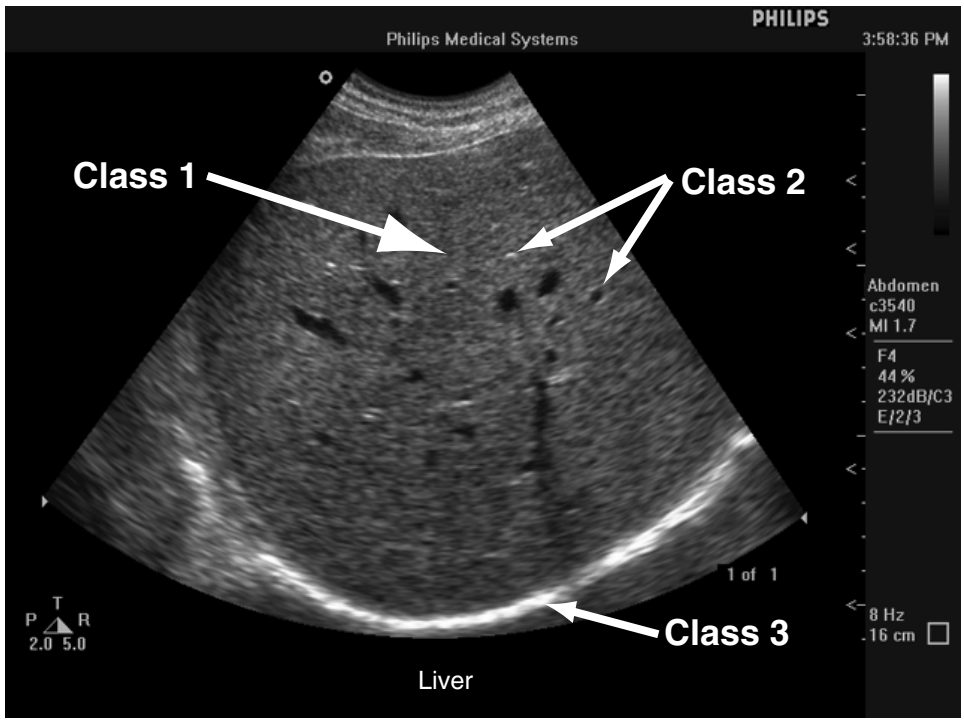

Figure 9.1 Ultrasound image of a liver showing four types of scattering effects (courtesy of Philips Medical Systems).

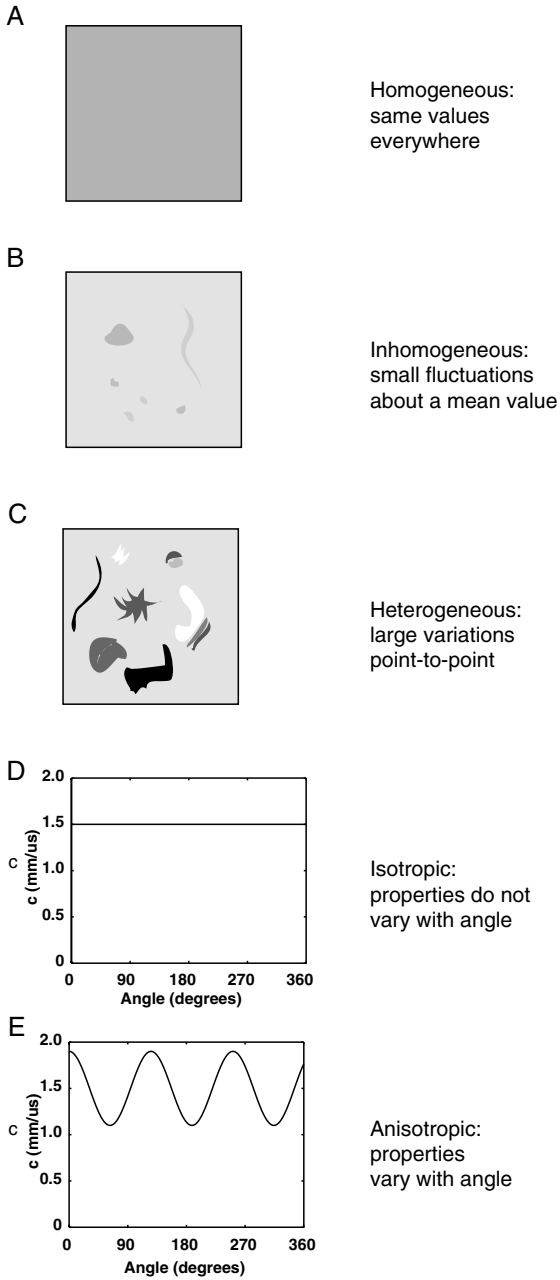

Figure 9.2 General terminology for tissue structures: (A) Homogeneous. (B) Inhomogeneous. (C) Heterogeneous. (D) Isotropic. (E) Anisotropic.

crossing region boundaries may experience reflection and transmission effects, possible mode conversion, refraction, and changes in sound speed and absorption, according to the appropriate length scales. For our purposes, the term "inhomogeneous" is used for tissues that are predominantly the same type with small fluctuations about a mean value (as depicted in Fig. 9.2b). In Figure 9.2c, a region enclosing a group of contiguous regions with different characteristics is called "heterogeneous." In this case, the tissue properties of the enclosed region vary with spatial position either through smaller subregions or, in the limit, from point to point. The term "isotropic" applies to tissue properties that do not vary with angular orientation (as in Figure 9.2d). If the properties do vary with the angle of insonification, then they are "anisotropic" (as in Figure 9.2e). Anisotropy occurs when tissue structure has a preferential structural orientation, such as muscular fibers.

It is helpful to know the general properties of homogeneous tissue first. The more important ones are listed in Table B2 in Appendix B. In this table, both the absorption and backscattering loss (at 180°) components of attenuation are listed. Recall that attenuation has both absorption and scattering components,

$$\alpha_T = \alpha + \alpha_s \tag{9.1}$$

Absorption is considered to be propagating energy that is converted to heat through mechanisms such as viscous and thermal conduction effects (as discussed in Section 4.1.2). These characteristics would fall under the Class 0 scattering and be assigned to homogeneous tissue regions. The scattering loss is caused by the partial interception by the receiving transducer of the angular distribution of backscattered energy. Another way of interpreting this scattering is that it occurs on several length scales simultaneously due to tissue structure. In addition to absorption (Class 0), this type of scattering may include Class 1 or diffusive subwavelength scattering. Typically, scattering loss is less than 20% of the overall attenuation for soft tissue, but there are exceptions (Nassiri and Hill, 1986a).

A way to determine how much energy is scattered away from the receiving transducer is to measure scattering as a function of angle. This approach also can aid in separating the contributions of changes in the density (dipole directivity) from those of the elastic constant (monopole directivity), each of which have a different angular scattering dependence, as was indicated by the Born approximation in Section 8.2.3.1. Nassiri and Hill (1986a, 1986b) have developed inhomogeneous statistical models for tissue based on the Born approximation and have obtained good experimental agreement. In this case, there are many effective scatterers per resolution cell, so that Class 1 scattering, in a statistical way, results in different scattering patterns. In addition, all tissue has loss that increases with frequency; therefore, all tissue includes Class 0 scattering.

Another Class 1 scatterer is blood. Blood cells have been modeled as subwavelength-sized spheres, cylinders, or disks (explained briefly in Section 8.2.2. and treated in more detail in Section 11.3). Flowing blood also falls in the Class 4 category.

An example of a Class 2 scatterer is an isolated microcalcification in the breast. Anderson *et al*. (1998) used a spherical scatterer as a model for this case. Their calculations for elastic and inelastic spheres are shown in Figure 9.3 for an

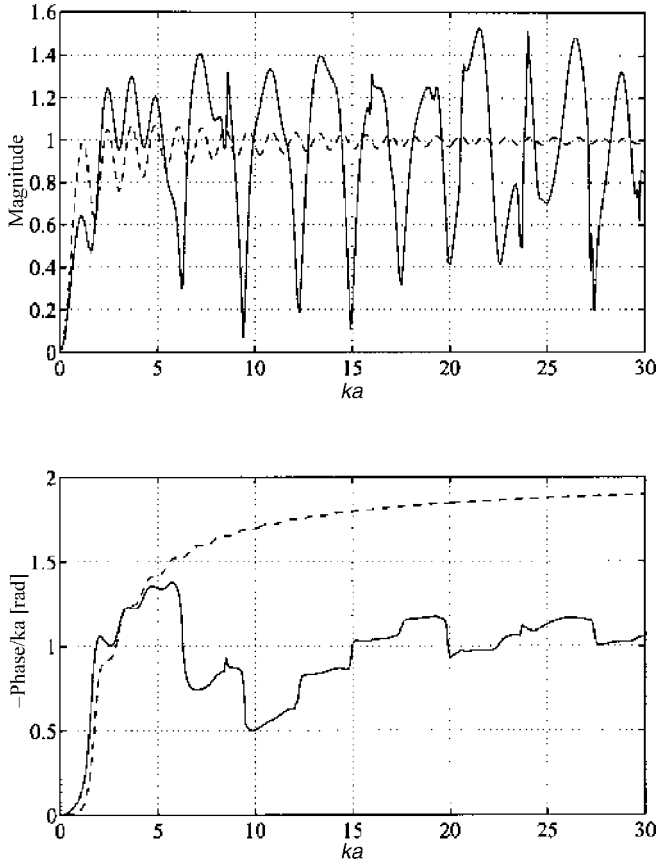

Figure 9.3 (Top) Magnitude of far-field scattering from a hydroxyapatite sphere simulated by a Faran model as an elastic sphere (solid line) and as a rigid sphere (dashed line). (Bottom) Corresponding phases scaled by $-1/ka$ to allow comparison with Hickling's results (from Anderson *et al.*, 1998, *IEEE*).

approximately Gaussian pulse with a 60% fractional bandwidth. By comparing these results with data (Figure 9.4), they concluded that microcalcifications behaved as elastic scatterers. This type of scatterer corresponds to a one-per-resolution cell or a Class 2.

9.3 PROPERTIES OF AND PROPAGATION IN HETEROGENEOUS TISSUE

9.3.1 Properties of Heterogeneous Tissue

Limited information is available on tissue-scattering properties in part because of the difficulty of making the measurements. Part of the problem in measuring tissue properties is the correction for system effects such as transducer spectral

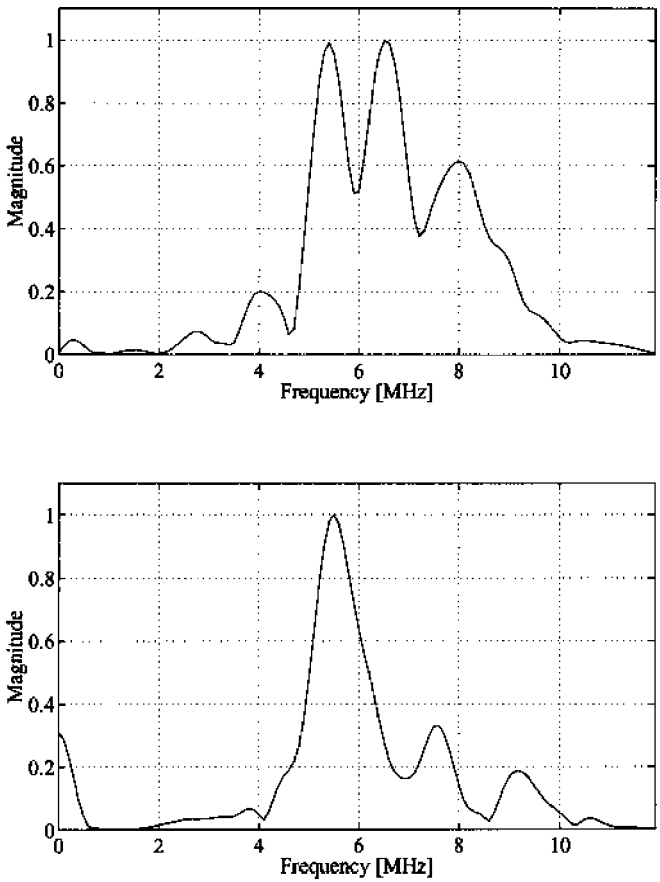

Figure 9.4 The magnitude spectra of radio frequency echoes from suspected *in vivo* microcalcifications in two different subjects. The similarity of the prominent peaks and nulls in the spectra to those of the elastic simulation of Figure 9.3 indicates elastic behavior. Higher absorption in the second case (bottom) reduces amplitudes at higher frequencies (from Anderson *et al.*, 1998, *IEEE*).

characteristics and directivity. In addition, scattering itself, in the frequency range commonly employed for medical imaging, is frequency dependent. The inferring of tissue properties from transducer measurements is an ongoing worldwide effort called "tissue characterization," which is described more fully in Section 9.5.

Before methods of tissue characterization are described, some of the issues and complexities of acoustic propagation in real tissue need to be examined. A number of early studies are summarized by Li (1997) and Bamber (1998). Because most ultrasound imaging is done through abdominal and chest walls, these have been studied extensively at the University of Rochester. Measurement-corrected data of the acoustic properties of abdominal and chest walls provide more direct information about the local spatial fluctuations of tissue properties.

The measurement of wall properties consisted of placing the wall specimen in a sealed chamber that has acoustically transparent windows and is filled with water. This chamber was aligned in a water tank between a diverging transmitter-transducer with a wide directivity and a mechanically scanned linear array acting as a receiver on the upper side of the specimen. For the chest walls (Hinkelman *et al*., 1997), a 96-element linear array designed to have small elements, 0.21 mm x 0.4 mm, was electronically switched, one element at a time, at each of 50 lateral positions to create a matrix of recorded-through transmission pulses equal to $96 \times 50 = 4800$ positions. A reference database was also recorded with no specimen in the tank. The effects of measurement geometry were removed by fitting a surface to the arrival time wave fronts and subtracting the fit from the data. The following features of the data were tabulated: waveform similarity, arrival time and energy level fluctuations, and full width half maximum (FWHM) correlation lengths. An average reference pulse was correlated with each pulse in a set to obtain a measure of waveform similarity, time delay fluctuations, and correlation lengths. Energy waveform values were calculated by integrating the squared amplitudes of the received signals. The resulting chest wall data are shown in Figure 9.5 as pictures of the two-dimensional spatial fluctuations of 16 samples, presented as pairs depicting time delay and energy fluctuations. The top row is a water reference. Note the similarity of features in most pairs.

Measurements for abdominal walls are compared to this data in Figure 9.6. The average root mean square (r.m.s) time delay fluctuations for 16 chest wall samples is 21 ns, as compared with 56 ns for abdominal walls. Just as speckle has been analyzed statistically, radio frequency (RF) data can be interpreted that way also. Correlation lengths, for example, can reveal both local and statistical information about the spacing between scatterers. Recall that in a convolution operation, the integrand consists of one function flipped from right to left and multiplied by another function (Appendix A); but in correlation, there is no flipping involved, so that it is expressed as $r(t) = x(t)^* y(-t)$. FWHM correlation lengths for chest walls and abdominal walls, for example, were 2.5 mm and 5.8 mm. The implications of these localized time domain delay differences are discussed in Section 9.8.

9.3.2 Propagation in Heterogeneous Tissue

The effect of tissue structure on wave propagation was also studied by the University of Rochester group. Hinkelman *et al*. (1996) developed a method for staining a cross section of an abdominal wall to identify tissue types. The stained wall cross sections were digitized and assigned acoustic values appropriate to each tissue type, as depicted by Figure 9.7. Mast *et al*. (1998, 1999) and Hinkelman *et al*. (1998) used these data to model plane wave propagation with a finite-difference time domain program through an abdominal wall, as depicted for sequential times in Figure 9.8.

Multiple scattering, refraction, and aberration are responsible for the complicated exiting wavefront. Smaller scatterers provide a low level of reverberation that trails after the larger, directly transmitted main wavefront; these signals contribute to image clutter. Simulations of focused beams propagating through abdominal walls, based on these data under linear and nonlinear conditions, are examined in Section

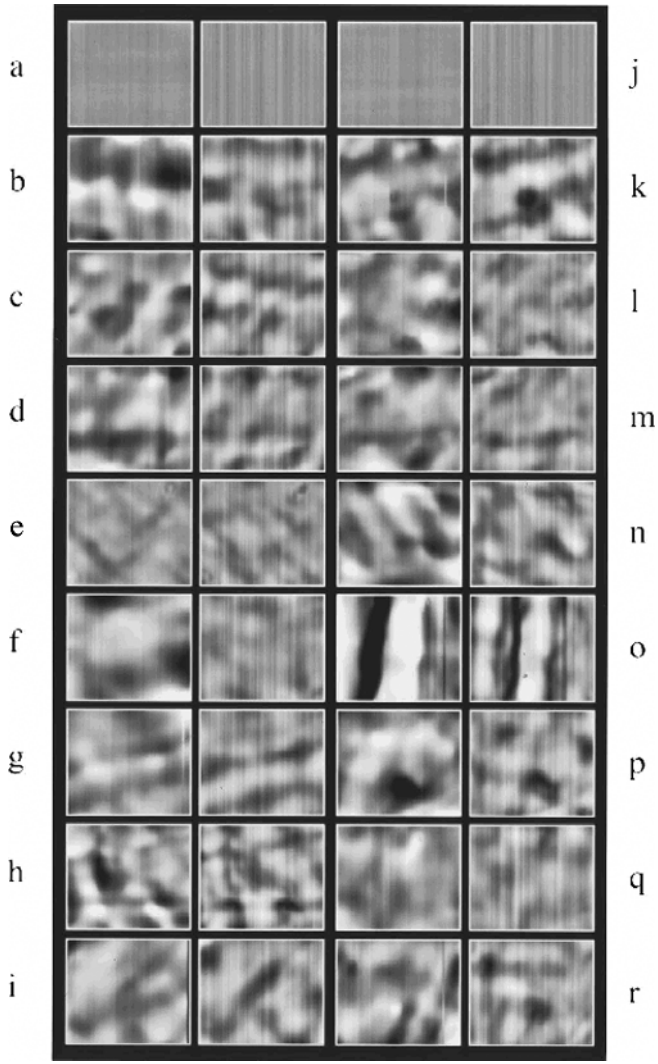

Figure 9.5 Arrival time and energy level fluctuations for two water paths and intercostal spaces of 16 chest wall samples. The first and third columns are arrival time panels; the second and fourth panels depict energy level fluctuations. The top row depicts two water measurements for reference. In the left panel of each pair, arrival time difference is shown on a linear scale with a maximum arrival time fluctuation of 150 ns represented by white and a minimum arrival time fluctuation of 250 ns represented by black. In the right panel of each pair, energy level fluctuations are shown on a logarithmic scale with a maximum positive excursion of 15 dB represented by white and a maximum negative excursion of 25 dB represented by black. In all panels, the horizontal coordinate is the array direction and spans a distance of 14.28 mm in 0.21-mm increments, while the vertical coordinate corresponds to position of the array in elevation and spans a distance of 11.60 mm with points interpolated from measurements at 0.40-mm intervals to produce data at 0.20-mm increments (from Hinkelman *et al.*, 1997, Acoustical Society of America).

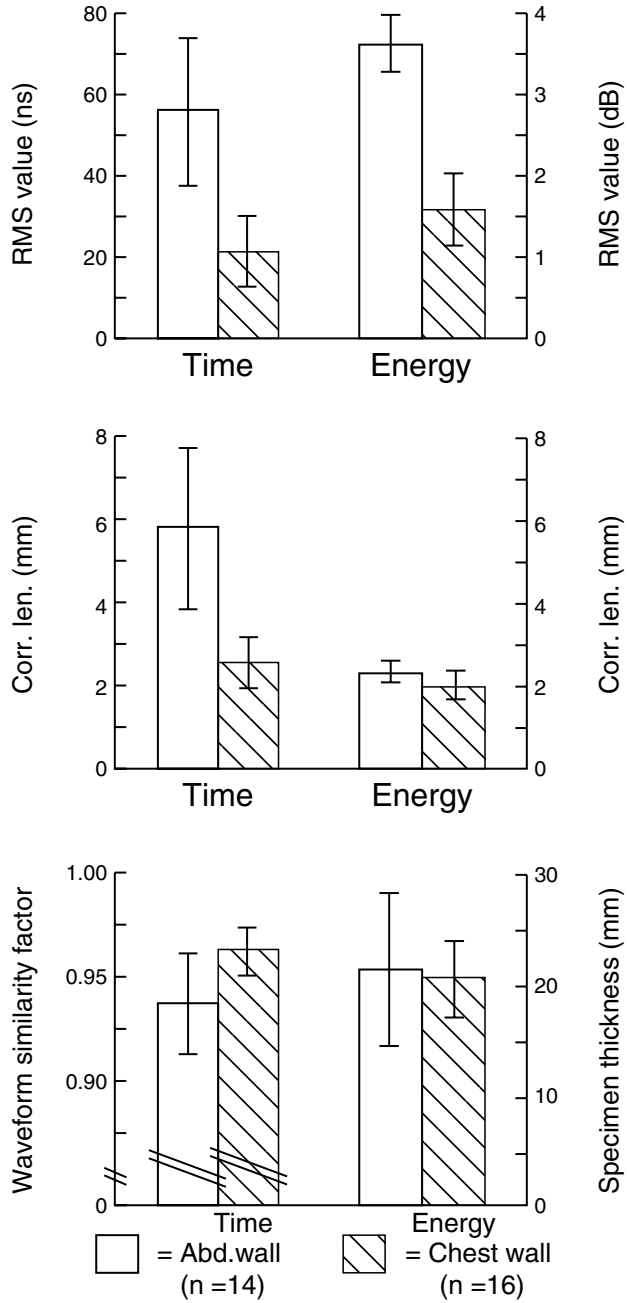

Figure 9.6 Comparison of chest wall and abdominal wall wavefront distortion statistics. In each chart, the average and standard deviation of the measurements within each group are shown. (from Hinkelman *et al.*, 1997, Acoustical Society of America).

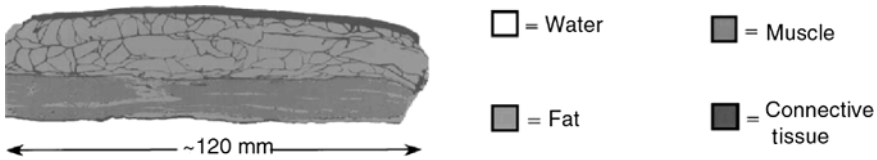

Figure 9.7 Cross-sectional tissue map of an abdominal wall with assigned acoustic properties (from Mast *et al.*, 1997) (see also color insert).

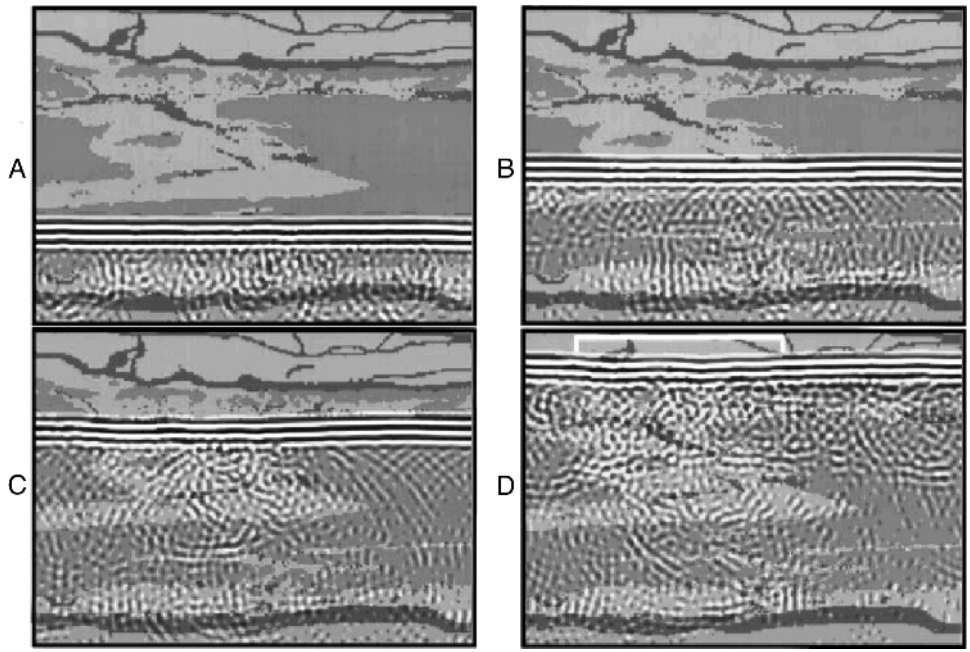

Figure 9.8 Propagation of a plane wave through a section of the abdominal wall sample depicted in Figure 9.7. Panels (A)–(D) show the upward progression of the main wavefront through the muscle layer including an aponeurosis comprised of fat and connective tissue, resulting in time-shift aberration across the wavefront. The area shown in each frame is 16.0 mm in height and 18.7 mm in width. The temporal interval between frames is 1.7 ms. Tissue is color coded according to that of Figure 9.7, while gray background represents water. Wavefronts are shown on a bipolar logarithmic scale with a 30-dB dynamic range. The wavefront represents a 3.75 MHz tone burst with white representing maximum positive pressure and black representing maximum negative pressure. A cumulative delay of about 0.2 ms, associated with propagation through the aponeurosis, is indicated by the square bracket in panel (D) (from Mast *et al.*, 1997, Acoustical Society of America) (see also color insert).

12.5.5. A calculated, focused wavefront from an array propagating through the breast is illustrated by Figure 9.9. Note the nearly circular wavefronts scattered off the tips of vertical septa, which appear to be the main disrupters of the plane wavefront. A sequential simulation of a plane wave propagating between ribs in a chest wall (shown in Figure 9.10) reveals multiple scattering from ribs that was observed in data sets (Hinkelman *et al.*, 1997; Mast *et al.*, 1999).

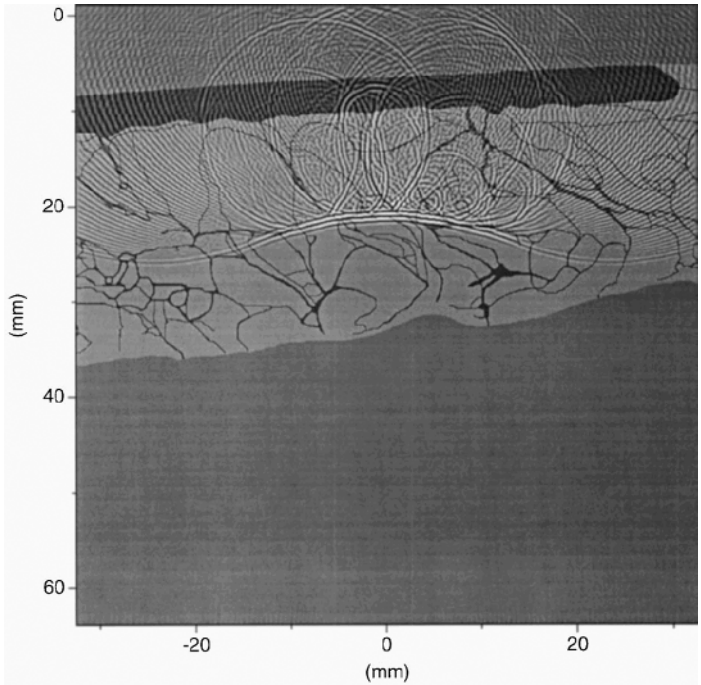

Figure 9.9 A converging focused pulse wavefront from a virtual array and secondary scattered wavefronts at an instant of time during propagation through a representative breast tissue map. The wavefront is superimposed on the map and displayed on a 60-dB bipolar logarithmic gray scale. In the map, dark gray denotes connective tissue or skin and light gray denotes fat (from Tabei *et al.*, 2003, Acoustical Society of America).

Scattering from real tissue includes three contributions. These simulations show only transmitted waves; however, they demonstrate that the main direct wavefronts are followed by a complex pattern of waves diffracted from tissue structures. The calculations provide a more realistic depiction of wave propagation (even though they are planar) than previous treatments of homogeneous tissue layers; however, they do not include the granularity necessary to include the third contribution, which is speckle. In summary, propagation in tissue has three parts: main wavefronts, lower level waves from diffracting structures, and speckle (diffusive waves from subwavelength tissue structures).

9.4 ARRAY PROCESSING OF SCATTERED PULSE-ECHO SIGNALS

If complicated scattering from heterogeneous tissue occurs, what is its effect on imaging? In Section 8.4.1, the steps of the imaging process were identified. First, a three-dimensional pulse packet from a focused beam races through tissue along a

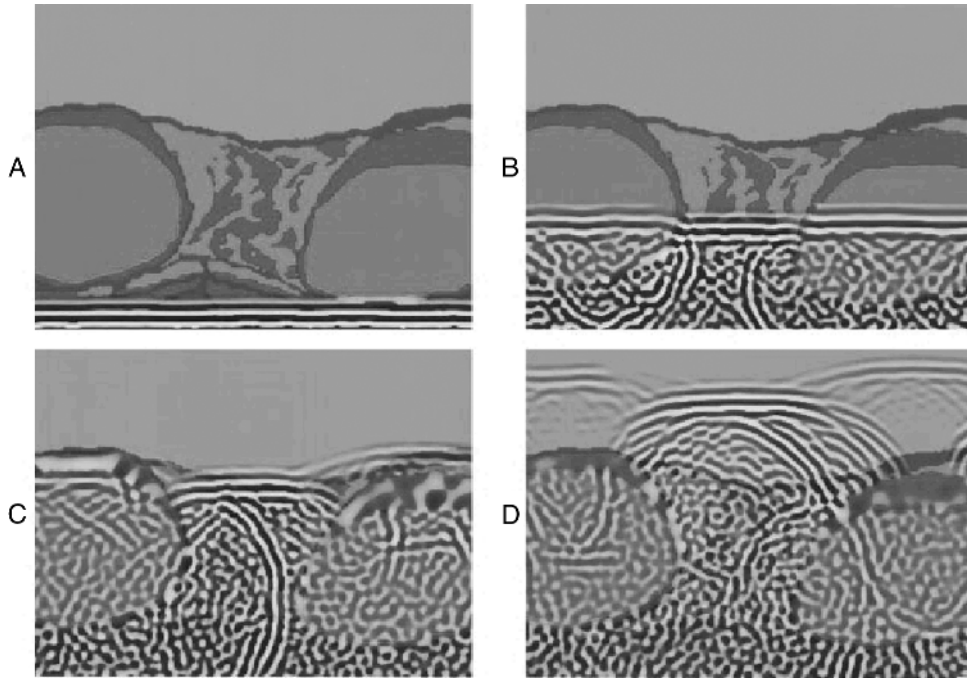

Figure 9.10 Simulation of 2.3-MHz plane wave tone burst wavefront propagating through a chest tissue map. In each map, blue denotes skin and connective tissue, cyan denotes fat, purple denotes muscle, orange denotes bone, and green denotes cartilage. Blood vessels appear as small water-filled (white) regions. Logarithmically compressed wavefronts are shown on a bipolar scale with black representing minimum pressure, white representing maximum pressure, and a dynamic range of 57 dB. Each panel shows an area that spans 28.27 mm horizontally and 21.20 mm vertically (from Mast *et al.*, 1999, Acoustical Society of America) (see also color insert).

designated vector direction, and it changes shape at each depth according to its point-spread function. Second, multiple scattering of the pulse happens at the depth location of each scatterer (z_i/c) over a broad angular range. Third, parts of the scattered wavefronts are intercepted by each element acting as a receiver with wide directivity at times ($2z_i/c$). Each element has a distinct spatial location and, therefore, intercepts different parts of scattered wavefronts and converts them into an electrical time record (volts).

We now have a look at a hidden aspect of imaging—what happens inside the beamformer after the three steps in the imaging process described earlier—when real data are received from a heart (Szabo and Burns, 1997). For the formation of an image line, array elements receive a time stream of data. In this example, 54 time records from active elements of a 2.5-MHz, 64-element phased array are shown in Figure 9.11 for an apical view of a heart. These time traces were captured in real time in the process of forming a cardiac sector image and are shown after focusing time alignment. Events between time samples 3200–3500 are caused by specular tissue reflections, and those events between 2200–2700 belong to a lung artifact. An ideal reflector will be aligned

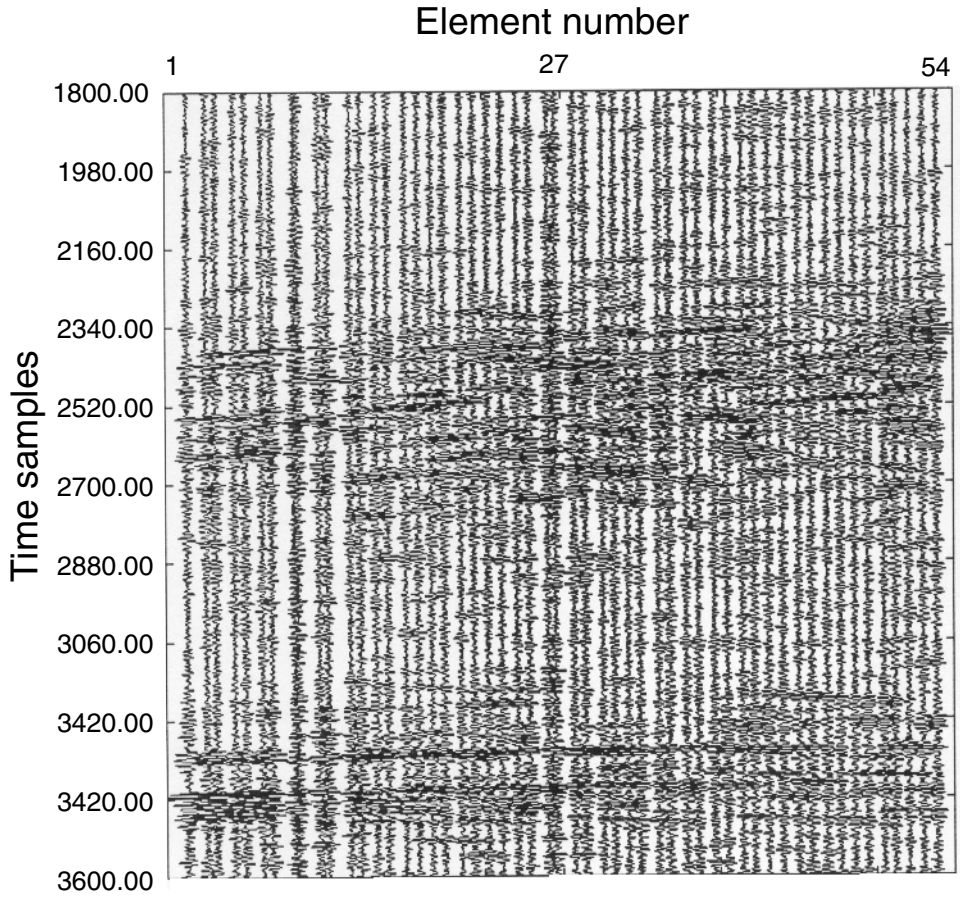

Figure 9.11 Raw RF data from line 72 (+8.25 degree steer direction) of an apical window data set. The data are shown for 54 traces of a 64-element transducer (traces 6–59) and for the time sample range of 1800–3600 or 90 μs. The horizontal events between time samples 3200–3500 correspond to specular tissue reflections, while the events between 2200–2700 correspond to a lung artifact. The data have been normalized to the maximum value in the plot (maximum = 65) (from Szabo and Burns, 1997, reprinted with permission of Kluwer Academic/Plenum Publishers).

across all traces and will form a horizontal wavefront. The wavefront at time sample 3300 comes close to this ideal, but it neither extends across all elements nor lines up completely across traces. Irregularities in terms of depth (vertical) time alignment along a wavefront are caused by aberration effects. What is surprising are the smaller signals, many of which are aligned across several traces; therefore, they cannot be random. These groups of similar waveforms, extending across a few traces and combining to form small wavefronts not aligned horizontally, indicate multiple scatters illuminated at various angles of incidence and reflecting in other angles according to their scattering shape (similar to those discussed in the last section).

What happens to all this information? The beamformer sums all these traces from elements into a final single-time record, which, after envelope detection, becomes a line in the image. This kind of beamformer operates on the principle of coherence (explained in Chapter 7). After focusing delay alignment, each time record is summed. Coherent waveforms, aligned in time, form large signals. Many of the smaller waveforms, which are coherent only across a few traces when summed with adjacent nonaligned signals in the same time slot, are suppressed. This summation processing shows the beauty and simplicity of the linear beamformer; coherent signals add, and noncoherent signals are rejected and appear as random, low-level clutter and speckle. Even though it is currently awkward in hardware and computationally intensive to utilize raw RF data such as that shown in Figure 9.11, beamformed RF data is utilized routinely by the methods of tissue characterization.

9.5 TISSUE CHARACTERIZATION METHODS

9.5.1 Introduction

The science of ultrasonic tissue characterization (UTC) is the untangling of hidden patterns in pulse-echo data to extract more information about tissue function and pathology than that seen in conventional images (Thijssen, 2000). Tissue characterization, as was originally conceived by Dr. J. J. Wild and J. M. Reid in 1952 (see Section 1.2), was a type of remote, painless ultrasound telehistology (a noninvasive way of determining the health of tissue or organ function through calculations and parameterized inferences from ultrasound data). The application of tissue characterization to detection of cirrhosis in the liver by Wells *et al*. (1969) and Mountford and Wells (1972) marked a turning point in the serious application of these methods. Hill and Chivers (1972) contributed to a scientific examination of scattering from tissue with the hope of retrieving quantitative data. Since then, this branch of medical ultrasound has undergone considerable development. Methods now include specialized measurements, signal processing, statistical analysis, and parameterized imaging.

In order to place these diverse UTC approaches in perspective, we can use the diagram in Figure 9.12, which serves as an introduction to the remaining contents of this chapter. The topics included here stretch the conventional use of the term ''tissue characterization'' but fit the definitions given previously. Most of UTC is based on RF signals either from beamformers prior to detection in imaging systems or from specialized measurements. The methods based exclusively on processing of RF data are basic spectral method, spectral features, integrated backscatter, and signal processing. Even conventional Doppler (see Chapter 11) can be considered to be a signal processing type of UTC because it calculates parameters based on RF pulse-echo data from flowing blood (Taylor and Wells, 1989). A number of other signal processing methods, such as color flow imaging (which determines blood flow velocity) and others that detect tissue movement and provide calculations and/or parameterized displays, will be described in Chapters 10 and 11.

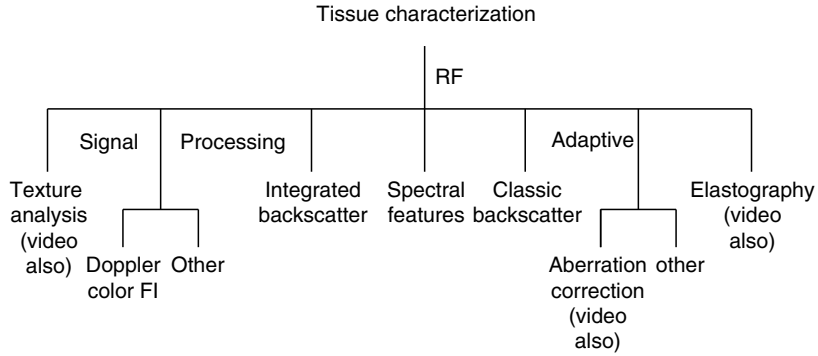

Figure 9.12 Diagram of ultrasound tissue characterization applications.

Several approaches can utilize video or RF data, the main one being texture analysis. Elastography, a collection of ways of imaging the stiffness of tissue use, can use either video or RF data. On the far right of Figure 9.12 are adaptive signal processing methods, such as aberration correction, that not only sense differences in tissue parameters but also alter the function of the imaging system in response to these sensed changes. Aside from the signal processing methods covered in the next two chapters, the topics in the diagram will be described in the following sections.

The breadth of the UTC science can only be highlighted briefly in this chapter. Whole books (Greenleaf and Sehgal, 1992; Shung and Thieme, 1993) have been written on these topics, and regular conferences on these topics such as the Tissue Characterization Symposia have been held for more than 25 years. From the last section, it is obvious that backscatter from real tissue is messy, which is why this field presents interesting challenges. Nonetheless, if we expand the concept of UTC to encompass the areas in Figure 9.12, there are a number of success stories and exciting developments for the future. Section 9.6 presents several UTC applications.

The usual starting point of UTC analysis is acquisition of raw RF signals because, as will be evident in the next chapter, the imaging systems add nonlinear processing on top of envelope detection to make images presentable over a large dynamic range. It is also possible to obtain tissue information from the video information in the image itself after removing this nonlinear processing, as discussed later.

9.5.2 Fundamentals

The foundations for UTC were explained in Chapter 8. A major goal in UTC is inverting or revealing the properties of the tissue through a backscatterer or another measured ultrasound parameter. A second, but even more important, goal is to use this acquired information to distinguish between states of tissue (healthy or diseased) or to detect changes in tissue property in response to a stimulus or, over longer periods of time, in response to natural processes or medication. A key problem in the untangling is undoing or correcting the spatial varying properties of the

measurement or imaging process. For example, a homogeneous tissue would appear to be inhomogeneous in an image simply from the variations in pressure from diffraction and absorption effects along the beam axes. These problems will be clarified soon. UTC approaches range from "proof of concept" experiments involving single lines of RF data from tissue samples *in vitro* (outside the body) to those involving data acquisition and processing from a system imaging a body in real time.

Since many of the physical aspects of these problems overlap, it is easier to start with the simplest approach. A framework for understanding the factors involved is essential (the central block diagram in Figure 2.14 is helpful for identifying factors symbolizing the physical mechanisms involved). These factors can be consolidated into an expanded version of Eq. (8.10b) for the received output voltage,

$$V_0(z,r,f) = E_{RT}(f)A_t(z,r,f)H_t(z,r,f)H_r(z,r,f)A_r(z,r,f)F_G(z,f)S(z,r,f) \tag{9.2a}$$

or, in terms of power (within a constant factor),

$$V_0V_0^* = E_{RT}E_{RT}^*A_tA_t^*H_tH_t^*A_rA_r^*F_GF_G^*SS^* \tag{9.2b}$$

where $F_G(z,f)$, a symbol for a generic filter and/or linear amplifier function, has been added. From a UTC viewpoint, the unknown tissue properties are frequency- and angle-dependent scattering and sometimes, frequency-dependent absorption, but these charateristics are distorted by the interrogating acoustic beam and the limitations of the electroacoustic transduction process. The beam and transducer act as imperfect samplers, both spatially (including geometric orientation, as well as limited angular range) and spectrally. The scattering properties are the sought-after signatures of the targets, and the effects of the array and transduction are somehow removed by calibration and compensated for, or minimized by, a number of methods. Most UTC approaches depend on comparisons of data to a comprehensive model of backscattering from tissue, such as, Eqs. (9.2a)–(9.2b) provide. An alternative is to extract attenuation rather than to backscatter information (Ce'spedes and Ophir, 1990).

Certain objects have unique scattering signatures in the frequency domain and, as a result, most of tissue characterization is done in the frequency domain. The most often-used parameter is the "backscattering coefficient." Sigelmann and Reid (1973) proposed a method for extracting a backscattering coefficient from power reflected from a volume containing scatterers such as blood with reference to the power reflected from a known flat plate. One of the first applications of backscatterer measurements was to blood by Shung *et al*. (1976). A recent twist on this theme is the use of blood as a reference scatterer to characterize nearby tissue (Pedersen *et al*., 2003). Measurements of blood are given in more detail in Chapter 11.

9.5.3 Backscattering Definitions

Most of the tissue characterization spectral methods are based on several assumptions to simplify the factors in Eq. (9.2) (Reid, 1993). The incident wave on the scatterer is assumed to be nearly plane insofar as a small volume of the scatterer is concerned

(a situation almost satisfied near the focal plane of a focusing transducer or the far field of a nonfocusing transducer). The scatterer or inhomogeneity in tissue is taken to be a small weak spherical scatterer that can be described well by the Born approximation, Eq. (8.8a). In terms of spectra, it is convenient to work with scattered power (W_s), which is related to the incident intensity (I_i) by

$$W_s = \sigma_t I_i \tag{9.3}$$

where σ_t is the scattering cross section. This reasoning, for a spherical scatterer, leads to the scattered intensity,

$$I_s = \sigma_t I_i / 4\pi r^2 \tag{9.4}$$

For a backscatterer that varies with angle, a differential scattering cross section is more appropriate, as

$$\sigma_d I_i = W_s / 4\pi \tag{9.5}$$

where the power is divided by 4π steradians in a unit sphere. Conversely, the total scattering cross section is the differential scattering cross section integrated over the solid angle about a spherical surface. In practice, the total cross section can be the sum of individual cross sections or may be integrated over a distribution of scatterers. Finally, there is the scattering cross section per unit volume, defined by

$$\sigma = \int_V \eta dv \tag{9.6a}$$

or

$$\sigma_d = \int_V \eta_d dv \tag{9.6b}$$

where η has units of inverse length compared to a cross section that has units of area.

9.5.4 The Classic Formulation

As discussed in Chapter 8, the scattering process involves the entire volume of tissue intercepted by the acoustic beam; therefore, a volume integration over this volume is involved for transmit. Likewise, the location of the receive beam relative to the scatterer (if it is not coincident with the transmit direction) is involved over the intercepted scattered volume; therefore, in general, two volume integrations are needed. Finally, a calibration method is convenient to obtain a more absolute measurement. In the original approach, a substitution method was applied to the problem. A nearly ideal plane reflector was placed in the position of the scattering volume under identical insonification conditions, and the voltage was recorded. The power ratio of scattered power to reference-reflected power gives an expression for mean value of the backscatter coefficient η_d (Reid, 1993) in an abbreviated form,

$$\bar{\eta}_d(f) = \frac{\int\int E_{RT} E_{RT}^* A_t A_t^* H_t H_t^* A_r A_r^* F_G F_G^* SS^* (dr_0')^3 (dr_0)^3}{\int\int E_{RT} E_{RT}^* A_t A_t^* H_t H_t^* A_r A_r^* F_G F_G^* (dr_0')^3 (dr_0)^3} = \frac{\langle V_0(f) V_0^*(f) \rangle \bar{r}^2}{V_{ref}(f) V_{ref}^*(f) 4 A S_{eff} l} \tag{9.7}$$

where A_r and A_t are attenuation factors appropriate for the different sample and reference paths, A is an overall attenuation correction factor, S_{eff} is an effective beam cross-sectional area, integration is over pulse length, $(l = c(t_2 - t_1)/2)$ and the intersection volume of the coincident beams, and $\bar{r}$ is the distance to the center of the sample.

In the original formulation, simplifications were made about the far field and beamwidth of the transducer and gate length of the received pulse, and after correction for the absorption of the sample and the water path, this ratio was shown to be proportional to the squared magnitude of the output voltage from the scattered region to the squared magnitude of the reference voltage. This narrowband approach was subsequently endorsed by the American Institute of Ultrasound in Medicine (1990) and led to further extensions of the original method.

9.5.5 Extensions of the Original Backscatter Methodology

Work at the University of Wisconsin (Madsen *et al*., 1984) provided a more general model for broadband applications and focusing transducers. Further work there, based on statistical continuum models, (Chen *et al*., 1993; Chen and Zagzebski, 1996) has shown that the backscatter increases with the number density of scatterers per volume fraction as a function of frequency. Waag and Astheimer (1993) developed a generalized backscattering approach for noncoincident transmitter and receivers. A way of extending the methodology to broadband applications (O'Donnell *et al*., 1979; Thomas *et al*., 1989), called the integrated backscatter approach, will be explained separately.

A more recent evolution of the original method, illustrated in Figure 9.13, is a general broadband approach to finding the backscatter coefficient (Chen *et al*., 1997) that utilizes a calibration waveform from a flat plate to obtain $E_{RT}(f)$ (see Section 8.3., Eq. (8.12)) and provides an analytical formulation for the entire pressure distribution in the beam as a function of frequency. Their expression is

$$\bar{\eta}_d(f) = \frac{\langle V_0(f)V_0^*(f)\rangle}{V_{ref}(2z_{ref},f)V_{ref}^*(2z_{ref},f)} \frac{|D_{ref}(2z_{ref},f)|^2}{\overline{TF}^4 A l \bar{D}_s(\bar{r},f)} \tag{9.8a}$$

where D_{ref} is the equivalent diffraction loss, DL_{equiv}, from Eq. (8.12); V_{ref} is the Fourier transform of round-trip output voltage $e_{RT}(t)$ at $2z_{ref}$ (explained in Section 8.3.1), A is an attenuation factor for the tissue and water paths taken outside of the diffraction integral (described in Section 7.9.4); and $\overline{TF}^4$ is the overall transmission factor from water to tissue and from tissue to water (on the return path),

$$\overline{TF}^4 = \frac{16(Z_2/Z_1)^2}{(1 + Z_2/Z_1)^4} \tag{9.8b}$$

where Z_1 is the coupling medium or water to the tissue, Z_2 is the acoustic tissue impedance, and $\bar{D}_s$ is a diffraction correction term that is known analytically or can be approximated (Chen *et al*., 1997). The last correction term is an improvement over other methods because it corrects for diffraction as a function of both frequency and

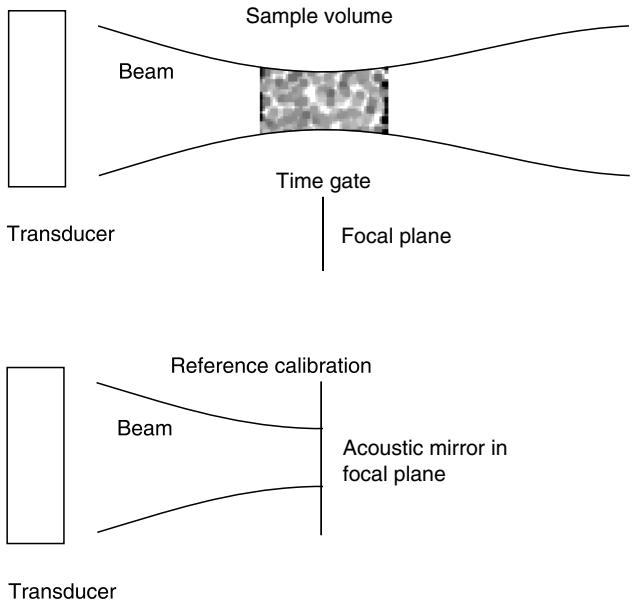

Figure 9.13 Configuration for classic backscatter measurement using the substitution method. (Top) Tissue measurement setup shown for a focusing transducer. (Bottom) Calibration setup with acoustic mirror.

distance in a convenient way; the tissue sample distance does not have to coincide with the reference distance. In addition, it includes the influence of the entire beam rather than a −3-dB beamwidth, as was used in the original method. This method has been found to be in excellent agreement with data, even for strongly focused transducers (Machado and Foster, 1999) after attenuation correction (D'Astous and Foster, 1986) was applied. This general method reduces to the Sigelmann–Reid technique under similar experimental conditions for nonfocusing transducers and to the approach of Madsen *et al*. (1984) for focusing transducers when the effect of the finite receive gate (a sliding time window, often apodized) is neglected.

9.5.6 Integrated Backscatter

Another approach that has been extremely successful for cardiac and other applications (discussed in more detail in Section 9.6.2) is integrated backscatter, which was developed at Washington University. The relative broadband integrated backscatter can be expressed as the ratio of the power spectrum averaged over the effective bandwidth of the transducer relative to that from a standard plane reflector in the focal zone of the transducer (O'Donnell *et al*., 1979; Thomas *et al*., 1989),

$$\bar{S}_r = \int_{f_0-\Delta f}^{f_0+\Delta f} \frac{|V_0(f)|^2}{|V_{ref}(f)|^2} df = \frac{\int_{-\infty}^{\infty} |v_0(t)|^2 dt}{\int_{-\infty}^{\infty} |v_{ref}(t)|^2 dt} \tag{9.9}$$

where the signal power spectrum is $|V_0(f)|^2$, that of the reference is $|V_{ref}(f)|^2$, and Δf is half the useable bandwidth, and the power or Parseval's theorem from Appendix A has been used to relate the frequency and time domain. Note that $|v_0(t)|$ is the envelope of the output time signal. Integrated backscatter can be corrected for attenuation, depending on the application.

An interesting property of the envelope $|V_0(t)|$ comes from the Fourier transform property is that the area in one domain is equal to the value of its transform at zero. Consider a simple example such as a Gaussian modulated sinusoidal time waveform, like those considered in Chapter 2, which is centered on delay time $t = t_{\text{delay}} = 2z/c$. If the envelope of the received signal is $e(t) = |v_0(t)|$, then the value of the envelope at $t = t_{\text{delay}}$ or equivalently, at the peak of a delayed signal, is

$$e(t - t_{delay}) = \mathcal{F}^{-1}\left[E(f)e^{-iz\pi f t_{delay}}\right] \tag{9.10a}$$

$$e_{peak} = e(0)|_{t=t_{delay}} = \int_{-\infty}^{\infty} E(f)e^{i2\pi f(t-t_{delay})} df|_{t=t_{delay}} = \int_{-\infty}^{\infty} E(f)df \tag{9.10b}$$

$$e_{peak} \approx \int |E(f)|df \tag{9.10c}$$

Where for a useable bandwidth, we assume that $|E(f)| \sim E(f)$ and that, alternatively, a similar result for the integral of the absolute value of the spectrum could be obtained by taking the absolute value of the whole integrand of the inverse Fourier transform and by using Schwartz's inequality.

9.5.7 Spectral Features

Other useful spectral features for tissue characterization have been proposed by Lizzi *et al*. (1983), Lizzi and Feleppa (1993), and Lizzi *et al*. (1997). By analyzing the frequency response of spherical scatterers of different sizes, they concluded that the slope of the backscattered spectrum, once corrected for attenuation and calibrated to a reflection from a plate (as in the other classical methods), was indicative of the size of the scatterers. Corrected data, in other words, were fit by a least-squares method, and the intercept and slope became useful spectral features. The intercept is related to the acoustic concentration (related to the scatterer volume concentration and the relative acoustic impedance). Finally, the midband slope value is also valuable and related in a statistical sense to integrated backscatter (Lizzi *et al*., 1997). Lizzi's group was also one of the first to appreciate that scattered power over small adjacent distances (Δx, etc.) was a spatial autocorrelation function in three dimensions. These autocorrelation functions are $R_D(\Delta x, \Delta y)$, directivity; $R_G(\Delta z)$, the axial time gate; and $R_Q(\Delta z)$, the relative impedance.

A classic UTC experiment is to tell the size of small subwavelength scatterers from the backscatter alone. Well, not quite alone. A reference model for the expected backscatter for a small sphere, such as that derived by J. J. Faran, Jr. (described in Section 8.2.3.1), is calculated over the frequency range of interest and compared to the backscatter.

Several research groups have studied the backscatter coefficient of many spheres in suspension without multiple scattering (Ueda and Ozawa, 1985; Romijn *et al*., 1989). Thijssen (2000) has shown that the slope of the backscattering coefficient at low frequencies (small *ka*) is related to the size of the scatterers (20 to 500 μm), as did Lizzi *et al*. (1983). In addition, Bridal *et al*. (1996) applied the standard methodology to a −6-dB spatial resolution cell of polystyrene beads in argose over a frequency range of 5–65 MHz with attenuation correction and renormalization. They compared their data to the Faran elastic sphere scattering theory. (It is remarkable that the size of scatterers as small as one sixth of a wavelength can be determined from the slope of their backscatter coefficient (shown in Figure 9.14)). Excellent absolute agreement for the spectral characteristics of spheres was also obtained by Hall *et al*. (1997). Chaturvedi and Insana (1996) explored the errors and limits of determining the sizes of small scatterers.

9.6 APPLICATIONS OF TISSUE CHARACTERIZATION

9.6.1 Radiology and Ophthalmic Applications

Determining the scatterers per unit volume can be helpful in discriminating between healthy and abnormal tissues. The slope of the backscatter coefficient approach has been successfully applied to eye tumors (Feleppa *et al*., 1986; Romijn *et al*., 1991; Thijssen *et al*., 1991), animal model melanomas (Romijn *et al*., 1989), renal glomeruli size estimation (Hall *et al*., 1996), and many other cases. In addition, it is sometimes possible to decipher a scattering component that is related to structural patterns in tissue (Thijssen, 2000).

Fellingham and Sommer (1984) predicted that the regularity of tissue structure would result in periodic peaks in the autocorrelation of backscattered pressure and that disease would disrupt this structure. By examining the RF data from *in vitro* samples of the liver and spleen, they were able to show some differences in ''mean scatterer spacing'' on the scale of millimeters for some diseased states.

An often-used technique in tissue characterization is to calculate and extract a relevant parameter, such as the midband value of the backscattering coefficient, and create a visual map of this parameter using a color map superimposed on the original B-mode image. Better discrimination is achieved by combining features (Lizzi *et al*., 1997; Lizzi and Feleppa, 1993). In some cases, even combined features are not enough because of overlapping regions. Feleppa *et al*. (2001) demonstrated that by using advanced techniques, such as neural network classification, differences between healthy and cancerous tissues in the prostate can still be determined. A combination of prostate-specific antigen (PSA) and spectral features were used to identify the

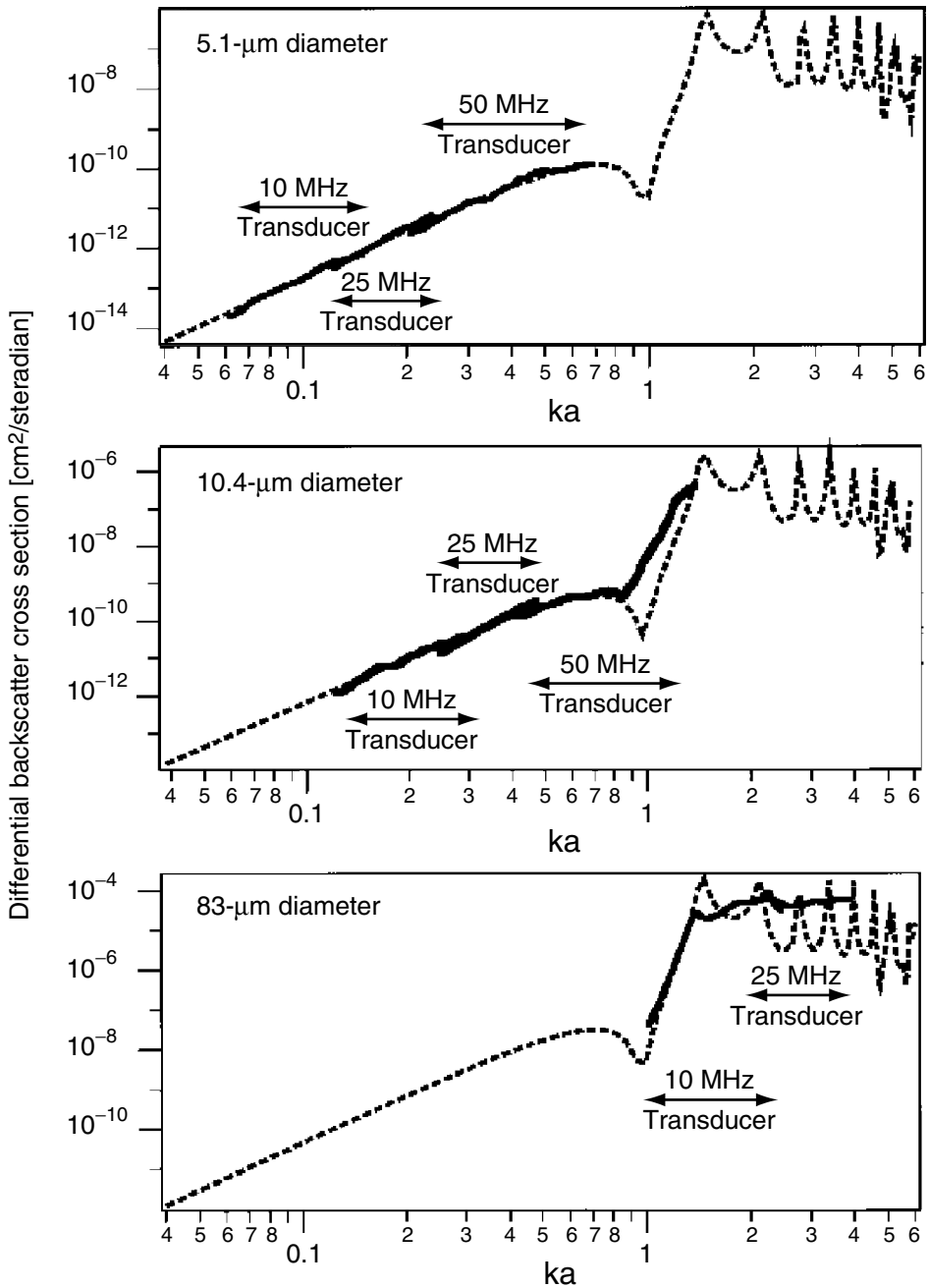

Figure 9.14 Comparison for simulation (solid lines) of backscatter from a sphere to backscatter data (dashed lines) as a function of *ka*. Theory was used to calculate the differential backscatter cross section for a single polystyrene sphere. Each data set is renormalized to align it to the single scatterer cross section curve (from Bridal *et al.*, 1996, Acoustical Society of America).

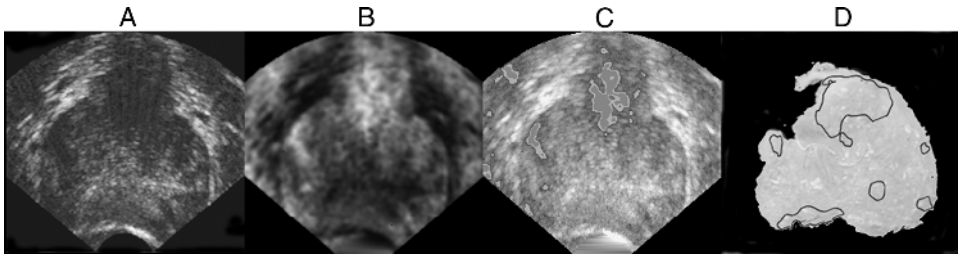

Figure 9.15 Images of the central plane of a prostate gland having an ultrasonically-occult anterior tumor as viewed from the apex of the prostate. (A) Computer-generated envelope-detected 'B-mode' image. (B) Grey-scale cancer-likelihood image (white = maximum likelihood). (C) Color-encoded overlay on a midband parameter image depicting the two highest levels of likelihood in red and orange. (D) Corresponding histological section that shows a 12-mm tumor protruding through the anterior surface and several smaller circular intracapsular foci of cancer and neoplasia as manually demarcated in ink bv the pathologist (from Feleppa *et al.*, 2001, reprinted with permission of Dynamedia, Inc.) (see also color insert).

likelihood of cancer occurring in different regions, as shown in the parameterized images of Figure 9.15. Note that the 12-mm tumor was not visible in conventional imaging and not identified by palpitation.

9.6.2 Cardiac Applications

Tissue characterization of the dynamic movements of the heart has led to new diagnostic tools, as well as a better understanding of heart function. Some background on the heart will be helpful in explaining how the heart is characterized by ultrasound methods. The heart is a tireless pump that squeezes out blood on myocardial contraction (systole) and fills up during the expansion phase (diastole). The heart pumps approximately 5–15 L of blood a minute. The strength of the heart is contained in the band of circumferential fibers that do the squeezing. Because these fibers have a preferential-organized direction, they have anisotropic acoustic properties (as plotted in Figure 9.16). Miller *et al.* (1989; 1998) measured these characteristics at Washington University, and their significant research on the heart is summarized in this section and in more detail in review articles.

These characteristics of anisotropy have been modeled well by the Born approximation for scattering from cylinders. This modeling shows that the direction of insonification relative to the arrangement of myocardial fibers is important. When the fibers are aligned perpendicular to the sound beam, maximum reflection occurs; when the fibers are parallel, reflection is minimum. Two important consequences of these effects (shown in Figure 9.17) are the variation of integrated backscatter and frequency-averaged attenuation with angle (Mottley and Miller, 1988; 1990). Both of these effects are seen in every cardiac image and are important in interpreting what is seen in these images.

Now imagine the heart twisting, moving, and stretching during each cardiac cycle so that the angle of insonification to the heart from a fixed location, such as the short axis acoustic window, keeps changing with time. One might think that it is totally

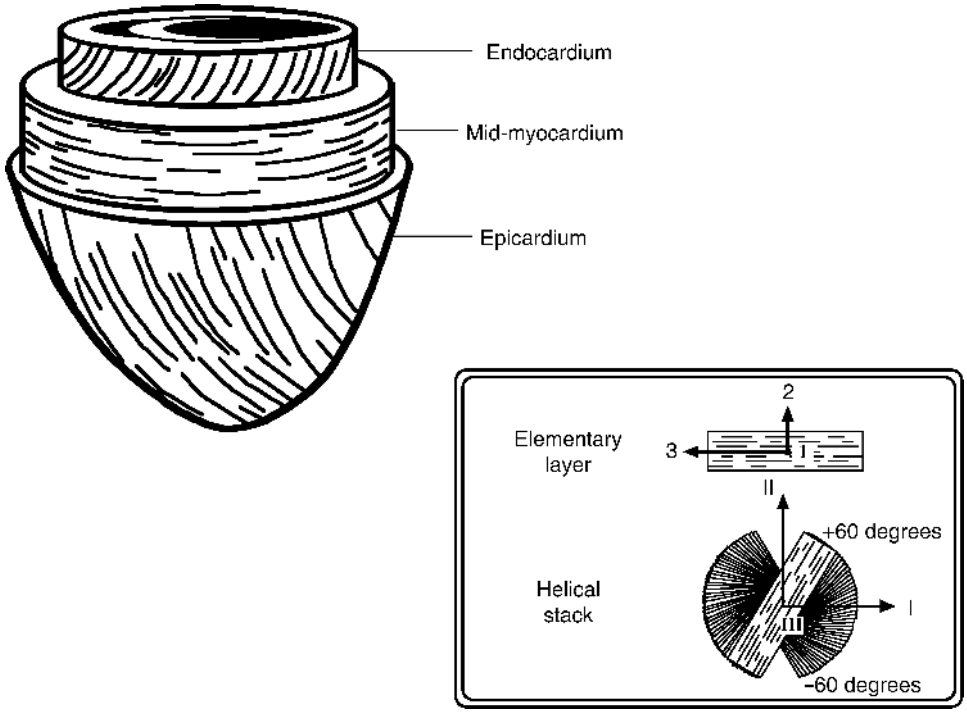

Figure 9.16 Arrangement of muscle layers of the heart showing the preferential directions of microfibers in the layers that cause anisotropy (courtesy of J. G. Miller).

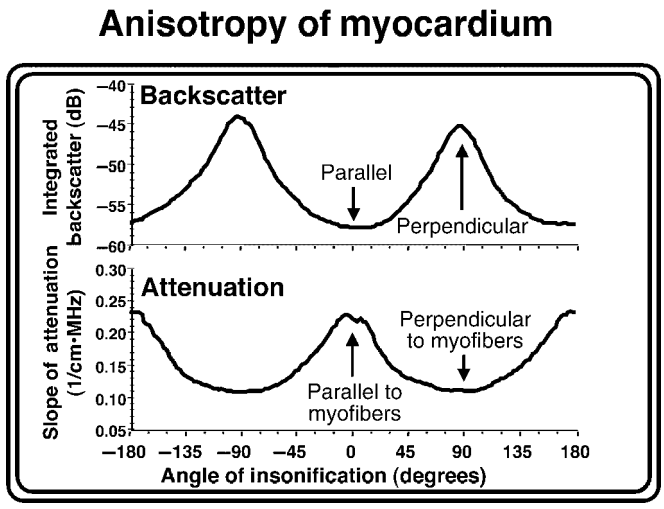

Figure 9.17 Angular variation of attenuation and integrated backscatter of the heart caused by anisotropy of myofibers (from Miller *et al.*, 1998, *IEEE*).

hopeless to attempt an interpretation of such a complicated configuration, but dynamic tissue characterization comes to the rescue. By looking at integrated backscatter features of the cardiac cycle, like those in Figure 9.18, researchers at Washington University were able to identify abnormalities of the heart. Accounting and correcting for anisotropy helps to determine a baseline pattern so that pathologies can be more readily identified.

Because heart diseases are major killers and debilitators, it is worth asking "What are the main pathologies of the heart?" The most important blood suppliers to the heart are the coronary arteries. Atherosclerosis is a disease in which the arteries are narrowed by plaque (a soft pasty material that can calcify), become fibrotic, or form into vulnerable plaque (a dangerous unstable sort that can turn into a thrombosis or blood clot). A symptom of atherosclerosis is arteriosclerosis (a hardening of the arteries). Ischemia is reduced blood flow as a result of mechanical obstruction of an artery. An infarct is tissue death caused by ischemia. A heart attack, or myocardial infarct, is the death of muscle cells of the heart and is often caused by the closing of an already constricted passage by a blood clot. Reperfusion is a mechanical (angioplasty) or chemical means (thrombolytic agents) of replenishing blood flow to an injured area to preserve heart function and reduce mortality and severe side effects of heart attacks.

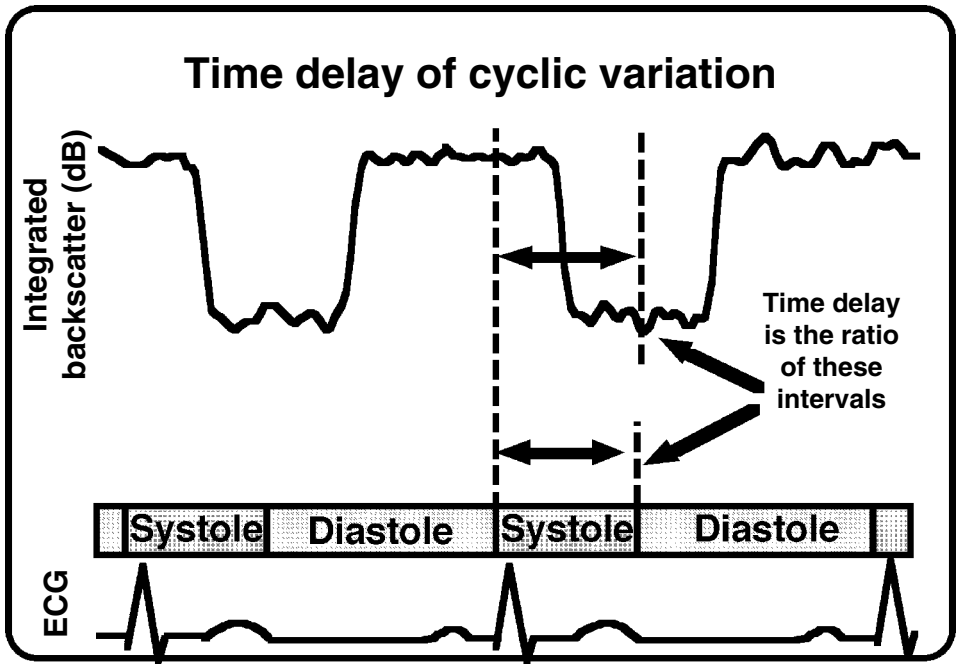

Figure 9.18 Characterization of the cyclic variation of integrated backscatter in terms of the variation in magnitude and the time delay relative to the start of systole, normalized to the systole interval (from Miller *et al., 1998, IEEE).*

Because the ability of the heart to function is severely compromised by these diseases, the heart cycle is affected. In particular, the features of the heart cycle described in Figure 9.18 can be used in identifying effects of disease such as infarcts, ischemia, and myopathy (a disease affecting the contractility of the heart), as well as the effects of reperfusion and other types of therapy. The effectiveness of using these features, after correction for the effects of anisotropy, are illustrated by Figure 9.19.

Ongoing studies of the heart have led to real-time improvements in echocardiology. For example, the need to capture both the weak and strong reflections from the muscle fibers has led to an anisotropic rational gain compensation method, as well as to a lateral gain compensation capability. The use of integrated backscatter was part of an algorithm to provide automatic real-time boundary detection of the left ventricle. These methods will be discussed in more detail in Chapter 10. The application of ultrasound contrast agents in combination with signal processing methods has also been highly successful in the diagnosis and tissue characterization of the heart (to be explained in Chapter 14).

9.6.3 High-Frequency Applications

High-frequency ultrasound is opening up new tissue landscapes not seen at conventional frequencies below 15 MHz. Three major high-frequency applications are utilizing the increased resolution to identify plaque in blood vessels intravascular ultrasound (IVUS), to reveal cellular structures and to examine small animals. These uses are opening up new insights into the progress of disease and cell death *in vivo*. The following discussion will show that high-frequency imaging is not just conventional imaging scaled down in resolution.

Consider a high-frequency spherically focusing transducer operating at 100 MHz with an $F\# = 1.33$ (Sherar *et al*., 1987; Foster *et al*., 1993) with an axial resolution of 28 μm and a FWHM of 17.5 um, as depicted in Figure 9.20. We can estimate a resolution cell volume as a −6-dB FWHM ellipsoid with a major axial axis and equal minor lateral axes in terms of wavelengths as in Figure 7.20, as

$$Vol = \frac{\pi}{6}(1.87\lambda)(1.17\lambda)^2 = 1.34c_0^3/f_c^3 \tag{9.11}$$

which gives a volume of $4.52 \times 10^3 \mu m^3$ for a center frequency of 100 MHz, a value that is 1000 times smaller than that for a more conventional B-mode frequency of 10 MHz, $4.52 \times 10^6 \mu m^3$.

What difference does this size make? Consider that cell size is on the order of microns. In a study of leukemia cells (Czarnota *et al*., 1997), the cell density was measured as approximately $10^{-3}/\mu m^3$. For this case, there would be 4.5 cells in a resolution cell at 100 MHz and 4500 cells at 10 MHz. Recall the class distinctions for scattering from Section 9.2 (Class 1 or diffusive scatterers are 25 or more per resolution cell, and Class 2 or diffractive scatterers are 1 per resolution cell). At 100 MHz, the scatterers are on the borderline between Classes 1 and 2; whereas, at 10 MHz, they are between Classes 1 and 0. At the higher frequency, scattering is more

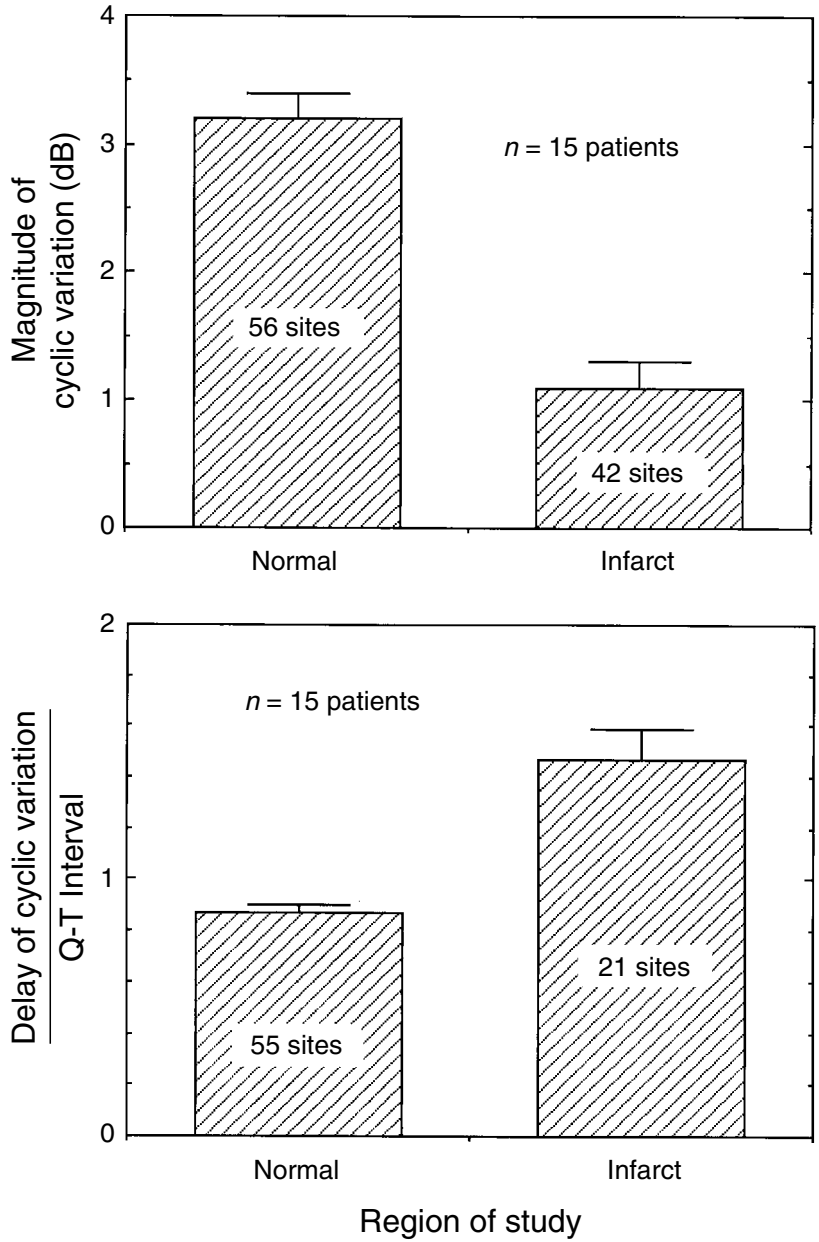

Figure 9.19 Results of a study of 15 patients with scars from old myocardial infarcts. Zones of scar exhibit reduced magnitude and increased time delay relative to healthy (noninfarct sites in the same patients (from Miller *et al.*, 1989, *IEEE*).

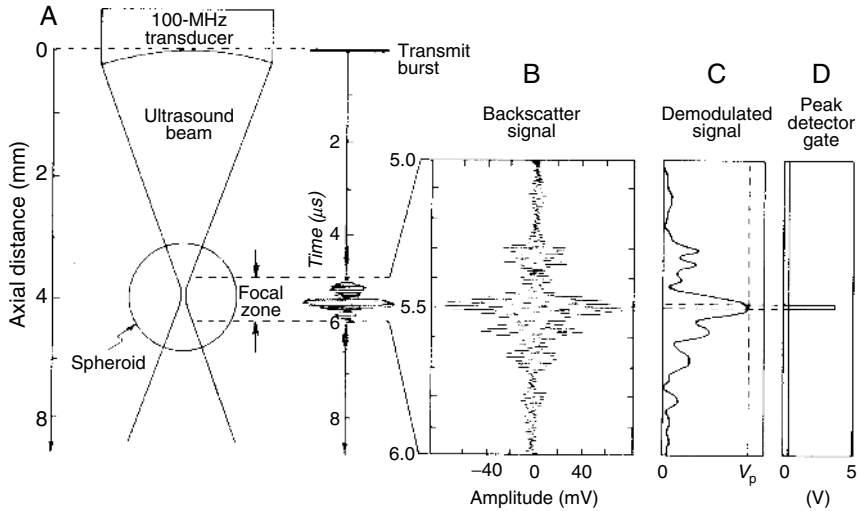

Figure 9.20 100-MHz backscatter microscope. (A) Sketch of beam and transmit signal. (B) Backscatter signal versus time. (C) Pulse-echo envelope. (D) Gate located at peak of echo envelope. Beam is scanned across an area consisiting of 256 × 256 measurements (from Sherar *et al.*, 1987, reprinted with permission of Nature, Macmillan Magazines Limited).

critically dependent on the size and arrangement of the individual scatterers, even though they are not resolvable.

To make this difference clearer, a high-frequency detection of the process of apoptosis will be discussed. Apoptosis is programmed cell death that can occur in cancer, embroynic development, or neurodegenerative disorders or can occur from diseases such as heart attacks or organ transplants or as a deliberate result of drug therapy.

In Figure 9.21 are a series of noninvasive images of programmed cell death by a toxic drug of apoptotic acute myeloid leukemia cells, taken by a 40-MHz ultrasound backscatter microscope (Czarnota *et al.*, 1999; 2001). Note the strong increase in backscatter brightness of speckle as the apoptotic process is maximized at 48 hours. The corresponding optical microscope views show differences in the size and arrangement of individual cells. At the 6-hour point, 95% of the cells underwent nuclear condensation or fragmentation; the nuclear diameter, originally 70% of the cell diameter, shrank to a nuclear diameter that is 40% of the cell diameter.

Because the cells themselves could not be resolved in the images, tissue characterization, in the form of spectral analysis developed by Lizzi's group and described in Section 9.5.7, was applied to the RF data from the images (Kolios *et al.*, 2002). Analysis of leukemia cells demonstrated significant changes in the scattering slope and in the midband value of the slope, which increased by 13 dB between healthy and apoptotic cells (shown in Figure 9.22). The slope values correlated with a decreasing mean scatterer radius.

As indicated by Figure 9.21, there are noticeable changes in the patterns and sizes of the cells during the process of apoptosis, and the number of cells on the order of a

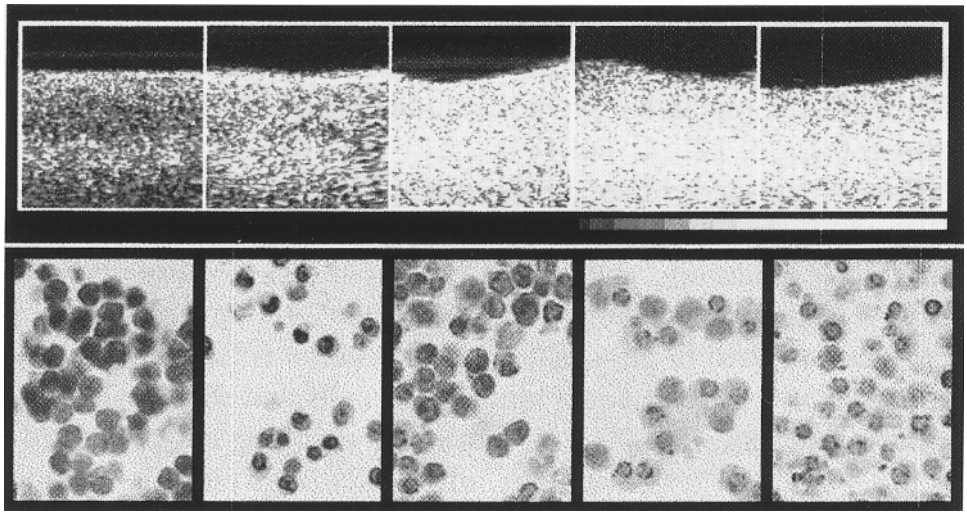

Figure 9.21 Ultrasound imaging of apoptosis and correlative histology. Sequential panels show cells at 0, 6, 12, 24, and 48 hours after treatment with a toxic drug. Each panel is approximately 5 mm wide. (Top row) 40-MHz ultrasound backscatter images of cells. (Bottom row) Optical microscopic images of stained cells; field of view is approximately 50 μm (from Czarnota *et al.*, 1999; 2001, reprinted with permission from Nature Publishing Group).

resolution cell is still countable. Unlike imaging at lower conventional frequencies, the backscatter appears to be more related to the specific arrangement of cells. Work is underway (Baddour *et al.*, 2002) to develop an ensemble model in which each cell is modeled as an elastic Faran–Hickling sphere (see Sections 8.2.3 and 9.2), and different patterns of cells, such as those in Figure 9.23, can be incorporated to mimic those observed during apoptosis. The model is producing results that match the observation that backscatter increases as the cells die and as their lattice structure becomes more randomized.

High-frequency, noninvasive backscatter imaging has been used for high-resolution internal evaluation of blood vessels (IVUS), the eye, and skin (Knapik *et al.*, 2000). Modes normally associated with conventional ultrasound, such as pulsed Doppler (Christopher *et al.*, 1997) and color flow imaging (Goertz *et al.*, 2000) (real-time modes described in detail in Chapter 11), have been miniaturized to work at high frequencies.

Surprisingly, one of the main motivations for creating a fully functional high-frequency imaging system is the mouse (Foster *et al.*, 2000). Mice share 90% of the same genes as humans, and many of their organs, such as the heart, liver, and kidneys, are similar to that of humans. Therefore, a mouse can serve as a model for human physiology and metabolism. The life span of a mouse is 18 to 33 months, and a human's is 50 to 90 years; therefore, 1 mouse day is roughly like 1 human month in terms of its equivalent length. Researchers can alter the mouse genome in predictable ways to express selected traits or susceptibility to disease. These transgenic mice can

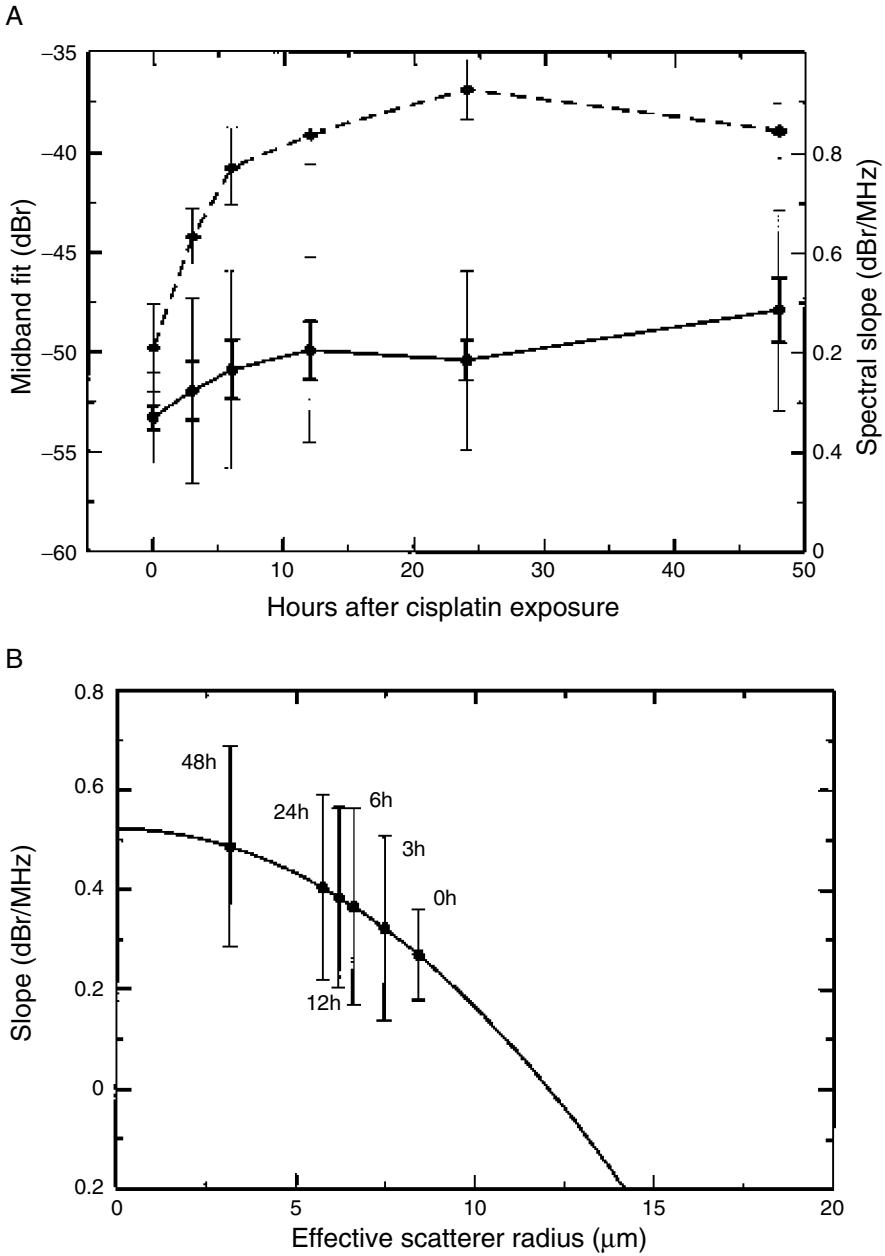

Figure 9.22 Spectral features of backscatter from leukemia at indicated times after exposure to a toxic drug. (A) Plot of spectral slope (solid curve, right axis) and midband slope value. (B) Plot of theoretical predictions of spectral slope versus scatterer radius compared to data from a 34-MHz transducer (from Kolios *et al.*, 2002, with permission from the World Federation of Ultrasound in Medicine and Biology).

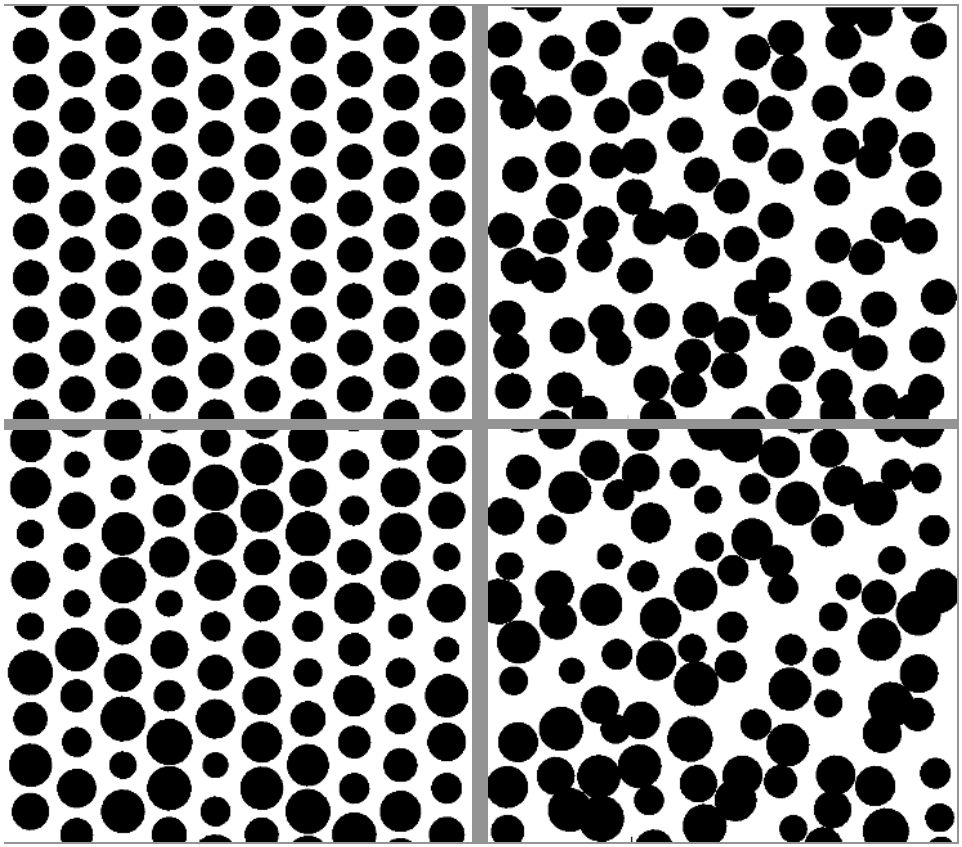

Figure 9.23 A few possible cell ensemble packings (only cell nuclei are shown). From left: perfect crystal, cell locations are allowed some degree of randomization, nucleus diameters are allowed some degree of randomization, both cell locations and nucleus diameters are randomized (from Baddour *et al.*, 2002, *IEEE*).

serve as models of disease progression as well as models of the effects of healing therapies and treatment strategies on an accelerated time scale.

High-frequency ultrasound can be used to study the physiology and morphology of mice noninvasively. High-resolution images of the internal growth of mice are now possible, as shown by the sequence of mouse embryo images in Figure 9.24 (Turnbull *et al.*, 1995; Aristizabal *et al.*, 1998; Srinivasan *et al.*, 1998; Turnbull, 1999; Turnbull *et al.*, 1999). These remarkable images are revealing growth patterns in ways never seen before.

In addition to cardiovascular disease, the progression of cancer has been studied (Turnbull *et al.*, 1996). Skin cancer or melanomas were monitored with 50-MHz ultrasound imaging from detection until their growth to a few millimeters in a few days. Sizes from images agreed to within a few percentage with the measured size of excised tumors.

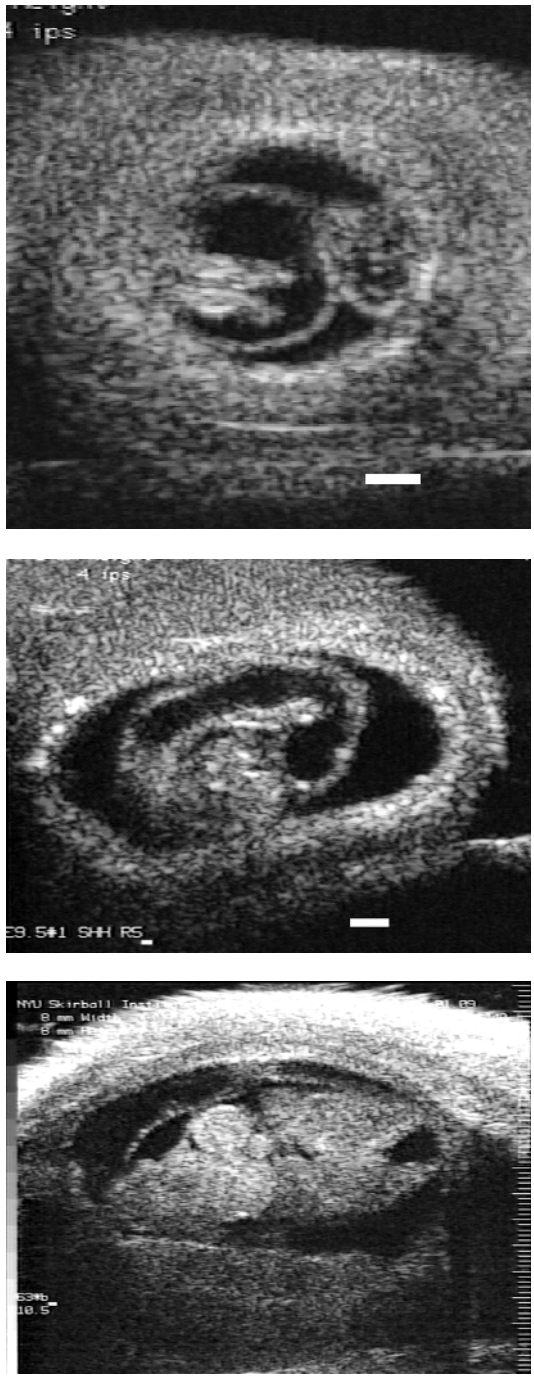

Figure 9.24 40-MHz ultrasound images of a live mouse embryo during development (courtesy of D.H. Turnbull).

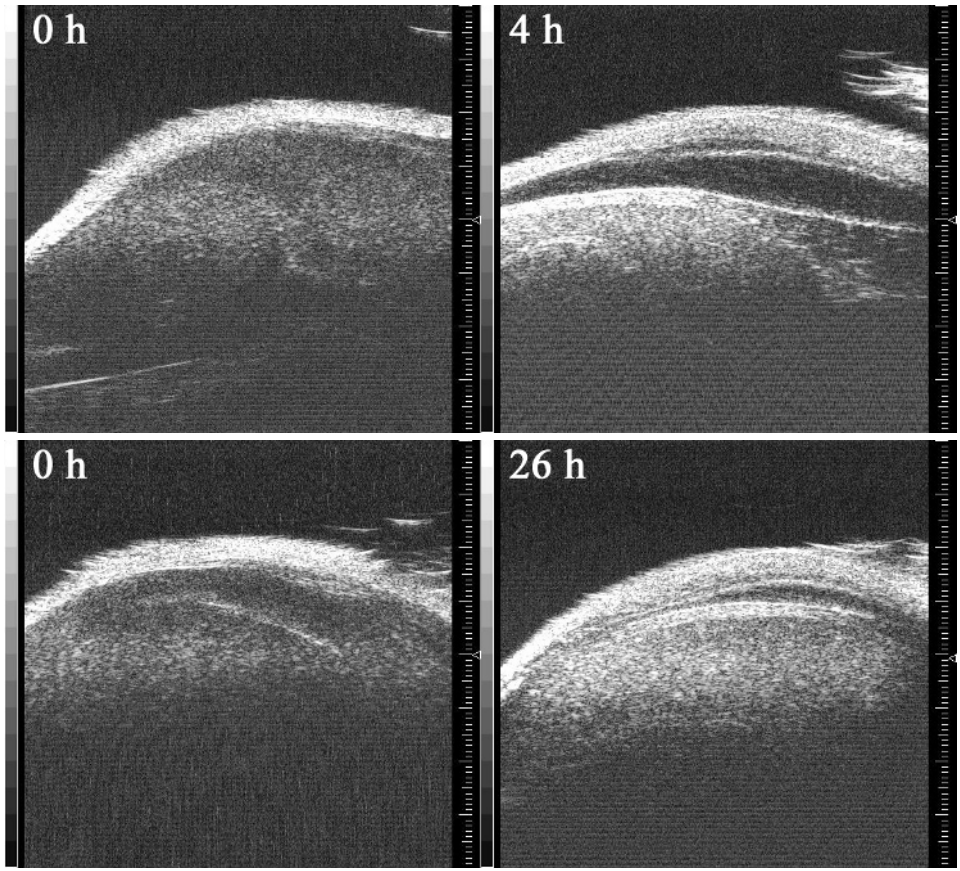

Figure 9.25 Ultrasonic B-mode images of human malignant melanoma tumors grown in mice (each row is a different mouse), immediately before laser irradiation during photodynamic treatment (0 h), and at two different time points after treatment (from Baddour *et al.*, 2002, *IEEE*).

Baddour *et al*. (2002) investigated the effect of photodynamic cancer therapy on human malignant melanoma in mice and monitored changes with 40-MHz ultrasound imaging. As shown in Figure 9.25, edema appeared as a bright region in the treated area, visible in the image 4 hours after treatment. By 26 hours, the edema had almost disappeared, and a very bright region was observed in the treated area. In these images, a combination of both high resolution and increased backscatter can be seen. As resolution increases, the number of scatterers per resolution cell dramatically decreases, yet the physical size of the cells stays the same; therefore, the cell size in wavelengths increases. What may be possible in the future is to take advantage of both the improved image definition and the added benefit of additional tissue structural information hidden in the backscatter (described earlier in this section).

9.6.4 Texture Analysis and Image Analysis

Most often, RF data are examined by individual lines; however, larger-scale structural information about tissues can also be found by combining data from different lines. Multiple line analysis can be done either in the RF or video domain.

As discussed earlier in Section 8.4.3, speckle is in part an artifact of the measurement system; however, textural differences in localized image regions can be indicative of tissue microstructure. Speckle and the image itself are also strongly affected by tissue absorption and diffraction, complicating the classification of tissue. Patterns in an image can be examined by second-order statistics in terms of the spatial autocovariance function. Thijssen (2000) points out that these statistics change with the number of scatterers within the resolution cell and other factors interfere.

Earlier methods did not account for these effects. Coolen *et al*. (1999) examined these sources of variability using first-order (mean and signal-to-noise ratios) and second-order statistics from the co-occurrence matrix of the data. After they corrected the video data for nonlinear imaging system effects, such as preprocessing and compression (to be described in Chapter 10), they found that the chief causes of variability were speckle noise and intervening inhomogeneous tissue along acoustic paths. By comparing these features with healthy liver and tumors, they were able to detect differences. Huisman and Thijssen (1998) investigated *in vivo* video data for the liver, and after exclusion of small blood vessels from their analysis, they discovered an inhomogeneous parenchyma background, fluctuations they hypothesized to be small perfusion variations on a subsegmental scale.

Another approach to overcome the interfering factors was developed by Hao *et al*. (2000). A gradient co-occurrence matrix and features from wavelet analysis were combined to form a vector for each pixel. At each location, this vector was compared to others on a global basis, as well as to its nearest neighbors on a ''geographic similarity'' basis for regional classification. This method was applied to 8.5-MHz intracardiac images of a pig under controlled laboratory conditions, and segmentation regions were compared to physicians' classification and histology (as shown in Figure 9.26).

9.7 ELASTOGRAPHY

B-mode ultrasound imaging, while an excellent all-around means of examining tissue, is poor at distinguishing stiff tissue from soft or compliant tissue. An important class of tissue, such as tumors and cirrhosis of the liver, grow out of the same tissue matrix material, and as a result, even though these types of tissue are stiffer or more fibrotic, they can be invisible under normal B-mode imaging. Palpation, a common method for looking for tumors or nodules in the breast, consists of pressing tissue by hand and looking for smaller displacements for hard nodules than those expected for soft tissue.

Ways of improving the ultrasonic contrast and detection of lesions, especially deep ones, were examined to replace the inexact and often fallible method of palpation. Sarvazyan (1993) suggested that high tissue contrast could be obtained by using shear

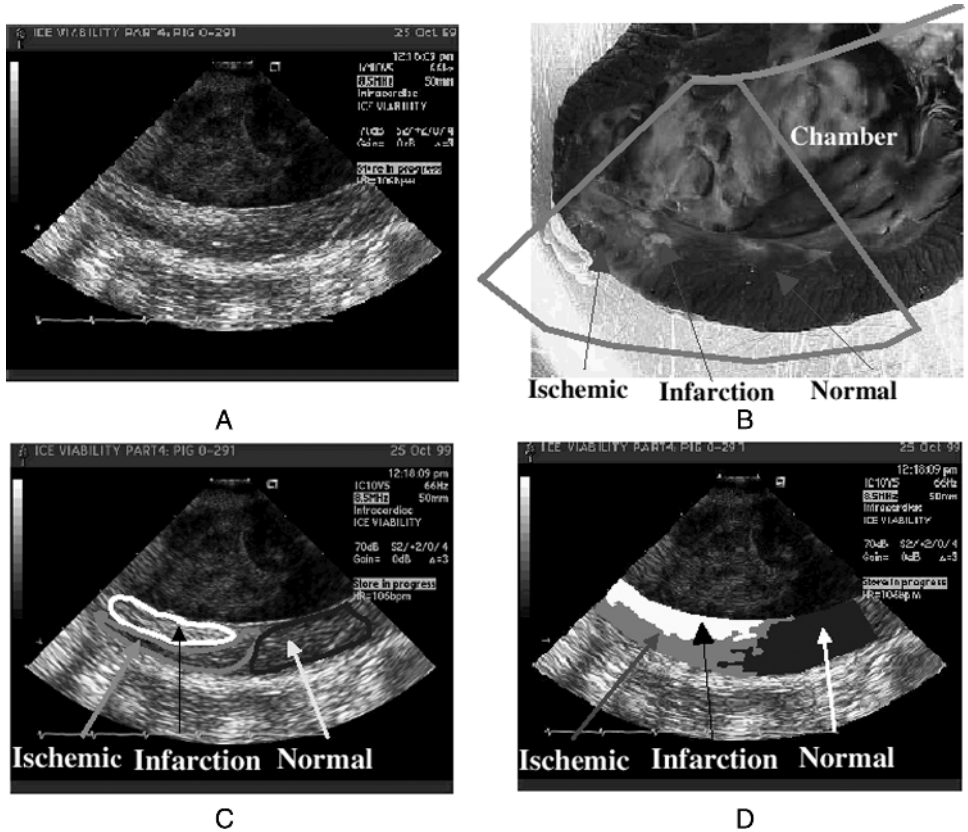

Figure 9.26 Segmentation of the ischemic myocardium. (A) Original ultrasound image. (B) The pathology gross image of the heart. (C) Three regions predicted by a cardiologist. (D) The segmented classification results (reprinted with permission from Hao, *et al.*, *Ultrasonics Symp. Proc.*, 2000, *IEEE*) (see also color insert).

waves; however, the transduction of shear waves and high absorption losses proved to be difficult barriers.

An appreciation for the elastic nature of tissue (presented in Section 3.3), which included shear waves, eventually led to a new area of investigation called elastography. Elastography, a branch of tissue characterization, is the measurement and/or depiction of the elastic properties of tissues. At the present time, elastography is an active area of research with already demonstrated clinical potential. While this term encompasses a number of diverse techniques, these techniques can be roughly categorized into three groups (shown in Figure 9.27). The dynamic method, sonoelasticity, incorporates a low-frequency vibrational source to shake the tissue in addition to the imaging transducer. Elastography, as originally conceived, consists of a static (or quasi-static) application of pressure during imaging. A newer set of applications, which is called "organic" here, relies on the natural movements of the body to supply the deformation of tissue needed for elastographic data.

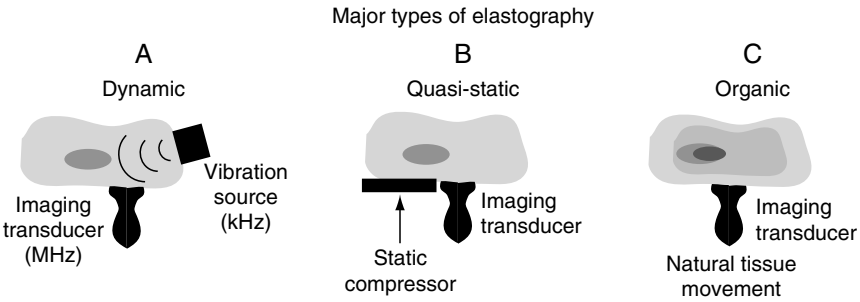

Figure 9.27 Main types of elastography: (A) sonoelasticity, (B) quasistatic, and (C) organic.

The basic operating principle of elastography involves the comparison of the spatial arrangement of tissue initially at equilibrium to itself after deformation. Recall Figure 3.8, which depicts a finger depressing a rectangular solid. As the vertical dimension of the block is decreased by the vertical pressure applied, the initial stress (T) is converted to lateral strains that cause the sides to bulge out. Mathematically, this phenomena is described by Hooke's law, $T = C: S$, Eq. (3.41b). Components of strain are combinations of the spatial derivatives of displacements in different directions, and stress and strain are related through a 6×6 elastic modulus matrix (C), which was described in Section 3.3.1. Elastography, then, is usually a determination of the relative displacements caused by a static or dynamic deformation, as well as a creation of a strain amplitude image. With more information, such as knowledge of the stress field at equilibrium and other factors, different elastic moduli can be calculated and represented as a parameterized image. Reviews of elastography can be found in Gao *et al*. (1996) and Ophir *et al*. (2000).

Early antecedents and forms of tissue elasticity detection were reviewed by Gao *et al*. (1996). One of the first successful forms of real-time elastography was sonoelasticity (Lerner *et al*., 1988; Parker and Lerner, 1992). As indicated in Figure 9.27a, a low-frequency (20–1000 Hz) vibration source was applied to the tissue of interest. This excitation caused the tissue to respond, and, depending on the shape of the tissue or organ and its structure and elastic boundary conditions, to resonate and form multiple reflected modes. These responses were detected by a modified color flow imaging system (a mode normally used to create an image of blood flow through Doppler detection, as described in Chapters 10 and 11). The resulting parameterized image was visualized as a green overlay on the B-mode image, with green-scale brightness proportional to vibration amplitude. Stiffer nonresponsive regions had lower amplitudes; for example, a hard tumor would appear as a dark region (as illustrated by Figure 9.28). Gao *et al*. (1995) derived a theory for sonoelasticity based on shear waves in a lossy elastic (viscoelastic) medium. Rubens *et al*. (1995) demonstrated that the sonoelasticity detected prostate cancer *in vitro* in real-time with better sensitivity than B-mode imaging. They found that 64% of pathologically confirmed tumors detected by this method were invisible by standard imaging.

Several groups have contributed to a growing body of research centered on methods that involve the deformation of tissue under an applied quasi-static load.

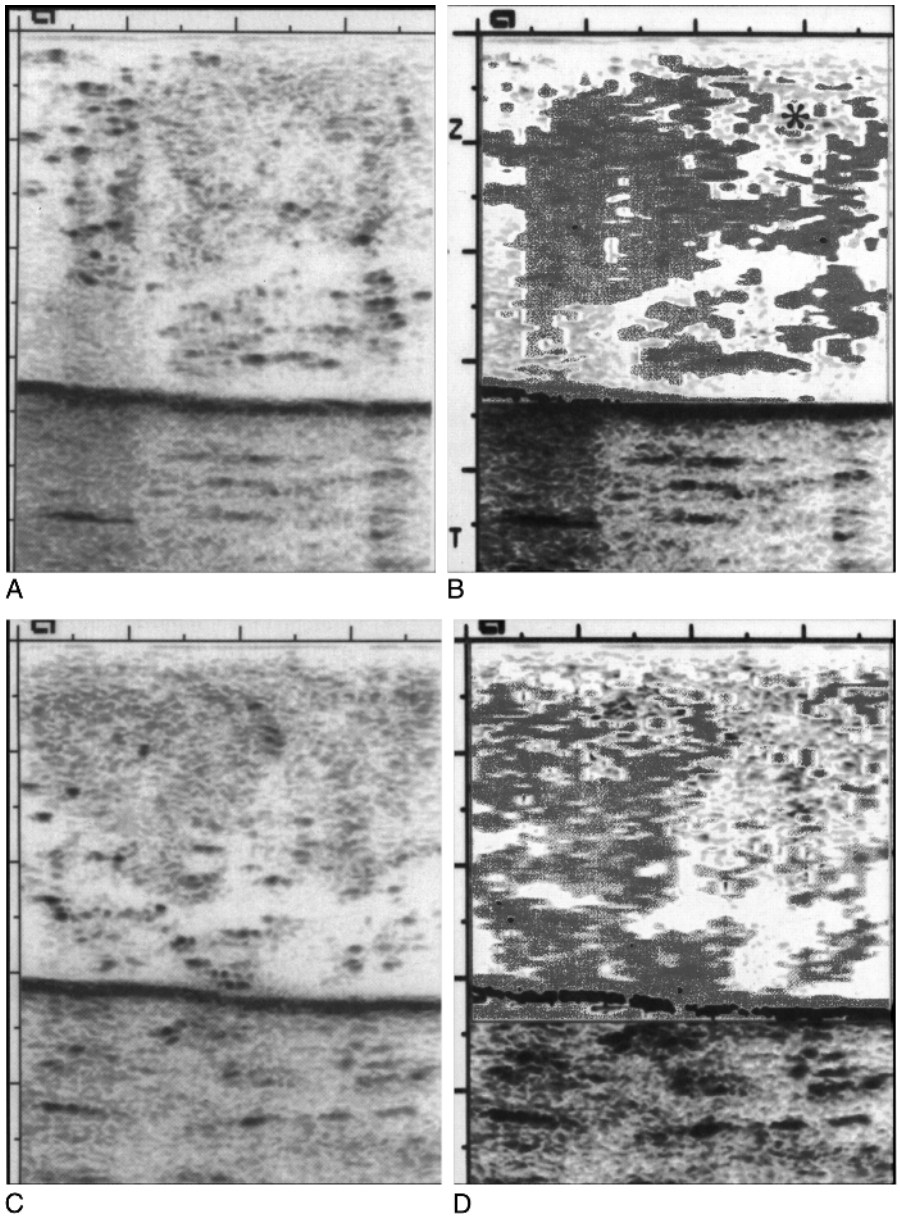

Figure 9.28 Diffuse carcinoma demonstrated at multiple frequencies in a 69-year-old man with no palpable abnormality and a serum PSA level of 6.7 ng/mL. (A) Standard prone transverse ultrasound image obtained at the base of the prostate demonstrates somewhat heterogeneous echo-texture. (B) Corresponding sonoelasticity image obtained at 50 Hz shows poor vibration diffusely, most pronounced posteriorly on the right (*). (C) A second section of the base, obtained slightly caudal to (A), shows a heterogeneous gray-scale pattern. (D) Corresponding sonoelasticity image obtained at 150-Hz documents absent bilateral posterior and right anterior vibration (from Rubens *et al.*, 1995, reprinted by permission of RSNA) (see also color insert).

Figure 9.27b Ophir *et al*. (2000) provides a comprehensive review of methods. Typically, a frame of RF lines is obtained for the tissue at equilibrium in a "precompression" state. Next, a small static uniaxial plane force is applied to the tissue, and once equilibrium is reached again for this "postcompression" state, another frame of RF data is acquired. The overall change in axial length is small ($dz/z < 1\%$), so the postcompression time records are shorter by $2dz/c$. These RF lines are zero-padded to the same length as the precompression data, and corresponding lines from the frames are cross-correlated. Locations from cross-correlation peaks from this operation indicate the delay changes of the deformations. Local axial strain can be estimated from the delay changes in a time window,

$$S_n = \frac{t_{n+1} - t_n}{2dz/c} \tag{9.12}$$

where t_n is the time shift for segment or time window n. The estimates of local strain for all RF lines can be combined to produce a strain image. A similar operation can be applied to obtain lateral strain and create two-dimensional images of strain (not just axial strain images). The amount of force applied must be enough to overcome noise but not great enough to cause decorrelation effects and remain in the linear range of elasticity. Two review articles (Gao *et al*., 1996; Ophir *et al*., 2000) detail a number of signal processing improvements (Insana *et al*., 1996), as well as a theoretical framework for estimating the quality of elastograms (Varghese and Ophir, 1997). Doyley *et al*. (2001) evaluated the performance of a freehand approach to creating strain elastograms using speckle tracking (Trahey *et al*., 1988).

Elastography has been applied to a number of tissues, including the prostate (Rubens *et al*., 1995; Krouskopf *et al*., 1998; Kallel *et al*., 1999a), breast (Parker and Lerner, 1992; Ce'spedes *et al*. 1993; Garra *et al*., 1997; Krouskopf *et al*., 1998), liver and kidney (Parker and Lerner, 1992), and muscle (Ce'spedes *et al*. 1993; Levinson *et al*., 1995), as well as to high intensity focused ultrasound (HIFU)-induced lesions in soft tissue (Kallel *et al*., 1999b). An example of a strain image made with the quasi-static method is given by Figure 9.29.

In these applications, the tissue was assumed to be stationary. In organic elastography (depicted in Figure 9.27c), the tissue deformation comes from the natural rhythms of the body. In particular, heartbeat can be an appropriate stimulus. Two major applications use the heartbeat as an appropriate stimulus: arterial contractions (de Korte *et al*., 1997; 2000) for IVUS imaging, and the heart motion itself (Konofagou *et al*., 2002) for echocardiology. Examples of IVUS elastograms are shown with the stimulus waveforms in Figure 9.30.

In addition to one-dimensional and two-dimensional strain images, orthogonal image planes can be acquired for the out-of-plane (or elevation plane) strain component to obtain a three-dimensional estimate of strain (Konofagou and Ophir, 1998). Either longitudinal or shear strain can be displayed. Without this extra data, a plane stress or plane strain approximation is made for image plane data. In fact, a number of approximations are often made in elastography, such as the isotropy, incompressibility, and linear elasticity of tissue. Fortunately, for isotropic materials, there are only two independent elastic moduli (as described in Section 3.3.1).

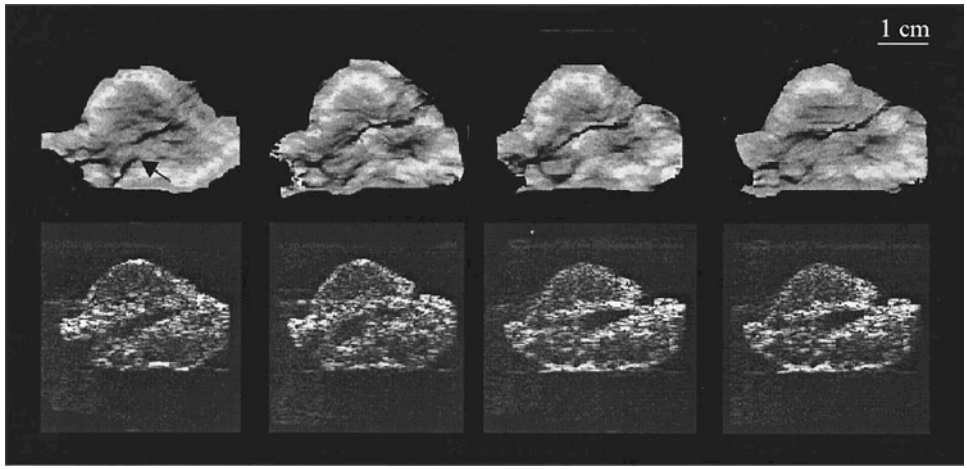

Figure 9.29 Parasagittal views near and at the center of a canine prostate *in vitro,* obtained from a Diasonics Spectra scanner at 5 MHz. (Top row) Axial strain elastograms, where white represents regions of low strain, and black represents regions of high strain. The apex is on the right, and the base is on the left. Observe the clear depiction of the urethra and of some of the ducts, the excellent contrast between the outer and the inner gland, and the visualization of the verumontanum as a low strain area located at the distal central part of the urethra (two center images). In these elastograms, black = soft; white = hard. (Bottom row) The corresponding sonograms from which the elastograms were computed (from Kallel *et al.*, 1999a, reprinted with permission of Dynamedia, Inc.).

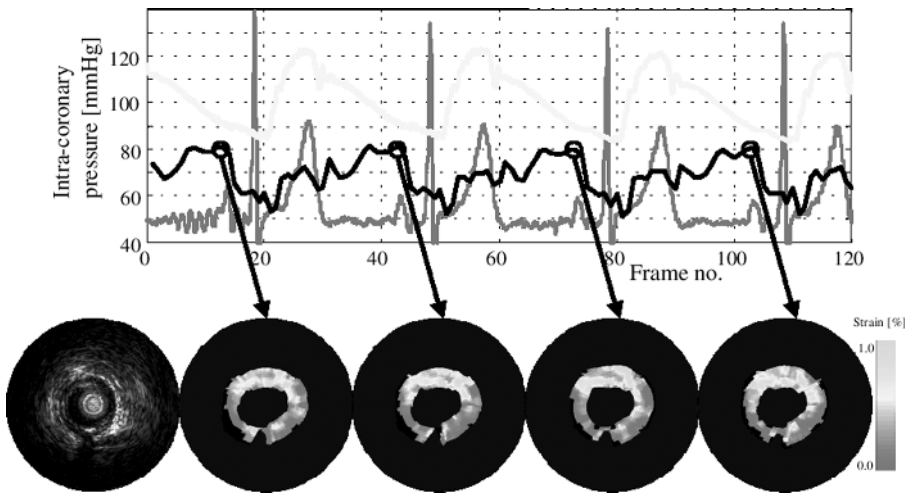

Figure 9.30 Reproducibility of IVUS elastography with elastic stimuli. The upper panel shows the physiologic signals. Echo frames acquired near end-diastole were used to determine the elastograms. The elastograms indicate that the plaque between 9 and 3 o'clock has high strain values, indicating soft material. The remaining part has low strain values, indicating hard material. At 6 o'clock a calcified spot is visible in the echogram, corroborating the low strain values (from de Korte *et al.*, 2000, *IEEE*) (see also color insert).

Because strain images are difficult to interpret, attempts have been made to calculate an elastic modulus and present it as an ''elastic modulus'' or ''stiffness'' image. Most often, the shear modulus is meant. One approach to finding this modulus is to either measure or assume the form of the stress field, in addition to measuring the strain field, and to invert Hooke's law. Other moduli (Ophir *et al*., 1999) can be determined and displayed, such as Young's modulus or Poisson's ratio (defined in Section 3.3.1). Alternatives are to predict the strain with a forward model, given the Young's modulus as a function of position, forces, and specific boundary conditions (O'Donnell *et al*. 1994; Skovoroda *et al*., 1994, 1995). Barbone and Bamber (2002) have examined the conditions necessary to obtain a unique solution for these inversions.

Most often, under clinical circumstances, information is incomplete. Gao *et al*. (1996) identified four areas that would aid the development of elastography. The first is expanding the limited amount of data on the elastic properties of different tissues (Fung, 1981), especially the differences between healthy and pathological types. The second involves a more complete accounting and incorporation of the spatial and spectral properties of mechanical sources in the methods used. Third, as this chapter has emphasized, the complex nature of tissue structure, responses, anisotropy, and losses need to be accounted for and modeled in a more realistic fashion. Fourth, very little is known about the *in vivo* boundary conditions of the tissues under examination; this information is necessary for more accurate inversions.

Despite these growth areas, elastography is already providing unique and valuable clinical information, especially for cancer detection, that cannot be obtained by other methods. As more information about the elastic characteristics of tissue is gathered and as the challenges of clinical application and signal processing are met, indications are that elastography will evolve into a valuable tissue characterization and ultrasound imaging method.

A combined imaging mode is magnetic resonance elastography (Greenleaf *et al*., 1998). By modulating the frequency and phase of a transverse acoustic wave relative to the magnetic field gradient of a magnetic resonance imaging (MRI) scanner, it is possible to image the progression of trasverse waves. From a computation of the local wavelength and knowledge of the density of the material, a quantitative image of the shear modulus can be created.

9.8 ABERRATION CORRECTION

If the design of a typical ultrasound standard-phased array beamformer is based on propagation into a homogeneous medium with speed of sound of 1.54 mm/μs, how well does it work in body with heterogeneous tissue? To first order, array imaging works reasonably well, mainly because of the similarity among the sound speeds in different types of tissues (discussed in Section 1.2). These beamformers depend on coherent phasing of identical waveforms, but as seen in Section 9.4, propagation in real tissue breaks up wavefronts and amplitude consistency. As a result, less than ideal performance is achieved (as discussed in Section 7.9.1 for defective or imperfect array elements). It is well known that some people are difficult to image. These topics lead

us to the subject of aberration (a term for focusing errors) and the possibility of correcting for these body propagation effects to recover the potential available in an imaging system.

The first place people have looked for the causes of aberration is the body wall, which can act as a dirty acoustic window by causing spatially localized differences in amplitude and time delay to waves from different elements in an array (as explained in Section 9.3.1). A cross section of an abdominal wall (as illustrated by Figure 9.7) indicates heterogeneity (the presence of several tissue types), inhomogeneity (variations within a type of tissue), and an irregular thickness. From the simulation, the wavefront of an incoming plane wave is broken up due to a number of effects: scattering, reverberation, refraction, and the cumulative differences in time delay passages through different thicknesses of the wall.

A variety of aberration correction methods have been devised to solve this difficult problem. Solutions usually involve two steps: determining the degree of aberration and correcting for it in an adaptive way. In addition, some methods are suited for real-time correction; others are novel algorithms for corrections based on previous information. Different classes of approaches are reviewed briefly as follows and end with a summary of the problems left to be solved.

Adaptive methods of aberration correction have been reviewed by Steinberg (1992), Ng *et al*. (1994), and Yi (1997). The earliest reported method was by Muller and Buffington (1974) for improving images degraded by atmospheric effects in telescopes. They showed that by maximizing the intensity integral J in the image plane through real-time adjustments of time delay,

$$J = \int I^2(u, v)dudv \tag{9.13}$$

the image can be corrected. Steinberg points out that this operation is equivalent to a multilag spatial correlation operation.

Unlike the astronomical case, small ''beacon'' point targets are not readily available in the body for the error-determining calibration step; therefore, these methods (Fink, 1992; Thomas and Fink, 1996) are limited in their application to medical ultrasound. In certain cases, like for kidney stones, they provide an alternative (Wu *et al*., 1991).

In the 1980s, research on microwave antennas and ultrasound demonstrated that random backscatter, such as that from tissue, can provide measurement of the phase error (Flax and O'Donnell, 1988; O'Donnell and Flax, 1988; Attia and Steinberg, 1989). Another approach was based on the idea embodied in Eq. (9.13), adjusting element delays to maximize regions of target brightness as a quality factor for both point like and diffuse targets (Nock *et al*., 1989; Trahey *et al*., 1990). These methods are based on the premise that the distortions occur in a thin-phase screen adjacent to the transducer. The disruption of coherence is considered to be primarily a phasing effect. Cross-correlation of signals on adjacent elements using a known reference or beacon target or, more practically, random backscatter from tissue, can provide measurement of the phase error. Once the error is known, a delay of the opposite sign and equal to the error is applied to compensate for aberration. Iteration can be applied to reduce the error.

There are a variety of implementations involving adjacent elements, groups of elements, or a summed array waveform for the reference waveform used for each correlation (Ng *et al*., 1994). Those using a small correction reference region are more sensitive to missing or partially inoperable elements (O'Donnell and Engeler, 1992), cumulative errors, and noise than others using larger refence areas. However, because of the van Cittert–Zernike theorem (see Section 8.4.5), elements decorrelate more toward the ends of the array for random scatterers, and this effect presents a possible limitation for large arrays. For 1.5-dimensional (1.5D) arrays, larger separations between elevation rows can cause delay jumps that are difficult to overcome in some situations.

With access to body wall measurements, Wang's group at the University of Rochester explored aberration correction for one-dimensional (1D) to two-dimensional (2D) arrays (Liu and Wang, 1995, 1998). They simulated aberration by passing a spherical wave front through the distortions of actual measured abdominal body wall data. Their method consisted of calculating a reference waveform based on all the waveforms received by the array and their cross-correlation properties, smoothing the delays obtained by cross-correlating each waveform by the reference waveform, correcting for known geometric delays, backpropagating the wavefront using an angular spectrum-of-waves approach until a waveform similarity criterion was maximized, smoothing the wavefront again to remove unusual spikes, and adjusting the wavefront by using arrival time estimates for time shift compensation. While this method is definitely not real-time, it showed that by backpropagating, lower beam sidelobes could be obtained.

This extra step indicates that the infinitely thin phase screen, assumed in other methods, may not be valid, and an approximation to a finite thickness wall could be obtained by placing the phase screen within the locaton of the wall. Further studies showed that improvements could be obtained by correcting the transmitted waveforms (Lacefield and Waag, 2001) as well as the received wavefronts, and by utilizing 2D arrays (Liu and Wang, 1998).

Li (1997) pointed out another overlooked problem in aberration correction: an overemphasis on the focal plane. The focal plane assumption inherent in most correction approaches is that the waveforms from all the elements should be identical or "redundant" under ideal conditions. Away from the focal plane, however, waveforms are no longer identical. Also, for echoes from unknown target distributions, there is no prior knowledge of what the wavefront was, even without aberrations. To overcome these problems, Li proposed a new common midpoint method in the near Fresnel zone (see Section 6.6.2); midpoint methods have been applied in seismic imaging. Li *et al*. (1997) applied the algorithm to phantoms and volunteers and found an improvement in approximately half the cases. A version of this method is evolving (Li, 2000; Li and Robinson, 2000a, 2000b) and has been demonstrated on phantoms.

Perhaps the most challenging aberration correction problem is the female breast (Zhu and Steinberg, 1993). In early experiments on aberration correction concentrated on the liver (O'Donnell and Flax, 1988), amplitude fluctuations were found to be negligible. The heterogeneity of the female breast causes significant refraction and multiple scattering, as is evident from measurements (Zhu and Steinberg, 1994)

and simulation (Tabei *et al*., 2003) and is seen in Figure 9.9. Zhu and Steinberg (1993) and Zhu, Steinberg, and Arenson (1993) conclude that amplitude as well as phase must be corrected for aberration. Liu and Wang (1994) and Odegaard *et al*. (1996) also reported that amplitude correction could be significant. Zhu and Steinberg (1993) show calculations supporting the need for 2D arrays for aberration correction in order to maintain high-quality imaging with low beam sidelobe levels for good contrast resolution. Others investigating 2D apertures for aberration correction include Trahey (1991), Liu and Wang (1995), Li and Robinson (2000a), and O'Donnell and Li (1991).

The most ambitious attempt at real-time adaptive imaging is reported by Rigby *et al*. (1998). Their system consisted of a 128-channel imaging GE LOGIQ 700 system modified to measure and modify delays to each active element with the computing power of 56 PC processors. Active elements of a 2.5–3.75 MHz 1.75D array could be selected via a multiplexer. The array configuration was a 6-row $\times$ 96-column linear array arranged like a 1.5D array except symmetric rows were not connected. The correction algorithm was similar to channel-to-channel correlation (Flax and O'Donnell, 1988; O'Donnell and Engeler, 1992) except a beam-summed waveform was used as a reference for each image line. Corrections were iterated frame-to-frame. Improved images were demonstrated on a phantom with a phase screen aberrator and a liver. Their report ended with two questions: Does the aberration correction provide any significant improvement in ultrasound imaging? Is the effort required to build the required 2D array system worthwhile?

Aberration correction remains a technological challenge. As the more realistic tissue simulations in Figures 9.8–9.10 show, there are many ways wavefront distortion occurs. The RF element data of a cardiac-phased array (plotted in Figure 9.11) reveals that wavefronts, even after normal focusing, are not aligned, are often tilted, and do not extend across all elements. In addition, an imaging transducer compresses a body wall, and its position varies with natural body motions. More on aberration can be found in Section 12.5.5, which shows the effect of body walls on harmonic imaging (see Figures 12.19–12.21), which provides partial imaging improvements.

9.9 WAVE EQUATIONS FOR TISSUE

For a homogeneous tissue medium with loss, the appropriate wave equation from Chapter 4 is

$$\nabla^2 p - \frac{1}{c_0^2}\frac{\partial^2 p}{\partial t^2} - L_\gamma * p = 0 \tag{9.14a}$$

This wave equation translates into the frequency domain in the following form for pressure (P):

$$\nabla^2 P - k_0^2 P - \gamma(\omega) P = 0 \tag{9.14b}$$

where

$$\gamma(\omega) = -\alpha(\omega) - i\beta_E(\omega) \tag{9.14c}$$

is from Chapter 4, and the wave number is $k_0 = \omega/c_0$.

In order to include local variations in sound speed and density as a function of position, the wave equations must change. The wave equation form most frequently used for the Born approximation (Fellingham and Sommer, 1984; Jensen, 1991; Ystad *et al.*, 1996; Angelsen, 2000) is adapted here to include general frequency power law loss. If the density and compressibility as a function of position are divided into an ambient term with a subscript (a) and a small perturbation term denoted by subscript (f) (Ystad *et al.*, 1996),

$$\rho(r) = \rho_a(r) + \rho_f(r) \tag{9.15a}$$

$$\kappa(r, \omega) = \kappa_a(r, \omega) + \kappa_f(r, \omega) \tag{9.15b}$$

and the following are introduced:

$$\varsigma(r) = \frac{\kappa_f(r, \omega)}{\kappa_a(r, \omega)} \tag{9.15c}$$

$$\psi(r) = \frac{\rho_f(r)}{\rho_a(r)} \tag{9.15d}$$

Then the wave equation in the frequency domain can be written as

$$\left(\nabla^2 + k_1^2\right)P - \gamma(r)P = -k_1^2\varsigma(r)P + \nabla[\Psi(r)\nabla P] \tag{9.16a}$$

in which

$$k_1^2(r, \omega) = \omega^2/c_a^2(r) = \omega^2\rho_a(r)\kappa_a(r) \tag{9.16b}$$

and

$$\gamma(r, f) = -\alpha(r, f) - i\beta_E(r, f) \tag{9.16c}$$

and the definitions in Chapter 4 for $\alpha(f)$, Eq. (4.6a), and $\beta_E(f)$, Eq. (4.18), can be used except that $\alpha_0(r)$ and $\alpha_1(r)$ are now functions of position. The time domain counterpart of Eq. (9.16a) can be written as

$$\nabla^2 p - \frac{1}{c_a^2}\frac{\partial^2 p}{\partial t^2} - L_\gamma(r) * p = \frac{\varsigma(r)}{c_a^2}\frac{\partial^2 p}{\partial t^2} + \nabla[\Psi(r)\nabla P] \tag{9.17}$$

where $L_\gamma(r)$, from Eq. (4.17), is now a function of position through $\alpha(r)$.

Note that the left-hand side of these wave equations can be considered to be the part describing propagation through the homogeneous ambient or average tissue material (Ystad *et al.*, 1996; Angelsen, 2000). This part of the equation provides geometric propagation through large-scale homogeneous regions. If the right-hand side is replaced by a delta function, $\delta(r - r_0)$, the solution is a freely propagating Green's function (Ystad *et al.*, 1996; Angelsen, 2000), modified for losses and dispersion. The right-hand side of Eqs. (9.2a)–(9.2b) represent perturbations to this background average value.

Full linear wave equations used for calculations of propagation in heterogeneous tissue are treated in more detail in Mast *et al.* (1997) and Wojcik *et al.* (1997).

Bibliography

Angelsen, B. A. J. (2000). *Ultrasound Imaging: Waves, Signals, and Signal Processing*. Emantec, Norway. A thorough analysis of scattering from tissue.

Bamber, J. C. (1997). *Encyclopedia of Acoustics*, Vol. 4. M. J. Crocker (ed.). John Wiley & Sons, New York, pp. 1703–1725. An overview of the properties of scattering from tissue.

Duck, F. A. (1990). *Physical Properties of Tissue: A Comprehensive Reference Book*. Academic Press, London.

Greenleaf, J. F. and Sehgal, C. M. (1992). *Biologic System Evaluation with Ultrasound*. Springer Verlag, New York. Resource on tissue function scattering, imaging, und characterization.

Kino, G. S. (1987). *Acoustic Waves: Devices, Imaging, and Signal Processing*. Prentice-Hall, Englewood Cliffs, NJ, pp. 300–357. Introduction to acoustic scattering.

Shung, K. K. and Thieme, G. A. (eds.). (1993). *Ultrasonic Scattering in Biological Tissues*. CRC Press, Boca Raton, FL. Provides details on tissue characterization.

References

American Institute of Ultrasound in Medicine. (July 13, 1990). *Standard Methods for Measuring Performance of Pulse-Echo Ultrasound Imaging Equipment*. Laurel, MD.

Anderson, M. E., Soo, M. S. C., and Trahey, G. E. (1998). Microcalcifications as elastic scatterers under ultrasound. *IEEE Trans. Ultrason. Ferroelec. Freq. Control* **45**, 925–934.

Angelsen, B. A. J. (2000). *Ultrasound Imaging: Waves, Signals, and Signal Processing*. Emantec, Norway.

Aristizabal, O., Christopher, D. A., Foster, F. S., and Turnbull, D. H. (1998). 40 MHz echocardiography scanner for cardiovascular assessment of mouse embryos. *Ultrasound in Med. & Biol*. **24**, 1407–1417.

Attia, H. A. and Steinberg, B. D. (1989). Self-cohering large antenna arrays using the spatial correlation properties of radar clutter. *IEEE Trans. Antenna and Prop*. **37**, 30–38.

Baddour, R. E., Sherar, M. D., Czarnota, G. J., Hunt, J. W., Taggart, L., Giles, A., Farnoud, N. R., and Kolios, M. C. (2002). High frequency ultrasound imaging of changes in cell structure including apoptosis. *IEEE Ultrason. Symp. Proc*., 1598–1603.

Bamber, J. C. (1998). Ultrasonic properties of tissue. *Ultrasound in Medicine*. F. A. Duck, A. C. Baker, and H. C. Starritt (eds.). Institute of Physics Publishing, Bristol, UK.

Barbone, P. E. and Bamber, J. (2002). Quantitative elasticity imaging: What can and cannot be inferred from strain images. *Physics in Med. & Biol*. **47**, 2147–2164.

Berkhoff, A. P., van Den Berg, P. M., and Thijssen, J. M. (1994). Simulation of wave propagation through aberiating layers of biological media, 1994 *IEEE Ultrasonics Symp. Proc*., 1797–1800.

Bridal, S. L., Wallace, K. D., Trousil, R. L., Wickline, S. A., and Miller, J. G. (1996). Frequency dependence of acoustic backscatter from 5 to 65 MHz ($0.06 < ka < 4.0$) of polystyrene beads in argose. *J. Acoust. Soc. Am*. **100**, 1841–1848.

Ce'spedes, I. and Ophir, J. (1990). Diffraction correction methods for pulse-echo acoustic attenuation estimation. *Ultrasound in Med. & Biol*. **16**, 707–717.

Ce'spedes, I., Ophir, J., Ponnekanti, H., and Maklad, N. (1993). Elastography: Elasticity imaging using ultrasound with application to muscle and breast in vivo. *Ultrason. Imag*. **15**, 73–88.

Chaturvedi, P., and Insana, M. F. (1996). Error bounds on ultrasonic scatterer size estimates. *J. Acoust. Soc. Am.* **100**, 392–399.

Chen, J.-F. and Zagzebski, J. A. (1996). Frequency dependence of backscatter coeffcient versus scatterer volume fraction. *IEEE Trans. Ultrason. Ferroelec. Freq. Control* **43**, 345–353.

Chen, J.-F., Zagzebski, J. A., and Madsen, E. L. (1993). Tests of backscatter coeffcient measurement using broadband pulses. *IEEE Trans. Ultrason. Ferroelec. Freq. Control* **40**, 603–607.

Chen, X., Phillips, D., Schwarz, K. Q., Mottley, J. G., and Parker, K. J. (1997). The measurement of backscatter coefficient from a broadband pulse-echo system: A new formulation. *IEEE Trans. Ultrason. Ferroelec. Freq. Control* **44**, 515–525.

Christopher, D. A., Starkoski, B. G., Burns, P. N., and Foster, F. S. (1997). High frequency pulsed Doppler ultrasound system for detecting and mapping blood flow in the microcirculation. *Ultrasound in Med. & Biol.* **23**, 997–1015.

Coolen, J., Engelbrecht, M. R., and Thijssen, J. M. (1999). Quantitative analysis of ultrasonic B-mode images. *Ultrason. Imag.* **21**, 157–172.

Czarnota, G. J., Kolios, M. C., Abraham, J., Portnoy, M., Ottensmeyer, F. P., Hunt, J. W., and Sherar, M. D. (1999). Ultrasound imaging of apoptosis: High-resolution non-invasive monitoring of programmed cell death in vitro, in situ and in vivo. *Br. J. Cancer* **81**, 520–527.

Czarnota, G. J., Kolios, M. C., Hunt, J. W., and Sherar, M. D. (2001). Ultrasound imaging of apoptosis: DNA-damage effects visualized. In "Methods in Molecular Biology," Chap. 20. *In Situ Detection of DNA Damage: Methods and Protocols*, Vol. 203. V. V. Didenko (ed.), Humana Press, Totowa, NJ.

Czarnota, G. J., Kolios, M. C., Vaziri, H., Benchimol, S., Ottensmeyer, F. P., Sherar, M. D., and Hunt, J. W. (1997). Ultrasonic biomicroscopy of viable, dead and apoptotic cells. *Ultrasound in Med. & Biol.* **23**, 961–965.

D'Astous, F. T. and Foster, F. S. (1986). Frequency dependence of ultrasound attenuation and backscatter in breast tissue. *Ultrasound in Med. & Biol.* **12**, 795–808.

de Korte, C. L., Ce'spedes, E. I., van der Steen, A. F. W., and Lancee, C. T. (1997). Intravascular elasticity imaging using ultrasound: Feasibility studies in phantoms. *Ultrasound in Med. & Biol.* **23**, 735–746.

de Korte, C. L., Doyley, M. M., Carlier, S. G., Mastik, F., van der Steen, A. F. W., Serruys, P. W., and Bom, N. (2000). High resolution IVUS elastography in patients. *IEEE Ultrason. Symp. Proc.*, 1767–1770.

Doyley, M. M., Bamber, J. C., Fuechsel, F., and Bush, N. L. (2001). A freehand elastographic imaging approach for clinical breast imaging: System development and performance evaluation. *Ultrasound in Med. & Biol.* **27**, 1347–1357.

Feleppa, E. J., Ennis, R. D., Schiff, P. B., Wuu, C.-S., Kalisz, A., Ketterling, J., Urban, S., Liu, T., Fair, W. R., Porter, C. R., and Gillespie, J. R. (2001). Spectrum-analysis and neural networks for imaging to detect and treat prostate cancer. *Ultrason. Imag.* **23**, 135–146.

Feleppa, E. J., Lizzi, F. L., Coleman, D. J., and Yaremko, M. M. (1986). Diagnostic spectrum analysis in ophthalmology. *Ultrasound in Med. & Biol.* **12**, 623–631.

Fellingham, L. A. and Sommer, F. G. (1984). Ultrasonic characterization of tisue structure in the in vivo human liver and spleen. *IEEE Trans. Sonics Ultrason.* **SU-31**, 418–428.

Fink, M. (1992). Time reversal of ultrasonic fields, Part I: Basic principles. *IEEE Trans. Ultrason. Ferroelec. Freq. Control*, **39**, 555–566.

Flax, S. W. and O'Donnell, M. (1988). Phase aberration correction using signals from point retlectors and diffuse scatterers: Basic principles. *IEEE Trans. Ultrason. Ferroelec. Freq. Control* **35**, 758–767.

Foster, F. S., Liu, G., Mehi, J., Starkoski, B. S., Adamson, L., Zhou, Y., Harasiecwicz, K. A., and Zan, L. (2000). High frequency ultrasound imaging: From man to mouse. *IEEE Ultrason. Symp. Proc.*, 1633–1638.

Foster, F. S., Pavlin, C. J., Lockwood, G. R., Ryan, L. K., Harasiewicz, K. A., Berube, L. R., and Rauth, A. M. (1993). Principles and applications of ultrasound backscatter microscopy. *IEEE Trans. Ultrason. Ferroelec. Freq. Control* **40**, 608–617.

Fung, Y. C. (1981). *Biomechanical Properties of Living Tissues*. Springer Verlag, New York.

Gao, L., Alam, S. K., Lerner, R. M., and Parker, K. J. (1995). Sonoelasticity imaging: Theory and experimental verification. *J. Acoust. Soc. Am.* **97**, 3875–3886.

Gao, L., Parker, K. J., Lerner, R. M., and Levinson, S. F. (1996). Imaging of elastic properties of tissue: A review. *Ultrasound in Med. & Biol.* **72**, 959–977.

Garra, B. S., Ce'spedes, E. I., Ophir, J. (1997). Elastography of breast lesions: Initial clinical results. *Radiology* **202**, 79–86.

Goertz, D. E., Christopher, D. A.,Yu, J. L., Kerbel, R. S., Burns, P. N., and Foster, F. S. (2000). High frequency colour flow imaging of the microcirculation. *Ultrasound in Med. & Biol.* **26**, 63–71.

Greenleaf, J. F., Ehman, R. L., Fatemi, M., and Muthupillai, R. (1998). Imaging elastic properties of tissue, Chap. 14. *Ultrasound in Medicine*, Medical Science Series. F. A. Duck, A. C. Baker, and H. C. Starritt (eds). Institute of Physics Publishing, Bristol, UK.

Greenleaf, J. F. and Sehgal, C. M. (1992). *Biologic System Evaluation with Ultrasound*. Springer Verlag, New York.

Hall, C. S., Marsh, J. N., Hughes, M. S., Mobley, J., Wallace, K. D., Miller, J. G., and Brandenbeurger. (1997). Broadband measurements of attenuation coefficient and backscatter coefficient for suspensions: A potential calibration tool. *J. Acoust. Soc. Am.* **101**, 1162–1171.

Hall, T. J., Insana, M. F., Harrison, L. A., and Cox, G. G. (1996). Ultrasonic measurement of glomerular diameters in normal adult humans. *Ultrasound in Med. & Biol.* **22**, 987–997.

Hao, X., Bruce, C., Pislaru, C., and Greenleaf, J. F. (2000). A novel region growing method for segmenting ultrasound images. *IEEE Ultrason. Symp. Proc.*, 1717–1720.

Hill, C. R. and Chivers, R. C. (1972). Investigations of backscattering in relation to ultrasonic diagnosis. *Ultrasonics in Biology and Medicine*. L. Filipeczynski (ed.). Polish Scientific Publishers,Warsaw, Poland, pp. 120–123.

Hinkelman, L. M., Metlay, L. A., Churukian, C. J., and Waag, R. C. (1996). Modified Gomori trichrome stain for macroscopic tissue slices. *J. Histotechnology* **19**, 321–323.

Hinkelman, L. M., Mast, T. D., Metlay, L. A., and Waag, R. C. (1998). The effect of abdominal wall morphology on ultrasonic pulse distortion, Part I: Measurements. *J. Acoust. Soc. Am.* **104**, 3635–3649.

Hinkelman, L. M., Szabo, T. L., and Waag, R. C. (1997). Measurements of ultrasonic pulse distortion produced by human chest wall. *J. Acoust. Soc. Am.* **101**, 2365–2373.

Huisman, H. J. and Thijssen, J. M. (1998). An in vivo ultrasonic model of liver parenchyma. *IEEE Trans. Ultrason. Ferroelec. Freq. Control* **45**, 739–750.

Insana, M. F., Bilgen, M., Chaturvedi, P., Hall, T. J., and Bertrandt, M. (1996). Signal processing strategies in acoustic elastography. *IEEE Ultrason. Symp. Proc.*, 1139–1142.

Jensen, J. A. (1991). A model for the propagation and scattering of ultrasound in tissue. *J. Acoust. Soc. Am.* **89**, 182–190.

Kallel, F., Price, R. E., Konofagou, E. E., Ophir, J. (1999a). Elastographic imaging of the normal canine prostrate. *Ultrason. Imag.* **21**, 201–215.

Kallel, F., Stafford, R. J., Price, R. E. Righetti, R., Ophis, J., and Hazle, J. D. (1999b). The feasibility of elastographic visualization of HIFU-induced thermal lesions in soft-tissues. *Ultrasound in Med. & Biol*. **25**, 641–647.

Knapik, D. A., Starkoski, B., Pavlin, C. J., and Foster, F. S. (2000). A 100–200 MHz ultrasound biomicroscope. *IEEE Trans. Ultrason. Ferroelec. Freq. Control* **47**, 1540–1547.

Kolios, M. C., Czarnota, G. J., Lee, M., Hunt, J. W., and Sherar, M. D. (2002). Ultrasonic spectral parameter characterization of apoptosis. *Ultrasound in Med. & Biol*. **28**, 589–597.

Konofagou, E. E., D'Hooge, J., and Ophir, J. (2002). Myocardial elastography: A feasibility study in vivo. *Ultrasound in Med. & Biol*. **28**, 475–482.

Konofagou, E. E., and Ophir, J. (1998). A new elastographic method for estimation and imaging of lateral displacements, lateral strains, corrected axial strains and Poisson's ratios in tissues. *Ultrasound in Med. & Biol*. **24**, 1183–1199.

Krouskopf, T. A., Wheeler, T. M., Kallel, F., Garra, B. S., and Hall, T. (1998). Elastic moduli of breast and prostate tissues under compression. *Ultrason. Imag*. **20**, 260–274.

Lacefield, J. C. and Waag, R. C. (2001). Evaluation of backpropagation methods for transmit focus compensation. *IEEE Ultrason. Symp. Proc*., 1495–1498.

Lerner, R. M., Parker, K. J., Holen, J., Gremiak, R., and Waag, R. C. (1988). Sono-elasticity: Medical elasticity images derived from ultrasound signals in mechanically vibrated targets. *Acoust. Imag*. **16**, 317–327.

Levinson, S. F., Shinagawa, M., and Sato, T. (1995). Sonoelastic determination of human skeletal muscle elasticity. *J. Biomech*. **28**, 1145–1154.

Li, Y. (1997). Phase aberration correction using near-field signal redundancy, Part I: Principles. *IEEE Trans. Ultrason. Ferroelec. Freq. Control*. **44**, 355–371.

Li, Y. (2000). Small element array algorithm for correcting phase aberration using near-field signal redundancy, Part I: Principles. *IEEE Trans. Ultrason. Ferroelec. Freq. Control* **47**, 29–48.

Li, Y. and Robinson, B. (2000a). Phase aberration correction using near-field signal redundancy, two-dimensional array algorithm. *IEEE Ultrason. Symp. Proc*., 1729–1732.

Li, Y. and Robinson, B. (2000b). Small element array algorithm for correcting phase aberration using near-field signal redundancy, Part II: Experimental results. *IEEE Trans. Ultrason. Ferroelec. Freq. Control* **47**, 49–57.

Li, Y. Robinson, B., and Carpenter, D. (1997). Phase aberration correction using near-field signal redundancy, Part II: Experimental results. *IEEE Trans. Ultrason. Ferroelec. Freq. Control* **44**, 372–379.

Liu, D.-L. and Waag, R. C. (1994). Correction of ultrasonic wavefront distortion using back-propagation and a reference waveform method for time-shift compensation. *J. Acoust. Soc. Am*. **96**, 649–660.

Liu, D.-L. and Waag, R. C. (1995). A comparison of ultrasonic wave distortion and compensation in one-dimensional and two-dimensional apertures. *IEEE Trans. Ultrason. Ferroelec. Freq. Control* **42**, 726–733.

Liu, D.-L. and Waag, R. C. (1998). Estimation and correction of ultrasonic wavefront distortion using pulse-echo data received in a two-dimensional aperture. *IEEE Trans. Ultrason. Ferroelec. Freq. Control* **45**, 473–490.

Lizzi, F. L., Astor, M., Fellepa, E. J., Shao, M., and Kalisz, A. (1997). Statistical framework for ultrasonic spectral parameter imaging. *Ultrasound in Med. & Biol*. **23**, 1371–1382.

Lizzi, F. L. and Feleppa, E. J. (1993). In vivo ophthalmological tissue characterization by scattering, Chap. 12. *Ultrasonic Scattering in Biological Tissues*. K. K. Shung and G. A. Thieme (eds.). CRC Press, Boca Raton, FL.

Lizzi, F. L., Greenbaum, M., Feleppa, E. J., and Elbaum, M. (1983). Theoretical framework for spectrum analysis in ultrasonic tissue characterization. *J. Acoust. Soc. Am.* **73**, 1366–1373.

Machado, J. C. and Foster, F. S. (1999). Validation of theoretical diffraction correction functions for strongly focused high frequency ultrasonic transducers. *Ultrason. Imag.* **21**, 96–106.

Madsen, E. L., Insana, M. F., and Zagzebski, J.A. (1984). Method of data reduction for accurate determination of acoustic backscatter coefficients. *J. Acoust. Soc. Am.* **76**, 913–923.

Mast, T. D., Hinkelman, L. M., Orr, M. J., Sparrow, V. W., and Waag, R. C. (1997). Simulation of ultrasonic pulse propagation, through the abdominal wall. *J. Acoust. Soc. Am.* **102**, 1177–1190.

Mast, T. D., Hinkelman, L. M., Metlay, L. A., Orr, M. J., and Waag, R. C. (1999). Simulation of ultrasonic pulse propagation, distortion, and attenuation in the human chest wall. *J. Acoust. Soc. Am.* **106**, 3665–3677.

Mast, T. D., Hinkelman, L. M., Orr, M. J., and Waag, R. C. (1998). The effect of abdominal wall morphology on ultrasonic pulse distortion, Part II: Simulations. *J. Acoust. Soc. Am.* **104**, 3651–3664.

Miller, J. G. *et al.* (1989). Myocardial tissue characterization: Clinical confirmation of laboratory results. *IEEE Ultrason. Symp. Proc.*, 1029–1036.

Miller, J. G. Barzilia, B., Milunski, M. R., Mohr, G. A., Pérez, J. E., Thomas III, L. J., Wear, K. A., Wichline, S. A., Vered, Z., and Sobel, B. E. (1998). Backscatter imaging and myocardial tissue characterization. *IEEE Ultrason. Symp. Proc.*, 1373–1381.

Mottley, J. G. and Miller, J. G. (1988). Anisotropy of the ultrasonic backscatter of myocardial backscatter of myocardial tissue, Part I: Theory and measurements in vitro. *J. Acoust. Soc. Am.* **85**, 755–761.

Mottley, J. G. and Miller, J. G. (1990). Anisotropy of the ultrasonic attenuation in soft tissues: Measurements in vitro. *J. Acoust. Soc. Am.* **88**, 1203–1210.

Mountford, R. A. and Wells, P. N. T. (1972). Ultrasonic liver scanning: The A-scan in the normal and cirrhosis. *Phys. in Med. & Biol.* **17**, 261–269.

Muller, R. A. and Buffington, A. (1974). Real-time correction of atmospherically degraded telescope images through image sharpening. *J. Opt. Soc. Am.* **64**, 1200–1209.

Nassiri, D. K. and Hill, C. R. (1986a). The differential and total bulk acoustic scattering cross-sections of some human and animal tissues. *J. Acoust. Soc. Am.* **79**, 2034–2047.

Nassiri, D. K. and Hill, C. R. (1986b). The use of angular acoustic scattering measurements to estimate structural parameters of human and animal tissues. *J. Acoust. Soc. Am.* **79**, 2048–2054.

Ng, G. C., Worrell, S. S., Freiburger, P. D., and Trahey, G. E. (1994). A comparative evaluation of several algorithms for phase aberration correction. *IEEE Trans. Ultrason. Ferroelec. Freq. Control* **41**, 631–643.

Nock, L., Trahey, G. E., and Smith, S. W. (1989). Phase aberration correction in medical ultrasound using speckle brightness as a quality factor. *J. Acoust. Soc. Am.* **85**, 1819–1833.

Odegaard, L., Halvorsen, E., Ystad, B., Torp, H. G., and Angelsen, B. (1996). Delay and amplitude focusing through the body wall; a simulation study. *IEEE Ultrason. Symp. Proc.*, 1411–1414.

O'Donnell, M., Bauwens, D., Mimbs, J. W., and Miller, J. G. (1979). Broadband integrated backscatter: An approach to spatially localized tissue characterization in vivo. *IEEE Ultrason. Symp. Proc.*, 175–178.

O'Donnell, M. and Engeler, W. E. (1992). Correlation-based aberration correction in the presence of inoperable elements. *IEEE Trans. Ultrason. Ferroelec. Freq. Control* **39**, 700–707.

O'Donnell, M. and Flax, S. W. (1988). Phase aberration measurements in medical ultrasound: Human studies. *Ultrasound Imag.* **10**, 1–11.

O'Donnell, M. and Li, R. G. (1991). Aberration corrected on a two-dimensional anisotropic phased array. *IEEE Ultrason. Symp. Proc.* 1183–1193.

O'Donnell, M., Skovoroda, A. R., Shapo, B. M., and Emelianov, S. Y. (1994). Internal displacement and strain imaging using ultrasonic speckle tracking. *IEEE Trans. Ultrason. Ferroelec. Freq. Control* **41**, 314–325.

Ophir, J., Alam, K. A., and Garra, B. (1999). Elastography: Ultrasonic estimation and imaging of the elastic properties of tissues. *J. Eng. Med.* **213**, 203–233.

Ophir, J., Garra, B., Kallel, F., Konofagou, E., Krouskop, T., Righetti, R., and Varghese, T. (2000). Elastographic imaging. *Ultrasound in Med. & Biol.* **26**, S23–S29.

Parker, K. J. and Lerner, R. M. (1992). Sonoelasticity of organs: Shear waves ring a bell. *J. Ultrasound Med.* **11**, 387–392.

Pedersen, P. C., Chakareski, J., and Lara-Montalvo, R. (2003). Ultrasound characterization of arterial wall structures based on integrated backscatter profiles. *Medical Imaging 2003: Ultrasonic Imaging and Signal Processing*. W. F. Walker and M. F. Insana (eds.), Proc. of SPIE, Vol. 50435, pp. 115–126.

Reid, J. M. (1993). Standard substitution methods for measuring ultrasonic scattering in tissues, Chapter 6. *Ultrasonic Scattering in Biological Tissues*. K. K. Shung and G. A. Thieme (eds.). CRC Press, Boca Raton, FL.

Rigby, K. W., Andarawis, E. A., Chalek, C. L., Haider, B. H., Hinrichs, W. L., Hogel, R. A., Lewe, W. M., Angle, M. G., McEathvon, B. T., Miller, S. C., Pestiman, S. M., Peters, M. A., Thomas, L. J., Krishnan, S., and O'Donnell, M. (1998). Realtime adaptive imaging. *IEEE Ultrason. Symp. Proc.*, 1603–1606.

Romijn, R. L., Thijssen, J. M., Oosterveld, B. J., and Verbeek, A. M. (1991). Ultrasonic differentiation of intracular melanoma: Parameters and estimation methods. *Ultrason. Imag.* **13**, 27–55.

Romijn, R. L., Thijssen, J. M., van Delft, J. L., de Wolff-Rouendaal, D., van Best, J., and Oosterhuis, J. A. (1989). In vivo ultrasound backscattering estimation for tumor diagnosis: An animal study. *Ultrasound in Med. & Biol.* **15**, 471–479.

Rubens, D. J., Hadley, M. A., Alam, S. K., Gao, L., Mayer, R. D., and Parker, K. J. (1995). Sonoelasticity imaging of prostate cancer: In vitro results. *Radiology* **195**, 379–383.

Sarvazyan, A. P. (1993). Shear acoustic properties of soft biological tissues in medical diagnostics. *J. Acoust. Soc. Am.* **93**, 2329.

Sherar, M. D., Noss, M. B., and Foster, F. S. (1987). Ultrasound backscatter microscopy images the internal structure of living tumour spheroids. *Nature* **330**, 493–495.

Shung, K. K., Sigelmann, R. A., and Reid, J. M. (1976). Scattering of ultrasound by blood. *IEEE Trans. Biomed. Eng.* BME-23, 460–467.

Shung, K. K. and Thieme, G. A. (eds.). (1993). *Ultrasonic Scattering in Biological Tissues*. CRC Press, Boca Raton, FL.

Skovoroda, A. R., Emelianov, S. Y., Lubinski, M. A., Sarvazyan, A. P., and O'Donnell, M. (1994). Thoeoretical analysis and verification of ultrasound displacement and strain imaging. *IEEE Trans. Ultrason. Ferroelec. Freq. Control* **41**, 302–313.

Skovoroda, A. R., Emelianov, S. Y., and O'Donnell, M. (1995). Tissue elasticity reconstruction based on ultrasonic displacement and strain images. *IEEE Trans. Ultrason. Ferroelec. Freq. Control* **42**, 747–765.

Sigelmann, R. A. and Reid, J. M. (1973). Analysis and measurement of ultrasound backscattering from an ensemble of scatterers excited by sine-wave bursts. *J. Acoust. Soc. Am.* **53**, 1351–1355.

Srinivasan, S., Baldwin, H. S., Aristizabal, O., Kwee, L., Labow, M., Artman, M., and Turnbull, D. H. (1998). Noninvasive *in utero* imaging of mouse embryonic heart development using 40 MHz echocardiography. *Circulation* **98**, 912–918.

Steinberg, B. D. (1992). A discussion of two wavefront aberration correction procedures. *Ultrason. Imag.* **14**, 387–397.

Szabo, T. L. and Burns, D. R. (1997). Seismic signal processing of ultrasound imaging data. *Acoustical Imaging*, Vol. 23. S. Lees and L. A. Ferrari (eds.). Plenum Press, New York, pp. 131–136.

Tabei, M., Mast, T. D., and Waag, R. C. (2003). Simulation of ultrasonic focus aberration and correction through human tissue. *J. Acoust. Soc. Am.* **113**, 1166–1176.

Taylor, K. W. and Wells, P. N. T. (1989). Tissue characterization *Ultrasound in Med & Biol.* **15**, 421–428.

Thijssen, J. M. (2000). Ultrasonic tissue characterization. *Acoustical Imaging*, Vol. 25. Plenum Press, New York, pp. 9–25.

Thijssen, J. M., Verbeek, A. M., Romijn, R. L., De Wolff-Rouzendaal, D., and Oosterhuis, J. A. (1991). Echographic differentiation of histological types of intraocular melanoma. *Ultrasound in Med. & Biol.* **17**, 127–138.

Thomas, J.-L., and Fink, M. A. (1996). Ultrasonic beam focusing through skull inhomogeneities with a time reversal mirror: Application to transskull therapy. *IEEE Trans. Ultrason. Ferroelec. Freq. Control* **43**, 1122–1129.

Thomas III, L. J., Barzilai, B., Perez, J. E., Sobel, B. E., Wickline, S. A., and Miller, J. G. (1989). Quantitative real-time imaging of myocardium based on ultrasonic integrated backscatter. *IEEE Trans. Ultrason. Ferroelec. Freq. Control* **36**, 466–470.

Trahey, G. E. (1991). An evaluation of transducer design and algorithm performance for two-dimensional phase aberration correction. *IEEE Ultrason. Symp. Proc.*, 1181–1187.

Trahey, G. E., Hubbard, S. M., and von Ramm, O. T. (1988). Angle independent ultrasonic blood flow detection by frame to frame correlation of B-mode images. *Ultrasonics* **26**, 271–276.

Trahey, G. E., Zhao, D., Miglin, J. A., and Smith, S. W. (1990). Experimental results with a real-time adaptive ultrasonic imaging system for viewing through distorting media. *IEEE Trans. Ultrason. Ferroelec. Freq. Control* **37**, 418–427.

Turnbull, D. H. (1999). In utero ultrasound backscatter microscopy of early stage mouse embryos. *Comput. Med. Imag. and Graph.* **23**, 25–31.

Turnbull, D. H., Bloomfield, T. S., Foster, F. S., and Joyner, A. L. (1995). Ultrasound backscatter microscope analysis of early mouse embryonic brain development. *Proc. of the National Academy of Sci.* **92**, 2239–2243.

Turnbull, D. H., Ramsay, J. A., Shivji, G. S., Bloomfield, T. S., From, L., Sauder, D. N., and Foster, F. S. (1996). Ultrasound backscatter microscope analysis of mouse melanoma progression. *Ultrasound in Med. & Biol.* **22**, 845–853.

Ueda, M. and Ozawa, Y. (1985). Spectral analysis of echoes for backscattering measurement. *J. Acoust. Soc. Am.* **77**, 38–47.

Varghese, T. and Ophir, J. (1997). A theoretical framework for performance characterization of elastography. *IEEE Trans. Ultrason. Ferroelec. Freq. Control* **44**, 164–172.

Wang, R. C. and Astheimer, J. P. (1993). Measurement system effects in ultrasonic scattering experiments, Chap. 8. *Ultrasonic Scattering in Biological Tissues*. K. K. Shung and G. A. Thieme (eds.). CRC Press, Boca Raton, FL.

Wells, P. N. T., McCarthy, C. F., Ross, F. G. N., and Read, A. E. A. (1969). Comparison of A-scan and compound B-scan in the diagnosis of liver disease. *Br. J. Radiol.* **42**, 818–823.

Wojcik, G., Fornberg, B., Waag, R., Carcione, L., Mould, J., Nikodym, L., and Driscoll, T. (1997). Pseudospectral methods for large-scale bioacoustic models. *IEEE Ultrason. Symp. Proc*. 1501–1506.

Wu, F., Fink, M., Mallart, R., Thomas, J. L., Chakroun, N., Casserreau, D., and Prada, C. (1991). Optimal focusing through aberrating media: A comparison between time reversal mirror and time delay correction techniques. *IEEE Ultrason. Symp. Proc.*, 1195–1199.

Ystad, B., Halvorsen, E., Odegaard, L., Angelsen, B. A. J., and Lygren, M. (1996). Wave equation based analysis of phase aberrations in inhomogeneous tissue. *IEEE Ultrason. Symp. Proc*., 1353–1356.

Zhu, Q. and Steinberg, B. D. (1993). Wavefront amplitude distortion and image sidelobe levels, Part I: Theory and Computer Simulations. *IEEE Trans. Ultrason. Ferroelec. Freq. Control* **40**, 743–753.

Zhu, Q. and Steinberg, B. D. (1994). Modeling, measurement and correction of wavefront distortion produced by breast specimens. *IEEE Ultrason. Symp. Proc*., 1613–1617.

Zhu, Q., Steinberg, B. D., and Arenson, R. L. (1993). Wavefront amplitude distortion and image sidelobe levels, Part II: In vivo experiments. *IEEE Trans. Ultrason. Ferroelec. Freq. Control* **40**, 754–762.

This page intentionally left blank

10 IMAGING SYSTEMS AND APPLICATIONS

Chapter Contents

10.1 INTRODUCTION

The modern diagnostic imaging system is continuing to evolve and, as a result, is becoming more complicated with new modes and features. System functions are the last blocks added to the overall block diagram (see Figure 2.14). This chapter introduces the basic principles of an imaging system and discusses signal processing techniques. Doppler and color flow imaging are deferred until the next chapter. An amazing variety of transducer types have been invented and adapted to specific clinical uses; therefore, the major clinical uses of ultrasound imaging systems need to be considered also.

In Figure 10.1, the external parts of an ultrasound imaging system are shown. The image display is mounted on a chassis with wheels for portability. On the right side,

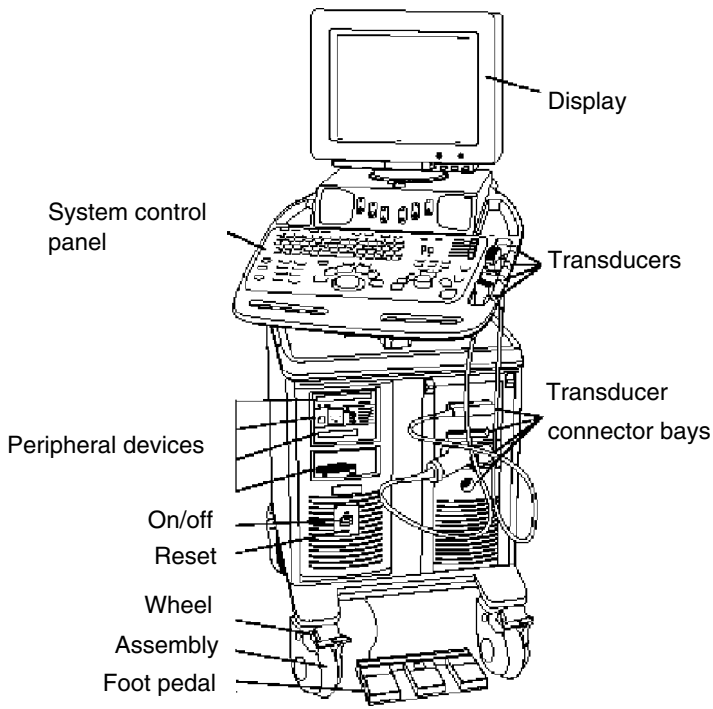

Figure 10.1 External parts of an ultrasound imaging system (courtesy of Philips Medical Systems).

several transducer arrays are stored, awaiting use, and they are attached to the system through several transducer connector bays in the front. Below the display is a keyboard and a number of knobs and switches for controlling the system. Peripheral devices, such as recording media and extra connectors, can be seen. The all-important on/off switch, which is sometimes difficult to find, is also identified.

10.2 TRENDS IN IMAGING SYSTEMS

Ultrasound imaging systems fall into the following commonly used categories: portable, low-end, mid-range, and high-end. The high-end systems are those with the latest and largest number of state-of-the-art features, and they generally produce the best images. Each manufacturer has unique features, called market differentiators, which distinguish their system from others manufactured by the same company, as well from those made by other companies. Over time, some features, because of the competitive nature of the industry, may migrate in altered form to imaging systems of rival manufacturers. Needless to say, because high-end systems have the most features and options, they are the most expensive. A mid-range system does not have some of the high-end features but has a full complement of options necessary to produce very good images in a variety of clinical applications. Low-end systems are usually limited in their functionality and are often designed to cover specific clinical applications. There are exceptions to these general categories.

The ultrasound imaging industry is undergoing dynamic change. One trend is that the new high-end features tend to migrate downward to mid-range systems and eventually to low-end systems over time. This migration is in part caused by the need to replace existing features with new ones to grow the market. Another major force is the parallel development in allied fields such as computation and electronics of enabling technologies (the invisible wind of change discussed in Chapter 1). These developments have already had a profound effect on what is possible with ultrasound as exemplified by the fully functional, portable imaging systems now available.

Portable imaging systems, which are a relatively new development, may provide a more restricted range of options (e.g., fewer transducers) or be fully functional with several transducer options in an extremely small package at a very low cost. Four portable systems were shown in Figure 1.13.

The Minivisor, the first fully portable, self-contained imaging system (mentioned in Chapter 1), is included for historical reference. The Sonosite system was the first modern portable of comparable size (about 6 lbs) and achieved its portability through custom designed ASICS. OptiGo, a portable also based on specialized chips, was designed for cardiac applications. Both of these systems offer color flow imaging and automated features to aid users. The Terason 2000 system achieves its small size and flexibility by leveraging laptop technology and its unique proprietary low power charge domain processor chip. The fully functional 128-channel system consists of a laptop, a 10-oz processor box, and the transducer. These systems were featured in an issue of the *Thoraxcentre Journal* (2001).

10.3 MAJOR CONTROLS

Because there are many controls for a typical ultrasound imaging system and their organization and names vary considerably from manufacturer to manufacturer, the following description is a short list of the major controls according to function. Note that even though the number of actual controls on an imaging system may seem bewildering at first, most systems start in a default set of control settings or ''presets'' that are optimized for a particular clinical application or transducer, so that with clinical training and moderate effort, such as the adjustment of the time gain compensation (TGC) controls, a reasonably good image can be obtained quickly.

A close-up of the system control panel of the same imaging system from Figure 10.1 is illustrated in Figure 10.2. On the right side, the TGC slide controls, transmit focus controls, and scan depth controls are evident.

The main controls identified in the system control panel (depicted in Figure 10.2) are the following:

Probe or transducer selection: Typically two to four transducers can be plugged into connectors in the imaging system, so this switch allows the user to activate one of the arrays at a time.

Mode selection: This provides the means for selecting a mode of operation, such as 2B-mode, color flow, M-mode, or Doppler, individually or in combination (duplex or triplex operation).

Depth of scan control: This adjusts the field of view (scan depth in centimeters).

Focus or transmit focal length selection: This allows the location of the transmit focal length to be moved into a region of interest. The depth location of the focal plane is usually indicated by a > symbol. (Multiple transmit foci can be selected in a

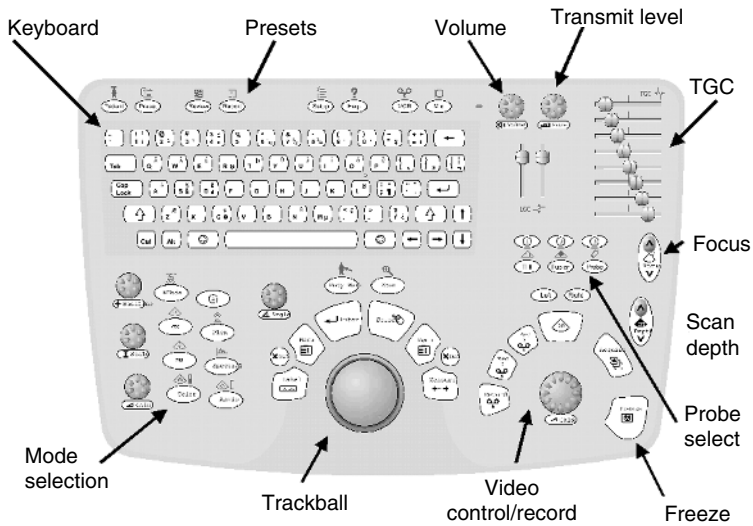

Figure 10.2 Keyboard and display of an ultrasound imaging system (courtesy of Philips Medical Systems).

splice or multiple transmit mode at the sacrifice of frame rate). In pulsed wave Doppler mode, the location of the focal length is often controlled by the center of the Doppler gate position.

Time gain compensation (TGC) controls (also depth gain compensation, time gain control, sensitivity-time control, etc.): These controls offset the loss in signal caused by tissue absorption and diffraction variations; they are usually in the form of slides for controlling amplifier gain individually in each contiguous axial time range. The image depth dimension is divided into a number of zones or stripes, each of which is controlled by a TGC control (discussed in Section 4.6). On some systems, these gains are adjusted automatically based on signal levels in different regions of the image. Some systems also provide the capability to adjust gains in the lateral direction (lateral gain compensation or additional control in the horizontal dimension). Other systems may have an automatic means of setting these controls based on parameters sensed in the signals in the image, sometimes called ''automatic TGC.''

Transmit level control: This adjusts drive amplitude from transmitters (it is done automatically on some systems). In addition to this control, a number of other factors alter acoustic output (discussed in more detail in Chapters 13 and 15). Feedback on acoustic output level is provided by thermal and mechanical indices on the display (also discussed in more detail in Chapters 13 and 15). A freeze control stops transmission of acoustic output.

Display controls: Primarily, these controls allow optimization of the presentation of information on the display and include a logarithmic compression control, selection of preprocessing and postprocessing curves, and color maps, as well as the ability to adjust the size of the images from individual modes selected for multimode operation. Provision is usually available for recording video images, playing them back, and comparing and sending them in various formats.

10.4 BLOCK DIAGRAM

The hidden interior of a digital imaging system is represented functionally by a generic simplified block diagram (shown by Figure 10.3). For now, the general operation of an imaging system is discussed (more details will be presented later).

A description of this block diagram follows:

User interface: Most of the blocks are hidden from the user, who mainly sees the keyboard and display, which are part of a group of controls called the ''user interface.'' This is the part of the system by which the user can configure the system to work in a desired mode of operation. System displays showing software configurable menus and controls (soft-keys) in combination with knobs or slider controls and switches, as well as the main image display monitor, provide visual feedback that the selected mode is operating. The user interface provides the means of getting information in and out of the system through connectors to the system. Main connections include a computer hookup to a local area network (LAN) to Digital Imaging and Communication in Medicine (DICOM) communication and networking, and to peripherals such as

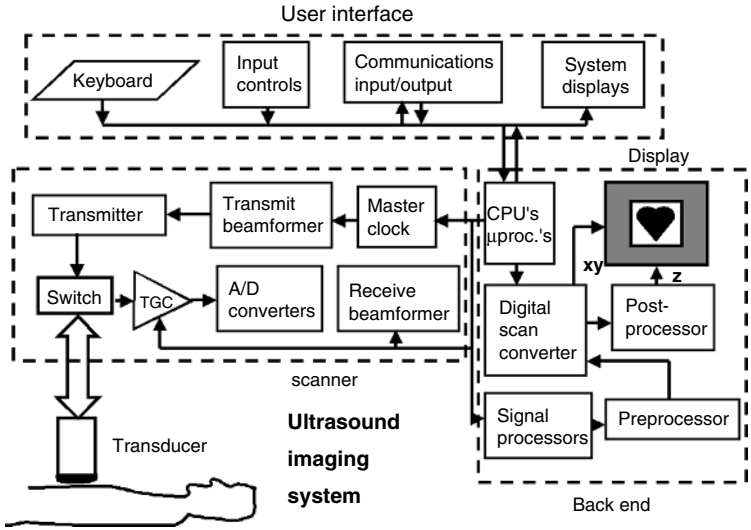

Figure 10.3 Block diagram of a generic digital ultrasound imaging system.

printers. Various recording devices, such as VCRs, and memory storage devices, such as read/write CD-ROMs and DAT drives, can be attached.

Controller (computers): A typical system will have one or more microprocessors or a PC that directs the operation of the entire system. The controller senses the settings of the controls and input devices, such as the keyboard, and executes the commands to control the hardware to function in the desired mode. It orchestrates the necessary setup of the transmit and receive beamformers as well as the signal processing, display, and output functions. Another important duty of the computer is to regulate and estimate the level of acoustic output in real time.

Front end: This grouping within the scanner is the gateway of signals going in and out of the selected transducer. Under microprocessor transmit control, excitation pulses are sent to the transducer from the transmitter circuitry. Pulse-echo signals from the body are received by array elements and go through individual user-adjustable TGC amplifiers to offset the weakening of echoes by body attenuation and diffraction with distance. These signals then pass on to the receive beamformer.

Scanner (beamforming and signal processing): These parts of the signal chain provide the important function of organizing the many signals of the elements into coherent timelines of echoes for creating each line in the image. The transmit beamformer sends pulses to the elements. Echo signals pass through an analog-to-digital (A/D) converter for digital beamforming. In addition, the scanner carries out signal processing, including filtering, creation of quadrature signals, and different modes such as Doppler and color flow.

Back end: This grouping of functions is associated with image formation, display, and image metrics. The input to this group of functions is a set of pulse-echo envelope lines formed from each beamformed radiofrequency (RF) data line. Image formation is achieved by organizing the lines and putting them through a digital scan converter

that transforms them into a raster scan format for display on a video or PC monitor. Along the way, appropriate preprocessing and postprocessing, log compression, and color or gray-scale mapping are completed. Image overlays containing alpha-numeric characters and other information are added in image planes. Also available in the back end are various metric programs, such as measuring the length of a fetal femur, calculating areas, or performing videodensitometry. Controls are also available for changing the format of the information displayed.

10.5 MAJOR MODES

The following are major modes on a typical imaging system:

Angio (mode): This is the same as the power Doppler mode (see Figure 11.23).

B-mode: This is a brightness-modulated image in which depth is along the z axis and azimuth is along the x axis. It is also known as "B-scan" or "2D mode." The position of the echo is determined by its acoustic transit time and beam direction in the plane. Alternatively, an imaging plane contains the propagation or depth axis (see Figure 9.1).

Color flow imaging (mode): A spatial map is overlaid on a B-mode gray-scale image that depicts an estimate of blood flow mean velocity, indicating the direction of flow encoded in colors (often blue away from the transducer and red toward it), the amplitude of mean velocity by brightness, and turbulence by a third color (often green). It is also known as a "color flow Doppler." Visualization is usually two-dimensional (2D) but can also be three-dimensional (3D) or four-dimensional (4D) (see Figure 10.6a).

Color M-mode: This mode of operation has color flow depiction at the same vector location where depth is the y deflection (fast time), and the x deflection is the same color flow line shown as a function of slow time. This mode displays the time history of a single color flow line at the same spatial position over time (see Figure 11.24).

Continuous wave (CW) Doppler: This Doppler mode is sensitive to the Doppler shift of blood flow all along a line (see Figure 11.13).

M-mode: This mode of operation is brightness modulated, where depth is the y deflection (fast time), and the x deflection is the same imaging line shown as a function of slow time. This mode displays the time history of a single line at the same spatial position over time (see Figure 10.4).

Doppler mode: This is the presentation of the Doppler spectrum (continuous wave or pulsed wave).

Color Doppler (mode): A 2D Doppler image of blood flow is color-coded to show the direction of flow to and away from the transducer (see Figure 10.6a).

Power Doppler (mode): This color-coded image of blood flow is based on intensity rather than on direction of flow, with a paler color representing higher intensity. It is also known as "angio" (see Figure 11.23).

Pulsed wave Doppler: This Doppler mode uses pulses to measure flow in a region of interest (see Figures 11.15 and 11.21).

Duplex: Presentation of two modes simultaneously: usually 2D and pulsed (wave) Doppler (see Figure 10.5).

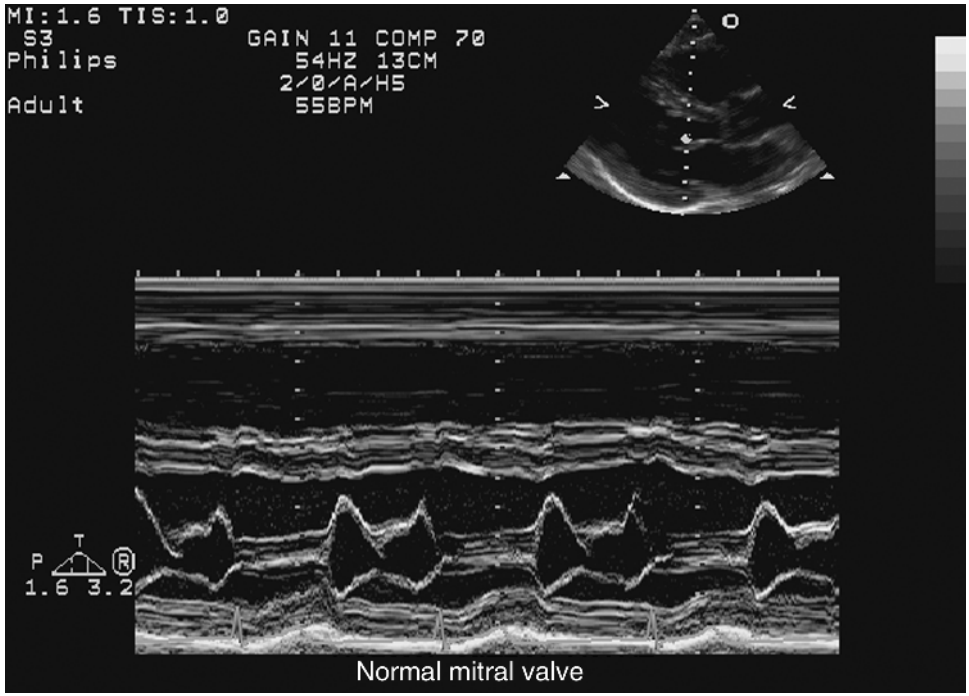

Figure 10.4 Duplex M-mode image. The insert (above right of the sector image) shows the orientation of the M-mode (courtesy of Philips Medical Systems).

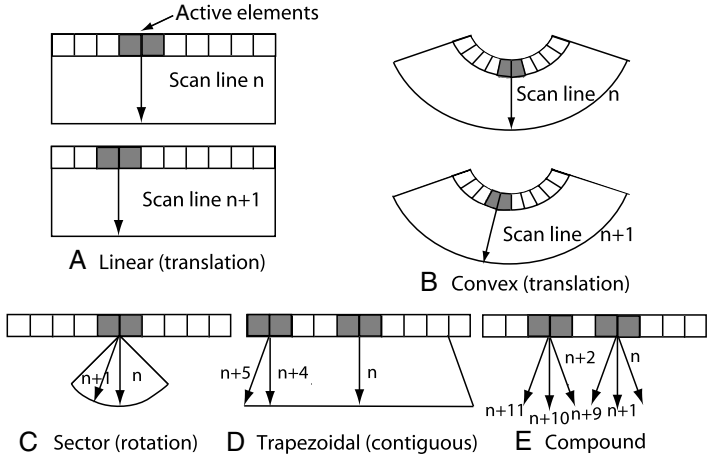

Figure 10.5 Time-sequenced image formats. (A) Basic linear (translation). (B) Convex curved linear (translation). (C) Basic sector (rotation). (D) Trapezoidal (contiguous: rotation, translation, and rotation). (E) Compound (translation and rotation at each active aperture position).

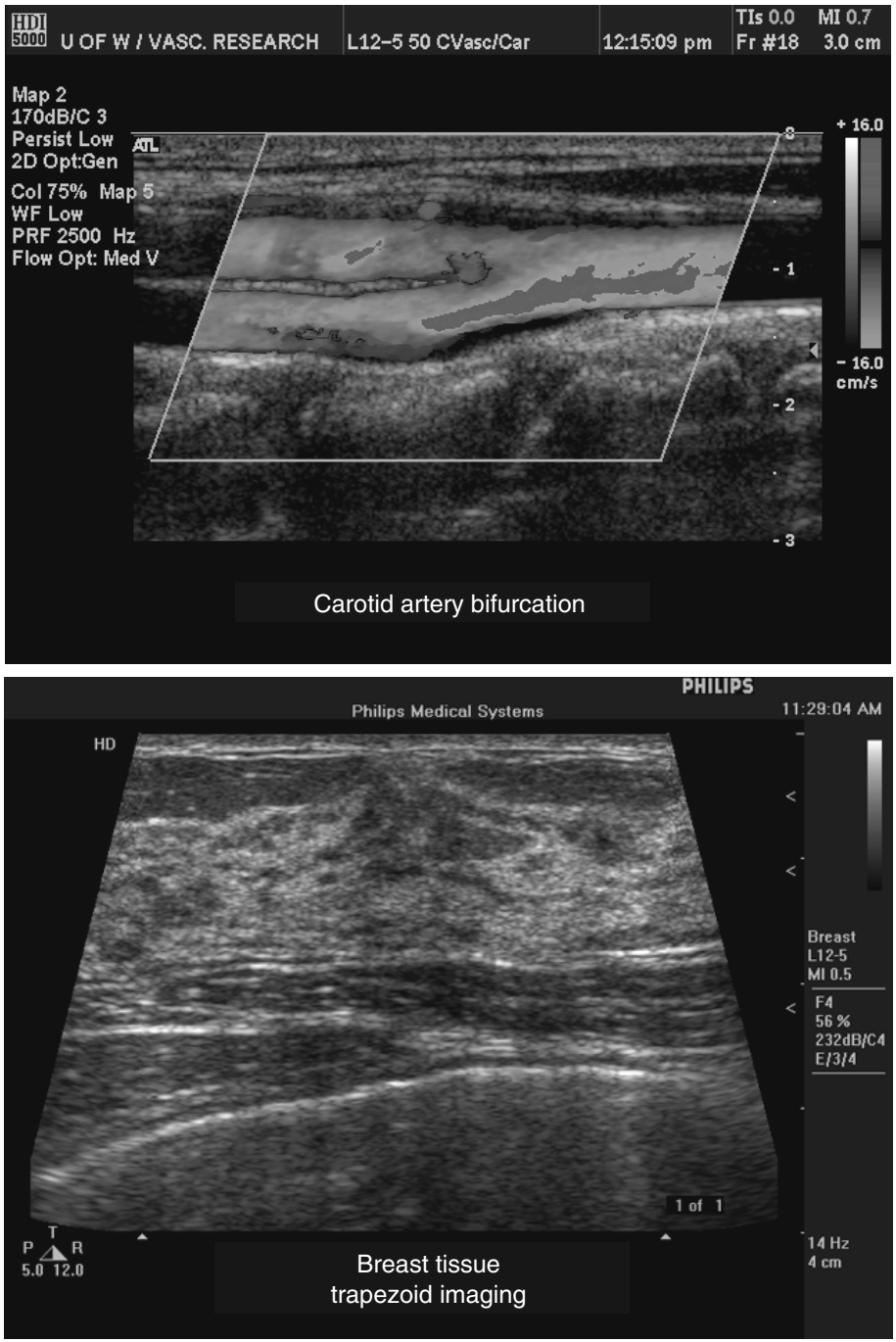

Figure 10.6 (A) Parallelogram-style color flow image from a linear array with steering. (B) Trapezoidal form at of a linear array with sector steering on either side of a straight rectangular imaging segment. Described as a contiguous imaging format in Chapter 1 (courtesy of Philips Medical Systems) (see also color insert).

Triplex: Presentation of three modes simultaneously: usually 2D, color flow, and pulsed Doppler (see Figures 11.13 and 11.15)
2D: (B-mode) imaging in a plane, with the brightness modulated
3D: This is a image representation of a volume or 3D object, such as the heart or fetus. Surface rendering can be used to visualize surfaces. Another image presentation is volume rendering, in which surfaces can be semitransparent or 2D slice planes through the object. Alternatively, there is simultaneous viewing of different 2D slice planes (side by side).
4D: A 3D image moving in time
Zoom: Video zoom is a magnification of a region of interest in the video image. Alternatively, acoustic zoom is a magnification of the region of interest in which acoustic and/or imaging parameters are modified to enhance the image, such as placing the transmit focus in the region of interest and/or increasing the number of image lines in the region.

10.6 CLINICAL APPLICATIONS

Diagnostic ultrasound has found wide application for different parts of the human body, as well as in veterinary medicine. The major categories of ultrasound imaging are listed below.

Major Imaging Categories:
Breast: Imaging of female (usually) breasts
Cardiac: Imaging of the heart
Gynecologic: Imaging of the female reproductive organs
Radiology: Imaging of the internal organs of the abdomen
Obstetrics (sometimes combined with Gynecologic as in OB/GYN): Imaging of fetuses *in vivo*
Pediatrics: Imaging of children
Vascular: Imaging of the (usually peripheral as in peripheral vascular) arteries and veins of the vascular system (called ''cardiovascular'' when combined with heart imaging)

Specialized applications have been honored by their own terminology. Many of these terms were derived from the location of the acoustic window where the transducer is placed, as well as the application. ''Window'' refers to an access region or opening through which ultrasound can be transmitted easily into the body. Note that transducers most often couple energy in and out of the body through the use of an externally applied couplant, which is usually a water-based gel or fluid placed between the transducer and the body surface. Transducers, in addition to being designed ergonomically to fit comfortably in the hand for long periods of use, are designed with the necessary form factors to provide access to or through the windows described later.

Major Imaging Applications:

(Note that ''intra'' (from Latin) means into or inside, ''trans'' means through or across, and ''endo'' means within.)

Endovaginal: Imaging the female pelvis using the vagina as an acoustic window

Intracardiac: Imaging from within the heart
Intraoperative: Imaging during a surgical procedure
Intravascular: Imaging of the interior of arteries and veins from transducers inserted in them
Laproscopic: Imaging carried out to guide and evaluate laparoscopic surgery made through small incisions
Musculoskeletal: Imaging of muscles, tendons, and ligaments
Small parts: High-resolution imaging applied to superficial tissues, musculature, and vessels near the skin surface
Transcranial: Imaging through the skull (usually through windows such as the temple or eye) of the brain and its associated vasculature
Transesophageal: Imaging of internal organs (especially the heart) from specially designed probes made to go inside the esophagus
Transorbital: Imaging of the eye or through the eye as an acoustic window
Transrectal: Imaging of the pelvis using the rectum as an acoustic window
Transthoracic: External imaging from the surface of the chest

10.7 TRANSDUCERS AND IMAGE FORMATS

10.7.1 Image Formats and Transducer Types

Why do images come in different shapes? The answer depends on the selected transducer, without which there would be no ultrasound imaging system. Our discussion emphasizes types of arrays (the most prevalent form of transducers in ultrasound imaging). The focus will be on widely used physical forms of arrays adapted for different clinical applications and their resulting image formats.

Early ultrasound imaging systems employed single-element transducers, which were mechanically scanned in an angular or linear direction or both (as described in Chapter 1). Most of these transducers moved in a nearly acoustically transparent cap filled with a coupling fluid. The first practical arrays were annular arrays that consisted of a circular disk cut into concentric rings, each of which could be given a delayed excitation appropriate for electronic focusing along the beam axis. These arrays also had to be rotated or scanned in a cap, and they provided variable focusing and aperture control for far better imaging than is available with fixed-focus, single-element transducers. A detailed description of the design and performance of a real-time, digital 12-element annular array ultrasound imaging system is available in Foster *et al*. (1989a, 1989b).

Another early array was the linear array (discussed in Chapter 1). The linear array may have up to 300–400 elements, but at any specific time, only a few (forming an active element group) are functioning at a time. The active contiguous elements form the active aperture. At one end of the array, an active element group turns on, as selected by a multiplexer (also called a "mux") that is receiving commands from the beamformer controller. Refer to Figure 10.5a, where the active elements are shaded to generate line number n. After the first pulse echoes are received for the first image

vector line (centered in the middle of this group), an element nearest the end of the array is switched off and the element next to the other end of the group is added as a new element. In this way, the next sequential line (numbered $n+1$) is formed, and this ''tractor-treading'' process continues as the active group slides along the length of the array, picking up and dropping an element at each line position. Switches are necessary if the number of elements in the array exceeds the number of receive channels available. The overall image format is rectangular in shape.

The main difference between a linear and a phased array is steering. The phased array has an active aperture that is always centered in the middle of the array, but the aperture may vary in the number of elements excited at any given time (discussed shortly). As shown in Figure 10.5c, the different lines are formed sequentially by steering until a sector (an angular section of a circle), usually about 90° in width, is completed. The phased array has a small ''footprint'' or contact surface area with the body. A common application for this type of an array is cardiac imaging, which requires that the transducer fit in the intercostal spaces between the ribs (typically 10–14 mm). The advantage of this array is that despite its small physical size, it can image a large region within the body.

Because it was easier to produce a fixed focal delay without steering for each line, linear arrays were the first to appear commercially (recall Chapter 1). In this tradition, convex linear arrays combined the advantage of a larger angular image extent with ease of linear array focusing without the need for electronic steering. Convex arrays may be regarded as linear arrays on a curved surface. As depicted in Figure 10.5b, a convex array has a similar line sequencing to a linear array except that its physical curvature directs the image line into a different angular direction. Because of the lack of steering, linear and convex arrays have a relaxed requirement for periodicity 1–3 wavelengths rather than the $\frac{1}{2}$ wavelength usually used for phased arrays.

Recent exceptions to this approach are linear arrays with finer periodicity so that they can have limited steering capability either for Doppler or color flow imaging. In this case, once the extent of steering is decided, periodicity can be determined from grating lobe calculations (see Chapter 7). Two common applications are parallelogram (also known as a steered linear) and trapezoidal imaging, in which sector-steered image segments are added to the ends of a rectangular image in a contiguous fashion (shown in Figure 10.5d). Actual imaging examples are given by Figure 10.7.

Another use of more finely sampled linear arrays with steering capabilities is compound imaging. As shown in Figure 10.5e, compound imaging is a combination of limited steering by an active group and translation of the active group to the next position for the next set of lines or image vectors. More information and imaging examples of a real-time implementation of this method will be discussed in Section 10.11.4.

The number of active elements selected for transmission is usually governed by a constant F number (F#). The −6-dB full width half maximum (FWHM) beamwidth can be shown to be approximately $FWHM = 0.4\lambda F/L = 0.4\lambda F\#$ from Eq. (6.9c). To achieve a constant lateral resolution for each deeper focal length (F), the aperture (L) is increased to maintain a constant F# until the full aperture available is reached. In a typical image, one transmit focal length is selected along with dynamic focusing on

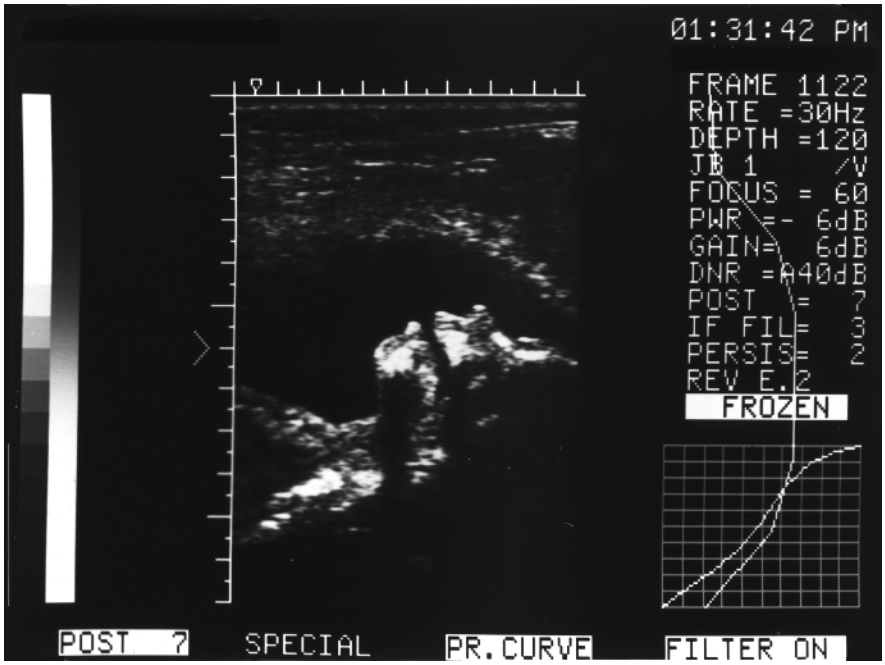

A

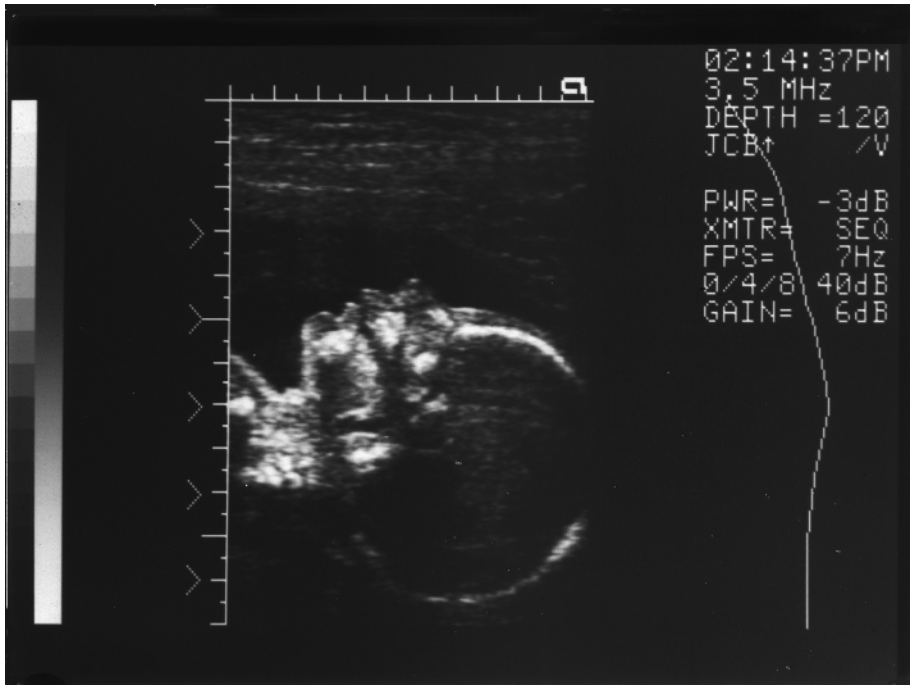

B

Figure 10.7 Transmit focusing of fetal head with (A) a single focus zone and (B) multiple spliced focal zones (courtesy of Siemens Medical Solutions, Inc. Ultrasound Group).

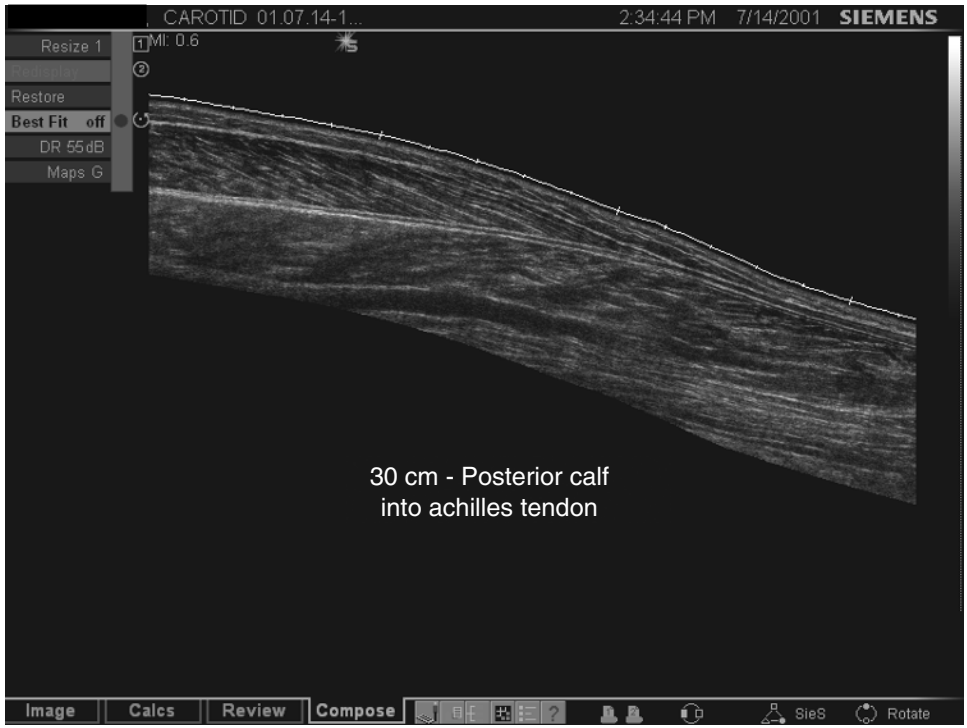

Figure 10.8 SieScape or panoramic image made by a transducer swept along a body surface (courtesy of Siemens Medical Solutions, Inc. Ultrasound Group).

receive. At the expense of frame rate, it is possible to improve resolution by transmitting at several different transmit focal lengths in succession and then splicing together the best parts. The strips or time ranges contain the best lateral resolution (like a layer cake) to make a composite image of superb resolution (Maslak, 1985). See Figure 10.7 for an example. For this method, a constant F# provides a similar resolution in each of the strips as focal depth is increased.

To overcome the small field of view limitation in typical ultrasound images, a method of stitching together a panoramic view (such as that shown in Figure 10.8) was invented. Even though the transducer is scanned freehand across the skin surface to be imaged, advanced image processing is used to combine the contiguously scanned images in real time (Tirulmalai *et al*., 2000). Other modes can also be shown in this type of presentation.

10.7.2 Transducer Implementations

Driven by many clinical needs, transducers appear in a wide variety of forms and sizes (as indicated by Figure 10.9). From left to right in this figure, there is a transesophageal probe mounted on the end of a gastroscope, a convex array, a linear array,

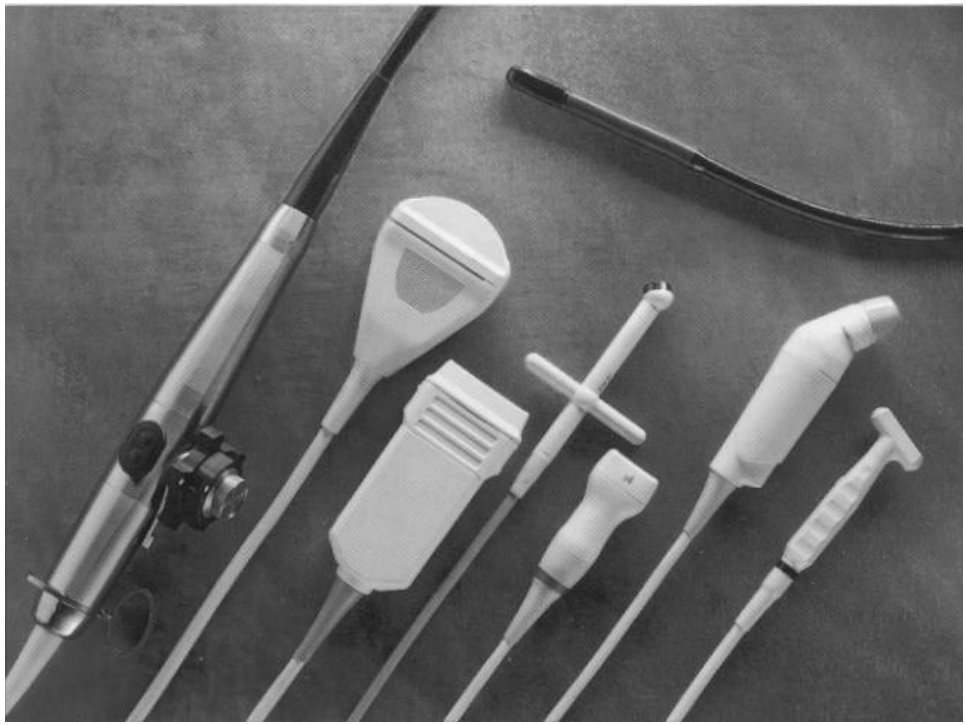

Figure 10.9 Transducer family portrait. From left to right, transesophageal array with positioning assembly, convex (curved) linear array, linear array, stand alone CW Doppler probe, phased array, transthoracic motorized rotatable phased array, and high-frequency intraoperative linear array (courtesy of Philips Medical Systems).

a ''stand-alone'' CW Doppler two-element transducer, a phased array, a motorized transthoracic array with an internal motor drive for 3D acquisition, and an intraoperative probe. The transesophageal probe (shown at the tip in the top center of the figure) is mounted in a gastroscope assembly (at extreme left of figure) to provide flexible positioning control of the transducer attitude within the throat. Transesophageal arrays couple through the natural fluids in the esophagus and provide cleaner windows to the interior of the body (especially the heart) than transducers applied externally through body walls. The endovaginal and transrectal probes (not shown) are designed to be inserted. The intraoperative and specialty arrays provide better access for surgical and near-surface views in regions sometimes difficult to access. These probes can provide images before, during, or after surgical procedures.

The more conventional linear, curved linear, and phased arrays have typical azimuth apertures that vary in length from 25 to 60 mm and elevation apertures that are 2–16 mm, depending on center frequency and clinical application. Recall that the aperture size in wavelengths is a determining factor. The number of elements in a 1D array vary from 32 to 400. Typical center frequencies range from 1 MHz (for

harmonic imaging) to 15 MHz (for high-resolution imaging of superficial structures). As discussed in Chapter 6, there has been a trend toward wider fractional bandwidths, which now range from 30–100%.

At first, array systems functioned at only one frequency because of the narrow fractional bandwidth available. As transducer design improved, wider bandwidth allowed for operation at a higher imaging frequency simultaneously with a lower-frequency narrowband Doppler or color flow mode (as indicated in Figure 10.10b). This dual frequency operation was made possible by two different transmit frequencies combined with appropriate receive filtering, all operating within the transducer bandwidth. The next generation of transducers made possible imaging at more than one frequency, as well as operation of the Doppler-like modes (see Figure 10.10c). At the present time (with new materials), this direction is continuing so that a single transducer array can function at multiple center frequencies (as shown in Figure 10.10d). This type of bandwidth means that one transducer can replace two or three others, permit harmonic imaging with good sensitivity, and provide higher image quality (to be described in Section 10.11.3). Broad bandwidths are also essential for harmonic imaging (to be described in Chapter 12).

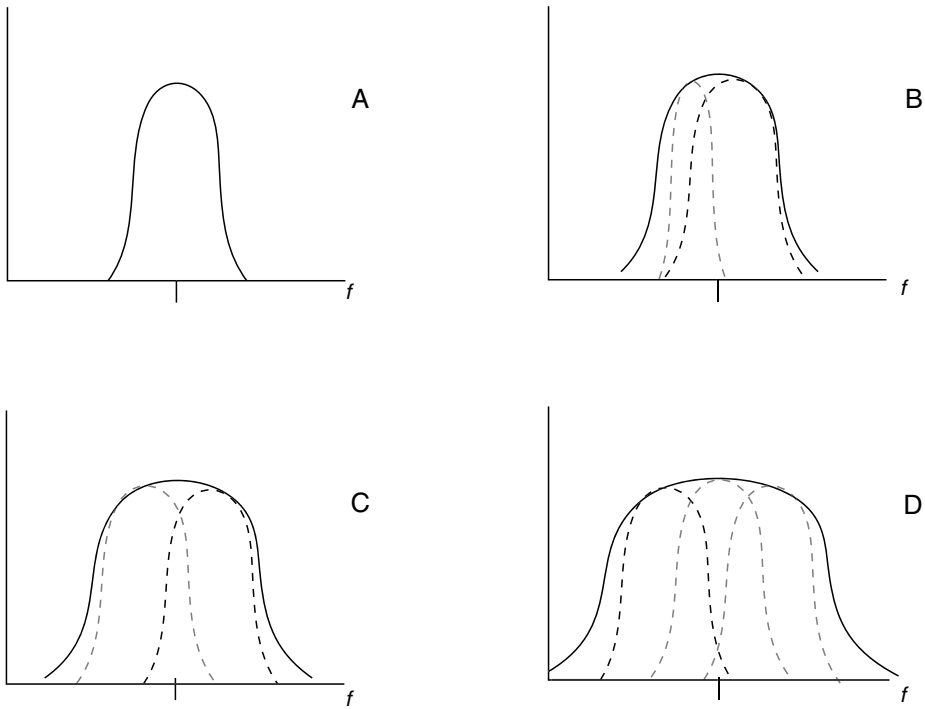

Figure 10.10 Stages of transducer bandwidth development. (A) Narrowband. (B) Dual mode. (C) Multiple mode. (D) Very wide band.

10.7.3 Multidimensional Arrays

As discussed in Chapter 7, most arrays are 1D with propagation along the z axis and electronic scanning along the x axis to form the imaging plane. Focusing in the elevation or yz plane is accomplished through a fixed focal length lens. A hybrid approach (a 1.5D array) achieves electronic focusing in the elevation plane by forming a coarsely sampled array in the y dimension at the expense of more elements. This number is a good compromise, however, compared to a complete 2D array, which usually requires about an n^2 channel count compared to n channels for 1D arrays. A way of reducing the number of electronic channels needed is to decrease the active number of elements to form a sparse array. All of these considerations were compared in Chapter 7. The main advantages of electronic focusing in the elevation are not only flexibility, but also improved resolution from coincident focusing in both planes and dynamic receive focusing in both planes simultaneously. The description of a real-time, fully populated 2D array with a nonstandard architecture is postponed until Section 10.11.6.

10.8 FRONT END

The front end is the mouth of the imaging system; it can talk and swallow. It has a number of channels, each of which has a transmitter and a switch (including a diode bridge) that allows the passage of high voltage transmit pulses to the transducer elements but blocks these pulses from reaching sensitive receivers (refer to the block diagram of Figure 10.3). Echoes return to each receiver, which consists of amplifiers in series, including one that has a variable gain for TGC under user control. The output of each channel is passed on to the receive beamformer.

10.8.1 Transmitters

The heartbeat of the system is a series of synchronized and precisely timed primitive excitation pulses (illustrated by Figure 10.11). The major factor in this heartbeat is the scan depth selected (s_d). The length of a line or vector, since each line has a vector direction, is simply the round-trip travel time ($2s_d/c_0$). As soon as one line has completed its necessary round-trip time, another line is launched in the next incremental direction required. For a simple linear array, the next line is parallel to the last one, whereas in a sector format, the next line is incremented through steering by a small angle.

The timing pulses associated with these events are the start of frame pulse, followed by the start of transmit. This last pulse actually launches a group of transmit pulses in parallel with the required delays to form a focused and steered beam from each active array element. The exact timing of these transmit pulses was described in Chapter 7. This process is repeated for each vector until the required number of lines (N) has been completed, after which a new start-of-frame timing pulse is issued by the system transmitter clock.

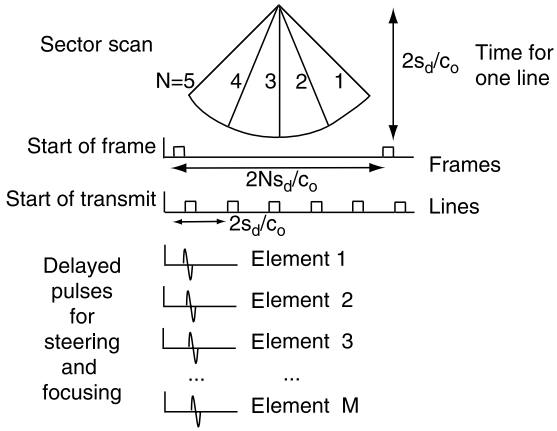

Figure 10.11 Pulse generation sequencing in an imaging system.

The rhythm of the system heartbeat can be interpreted as a repetitive timing sequence with a duty cycle. For the example shown in Figure 10.11, assume a scan depth of $s_d = 150$ mm, as well as 5 lines per frame and 6 active elements. The round-trip time for one line is $2s_d/c = 200\,\mu$s; this will be the start of the transmit pulse interval between each line. The time for a full frame is N lines/frame or, in this case, $5 \times 200\,\mu$s/frame $= 1000\,\mu$s/frame or 1000 frames/sec. The number of lines is only 5 for this example. A more realistic number of lines is 100, in which case the time for a full frame would be 20 ms or a frame rate of 50 frames/sec.

Finally, depicted in the bottom of Figure 10.11 is a sequence of delayed pulses (one for each active element of the array) to steer and focus the beam for that line. Note that these pulses are launched in parallel with each start of transmit. These transmit pulses have a unique length or shape for the mode and frequency chosen. For example, instead of one primitive transmit pulse such as a single cycle of a sine wave for 2D imaging, a number (m) of primitive pulses in succession can be sent to form an elongated pulse for Doppler mode. The duty cycle is taken to be the ratio of the length of the basic transmit sequence per line divided by the round-trip time. In practice, a vector line may be repeated by another one in the same direction or by one in a different mode in a predetermined multimode sequence necessary to build a duplex or a triplex image (Szabo *et al*., 1988).

10.8.2 Receivers

In order to estimate the dynamic range needed for a front end, typical echo levels in cardiac imaging will be examined. Numbered amplified backscattered echoes from the heart are illustrated by Figure 10.12b for the beam path shown through a cross section of the heart in Figure 10.12a (Shoup and Hart, 1988). With reference to the indexing of the echoes, the first waveform corresponds to feed-through during the

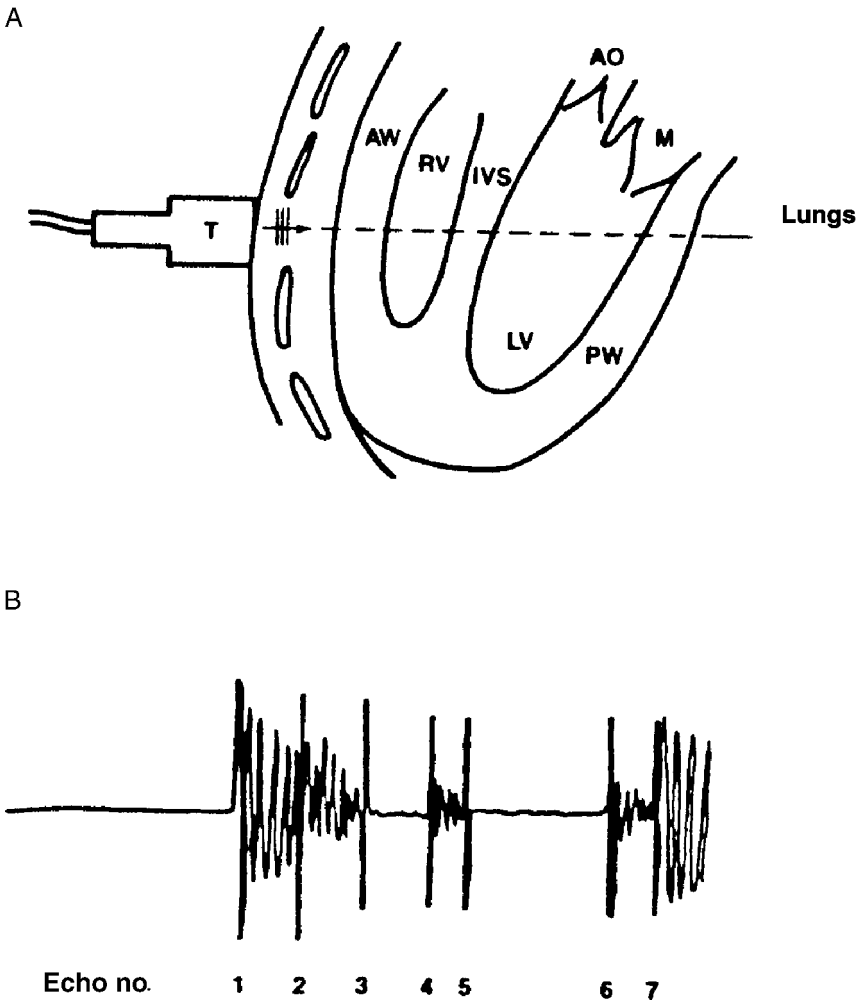

Figure 10.12 (A) Echo path through the heart. AW = anterior wall, RV = right ventricle, IVS = intraventricular septum, LV = left ventricle, AO = aortic valve, M = mitral valve, PW = posterior wall. (B) Amplified echoes corresponding to path in (A) (from Shoup and Hart, 1988, *IEEE*).

excitation pulse. Echo 2 is caused by the reflection factor (RF) between the fat in the chest wall and muscle of the anterior wall; this kind of signal is on the average about −55 dB below that obtained from a perfect (100%) reflector. Echo 3 is the echo from the reflection between blood and the tissue in the wall; it has a similar absolute level. Between echoes 3 and 4 is the backscatter from blood, which is at the absolute level of −70 dB compared to a 100% reflector and falls below the scale shown. The large echo number 7 is from the posterior wall lung interface; it is a nearly perfect reflector (close to 0 dB absolute level). In order to detect blood and the lung without saturating, the

receivers require a dynamic range of at least 70 dB for cardiac imaging. TGC amplification (mentioned in Chapter 4) was applied to the echoes in Figure 10.12b. The absolute values of the echoes were determined independently from RF data and a reference reflector. There is an individual front-end amplifier for each channel (usually 64 or 128 total) in the system. Each amplifier typically covers a range of 55–60 dB. For digital conversion, sampling rates of 3–5 times the highest center frequency are needed to reduce beamforming quantization errors (Wells, 1993). A means of time shifting for the dynamic receive beamformer at higher rates, closer to 10 times the center frequency, would be preferable to achieve low beam sidelobes (Foster *et al*., 1989). Modern imaging systems can have dynamic ranges in excess of 100 dB, and some have the sensitivity to image blood directly in B-mode at high frequencies (see Chapter 11) and to detect weak harmonic signals (see Chapters 14 and 15).

10.9 SCANNER

10.9.1 Beamformers

In Chapter 7, the operation of transmit and receive beamformers was discussed. The practical implementation of these beamformers involves trade-offs in time and amplitude quantization. In addition, more complicated operations have been implemented. In order to speed up frame rate, basic parallel beamforming is a method of sending out a wide transmit beam and receiving several receive beams (as explained in Section 7.4.3). The discussion of real-time compound imaging (Entrekin *et al*., 2000), which involves the ability of the beamformer to send out beams along multiple vector directions from the same spatial location in a linear array, is deferred until Section 10.11.4.

10.9.2 Signal Processors

10.9.2.1 Bandpass filters

This signal processing part of the system takes the raw beamformed pulse-echo data and selectively pulls out and emphasizes the desired signals, combines them as needed, and provides real and quadrature signals for detection and modal processing. This section covers only processing related to B-mode imaging. Chapter 11 covers color flow imaging and Doppler processing. Digital filters operate on the data from the A/D converters (shown in the block diagram, Figure 10.3). Bandpass filtering is used to isolate the selected frequency range for the desired mode within the transducer passband (recall Figure 10.10). The data may also be sent to several bandpass filters to be recombined later in order to reduce speckle (see Section 10.11.3). Another important function of bandpass filtering is to obtain harmonic or subharmonic signals for harmonic imaging (to be covered in more detail in Chapter 12). In Chapter 4, absorption was shown to reduce the effective center of the signal spectrum with depth. The center frequency and shape of bandpass filters can be made to vary with depth to better track and amplify the desired signal (see Section 10.11.2).

10.9.2.2 Matched filters

Another important related signal processing function is matched filtering. In the context of ultrasound imaging, this type of filter has come to mean the creation of unique transmit sequences, each of which can be recognized by a matched filter. One of the key advantages of this approach is that the transmit sequence can be expanded in time at a lower amplitude and transmitted at a lower peak pressure amplitude level, with benefits for reducing bioeffects (see Chapter 15) and contrast agent effects (see Chapter 14). Other major advantages include the ability to preserve axial resolution with depth, and increased sensitivity and tissue penetration depth.

Matched filtering actually begins with the transmit pulse sequence. In this case, the transmit waveform is altered into a special shape or sequence, $s(t)$. This transmission encoding can be accomplished by sending a unique sequence of primitive pulses of different amplitudes, polarities, and/or interpulse intervals. In the case of binary sequences, a ''bit'' is a primitive pulse unit that may consist of, for example, half an RF cycle or several RF cycles.

Two classic types of transmit waveforms, $x(t)$, a coded binary sequence and a chirped pulse, have been borrowed from radar and applied to medical ultrasound (Lee and Ferguson, 1982; Lewis, 1987; Cole, 1991; O'Donnell, 1992; Chiao and Hao, 2003). The appropriate matched filter in these cases is $x^*(-t)$. The purpose of a matched filter is to maximize signal-to-noise, defined as the ratio of the peak instantaneous output signal power to the root mean square (r.m.s.) output noise power (Kino, 1987). A simple explanation of how the output power can be maximized can be given through Fourier transforms. Consider a filter response,

$$y(t) = x(t) * h(t) \tag{10.1}$$

where $x(t)$ is the input, $y(t)$ is the output waveform, and $h(t)$ represents the filter. Let the matched filter be

$$h(t) = Ax^*(-t) \tag{10.2}$$

where A is a constant and * represents the conjugate. For this filter, the output becomes

$$y(t) = Ax(t) * x^*(-t) = A\int_{-\infty}^{\infty} x(\tau)x^*(\tau - t)d\tau = A\int_{-\infty}^{\infty} x^*(\tau)\,x(\tau + t)d\tau \tag{10.3}$$

but from the Fourier transform, the output can be rewritten as

$$y(t) = A\int_{-\infty}^{\infty} X(f)X^*(f)e^{i2\pi ft}df = A\int_{-\infty}^{\infty} |X(f)|^2 e^{i2\pi ft}df \tag{10.4}$$

In other words, the matched filter choice of Eq. (10.2) leads to an autocorrelation function, Eq. (10.3), which automatically maximizes the power spectrum, Eq. (10.4) (Bracewell, 2000) and consequently, maximizes the ratio of the peak signal power to the r.m.s. noise power (Kino, 1987).

A simple example of a coded waveform is a three bit Barker code. This code can be represented graphically (shown in Figure 10.13), or it can be represented mathemati-

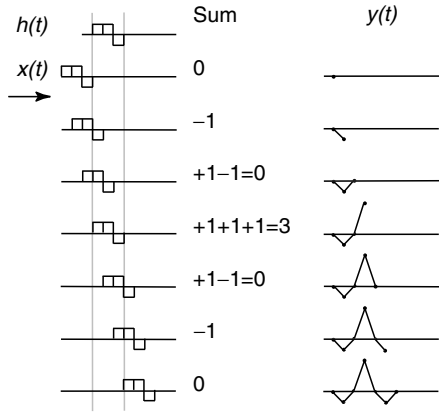

Figure 10.13 Output of a three-bit Barker code. (Top) Receive correlator sequence $h(t)$ versus time units. (Below) Input sequence $x(t)$ shown as incrementing one time unit or one bit at a time through the correlator with the corresponding summation and output waveform.

cally as the binary sequence [+1+1−1]. Binary codes have unique properties and solve the following mathematical puzzle: What sequence of ones and minus ones, when correlated with itself, will provide a gain in output (y) with low sidelobes?

In the top of Figure 10.13 is a plot of the correlation filter $h(t)$ against unit time increments. Recall that the convolution operation involves flipping the second waveform right to left in time and integrating (see Appendix A). Physically, correlation is the operation of convolution of $x(t) * x^*(-t)$. This integration consists of a double reversal in time (once for the convolution operation and once for the receive filter). The net result is a receive waveform that is back to its original orientation in time. The operation is simplified to sliding one waveform, $x(t)$, past the second, $x(t)$, left to right. Each row in this figure shows an input waveform sliding from left to right, one time unit interval at a time, until the waveform has passed through the correlator. Integration at each slot is easy: First, determine the amplitude values of $h(t)$ and $x(t)$ multiplied together, such as $-1 \times -1 = 1$, at each time interval overlap position; second, sum all the product contributions from each time interval in the overlap region to obtain the amplitude value for the time position in the row. In the last row, connect the dots at each time interval to get $y(t)$. The repeating triangular shapes within $y(t)$ can be recognized as the convolution, or correlation in this case, of two equal rectangles, $\Pi(t)$, that slide past each other to form triangle functions; these steps complete the description of $y(t)$ between the dots we calculated in Figure 10.13. Note the main features of $y(t)$: a peak equal to n bits (three) and two satellite time sidelobes of amplitude -1. From maximum amplitudes of plus or minus one, a gain of three has been achieved by encoding.

Fortunately, MATLAB makes these kinds of calculations trivial. We can obtain graphical results with three lines of code:

$$\begin{aligned} &x = [0\ 1\ 1\ -1\ 0]'; \\ &y = x\,\mathrm{corr}(x) \\ &\mathrm{plot}(y); \end{aligned} \tag{10.5}$$

The first line forms the Barker sequence, allowing for zeros to get the full depiction of the output. The autocorrelation function is the cross-correlation function xcorr.m with one argument. The reader is encouraged to play with the program barkerplot.m to verify that as the number of bits, N, is increased, the peak increases in proportion and the ratio of peak amplitude level to maximum sidelobe level improves.

A family of codes with more impressive performance is the pseudo-random binary M-sequence code of ones and zeros that is shown in the lower right-hand corner of Figure 10.14 (Carr *et al.*, 1972) along with the output, $y(t)$. Here the sidelobe ratio is -15.84 dB. Note that for an acoustic transmitter, ones and zeros may translate into either a series of "ones" (regarded as positive primitive pulses, $+1$) and "zeros" (regarded as primitive pulses with a 180° phase reversal or negative-going pulses, -1).

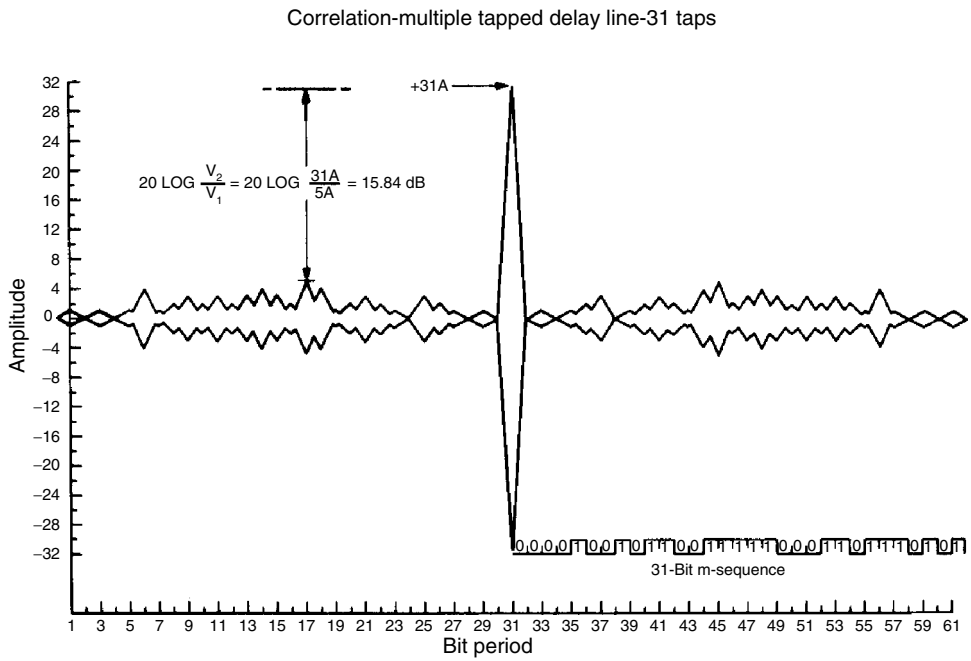

Figure 10.14 Theoretical plot of amplitude versus bit period for the correlation of a 31-bit maximal length (M) sequence. The peak-to-sidelobe ratio for this sequence is -15.84 dB (from Carr *et al.*, 1972, *IEEE*).

There are several families of codes, each with advantages and disadvantages. Each bit or primitive pulse alone will evoke a round-trip response from the transducer, which fixes the minimum resolution available. In the usual case without a coded sequence, a transmit pulse might consist of a half-period pulse or a full-period pulse (e.g., a single *sine* wave) corresponding to the desired frequency of excitation. Receive amplitude levels can be raised by increasing the applied transmit voltage. At some pressure level (described in Chapter 15), a fixed limit is reached for safety reasons so that the voltage can no longer be increased. One advantage of coded sequences is that a relatively low voltage A can be applied, and a gain of NA is realized on reception after the correlation process. Another advantage of coded sequences is that certain orthogonal codes, such as Golay codes, allow the simultaneous transmission of a number of beams in different vector directions, which are sorted out on decoded reception through matched correlators (Lee and Ferguson, 1982; Shen and Ebbini, 1996; Chiao *et al.*, 1997; Chiao and Hao, 2003) as is shown in Figure 10.15.

Another important class of coded matched filter functions are chirps (Lewis, 1987; Cole, 1991; Genis *et al.*, 1991). A methodology borrowed from radar, a transmit waveform, $x(t)$, consists of a linear swept frequency modulated (FM) pulse of duration T. The result of matched filtering is a high-amplitude short autocorrelation pulse. If a chirp extends over a bandwidth B, the correlation gain (G) through a matched filter $x^*(-t)$, a mirror image chirp, is $G = TB$ (Kino, 1987). Examples of a chirp and compressed pulses from flat targets are given in Figure 10.16. A third waveform depicts the transmitted upchirp waveform. A useful parameter is the instantaneous frequency, defined as

$$f_i = \left(\frac{1}{2\pi}\right)\frac{d\phi}{dt} \tag{10.6}$$

where ϕ is the phase of the analytic signal as a function of time (see Appendix A). For the transmit chirp of Figure 10.16, the instantaneous frequency as a function of time

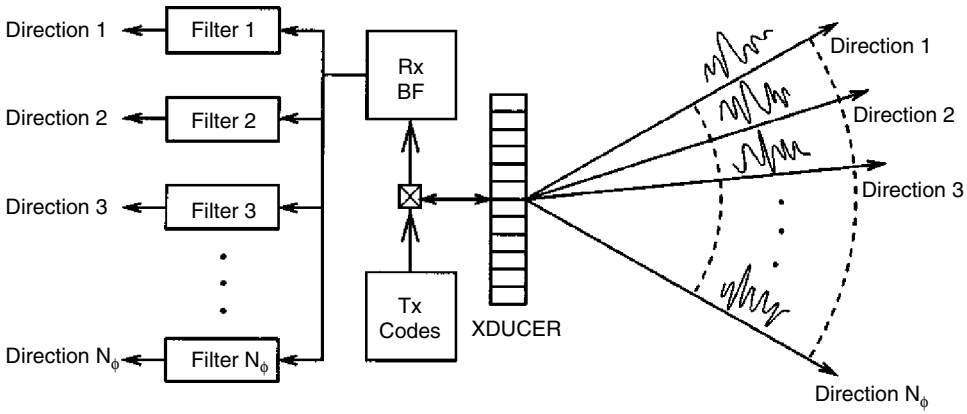

Figure 10.15 Simultaneous multibeam encoded ultrasound imaging system (from Shen and Ebbini, 1996, *IEEE*).

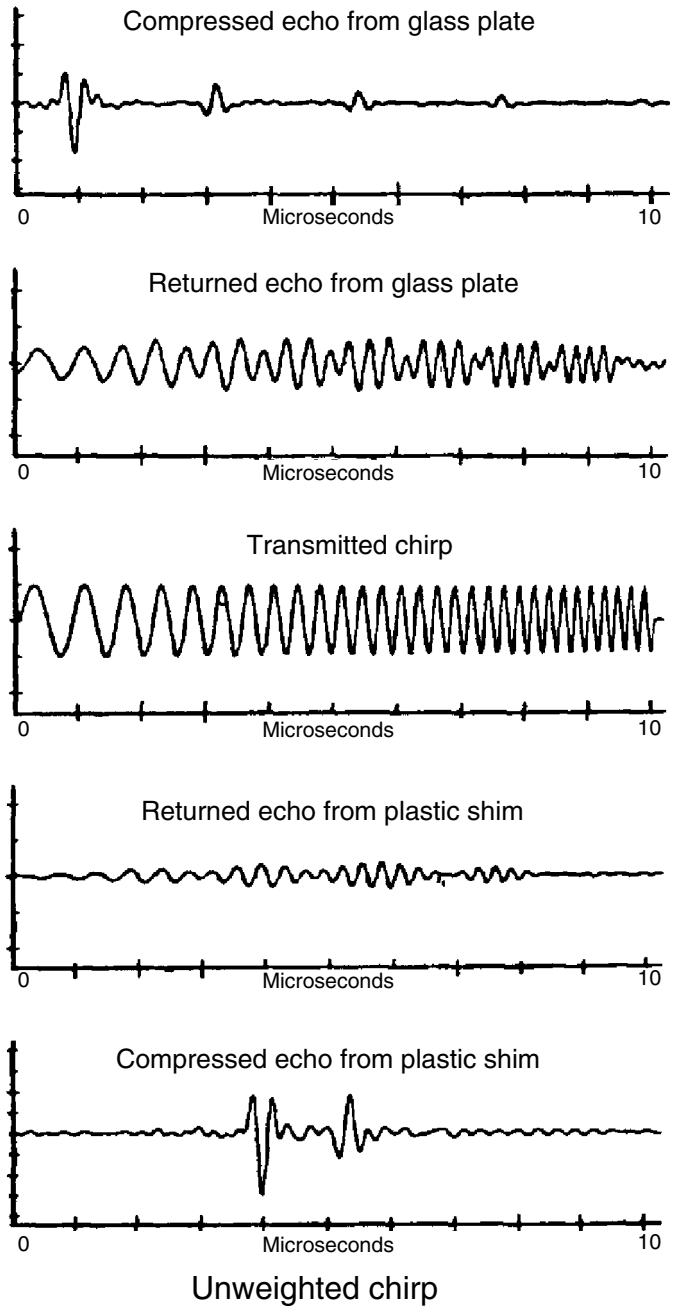

Figure 10.16 A chirp extending from 5 to 9 MHz (middle panel) and returned (uncompressed) and compressed pulse echoes from a glass plate and a plastic shim (from Lewis, 1987, *IEEE*).

is an ascending line from 5 to 9 MHz. The second panel from the top of Figure 10.16 shows the received echoes for a glass plate. After passing through the matched filter, these echoes are compressed to give excellent resolution and indicate multiple internal reflections into the top panel. A pair of similar echo signals for a plastic plate with higher internal absorption is shown in the lower two panels of Figure 10.16. The pros and cons of this methodology are discussed in the previous references. Both orthogonal codes and chirped waveform matched filters have been implemented on commercial systems.

10.10 BACK END

10.10.1 Scan Conversion and Display

The main function of the back end (refer to Figure 10.3, the block diagram) is to take the filtered RF vector line data and put it into a presentable form for display. These steps are the final ones in the process of imaging (described in detail in Section 8.4). An imaging challenge is to take the original large dynamic range, which may be originally on the order of 120 dB, and reduce it down to about 30 dB, which is the maximum gray-scale range that the eye–brain system can perceive. The limits and description of human visual perception is beyond the scope of this work, and they are described in more detail in Sharp (1993). As we have seen, the initial step is taken by the TGC amplifiers, which reduce the dynamic range to about 55–60 dB. The beamformed digitized signals are converted to real (I) and quadrature (Q) components (delayed from the I signal by a quarter of the fundamental period). These components can be combined to obtain the analytic envelope of the signal through the operation $\sqrt{I^2 + Q^2}$.

In Figure 10.17, the envelope detection begins the back-end processing. This step is followed by an amplifier that can be controlled by the user to operate linearly at one extreme, or as a logarithmic amplifier at the other extreme, or as a blend between the two extremes to achieve further dynamic range compression. For example, in the case in which soft-tissue detail and bright specular targets coexist in the same image, the logarithmic characteristic of the amplifier can reduce the effects of the specular reflections on the high end of the scale. The preprocessing step, not done in all systems, slightly emphasizes weak signals as the number of bits is reduced, for example, from 10–7 bits after digitization.

So far, a number of vectors (lines with direction) have undergone detection, amplification, preprocessing (if any), and resampling to a certain number of points per line for suitable viewing. In order to make a television or PC-style rectangular image, this information has to be spatially remapped by a process called scan conversion. If the vectors were displayed in their correct spatial positions, the data would have missing information when overlaid on a rectangular grid corresponding to pixel locations in a standard raster scan, such as the NTSC TV. Sector scanning is one of the more challenging formats to convert to TV format (as illustrated by Figure 10.18). An enlargement of the polar coordinate scan lines overlaid on the raster rectangular pixel

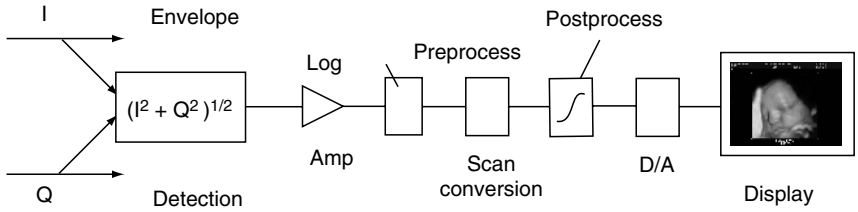

Figure 10.17 Block diagram for back-end processing used for image display (courtesy of Philips Medical Systems).

grid indicates the problem. Not only do the scan lines rarely intersect the pixel locations, but also each spatial position in the sector presents a different interpolation because the vectors change angle and are closer toward the apex of the sector. Early attempts at interpolation caused severe artifacts, such as Moire's pattern, and unnatural steps and blocks in the image. This problem can be solved by a 2D interpolation method (Leavitt *et al.*, 1983), which is shown in the bottom of Figure 10.18. The actual vector points are indicated along the bold scan lines with the pixel locations marked by crosses. To obtain the interpolation at a desired point (Z), first the radius from the apex to the intended pixel point is determined. Second, the angle of a radial line passing through Z is found. The generalized 2D interpolation formula is

$$Z(r, \theta) = \sum_n \sum_m S(r - n\Delta r, \theta - m\Delta\theta)\, Z(n\Delta r, m\Delta\theta) \tag{10.7}$$

where S is a 2D triangular function.

The next step is one in which the amplitudes in the rectangular format undergo a nonlinear mapping called postprocessing. A number of postprocessing curves are selectable by the user to emphasize low- or high-amplitude echoes for the particular scan under view. This choice determines the final gray-scale mapping, which is usually displayed along with the picture. In some cases, pure B-mode images undergo an additional color mapping (sometimes called colorization) in order to increase the perceived dynamic range of values. Finally, a digital-to-analog (D/A) conversion occurs for displaying the converted information. The usual video controls such as brightness and contrast are also available, but they play a minor role compared to the extensive nonlinear mapping processes the data has undergone. Image plane overlays are used to present graphic and measurement information. Color flow display (to be covered in Chapter 11) also undergoes scan conversion and is displayed as an image plane overlaid on the gray-scale B-mode plane. In addition, most systems have the capability to store a sequence of frames in internal memory in real time for cine loop display.

10.10.2 Computation and Software

Software plays an indispensable and major role in organizing, managing, and controlling the information flow in an imaging system, as well as in responding to external

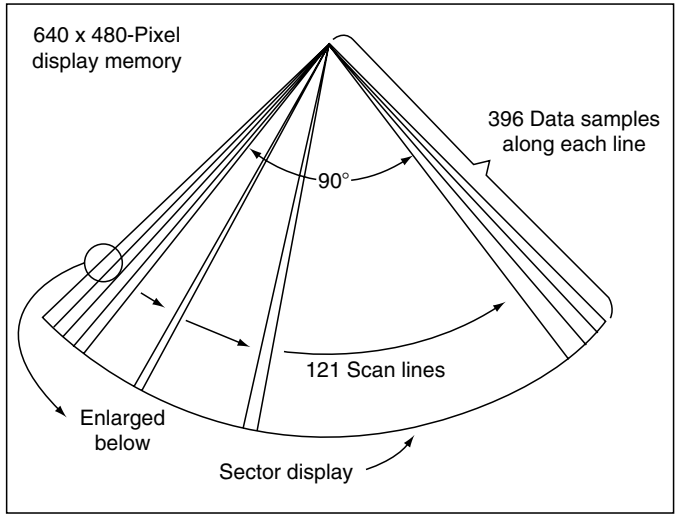

A

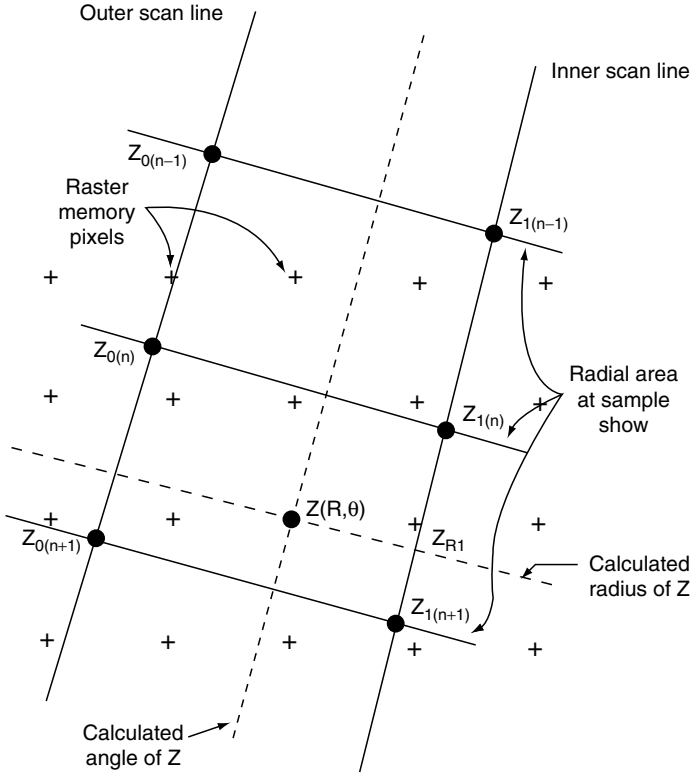

B

Figure 10.18 (A) Image vectors in a sector scan display overlaid on desired rectangle format. (B) Magnified view comparing vector data in polar coordinates to rectangular pixel positions (Reprinted by permission of Hewlett Packard, from Leavitt *et al.*, 1983, Hewlett Packard).

control changes or interrupts. First, it starts and stops a number of processes such as the transmit pulse sequence. Interrupts or external control changes by the user are sensed, and the appropriate change commands are issued. The master controller may have other slave microprocessors that manage specific functional groups, such as beamforming, image scan conversion and display, calculations and measurements of on-screen data, hardware, and digital signal processing (DSP) chips. The controller also manages external peripheral devices such as storage devices and printers as well as external communication formats for LAN and DICOM. The controller also supervises the real-time computation of parameters for the output display standard (to be described in Chapter 15), as well as acoustic output management and control.

10.11 ADVANCED SIGNAL PROCESSING

10.11.1 High-End Imaging Systems

The difference between a basic ultrasound imaging system and a high-end system is image quality. High-end systems employ advanced signal processing to achieve superior images. Acuson was the first to recognize that a "high-end" system could be successful in the clinical marketplace. The first Acuson images were known for their spatial resolution, contrast, and image uniformity (Maslak, 1985). Soon other manufacturers took up the challenge, and the striving for producing the best image continues today.

Three examples of advanced processing for enhancing image quality are attenuation compensation, frequency compounding, and spatial compounding (Schwartz, 1993). Usually separate signal processing paths and functions are combined in new ways to achieve improved images. In Figure 10.19 is a block diagram of an ultrasound imaging system; it has several differences from the block diagram of Figure 10.3. To the right of the transducer are scanner functions: beamforming and filtering. The remaining functions are back-end functions of image detection, logarithmic compression, and frame generation. At the bottom of the figure are a number of new blocks (numbered 1–4). Not all the steps of image information are included in this diagram, which is more symbolic and emphasizes differences in signal processing more than traditional imaging architectures. Controlling software to manage the interplay between different functions is assumed.

10.11.2 Attenuation and Diffraction Amplitude Compensation

TGC is an approach available to imaging system users to manually adjust for the changes in echo-amplitude caused by variations in beam-formation along the beam axis and by absorption. Better image improvements can be obtained by analyzing the video data and adaptively remapping the gain in an image in a 2D sense. At least two different approaches have appeared in literature (Melton and Skorton, 1981; Hughes and Duck, 1997). The first method senses differences in RF backscatter and adaptively changes TGC gains. The second analyzes each line of video data to read just the

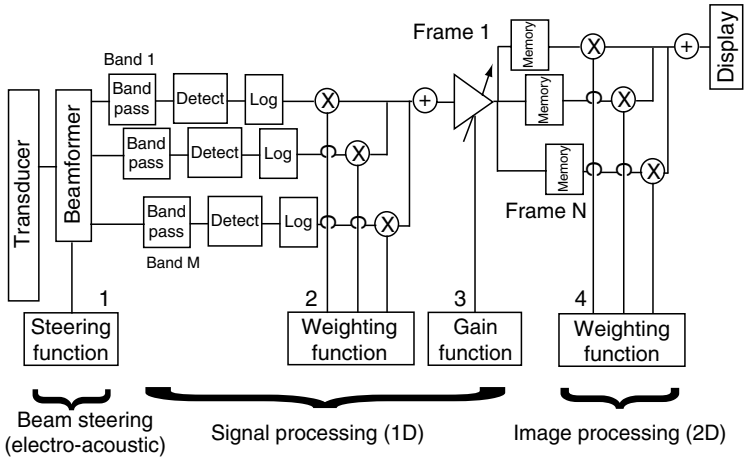

Figure 10.19 Imaging system architecture with signal processing enhancements. The lower blocks are numbered as (1) steering function, (2) spectral weighting function, (3) gain function, and (4) weighting function (courtesy of G. A. Schwartz, Philips Medical Systems).

intensity levels as a function of time, based on an algorithm, and it leads to an image renormalized at each spatial point. This last approach is more suitable for imaging systems because it can be accomplished in software without major hardware changes.

Using this method as an example, we return to Figure 10.19, block 3 (gain function). The triangle above it symbolizes a variable gain control. A line of video data, corrected for previous video processing and TGC settings, passes through the amplifier and is sent down to the gain control or video analyzer software (not shown in diagram). This line of data is analyzed by an adaptive attenuation estimation algorithm, and the renormalization factor or new gain is determined for each time sample and is sent back through the adjusted amplifier. Only the renormalized values of video information pass through the normal digital scan conversion process (not shown) to create a compensated image frame that is stored in frame memory.

10.11.3 Frequency Compounding

The concept of frequency diversity to reduce speckle was discussed in Section 8.4.6. Until the 1980s, some clinicians valued the grainy texture of speckle, believing it to contain tissue information. In Chapter 8, speckle was shown to be mainly artifactual. Images of the same tissue taken by different transducers at various frequencies present different-looking speckle. Researchers have shown (Abbot, 1979; Melton and Magnin, 1984; Trahey *et al.*,1986) the benefits of smoothing out speckle through a scheme of subdividing the pulse-echo spectrum into smaller bandwidths and then recombining them. Through frequency diversity, improved contrast is obtained and more subtle gradations in tissue structure can be distinguished.

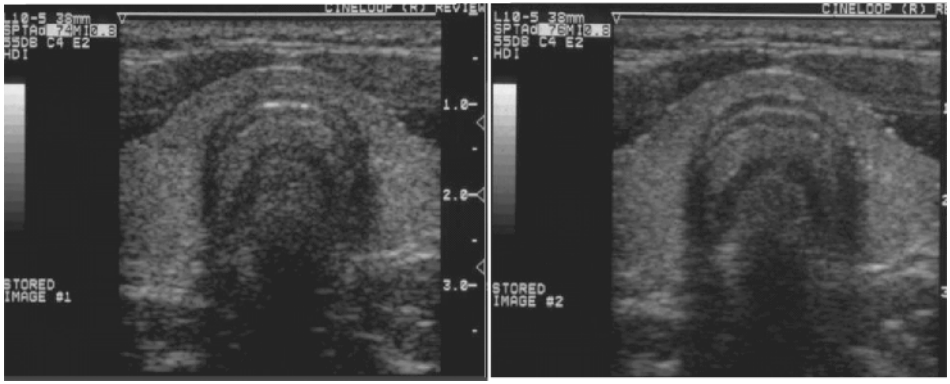

Figure 10.20 (Left) Conventional imaging. (Right) Frequency compounding (courtesy of G. A. Schwartz, Philips Medical Systems).

A way in which frequency compounding can be implemented is illustrated by Figure 10.19. RF data from a summed beamformed line are sent in parallel to a number (M) of bandpass filters and detection. Each detected signal path is assigned a weight according to a spectral weighting function (block 2) and summed to form a final composite line for scan conversion. Because speckle depends on the constructive and destructive interference at a particular frequency, this 1D summing process reduces the variance of the speckle. Clinical images with and without frequency compounding are compared in Figure 10.20.

10.11.4 Spatial Compounding

While spatial diversity was also named as a way of reducing speckle in Section 8.4.6, there is a more important reason for using it—new backscattering information is introduced into an image. Artifacts are usually thought of as echo features that do not correspond to a real target or the absence of a target. A more subtle artifact is a distortion or a partial depiction of an object. Obvious examples are echoes from a specular reflector, that are strongly angle dependent (as covered by Section 8.4.2). In that section, three angular views of a cylinder were shown in Figure 8.11. That cylinder is revisited in Figure 10.21 (once as seen by conventional imaging and also as seen by compound imaging). When viewed on a decibel scale, there is considerably more echo information available for the cylinder viewed from wider angles.

The implementation of real-time spatial compounding involves 1D and 2D processing. To generate a number (N) of different looks at an object, translation and rotation operations are combined in an array (as explained in Section 10.7). To acquire the necessary views efficiently, in addition to the normal (zero-degree) line orientation frame, N-1 single steered frames are also taken (as in Figure 10.6). A scheme for accomplishing compounding in real time is depicted in Figure 10.22. The moving average of N frames create each spatial compound frame. In the overall block diagram of Figure 10.19, a sequence of N steered angles is entered through

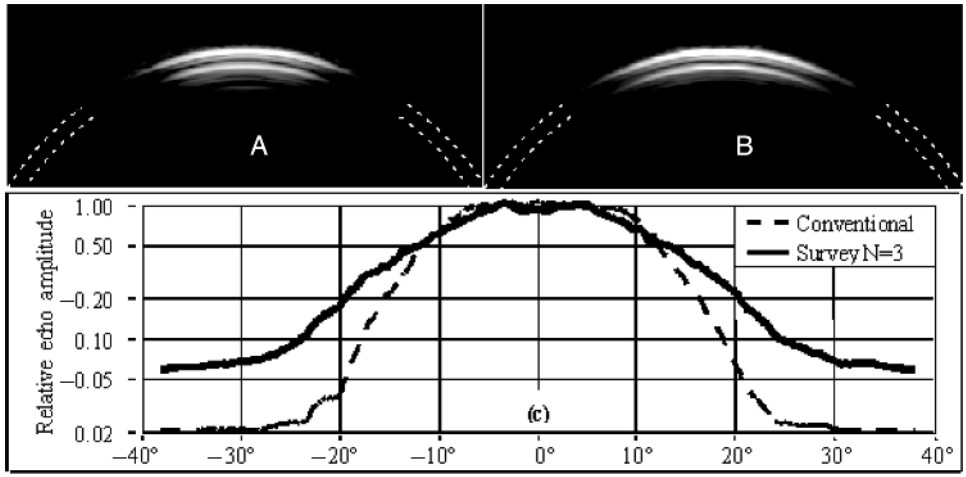

Figure 10.21 Specular reflection from a cylindrical reflector for (A) conventional and (B) compound imaging for steering angles of 17°, 0°, and −17°. (C) Corresponding echo amplitudes received by a 5–12 MHz linear array are plotted as a function of angular position (courtesy of Entrekin *et al.*, 2000, reprinted with permission of Kluwer Academic/Plenum Publishers).

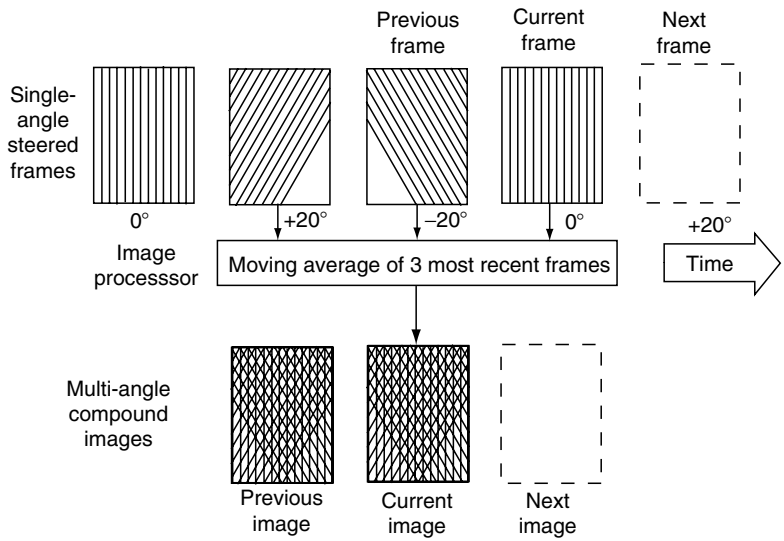

Figure 10.22 Steps of real-time spatial compounding. In a sequence of steered frames, the scan-converted frames are combined with a temporal moving average filter to form compound images (courtesy of Entrekin *et al.*, 2000, reprinted with permission of Kluwer Academic/Plenum Publishers).

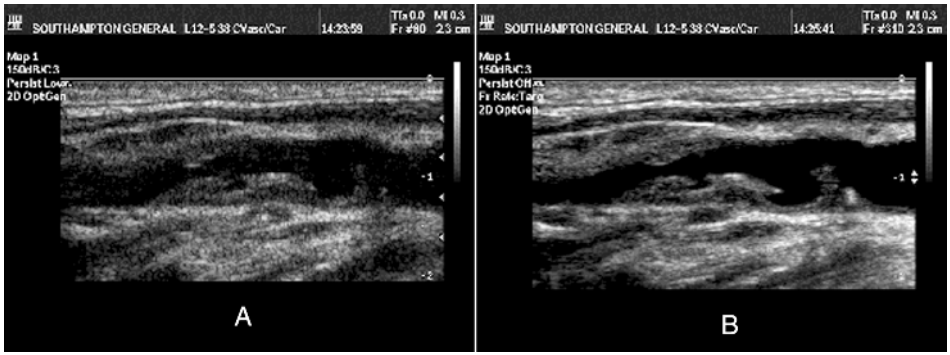

Figure 10.23 (A) Conventional and (B) compound views of an ulcerated carotid artery plaque as viewed with a 5–12 MHz linear array (courtesy of Entrekin *et al.*, 2000, reprinted with permission of Kluwer Academic/Plenum Publishers).

block 1. The *N*-scan-converted single-angle steered frames arrive in the back end where, according to a prescribed spatial compounding function of block 4, each frame *N* is assigned line and overall 2D frame weighting. Finally, the weighted frames are combined in an averaging operation (symbolized by the summing operation) before display.

Enhanced lesion detection, or the increase in contrast between a cyst and its surrounding material, as well as speckle signal-to-noise have been demonstrated for real-time spatial compounding (Entrekin *et al.*, 2000). Even though the views are not totally independent, these improvements follow a $\sqrt{N}$ trend. Figure 10.23 compares conventional and spatially compounded images of ulcerated plaque in a carotid artery. Enhanced tissue differentiation, contrast resolution, tissue boundary delineation, and the definition of anechoic regions are more evident in the spatially compounded image. One drawback of this method is that temporal averaging may result in the blurring of fast-moving objects in the field of view. This effect can be reduced by decreasing the number of frames (*N*) averaged; appropriate numbers have been determined for different clinical applications (Entrekin *et al.*, 2000).

10.11.5 Real-Time Border Detection

In order to determine the fast-moving changes of the left ventricle of the heart, a 2D signal processing method has been developed to track the endocardial border. This approach is based on automatically detecting the difference between the integrated backscatter of blood and the myocardium (heart muscle) (Loomis *et al.*, 1990; Perez *et al.*, 1991) at each spatial location. Implementation of this approach combines a blood–tissue discriminator filter and an algorithm for incoming pulse echoes with 2D signal processing to present a real-time display of the blood–tissue border. This border can be used for real-time calculations of related cardiac parameters.

Another cardiac problem of interest is akinetic motion of the heart due to injury, disease, or insufficient arterial blood supplies. The net effect is that the heart wall of the left ventricle no longer contracts and expands uniformly during the cardiac cycle,

and some local regions lag behind. The border-tracking algorithm described earlier can be applied to this problem. The change in border position from the previous frame is determined, and this change is assigned a unique color. From frame to frame, during either a contraction or expansion phase, the sequence of color changes are added to each other to paint an overall picture of wall motion (as depicted in Figure 10.24a). This ideal picture shows that borders have uniform thickness during a normal contracting cycle; tracking is synchronized with the electrocardiogram (ECG). In real time, this process has been used to track the walls of the left ventricle (shown in Figure 10.24b). Locally nonuniform expansion and contraction of the chamber can be detected from irregularities in the color patterns.

10.11.6 Three- and Four-Dimensional Imaging

One of the drawbacks of 2D ultrasound imaging is the skill and experience required to obtain good images and to make a diagnosis. Imaging in this way is demanding in terms of keeping track of the spatial relationships in the anatomy, and part of using this skill is being able to do 3D visualization in one's head during an exam. An ultrasound exam does not consist of just picture-perfect images such as those in this chapter. Instead, pictures are selected from a highly interactive searching process, during which many image planes are scanned in real time.

The primary goal of 3D ultrasound imaging is the user-friendly presentation of volume anatomical information with real-time interactive capabilities. This goal is challenging in terms of the acquisition time required, the amount of data processed, and the means to visualize and interact with the data in a diagnostically useful and convenient way. Image interpretation becomes simpler because the correct spatial relationships of organs within a volume are more intuitively obvious and complete, thereby facilitating diagnosis, especially of abnormal anatomy such as congenital defects and of distortions caused by disease. The probability of finding an anomaly has the potential of being higher with 3D than with manual 2D scanning because the conventional process may miss an important region or not present sufficient information for interpretation and diagnosis.

The process of 3D imaging involves three steps: acquisition, volume rendering, and visualization. For more details, excellent reviews of 3D imaging by Nelson and Pretorius (1998) and Fenster and Downey (1996) are recommended.

Acquisition is a throwback to the days of mechanical scanning discussed in Chapter 1, except with arrays substituted for single-element transducers. At any instant of time, the array is busy creating a scan plane of imaging data; however, in order to cover a volume, it is also mechanically scanned either through translation, rotation, or fanning. A major difference for 3D imaging is that position data must be provided for each image plane. As in the early mechanical scanning days, this information is provided by either built-in (or built-on) position sensors or by internal/external position controllers, by which the spatial location and or orientation of the array is changed in a prescribed way. The built-on sensors allow freehand scanning. Because acquisition time is on the order of seconds, data are often synchronized to the ECG, M-mode, or Doppler signals, so that, for example, enough frames are acquired at the

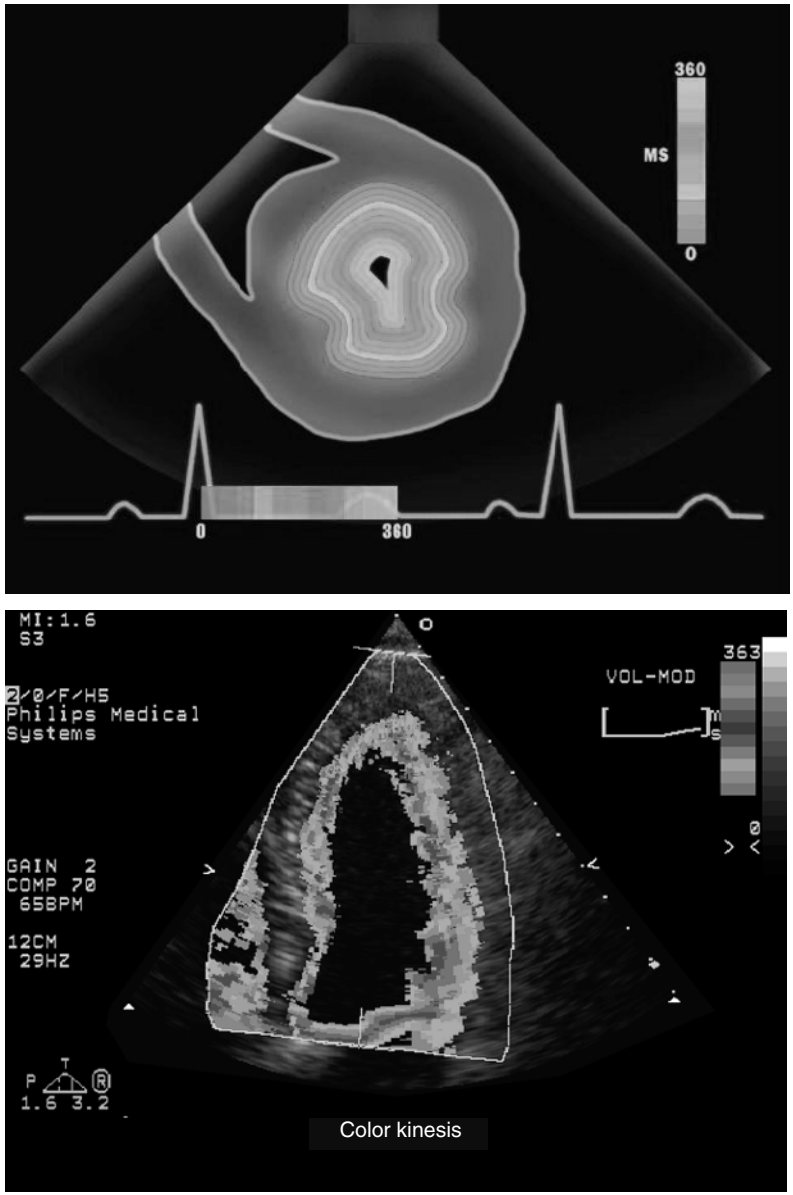

Figure 10.24 (A) Artist's depiction of color-kinesis automatic border-tracking algorithm, showing uniform contraction and synchronization to ECG. (B) Algorithm in operation shows severe akinetic behavior near the bottom of a left ventricle. Note the lack of motion near the base of the septal wall (lower left) and large motion on the opposite side of the chamber (lower right) (courtesy of Philips Medical Systems) (see also color insert).

same point in a cardiac cycle to create a volume. To create 4D images, time as well as position information is necessary for each acquired image plane. A recent innovation is the real-time 2D array, for which a volume of data can be acquired rapidly and completely electronically without moving the array.

The next step of the 3D process is that the video data in the image planes are interpolated into a volume of data in their correct spatial position. The 3D counterpart to pixels in 2D imaging is the voxel. Adequate sampling is important because a considerable amount of interpolation is involved. The quality of individual image planes is reflected in the final 3D images so that speckle, unequal resolution throughout the field of view, signal-to-noise, and patient movement are important. In this regard, a 2D array, in which the elevation and azimuth focusing are collocated, contributes to more resolution uniformity.

The visualization software takes the volume data and presents it in an interactive way for imaging. This step presents a challenge for some ultrasound data from soft tissues that do not have enough contrast for definitive segmentation. Slice presentation is the simultaneous display of several image planes that can be selected interactively from arbitrary locations and orientations within the volume. These slices are also referred to as multiplanar reformatting (MPR) views. Recently, techniques have been created for directly viewing the 3D matrix of echo signals. Such techniques are referred to as "volume rendering," and they produce surfacelike images of the internal anatomy. Although similar in presentation, such techniques should be distinguished from the more common surface-rendering techniques, which are used in computer animations and games and motion pictures. The most popular images of this kind are those of the fetus (see Figure 1.12), in which it is easier to distinguish between the fetal body and the surrounding amniotic fluid. Volume rendering is also applicable to functional information; for example, one can use color flow 4D imaging to visualize both normal and pathologic flows in 3D space. Ease of use of the interactive visualization software is an ongoing concern and focus of development.

A more recent change in visualization capability is the introduction of a real-time 2D array by Philips Medical Systems (see Section 7.9.2). This array has the equivalent of combined front-end and micro-beamforming functions in the handle of the transducer. Electronic 3D scanning in real time provides rapid acquisition of volume data and simultaneous viewing of different image planes as well. A frame from a real-time 4D sequence of the opening and closing of heart valves is shown in Figure 10.25.

10.12 ALTERNATE IMAGING SYSTEM ARCHITECTURES

This chapter completes the central block diagram of Figure 2.14. Blocks *F* (for filtering), *D* (for detection), and *D* (for display) provide the last pieces of the imaging system. The overall structure in this diagram (the linear phased array architecture), borrowed from electromagnetic array antennas, has had a surprisingly long run. This type of beamformer is straightforward to implement, real time, simple, and robust, and it has high angular selectivity. No contenders have been demonstrated to be

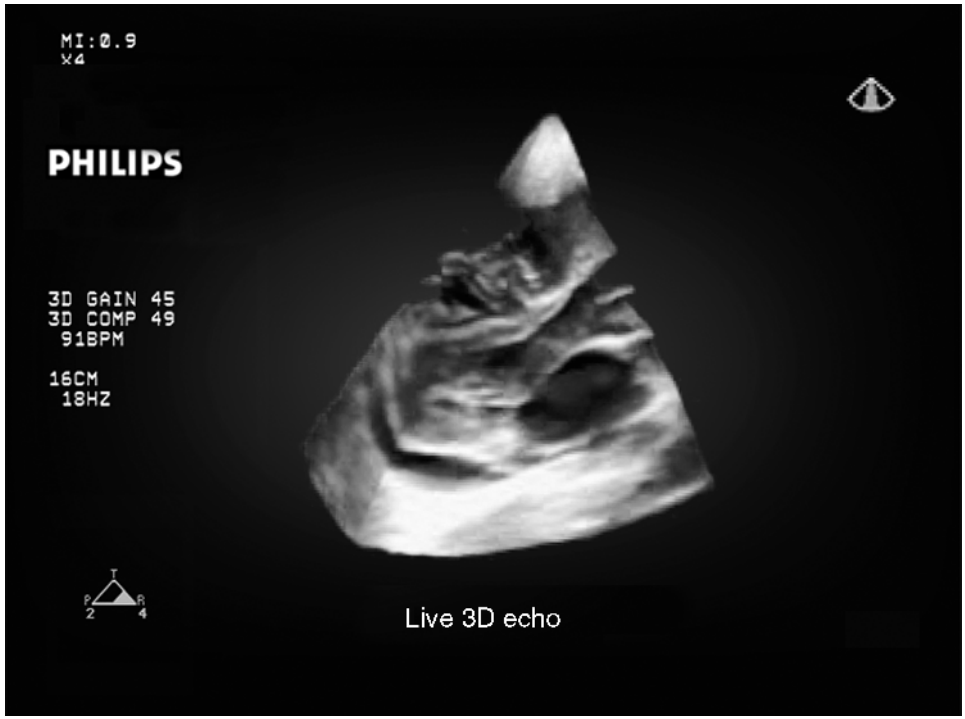

Figure 10.25 Real-time 4D image frame of heart valve motion (courtesy of Philips Medical Systems).

improvements over the original architecture in a clinical setting. The present beamformer has two chief limitations: lack of speed and flexibility.

An example of the flexibility issue is its inability to handle aberration well. This last problem has been addressed by several schemes (as discussed in Chapter 9). Adaptive imaging systems for this purpose were described by Krishnan *et al*. (1997) and Rigby *et al*. (2000). Another adaptive scheme for minimizing the effects of off-axis scatterers was described by Mann and Walker (2002). A scheme for extracting more angular backscattering information for imaging was presented by Walker and McAllister (2002).

In terms of improving speed, novel methods have been proposed (von Ramm *et al*., 1991). The key limitation in conventional systems is the pulse-echo round-trip time that adds up, line by line. Several alternative methods employ broad transmit beams to overcome the long wait for images. Lu (1997, 1998) has devised a very fast frame-rate system based on a plane wave transmission, X-receive beams, and a Fourier transform technique. A new company, Zonare, has been formed based on an architecture that includes the transmission of several (approximately 10) broad plane wave-beams per frame and fast acquisition and signal processing (Jedrzejewicz *et al*., 2003). Jensen and his colleagues at the University of Copenhagen have developed a fast synthetic aperture system that includes broad-beam transmit insonification. They provide a discussion of other limitations of conventional imaging, such as fixed transmit focus-

ing (Jensen *et al*., 2002). These systems have the potential for more than just speed; they may be able to acquire more complete information-laden data sets, as well as have time to provide more sophisticated and tissue-appropriate processing and to extract relevant parameters for diagnostic imaging.

Bibliography

Foster, F. S., Larson, J. D., Mason, M. K., Shoup, T. S., Nelson, G., and Yoshida, H. (1989a). Development of a 12 element annular array transducer for realtime ultrasound imaging. *Ultrasound in Med. & Biol*. **15**, 649–659. Details the design of an annular array digital imaging system.

Foster, F. S., Larson, J. D., Pittaro, R. J., Corl, P. D., Greenstein, A. P., and Lum, P. K. (1989b). A digital annular array prototype scanner for realtime ultrasound imaging. *Ultrasound in Med. & Biol*. **15**, 661–672. Another article detailing the design of an annular array digital imaging system.

Hewlett Packard Journal **10**, Vol. 34. (Oct. 1983). Describes the operation of HP's first generation of imaging systems in detail.

Hewlett Packard Journal **12**, Vol. 34. (Dec. 1983). A special issue that continues the description in the above reference.

Kino, G. S. (1987). *Acoustic Waves: Devices, Imaging, and Analog Signal Processing*. Prentice-Hall, Englewood Cliffs, NJ. Provides acoustic imaging theory and applications available on CD-ROM from IEEE-UFFC Group.

Kremkau, F. W. ( ). *Diagnostic Ultrasound: Principles and Instruments*. This introductory book investigates the topic of imaging systems in more depth. It has a wealth of information that is clearly presented at an easily understood level.

Morgan, D. P. (1991). *Surface Wave Devices*. (Available on CD-ROM from IEEE-UFFC Group.) Ferroelec and Freq. Control Society. Additional information about signal processing, encoding, and chirped waveforms for an allied field and surface acoustic wave devices.

References

Bracewell, R. (2000). *The Fourier Transform and Its Applications*, Chap. 17. McGraw Hill, New York.

Carr, P. H., DeVito, P. A., and Szabo, T. L. (1972). The effect of temperature and Doppler shift on the performance of elastic surface wave encoders and decoders. *IEEE Trans. Sonics Ultrason*. **SU-19**, 357–367.

Chiao, R. Y. and Hao, X. (2003). Coded excitation for diagnostic ultrasound: A system developer's perspective. *Ultrason. Symp. Proc*., 437–448.

Chiao, R. Y., Thomas, L. J., and Silverstein, S. D. (1997). Sparse array imaging with spatially-encoded transmits. *IEEE Ultrason. Symp. Proc*., 1679–1682.

Cole, C. R. (1991). Properties of swept FM waveforms in medical ultrasound imaging. *IEEE Ultrason. Symp. Proc*., 1243–1248.

Entrekin, R. R., Jago, J. R., and Kofoed, S. C. (2000). Real-time spatial compound imaging: Technical performance in vascular applications. *Acoustical Imaging*, Vol. 25. Halliwell, M. and Wells, P. N. T. (eds.). Kluwer Academic/Plenum Publishers, New York, pp. 331–342.

Fenster, A. and Downey, D. B. (1996). 3-D ultrasound imaging: A review. *IEEE Eng. Med. Bio.* **15**, 41–49.

Foster, F. S., Larson, J. D., Mason, M. K., Shoup, T. S., Nelson, G., and Yoshida, H. (1989a). Development of a 12 element annular array transducer for realtime ultrasound imaging. *Ultrasound in Med. & Biol.* **15**, 649–659.

Foster, F. S., Larson, J. D., Pittaro, R. J., Corl, P. D., Greenstein, A. P., and Lum, P. K. (1989b). A digital annular array prototype scanner for realtime ultrasound imaging. *Ultrasound in Med. & Biol.* **15**: 661–672.

Genis V., Obeznenko, I., Reid, I. M., and Lewin, P. (1991). Swept frequency technique for classification of the scatter structure. *Proc. of Annual Conf. on Engineering in Med. and Biol.* 13: 167–168.

Hughes, D. I. and Duck, F. A. (1997). Automatic attenuation compensation for ultrasonic imaging. *Ultrasound in Med. & Biol.* **23**, 651–664.

Jedrzejewicz, T., McLaughlin, G., Napolitano, D., Mo, L., and Sandstrom, K. (2003). Zone acquisition imaging as an alternative to line-by-line acquisition imaging. *Ultrasound in Med. & Biol.* **29**, No. 5S, S69–70.

Jensen, J. A., Nikolov, S. I., Misaridis, T., and Gammelmark, K. L. (2002). Equipment and methods for synthetic aperture anatomic and flow imaging. *Ultrason. Symp. Proc.*, 1518–1527.

Kino, G. S. (1987). *Acoustic Waves: Devices, Imaging, and Analog Signal Processing*. Prentice-Hall, Englewood Cliffs, NJ.

Krishnan, S., Rigby, K. W., and O'Donnell, M. (1997). Adaptive aberration correction of abdominal images using PARCA. *Ultrason. Imag.* **19**, 169–179.

Leavitt, S. C., Hunt, B. F., and Larsen, H. G. (1983). A scan conversion algorithm for displaying ultrasound images. Hewlett Packard J. **10**, Vol. 34., 30–34.

Lee, B. B., and Ferguson, E. A. (1982). Golay codes for simultaneous multi-mode operation in phased arrays. *IEEE Ultrason. Symp. Proc.*, 821–825.

Lewis, G. K. (1987). Chirped PVDF transducers for medical ultrasound imaging. *IEEE Ultrason. Symp. Proc.*, 879–884.

Lu, J.-yu. (1997). 2D and 3D high frame rate imaging with limited diffraction beams. *IEEE Trans. Ultrason. Ferroelec. Freq. Control* **14**, 839–856.

Lu, J-yu. (1998). Experimental study of high frame rate imaging with limited diffraction beams. *IEEE Trans. Ultrason. Ferroelec. Freq. Control* **45**, 84–97.

Mann, J. A., and Walker, W. F. (2002). A constrained adaptive beamformer for medical ultrasound: Initial results. *IEEE Ultrason. Symp. Proc.*, 1763–1766.

Maslak, S. M. (1985). Computed sonography. *Ultrasound Annual 1985*. R. C. Sanders and M. C. Hill (eds.). Raven Press, New York.

Melton Jr., H. E. and Skorton, D. J. (1981). Rational-gain-compensation for attenuation in ultrasonic cardiac imaging. *Ultrason. Symp. Proc.*, 607–611.

Morgan, D. P. (1991). *Surface Wave Devices*. For signal processing Elsevier, Amsterdam.

Nelson, T. R. and Pretorius, D. H. (1998). Three-Dimensional ultrasound imaging. *Ultrasound in Med. & Biol.* **24**, 1243–1270.

O'Donnell, M. (1992). Coded excitation system for improving the penetration of real time phased-array imaging systems. *IEEE Trans. Ultrason. Ferroelec. Freq. Cont.* **39**, 341–351.

Perez, J. E., Waggoner, A. D., Barzilia, B., Melton, H. E., Miller, I. G., and Soben, B. E. (1991). New edge detection algorithm facilitates two-dimensional echo cardiographic on-line analysis of left ventricular (LV) performance J. Am. Coll. Cardiol. 17: 291A.

Rigby, K. W., Chalek, C. L., Haider, B., Lewandowski, R. S., O'Donnell, M., Smith, L. S., and Wildes, D. S. (2000). In vivo abdominal image quality using real-time estimation and correction of aberration. *IEEE Ultrason. Symp. Proc*., 1603–1606

Schwartz, G. S. (2001). Artifact reduction in medical ultrasound. *J. Acoust. Soc. Am*. **109**, 2360.

Sharp, P. F. (1993). *Advances in Ultrasound Techniques and Instrumentation*, Chap. 1. P. N. T. Wells (ed.). Churchill Livingstone, New York.

Shen, J. and Ebbini, E. S. (1996a). A new coded-excitation ultrasound imaging system, Part I: Basic principles. *IEEE Trans. Ultrason. Ferroelec. Freq. Control* **43**, 141–148.

Shen, J. and Ebbini, E.S. (1996b). A new coded-excitation ultrasound imaging system, Part II: Operator design. *IEEE Trans. Ultrason. Ferroelec. Freq. Control* **43**, 131–140.

Shoup, T. A. and Hart, J. (1988). Ultrasonic imaging systems. *Ultrason. Symp. Proc*., 863–871.

Szabo, T. L., Melton Jr., H. E., and Hempstead, P. S. (1988). Ultrasonic output measurements of multiple mode diagnostic ultrasound systems. *IEEE Trans. Ultrason. Ferroelec. Freq. Control* **35**, 220–231.

Tirumalai, A. P., Lowery, C., Gustafson, G., Sutcliffe, P., and von Behren, P. (2000). Extended-field-of-view ultrasound imaging. *Handbook of Medical Imaging*, Vol. 3: Display and PACs. Y. Kim and S. C. Horii (eds.). SPIE Press Vol. PM81.

von Ramm, O.T., Smith, S. W., and Pavy Jr., H. E. (1991). High-speed ultrasound volumetric imaging system, Part II: Parallel processing and image display. *IEEE Trans. Ultrason. Ferroelec. Freq. Control* **38**, No. 2, 109–115.

Walker, W. F. and McAllister, M. J. (2002). Angular scatter imaging: Clinical results and novel processing. *IEEE Ultrason. Symp. Proc*., 1528–1532.

Wells, P. N. T. (1993). *Advances in Ultrasound Techniques and Instrumentation*. Churchill Livingstone, New York.

11 DOPPLER MODES

Chapter Contents

11.1 INTRODUCTION

Doppler ultrasound and imaging are focused on the visualization and measurement of blood flow in the body. This is a technological achievement because, until recently, the received echoes from the acoustic scattering from regions of blood, such as those in the chambers of the heart, were at levels so low that they could not be seen or appeared as black in an ultrasound image. Even when blood cannot be seen directly, its movement can be detected. Now images of blood circulation, called color flow imaging (CFI), as well as precise continuous wave (CW) and pulsed wave (PW) Doppler measurements of blood flow, are routine on imaging systems. In this specialized area of ultrasound, interrogating beams are sent repeatedly in the same direction and are compared to each other to determine the movement of blood scatterers over time. All the usual physics of ultrasound apply, including beam directivity, transducer bandwidth, absorption, and the scattering properties of the tissue (blood). Doppler detection is a blend of physics and specialized signal processing techniques required to extract, process, and display weak Doppler echoes. Doppler techniques provide critical diagnostic information noninvasively about the fluid dynamics of blood circulation and abnormalities.

11.2 THE DOPPLER EFFECT

Most of us have heard of the Doppler effect, which is the perceived change in frequency as a sound source moves toward or away from you. Since sound is a mechanical disturbance, the frequency perceived is the effective periodicity of the wavefronts. If the source is moving directly toward the observer with a velocity (c_s) in a medium with a speed of sound (c_0) then the arriving crests appear closer together, giving the observer the acoustic illusion of a higher frequency. As illustrated in Figure 11.1, the perceived frequency depends on the direction in which the source is moving toward or away from the observer. Pierce (1989) has shown that the perceived frequency is related to the vector dot product of the source (c_s) and unit observer (u_0) vectors, which differ by an angle θ, $v_x = c_s \cdot u_0 = c_s \cos\theta$,

$$f = f_0 + (f_D/c_0)c_s \cdot u_0 \tag{11.1a}$$

and solving for the Doppler frequency (f_D) in terms of the transmitted frequency (f_0),

$$f_D = \frac{f_0}{1 - (c_s/c_0)\cos\theta} \tag{11.1b}$$

leads to a Doppler shift, correct to first order when $c_S = c_0$,

$$\Delta f = f_D - f_0 = f_0(c_s/c_0)\cos\theta \tag{11.1c}$$

From this equation, the perceived frequencies for the observers in Figure 11.1 can be calculated for a 10-kHz source tone moving at a speed of 100 km/hr ($v = 27.78\, m/s$)

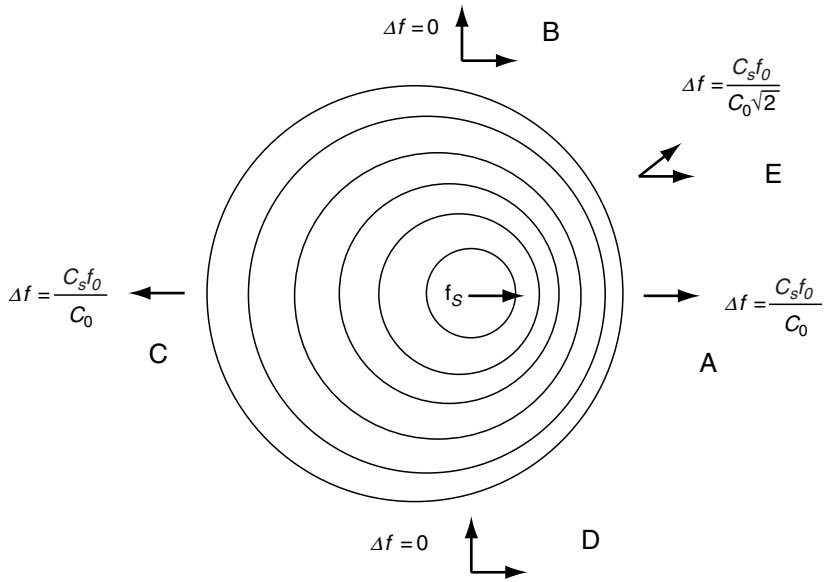

Figure 11.1 Doppler-shifted wave frequencies from a moving source as seen by observers at different location and at the following angles relative to the directions of the source: (A) 0°; (B) 90°; (C) 180°; (D) 270°; (E) 45°.

in air ($c_0 = 330\,m/s$). Observers B and D, at 90° to the source vector, hear no Doppler shift. Observer A detects a frequency of 10,920 Hz, while observer C (here, $\theta = \pi$) hears 9,220 Hz.

A similar argument yields an equation for a stationary source and a moving observer with a velocity (c_{obs}),

$$f = [1 + (v_{obs}/c_0)\cos\theta]f_0 \tag{11.2}$$

The Doppler effect plays with our sense of time, either expanding or contracting the timescale of waves sent at an original source frequency (f_0). Furthermore, it is important to bear in mind the bearing or direction of the sound relative to the observer in terms of vectors.

Now consider a flying bat intercepting a flying mosquito based on the Doppler effect caused by the relative motion between them (see Figure 11.2). It is straightforward to show that if the mosquito source has a speed of c_s, and the bat has a speed of c_{obs}, the corresponding equation for the Doppler-shifted frequency is

$$f = f_0[1 + (c_{obs}/c_0)\cos\theta]/[1 - (c_s/c_0)\cos\theta] = f_0[c_0 + c_{obs}\cos\theta]/[c_0 - c_s\cos\theta] \tag{11.3}$$

In other words, the flying mosquito perceives the bat signal as being Doppler shifted, and the bat hears the echo as being Doppler shifted again due to its motion. Of course, this situation is simplified greatly, as is Figure 11.1, because it is depicted two-dimensionally. This description has been adequate for most medical ultrasonics, in

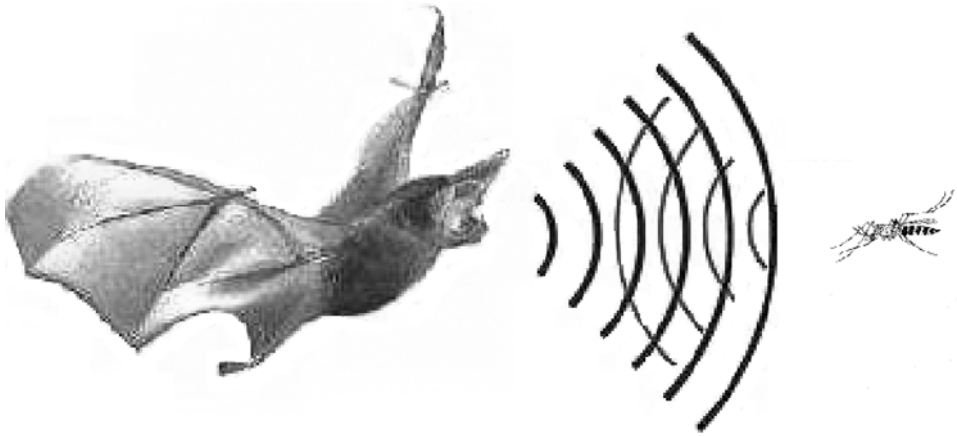

Figure 11.2 Bat detects insect target with ultrasound pulse echoes.

which imaging is done in a plane, until the comparatively recent introduction of 3D imaging.

The aero-duel between the bat and insect is played out three-dimensionally in real-time. The poor mosquito beats its wings about 200 flaps/sec, which is the annoying whine you may hear just as you are about to fall asleep on a hot night. The moth also acts as an acoustic sound source at a softer 50 flaps/sec. Enter the bat which, depending on the type, has an ultrasound range between 20 and 150 kHz (e.g., the range of the horseshoe bat is 80–100 kHz). This corresponds to an axial resolution of 2–15 mm, which is perfect for catching insects. The bat emits an encoded signal, correlates the echo response in an optimum way (shown to be close to the theoretical possible limit), adapts its transmit waveform as necessary as it closes in on its target, changes its flight trajectory, and usually intercepts the insect with a resolution comparable to the size of its mouth, all in real time. Researchers are still trying to understand this amazing feat of signal processing and acrobatics and how a bat utilizes the Doppler shift between it and a fast-moving insect in 3D and while changing trajectories. Studies have shown how a bat interprets the following clues: Doppler shift (the relative speed of prey); time delay (the distance to the target); frequency and amplitude in relation to distance (target size and type recognition); amplitude and delay reception (azimuth and elevation position); and flutter of wings (attitude and direction of insect flight). One of the key signal processing principles a bat utilizes is the repetitive interrogation of the target so that the bat can build an image of the location and speed of its prey, pulse by pulse.

One of the earliest instances of pulse-echo Doppler ultrasound is in the original patent submitted by Constantin Chilowsky and Paul Langevin (1919) in 1916. Recall from Chapter 1 that their invention made underwater pulse-echo ranging technologically possible as a follow-up to earlier patents by Richardson (1913) (who also mentioned the Doppler shift but as a problem) for acoustic iceberg detection to prevent another Titanic disaster. In their patent, they mention a method to detect

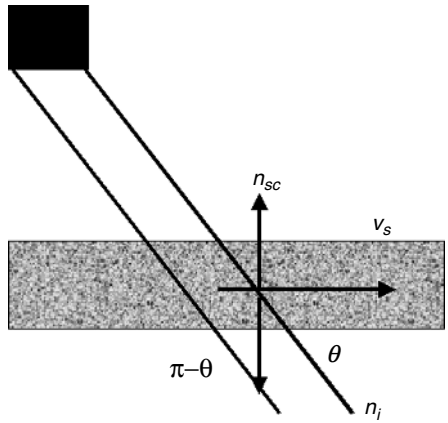

Figure 11.3 Sound beam intersecting blood moving at velocity v in a vessel tilted at angle θ.

relative motion between the observer and target by comparing the Doppler-shifted frequency from the target to the frequency of a stable source.

The dot product results from the moving source, and moving observer cases can be applied to the simplified situation of a transducer sensing the flow of blood in a vessel flowing with velocity and direction (v_t) at an angle (θ) to the vessel, as depicted in Figure 11.3. In this case, the transducer is infinitely wide and the intervening tissues have negligible effect. The blood velocity is much smaller than the speed of sound in the intervening medium (c_0). The signal as seen from an observer riding the moving blood appears to be Doppler shifted,

$$\omega_T = \omega_2 + c_D \cdot k_i = \omega_0 + c_D \cdot \left(\frac{\omega_i}{c_0}\right) n_i \tag{11.4a}$$

where ω_T is the shifted angular frequency, ω_2 is the angular frequency seen by the scattering object from a moving coordinate system, ω_i is the incident angular frequency, c_D is the Doppler velocity, and n_i is in the direction of the incident k vector along the beam. The returning scattered signal along unit vector n_{sc} appears to be from a moving source and is Doppler shifted,

$$\omega_R = \omega_2 + c_D \cdot k_{sc} = \omega_2 + c_D \cdot \left(\frac{\omega_{sc}}{c_0}\right) n_{sc} \tag{11.4b}$$

where ω_R is the shifted angular frequency, ω_{sc} is the scattered frequency Doppler, and n_{sc} is in the direction of the scattered k vector back toward the transducer. For a coincident transmitter and receiver, the overall Doppler shift can be found by subtracting the ω_R from ω_T and letting $\omega_{sc} \approx \omega_i \approx \omega_0$ to first order,

$$\omega_R - \omega_T = \omega_0(c_D/c_0)[1 + \cos(\theta) - \cos(\pi - \theta)] = \omega_0(c_D/c_0)[2\cos\theta] \tag{11.4c}$$

or in the form of the classic Doppler shift frequency,

$$f_D = \Delta f = f_R - f_T = [2(v/c_0)\cos\theta]f_0 \tag{11.4d}$$

Before looking at ways that this Doppler shift can be implemented in instrumentation, it is worth understanding more about the properties of blood and how it interacts with sound.

11.3 SCATTERING FROM FLOWING BLOOD IN VESSELS

Even though it is a fluid, blood is considered to be a highly specialized connective tissue. One of the main purposes of blood is to exchange oxygen and carbon dioxide between the lungs and other body tissues. There are typically 5 L of blood in an adult, or about 8% of total body weight. Blood is continually changing the suspension of red blood cells, white blood cells, and platelets in a solution called plasma. Red blood cells (erythrocytes) are the most plentiful, with about 5 million cells per microliter. Each cell is a disk that is concave on top and bottom (like the shape of a double concave lens with a smooth-rounded outer ridge encompassing it) and about 7μm in diameter and 2μm in thickness. For adequate combination with oxygen, red blood cells must have a normal amount of hemoglobin (a red protein pigment that depends on the iron level in the body). White blood cells, or leukocytes, are about twice as big as red blood cells, but there are fewer of them (only 4000–10,000 in a microliter). Platelets, which have a cross section that is 1/1000 that of red blood cells, are fragments and are also fewer in number than red blood cells (about 250,000–450,000 per microliter). A standard laboratory measurement is hematocrit, which is the ratio of the volume of red blood cells, packed by a centrifuge operation, to the overall blood volume. A typical ratio of hematocrit for a normal person is 45%; other values may indicate health problems.

The consistency of blood can change in different parts of the circulatory system. The viscosity of blood is 4.5–5.5 times that of water. Red blood cells can clump together or aggregate. A particular type of grouping is rouleau, which is a long chain of stacked cells. These groupings have a dramatic effect on ultrasound backscatter in veins. Not only is blood changing, breath by breath, but it is also being replenished; red blood cells last about 120 days, and white blood cells last less than 3 days.

Blood is also sensitive to vessel architecture. To first order, if blood is considered to be an incompressible Newtonian fluid in a long rigid tube with a changing diameter (shown in Figure 11.4), the mean fluid velocity averaged over a cross section ($\bar{v}$) obeys the following steady-state relation (Jensen, 1996):

$$A(z_1)\bar{v}(z_1) = A(z_2)\bar{v}(z_2) \tag{11.5a}$$

where z is the tube axis. The volumetric flow rate (Q) is constant through changes in tube cross section,

$$Q = A(z)\bar{v}(z) \ (\mathrm{m}^3/\mathrm{s}) \tag{11.5b}$$

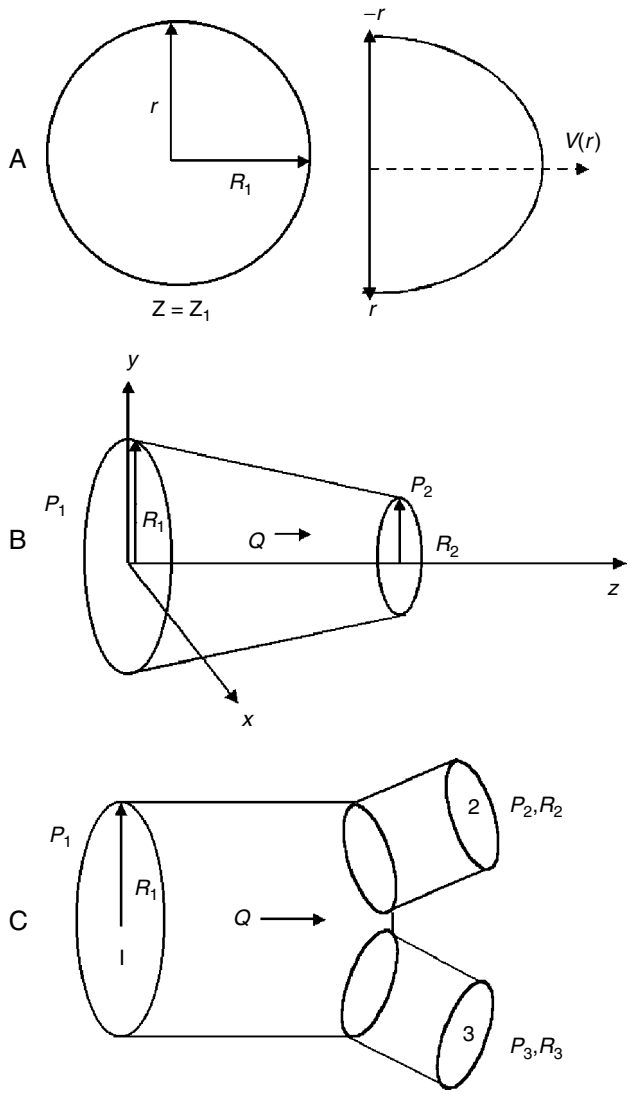

Figure 11.4 Fluid flow in vessels containing a Newtonian fluid. (A) Parabolic velocity distribution in vessel cross section. (B) Fluid flow constant for different cross sections. (C) Flow into branches.

and is analogous to current in a wire. In the case of narrowing, the fluid velocity increases by the ratio of the square of the radii.

The pressure drop for a tube with a constant radius, similar to voltage drop in the electrical analogy (Jensen, 1996), is called Poiseuille's law,

$$\Delta P = P(z_2) - P(z_1) = R_f Q \tag{11.5c}$$

where R_f is viscous resistance. Laminar flow in a long rigid tube has a parabolic distribution of fluid velocity across its diameter, with v_o, the maximum value in the tube center,

$$v(r) = \left(1 - \frac{r^2}{R^2}\right) v_o \tag{11.6a}$$

For a parabolic flow distribution, the resistance for an outer diameter R is (Jensen, 1996)

$$R_f = 8\mu l/(\pi R^4) \tag{11.6b}$$

where μ is viscosity in $kg/(m \cdot s)$ and l is the tube length over which the pressure drop occurs. If a circular rigid tube branches into n smaller circular tubes of different outer diameters (R_n), the volumetric flow rate is conserved, and fluid velocity in each branch (v_n) is related by

$$\pi R_0^2 v_0 = \sum_{n=1}^{N} \pi R_n^2 v_n \tag{11.7}$$

Bernoulli's law expresses the conservation of energy for fluid flow in a tube, including potential, kinetic, and thermal energies. From this law, which is more general than Poiseuille's law, it is possible to relate the pressure drop to changes in geometry or fluid velocity. A simplified version for constant temperature and height is

$$P_1 + \frac{1}{2}\rho v_1^2 = P_2 + \frac{1}{2}\rho v_2^2 \tag{11.8}$$

This important relation shows that where pressure is high, fluid velocity is low and vice versa. For example, when a parabolic velocity distribution occurs, as in Eq. (11.6a), Bernoulli's law indicates that pressure will be highest at the walls of the vessel and lowest in the center.

Realistically, blood is not an incompressible fluid but has a viscosity that changes with shear flow rate. Furthermore, vessels are not long, rigid tubes but are elastic with curved, complicated branching geometries. Finally, from the pumping of the heart, the flow is pulsatile and sometimes turbulent (not a steady flow). These practical considerations indicate that the previous equations are rough guidelines; reality is far more complicated. Despite these problems, Doppler ultrasound provides a remarkable, noninvasive dynamic depiction of blood flow *in vivo* that cannot be obtained by any other method.

How does sound interact with blood? Viewed as a homogeneous tissue, blood has an acoustic impedance and sound speed that depend on the red blood cell content, but typically it is $Z = 1.63$ megaRayls and $c = 1.57\text{mm}/\mu\text{s}$ (Bamber, 1986). Early measurements by E. L. Carstensen and H. P. Schwan (1959) of acoustic absorption for different concentrations of hemoglobin and sound speed dispersion agree well with the time causal relations of Chapter 4 (shown in Figure 11.5). Hemoglobin is a red-iron–containing pigment that gives red blood cells their color. The hematocrit is the percentage of whole blood that is comprised of red blood cells.

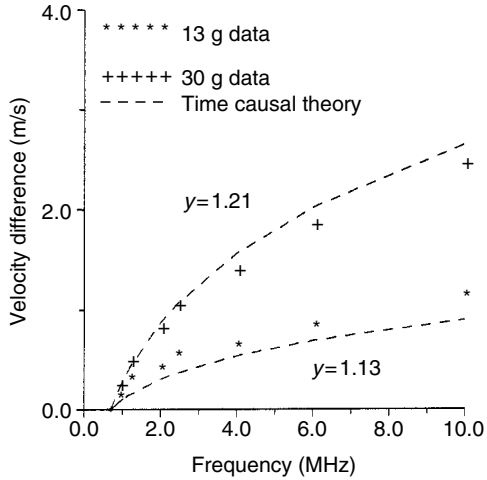

Figure 11.5 Absorption of hemoglobin solutions versus frequency for concentrations of 13 and 30 g/100 cm^3. Power law fits to data of Carstensen and Schwan (1959) have exponents $y = 1.21$ (top curve) and $y = 1.13$ (bottom curve) (from Szabo, 1993).

What are the backscattering properties of blood as a tissue? R. A. Sigelmann and J. M. Reid (1973) developed one of the first calibrated tissue characterization methods to measure backscatter from blood. Even though blood has been modeled as a continuous inhomogenous medium (Angelsen, 1981), it is most often regarded as a collection of red blood cells because they predominate over other cell types. Because of the small size of red blood cells ($\sim 7\,\mu$m) relative to an insonifying wavelength (750–150 μm for 2–10 MHz), initially they were modeled as Rayleigh scatterers with backscattering proportional to the fourth power of frequency. Shung (1982) showed that by modeling the cells as cylinders, better agreement was obtained than modeling the cells as spheres (shown in Figure 11.6). Coussios (2002) simulated cells as disks and found a fourth power of frequency using the Born approximation. Cylinders and discs have a strong preferential directivity that agrees with the fact that blood appears to be anisotropic (Teh and Cloutier, 2000). The arrangement of cells into rouleaux and rouleau networks further increases the degree of anisotropy and the directional dependence of backscatter. Furthermore, backscatter is flow dependent (Wang *et al.*, 1997; Fontaine *et al.*, 1999; Teh and Cloutier, 2000). Wang *et al.* (1997) found, for example, that backscatterer was lower in the vena cava than in the aorta, where flow was faster. The backscatter peaks at about 26% hematocrit; consequently, it is not a monotonic or single-valued function of hematocrit.

Millions of red blood cells have been analyzed statistically, and they were found to have a Rayleigh distribution (Mo and Cobbold, 1986). Like tissue microstructure and the resultant texture discussed in Chapter 8, the granular and apparent random nature of red blood cells also produce specklelike behavior at conventional Doppler frequencies.

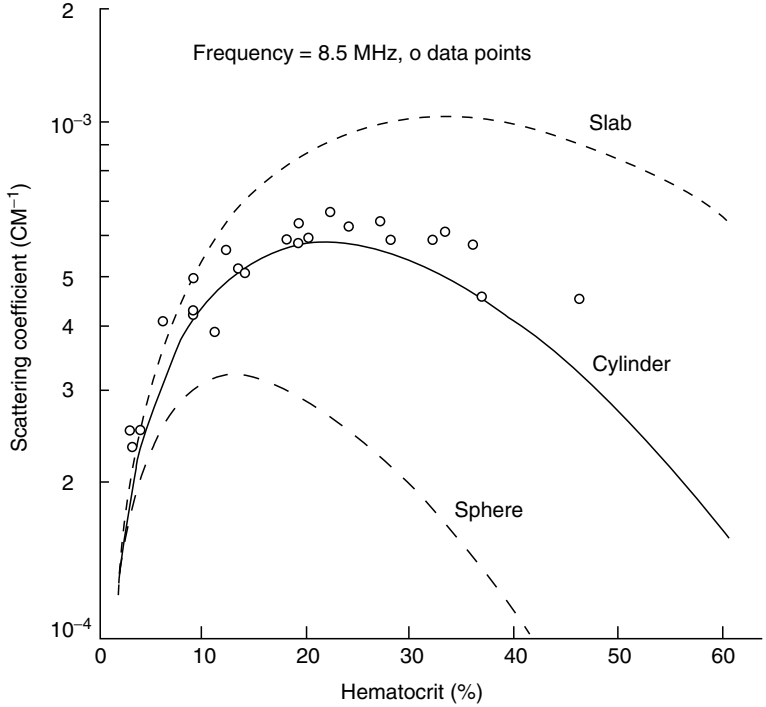

Figure 11.6 Backscattering of blood versus hematocrit compared with models of cells as spheres or cylinders (from Shung, 1982, *IEEE*).

Measurements at higher frequencies where wavelengths approach the dimensions of red blood cells (43–23 μm for 35–65 MHz) demonstrate different behavior. Absorption of blood measured by Lockwood *et al*. (1991) approaches that of other tissue (half that of the arterial wall) in Figure 11.7. Likewise, backscatter coefficients for flowing blood are comparable with those for some vascular tissues; they increase at high flow rates (as shown in Figure 11.8), and they have similar power law dependence ($y \sim 1.4$). As shown later in Section 11.8, the echogenecity of blood is sufficient at higher imaging frequencies to allow the direct visualization of blood. By using their dual-gated Doppler system, Nowicki and Secomski (2000) and Secomski *et al*. (2003) demonstrated that the speed of sound and attenuation are monotonic functions of hematocrit, even though acoustic power is not (Figure 11.9).

11.4 CONTINUOUS WAVE DOPPLER

Compared to the bat, Doppler medical ultrasound seems to be comparatively simple. Satomura (1957) reported CW experiments with Doppler-shifted ultrasound signals produced by heart motion. His work marked the beginning of many Doppler developments for diagnosis.

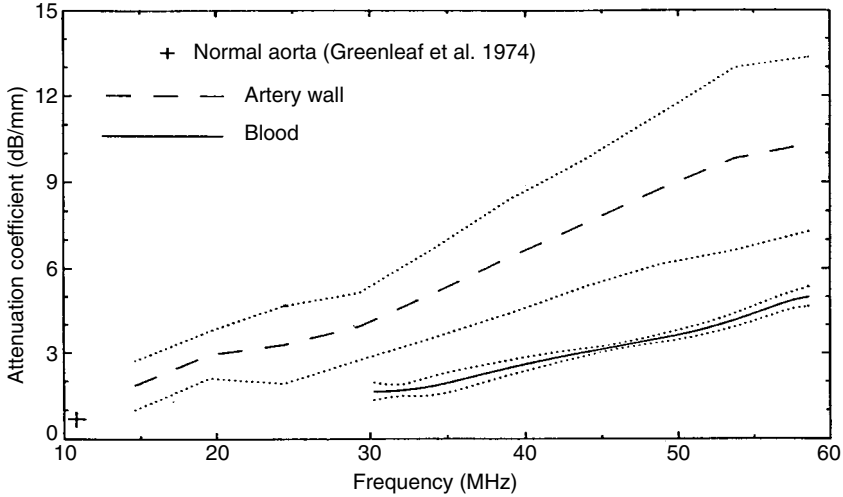

Figure 11.7 Attenuation measurements in artery samples and blood, summarized with the standard deviation in the data shown as dotted lines. Attenuation of human aorta measured at 10 MHz and 20° C by Greenleaf *et al.* (1974) inserted for comparison (from Lockwood *et al.*, 1991, reprinted with permission from the World Federation of Ultrasound in Medicine and Biology).

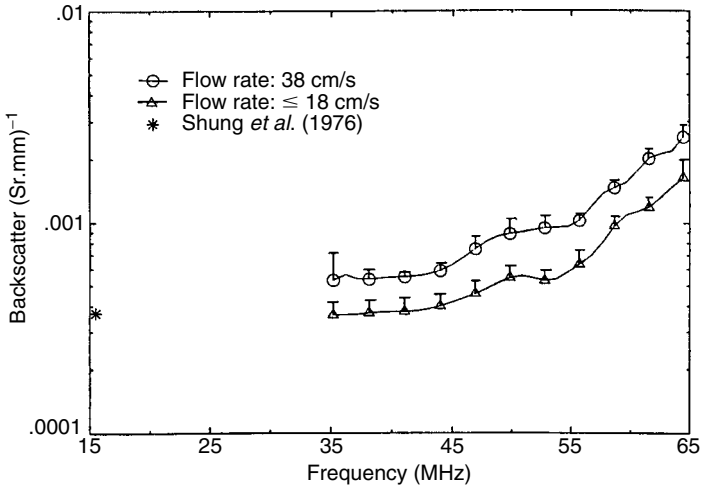

Figure 11.8 Summary of scattering measurements of flowing blood. Data measured by Shung *et al.* (1976) at 15 MHz inserted for comparison (from Lockwood *et al.*, 1991, reprinted with permission from the World Federation of Ultrasound in Medicine and Biology).

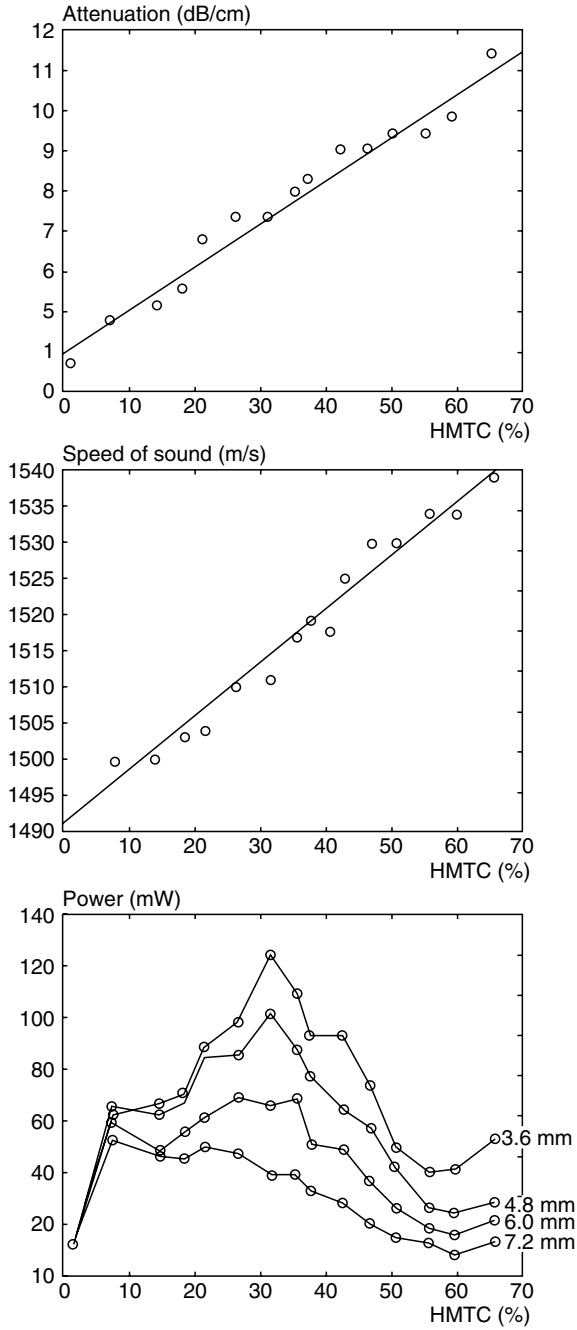

Figure 11.9 (Top) Attenuation versus hematocrit. (Middle) Speed of sound versus hematocrit. (Bottom) Power versus hematocrit for four gate settings (from Nowicki and Secomski, 2000, *IEEE*).

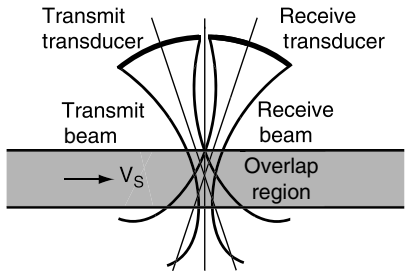

Figure 11.10 Split stand-alone CW Doppler transducer showing split faces and the intersection of transmit and receive beams.

Early Doppler systems were completely analog with high sensitivity and selectivity. The classic CW Doppler subsystem is still a mainstay of modern ultrasound imaging systems. The "stand-alone" CW probe usually consists of a spherically concave transducer split in halves for transmit and reception (Evans and Parton, 1981). Actually, the centers of the halves are tilted slightly so that the transmit and receive beams intersect over a region of interest (as shown in Figure 11.10). To a good approximation, the Doppler Eq. (11.4d) still works for this geometry, with the centerline between halves serving as the angle reference line.

The halves are connected to a CW Doppler system similar to the one shown in Figure 11.11. By incorporating the transmit signal at f_0 into the receive signal path, the Doppler signal can be extracted with its amplitude and phase preserved. The processing is straightforward and is symbolized by the spectral graphs at different stages (signposted by letters), of the Doppler system in Figure 11.11. In this figure, single lines show CW spectra, solid lines show real spectra, and dashed lines show

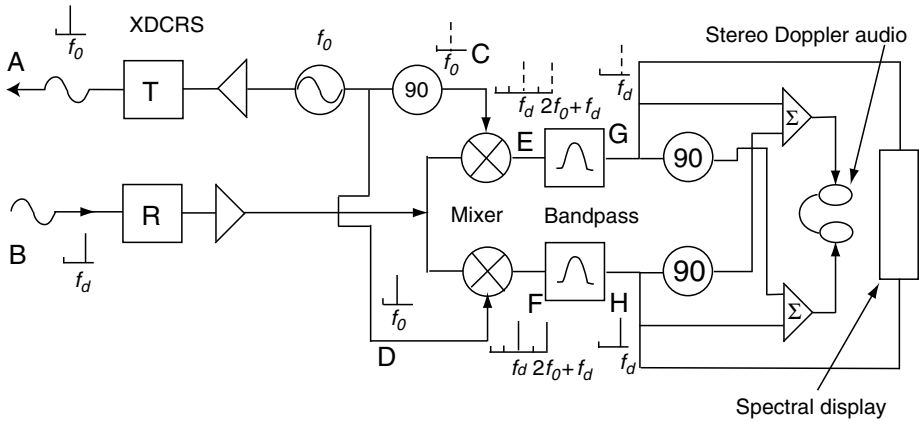

Figure 11.11 Block diagram for CW Doppler ultrasound system for a split stand-alone transducer.

imaginary (shifted by 90°) spectra. The transmitted signal is a CW *cosine* at *A*. The Doppler-shifted signal is received at *B*, and it enters a pair of multiplier mixers. The top mixer multiplies a 90° shifted source signal, sin ($\omega_0 t$), with the echoes to produce, at *E*, an imaginary Doppler signal, (f_D), near $f = 0$ and one near $2f_0$. Similarly, the lower mixer creates, at *F*, real spectra at those frequencies. Bandpass filters remove both $f = 0$ signals due to stationary tissue and the Doppler near $2f_0$ to supply an "I" (for in-phase) signal at *H* and a quadrature "Q" signal at *G*. These two signals combined can be considered to be an analytic signal (see Appendix A) with only a positive Doppler-shifted frequency. Recall that the analytic signal can be created with a Hilbert transform (Appendix A). It comes as no surprise that, except for front end amplification, all the processing can also be done digitally after analog-to-digital (A/D) conversion through Hilbert transforming and digital filtering. Furthermore, the spectral display can be conveniently performed by a fast Fourier transform (FFT). The remaining processing in the system, consisting of phase shifts, separates the signals into a forward flow and a reverse flow for stereo audio enjoyment.

By a fortuitous coincidence, the Doppler-shifted frequencies fall within the human hearing range for typical ultrasound frequencies in combination with most of the blood velocities encountered in the body. Typical values are calculated for different angles from the Doppler equation, Eq. (11.4d), and plotted in Figure 11.12. These velocities extend from about 150 mm/s in the vena cava to 3000 mm/s in the ascending aorta. Just as physicians have learned to use the stethoscope, expert users of CW Doppler can detect abnormalities in flow just by listening, as Robert Hooke foresaw more than 300 years ago (see Chapter 1).

While stand-alone probes are regarded as being extremely sensitive, a more convenient way of obtaining CW signals is to use an imaging array. The most common configuration is to split an array into two sections (subarrays) for transmit and receive. Steering and focusing are under electronic control and provide much more flexibility than the fixed-focus stand-alone probe. Furthermore, system signal processors and computers can be used for computation and display. While stand-alone users "fly blind," in that there are no visual cues to guide the correct placement of the sensitive beam area, CW in arrays can be combined with B-mode or color flow imaging to locate and align the Doppler beam with a vessel or region of interest as described in duplex and triplex modes in Chapter 10.

An example of a triplex mode, including color flow imaging overlaid on a gray-scale image and CW Doppler, is illustrated by Figure 11.13. At the top of the display is a small insert showing a complete gray-scale heart image with a color flow overlay. Even though color flow imaging will be discussed later, the reader should appreciate that this image is a global view of the flow in the left ventricle of the heart. The color code at the right indicates that orange represents positive velocities flowing toward the transducer, and blue represents those flowing in a direction away from the transducer. The line through this colored region and the apex is the direction of the CW Doppler measurement; it includes mainly blue with a few small orange regions.

The spectral display in gray depicts Doppler-shifted frequencies representing velocities as a function of time. From left to right, there seems to be a pattern that almost repeats itself. This pattern can be thought of in terms of two timescales: slow time and

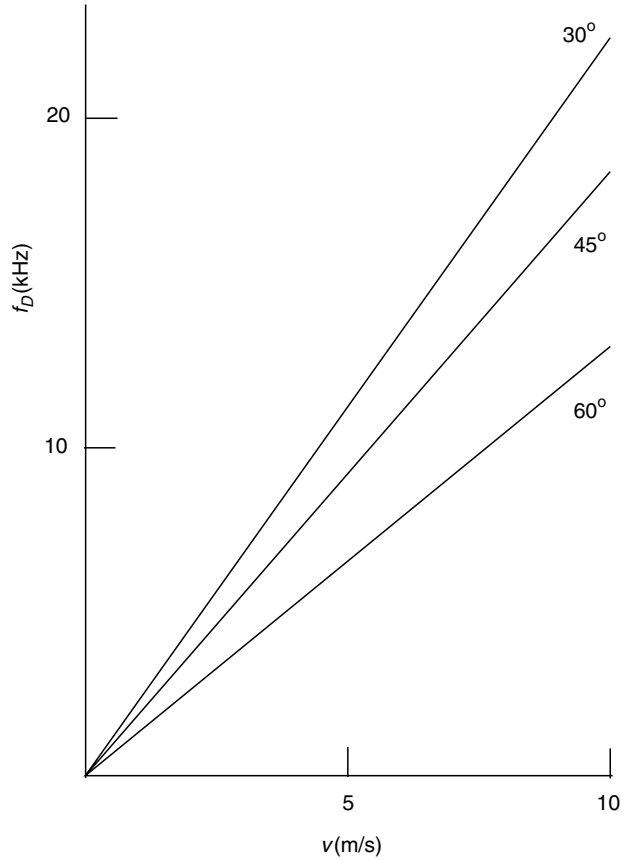

Figure 11.12 Doppler shift frequencies for source frequency of 2 MHz as a function of velocities (v) for different angles with $c_0 = 1.54\ km/s$.

fast time. A time window (T) is used to calculate a fast time snapshot spectrum of the flow. This process is continually repeated with the next time window placed to the left of the one before it. The overall scale of several repetitions can be considered to be slow time; there is a horizontal slow timescale in beats per minute above the spectrogram. As a new snapshot is displayed on the left end of the slow timescale, the last one on the right disappears, so the visual effect is that time records are scrolling to the right on the display. A careful look reveals that each snapshot is not identical but represents a live indication of the dynamic changes happening during cardiac cycles. As expected from the color flow image, both positive and negative velocities are shown characteristic of the backflow that occurs in regurgitation. The spectrum has a velocity scale to the right in meters per second. The granular appearance of the spectrogram resembles speckle.

To examine the influence of other major physical effects on Doppler processing, it is helpful to apply a block diagram approach to the overall system, as depicted in

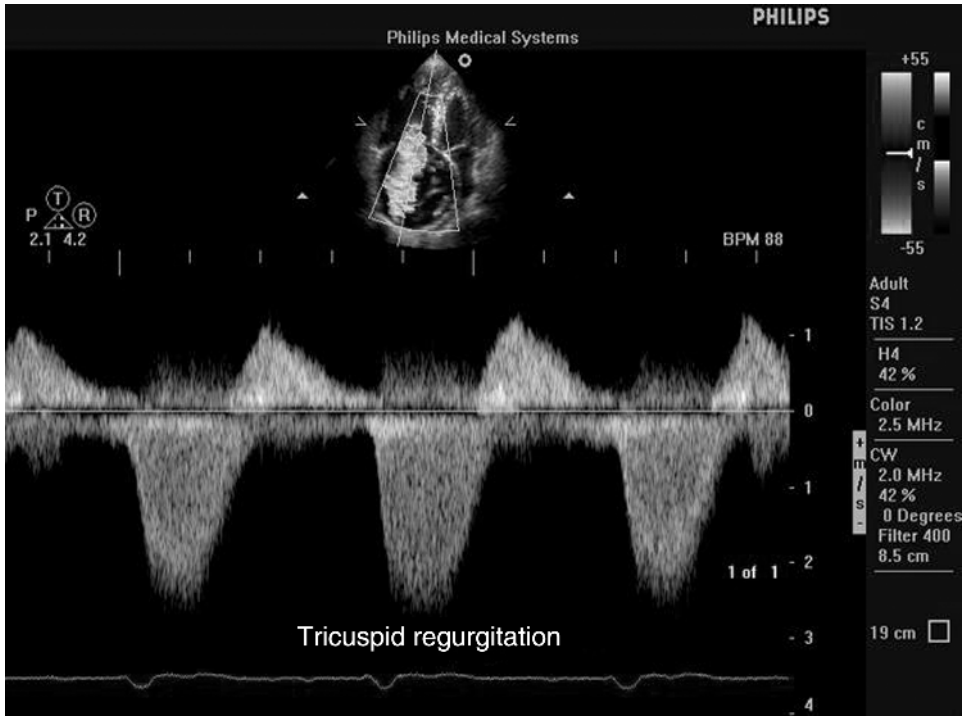

Figure 11.13 Duplex imaging mode of tricuspid regurgitation for CW Doppler velocity display with a color flow image insert (above) with direction of CW line (courtesy of Philips Medical Systems) (see also color insert).

Figure 11.14. Many of the individual blocks are recognizable from their use in the overall block diagram (see Figure 2.14). In the system are the already discussed source, bandpass filter, time gate, FTT, and audio detector. The physical processes out of the Doppler box, representing points *A* through *B* for the round-trip path in the time domain, can be represented by

$$v_B = s *_r (h_t *_t h_r) *_t a_r *_t a_t *_t e_{RT} *_t v_a \tag{11.9}$$

where v_a is the excitation voltage. The transducer impulse response, $e_{RT} = e_g *_t e_t$, has little effect since only a narrow bandwidth transducer with good efficiency (light or air backing) is required. Attenuation, symbolized on transmit and receive paths by a_t and a_r, to the target and back is practically a constant factor at a single frequency and depth. The major physical factors are the beam diffraction (represented by h) and the scatterers (s). The individual unresolved blood cells, moving at different velocities from positions within the vessel that are insonified by the beam, cause a statistical specklelike variation and resultant Doppler shifts.

Newhouse *et al*. (1980) have shown that the distribution of red blood cells caught in the sound beam cause transit time broadening, which is caused by the geometric extent (or broadening) of the beam. Recall from Chapter 7 that the cross section of a

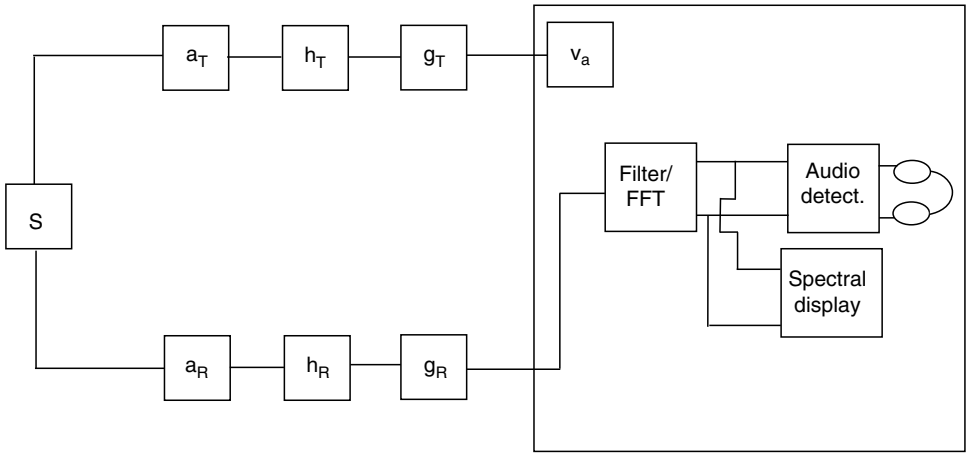

Figure 11.14 Block diagram for CW Doppler ultrasound system and related physical effects.

beam, especially in the focal plane, can be described as a function of a lateral dimension or angle, as well as a function of frequency. This effect is also present for the Doppler case. Newhouse *et al*. (1980) utilized the focal plane, or far field, full width half maximum (FWHM) beamwidth formula ($w = 0.8\lambda F/a = 0.8c_0F/(af_0)$ to derive an estimate for the spectral broadening of the Doppler spectrum from a circular beam,

$$\Delta f_D/f_D = (0.8\lambda F/a)\tan\theta = [0.8c_0F/(af_0)]\tan\theta \tag{11.10}$$

Cobbold *et al*. (1983) examined the effects of beam misalignment with the vessel and attenuation effects (which they found to be small when the beam size was comparable to the vessel diameter) on the mean velocity. This is a key parameter in estimating volumetric flow. In summary, the block diagram proposed provides a comprehensive way of accounting for important factors affecting Doppler signals.

11.5 PULSED WAVE DOPPLER

11.5.1 Introduction

To overcome range ambiguity, which is the well-known limitation of CW Doppler (which is sensitive to whatever vessels intersect its entire beam), PW Doppler (Wells, 1969a; Baker, 1970) was devised to control the region of active insonification. Like the bat, a pulsed Doppler system sends ultrasound pulses of a chosen length repetitively to a target at a certain range. Another duplex image (in Figure 11.15) shows PW Doppler in combination with a color flow image. In this case, superimposed on the image is a line with a marker indicating the pulse length, range depth, and direction; below is the Doppler velocity spectrum in a display similar to that used for the CW Doppler in Figure 11.13. Both the range and interrogating pulse length are

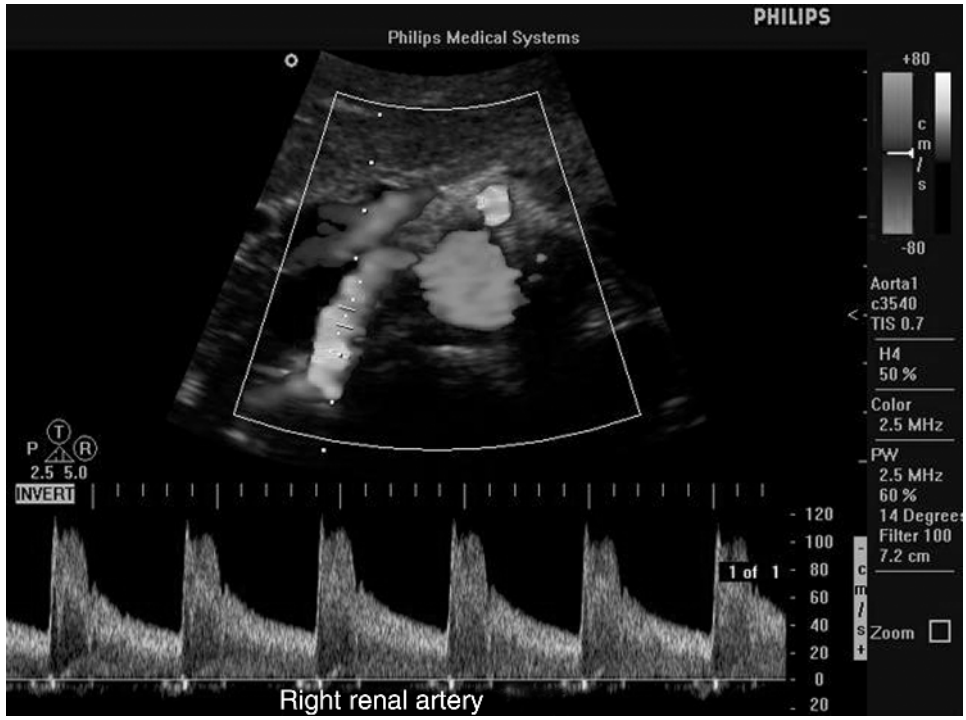

Figure 11.15 Duplex imaging mode of a right renal artery for PW Doppler velocity display, with a color flow image insert (above) with direction of PW line and Doppler gate position (courtesy of Philips Medical Systems) (see also color insert).

controllable. From the image, an angle to the vessel can be determined and entered into some systems to correct for the Doppler *cosine* angle variation.

Range-gated pulsed Doppler systems are different from CW systems in important ways, even though they may seem similar superficially. Unlike the CW model of Doppler-shifted wavefronts of Figure 11.1, finite length pulses are used. In addition to expected time dilation or contraction by the Doppler effect, changes in pulse delay arrival time are also involved (Wilhjelm and Pedersen, 1993a; Jensen, 1996). For a transmitted waveform, $v_A(t)$, Jensen (1996) has shown that the received Doppler-shifted output signal has the form (assuming no absorption or diffraction effects), of

$$v_B(t) = v_A\left[\Psi\left(t - \frac{2d_0}{\Psi c_0}\right)\right] = v_A\left[\Psi t - \frac{2d_0}{c_0}\right] \tag{11.11a}$$

where d_0 is the distance to the target, and the Doppler scaling factor Ψ is

$$\Psi = 1 - \frac{2c_D \cos\theta}{c_0} = 1 - \delta_D \tag{11.11b}$$

that appears in Eq. (11.11a) as a timescaling factor for dilation or contraction and also as a time delay modifier, and $\delta_D = 2c_D \cos\theta / c_0$, is an often-used constant.

In CW Doppler, the Doppler-shifted received frequency is compared to the transmitted frequency; however, in range-gated Doppler, each received echo is compared to a similar echo resulting from the previous transmission. The relative delay between Doppler-shifted echoes from consecutive pulses is simply (Bonnefous *et al.*, 1986; Wilhjelm and Pedersen, 1993a; Jensen, 1996)

$$t_d = \frac{2\Delta z}{c_0} = \frac{2T_{PRF}c_D \cos\theta}{c_0} = \delta_D T_{PRF} \tag{11.11c}$$

where Δz is the distance traveled away from the transducer and T_{PRF} is the time between transmit pulses, and PRF is pulse repetition frequency.

This comparison has the important consequence that it is relatively insensitive to the absorption and diffraction effects on the paths through intervening tissues to the target site. Pulse to pulse, these factors do not change much, so they are compared on a consistent basis; however, they affect overall sensitivity. Otherwise, absorption would cause a considerable downshift (on a Doppler scale) in the center frequency of the transmitted pulse (as discussed at the end of Chapter 4); consequently, it would generate a false Doppler signal (Jensen, 1996). Note that for the CW case, variations and loss caused by the diffraction of the beam and increasing absorption loss with depth can contribute to a diminishing sensitivity, which can be a problem for a real system with noise and limited dynamic range. Pulsed Doppler, when implemented on arrays, provides a number of advantages: a larger variable aperture, electronically controlled focusing and steering, and the ability to vary the sample volume by adjustment of the pulse length.

11.5.2 Range-Gated Pulsed Doppler Processing

Before beginning the derivation of equations for pulsed Doppler, it is worth discussing the primary difference between pulsed and continuous wave Doppler. This difference is sampling. Just as array elements behave as spatial samplers (as discussed in Chapter 7), Doppler pulses act as time domain samplers. The repetitive nature of these pulses can be most conveniently represented by the *shah* or sampling function from Appendix A. Recall that the Fourier transform of the *shah* function is a replicating function in the frequency domain, which will allow us to characterize the Doppler spectrum. This approach will also easily show the consequence of undersampling, which is the chief limitation of pulsed Doppler. This section will end with an expression for the Doppler-shifted frequencies for the pulsed approach.

As described in Chapter 10, a master clock sends pulses repetitively at a pulse repetition frequency (f_{PRF}) along the same direction that is selected by the user. Parameters of interest are depicted by Figure 11.16. The time between pulses is the pulse repetition interval, $PRI = T_{\mathrm{PRF}} = 1/f_{PRF}$. Each pulse is an M period of the fundamental f_0, or the gate length is

$$T_g = MT = M/f_0 \tag{11.12a}$$

The tone bursts transmitted at intervals T_{PRF} can be described approximately as

$$v_A(t) = g(t)^* {}_t III(t/T_{PRF}) \tag{11.12b}$$

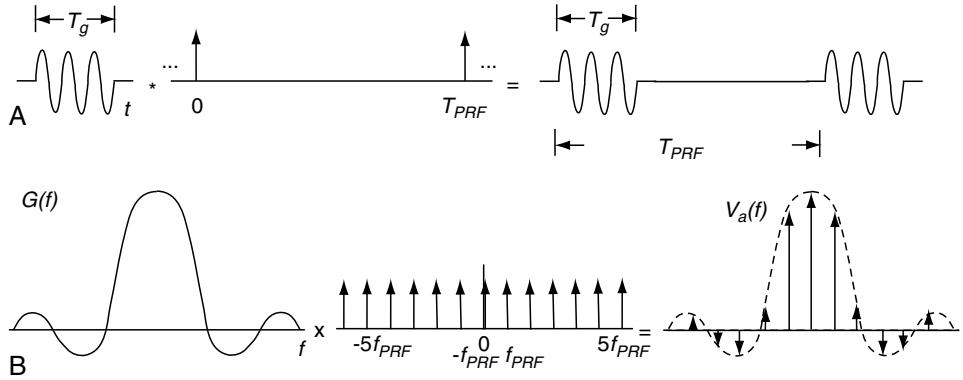

Figure 11.16 (A) Repeating transmit pulse parameters. (B) Spectrum of repeating pulses.

$$v_A(t) = \prod(t/T_g)\,\sin(\omega_0 t)^*\,{}_t III(t/T_{PRF}) \tag{11.12c}$$

$$v_A(t) = \sum_{n=-\infty}^{\infty} \prod[(t - nT_{PRF})/T_g]\,\sin[\omega_0(t - nT_{PRF})] \tag{11.12d}$$

where the *rect* and the *shah* replicating functions have been used from Appendix A and $g(t)$ describes the individual pulse. Equation (11.12) is depicted graphically at the top of Figure 11.16. From the Fourier transform of this equation and the application of the Fourier transform sampling property of the *shah* function, an interesting spectrum is obtained:

$$V_A(f) = (-iT_{PRF}T_g/2)\{\,sinc[T_g(f - f_0)] - sinc[T_g(f + f_0)]\}III(f/f_{PRF}) \tag{11.13a}$$

$$V_A(f) = (-iT_{PRF}T_g/2)\sum_{n=-\infty}^{\infty}\{\,sinc[T_g(nf_{PRF} - f_0)] - sinc[T_g(nf_{PRF} + f_0)]\}\delta(f - nf_{PRF}) \tag{11.13b}$$

where the graphical representation of this equation is in the bottom of Figure 11.16. A consequence of the repetitious life of the transmitted pulses is that their spectra appear as lines modulated by the *sinc*-shaped functions centered on $\pm nf_0$. A similar calculation from Magnin (1986) for $g(t)$ as a Gaussian envelope instead of a tone burst is plotted in Figure 11.17a. Here his corresponding notation is $f_s = f_0$, and $PRI = T_{PRF}$.

Typically the Doppler range gate (pulse) is placed on a vessel or region of interest, and pulse and transmit beam characteristics are optimized for the range delay $t_0/2$. Two types of echoes are a stationary pulse and a Doppler-shifted pulse, returning at an approximate round-trip time of t_0. By applying Eq. (11.9) to Eq. (11.12), an expression for the received echoes can be derived. First the stationary echoes,

$$v_{BS}(t) = \sum_{n=-\infty}^{\infty} \prod[(t - t_0 - nT_{PRF})/T_g]\,\sin[\omega_0(t - t_0 - nT_{PRF})] \tag{11.14a}$$

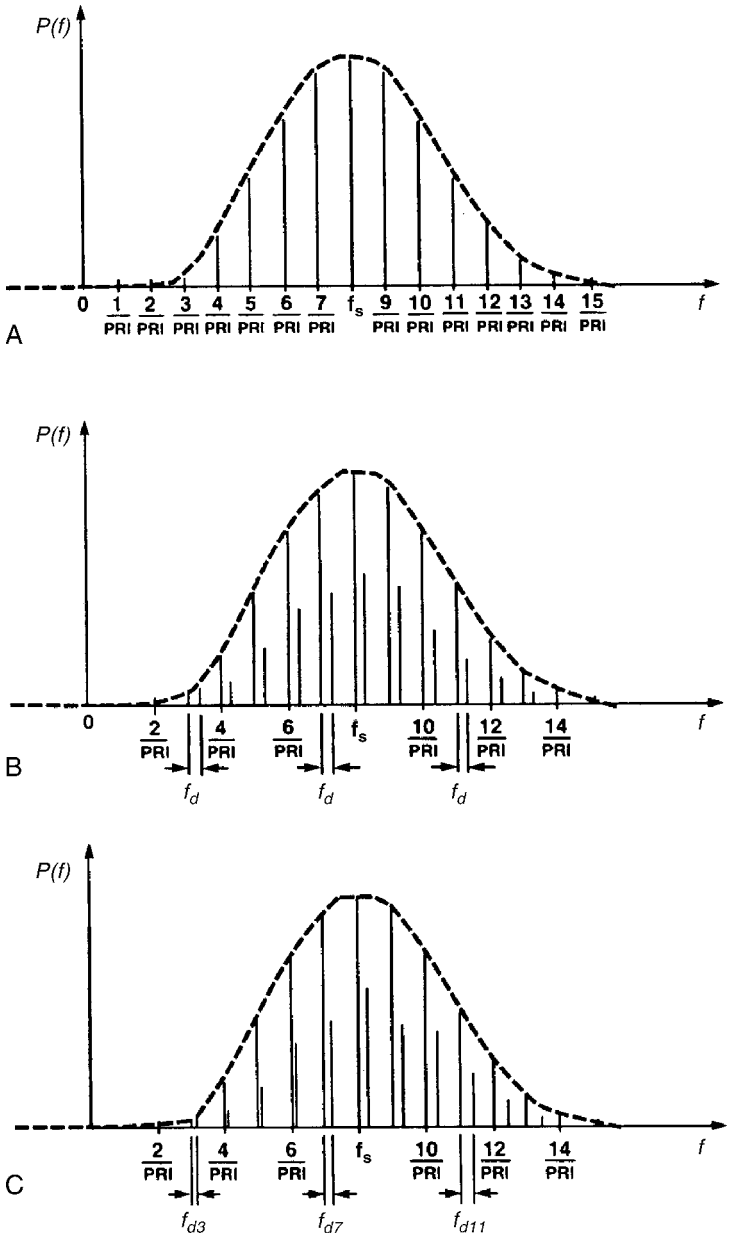

Figure 11.17 (A) Spectra of stationary objects for a Gaussian transmit pulse. (B) Equally shifted Doppler spectra compared to spectra from echoes from stationary objects. (C) Correctly shifted Doppler spectra compared to spectra from echoes from stationary objects (from Magnin, 1986, reprinted by permission of Hewlett Packard).

and then the Doppler-shifted echoes, simply delayed by t_0 from the result of Eq. (11.12d)

$$v_{BD}(t) = \sum_{n=-\infty}^{\infty} \prod \left[\Psi(t - (t_0/\Psi) - (nT_{PRF}/\Psi))/T_g\right] \sin[\Psi\omega_0(t - (t_0/\Psi) - (nT_{PRF}/\Psi))] \tag{11.14b}$$

where the arguments in parentheses can be rewritten as

$$[t - (t_0/\Psi) - (nT_{PRF}/\Psi)] = [t - t_0 - nT_{PRF} - \delta_D(t_0 + nT_{PRF})] \tag{11.14c}$$

Note that by letting $c_D = 0$, $\delta_D = 0$, $\Psi = 1$, Eq. (11.14b) reduces to the stationary target version, Eq. (11.14a), and therefore, this equation covers both types of echoes. The last equation can be rewritten as

$$v_{BD}(t) = \prod \left(t\Psi/T_g\right) \sin(\Psi\omega_0 t) * III[(t - t_0)/T_{PRF}] \tag{11.14d}$$

where the relation $\delta(ax) = \delta(x)/|a|$ and the definition of the *shah* function have been applied to obtain

$$v_{BD}(t) = \prod \left(t\Psi/T_g\right) \sin(\Psi\omega_0 t) \sum_{n=-\infty}^{\infty} (1/\Psi)\delta[t - (nT_{PRF} + t_0)/\Psi] \tag{11.14e}$$

By Fourier transforming these echoes, Eq. (11.14e), their spectra are obtained,

$$V_{BD}(f) = \frac{-iT_g}{2\Psi} \left\{ sinc\left[(T_g/\Psi)(f - \Psi f_0)\right] - sinc\left[(T_g/\Psi)(f + \Psi f_0)\right] \right\} * III(f/f_{PRF}) \exp(-i2\pi f t_0) \tag{11.15a}$$

$$V_{BD}(f) = G(f) * \sum_{n=-\infty}^{\infty} \Psi\delta[f - nf_{PRF}\Psi] \tag{11.15b}$$

where $G(f) = \{\ \}$ in Eq. (11.15a) is the Fourier transform of the pulse function $g(t)$, and if a similar scaling relation was used for the impulse functions,

$$V_{BD}(f) = \Psi G(f)^* \sum_{n=-\infty}^{\infty} \delta[f - nf_{PRF} + \delta_D nf_{PRF}] \tag{11.15c}$$

Except for a time delay to the target, the spectrum of stationary echoes ($\delta_D = 0$ in the previous equation) is similar to that of the repeated transmitted pulses. There may be an expectation that the Doppler spectra should be shifted by a constant frequency,

$$f_d = \delta_D f_{PRF} \tag{11.16}$$

for each of the PRF harmonic frequencies, as illustrated by Figure 11.17b for a Gaussian envelope, $G(f)$; however, this relation is incorrect. Magnin (1986) pointed out that the actual counterintuitive result of Eq. (11.15c) is that the Doppler shift actually increases with PRF harmonic number n, or $\delta_D nf_{PRF}$, as shown in Figure

11.17c. This analysis shows that for a single scatterer moving at a constant velocity (c_D), pulsed Doppler produces a distribution of unequal harmonic Doppler shifts.

The remarkable aspect of Doppler detection is that stationary signals are typically 40 dB (100 times) larger than the amplitudes of Doppler echoes, and the Doppler shift can be less than 1 KHz or only a few parts out of 10,000 relative to the transmit frequency. Furthermore, because time delay shifts are small for Doppler echoes, they can overlap the stationary echoes. This feat of engineering is accomplished by quadrature sampling the returning echoes and by other filtering (shown in the next few sections).

11.5.3 Quadrature Sampling

Quadrature sampling is needed to differentiate between forward and reverse flows. Principles of this detection method can be understood by reference to Figure 11.18. At the top of this figure are pulses gliding slowly to the left or right, representing the Doppler time-shifted echoes described in Eq. (11.14b). If the samples occur at $t_0 + nT_{PRF}$, there are timing circumstances where the in-phase sampler cannot distinguish between forward and reverse directions, even though the equivalent Doppler frequency can be determined correctly from the resulting detected period. In this example, the period is

$$f_D = 1/4T_{PRF} = f_{PRF}/4 \tag{11.17a}$$

Note also that the time shift from one pulse to the next sequential pulse at sample times (pulse repetition intervals of T_{PRF}) is

$$t_D = T_{PRF}/4 \tag{11.17b}$$

If the sampling times are done a quarter period later, at $1/4f_0$, the quadrature sampler, in this example, is able to discriminate between the flow directions (as shown at the bottom of Figure 11.18).

In order to derive equations that represent this sampling process, the *shah* function is applied to Eq. (11.14d),

$$v_{BD}^S(t) = v_{BD}(t)III[(t - t_0)/T_{PRF}] \tag{11.18a}$$

to indicate sampling at times $t_0 + mT_{PRF}$, as required,

$$v_{BD}^S(t) = [g(t)/\Psi] \sum_{m=-\infty}^{\infty} \sum_{n=-\infty}^{\infty} \delta[t - t_0 - nT_{PRF} - \delta_D(t_0 + nT_{PRF})]\delta(t - t_0 - mT_{PRF}) \tag{11.18b}$$

This double sum can be reduced to a single sum through timing arguments explained by Newhouse and Amir (1983) or by using matched indices $m = n$,

$$v_{BD}^S(t) = [g(t)/\Psi] \sum_{n=-\infty}^{\infty} \delta[t - \delta_D(t_0 + nT_{PRF})]. \tag{11.18c}$$

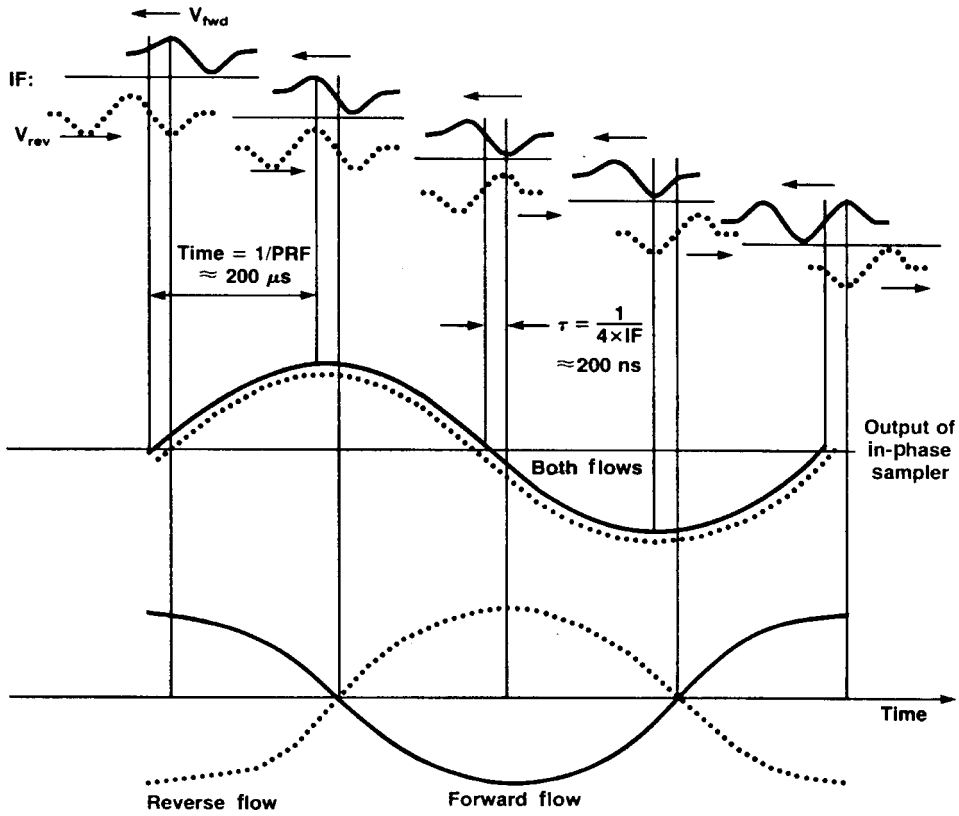

Figure 11.18 Quadrature sampling of forward and reverse flows for a pulsed Doppler system. (Top:) Echoes for five PRF intervals containing both forward and reverse flow Doppler time shifts. (Center:) Output of a single (in-phase) sampler for both echoes. (Bottom:) Output of second (quadrature) sampler allows differentiation of forward and reverse flows by phase encoding (from Halberg and Thiele, 1986, reprinted by permission of Hewlett Packard).

As first shown by Newhouse and Amir (1983), the sampled waveform is reversed and scaled in time by the Doppler factor δ_D and sampled at times $t_0 + nT_{PRF}$. Note that for no shift, the transmitted waveform is unchanged.

Finally, the spectrum of the sampled waveform is

$$V_{BD}^{S}(f) = V_{BD}(f) * f_{PRF}[III(f/f_{PRF}) \exp(-i2\pi f t_0)] \tag{11.19a}$$

which by similar arguments can be reduced to a single sum,

$$V_{BD}^{S}(f) = G(f) \exp(-i2\pi f t_0) \Psi f_{PRF} \sum_{n=-\infty}^{\infty} \delta(f - \delta_D m f_{PRF}) \tag{11.19b}$$

$$V_{BD}(f) = \frac{-iT_g}{2T_{PRF}} \{sinc(T_g f) \exp(-i4\pi f t_0)\} * \{\delta[\Psi(f - f_0)] - \delta[\Psi(f + f_0)]\} \sum_{n=-\infty}^{\infty} \delta(f - \delta_D n f_{PRF}) \tag{11.19c}$$

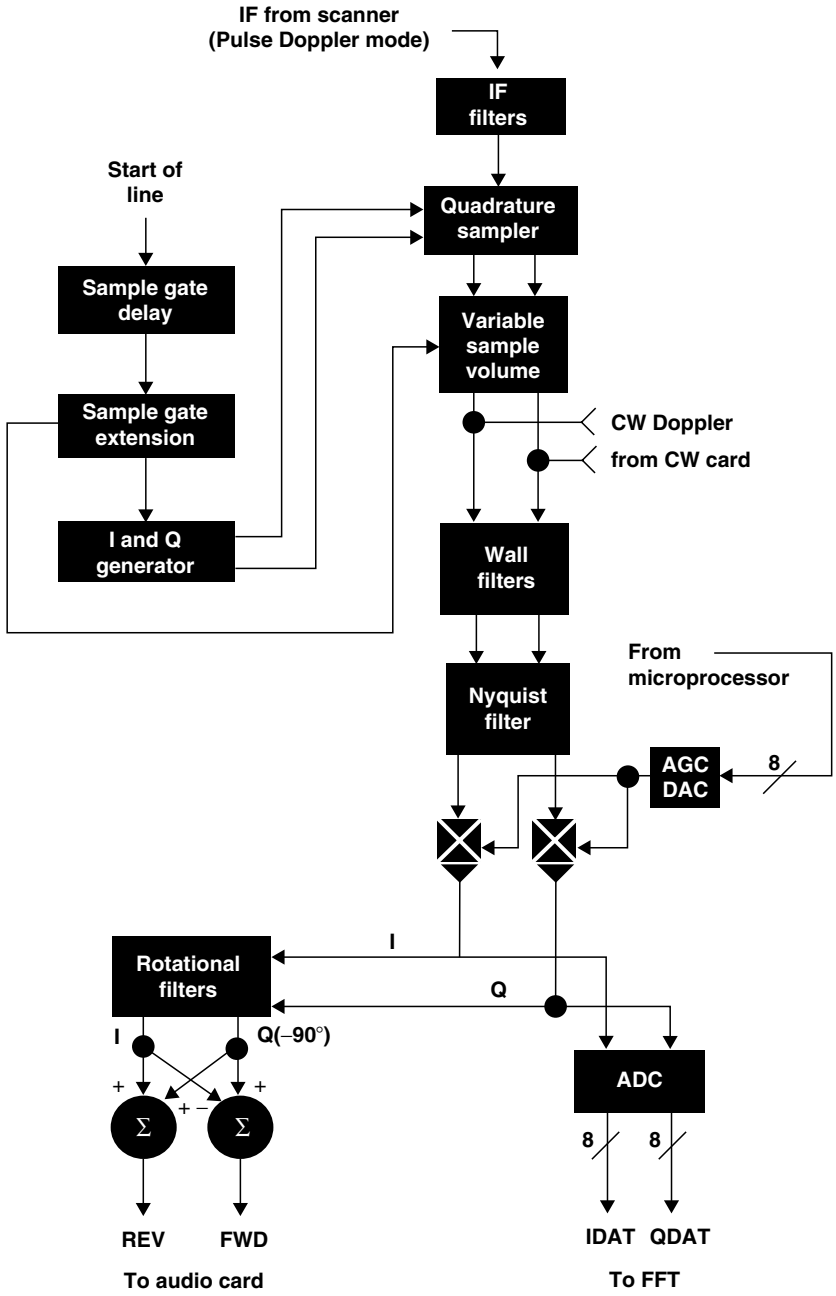

Figure 11.19 Block diagram of range-gated Doppler system (from Halberg and Thiele, 1986, reprinted by permission of Hewlett Packard).

$$V_{BD}(f) = \frac{-iT_g}{2T_{PRF}} \left\{ sinc(T_g f) e^{(-i4\pi f t_0)} \right\} * \left\{ \sum_{n=-\infty}^{\infty} \delta[f - (\delta_D n f_{PRF} - \delta_D f_0 - f_0)] + \sum_{n=-\infty}^{\infty} \delta[f - (\delta_D n f_{PRF} + \delta_D f_0 + f_0)] \right\} \tag{11.19d}$$

11.5.4 Final Filtering and Display

Equation (11.19d) represents the quadrature-sampled signal. With reference to the pulsed Doppler block diagram in Figure 11.19, the next steps are the wall filter and Nyquist filtering.

After Nyquist filtering at $f_{PRF/2}$ (one of the next steps in the signal processing from the block diagram of Fig. 11.19), the higher frequencies are eliminated. From Eq. (11.19d), the sampling repetitions end up at a single frequency when $mf_{PRF} = f_0$. Ironically, after all this processing, the pulsed Doppler appears at frequencies, $f_D = \pm\delta_D f_0$. Even though this is the same frequency obtained by Doppler frequency shifting in the CW case, Jensen (1996) points out that for the pulsed Doppler case, this coincidence is a result of the Doppler time shift and the way the pulsed Doppler is implemented. He has derived results for pulsed Doppler in more detail and has accounted for a finite number of Doppler pulses that produce the observed bandwidth Doppler spectrum rather than the spectral lines obtained here.

In addition to Nyquist filtering, special filtering is necessary to remove stationary or slowly moving vessel or tissue walls. As illustrated symbolically in Figure 11.20, this high-pass filter, also known as the "wall filter" because of its steep cutoff

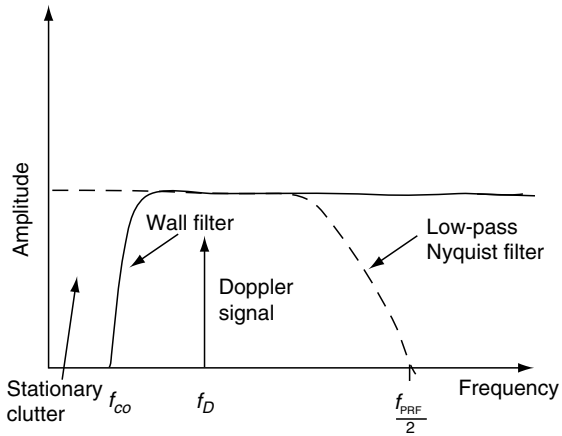

Figure 11.20 Symbolic depiction of Doppler-detected frequency (f_D) and the Nyquist low-pass filter with a $f_{PRF}/2$ cutoff frequency and a wall filter with a user-selectable cutoff.

characteristic, eliminates low Doppler frequencies that correspond to slow movements. In some systems the cutoff frequency is user-selectable to best suit the clinical application.

The last steps in Doppler processing involve automatic gain amplification as well as routing to an FFT processor for spectral display and to phase shifters for audio output of the detected Doppler signals. For the latter, an extra 90° in phase is added to or subtracted from each output so that they are 180° out of phase at the speakers.

In a quadrature or analytic signal representation, the forward flows might have a +90° encoding (phase difference between the in-phase and quadrature channels), whereas the reverse flow would be −90° encoded. By "delaying" the quadrature channel by 90° (with respect to the in-phase channel), the forward flow could then be extracted by taking the summed signal (common mode), whereas the reverse flow could be derived from the difference signal. These isolated forward and reverse flow signals are then directed to the audio speakers.

11.5.5 Pulsed Doppler Examples

In order to appreciate the engineering and clinical trade-offs for pulsed Doppler, as well as to clarify the significance of the variables, a practical example will be helpful. Consider blood flowing at a velocity of 2 m/s in a vessel that is insonified at an angle of 60° at a depth of 5 cm with a transmit frequency of 2.5 MHz (assume $c_0 = 1.154\,\text{cm}/\mu\text{s}$). The round-trip echo time is

$$t_{RT} = z(2/c_0) = 5{\cdot}13 = 65\mu s \tag{11.20a}$$

For a tone burst of 10 cycles, the gate length is

$$T_g = m/f_0 = 10/2.5 = 4\mu s \tag{11.20b}$$

The minimum pulse repetition interval is

$$T_{PRF} = t_{RT} + T_g = 65 + 4 = 69\mu s \tag{11.20c}$$

so that the maximum PRF is

$$f_{PRF} = 1/T_{PRF} = 14.5\,kHz \tag{11.20d}$$

resulting in a Nyquist frequency of

$$f_{NYQ} = f_{PRF}/2 = 7.25\,kHz \tag{11.20e}$$

A Doppler factor of

$$\delta_{\mathrm{D}=2\mathrm{v}\cos\theta/\mathrm{c}_0} = 2 \times 2 \times \cos(\pi/3)/1540 = 1.3\mathrm{e}-3 \tag{11.20f}$$

results in a Doppler frequency of

$$\mathrm{f_D} = \delta_D f_0 = 3.25\,\mathrm{kHz} \tag{11.20g}$$

and a Doppler time shift of

$$t_{\mathrm{D}} = \delta_{\mathrm{D}}\mathrm{T_{PRF}} = 0.0897\mu\mathrm{s} \tag{11.20h}$$

Fortunately, the Doppler frequency is less than the Nyquist frequency. From the Nyquist frequency, the maximum detectable velocity from the Doppler frequency equation ($\theta = 0$) is

$$v_{\max} = c_0 f_{NYQ}/(2f_0) = 2.23\, m/s \tag{11.20i}$$

The obvious sampling rate limitation is one of the weaknesses of pulsed Doppler. Velocities faster than the previous value permitted by the Nyquist rate appear out of their proper place in the spectrum or "alias."

While our analysis has dealt with an idealized single Doppler frequency, clinical Doppler involves a spread of shifted frequencies from several causes. As in the block diagram for CW Doppler in Figure 11.14, a similar diagram could be constructed for PW Doppler. While the physical effects are similar, the sampling mechanism in PW Doppler results in absorption and diffraction effects only at the gate depth, whereas these physical factors affect CW Doppler along a larger region formed by the intersection of the transmit and receive beams. A better model for the blood scatterers, $s(r, t)$, in such a block diagram would involve a statistical distribution of cells, describing their whirling and changing in time, as well as their moving at a parabolic or abnormal spread of velocities across the width of a vessel or chamber. These effects result in a widening of the Doppler and its granular appearance (as depicted in Figure 11.15). Further broadening occurs as a result of the finite beamwidth of the interrogating beam interacting with the sample volume of blood. The extent of this volume narrows as particle velocities increase, which implies that short pulses are needed (short T_g). However, better spectral sensitivity and penetration (see Eq. (11.15a)) is obtained by narrow bandwidths, which are obtained with longer pulses (a contradictory trade-off).

Imaging systems often provide calculations of Doppler parameters. An example is shown for the superficial femoral artery in Figure 11.21. Shown are the mean velocity, the average value, and the systolic-to-diastolic (S/D) velocity ratio. The mean velocity combined with the volumetric flow equation, Eq. (11.5b), can be used to estimate volume flow; this application favors a longer pulse needed to capture the entire cross section of a vessel.

In an important application, the pressure drop across a stenotic valve can be estimated from Bernoulli's law, Eq. (11.8), (Hattle and Angelsen, 1985) as

$$P_1 - P_2 = 4v_2^2 \tag{11.21}$$

in which the blood velocity is in m/s and pressure is in mmHg. The velocity at the valve is measured by Doppler ultrasound, $v_2 = c_D$, and if the change in pressure as determined by this equation exceeds 50 mmHg, the valve most likely needs to be replaced or repaired. In this case, the high velocities appear as a narrow jet that is best found with a wide-focus CW beam.

Standard deviation provides a quantitative measure of the breadth of the velocity distribution. Hattle and Angelsen (1985) summarize clinical applications of Doppler measurements.

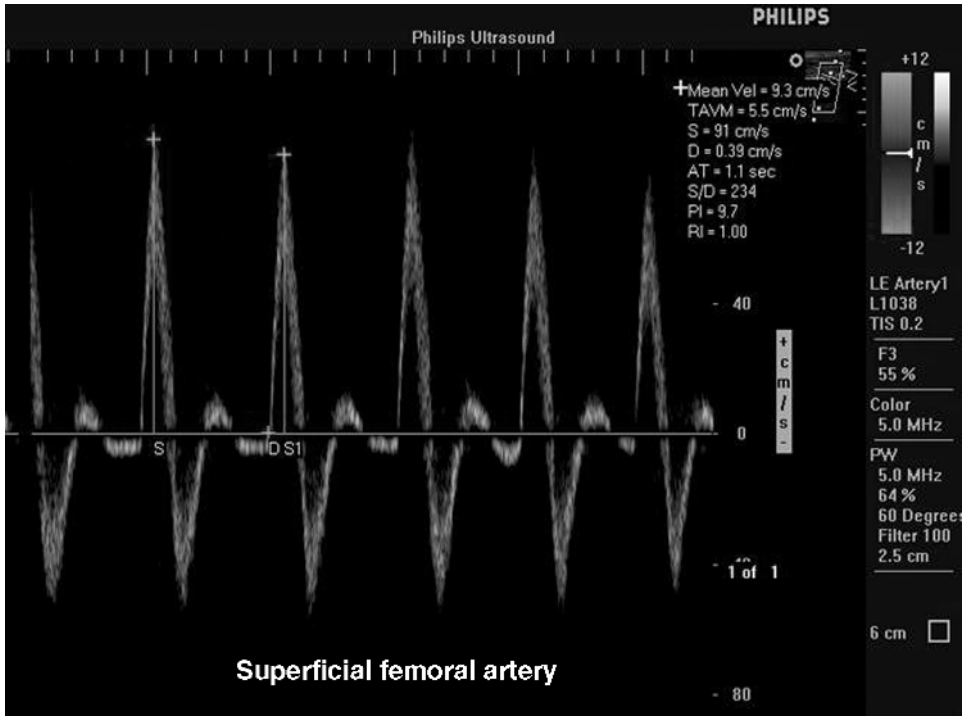

Figure 11.21 Duplex-pulsed Doppler display for a superficial femoral artery with calculations displayed and a small image in the upper-right corner (courtesy of Philips Medical Systems).

11.6 COMPARISON OF PULSED AND CONTINUOUS WAVE DOPPLER

Table 11.1 summarizes PW and CW Doppler. It is assumed that the PW Doppler is from an array, whereas the CW Doppler is obtained either from a fixed (stand-alone) probe or an array (steerable CW). Steerable CW Doppler can be regarded as being at the extreme of the PW Doppler continuum.

TABLE 11.1 CW and PW Doppler Comparisons

Topic	Fixed CW Doppler	Steerable CW Doppler	PW Doppler
Resolution	At intersection of transmit and receive	At intersection of transmit and receive	Range-gated
Focusing	Fixed focus and amplitude	Electronic focusing with gain	Electronic focusing with gain
Steering	Mechanical	Electronic	Electronic
Visual aid for placement	None	Line, duplex, triplex imaging	Gate, duplex, triplex imaging
Aliasing	No	No	Yes
Absorption and diffraction	At intersection of transmit and receive	At intersection of transmit and receive	At gate position

11.7 ULTRASOUND COLOR FLOW IMAGING

11.7.1 Introduction

Color flow imaging (CFI) is one of the big technological breakthroughs of diagnostic ultrasound imaging. The real-time display of the blood velocity and direction is both an outstanding technical achievement and clinical success story. By providing a moving color picture that is a global view of dynamic blood flow, this modality enabled the finding of previously overlooked jets from stenotic and other flow abnormalities, such as leaking heart valves (shown as regurgitation shown in Figure 11.15), flow reduction, and occlusion from atherosclerotic plaque. Combined with conventional Doppler, CFI provides a global view for accurate Doppler line placement, which previously was a "blind" and difficult procedure. These contributions of CFI have increased diagnostic confidence in the sense that anomalies can be detected quickly and not be overlooked.

Early attempts at making a Doppler image included multigate Doppler or Doppler that was swept mechanically through a number of vector directions (Nowicki and Reid, 1981). Because blood is fast moving, considered quasi-stationary for only 5–100 ms at different locations (Magnin, 1987), these methods could not keep up. Also unlike PW Doppler, in which FFTs were calculated only during the range-gate interval, much longer scan depths were needed. These factors meant that only 3–12 (typically 8) sample points were available per depth (Magnin, 1987). For so few points FFTs had a large variability and were not fast enough. One manufacturer had an FFT-based estimator but is no longer in business (Kimme-Smith *et al*., 1989). Even faster and more robust mean frequency estimators had to be devised to determine blood flow velocity. Furthermore, the kind of information normally presented in a spectrogram had to be displayed in a way that could be comprehended quickly at each spatial location.

11.7.2 Phase-Based Mean Frequency Estimators

An instantaneous frequency can be defined as (Bracewell, 2000)

$$f_i = \frac{1}{2\pi}\frac{\partial \phi}{\partial t} \tag{11.22}$$

For the continuous case, a Doppler signal after quadrature sampling and mixing can be combined into an exponential (Jensen, 1996) or complex phasor,

$$v_D(t) = A\exp[-i(2\pi f_0 \delta_D t + constant)] \tag{11.23}$$

which has a familiar instantaneous frequency,

$$f_i = \frac{1}{2\pi}\frac{\partial \phi}{\partial t} = \frac{1}{2\pi}\frac{\partial(2\pi f_0 \delta_D t + constant)}{\partial t} = \delta_D f_0 \tag{11.24}$$

In the general case, more than a single frequency is involved. Equation (11.22) still holds for multiple frequencies but must be approximated for the discrete case needed for CFI.

What is really needed is the mean frequency for N samples. If a number of time samples (N) are taken from repetitive insonifications at the same depth, each sample can be turned into a pair of $I(nT_{PRF})$ and $Q(nT_{PRF})$ through the quadrature process. Note that the I and Q components can be regarded as the Cartesian projections of a phasor or vector with a magnitude and angle. For this set of samples, an instantaneous envelope, $A(nT_{PRF})$, can be determined from the square root of the sum of the squares, as described for an analytic signal in Appendix A. The instantaneous phase can be found from $\phi(n) = \arctan[Q(n)/I(n)]$. First the continuous case can be found from the definition of phase in terms of the arctangent; second, the derivative of the arctangent (Evans, 1993; Jensen, 1996) gives

$$\frac{d\phi}{dt} = \frac{I(t)dQ(t)/dt - Q(t)dI(t)/dt}{I^2(t) + Q^2(t)} \tag{11.25a}$$

A discrete finite difference approximation of this derivative and averaging yields an approximate instantaneous frequency estimator,

$$\bar{f} \approx \frac{1}{2\pi T_{PRF}} \frac{\sum_{n=1}^{N} I(n)Q(n-1) - Q(n)I(n-1)}{\sum_{n=1}^{N} I^2(n) + Q^2(n)} \tag{11.25b}$$

where here the index n is meant to identify each unique phasor in a time sequence of phasors. A simpler mean frequency estimator is to approximate instantaneous frequency by changes in phase (Brandestini, 1978) from one sample to another, as

$$\bar{f} \approx \frac{\Delta\phi}{2\pi\Delta T} = \frac{1}{2\pi N T_{PRF}} \sum_{n=1}^{N} \{\arctan[Q(n)/I(n)] - \arctan[Q(n-1)/I(n-1)]\} \tag{11.26}$$

An alternative estimator is the autocorrelator (Kasai *et al*, 1983). A geometric interpretation of this approach is that the tangent of the difference between phasors,

$$\tan(\phi_n - \phi_{n-1}) = \frac{\sin(\phi_n - \phi_{n-1})}{\cos(\phi_n - \phi_{n-1})} = \frac{\sin\phi_n \cos\phi_{n-1} - \cos\phi_n \sin\phi_{n-1}}{\cos\phi_n \cos\phi_{n-1} - \sin\phi_n \sin\phi_{n-1}} \tag{11.27}$$

can be used to estimate the mean frequency through a discrete approximation of the sum of these tangents,

$$\bar{f} \approx \frac{1}{2\pi T_{PRF}} \arctan \left[\frac{\sum_{n=1}^{N} I(n)Q(n-1) - Q(n)I(n-1)}{\sum_{n=1}^{N} I(n)I(n-1) + Q(n)Q(n-1)} \right] \tag{11.28}$$

This formulation can be related to autocorrelation through an alternate definition of mean frequency in terms of the power spectrum, $P(f)$ (Angelsen, 1981; Kasai *et al.*, 1983). Consider first the definition of an autocorrelation function (see Appendix A),

$$R(\tau) = v(\tau) * v^*(-\tau) = \int_{-\infty}^{\infty} v(u)v^*(u-\tau)du \tag{11.29a}$$

which is related to the power spectrum through a Fourier transform,

$$R(\tau) = \int_{-\infty}^{\infty} V(f)V^*(f)e^{i2\pi f\tau}df = \int_{-\infty}^{\infty} |V(f)|^2 e^{i2\pi f\tau}df \tag{11.29b}$$

where the power spectrum is $P(f) = |V(f)|^2$. The mean frequency can be obtained from the Fourier transform derivative theorem (see Appendix A), and the autocorrelation function at zero lag, $\tau = 0$, Eq. (11.29b),

$$\bar{f} = \frac{\int_{-\infty}^{\infty} fP(f)df}{\int_{-\infty}^{\infty} P(f)df} = \frac{\int_{-\infty}^{\infty} i2\pi fP(f)df}{i2\pi \int_{-\infty}^{\infty} P(f)df} = \frac{-i}{2\pi}\frac{dR(0)}{dt} \tag{11.30}$$

This relation is approximated as

$$\bar{f} = \frac{1}{2\pi}\frac{d\phi}{dt} \approx \frac{\phi(T_{PRF})}{2\pi T_{PRF}} \tag{11.31}$$

in which ϕ is the phase of the autocorrelation function since $R(\tau) = |R(\tau)|\exp[i\phi(\tau)]$. Finally, the autocorrelation function, as defined by Eq. (11.29a), is integrated over N transmits (Kasai *et al.*, 1983),

$$R(T_{PRF}, t) = \int_{t-NT_{PRF}}^{t} v(t)v^*(t-T_{PRF})dt \tag{11.32a}$$

If $v(t) = I(t) + iQ(t)$, this integral becomes

$$R(T_{PRF}, t) = \int_{t-NT_{PRF}}^{t} [v_{REAL}(t, T_{PRF}) + iv_{IMAG}(t, T_{PRF})]dt \tag{11.32b}$$

where

$$v_{REAL}(t, T_{PRF}) = I(t)I(t-T_{PRF}) + Q(t)Q(t-T_{PRF}) \tag{11.32c}$$

$$v_{IMAG}(t, T_{PRF}) = I(t-T_{PRF})Q(t) - I(t)Q(t-T_{PRF}) \tag{11.32d}$$

A numerical implementation of Eq. (11.32a) is to replace the integral with a sum over N repetitions and associate the terms in Eqs. (11.32c) and (11.32d) with indices, $t = n$, $t - T_{PRF} = n - 1$. Finally, the phase can be determined from the arctangent of

the summed imaginary terms over the real terms, and the mean frequency is found from Eq. (11.31), which gives the result of Eq. (11.28).

Evans (1993) has reviewed the three methods, and the instantaneous frequency method, Eq. (11.25b), appears to be the least accurate. The autocorrelator is the most robust, and it or variants of it are probably the most widely used (Kimme-Smith *et al*., 1989). The phase detector (also called an instantaneous frequency detector in the literature), Eq. (11.26), is intermediate in its performance.

11.7.3 Time Domain–Based Estimators

Time domain cross-correlation approaches based on the Doppler time shift have been proposed (Embree and O' Brien, 1985, 1990; Bonnefous and Pesque, 1986). These Doppler methods could exceed the aliasing limits of the phase-based algorithms to a limited extent, and they could use shorter pulses to improve axial resolution. Although the shorter pulse trains would have the same compromise in sensitivity as the earlier methods, they would have reduced spectral spread.

The basic principle is that the position of a cross-correlation gives the measurement of the Doppler time shift by red blood cell scatterers (Bonnefous *et al*., 1986).

$$R_{cn}(\tau, t) = \int_{t}^{T_g+t} v_n(t')v_{n+1}(t'+\tau)dt' \tag{11.33a}$$

but the successive echo is delayed by the Doppler time shift (τ_D)

$$v_{n+1}(t) = v_n(t-\tau_D) \tag{11.33b}$$

so that,

$$R_{cn}(\tau, t) = \int_{t}^{T_g+t} v_n(t')v_n(t'+\tau-\tau_D)dt' = R_n(\tau-\tau_D) \tag{11.33c}$$

where R_n is an autocorrelation function that is maximum when $\tau = \tau_D$. When the time between repetitions is T_{PRF}, the Doppler velocity from the Doppler time shift equation is

$$v_D = \frac{c_0\tau_D}{2T_{PRF}\cos\theta} \tag{11.33d}$$

Bonnefous *et al*. (1986) described how this approach can be used as a color flow velocity estimator. They demonstrated that higher velocities can be detected with this method without aliasing. The blood scatterers must not have moved so much that there will be insufficient overlap to obtain a high cross-correlation between consecutive transmits; this condition is usually met in practice.

Hein and O'Brien (1993c) provided a review of cross-correlation methods for Doppler detection of blood flow and tissue motion. They indicated that the phase-based Doppler detection methods are biased by the center frequency.

11.7.4 Implementations of Color Flow Imaging

All of the estimators described have qualities of being fast, robust, and efficient; consequently, they have been implemented in hardware and digital signal processors (DSPs). The initial signal processing is similar to that used to create I and Q paths for PW Doppler except that wall filters follow analog-to-digital (A/D) conversion. The wall filters can be feedback recursive filters of the moving target indicator (Magnin, 1987) or the delay line canceller type (Evans, 1993). After filtering, the signals enter the mean frequency estimator and turbulence estimators. The results of these calculations then enter a display encoder and digital scan conversion. The time domain method differs substantially from the phase-based methods in that quadrature sampling is not necessary, so that after wall filtering, the signals are processed by a cross-correlator.

All methods undergo a color mapping scheme that can vary among manufacturers, so only the basic concepts can be dealt with here (Magnin, 1987). A color image is overlaid on a standard gray-scale image. The colors chosen are not the actual colors of blood but represent blood flow velocity and direction. Colors are assigned to the direction of flow relative to the transducer, for example, with red for flow toward the transducer and blue for flow away from it. Green, another primary color can be added to indicate turbulence. Either the hue of the color is increased as the velocity increases or alternatively, the intensity is increased. In Figure 11.15, the red/blue scheme is shown with increasing intensity.

Frame rate is always at a premium, and it depends on the total number of vectors or transmit events and the scan depths. In multiple modes, and color flow always includes a gray-scale B-scan image, it is possible to have not only different-shaped pulses but also different scan depths (Szabo *et al*., 1988). To catch fast-moving flow, frame rate can be increased by giving the user the option of reducing the size of the region of interest for CFI (as shown in the inset of Figure 11.13). Figure 11.15 shows a triplex image CFI and a gray-scale and PW Doppler. The ability to display several modes at once (Barber *et al*., 1974) is very useful clinically, especially for the placement of Doppler lines, but this also increases frame rate and both processing and line sequencing complexity.

While there is no doubt of CFI's usefulness, its limitations must also be kept in mind. First, mean blood flow velocity is estimated on the basis of a few time samples; therefore, the values obtained will not be as accurate as PW and CW Doppler measurements based on longer dwell times (length of time during which a transducer is held at the same position), many more sample points, and more precise FFT algorithms. Second, the velocity values derived from CFI have an implicit *cosine* θ variation with no correction for this part of the Doppler effect. As an example, consider a sector scan in which the middle vector line is perpendicular to a vessel with blood flowing left to right. Under certain conditions, a CFI of this situation will display blood as flowing left to right on the left side of the image, as stopping at dead center ($\cos 90 = 0$), and as reversing flow on the right half of the image. This kind of geometry is avoided in clinical practice, with the flow vectors always at some angle to the vessel. A third cautionary observation is that aliasing can occur (the mapping of high velocities into lower ones); these situations are often unusual enough to be noticed. Fourth, changes in flow velocity can occur out of the imaging plane and be mapped into the field of view. Fifth, "flash artifacts" can occur (the incorrect

mapping of moving blood onto tissue regions). This effect may be caused by tissue movement or by an inappropriate setting or limitation of the wall filter.

11.7.5 Power Doppler and Other Variants of Color Flow Imaging

A variation of CFI is called power Doppler, or ultrasound angiography (Rubin *et al*., 1994; Babock *et al*., 1996; Chen *et al*., 1996), and is a color representation of Doppler amplitude. An example of this modality is given by Figure 11.22, which shows an image of a renal transplant. Here Doppler intensity is shown as a change in the color intensity of red to yellow. Curious features of power Doppler are an absence of information about velocity direction and dependence on angle. If there is a sufficient Doppler signal, usually the presence of fluctuations of the backscatter with angle will be enough to show flow even at 90°. What is being displayed is the integral of power density or

$$\int_{-\infty}^{\infty} P(f)df = \int_{-\infty}^{\infty} |V(f)|^2 df \approx \sum_{n=1}^{N} I^2(n) + Q^2(n) \tag{11.34}$$

As apparent from Figure 11.22, this modality has more capability than standard CFI to show flow in smaller vessels. The two modes are compared in Figure 11.23. In the

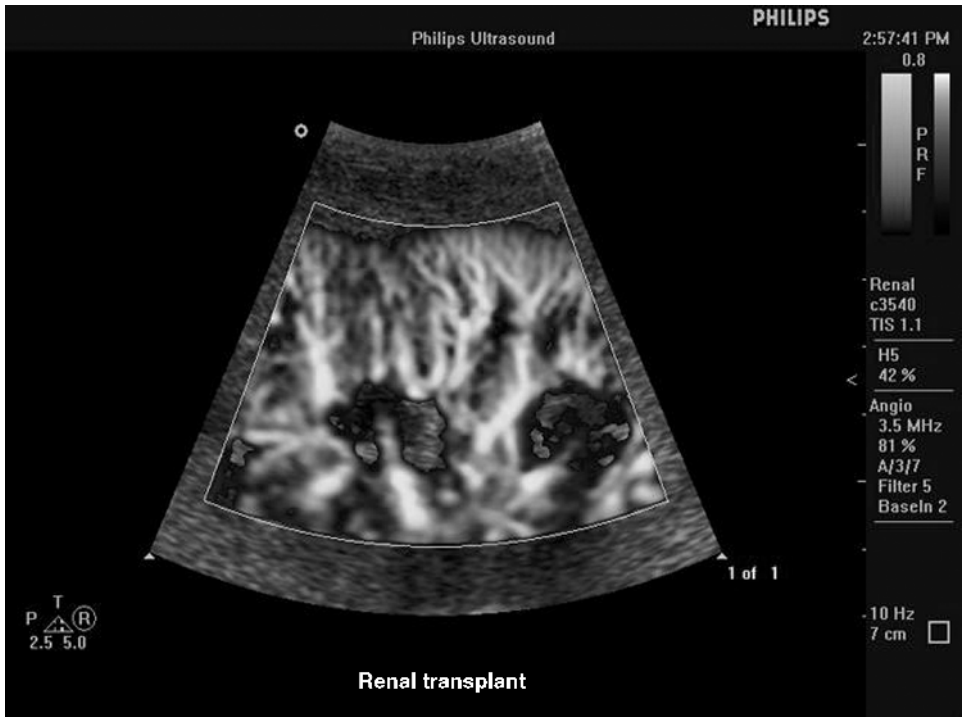

Figure 11.22 Power Doppler image of the arterial tree in a renal transplant (courtesy of Philips Medical Systems) (see also color insert).

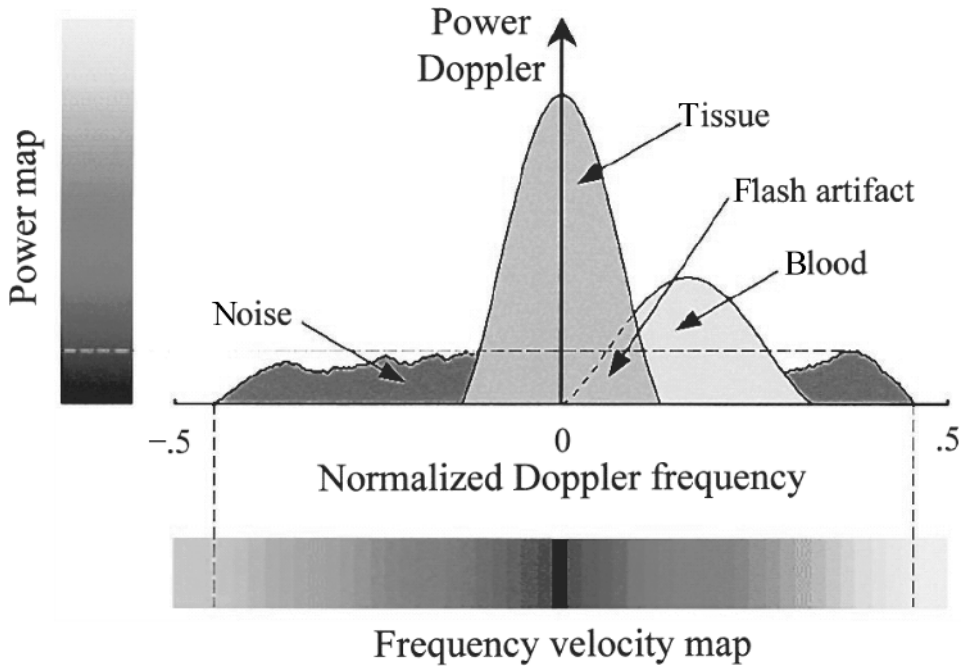

Figure 11.23 Power Doppler, a mapping of power to a continuous color range, is compared to color flow imaging (CFI). The direction and Doppler velocity are encoded as a dual display in which colors represent velocities in terms of the Doppler spectrum and also the direction of flow to and from the transducer (from Frinking *et al.*, 2000, reprinted with permission from the World Federation of Ultrasound in Medicine and Biology) (see also color insert).

power Doppler mode (Burns *et al.*, 1994; Powers *et al.*, 1997; Frinking *et al.*, 2000), the power of the Doppler signal without phase information is displayed as a range of colors instead of spectral data. Noise arriving in the Doppler receiver at high gains is mapped to a small band of color in contrast to CFI, in which noise is spread across the spectrum as many colors. This containment of noise in the power Doppler mapping contributes to an effective increase in the dynamic range displayed. In CFI, moving tissue can overlap blood signals and appear as flash artifacts, but in power Doppler, this overlap appears as the same power amplitudes.

In the power Doppler mode, the total power is more dependent on flow amplitude and less on random fluctuations, which cause phase interference effects in standard CFI. As a result, the power is integrated in amplitude across all the red blood cells in the beam without regard to phase. The increase in detection of moving cells is displayed as an increasingly paler color. In this mode, power is less affected by angular *cosine* effects; this contributes to sensitivity improvement. Even at right angles, some signal is present because of the spreading effects (discussed in Section 11.3). Another advantage is that aliasing at high velocities has little effect on the displayed power. These factors contribute to higher sensitivity for the depiction of small vessels, as evident in Figure 11.22.

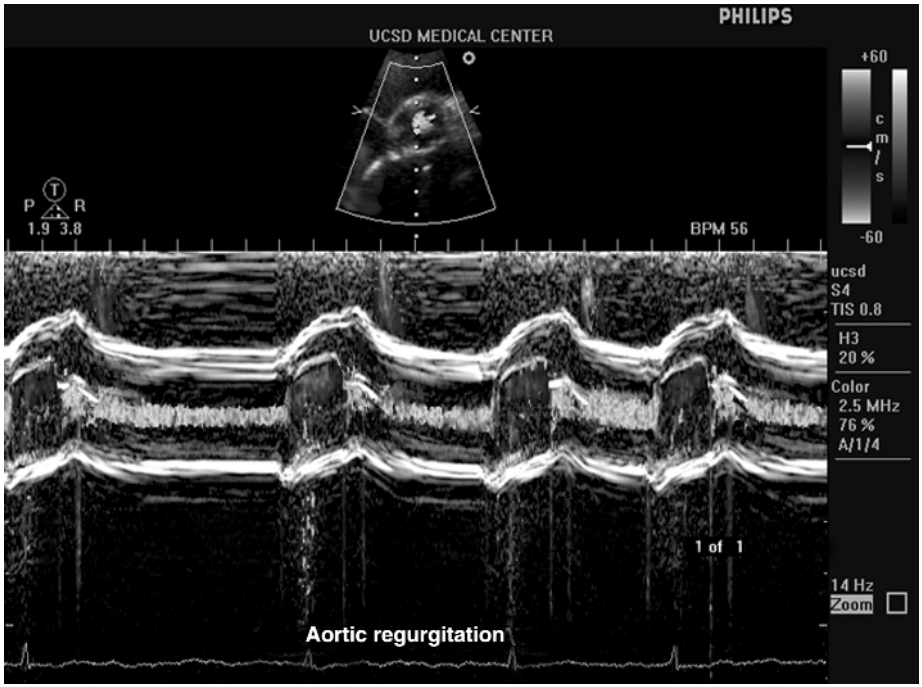

Figure 11.24 Color M-mode depiction of a leaky tricuspid valve (courtesy of Philips Medical Systems) (see also color insert).

For examination of flow at one location, a different mode, called color M-mode, can be used (as illustrated by Figure 11.24). In this case, a color flow vector line is updated in fast time and displayed in slow time as with a standard M-mode format. Note how the passage of blood through a valve is depicted in detail.

11.7.6 Future and Current Developments

Work is ongoing to improve Doppler methodology, primarily to overcome the limitations and extend its usefulness. Routh (1996) has reviewed Doppler imaging developments, and Ferrara and Deangelis (1997) have reviewed CFI comprehensively. Angle-independent CFI algorithms are reviewed by Ramamurthy and Trahey (1991) and Routh (1996). An active area is the development of new velocity estimators such as correlation (Hein *et al*., 1993a, 1993b) and wideband maximum likelihood (Ferrara and Algazi, 1991a, 1991b) as well as ways of eliminating or correcting for aliasing. One way of determining the true corrected velocity and its vector direction is through the use of spatially separated Doppler transducers to determine the location and angle to the target. Presenting all this vector information in an image is a challenge in itself. Similar to other 3D imaging acquisition methods, 3D CFI images have been made. Interest in measuring flow in the microvasculature is growing and requires special methods, including algorithms, to detect extremely slow flow, higher frequencies, and

contrast agents. Contrast agents, which are microbubbles that act as highly acoustically reflective blood tracers to enhance sensitivity, will be discussed in Chapter 14. Doppler has been applied to sonoelasticity (Lerner *et al*., 1990), to sensing streaming in breast cysts (Nightingale *et al*., 1995), and detecting wall motion (Hein and O'Brien, 1993c).

11.8 NON-DOPPLER VISUALIZATION OF BLOOD FLOW

As discussed earlier, scattering from red blood cells is very weak. With the development of imaging systems in the mid and late 1990s with large dynamic ranges and better signal processing capabilities, it became possible to visualize blood flow more directly in B-mode. One means of achieving the direct flow is to employ higher frequencies at which the backscattering coefficient of blood becomes more comparable to that of tissue (recall Figure 11.8). An example of this visualization is shown at 12 MHz for a high-frequency linear array in Figure 11.25.

Far better visualization of blood flow, even at low frequencies, can be obtained by advanced signal processing methods. B-mode blood flow imaging, called "B-flow" (Chiao *et al*., 2000) and demonstrated in Figure 11.26, provides high frame rate blood flow visualization through a two-step process.

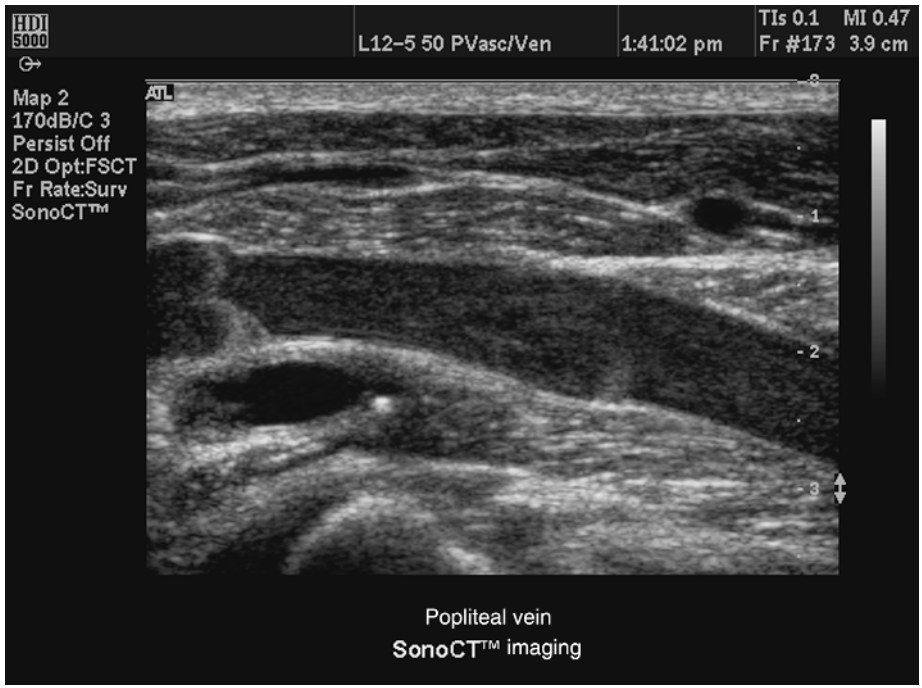

Figure 11.25 Visualization of blood flow in popliteal vein at high frequencies at 12 MHz with linear array (courtesy of Philips Medical Systems).

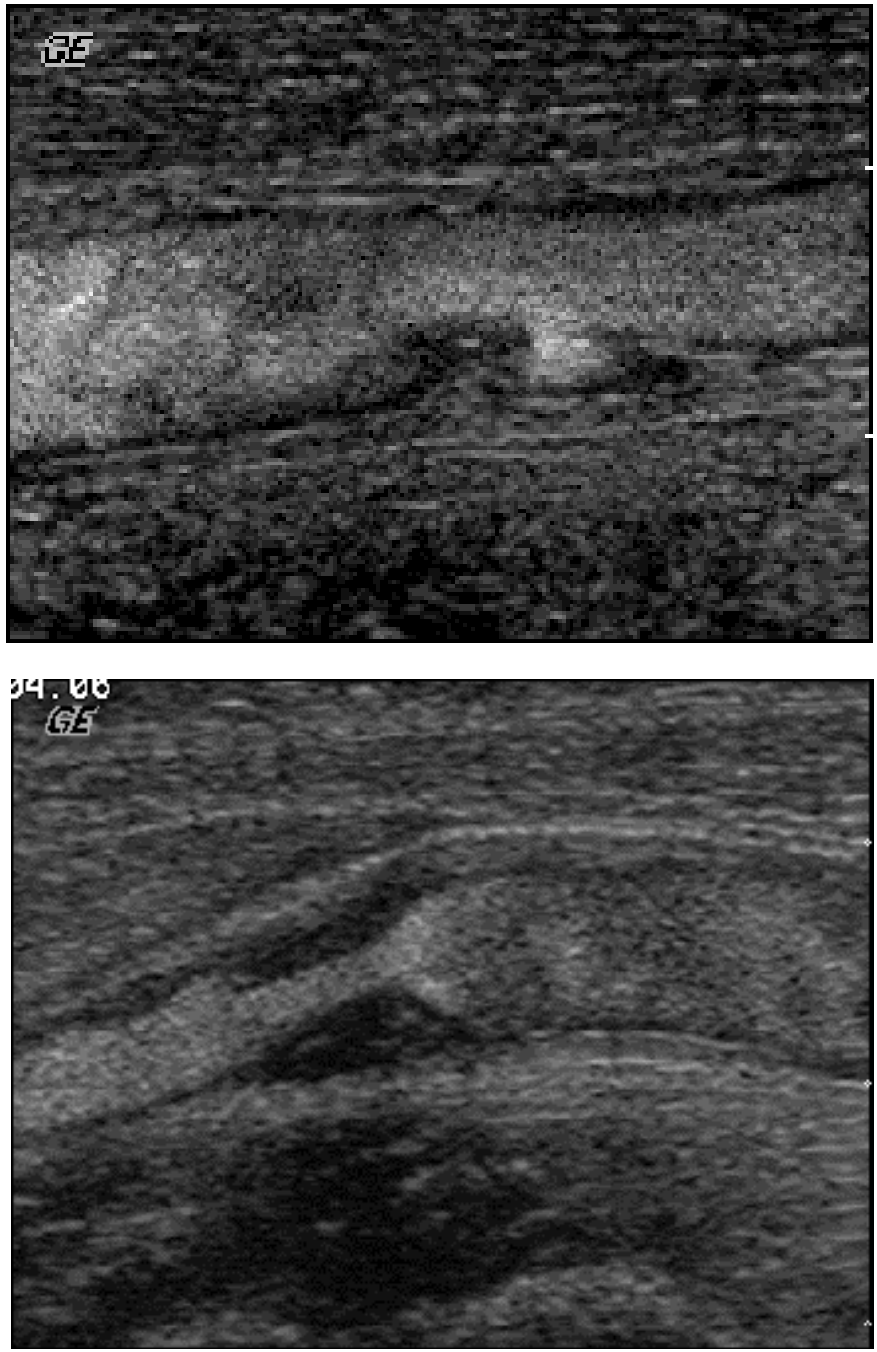

Figure 11.26 B-mode blood flow imaging of (A) an ulcerated plaque and (B) a carotid artery stenosis (from Chiao *et al.*, 2000, *IEEE*).

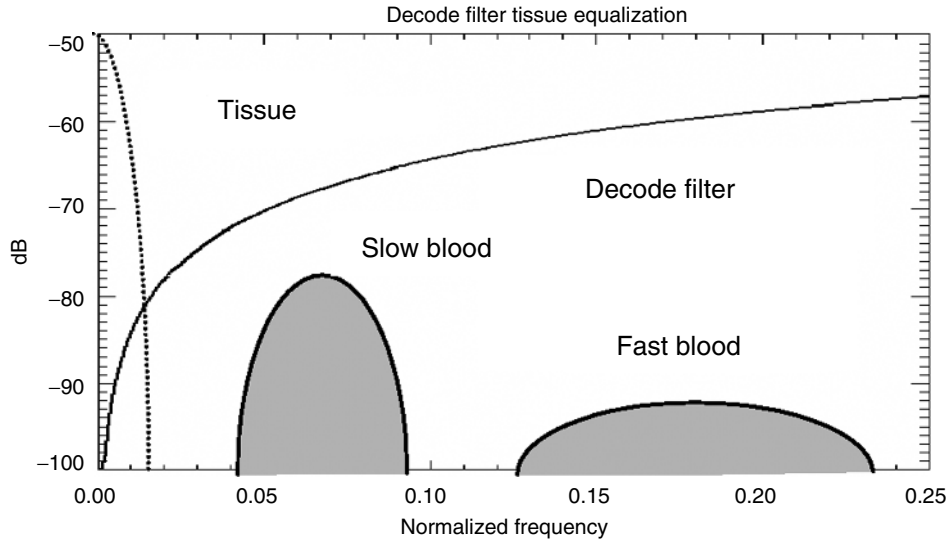

Figure 11.27 Equalization filter curve based on decoded echoes from successive transmit events along the same vector direction. Also shown are signal levels for slowly moving tissue, as well as slow and fast blood flow (from Chiao *et al.*, 2000, *IEEE*).

First, the Doppler dilemma of short pulse length (good resolution) versus high sensitivity (long pulse length) is solved by using long-encoded pulses that are later decoded on reception. As discussed in Chapter 10, coded excitation can be applied to achieve high pulse compression and sensitivity on reception through the selection of codes with low time sidelobes (Golay codes). Representing blood scattering and tissue in the same image, even after improved sensitivity, requires a second step called ''tissue equalization.'' A filter devised to discriminate between blood movement and more stationary tissue assigns an image brightness based on the decorrelation between successive echoes along each vector direction, frame to frame. The equalization filter is illustrated by Figure 11.27. From the images, the flow (especially that which is more turbulent due to factors discussed in Section 11.3) is enhanced and the surrounding tissue is more muted.

11.9 CONCLUSION

In summary, the bat's use of repetitive ultrasound pulses and matched filtering to measure the speed of a target have been mimicked (unknowingly) by the developers of pulsed wave Doppler. The bat actually uses more of a chirplike signal, which is recompressed on reception with its own adaptive matched filter. Wilhjelm and Pedersen (1993a, 1993b) applied chirped pulses to Doppler ultrasound but concluded that the resulting time sidelobes upon recompression (see Chapter 10) produced

detrimental artifacts that were detrimental for clinical use. The B-flow method, though not a Doppler technique, is closer in spirit to the matched filtering of the bat. A primary disadvantage of PW Doppler is that the Doppler line must be swept around to locate blood flow, which is a tedious and time-consuming procedure. As described earlier, the bat employs senses other than ordinary hearing to create a mental dynamic picture of its moving prey. In ultrasound, a visual color flow picture is obtained by sweeping the beams over a wide area through color flow imaging.

Bibliography

Brock-Fisher, G. A. M., Poland, M. D., and Rafter, P. G. (Nov. 26, 1996). *Means for Increasing Sensitivity in Non-Linear Ultrasound Imaging Systems*, US patent 5,577,505.

Evans, D. H. (1993). *Advances in Ultrasound Techniques and Instrumentation*, Chap. 8. P. N. T. Wells (ed.). Churchill Livingstone, New York. A review of color flow imaging.

Evans, D. H., McDicken, W. N., Skidmore, R., and Woodcock, J. P. (1989). *Doppler Ultrasound Physics: Instrumentation and Clinical Applications*. John Wiley & Sons, Chichester, UK. An older text with valuable information.

Ferrara, K. and Deangelis, G. (1997). Color flow mapping. *Ultrasound in Med. & Biol*. **23**, 321–345. A review of color flow imaging.

Hattle, L. and Angelsen, B. (1985). *Doppler Ultrasound in Cardiology: Physical Principles and Clinical Application*, 2nd ed., Lea and Ferbiger, Philadelphia. A classic text on Doppler principles.

Jensen, J. A. (1996). *Estimation of Blood Velocities Using Ultrasound*. Cambridge University Press, Cambridge, UK. A recommended book for more details about Doppler and Doppler-related imaging and the measurement of blood flow.

Magnin, P. A. (1987). A review of Doppler flow mapping techniques. *IEEE Ultrason. Symp. Proc*., 969–977. An explanation of color flow imaging methodologies.

Routh, H. F. (1996). Doppler ultrasound. *IEEE Eng. in Med. Biol*. **15**, 31–40. A review of Doppler ultrasound.

Wells, P. N. T. (1998). Current Doppler technology and techniques, Chap. 6. In *Ultrasound in Medicine*, Medical Science Series, F. A. Duck, A. C. Baker, and H. C. Starritt (eds.). Institute of Physics Publishing, Bristol, UK. A concise introduction to the essential measurement and imaging methods of Doppler ultrasound.

References

Angelsen, B. A. J. (1981). Instantaneous frequency, mean frequency, and variance of mean frequency estimators for ultrasonic blood velocity Doppler signals. *IEEE Trans. Biomed. Eng*. **BME-28**, 733–741.

Babock, D. S., Patriquin, H., La Fortune, M., and Dauzal, M. (1996). Power Doppler sonography: Basic principles and clinical applications in children. *Pediatr. Radiol*. **26**, 109–115.

Baker, D. W. (1970). Pulsed ultrasonic Doppler blood-flow sensing. *IEEE Trans. Sonics Ultrason*. **SU-17**, 170–185.

Bamber, J. C. (1986). *Physical Principles of Medical Ultrasonics*, Chap. 14. C. R. Hill (ed.). John Wiley & Sons, Chichester, UK.

Bonnefous, O. and Pesque, P. (1986). Time-domain formulation of pulse-Doppler ultrasound and blood velocity measurement by cross-correlation. *Ultrason. Imag.* **8**, 73–85.

Bonnefous, O., Pesque, P., and Bernard, X. (1986). A new velocity estimator for color flow mapping. *IEEE Ultrason. Symp. Proc.*, 855–860.

Bracewell, R. (2000). *The Fourier Transform and its Applications*. McGraw-Hill, New York.

Brandestini, M. (1978). Topoflow: A digital full range Doppler velocity meter. *IEEE Trans. Sonics Ultrason.* **SU-25**, 287–293.

Carstensen, E. L. and Schwan, H. P. (1959). Acoustic properties of hemoglobin solutions. *J. Acoust. Soc. Am.* **31**, 305–311.

Chen, J.-F., Fowlkes, J. B., Carson, P. L., Rubin, J. M., and Adler, R. S. (1996). Autocorrelation of integrated power Doppler signals and its application. *Ultrasound Med Biol.* **22,** 1053–1057.

Chiao, R. Y., Mo, L. Y., Hall, A. L., Miller, S. C., and Thomenius, K. E. (2000). B-mode blood flow (B-flow) imaging. *IEEE Ultrason. Symp. Proc.*, 1469–1472.

Chilowsky, C. and Langevin, P. (April 17, 1919). *Improvements in and Connected with the Production of Submarine Signals and the Location of Submarine Objects*, UK patent 125,122.

Cobbold, R. S. C., Vetlink, P. H., and Johnston, K. W. (1983). Influence of beam profile and degree of insonation on the CW Doppler ultrasound spectrum and mean velocity. *IEEE Trans. Sonics Ultrason.* **SU-30**, 364–370.

Coussios, C.-C. (2002). The significance of shape and orientation in single particle weak-scatterer models. J. Acoust. Soc. Am. **112**, 906–915.

Embree, P. M. and O'Brien Jr., W. D. (1985). The accurate ultrasonic measurement of the volume flow of blood by the time domain correlation, *IEEE Ultrason. Symp. Proc.*, 963–966.

Embree, P. M. and O'Brien Jr., W. D. (1990). Volumetric blood flow via time domain correlation: Experimental verification, *IEEE Trans. Ultrason. Ferroelec. Freq. Control* **37**, 176–189.

Evans, D. H. (1993). *Advances in Ultrasound Techniques and Instrumentation*, Chap. 8. P. N. T. Wells (ed.). Churchill Livingstone, New York.

Evans, D. H. and Parton, L. (1981). The directional characteristics of some ultrasonic Doppler blood-flow probes, *Ultrasound in Med. Biol.* **7**, 51–62.

Ferrara, F. W. and Algazi, V. R. (1991a). A new wideband spread target maximum likelihood estimator for blood velocity estimation, Part I: Theory. *IEEE Trans. Ultrason. Ferroelec. Freq. Control* **38**, 1–16.

Ferrara, F. W. and Algazi, V. R. (1991b). A new wideband spread target maximum likelihood estimator for blood velocity estimation, Part II: Evaluation of estimators with experimental data. *IEEE Trans. Ultrason. Ferroelec. Freq. Control* **38**, 17–26.

Ferrara, K. and Deangelis, G. (1997). Color flow mapping. *Ultrasound in Med. & Biol.* **23**, 321–345.

Fontaine, I., Bertrand, M., and Cloutier, G. (1999). A system-based simulation model of the ultrasound signal backscattered by blood. *IEEE Ultrason. Symp. Proc.,* 1369–1372.

Frinking, P. J. A., Boukaz, A., Kirkhorn, J., Ten Cate, F. J., and De Jong, N. (2000). Ultrasound contrast imaging: Current and new potential methods. *Ultrasound in Med. & Biol.* **26**, 965–975.

Greenleaf, J. F., Duck, F. A., Samayoa, W. F., and Johnson, S. A. (1974). Ultrasound data acquisition and processing system or atherosclerotic tissue characterization. *IEEE Ultrason. Symp. Proc.,* 1561–1566.

Halberg, L. I. and Thiele, K. E. (1986). Extraction of blood flow information using Doppler-shifted ultrasound. *HP Journal* **37**, 35–40.

Hattle, L. and Angelsen, B. (1985). *Doppler Ultrasound in Cardiology: Physical Principles and Clinical Application*, 2nd ed., Lea and Febiger, Philadelphia.

Hein, I. A. and O'Brien Jr., W. D. (1993a). A real-time ultrasound time domain correlation blood flowmeter: Part I: Theory and design. *IEEE Trans. Ultrason. Ferroelec. Freq. Control*. **40**, 775–778.

Hein, I. A. and O'Brien Jr., W. D. (1993b). A real-time ultrasound time domain correlation blood flowmeter: Part II: Performance and experimental verification. *IEEE Trans. Ultrason. Ferroelec. Freq. Control* **40**, 778–785.

Hein, I. A., and O'Brien Jr., W. D. (1993c). Current time-domain methods for assessing tissue motion by analysis from reflected ultrasound echoes: A review. *IEEE Trans. Ultrason. Ferroelec. Freq. Control* **40**, 84–102.

Jensen, J. A. (1996). *Estimation of Blood Velocities Using Ultrasound*. Cambridge University Press, Cambridge, UK.

Kasai, C., Namekawa, K., Koyano, A., and Omoto, R. (1983). Real-time two dimensional blood flow imaging using an autocorrelation technique. *IEEE Trans. Sonics Ultrason*. **SU-32**, 458–464.

Kimme-Smith, C., Tessler, F. N., Grant, E.G., and Perella, R. R. (1989). Processing algorithms for color flow Doppler. *IEEE Ultrason. Symp. Proc.*, 877–879.

Lerner, R. M., Huang, S. R., and Parker, K. J. (1990). Sonoelasticity images derived from ultrasound signals in mechanically vibrated tissues. *Ultrasound in Med. & Biol*. **15**, 231–239.

Lockwood, G. R., Ryan, L. K., Hunt, J. W., and Foster, F. S. (1991). Measurement of the ultrasonic properties of vascular tissues and blood from 35–65 MHz. *Ultrasound in Med. & Biol*. **17**, 653–666.

Magnin, P. A. (1986). Doppler effect: History and theory. *HP Journal* **37**, 26–31.

Magnin, P. A. (1987). A review of Doppler flow mapping techniques. *IEEE. Ultrason. Symp. Proc.*, 969–977.

Mo, L. Y. L., and Cobbold, R. S. C. (1986). "Speckle" in continuous wave Doppler ultrasound spectra: A simulation study. *IEEE Trans. Ultrason. Ferroelec. Freq. Control* **33**, 747–753.

Newhouse, V. L., and Amir, L. (1983). Time dilation and inversion properties and the output spectrum of pulsed Doppler flowmeters. *IEEE Trans. Sonics Ultrason*. **SU-30**, 174–179.

Newhouse, V. L., Furgason, E. S., Johnson, G. F., and Wolf, D. A. (1980). The dependence of ultrasound Doppler bandwidth on beam geometry. *IEEE Trans. Sonics Ultrason*. **SU-25**, 50–59.

Nightingale, K. R., Kornguth, P. J., Walker, W. F., Mc Dermott, B. A., and Trahey, G. E. (1995). A novel technique for differentiating cysts from solid lesions: Preliminary results in the breast. *Ultrasound in Med. & Biol*. **21**, 745–751.

Nowicki, A. and Reid, J. M. (1981). An infinite gate-pulsed Doppler. *Ultrasound in Med. & Biol*. **7**, 41–50.

Nowicki, A. and Secomski, W. S. (2000). Estimation of hematocrit by means of dual-gate power Doppler. *IEEE Ultrason. Symp. Proc.*, 1505–1508.

Pierce, A. D. (1989). *Acoustics*. Acoustical Society of America, Woodbury, NY.

Ramamurthy, B. S. and Trahey, G. E. (1991). Potential and limitations of angle-independent flow detection algorithms using radio-frequency and detected echo signals. *Ultrason. Imag*. **13**, 252–268.

Richardson, L. F. (March 27, 1913). *Apparatus for Warning a Ship at Sea of its Nearness to Large Objects Wholly or Partly Under Water*, UK patent 11,125.

Routh, H. F. (1996). Doppler ultrasound. *IEEE Eng. in Med. Biol*. **15**, 31–40.

Rubin, J. M., Bude, R. O., Carson, P. L., Bree, R. L., and Adler, R. S. (1994). Power Doppler ultrasound: A potential useful alternative to mean-frequency-based color Doppler ultrasound. *Radiology* **190**, 853–856.

Satomura, S. (1957). Ultrasonic Doppler method for the inspecion of cardiac function. *J. Acoust. Soc. Am*. **29**, 1181–1185.

Secomski, W., Nowicki, A., Guidi, F., Tortoli, P., and Lewin, P. A. (2003). Noninvasive in vivo measurements of hematocrit. *J. Ultrasound Med*. **22**, 375–384.

Shung, K. K. (1982). On the scattering of blood as a function of hematocrit. *IEEE Trans. Sonics Ultrason*. **SU-29**, 327–331.

Shung, K. K., Sigelmann, R. A., and Reid, J. M. (1976). Scattering of ultrasound by blood. *IEEE Trans. Biomed. Eng*. **BME-23**, 460–467.

Sigelmann, R. A., and Reid, J. M. (1973). Analysis and measurement of ultrasound backscattering from an ensemble of scatterers excited by sine-wave bursts. *J. Acoust. Soc. Am*. **53**, 1351–1355.

Szabo, T. L. (1993). *Linear and Nonlinear Acoustic Propagation in Lossy Media*, Ph.D. thesis. University of Bath, Bath, UK.

Szabo, T. L., Melton Jr., H. E., and Hempstead, P. S. (1988). Ultrasonic output measurements of multiple mode diagnostic ultrasound systems. *IEEE Trans. Ultrason. Ferroelec. Freq. Control* **35**, 220–231.

Teh B.-G. and Cloutier, G. (2000). Modeling and analysis of ultrasound backscattering by spherical aggregates and rouleaux of red blood cells. *IEEE Trans. Ultrason. Ferroelec. Freq. Control* **47**, 1025–1035.

Wang, S. H., Lin, Y. H., and Shung, K. K. (1997). In vivo measurements of ultrasonic backscatter from blood. *IEEE Ultrason. Symp. Proc.*, 1161–1164.

Wilhjelm, J. E. and Pedersen, P. C. (1993a). Target velocity estimation with FM and PW echo ranging Doppler systems, Part I: Signal analysis. *IEEE Trans. Ultrason. Ferroelec. Freq. Control* **40**, 366–372.

Wilhjelm, J. E. and Pedersen, P. C. (1993b). Target velocity estimation with FM and PW echo ranging Doppler systems, Part II: Systems analysis. *IEEE Trans. Ultrason. Ferroelec. Freq. Control* **40**, 373–380.

Wells, P. N. T. (1969a). A range gated Doppler system. *Med. Biol. Eng*. **7**, 641–652.

Wells, P. N. T. (1969b). *Physical Principles of Ultrasonic Diagnosis*. Academic Press, London.

12.1 INTRODUCTION

Nonlinear effects are important for harmonic imaging, contrast agents, and acoustic output measurements. The effects of nonlinearity combine and interact with all the other major components of imaging (attenuation, focusing, and signal processing), and, therefore, they cannot be understood in isolation. In addition, linearity (a fundamental design assumption for imaging systems), based on proportionality and superposition, must be reexamined to work with nonlinearity. This chapter explores what nonlinearity is and how it extends and challenges our understanding of linear wave propagation. Contrast agents are discussed separately in Chapter 14.

What is nonlinearity? Nonlinearity is a property of a medium by which the shape and amplitude of a signal at a location are no longer proportional to the input excitation. In a fluid, for example, the relation between variations in pressure and changes in density from equilibrium values is no longer linear (as shown for water by Figure 12.1). Two curves are depicted, and each one is an approximation to the actual nonlinear relationship. Until now, an assumption has been made that for infinitesimal amplitudes, linearity holds, as described by,

$$p - p_0 = A\left(\frac{\rho - \rho_0}{\rho_0}\right) = \left[\rho_0\left(\frac{\partial p}{\partial \rho}\right)_{S,\,\rho=\rho_0}\right]\left(\frac{\rho - \rho_0}{\rho_0}\right) = \rho_0 c_0^2\left(\frac{\rho - \rho_0}{\rho_0}\right) \qquad (12.1a)$$

where P_0 and ρ_0 are the pressure and density at equilibrium in a fluid (similar relations can be found for gases and solids). Here, $A = \rho_0 c_0^2$ is a linear constant taken for $\rho = \rho_0$ and at a specific entropy. The assumption is made that the process is adiabatic, meaning that there is no heat transfer during the rapid fluctuations of an acoustic wave. A better approximation is to include the next term in a Taylor expansion series (Beyer, 1997) for the pressure as a function of density,

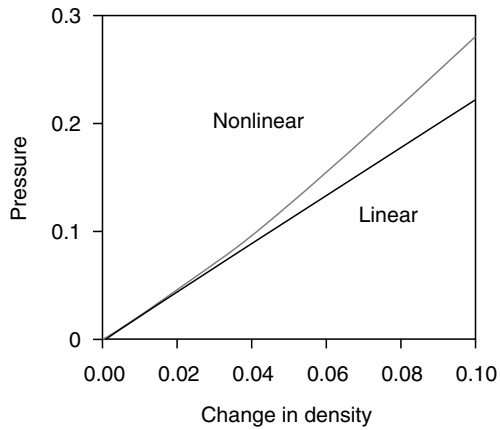

Figure 12.1 Linear and nonlinear characteristics of pressure versus density for water.

$$p - p_0 = A\left(\frac{\rho - \rho_0}{\rho_0}\right) + B\left(\frac{\rho - \rho_0}{\rho_0}\right)^2 + \ldots \tag{12.1b}$$

called the "nonlinear equation of state," with B defined as

$$B = \left[\rho_0^2 \left(\frac{\partial^2 p}{\partial \rho^2}\right)_{S,\ \rho=\rho_0}\right] \tag{12.1c}$$

Equation 12.1b is plotted as the nonlinear curve in Figure 12.1.

A simple measure of the relative amount of nonlinearity is the ratio of B/A. More common, however, is the coefficient of nonlinearity, β (not to be confused with the wave number propagation factor), which is defined as

$$\beta = 1 + B/2A \tag{12.2}$$

which will be related later to the speed of sound in a nonlinear medium. Not only is water nonlinear, but also so are all tissues (as shown in the graph of β in Figure 12.2). Coefficients for tissue fall in the range of 3 to 7 (water to fat) (Duck, 1990). Note that tissues are only slightly more nonlinear than water. Contrast agents (discussed in Chapter 15) can have nonlinearity coefficients of more than 1000 in high concentration (Wu and Tong, 1994).

In addition to tissues being nonlinear, so are many physical phenomena in the world around us. Linear approximations to reality are used for convenience, simplified understanding, and design control. Nonlinear approximations are more accurate, but they are more complicated for use in simulation and design. Because the effects of nonlinearity are amplitude dependent, in acoustics they are also called "finite amplitude" (as opposed to linear theory, which is based on infinitesimal amplitudes).

Nonlinearity produces strange behavior not predictable by our usual linear viewpoint. The major consequences of acoustic propagation in a nonlinear medium are

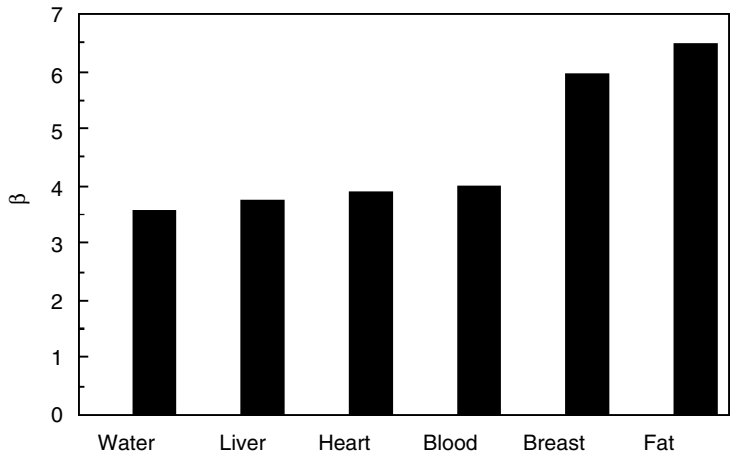

Figure 12.2 Coefficients of nonlinearity for tissues and water.

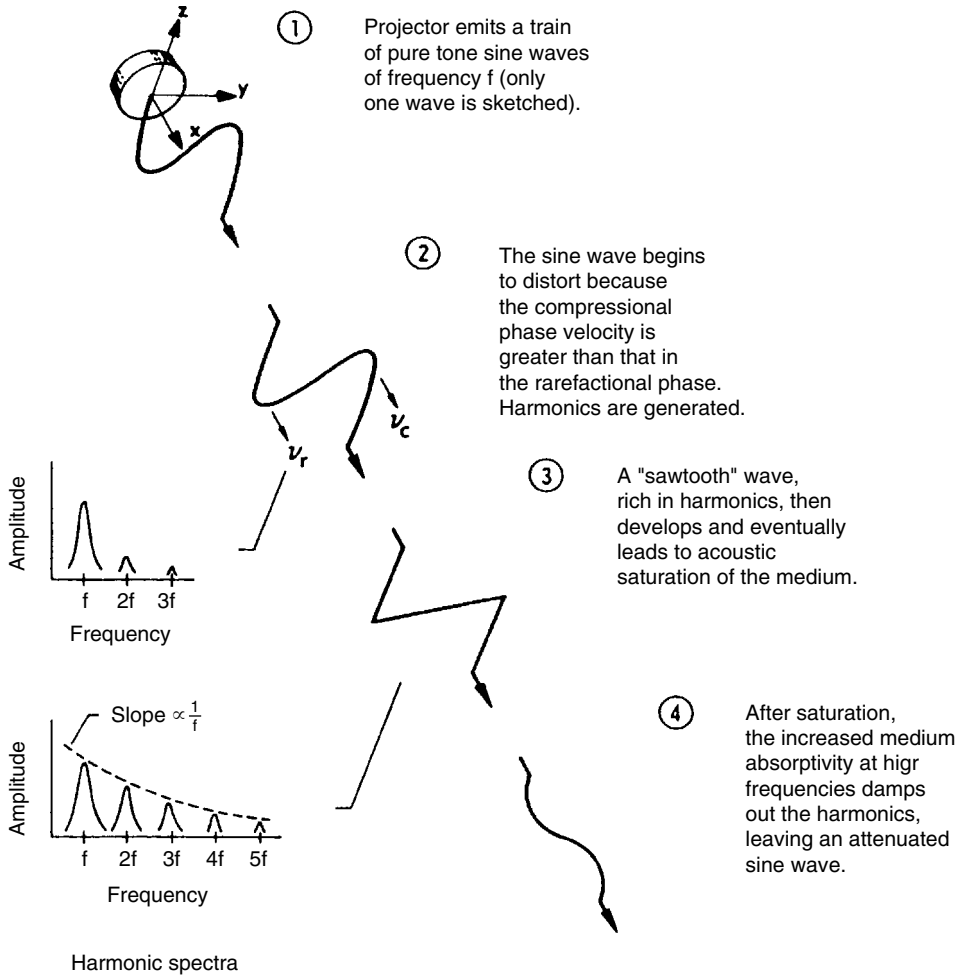

Figure 12.3 Evolution of a shock wave beginning from a plane sinusoidal wave source. Note that even though a transducer source is shown, the waveforms are those of an infinite plane wave transmitter (from Muir and Carstensen, 1980, reprinted with permission from the World Federation of Ultrasound in Medicine and Biology).

cumulative pulse and beam distortion, harmonic generation, and ultimately, saturation. Consider the stages of waveform evolution in Figure 12.3. At the top of this figure, one cycle of a long tone burst of a single-frequency plane wave is shown as the input to a nonlinear medium. As the signal propagates, distortion begins and simultaneously creates low levels of harmonics. Next in the sequence, the cumulative distortion eventually leads to a sawtooth, or "N"-shaped waveform or "shock wave," which has frequencies at harmonic multiples of the fundamental. If the fundamental is called the "first" harmonic and each harmonic is designated by *n*,

the amplitude of each harmonic in the spectrum falls off by n^{-1} for this waveform. Finally, at great distances and at higher frequencies, only an attenuated low-amplitude "old age" waveform is left that is no longer proportional to the original emitted amplitude.

Even though the use of these harmonics for imaging became widespread on ultrasound imaging systems by the late 1990s, nonlinear acoustics has been a growing branch of acoustics for more than 240 years (Blackstock, 1998). Intense development in this area has occurred in the last 40 years (Bjorno, 2002). Three major areas that spurred this interest in nonlinear acoustics are sonic booms (shock waves generated by supersonic sources such as jet planes) beginning in the 1950s, the application of parametric arrays to increase resolution in sonar (1960s to present), and, of course, biomedical ultrasound (1970s to present). Parametric arrays employ high-intensity sound and the ability of water as a highly nonlinear medium to create narrow beams at difference frequencies (Westervelt, 1963; Berktay and Al-Temini, 1969). A key enabling technology for nonlinear acoustics was the high-speed digital computer, which was necessary for the numerical solution of nonlinear equations. Improvements in wideband transducers and experimental techniques made possible the verification of newly developed models for sound propagation in nonlinear media. Other expanding areas of nonlinear acoustics include thermoacoustic refrigerators, sonochemistry, cavitation and bubble dynamics, high-power industrial and surgical applications, and nondestructive testing and evaluation (Tjotta, 2000; Bjorno, 2002).

In regard to nonlinear developments specifically related to harmonic imaging, one of the first was a demonstration of harmonic images by Muir (1980) for sonar applications. He created underwater harmonic images formed by the bandpass filtering output of a scanned wideband hydrophone at each of several harmonics (as illustrated by Figure 12.4). Second harmonic images were also reported in acoustic microscopy (Kompfner and Lemons, 1976; Germain and Cheeke, 1988.) Muir and Carstensen (1980) argued that ultrasound imaging systems were capable of generating distorted waves in nonlinear media such as water and tissue. There were indications through related acoustic measurements in water with hydrophones and other means that ultrasound imaging systems generated harmonics in water in the late 1970s and early 1980s (Carson *et al*., 1978; Carstensen *et al*., 1980; Bacon, 1984). Conclusive evidence (Duck and Starritt, 1984) in the form of acoustic output measurements of clinical systems in water with wideband hydrophones began to appear in the early 1980s. Until recently, bandpass filters in ultrasound imaging systems removed all harmonic frequencies so that nonlinear effects from tissues went unnoticed. The first deliberate attempts at medical harmonic imaging in its present form were for imaging highly nonlinear contrast agents at the second harmonic (to be discussed in more detail later in Chapter 14). An earlier form on nonlinear imaging, called "B/A imaging," was investigated in laboratories but did not find clinical application. Starritt *et al*. (1985, 1986) confirmed that harmonics could also be generated in tissue. Tissue harmonic imaging was reported by several groups (Ward *et al*., 1996, 1997; Averikou *et al*., 1997). By the late 1990s, the benefits of tissue harmonic imaging without contrast agents became commonplace on ultrasound imaging systems. Harmonic imaging with contrast agents is covered in Chapter 14.

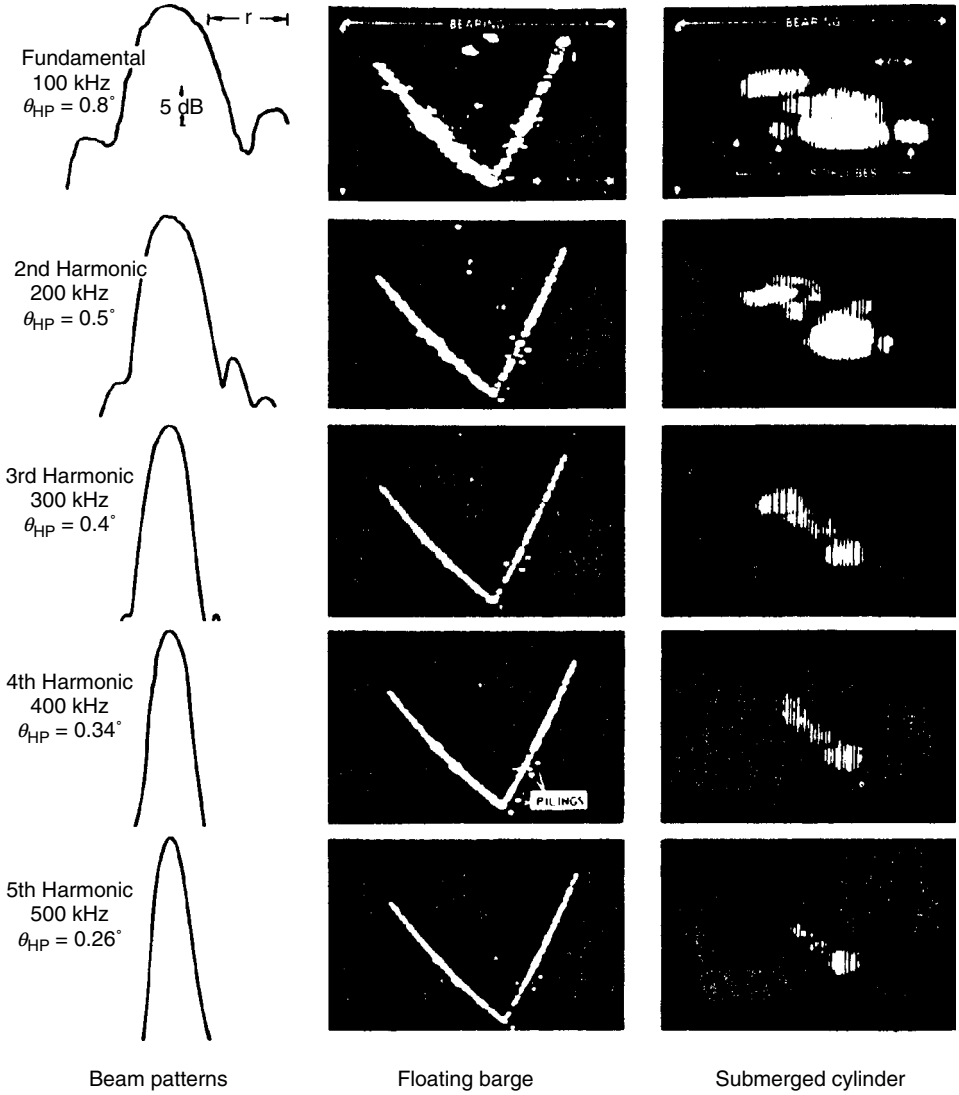

Figure 12.4 Harmonic images of a barge and a submerged cylinder in water produced by filtering out harmonic frequencies from a wideband angle–scanned hydrophone receiver mounted above a narrowband transmitter. Beams at the fundamental frequency up to the fifth harmonic are shown at the left (from Muir, 1980, reprinted with permission from Kluwer Academic/Plenum Publishers).

12.2 WHAT IS NONLINEAR PROPAGATION?

An interesting consequence of the quadratic dependence of pressure on density is a change in sound speed between the compressional (positive as shown in Figure 12.5) and rarefactional (negative) half cycles of a signal. For a sinusoidal plane wave signal

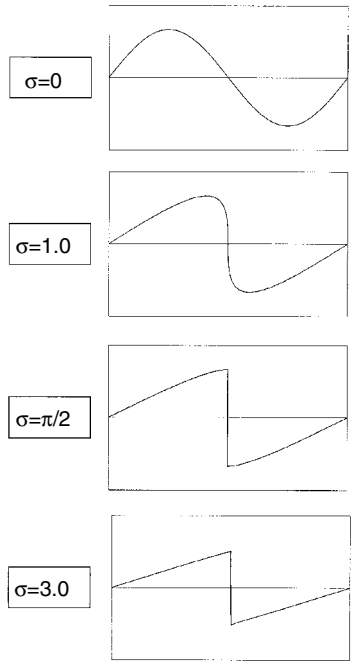

Figure 12.5 Successive waveforms for an initially sinusoidal plane wave shown for increasing normalized distances (σ) from the source (from Duck, 2002, reprinted with permission from the World Federation of Ultrasound in Medicine and Biology).

in a lossless nonlinear medium, the speed of sound for a displacement amplitude u is given by

$$dz/dt = c_0 + \beta u, \tag{12.3}$$

so that positive half cycles speed up by an extra factor βu, and the negative ones, where the displacement u is negative, slow down by βu, as shown in Figure 12.5 for increasing normalized distances denoted by a parameter (σ). This sound speed dependence is definitely a finite amplitude effect. The positive peaks move forward toward the zero crossing, whereas the negative peaks retreat toward the zero crossing behind them. In this idealized case, when the peaks have moved $\pi/2$ from their original positions, they coincide at the zero crossing and form a sawtooth with an infinite slope at the zero crossing (π) position. The condition in which the slope first becomes infinite is called shock formation. Past this point, the wave amplitude becomes smaller. Equation (12.3) also indicates that this change in sound speed can create increased distortion either if the medium is more nonlinear (larger β) or if the displacement amplitude u is larger. Overall, the two contributions to nonlinear

distortion are both the equation of state and the local convective nonlinearity caused by the displacement on the sound speed. As an example, $B/A = 5$ for water, so that from the definition of $\beta = 1 + 2.5$, Eq. (12.2), the first term or convective contribution to distortion is one third of the total, with the nonlinearity of the medium accounting for the remaining two thirds (Duck, 2002).

The normalized distance nonlinearity parameter σ for a plane wave is useful in predicting distortion. The acoustic Mach number ε is defined as

$$\varepsilon = u_0/c_0 \tag{12.4a}$$

and can also be expressed as

$$\varepsilon = p_0/(\rho_0 c_0^2) = \sqrt{2I/(\rho_0 c_0^3)} \tag{12.4b}$$

where I is the time average intensity, and initial pressure at the source is $p_0 = \rho_0 c_0 u_0$. Finally, the nonlinearity parameter can be expressed as

$$\sigma = \beta \varepsilon k z = \frac{\beta p_0 2\pi f z}{\rho_0 c_0^3} \tag{12.4c}$$

where k is the wave number, $k = \omega/c_0$, and z is the distance from the source. The importance of Eq. (12.4c) is that it predicts increasing distortion when any of the following increase: nonlinearity (β), frequency (f), amplitude (p_0), or distance (z). Note that in accordance with Figure 12.5, shock occurs when $\sigma = 1$ or at the shock distance, $z = l_s = 1/(\beta \varepsilon k)$. For this value of σ, a vertical discontinuity appears in the waveform. For values between 1 and 3, a transition region exists, and when it exceeds 3, the sawtooth region begins,

$$p(x, \tau) = p_0 \sum_{n=1}^{\infty} \frac{2}{n(1+\sigma)} \sin(n\omega\tau + \phi) \tag{12.4d}$$

in which retarded time, $\tau = t - z/c_0$, is used, and phase $\phi = 0$.

Another peculiar property of sound in a nonlinear medium is that propagation has a cumulative distortion with distance. Because of quadratic dependence of pressure on density changes, an analogy can be made with another nonlinear device (the square law mixer in electronics). Consider the nonlinear medium to be made up of a series of distributed mixers that are each an infinitesimal distance (Δz) from each other (as depicted in Figure 12.6). If the change in density is a sinusoid of frequency $\omega_0 = 2\pi f_0$ that is injected into the mixer chain, then from Eq. (12.1b), the square law mixer output would be

$$p - p_0 = A\cos\omega_0 t + B\cos^2\omega_0 t \tag{12.5a}$$

$$p - p_0 = A\cos\omega_0 t + (B/2)(1 + \cos 2\omega_0 t) \tag{12.5b}$$

The fundamental and the second harmonic output feed the next mixer, and repeating the same square law process yields harmonic frequencies of f_0, $2f_0$, $3f_0$, and $4f_0$. At each position, the newly distorted waveform (represented here by its spectrum) recreates itself by interacting with the nonlinear (square law) properties of the

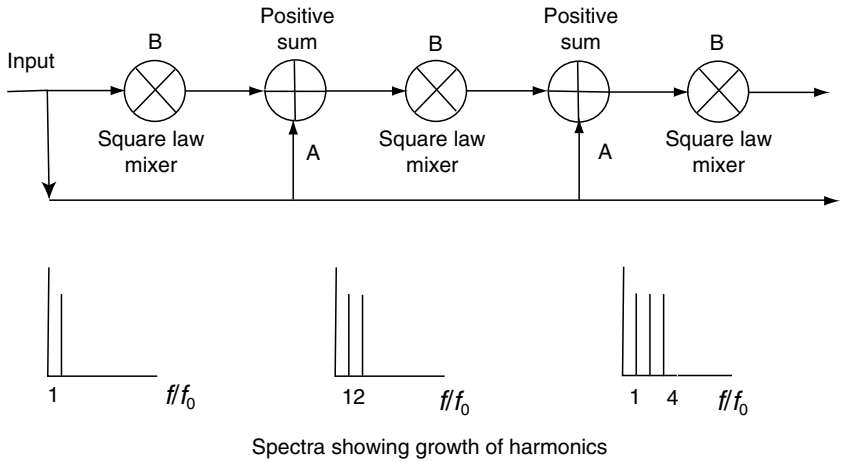

Figure 12.6 Propagation through a nonlinear medium modeled as a chain of square law mixers and summing nodes, each of which is separated by an infinitesimal distance. The number of harmonics grows as the original input of frequency (f_0) creates new frequencies at each stage.

medium. This process is represented by a idealized chain of mixers at each infinitesimal spatial location, in which progression in distance increases the number of harmonics exponentially. The purpose of this analogy is to demonstrate a harmonic generating process; the actual creation of harmonics is more complicated than shown here and is covered in more detail later.

A third unusual property of acoustic propagation in a nonlinear medium, in addition to amplitude- and nonlinearity-dependent sound speed and cumulative distortion with multiple harmonic generation, is acoustic saturation. In a linearized world, amplitudes at spatial positions are proportional without limit to the input or beginning amplitude at the source. As illustrated by Figure 12.5, for a lossless ideal nonlinear medium, amplitude of an increasingly distorted wave shape peaks and then diminishes past values of $\sigma > \pi/2$.

The overall saturation effect can be seen in Figure 12.7, in which the nonlinear characteristic tracks the linear one initially and then approaches a plateau (saturation level). The difference between the expected extrapolated linear increase in amplitude at a position in a nonlinear medium based on unrealistic linear assumptions and that actually obtained is called ''extra or excess attenuation.'' This attenuation is caused by absorption, as well as the type of distortion that occurs at long propagation distances in the medium and that alters the coherent phasing of harmonic components to reduce amplitude. Note that a linear extrapolation made from the origin to any point on the nonlinear region of the saturated curve would result in an underestimate of the amplitude to the left of the point.

Duck (1998) has presented two expressions for the maximum acoustic pressure in the plateau region that can be reached at any distance (z) from a source of frequency (f_0). The first expression is for plane waves,

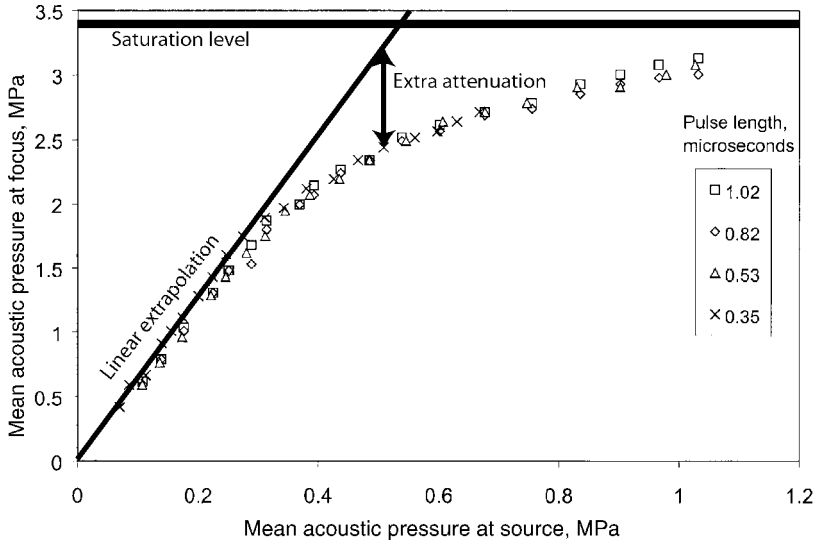

Figure 12.7 Hydrophone measurements at different pulse lengths versus increasing transmit levels that demonstrate the start of acoustic saturation phenomena in a pulsed diagnostic beam. No dependence on pulse length was observed over the range 0.35–1.02 μ sec. Extra attenuation is the difference between a linear extrapolation from low amplitudes and the nonlinear characteristic (adapted from Duck, 2002, reprinted with permission from the World Federation of Ultrasound in Medicine and Biology).

$$p_{sat,p} = \frac{\rho_0 c_0^3}{2\beta f_0 z} \tag{12.6a}$$

and the second approximate expression is for a circularly symmetric focusing transducer with a focal length (F) and a low amplitude focal gain of G (Naugol'nykh and Romanenko, 1959),

$$p_{sat,F} = \frac{\rho_0 c_0^3}{2\beta f_0 F} \frac{G}{\ln G} \tag{12.6b}$$

In more lossy media other than water, absorption plays a stronger role in determining levels of saturation (Blackstock *et al.*, 1998). Beamforming also alters the situation, and for tightly focused beams, Eq. (12.6b) underestimates experimentally observed saturation levels (Sempsrott and O'Brien, 1999).

12.3 PROPAGATION IN A NONLINEAR MEDIUM WITH LOSSES

How does acoustic propagation in nonlinear water compare with that in a typical tissue that has a frequency power law absorption characteristic? Because the effects of absorption increase with frequency and distance, absorption acts as a low-pass filter to reduce the amplitudes of higher harmonics, as well as signal amplitude. Absorption

and nonlinearity are always involved interactively in competition by reducing and creating harmonics and distortion. A measure of which one will win this contest is the Gol'dberg number (1957),

$$\Gamma = \sigma/(\alpha z) \tag{12.7}$$

Nonlinear distortion or shock begins when $\Gamma = 1$. For increasing values of Γ greater than 1, nonlinear distortion becomes more dominant; whereas for values less than 1, absorption prevents significant distortion from developing.

Gol'dberg numbers for water and tissues are compared at a typical diagnostic pressure of 5 MPa and a midrange frequency of 5 MHz in Figure 12.8. What is unusual about this chart is the large Gol'dberg number for water ($\Gamma = 266$), which is clearly in a class by itself when compared to Gol'dberg numbers for tissue, which are all less than 14. These numbers indicate that distortion is extremely easy to achieve in water, even for small amplitudes, compared to tissue. Experimentally, these effects have been observed in acoustic output measurements made in water, but extrapolating data to equivalent values in tissue is an extremely challenging nonlinear problem (Szabo *et al.*, 1999). Both the amplitudes and the severity of distortion are markedly different in water than in tissues. For water, the power exponent $y = 2$ (from Chapter 4), so that Γ increases with amplitude and inversely with frequency. In contrast, for tissues, $y \approx 1$; therefore, Γ is nearly independent of frequency and changes with amplitude.

Acoustic propagation in a lossy nonlinear medium is a balance between absorption and harmonic replenishment from lower frequencies. In some cases, the loss slope at greater distances can be less than that expected from linear absorption (Haran and Cook, 1983).

An important consequence of the interaction of nonlinear effects and absorption is enhanced heating. Heating in tissue is related directly to absorption (to be explained in Chapter 13). The spectrum of a distorted waveform in a nonlinear medium contains many harmonics, each of which is being attenuated more at higher frequencies.

Figure 12.8 Gol'dberg numbers for tissue and water for a pressure of 5 MPa and a frequency of 5 MHz (from Szabo *et al.*, 1999, with permission from the American Institute of Ultrasound in Medicine).

As a result, the amount of energy lost in heating has increased over what would have occurred at the lower-frequency fundamental rate. Estimates of heating have been made on weak shock absorption (Bacon and Carstensen, 1990; Dalecki *et al*., 1991), in which nonlinearity plays a dominant role. Numerical techniques are necessary for accurate prediction of the close interaction of nonlinear and absorption in tissue (Haran and Cook, 1983; Christopher and Carstensen, 1996; Divall and Humphrey, 2000; Ginsberg and Hamilton, 1998).

12.4 PROPAGATION OF BEAMS IN NONLINEAR MEDIA

The accurate prediction of sound fields in nonlinear media evolved rapidly once the theory was developed, efficient numerical means of computing became available, and broadband hydrophones validated the predictions. A key development was the derivation of the Khokhlov-Zablotskaya-Kuznetsov (KZK) wave equation under the paraxial approximation (Kuznetsov, 1971). This equation combines nonlinearity and diffraction, as well as absorption, in a numerically suitable form. By the mid-1980s, a numerical frequency domain KZK algorithm was devised to run on computer workstations (Aanonsen *et al*., 1984). Other programs soon followed (as described in Section 12.6). Careful wideband hydrophone measurements in water by Baker *et al*., (1988), Baker (1989) and others (Ten Cate, 1993; Nachef *et al*., 1995; Averikou and Hamilton, 1995) verified the accuracy and utility of these programs.

An example of the agreement with the KZK algorithm (Baker, 1992; Humphrey, 2000) with data for the fundamental and harmonics of a focusing transducer radiating into water is shown in Figure 12.9. Note the absence of harmonics close to the transducer. Progressively longer distances are required for the higher harmonics to build up, which is a trend expected from σ, Eq. (12.4c). For harmonics, the ascent into the focal region is steeper than for the fundamental. As the harmonic number goes up, each higher harmonic peaks at a progressively deeper depth compared to the fundamental; consequently, with harmonic imaging, a deeper focal region is achieved than that expected under linear circumstances.

Graphs of measurements in the focal plane of the fundamental and second harmonic (Averikou and Hamilton, 1995) are shown in Figure 12.10. Not only is the main lobe narrower for the second harmonic, but the number of sidelobes has increased.

In addition, similar measurements by Baker (1992) and Ten Cate (1993) provide insights into the characteristics of a harmonic beam. First, the beamwidths of the harmonics in the far field (nonfocusing aperture) or focal plane are narrower than that of the fundamental by $1/\sqrt{n}$. Thus, the second harmonic beamwidth is 0.707 narrower. Second, a natural apodization occurs so that the sidelobe levels are progressively lower as the harmonic number increases. This effect can be explained by the fact that as the amplitude falls off away from the beam axis, so does harmonic generation, as expected by the trend in Eq. (12.4c). Third, ''finger'' or extra sidelobes appear. Typically for every sidelobe width of the fundamental, n sidelobes fill in (as apparent from Figure 12.10). Ten Cate (1993) has shown that these sidelobes fall

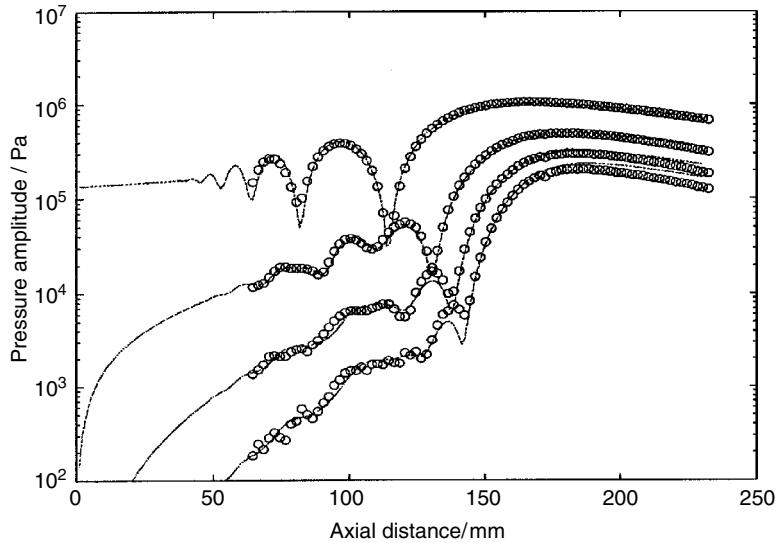

Figure 12.9 Axial variation of fundamental up to fourth harmonic for a circular focusing transducer with $a = 19$ mm, a linear focal gain of 9.2 (Eq. (6.33a)), and fundamental 2.25 MHz. Experiment is shown by dots, and theory is shown by lines. Note that this set of curves is based on a source pressure of $p_0 = 135$ kPa (reprinted from Humphrey, 2000, with permission from Elsevier).

off as $1/x$ in the transverse direction x. Note that these measurements were continuous wave (CW), so some filling in of the nulls will occur for pulses with a moderate or wide bandwidth. Fourth, harmonic amplitude levels on the beam axis can be even higher than expected for a sawtooth wave ($1/n$ levels for the nth harmonic). In water, the second harmonic can be as large as several decibels below the fundamental in the focal region or in the far field for a spherically focusing aperture.

Nonlinear wave distortion for beams is completely different in appearance from those predicted for infinite plane waves. In Figure 12.11 are waveforms measured by Baker (1989) with a hydrophone in the far field of a piston source as the voltage drive to the transducer was increased. Here wave shapes change from an initial sinusoid to a characteristic waveform at high amplitudes that is not a sawtooth but has a pronounced high-amplitude compressional peak and a shallower rarefactional peak. Note that these represent a family of different waveforms and beamshapes that depend on the source amplitude.

What is the cause of this asymmetry? Parker and Friets (1987) suggested that the phasing of each harmonic is a major contributor to changing wave shapes. They have shown that by adding a constant phase ϕ to the Fourier series coefficients describing a sawtooth, Eq. (12.4d), different shapes can be obtained. If $\phi = \pi/4 = 0.785$ radian, the resulting waveform (Figure 12.12) is remarkably like those for high-amplitude pressures in Figure 12.11. Hart and Hamilton (1988) demonstrated through computations of the KZK equation that the phase of each harmonic of a focused beam is at

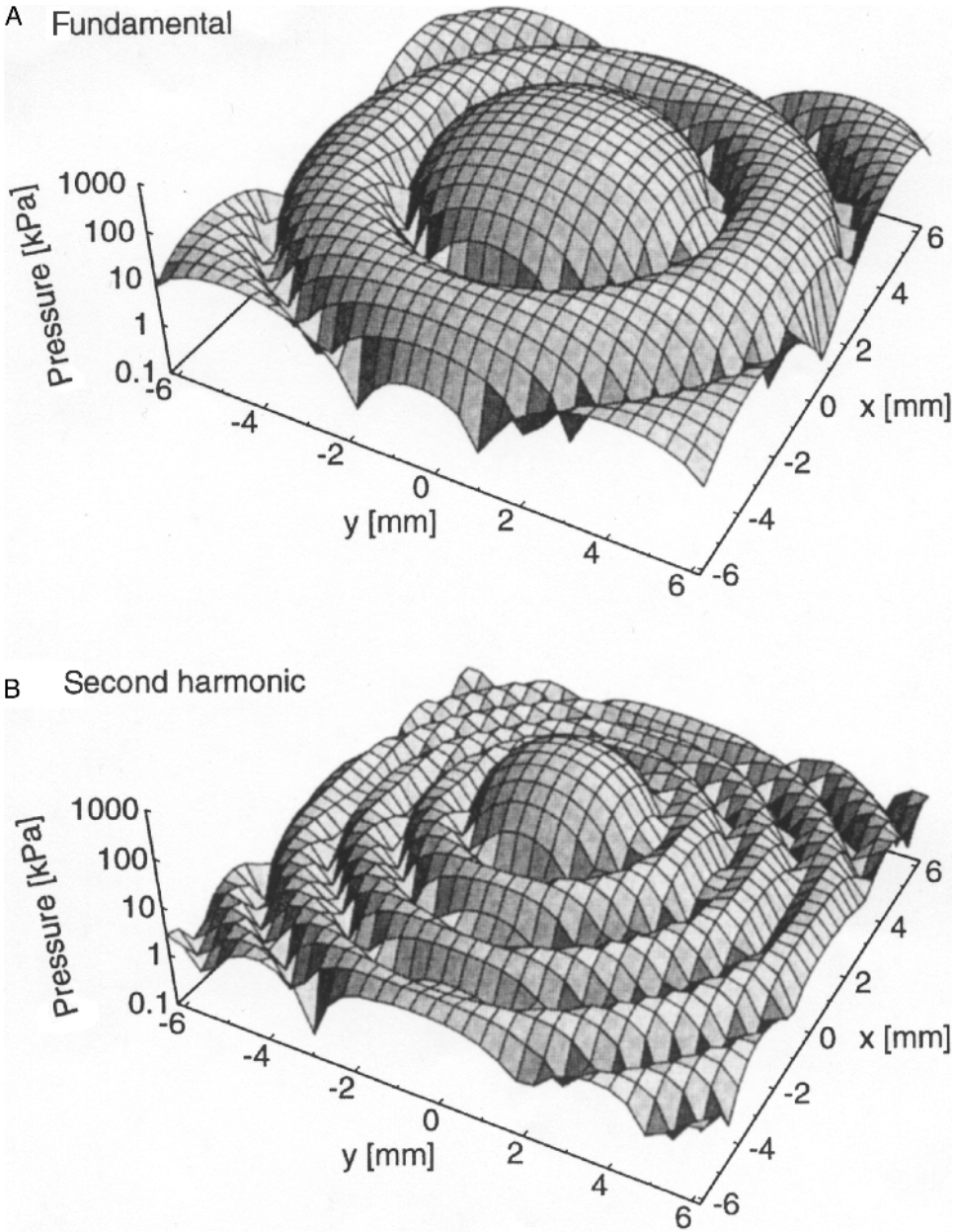

Figure 12.10 Measurements of (A) fundamental and (B) second harmonic in the focal plane for CW 2.25-MHz transducer with $a = 18.8$ mm and $F = 160$ mm (from Averikou and Hamilton, 1995, Acoustical Society of America).

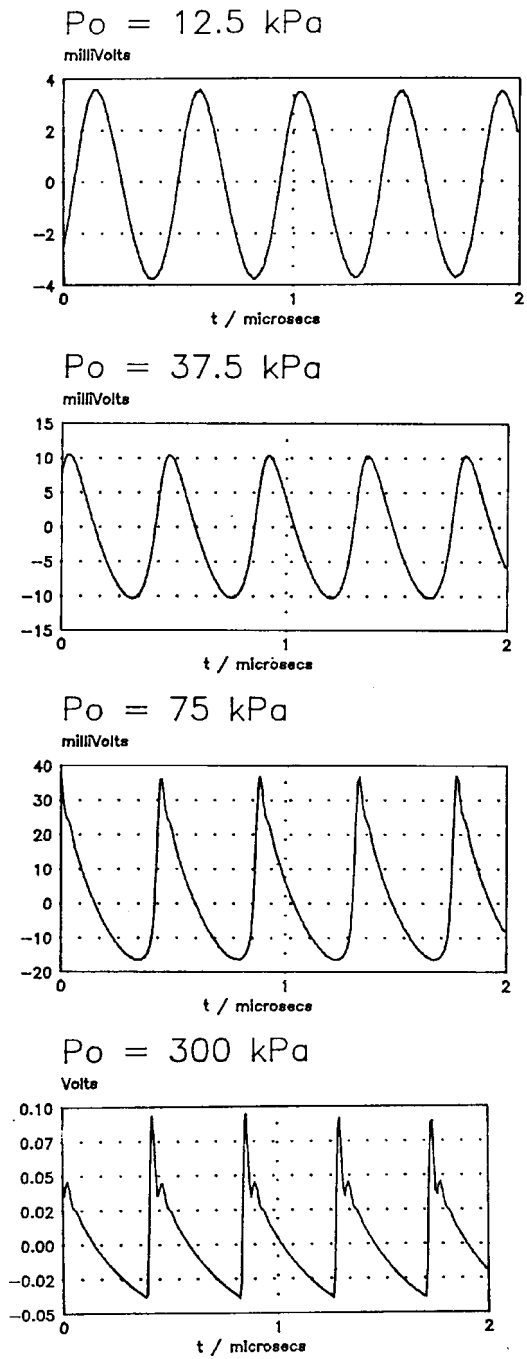

Figure 12.11 Hydrophone measurements of pressure at $z = 700$ mm, the far field of a piston source ($a = 19$ mm) operating CW at 2.25 MHz as the drive voltage to the transducer is increased (from Baker, 1989, courtesy of A. C. Baker).

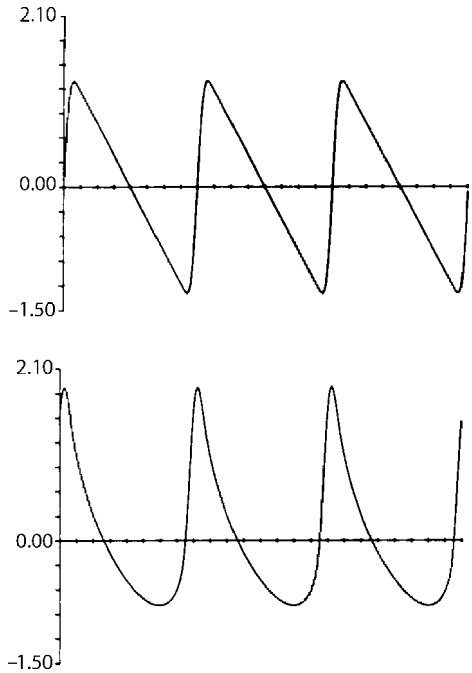

Figure 12.12 (Bottom) Waveform resulting from adding a constant phase of $\phi = \pi/4$ between harmonics in the standard Fourier series for a sawtooth (Top) (from Parker and Friets, 1987, *IEEE*).

least 90° greater than the previous harmonic. Hansen *et al.* (2001) have also shown that it is the phase associated with each harmonic, especially the lower ones, that causes the asymmetry. Away from the simplified circumstances of the far field, contributions from the diffraction of the beam cause a variety of distorted asymmetric waveform shapes.

For the case of a pulsed waveform, Baker and Humphrey (1992) applied a Fourier approach to describing the source waveform at the fundamental frequency (as demonstrated by Figure 12.14). This waveform became the input pulse to a KZK simulation program to calculate the waveform at 700 mm (Figure 12.14), which has typical asymmetric behavior and the harmonic buildup in the spectrum, both due to cumulative nonlinear distortion. Even though the propagation develops nonlinearly at any spatial location, the waveform and its spectrum there can be evaluated by linear fast Fourier transform (FFT) methods.

Most imaging systems use rectangular arrays, which behave differently than the spherically focused apertures just discussed. Because a rectangular array aperture usually has two means of focusing that are not coincident, nonlinear distortion can be more complicated than for the spherically focused case. Except for the situation in which both the elevation and azimuth focal lengths coincide, axial pressures tend to

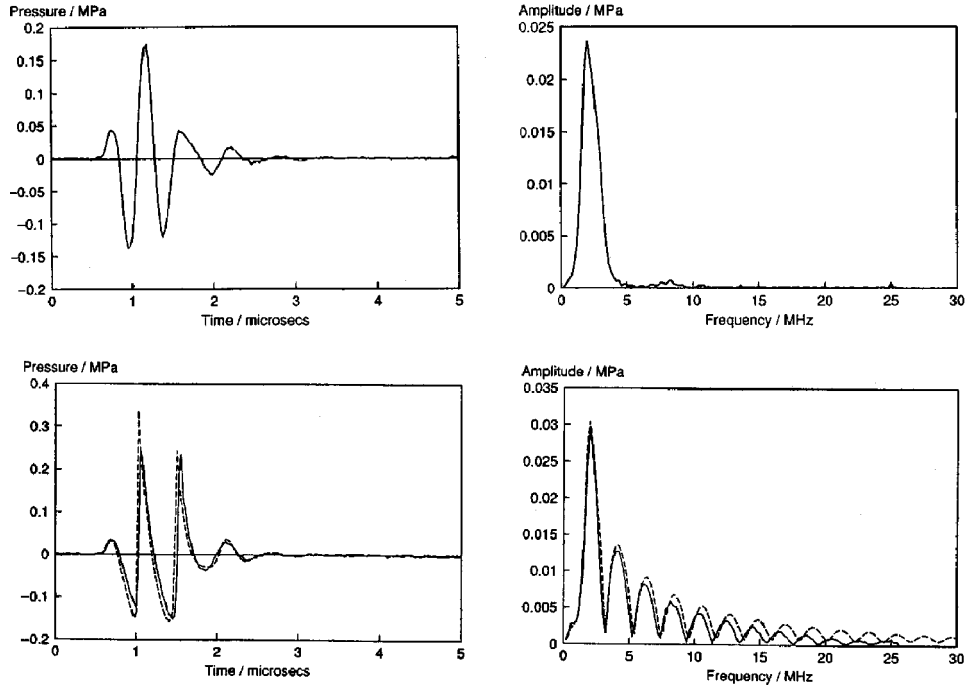

Figure 12.13 (Top) A 2.25-MHz waveform at source measured at $z = 15$ mm on-axis and used for simulation, with its spectrum on the right. (Bottom) Pressure waveform and spectrum simulated by KZK model and compared to data at 700 mm on-axis (from Baker and Humphrey, 1992, Acoustical Society of America).

be less than a circular aperture of the same area. The trends for nonlinear, circularly symmetric beams apply to rectangular apertures as well. For example, a similar buildup of the second harmonic axial pressure relative to that of the fundamental is shown in Figure 12.14.

The beam cross sections for a rectangular aperture in Figure 12.15 reveal fingers and natural apodization effects seen in the spherical case. Predictions of fields from rectangular apertures include another dimension and therefore involve approximately a factor of $N^{4/3}$ times the two-dimensional computations for the circular case.

Do arrays have grating lobes at the second harmonic? Consider a standard-phased array with half-wavelength, element-to-element spacing. At the second harmonic, this spacing would be a wavelength that usually corresponds to grating lobes outside of a normal $+/-$ 45° sector scan. In this case, no second harmonic grating lobes are generated at the transmit aperture at the fundamental frequency. As a result, the aperture has neither the starting pattern nor sufficient amplitude to serve a "seed" to grow grating lobes. Recall from Chapter 7 that grating lobes are weaker than the main lobe from the angular weighting of the element directivity function. In the case of a linear array that normally has an undersampled periodicity, or the initial aperture pattern necessary for generating grating lobes, the reduced amplitude of these grating lobes would most likely not survive the nonlinear natural apodization process. Because

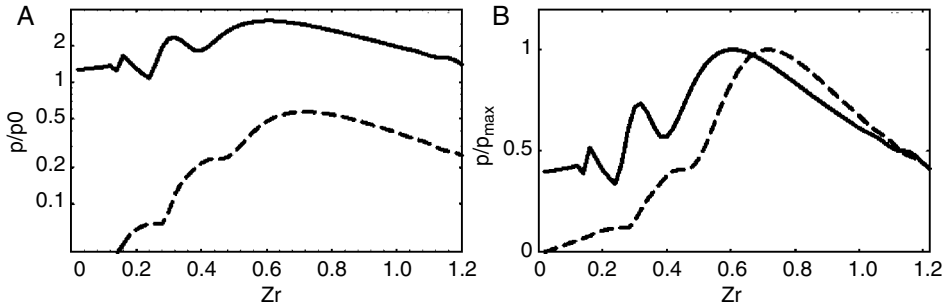

Figure 12.14 Normalized axial pressure along z for a 2-MHz pulsed rectangular array P4-2 radiating into a simulated tissue medium. The aperture (a_x), is 10.8 mm, and the focal distance (F) is 100 mm. Normalized distance is $z_r = z/F$. (A) Fundamental and second harmonic on logarithmic scale. (B) Fundamental and second harmonic normalized on a linear scale (from Averkiou, 2000, *IEEE*).

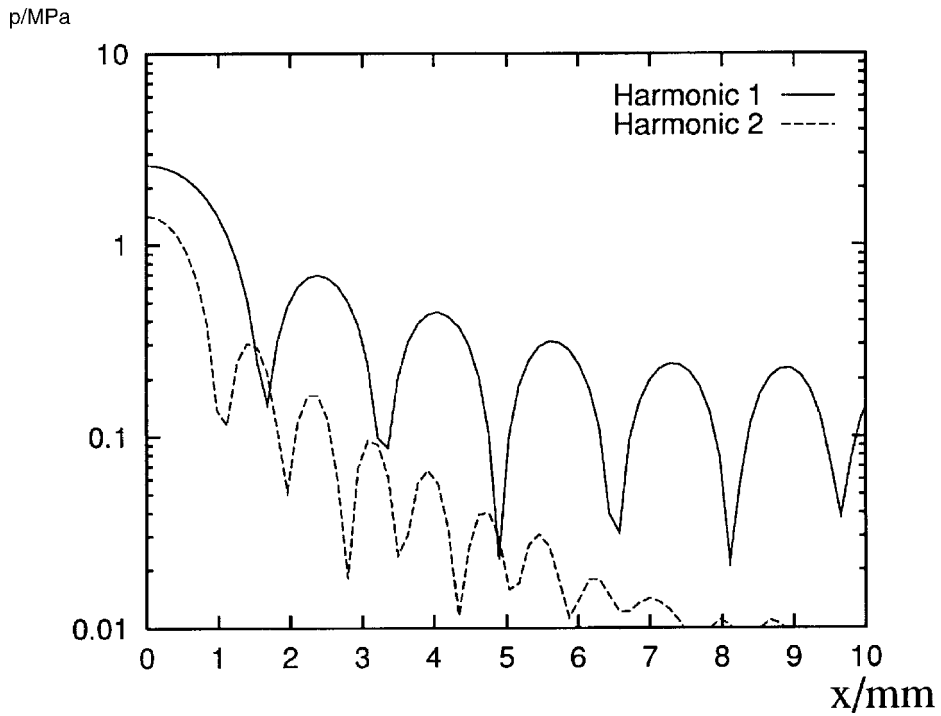

Figure 12.15 (Solid line) Theoretical half-beam azimuth cross sections in tissue for a 3.0-MHz array, 15 mm (azimuth) × 10 mm (elevation), with a coincident 50 mm focal length. Calculations are for the focal plane with a 1-MPa source pressure. (Dashed line) The calculations were performed for a source pressure of 1.0 MPa and show the cross section in the focal plane (from Humphrey, 2000, with permission from Elsevier).

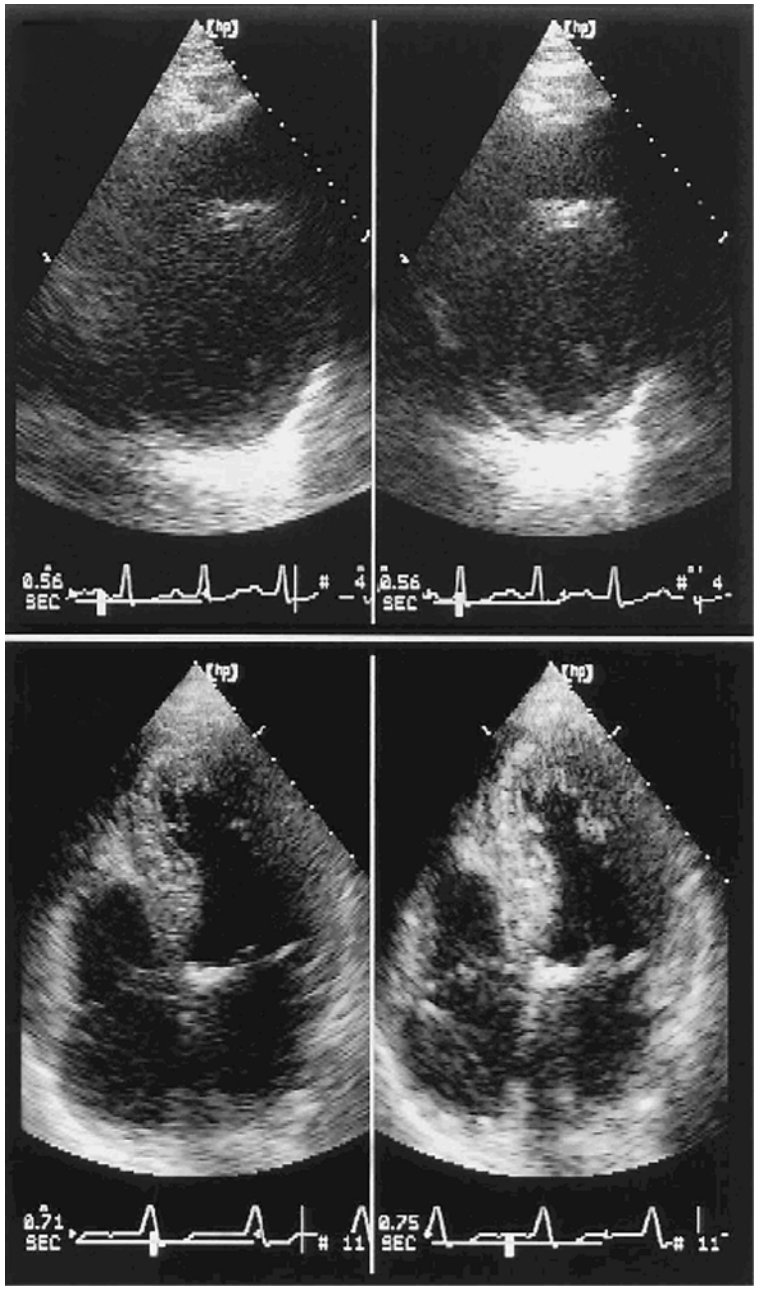

Figure 12.16 Representative cardiac images obtained on a difficult-to-image patient with fundamental imaging (left) and second harmonic imaging (right) for parasternal short-axis (upper panel) and apical four chamber (lower panel) views (from Spencer *et al.*, 1998, reprinted with permission from Excerpta Medica, Inc.).

of the low sidelobe levels of nonlinear beams, a spatially undersampled array in a receive mode would not detect significant echoes in the receive grating lobe regions.

12.5 HARMONIC IMAGING

12.5.1 Introduction

Tissue harmonic imaging (THI), also known as "native harmonic imaging," has been praised as being a breakthrough in ultrasound imaging that is as important as Doppler or color flow imaging. Equally unexpected was its accidental discovery on imaging systems and rapid commercialization in a few years. Originally, work on harmonic imaging was motivated by the need to image contrast agents. Because of the high reflectivity and extremely nonlinear properties of contrast agents, imaging system manufacturers filtered out the second harmonic of the returning echoes to separate the echoes of contrast agents from the assumed linear tissue background reflections.

Engineers and clinicians, unacquainted with the fact that tissues were also nonlinear, were puzzled to find the tissue background still in the second harmonic image and at first suspected their instrumentation. The linearity of an imaging system is checked easily. One way of validating that tissues are nonlinear is to gradually increase transmit amplitude (Muir, 1980) and to monitor the corresponding echo levels at the second harmonic and fundamental. Of course, there should be no second harmonic signal if the tissue is linear, and the echoes at the fundamental should track the transmit levels in a proportional fashion. In this way, tissue was found to behave as a nonlinear medium.

Once harmonic imaging had been implemented on imaging systems, an even bigger surprise was that clinicians began to favor the second harmonic images of tissue over those at the fundamental frequency. Examples of fundamental and second harmonic cardiac images are shown in Figure 12.16. The greater clarity, contrast, and details of the harmonic images are evident and have been quantitatively verified (Spencer *et al*., 1998; Kornbluth *et al*., 1998). These images emphasize another major discovery: People who were imaged poorly or not at all with conventional fundamental frequency ultrasound could be examined by second harmonic imaging. People who are difficult to image with ultrasound (about 30% of the population) are often those who have the greatest need to be imaged because of their health disorders. There are many examples of improvements in noncardiac applications as well (as illustrated by Figure 12.17 for the gallbladder). With all these clinical benefits, it is no wonder that harmonic imaging gained rapid acceptance and incorporation into new scanners.

Despite the significant advantages offered by harmonic imaging, their scientific basis has been explained only partially (Spencer *et al*., 1998; Tranquart *et al*., 1999; Averkiou, 2000; Humphrey, 2000; Li and Zagzebski, 2000; Duck, 2002). To those not familiar with nonlinear acoustics, THI appears to defy the well-known physical laws of linear acoustics; furthermore, contributing effects are difficult to isolate individually. The following discussion will comprehensively cover some of the reasons behind the success of harmonic imaging and its limitations in clinical circumstances.

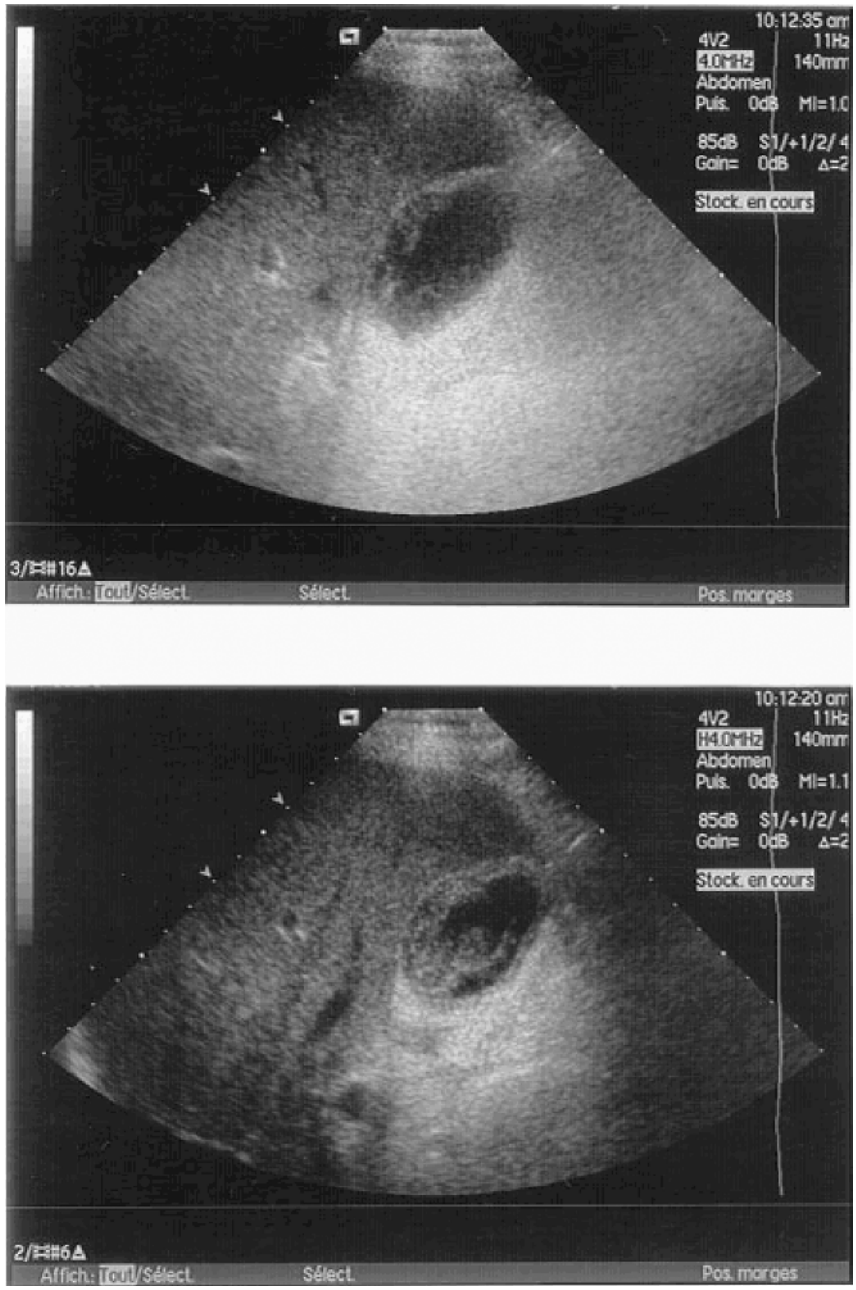

Figure 12.17 Images at the fundamental (top) and second harmonic (bottom) of chronic cholecystitis. Note that the harmonic image contains much more detail and contrast, as well as the contents and wall of the gall bladder (from Tranquart *et al.*, 1999, reprinted with permission from the world Federation of Ultrasound in Medicine and Biology).

Where possible, three types of imaging alternatives will be compared for arrays with coincident azimuth and elevation focusing: conventional fundamental frequency imaging, second harmonic imaging, and conventional imaging at twice the fundamental frequency. Results are summarized in Table 12.1. Familiar topics, such as focusing, arrays, scattering from tissue, and signal and image processing, will be revisited from an unusual point of view that will seem baffling to those with linear expectations. Harmonic imaging, which involves both the nonlinearities of tissues and contrast agents, is deferred until Chapter 14.

12.5.2 Resolution

Resolution is considered to be best in the focal plane. At this location, the axial resolution is a measure of pulse length, $\tau = m/f_0$ cycles of the fundamental (f_0). For the double fundamental frequency case, the axial resolution is half that of the fundamental, $\tau/2 = m/2f_0$. At the second harmonic, the envelope of the pulse remains the same as that of the fundamental or $\tau = 2m/2f_0$. This effect can be seen indirectly in Figure 12.13, in which a highly distorted pulse has the same pulse length as the linear pulse. Examples of fundamental and second harmonic simulated pulses for medical imaging with similar envelopes can be found in Averkiou (2000).

A more direct measure of harmonic axial resolution was made by Ward *et al.* (1997) when they measured harmonic-rich echoes from a wire target with a broadband hydrophone. Their results in Figure 12.18 indicate a second harmonic pulse length approximately the same length as the fundamental with the higher harmonics slightly shorter, perhaps because of absorption.

From previous discussions in Section 7.5.2, spatial resolution can be quantified in terms of detail resolution, corresponding to a −6-dB beamwidth and contrast resolution that corresponds to the −40-dB beamwidth. Detail resolution is a measure of how well small objects are resolved. Contrast resolution is a measure of how well subtle differences in tissue can be distinguished, as well as of the overall range of amplitude reflectivities that are possible to see.

TABLE 12.1 Comparison of Parameters for Fundamental, Twice Fundamental (Linear), and Second Harmonic Modes (m = number of cycles, and L = physical aperture)

Mode	$\mathbf{f_0}$	$\mathbf{2f_0}$	$\mathbf{f_{2H}}$
Parameter			
Axial resolution	m/f_0	$m/2f_0$	m/f_0
Azimuth FWHM	W_0	$W_0/2$	$W_0/\sqrt{2}$
−40-dB beamwidth	W_{40}	$W_{40}/2$	$W_{402H} \ll W_{40}$
Sidelobe level	SL_0	SL_0	$SL_{2H} \ll SL_0$
Focusing gain	G_0	$2G_0$	Variable
Depth of field	DOF_0	$DOF_0/2$	Variable
Grating lobe level	GL_0	$GL_0/4$	~ 0

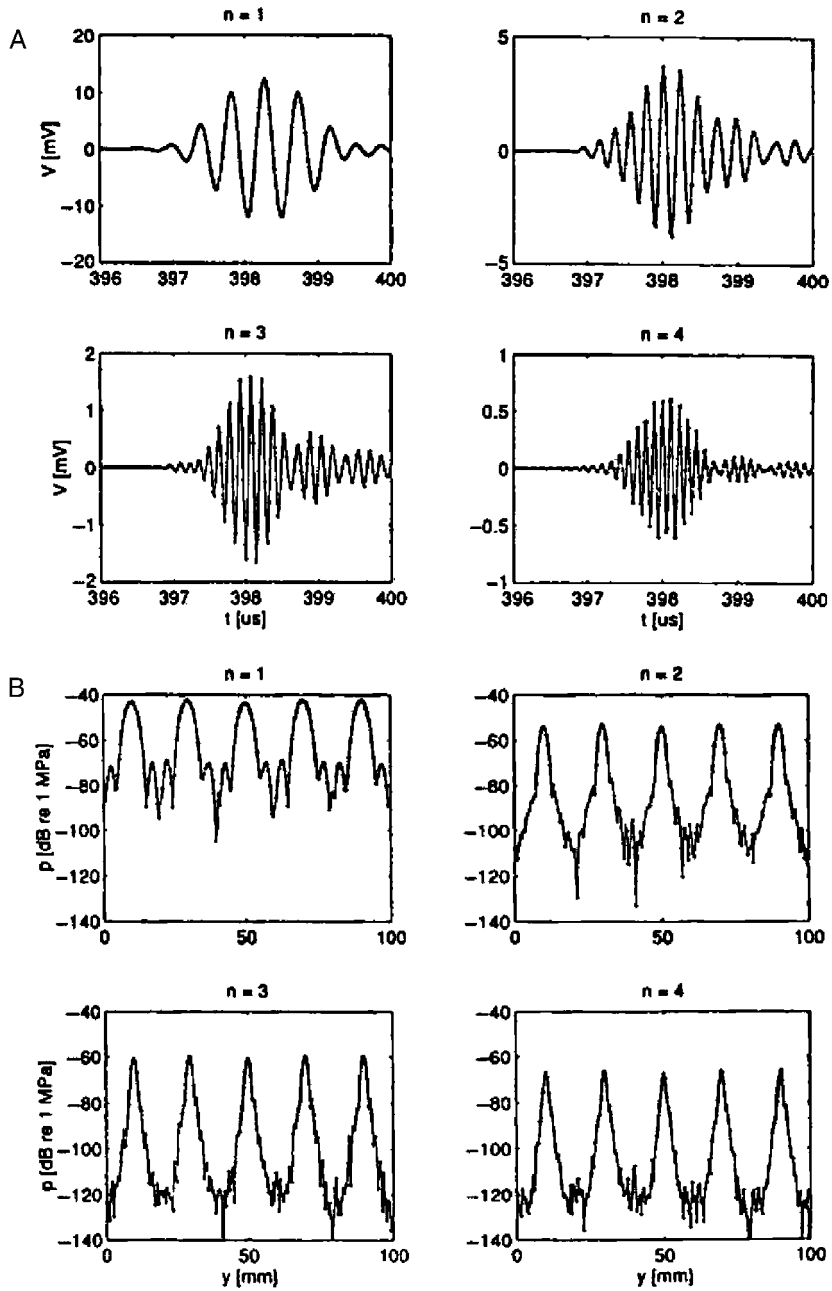

Figure 12.18 Relected pulse echoes (A) and beam profiles (B) from a row of wire targets in water as measured by a hydrophone and a source pressure of 400 kPa. The echoes were bandpass filtered to obtain the fundamental ($n = 1$) and harmonics up to the fourth ($n = 4$) components of the signals (from Ward *et al.*, 1997, Acoustical Society of America).

For the spatial resolution in the focal plane, if the −6-dB fundamental one-way beamwidth, w_0 = FWHM, then at $2f_0$, it is $w_0/2$; at the second harmonic, f_{2H}, it is $w_0/\sqrt{2}$ (as apparent from Figures 12.15 and 12.18).

What is more remarkable is the contrast resolution of harmonic beams, which is at the −40-dB beamwidth level. For the case depicted in Figure 12.15, this corresponds to a fundamental −40-dB half beamwidth of $x = 52.5$ mm compared to a half beamwidth of only 7 mm for the harmonic. As discussed in Section 7.5.2 and Chapter 9, the transmitted beam has opportunities not only to interact with strong scatterers anywhere in its beam pattern, but also to integrate the cumulative volume under its sidelobes in the case of diffusive tissue scattering. For the array operating at $2f_0$, with proper $\lambda/2$ spacing, the corresponding half beamwidth is still half of that at the fundamental or, in this case, about 26 mm. Since transmit beams are shown in Figure 12.15 (the −20-dB beamwidth is also of interest), they are about 6 mm for f_0, 2.4 mm for the second harmonic and 3 mm for $2f_0$.

Finally, for receive beamforming, the backscattered echoes are usually considered to be low enough in amplitude to propagate linearly (Li and Zagzebski, 2000); however, the second harmonic and $2f_0$ beams, being at the same frequency, are similar and narrower than the fundamental beam at f_0.

12.5.3 Focusing

While resolution is an aspect of focusing, a somewhat better picture of the overall effects of focusing can be depicted in a contour plot of a field from a focusing array in the azimuth plane (such as in Figure 12.19). While these are contours for a focused transducer in an attenuating tissuelike medium, the one-way general characteristics hold for rectangular arrays as well. Here simulations are for a rectangular array radiating into a lossy medium with 0.3 dB/MHz^2-cm. There is excellent correspondence between the contour features of the f_0 and $2f_0$, as expected from the focal scaling law of Chapter 6. According to Eq. (6.34), the higher-frequency beam focuses more deeply—approximately 56 and 72 mm for the peak values, not accounting for losses (also see Figure 12.14). The aperture at twice the fundamental frequency has twice the number of wavelengths so that the focal range and depth of field is compressed into a shorter physical distance. While the resolution of the $2f_0$ beam is roughly half in the focal region and the focal gain is double that of the fundamental beam, the beamwidth in the near Fresnel zone close to the aperture is similarly wide. A consequence of the shorter depth of field and increased absorption at higher frequencies is a much shorter penetration depth for the $2f_0$ beam.

By comparison, for the harmonic beam, resolution in the focal region is nearly as good as it is in the $2f_0$ beam, but in the near Fresnel zone, it differs. Close to the aperture, where the harmonics have not had sufficient distance to build up, there is a dead zone, and beyond it is a weak field and a sudden rapid buildup to the focal region. The harmonic focal region starts slightly deeper than that of the fundamental and maintains good resolution over greater axial range than the the $2f_0$ beam. This combination of characteristics (an insensitivity in the near Fresnel zone and high resolution over an extended depth of field) is fortuitous for THI. Finally, note that

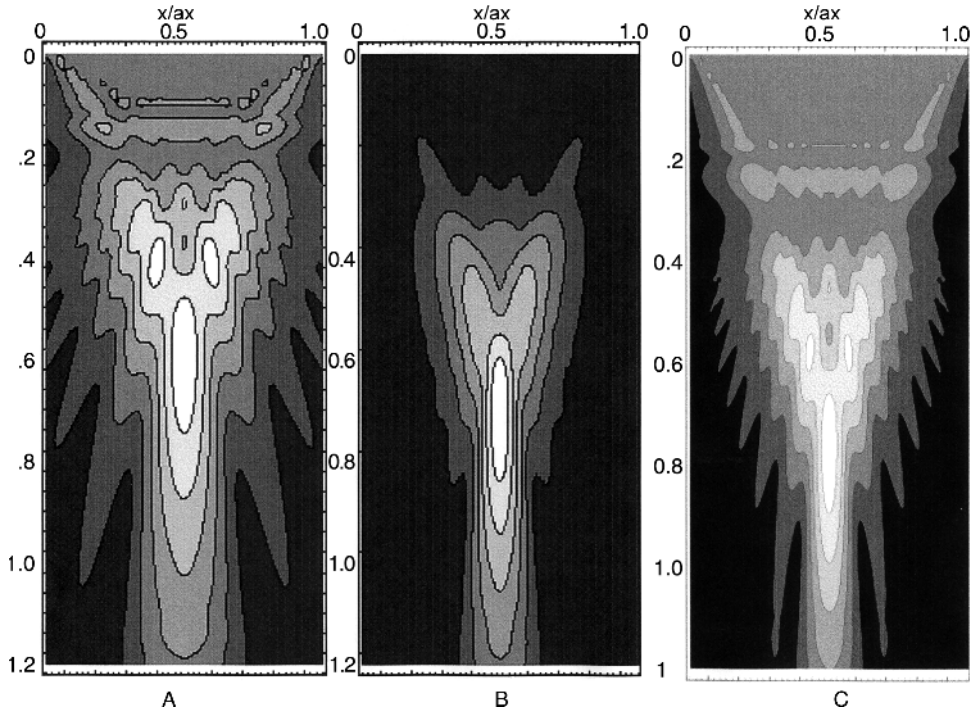

Figure 12.19 Azimuth plane contour beam plots for (A) fundamental, (B) second harmonic, and (C) twice the fundamental (linear) of a 2-MHz pulsed rectangular phased array P4-2 radiating into a simulated tissue medium. The aperture (a_x), is 10.8 mm, the focal distance (F) is 100 mm, and $z_r = z/F$ is the vertical axis. The six contour levels represent zero to maximum (white) on a linear scale (adapted from Averkiou, 2000, *IEEE* and courtesy of M.A. Averkiou).

any set of harmonic beam profiles is dependent on amplitude, so there is a family or sets of profiles for an aperture.

12.5.4 Natural Apodization

Because harmonic generation is strongest along the beam axis, pressure amplitude away from the main axis in a transverse direction falls off at a greater rate than the linear case. As evident in Figure 12.15, not only is the main lobe narrower, but also the sidelobes decrease in an enhanced way over the linear fundamental case. Under linear conditions, this type of apodization would come at the expense of a wider beam in the focal plane, as well as a decreased on-axis amplitude or focal gain. Recall from Section 7.4.2 that to decrease sidelobes under linear conditions, the source aperture is amplitude tapered toward its ends, which decreases aperture area and, consequently, focal gain. With harmonics, the full untapered aperture can be used to achieve apodization without the disadvantages that occur under linear conditions. If apodization is employed with harmonics, the beam sidelobes fall even more rapidly than the linear case.

For the two linear cases at f_0 and $2f_0$ with no original apodization at the aperture, the sidelobes fall at the same rate ($\sim 1/x$). An explanation of why the harmonic sidelobes fall much faster (as demonstrated by Figure 12.15) is that as the beam evolves into a main lobe, the center has the strongest amplitude and greatest potential to generate harmonics. The sides of the main lobe are lower in amplitude and generate less harmonics. This relationship is expressed by the nonlinearity parameter (σ), which is proportional to amplitude according to Eq. (12.4c). Recall that nonlinear beams continually recreate themselves as they propagate, so the effect of diminishing amplitudes on the sides of the beam is cumulative.

During imaging, strong off-axis scatterers, as well as large soft scatterers that extend over a significant sidelobe region, can be mapped onto an image line. This strong concentration of energy in a harmonic beam provides a high selectivity against off-axis scattering. In the case of intercostal imaging, both the narrow beamwidth and dead zone properties of the harmonic beam minimize the pressure amplitudes reaching the ribs and scattering back toward the transducer.

In this kind of situation, the part of the beam controlled by the elevation aperture and focusing is often overlooked. Because of its fixed focal length, the beam in the elevation plane can be wide in a region in which the elevation and azimuth focal lengths are no longer coincident. For the harmonic beam, the steeper falloff of pressure, especially at larger distances from the beam axis, significantly reduces the sidelobe volume in which unwanted targets can lie and be mapped into the image.

Fedewa *et al*. (2001) compared the spatial coherence of beams at harmonic and fundamental frequencies by measuring backscatter from a tissue-mimicking phantom. They found that while fundamental frequency data corresponded to the autocorrelation function of the transmit aperture in accordance with the van Cittert–Zernike theorem (discussed in Section 8.4.5), the spatial coherence of the harmonic was lower. To determine the effective apodization at these two frequencies, beams filtered at these frequencies were measured in the focal plane and linearly back-propagated to the aperture using the angular spectrum of waves. The known apodization was recovered at the fundamental, and its autocorrelation function matched the spatial coherence data at this frequency. As discussed earlier, the same physical aperture operating linearly at twice the fundamental frequency results in a similarly shaped beam, but it is narrower by a scale factor of one half. By back propagation at the same frequency, the effective second harmonic apodization was found to be narrower than the full aperture, and similar processing brought agreement with the harmonic spatial coherence data. Under linear conditions, apodization results in a wider focal plane beam. In this case, the narrower effective second harmonic apodization corresponds to a harmonic beamwidth that is $1/\sqrt{n}$ of that at the fundamental but wider than the beamwidth expected at twice the fundamental ($2f_0$) under linear conditions.

12.5.5 Body Wall Effects

Heterogenities in the body wall cause multiple reverberations (as discussed in Chapter 9). These low-level echoes become clutter and haze (or acoustic noise) in

an image. Because of their low amplitude and lack of coherence, they do not generate significant harmonics. Since their spectral content remains within the fundamental pass band, the reverberation echoes can be removed effectively by second harmonic bandpass filtering.

Aberration is a deformation of an ideal focusing wavefront caused by propagation variations in path lengths from different parts of the aperture to the focal point. Several factors contribute to these time delay differences along various path lengths: nonuniformly thick tissue layers of different sound speeds and scattering from and through heterogeneous structures. Focusing designs for imaging systems are based on the assumption of a homogeneous medium with a constant speed of sound of 1.54 mm/μs.

For propagation through multiple heterogeneous body wall layers, the focusing wavefront continues to deviate from the ideal as it propagates. Adjacent element paths with slightly different average sound speeds undergo a phase change that is proportional to frequency,

$$\phi_{ERROR} = 2\pi f \Delta r \left(\frac{1}{c_0 + \Delta c} - \frac{1}{c_0} \right) \approx - \frac{2\pi f \Delta r}{c_0} \frac{\Delta c}{c_0} \tag{12.8}$$

where the path difference is Δr and the difference in sound speeds is Δc. This relation indicates that for the same tissue structure, the phase error will increase with frequency. Returning to our comparison, we conclude that aberration should be worse for $2f_0$ compared to the fundamental. For the second harmonic, a curious phenomenon occurs. As the wavefront propagates through the body wall, it starts with the phase error of the fundamental because the harmonic has not had sufficient distance to grow yet; consequently, one would expect the harmonic beam to be better than the $2f_0$ beam.

Christopher (1997) used the University of Rochester body wall data (described in Chapter 9) to run simulations of the effects of aberration on fundamental frequency and second harmonic beams. The data were translated into phase screens with jitter to simulate the aberration. He compared fundamental frequency (f_0) beams, second harmonic beams, and double fundamental frequency ($2f_0$) beams. He found that they all suffered a loss in absolute main lobe sensitivity and that the sidelobe levels of the second harmonic were significantly lower. On receive beamforming, the second harmonic and $2f_0$ beams suffer the same aberration effects (worse than that from the f_0 beam).

Wojcik *et al*. (1998) also ran nonlinear simulations with the same data; however, their finite difference approach allowed the inclusion of realistic structural detail and reflections. Their baseline simulation in Figure 12.20 is for the piecewise continuous succession of homogeneous flat layers. Since the sound speeds in these materials are similar, the overall beam-shapes are only slightly altered from what would be expected for one continuous homogeneous tissue. The beams are similar in shape to those of Figure 12.19, except for the standing waves in the first two layers apparent in the axial plots. The second simulation (Figure 12.21), also for a focal length of 5 cm, includes marbling and irregular interfaces. In this sequence, the strong reverberations near the entrance of the beam are missing from the second harmonic beam. In addition, the

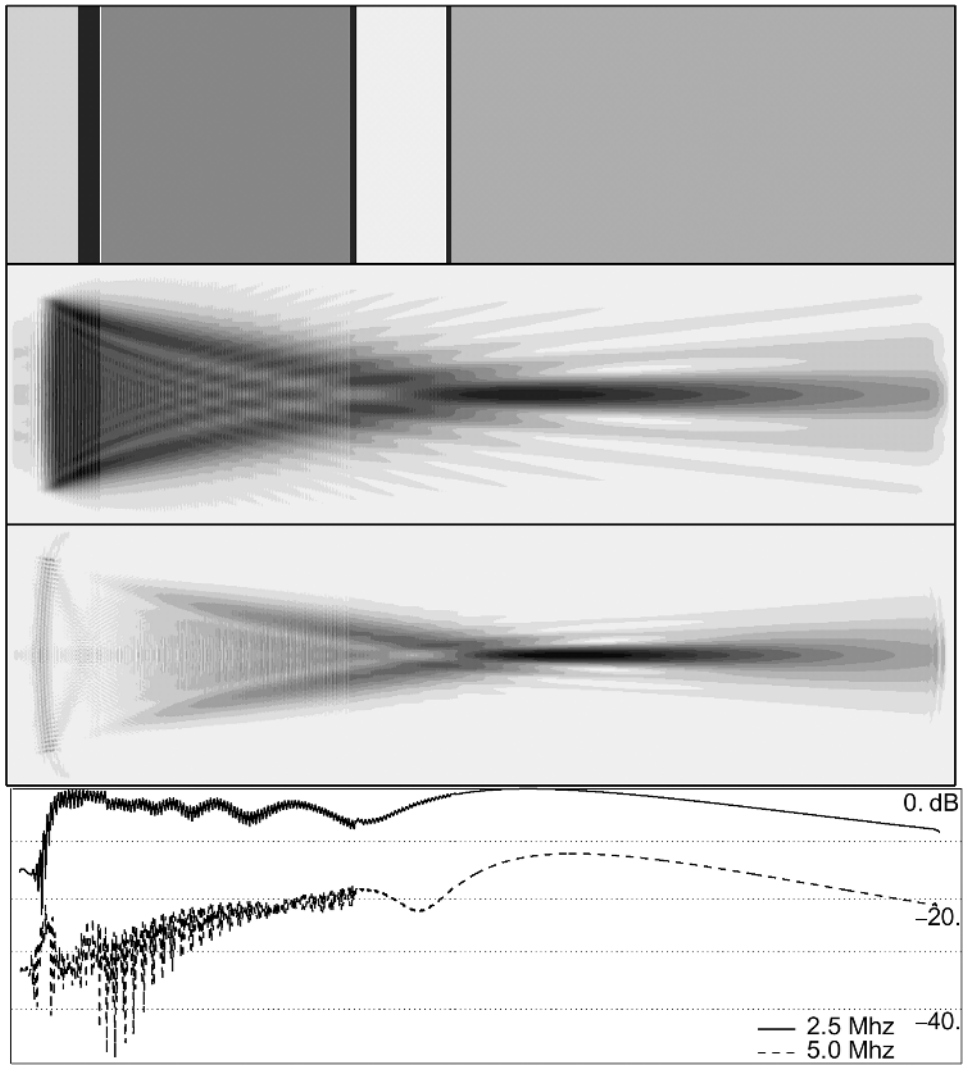

Figure 12.20 (Top panel) Acoustic propagation through an idealized piecewise continuous homogeneous abdominal wall section. Color coding for layers from left to right is water, fat, muscle, and liver, with black representing connective tissue. Size is 1.5 cm × 5 cm. Spectral amplitude distributions rate for the 2.5-MHz fundamental (second panel from top) and 5-MHz second harmonic (third panel from top) as well as along the beam axis (bottom panel) for a 1.5-cm aperture with a 5-cm focal length. The scale on the middle two figures is 2 cm (vertical) × 8 cm (horizontal) (from Wojcik *et al.*, 1998, *IEEE*).

second harmonic main lobe remains more tightly focused to a deeper depth than the fundamental. In another wall sample with more marbling in the muscle layer, MS3 (shown in Figure 12.22), the harmonic beam offers a more modest improvement. For this case, as the focal length is changed from 5 to 10 cm, the harmonic and fundamental beams both fail to focus. This result makes sense even under linear

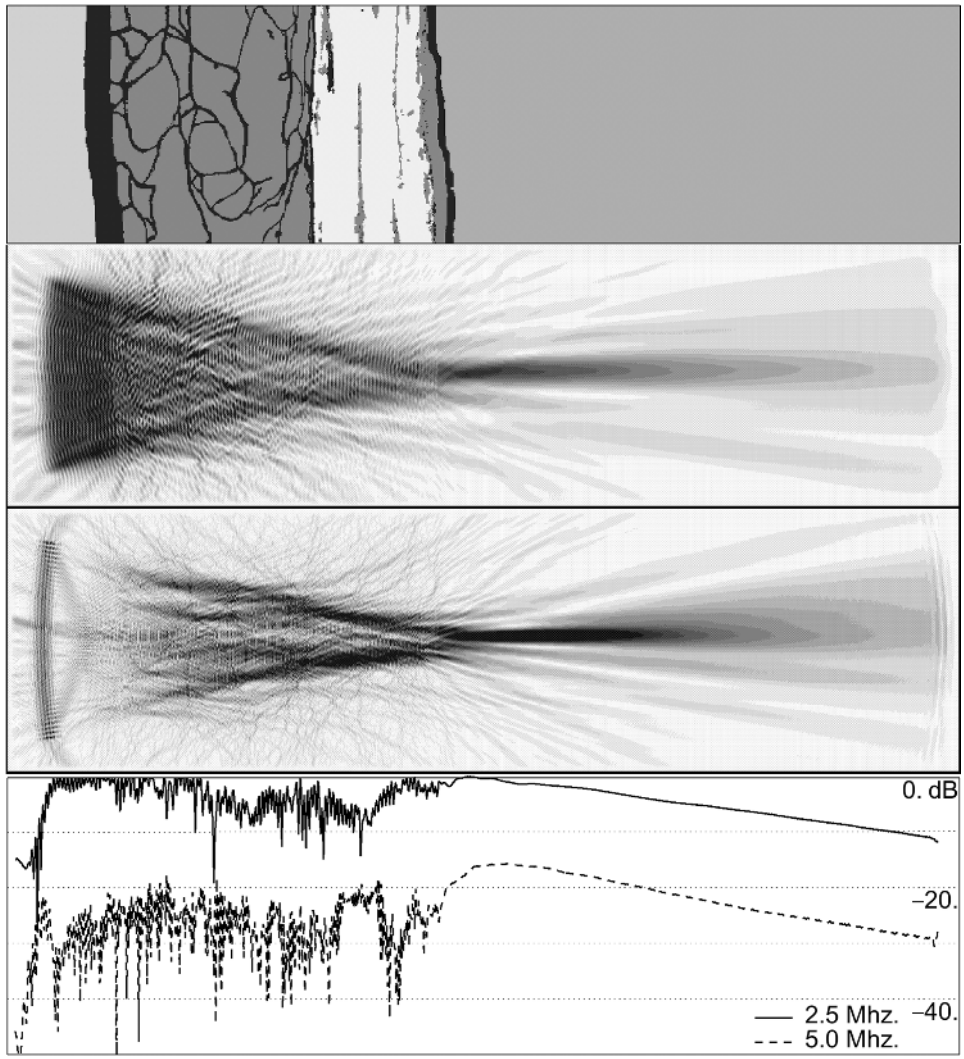

Figure 12.21 (Top panel) Acoustic propagation through abdominal wall section MS2. Color coding for layers from left to right is water, fat, muscle, and liver, with black representing connective tissue. Size is 1.5 × 5 cm. Spectral amplitude distributions are for the 2.5-MHz fundamental (second panel from top) and 5-MHz second harmonic (third panel from top), as well as along the beam axis (bottom panel) for a 1.5-cm aperture with a 5-cm focal length. The scale on the middle two figures is 2 cm (vertical) × 8 cm (horizontal) (from Wojcik *et al*., 1998, *IEEE*).

conditions because the ideal delay curve for a deeper focus is flatter and more susceptible to disruption by even small time delay errors. Studies of harmonic aberration correction by Christopher (1997) and Liu *et al*. (2001) have verified that the harmonic beam is more robust with aberration and can be further improved by correction methods.

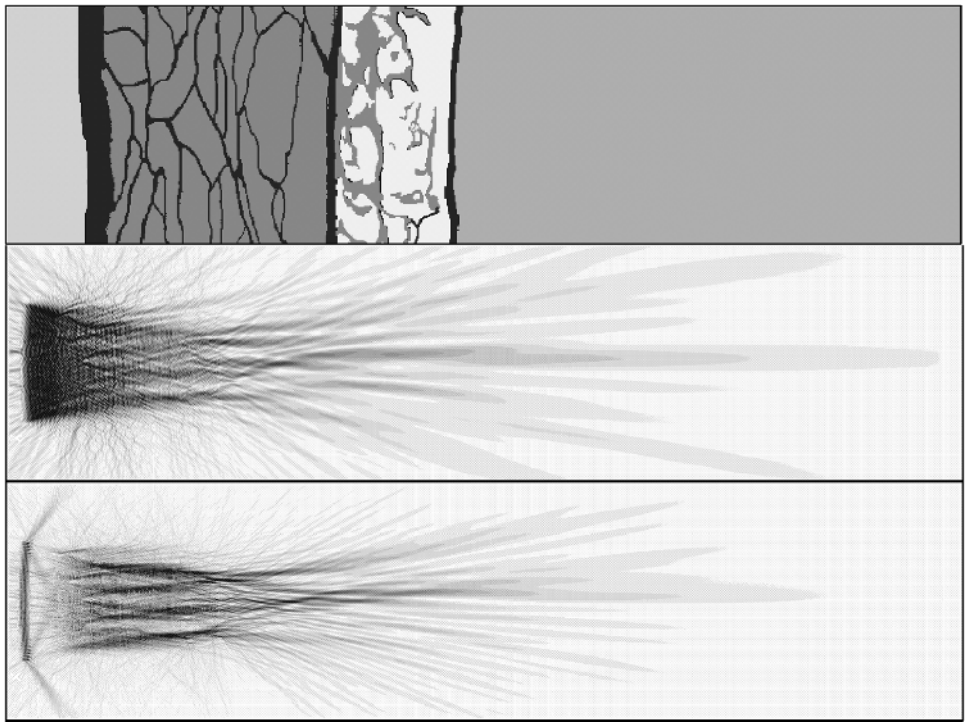

Figure 12.22 (Top panel) Acoustic propagation through abdominal wall section MS3. Color coding for layers from left to right is water, fat, muscle, and liver, with black representing connective tissue. Size is 2×10 cm. Spectral amplitude distributions are for the 2.5-MHz fundamental (second panel) and 5 MHz second harmonic (third panel) for a 2-cm aperture with a 10-cm focal length. The scale on the bottom two figures is 4 cm (vertical)×16 cm (horizontal) (from Wojcik *et al.*, 1998, *IEEE*).

12.5.6 Absorption Effects

Absorption effects are closely related to beamforming under nonlinear conditions. Aside from the fundamental to second harmonic conversion efficiency that is dependent on source amplitude level, the rate at which harmonic beams decay may be less than a comparable fundamental frequency beam propagating linearly at the same frequency. Figures 12.20–12.22 include absorption loss. From Figure 12.22, the deeper focal region of the second harmonic has not only a sharper focus, but also a comparable axial amplitude in the focal region relative to the fundamental despite its higher frequency. A major contributor to this high harmonic amplitude is the continual interplay between beam formation, harmonic buildup and replenishment, and absorption. The total apparent absorption for the second harmonic beam is less than expected for a beam at twice the frequency ($2f_0$) because the preconverted amplitude gets a ''free ride'' part of the way. Perhaps it is not exactly a free ride, but consider that the preconverted amplitudes are attenuated at the lower fundamental frequency rate

for a portion of its propagation path, whereas a fundamental beam at $2f_0$ is absorbed at a higher rate along all of its path.

Of course, if the absorption is much stronger than the second harmonic replenishment with distance, it will eventually reduce penetration. In their study of harmonic imaging at higher frequencies, 20 MHz fundamental, Cherin *et al*. (2000) found that some of the benefits of harmonic imaging were offset by the greater absorption at these frequencies.

12.5.7 Harmonic Pulse Echo

While the previous discussion has concentrated on transmit nonlinear phenomena, imaging involves scattering and the return paths of the echoes. Some of the first pulse-echo studies at harmonic frequencies were done with high-frequency acoustic microscopes (Kompfner and Lemons, 1976; Germain and Cheeke, 1988.) Scattering in a nonlinear medium has been studied for beams obliquely reflected from a flat or curved boundary (Landsberger and Hamilton, 2000; Makin *et al*., 2000), and good agreement with theory has been obtained. For phantom imaging, an approach involving the nonlinear KZK equation on transmit and linear scattering from point targets has proved useful for simulation (Li and Zagzebski, 2000). Controlled comparisons of fundamental and harmonic imaging (van Wijk and Thijssen, 2002) indicated improved tissue-to-clutter ratios for the harmonics, as well as large differences among other criteria that were possibly caused by different implementations of harmonics on imaging systems by manufacturers. Other than the images themselves, limited experimental data on clinical style echoes is available. An exception is the high-frequency harmonic study of Cherin *et al*. (2000), in which a fundamental frequency of 20 MHz was used. Pulse-echo second harmonic beam cross sections reflected from a point target were measured and were found to be similar to those at $2f_0$; their similarity may in part be caused by the strong absorption effects at this frequency, which were also noticeable in images of mice presented in the study.

The clinical value of THI is indisputable, as demonstrated by a growing number of studies in the literature (Spencer *et al*., 1998); however, under some circumstances, fundamental imaging will perform better. For example, harmonic imaging may offer no added diagnostic information in some higher-frequency imaging situations or for normally easy-to-image patients. More work needs to be done to determine the benefits and limitations of harmonic imaging. In recognition of this trade-off, some imaging system manufacturers can blend fundamental and harmonic images to improve image quality and to reduce speckle.

The emphasis on transmit harmonic beam characteristics in this chapter can be justified by the fact that it ultimately limits the resolution attainable. Under linear conditions this is the case because dynamic receive focusing is applied uniformly at each depth in the image and overall resolution is roughly the product of the transmit and receive beam profile at each depth. Despite the lack of information about harmonic scattering from tissues, one would expect that dynamic receive focusing provides similar imaging benefits at the harmonic.

One of the striking characteristics of harmonic imaging is its improved contrast compared to an image at the fundamental. The usual explanations offered are improved contrast resolution and reduced clutter or better acoustic signal-to-noise in the image. Reverberations and multiple scatterings are mainly incoherent and follow the main reflected signals back to the transducer on receive to create high clutter levels. These trailing spurious signals are small in amplitude, do not generate harmonics, and are filtered out at the second harmonic frequency. In addition, the high selectivity of harmonic beams avoids possible detrimental reflectors such as ribs and cartilage.

There may be another reason for the observed enhanced contrast seen in harmonic images. The second harmonic generation process depends on the square of the fundamental pressure (as indicated by Figure 12.1); therefore, for a given increase in input pressure, the second harmonic will give a disproportionally larger relative amplitude compared to a strictly proportional linear response. This effect is exaggerated in the nonlinear case as input amplitude is increased. In Chapter 10, a process was described by which the detected image signals can undergo a nonlinear post processing mapping procedure to emphasize or deemphasize strong or weak echo amplitudes, according to the particular curve selected by the user. A similar mapping of gray levels from the original range in a stored image or negative to the output media or final image is commonly used in photography. The acoustic nonlinear generation process is a relationship that can be regarded as an imaging preprocessor characteristic that for a given change in input pressure level, provides a larger relative second harmonic pressure change (enhanced contrast) than that obtained under linear circumstances.

Little work has been done on scattering from real tissue structures under nonlinear conditions. Early attempts at harmonic imaging, then called B/A imaging, provided some interesting preliminary results even though this research methodology was too awkward to be implemented commercially, as summarized by Duck (2002). Typically, a high-power pumping signal and an imaging probe were required. Extensive measurements of B/A from eq. (12.5a) have been made of healthy and diseased tissue (Law *et al*., 1981, 1985; Yongchen *et al*., 1986; Duck, 1990; Zhang and Dunn, 1991; Everbach, 1997; Labat *et al*., 2000). Zhang *et al*. (1991) provided intriguing data that indicate if the chemical composition of tissue is unchanged but its structure is changed, or if the B/A of the tissue has a structural dependency.

12.6 HARMONIC SIGNAL PROCESSING

Harmonic imaging imposes extra requirements on an imaging system. Because harmonics may be 20–30 dB or lower than a fundamental signal, a system must have a large dynamic range. Penetration is even more dependent on electronic signal-to-noise ratios at these high frequencies. Several signal processing methods have been devised to improve sensitivity and to remove the desired harmonic information selectively.

Figure 12.23 shows the basic principle of extracting harmonic information from the receive echoes by filtering. An important aspect of this filtering process is enough transducer bandwidth to recover the harmonic signal bandwidth with adequate

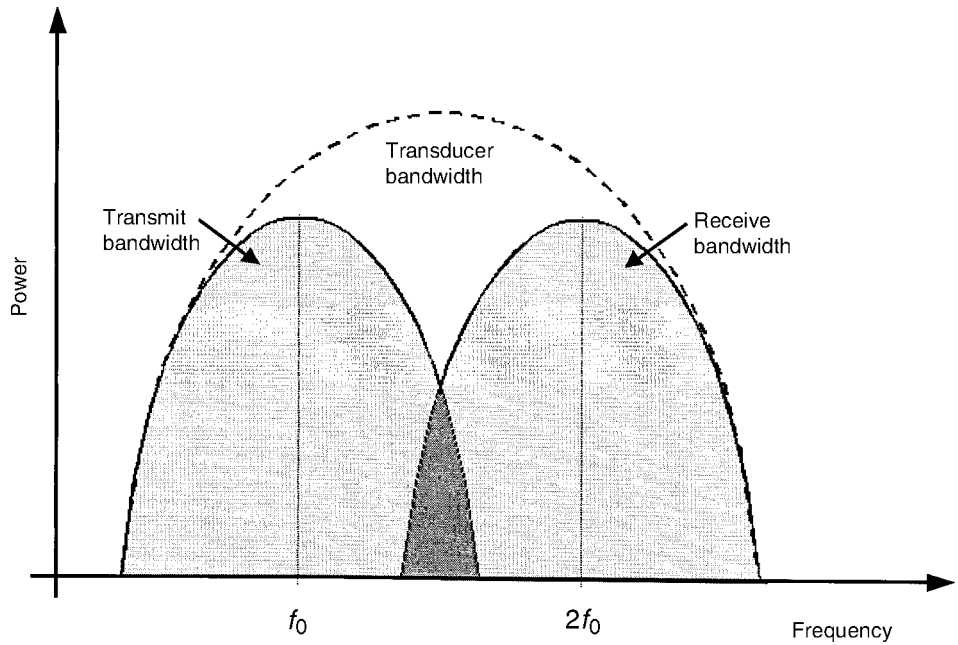

Figure 12.23 Spectral overlap of transmit and receive passbands (solid regions) and second harmonic signal (dashed curve) within transducer bandwidth. Overlap region highlighted in black with unwanted transmitted signal in harmonic band (adapted from Frinking *et al.,* 2000, reprinted with permission from the world Federation of Ultrasound in Medicine and Biology).

sensitivity and minimal distortion. The usual method is to filter out only a band of frequencies centered at the harmonic frequency (Muir, 1980). In the case of harmonic imaging of contrast agents, filtering can occur at subharmonics of the transmitted frequency, as discussed in Chapter 14 (Shi and Forsberg, 2000).

Transmission control of fundamental signals is more critical for harmonic imaging. If the transmitted spectra overlaps the receive bandwidth (as indicated in Figure 12.23), a kind of harmonic acoustic noise is created that can interfere with the pure harmonic echoes (as illustrated in Figure 12.24). The most straightforward way of dealing with this problem is to transmit longer pulses to narrow the transmit spectrum and reduce the overlap, but axial resolution suffers as a consequence. Reduction of transmission into the harmonic region implies extremely good transmitter control, otherwise even small transmitted harmonics comparable in magnitude to weak harmonic echoes can swamp, interfere with, or distort tissue-generated harmonics and beams. This effect is illustrated by an imperfect transmitted signal in which unwanted harmonic content is more than 25 dB below the peak at the fundamental frequency in Figure 12.24. In terms of the mixer analogy, unwanted frequencies in the source pulse enter the nonlinear generation process and become scrambled so that expected harmonic levels that depend on coherence are not obtained. In other words, a kind of harmonic noise is created that is unrelated to the echoes at the desired harmonic frequencies.

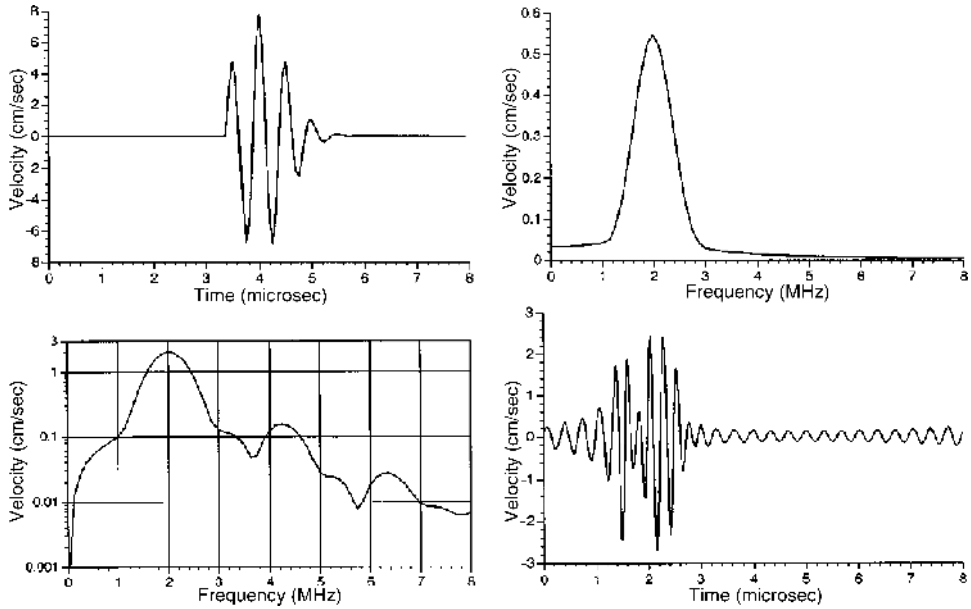

Figure 12.24 (Top left) An imperfect 2-MHz on-axis source particle velocity waveform. (Top right) Corresponding source spectrum. (Bottom left) Spectrum at focal plane with significant transmit overlap past 3 MHz. (Bottom right) Pulse reconstructed from frequencies from 3 to 8 MHz from the focal spectrum (from Christopher, 1997, *IEEE*).

For imaging systems that have frequency agility (the capability to transmit and receive on several possible frequencies within the transducer bandwidth) not only on receive but also on transmit, other solutions are possible for eliminating overlap and, consequently, improving harmonic dynamic range. Pulse inversion is a method in which an inverted pulse is sent in the next acoustic vector line in the same direction and is summed as part of the detection process to cancel the linear (fundamental) component of the echoes, as illustrated in Figure 12.25 (Simpson *et al*., 1999; Jiang *et al*., 1998; Bruce *et al*., 2000). Originally developed for Doppler and contrast agents, it has been successfully applied to B-mode imaging (Averkiou, 2000).

Another method for reducing fundamental is called ''power or amplitude modulation,'' in which fundamental signals at a low amplitude and at a normal high amplitude are transmitted on sequential lines in the same direction. The lower signal, mainly linear and centered at the fundamental, is amplified to the level of and subtracted from the harmonic signal (Brock-Fisher *et al*., 1996; Christopher, 1997; Jiang *et al*., 1998; Averkiou, 2000) to extract the harmonic content (as illustrated by Figure 12.26). Note that the standard pulse inversion process emphasizes even harmonics and cancels odd ones (including the fundamental), whereas the amplitude modulation deemphasizes the fundamental and keeps higher harmonics. Both these methods have the drawbacks of reducing frame rate by a factor of two and of sometimes failing to keep up with fast moving tissue movements. Methods have been developed (Bruce *et al*., 2000) to solve these limits.

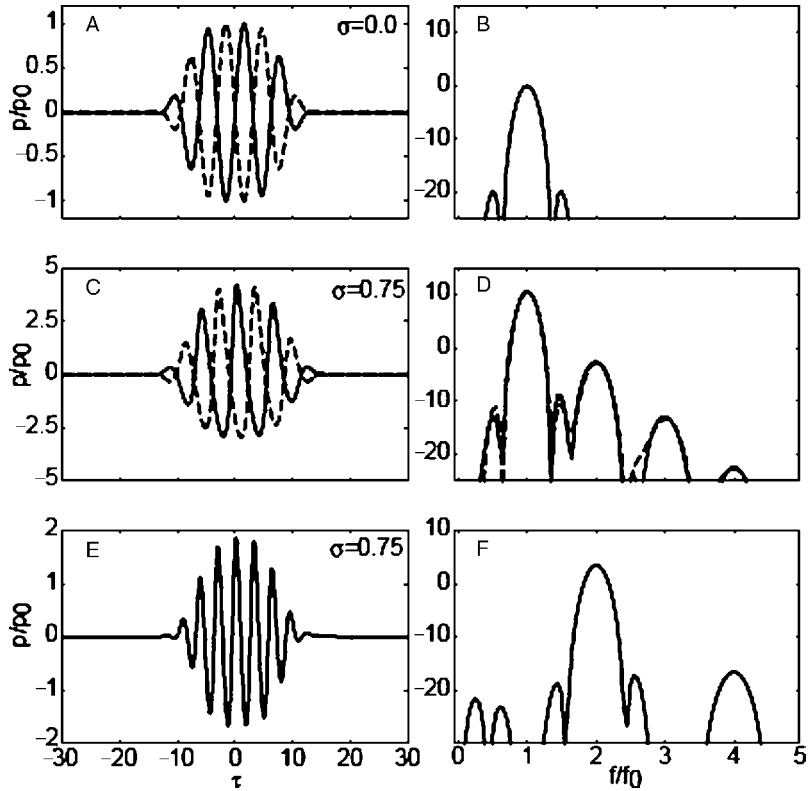

Figure 12.25 Principles of pulse inversion. Here $\sigma = z/F$. Principles of pulse inversion: (A) positive (solid line) and inverted (dashed line) pulses at source; (B) spectral magnitudes in dB of pulses in (A); (C) positive and negative pulses after nonlinear propagation in water to a depth of ¾ of the focal length; (D) spectra of pulses in (C); (E) sum of pulses in (C); (F) spectrum of sum in (E) (from Averkiou, 2000, *IEEE*).

Other approaches for harmonic reduction have also been reported, including one using the fact that higher-order harmonics regenerate other harmonics and the fundamental frequency, as evident from the mixer model (Haider and Chiao, 1999). Related methods include distorting (Christopher, 1999) or encoding the fundamental and applying signal processing to remove the harmonic (Takeuchi, 1996; Kim *et al*., 2001).

12.7 OTHER NONLINEAR EFFECTS

In a nonlinear medium, acoustic waves experience two other effects: radiation force and acoustic streaming (Beyer, 1997; Nyborg, 1998). A progressive sound wave creates a small force that travels along the beam. As will be described in Chapter 13, if an absorbing target is placed in the path of the beam, it will be displaced. This target movement is proportional to acoustic intensity and is a way of measuring

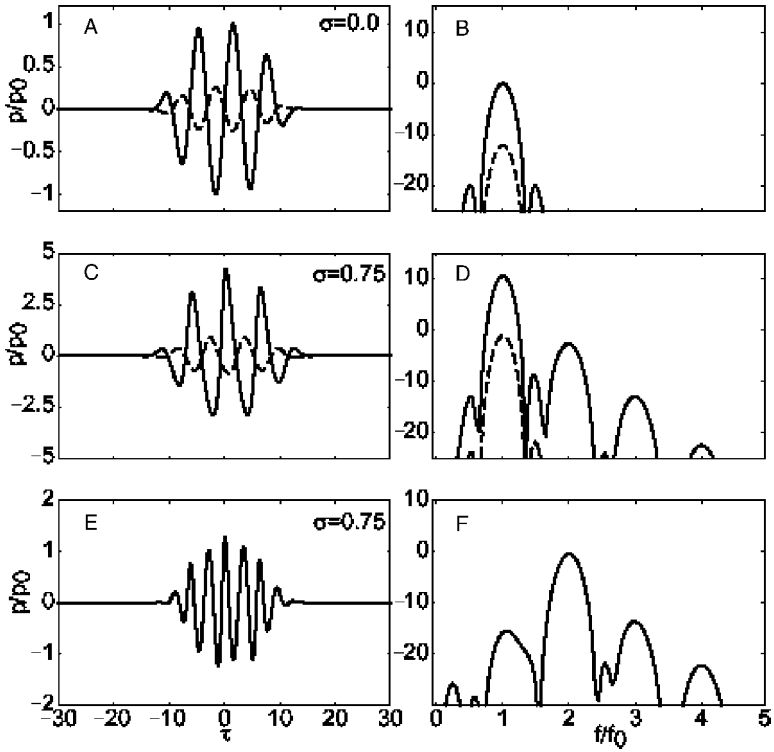

Figure 12.26 Principles of power or amplitude modification imaging: (A) dashed line, pulse ¼ the amplitude of other pulse (solid line); (B) spectral magnitudes in dB of pulses in (A); (C) pulses after nonlinear propagation in water to $\sigma = z/F = 3/4$; (D) spectra of pulses in (C); (E) sum of pulses in (C) with smaller pulse multiplied by 4; (F) spectrum of sum in (E) (from Averkiou, 2000, *IEEE*).

acoustic power with a device called a force balance. The pressure gradient of an acoustic beam pushes away the fluid and causes acoustic streaming. A measurement of acoustic streaming in a water glycerine solution is presented in Figure 12.27.

The radiation force (F) is simply related to the time-averaged intensity in the beam integrated over the surface area (S) of a target,

$$F = \int I_i dS/c_0 = \int (p_0^2/2\rho_0 c_0^2) dS = W/c_0 \tag{12.8}$$

where W is time-averaged acoustic power. This Langevin radiation pressure (times area) is a constant that does not vary with time fluctuations of the beam, but its time-averaged value is proportional nonlinearly to the square of the pressure amplitude. This type of pressure is defined as the difference between the mean pressure at an absorbing (or reflecting) wall and the pressure immediately behind the wall. For a typical diagnostic acoustic beam of 100 mw/cm^2, the force is on the order of 7 μg, so a sensitive microbalance is needed to measure it. The actual force depends on the interface and the angle of the beam to it (Duck, 1998).

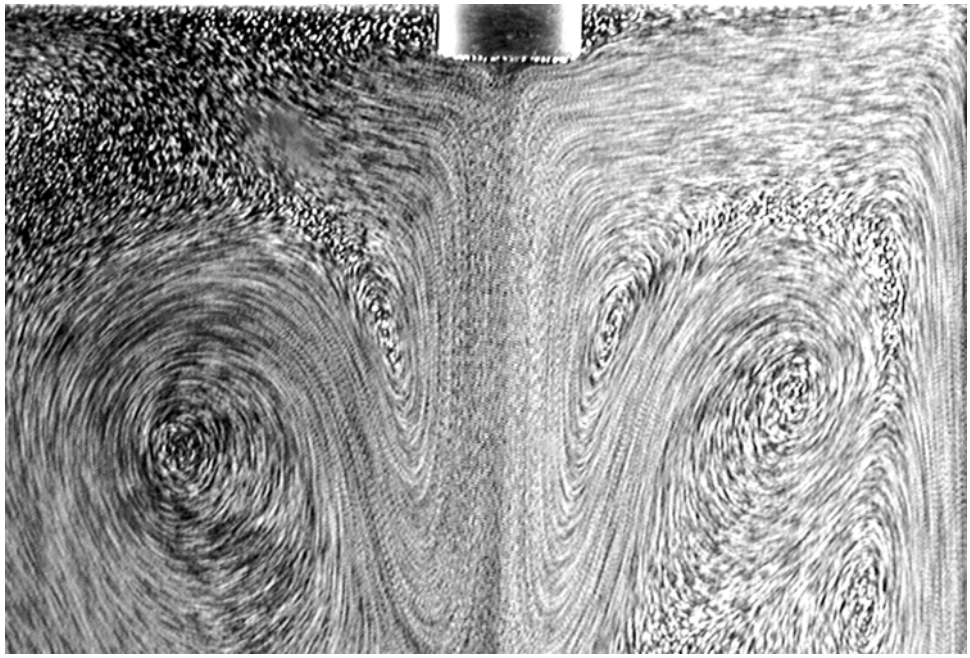

Figure 12.27 Visualization of acoustic streaming from a plane piston transducer radiating into a water gylcerine solution, as measured by the 32-MHz pulsed Doppler method (from Nowicki *et al.*, 1998, reprinted with permission from Excerpta Medica, Inc.).

In the free field of a beam, the pressure has a complicated pattern that can be thought of as consisting of pressure gradients. If the medium is lossy, then absorption is a mechanism by which some of the pressure is converted to heat. For a tissue with an absorption α, the heat generated at a time-averaged rate per unit volume is given locally by q_v,

$$q_v = 2\alpha I_i(t, r) \tag{12.9}$$

based on the assumption that the pressure and particle velocity are in phase. The value for the time-averaged intensity (I_i) is often based on the focused field of the transducer. For a focused beam, the heating is maximum near the focal point, and elsewhere, the extent and magnitude of the heating follows the shape of the focused field. If the medium is nonlinear, then α is enhanced and so is the heating.

Another effect related to the pressure gradients in the beam is acoustic streaming (Starritt *et al.*, 1989; Wu *et al.*, 1998). A free-field radiation pressure, described by Rayleigh for a nonlinear medium, has tensorial or vectorial dependence on the pressure field and its direction, and it is related to the shape of the beam. Acoustic streaming is connected to this radiation pressure gradient, and along the beam axis, the streaming velocity (v) is approximately

$$v(r) = [2\alpha I_i(r)][\rho/(c_0\eta)]\left(d^2G\right) \tag{12.10}$$

where the first term can be recognized as similar to heating in Eq. (12.9), the second term is inversely proportional to viscosity (η), and the third term is dependent on geometric factors of the beam (d), the beam diameter, and a geometric constant (G) (Duck, 1998). Again, α can be considered to be enhanced by nonlinear effects. Also, because of natural apodization caused by the nonlinear medium, the pressure or intensity field itself is modified over the linear case. Finally, streaming affects temperature rises in nonlinear media.

12.8 NONLINEAR WAVE EQUATIONS AND SIMULATION MODELS

Considerable progress has been made in the understanding and modeling of waves in nonlinear media through appropriate wave equations. These wave equations fall into three major types: one-dimensional diffusion (Burgers), three-dimensional parabolic (KZK), and full wave (Westervelt). In general, they can only be solved numerically (the Burgers equation can be solved by a mathematical transform). They are presented in time domain forms, but they are most often solved in the frequency domain.

A key vehicle for describing the essential nature of wave propagation in nonlinear media with simple quadratic power law absorption in one dimension is the Burgers equation for pressure as a function of a retarded time scale (τ) for a fluid medium (Beyer, 1997; Hamilton and Morfey, 1998), as

$$\hat{p}_z - \alpha_0 \hat{p}_{\tau\tau} = \left[\bar{\beta}/\left(c_0^3 \rho_0\right)\right] \hat{p} \hat{p}_\tau \tag{12.11}$$

in which a retarded time (τ) and the abbreviated notation from Section 4.7.3 are convenient. Note that the form can be regarded as an inhomogeneous lossy one-way wave equation with a nonlinear source term on the right-hand side (r.h.s). An exact analytic solution to this equation is possible through a substitution of variables as well as approximate, series solutions (Blackstock, 1966). The sawtooth equation, Eq. (12.4c), is one solution for large Γ (Blackstock *et al.*, 1998). This equation is only appropriate for media with a quadratic frequency power law exponent such as water, which has no sound speed dispersion. Blackstock (1985) suggested that the Burgers equation could be applied to other types of losses by replacing the second term with a loss operator. This equation has been extended to media with a power law loss in the following general form (Szabo, 1993):

$$\hat{p}_z - L'_{\alpha,\, y,\, \tau} *_\tau \hat{p} = \left[\bar{\beta}/\left(c_0^3 \rho_0\right)\right] \hat{p} \hat{p}_\tau \tag{12.12}$$

where the time causal operator ($L'_{\alpha,\, y,\, \tau}$) was described at the end of Chapter 4. This equation includes dispersion necessary to describe losses in tissue and many other media, and it reduces to the Burgers equation for $y = 2$. Haran and Cook (1983) have studied losses in tissues under nonlinear conditions. A more recent contribution, properly accounting for power law dispersion, can be found in Wallace *et al.* (2001). They point out that because of phasing of harmonic components, sound speed dispersion can play a significant role in determining waveform distortion. Methods for frequency domain calculations can be found in Hamilton (1998).

A considerable amount of research on sound beams in nonlinear media was published in the Soviet literature and later consolidated in the book, *Nonlinear Theory of Sound Beams* (Bakhvalov *et al*., 1987). A key development was the Khokhlov-Zablotskaya-Kuznetsov (KZK) (Kuznetsov, 1971) wave equation under the paraxial or Fresnel approximation,

$$\nabla_{\perp}^2 \hat{p} - \frac{2}{c_0}\hat{p}_{z\tau} + (2\alpha_0/c_0)\hat{p}_{\tau\tau\tau} = -\left[\bar{\beta}/\left(c_0^4\rho_0\right)\right]\hat{p}_{\tau\tau}^2 \tag{12.13}$$

where the notation is from Chapter 4. Again, this equation can be considered as a parabolic (one-way) wave equation with the third term describing loss and the r.h.s. being a nonlinear source term. When the r.h.s. is set to zero, the equation applies to linear media with loss. The KZK equation combines nonlinearity, diffraction under the parabolic (Fresnel) approximation, and absorption for a quadratic loss medium (water) in a numerically suitable form.

Programs for the prediction of circularly symmetric beams were developed in the Soviet Union, and many of the figures for the book (Bakhvalov *et al*., 1987) were computations from these programs. A concentration of nonlinear analysis and theory by Naze Tjotta and Tjotta and others in Norway laid the theoretical foundation (Berntsen *et al*., 1984; Naze Tjotta and Tjotta, 1981) for several computer programs, including a numerical implementation of the KZK equation (Aanonsen *et al*., 1984; Hamilton *et al*., 1985; Berntsen and Vefring, 1986; Berntsen, 1990), which is also known as the Bergen code. This finite difference method uses a Fourier series approach to solve the necessary coupled differential equations for harmonics in the frequency domain.

To appreciate the complexity of KZK equation computations, consider that for each individual path length from a point on the aperture to a field point, there is a different amount of distortion. Unlike a direct diffraction computation for a selected plane in a linear lossy medium, a calculation for a nonlinear medium requires that all the intervening beam-shapes must be calculated first so that the required amount of cumulative waveform distortion can develop. At each spatial position, every frequency leads to a sum and difference frequency (somewhat analogous to the mixer model), so that because of the growing number of harmonics generated, KZK programs are computationally intensive. For N total harmonics, computations on the order of N^2 are required for each spatial grid point.

The original formulation of the KZK included frequency-squared loss appropriate for water. A modification of the KZK equation that applies to power law absorbing media and includes dispersion (Szabo, 1993) is

$$\nabla_{\perp}^2 \hat{p} - \frac{2}{c_0}\hat{p}_{z\tau} - L_{\alpha,y,\tau} *_{\tau} \hat{p} = -\left[\bar{\beta}/\left(c_0^4\rho_0\right)\right]\hat{p}_{\tau\tau}^2 \tag{12.14}$$

This equation reduces to Eq. (12.13) for $y = 2$. Absorption can also be included in the frequency domain by changing the Fourier coefficient of the nth harmonic (Watson *et al*., 1990) as a multiplicative propagation factor.

Versions of the frequency domain KZK equation have been extended to pulsed fields using a Fourier series pulse decomposition (Baker, 1991; Baker and Humphrey,

1992; Cahill and Baker, 1998) to focusing (Hart and Hamilton, 1988) and to rectangular geometries (Kamakura *et al*., 1992; Sahin and Baker, 1993; Berg and Naze Tjotta, 1993; Baker *et al*., 1995). If the circularly symmetric case involves M calculations, the rectangular case adds another dimension and increases computation by a factor $M^{4/3}$.

For pulsed fields, a more direct approach is solving the KZK in the time domain. The evolution of this approach, which began with the Soviet work (Bakhvalov *et al*., 1987), continued with Bacon (1984) and developed into a different KZK approach at the University of Texas in Austin (Lee and Hamilton, 1995), with added relaxation effects (Cleveland *et al*., 1996) and focusing for rectangular apertures (Averkiou, 2000). In the time domain, the operators are on the order M; however, many time points are required to capture steep shock fronts (Too and Ginsberg, 1992).

Because of limitations of the KZK approach, one-way propagation, and results trusted for propagation angles of less than 20° (Froysa, 1991), interest in numerical implementations of the full nonlinear wave equation has continued. Westervelt (1963) derived a full wave, nonlinear local wave equation that described cumulative distortion,

$$\nabla^2 p - \frac{1}{c_0^2} p_{tt} + \frac{2\alpha_0}{c_0} p_{ttt} = -\left[\bar{\beta}/\left(c_0^4 \rho_0\right)\right] p_{tt}^2 \tag{12.15}$$

Although the initial relevance for this equation was for parametric arrays, (Westervelt, 1963; Berktay, 1965; Berktay and Al-Temini, 1969), it has more general applicability. A version of this equation for power law media (Szabo, 1993) is

$$\nabla^2 p - \frac{1}{c_0^2} \frac{\partial^2 p}{\partial t^2} - L_{\alpha,y,t} * p = -\left[\bar{\beta}/\left(c_0^4 \rho_0\right)\right] p_{tt}^2 \tag{12.16}$$

where symbols are from Chapter 4. A numerical solution to Eq. (12.15) with thermoviscous-type losses has been applied to HIFU surgical applications (Hallaj *et al*., 2001). Another time domain approach is a different wave equation called the nonlinear progressive equation (NPE) (McDonald and Kuperman, 1987). Too and Ginsberg (1992) have developed a version for sound beams. Li and Zagzebski (2000) have used this approach for evaluating image quality for harmonics.

Several approaches utilize a substep or hybrid (known as operator-splitting) scheme for computation. In the Pestorious (1973) algorithm, propagation is reduced to small alternating steps. Here nonlinear effects and thermoviscous absorption are computed using weak shock theory. Then other absorption effects are computed in the frequency domain, and, finally, these results are inverse Fourier transformed back to the time domain for the next nonlinear incremental step. Christopher and Parker (1991) have developed an algorithm in which diffraction and attenuation are computed in the angular spectrum domain as an incremental substep followed by a substep in which nonlinear effects are computed via a frequency domain solution to the Burgers equation. The advantage of their approach is that there is no angular restriction as in the KZK methods; strong nonlinearities, appropriate for modeling lithotripters, can be accomodated, as well as multiple layers (without reverberations). In a later version, the

nonlinear substep was computed in the time domain (Christopher, 1993). Another split-step, full wave algorithm operates entirely in the time domain (Tavakkoli *et al*., 1998) and uses an exact Rayleigh integral for the diffraction substep, a material impulse response–like function for the absorption–dispersion substep, and an analytic Poisson solution for a lossless medium for the nonlinear substep. Good agreement has been obtained with data (Remenieras *et al*., 2000). Ginter (2000) has accounted for energy conservation and power law attenuation in his approach.

Figures 12.20–12.22 were generated by a finite difference pseudo-spectral full wave solver using six processors running in parallel (Wojcik *et al*., 1998, 1999a). This method accounts for multiple reflections, absorption, and nonlinearity and employs perfectly matched layers at the boundaries. A series of experiments in water and through tofu as a tissue mimic agreed well with computations (Wojcik *et al*., 1999b).

Finally, there are indications that as computing speed increases, nonlinear propagation programs will become more widely available. Several groups are working on new and approximate methods for nonlinear propagation. Indications are that these programs may operate through MATLAB interfaces.

12.9 SUMMARY

Nonlinear acoustics, as applied to diagnostic ultrasound imaging, is a fortuitous combination of parameters. As summarized in Table 12.1, THI offers several unique advantages over conventional imaging. Because the harmonics are created along the axis of the beam, reverberations and acoustic noise can be removed by signal processing. Objectional off-axis scatterers are substantially reduced by the reduced harmonic beam volume. Aberration effects appear to be somewhat reduced but not eliminated. Surprisingly robust, harmonic imaging provides a means of imaging some people who are impossible to examine by conventional techniques. The superior contrast of harmonic images also enhances its diagnostic capability.

THI is still not fully understood. The numerical computational barriers are being reduced by the inevitable improvements in computational rates and by several more user-friendly approximate nonlinear propagation models currently under development. Signal processing methods, discussed in application to contrast agents in Chapter 14, continue to improve sensitivity and contrast resolution. Implementation of these techniques varies from manufacturer to manufacturer (van Wijk and Thijjsen, 2002). While the basic physical principles of nonlinear propagation are understood, their optimization to various clinical applications is still evolving.

BIBLIOGRAPHY

Averkiou, M. A. (2000). Tissue harmonic imaging. *IEEE Ultrason. Symp. Proc*., 1561–1566. A recommended summary of harmonic imaging and related signal processing

Baker, A. C. (1998). Nonlinear effects in ultrasonic propagation. In *Ultrasound in Medicine*. F. A. Duck, A. C. Baker, H. C. Starritt (eds.). I.O.P. Publishing, Bristol, UK, pp. 23–28. A brief summary of the measurement and simulation of nonlinear harmonic beams.

Bakhvalov, N. S., Zhileikin, Y. M., and Zabolotskaya, E. A. (1987). *Nonlinear Theory of Sound Beams*. American Institute of Physics, New York. A treatise on the characteristics of beams in nonlinear media and their simulation.

Berktay, H. O. (1965). Parametric amplification by the use of acoustic nonlinearities and some possible applications. *J Sound Vib*. **2**, 462–470. An early treatment of the principles of nonlinear acoustics and beams.

Beyer, R. T. (1997). *Nonlinear Acoustics*. Acoustical Society of America, Woodbury, NY. Reprint from Naval Ship Systems Command, 1974. A longtime classic on nonlinear acoustics.

Duck, F. A. (1999). Acoustic saturation and output regulation. *Ultrasound in Med. & Biol*. **25**, 1009–1018.

Duck, F. A. (2002). Nonlinear acoustics in diagnostic ultrasound. *Ultrasound in Med. & Biol*. **28**, 1–18. A comprehensive review of nonlinear propagation effects beams and harmonic imaging.

Encyclopedia of Acoustics. (1997). M. S. Crocker (ed.). John Wiley & Sons, New York. Short articles on many aspects of both linear and nonlinear acoustics.

Frinking, P. J. A., Boukaz, A., Kirkhorn, J., Ten Cate, F. J., and De Jong, N. (2000). Ultrasound contrast imaging: Current and new potential methods. *Ultrasound in Med. & Biol*. **26**, 965–975. Article includes a review of nonlinear signal processing.

Humphrey, V. F. (2000). Nonlinear propagation in ultrasonic fields: Measurements, modelling and harmonic imaging. *Ultrasonics* **38**, 267–272. A recommended overview article on nonlinear acoustics and harmonic imaging.

Nonlinear Acoustics. (1998). M. F. Hamilton and D. T. Blackstock (eds.). Academic Press, San Diego. A thorough theoretical overview of nonlinear acoustics.

Novikov, B. K. Rudenko, O. V., and Timoshenko, V. I. (1987). Nonlinear underwater Acoustics. American Institute of Physics, New York 1987 Nonlinear underwater acoustic applications of beams and arrays.

Starritt, H. C., Duck, F. A., and Humphrey, V. F. (1989). An experimental investigation of streaming in pulsed diagnostic ultrasound beams. *Ultrasound in Med. & Biol*. **15**, 363–373.

Starritt, H. C., Duck, F. A., and Humphrey, V. F. (1991). Forces acting in the direction of propagation in pulsed ultrasound fields. *Phys. Med. Biol*. **36**, 1465–1474.

Wu, J., Winkler, A. J., and O'Neill, T. P. (1998). Effect of acoustic streaming on ultrasonic heating. *Ultrasound in Med. & Biol*. **24**, 153–159.

References

Aanonsen, S. I., Barkve, T., Naze Tjotta, J., and Tjotta, S. (1984). Distortion and harmonic generation in the nearfield of a finite amplitude sound beam. *J. Acoust. Soc. Am*. **75**, 749–768.

Averkiou, M. A. (2000). Tissue harmonic imaging. *IEEE Ultrason. Symp. Proc*., 1561–1566.

Averkiou, M. A., and Hamilton, M. F. (1995). Measurements of harmonic generation in a focused finite-amplitude sound beam. *J. Acoust. Soc. Am*. **98**, 3439–3442.

Averkiou, M. A., Roundhill, D. N., Powers, J. E. (1997). A new imaging technique based on the nonlinear properties of tissues. *IEEE Ultrason. Symp. Proc*., 1561–1566.

Bacon, D. R. (1984). Finite amplitude distortion of the pulsed fields used in diagnostic ultrasound. *Ultrasound in Med. & Biol*. **10**, 189–195.

Bacon, D. R. and Carstensen, E. L. (1990). Increased heating by diagnostic ultrasound due to nonlinear propagation. *J. Acoust. Soc. Am*. **88**, 26–34.

Baker, A. C. (1989). *Finite Amplitude Propagation of Focused Ultrasonic Waves in Water*, Ph. D. dissertation. University of Bath, Bath, UK.

Baker, A. C. (1991). Prediction of nonlinear propagation in water due to diagnostic medical ultrasound equipment. *Phys. Med. Biol*. **36**, 1457–1464.

Baker, A. C. (1992). Nonlinear pressure fields due to focused circular apertures. *J. Acoust. Soc. Am*. **91**, 713–717.

Baker, A. C., Anastasiadis, K., and Humphrey, V. F. (1998). The nonlinear pressure field of a plane circular piston: Theory and experiment. *J. Acoust. Soc. Am*. **84**, 1483–1487.

Baker, A. C., Berg, A. M., Sahin, A., and Naze Tjotta, J. (1995). The nonlinear pressure field of plane, rectangular apertures: Experimental and theoretical results. *J. Acoust. Soc. Am*. **97**, 3510–3517.

Baker, A. C. and Humphrey, V. F. (1992). Distortion and high frequency generation due to nonlinear propagation of short ultrasonic pulses from a plane circular piston. *J. Acoust. Soc. Am*. **92**, 1699–1705.

Bakhvalov, N. S., Zhileikin, Y. M., and Zabolotskaya, E. A. (1987). *Nonlinear Theory of Sound Beams*. American Institute of Physics, New York.

Berg, A. M. and Naze Tjotta, J. (1993). Numerical simulation of sound pressure field from finite amplitude, plane or focusing, rectangular apertures. *In Advances in Nonlinear Acoustics*. H. Hobaek (ed.). Elsevier, London, pp. 309–314.

Berktay, H. O. (1965). Possible exploitation of nonlinear acoustics in underwater transmitting applications. *J. Sound Vib*. **2**, 435–461.

Berktay, H. O. and Al-Temini, C. A. (1969). Virtual arrays for underwater applications. *J. Sound Vib*. **9**, 295–307.

Berntsen, J. (1990). Numerical calculations of finite amplitude sound beams. *Frontiers of Nonlinear Acoustics*. M. F. Hamilton and D. T. Blackstock, (eds.). Elsevier, London, pp. 191–196.

Berntsen, J., Naze Tjotta, J., and Tjotta, S. (1984). Nearfield of a large acoustic transducer, Part IV: Second harmonic and sum frequency radiation. *J. Acoust. Soc. Am*. **75**, 1383–1391.

Berntsen, J. and Vefring, E. (1986). *Numerical Computation of a Finite Amplitude Sound Beam*, Tech. Report 82. Dept. of Math., Univ. of Bergen, Bergen, Norway.

Beyer, R. T. (1997). *Nonlinear Acoustics*. Acoustical Society of America. Woodbury, NY. Reprint from Naval Ship Systems Command, 1974.

Bjorno, L. (2002). Forty years of nonlinear ultrasound. *Ultrasonics*.

Blackstock, D. T. (1966). Connection between the Fay and Fubini solutions for plane sound waves of finite amplitude. *J. Acoust. Soc. Am*. **39**, 1019–1026.

Blackstock, D. T. (1985). Generalized Burgers equation for plane waves. *J. Acoust. Soc. Am*. **77**, 2050–2053.

Blackstock, D. T. (1998). *Nonlinear Acoustics*, Chapt. 1. M. F. Hamilton and D. T. Blackstock (eds.). Academic Press, San Diego. pp. 1–23.

Blackstock, D. T., Hamilton, M. F., and Pierce, A. D. (1998). *Nonlinear Acoustics*, Chapt. 4. M. F. Hamilton, and D. T. Blackstock (eds.). Academic Press, San Diego.

Brock-Fisher, G. A., Poland, M. D., and Rafter, P. G. (Nov. 26, 1996). *Means for Increasing Sensitivity in Non-Linear Ultrasound Imaging Systems*, US patent 5,577,505.

Bruce, F. B., Averkiou, M. A., Skyba, D. M., and Powers, J. E. (2000). A generalization of pulse inversion Doppler. *IEEE Ultrason. Symp. Proc*., 1561–1566.

Cahill, M. D. and Baker, A. C. (1998). Numerical simulation of the acoustic field of a phased-array medical ultrasound scanner. *J. Acoust. Soc. Am*. **104**, 1274–1283.

Carson, P. J., Fischella, P. R., and Oughton, T. V. (1978). Ultrasonic power and intensity produced by diagnostic ultrasound equipment. *Ultrasound in Med. & Biol*. **3**, 341.

Carstensen, E. L., Law, W. K., McKay, N. D., and Muir, T. G. (1980). Demonstration of nonlinear acoustical effects at biomedical frequencies and intensities. *Ultrasound in Med. & Biol*. **6**, 359–368.

Cherin, E., Poulsen, J. K., van der Steen, A. F. W., and Foster, F. S. (2000). Comparison of nonlinear and linear imaging techniques at high frequency. *IEEE Ultrason. Symp. Proc*., 1561–1566.

Christopher, T. (1993). A nonlinear plane-wave algorithm for diffractive propagation involving shock waves. *J. Comp. Acoust*. **1**, 371–393.

Christopher, T. (1997). Finite amplitude distortion-based inhomogeneous pulse echo ultrasonic imaging. *IEEE Trans. Ultrason. Ferroelec. Freq. Control* **44**, 125–139.

Christopher, T. (1999). Source prebiasing for improved second harmonic bubble response imaging. *IEEE Trans. Ultrason. Ferroelec. Freq. Control* **46**, 556–563.

Christopher, T. and Carstensen, E. L. (1996). Finite amplitude distortion and its relationship to linear derating formulae for diagnostic ultrasound systems. *Ultrasound in Med. & Biol*. **22**, 1103–1116.

Christopher, T. and Parker, K. J. (1991). New approaches to nonlinear diffractive field propagation. *J. Acoust. Soc. Am*. **90**, 488–499.

Cleveland, R. O., Hamilton, M. F., and Blackstock, D. T. (1996). Time-domain modeling of finite-amplitude sound in relaxing fluids. *J. Acoust. Soc. Am*. **99**, 3312–3318.

Dalecki, D., Carstensen, E. L., and Parker, K. J. (1991). Absorption of finite amplitude focused ultrasound. *J. Acoust. Soc. Am*. **89**, 2435–2447.

Divall, S. A. and Humphrey, V. F. (2000). Finite difference modelling of the temperature rise in nonlinear medical ultrasound fields. *Ultrasonics* **38**, 273–277.

Duck, F. A. (1990). *Physical Properties of Tissue: A Comprehensive Reference Book*. Academic Press, London.

Duck, F. A. (1998). Radiation pressure and streaming, Chapt. 3. In *Ultrasound in Medicine*, Medical Science Series. F. A. Duck, A. C. Baker, and H. C. Starritt (eds.). Institute of Physics Publishing, Bristol, UK.

Duck, F. A. (2002). Nonlinear acoustics in diagnostic ultrasound. *Ultrasound in Med. & Biol*. **28**, 1–18.

Duck, F. A. and Starritt, H. C. (1984). Acoustic shock generation by ultrasonic imaging equipment. *Br. J. Radiol*. **57**, 231–240.

Everbach, E. C. (1997). Parameters of nonlinearity of acoustic media. *Encyclopedia of Acoustics*. M. J. Crocker (ed.). John Wiley & Sons, New York.

Fedewa, R. J., Wallace, K. D., Holland, M. R., Jago, J. R., Ng, G. C., Reilly, M. W., Robinson, B. S., and Miller, J. G. (2001). Statistically significant differences in the spatial coherence of backscatter for fundamental and harmonic portions of a clinical beam. *Proc IEEE Ultrason. Symp*. 1481–1484.

Frinking, P. J. A., Boukaz, A., Kirkhorn, J., Ten Cate, F. J., and De Jong, N. (2000). Ultrasound contrast imaging: Current and new potential methods. *Ultrasound in Med. & Biol*. **26**, 965–975.

Froysa, K. E. (1991). *Linear and Weakly Nonlinear Propagation of a Pulsed Sound Beam*, Ph. D. dissertation. Dept. of Math., Univ. of Bergen, Bergen, Norway.

Germain, L. and Cheeke, J. D. N. (1988). Generation and detection of high-order harmonics in liquids using a scanning acoustic microscope. *J. Acoust. Soc. Am*. **83**, 942–949.

Ginsberg, J. H. and Hamilton, M. F. (1998). *Nonlinear Acoustics*, Chapt. 11. M. F. Hamilton, and D. T. Blackstock (eds.). Academic Press, San Diego.

Ginter, S. (2000). Numerical simulation of ultrasound-thermotherapy combining nonlinear wave propagation with broadband soft-tissue absorption. *Ultrasonics* **37**, 693–696.

Gol'dberg, Z. A. (1957). On the propagation of plane waves of finite amplitude. *Sov. Phys. Acoust*. **3**, 340–347.

Haider, B., and Chiao, R. Y. (1999). Higher order nonlinear ultrasonic imaging. *IEEE Ultrason. Symp. Proc*., 1527–1531.

Hallaj, I. M., Cleveland, R. O., and Hynynen, K. (2001). Simulations of the thermo-acoustic lens effect during focused ultrasound surgery. *J. Acoust. Soc. Am*. **109**, 2245–2253.

Hamilton, M. F. (1998). *Nonlinear Acoustics*, Chapt. 8. M. F. Hamilton, and D. T. Blackstock (eds.). Academic Press, San Diego.

Hamilton, M. F. and Morfey, C. L. (1998). *Nonlinear Acoustics*, Chapt. 3. M. F. Hamilton, and D. T. Blackstock (eds.). Academic Press, San Diego.

Hamilton, M. F., Naze Tjotta, J., and Tjotta, S. (1985). Nonlinear effects in the farfield of a directive sound source. *J. Acoust. Soc. Am*. **78**, 202–216.

Hansen, R., Angelsen, B. A. J., and Johansen, T. F. (2001). Reduction of nonlinear contrast agent scattering due to nonlinear wave propagation. *IEEE Ultrason. Symp. Proc*., 1725–1728.

Haran, M. E. and Cook, B. D. (1983). Distortion of finite amplitude ultrasound in lossy media. *J. Acoust. Soc. Am*. **73**, 774–779.

Hart, T. S. and Hamilton, M. F. (1988). Nonlinear effects in focused sound beams. *J. Acoust. Soc. Am*. **84**, 1488–1496.

Humphrey, V. F. (2000). Nonlinear propagation in ultrasonic fields: Measurements, modelling and harmonic imaging. *Ultrasonics* **38**, 267–272.

Jiang, P., Mao, Z., and Lazenby, J. C. (1998). A new tissue harmonic imaging scheme with better fundamental frequency cancellation and higher signal-to-noise ratio. *IEEE Ultrason. Symp. Proc*., 1589–1594.

Kamakura, T., Tani, M., and Kumamoto, Y. (1992). Harmonic generation in finite amplitude sound beams from a rectangular aperture source. *J. Acoust. Soc. Am*. **91**, 3144–3151.

Kim, D. Y., Lee, J. C., Kwon, S. J., and Song, T. K. (2001). Ultrasound second harmonic imaging with a weighted chirp pulse. *Proc. IEEE Ultrason. Symp*., 1477–1480.

Kompfner, R. and Lemons, R. A. (1976). Nonlinear acoustic microscopy. *Appl. Phys. Lett*. **28**, 295–297.

Kornbluth, M., Liang, D. H., Paloma, A., and Schnittger, I. (1998). Native harmonic imaging improves endocardial border definition and visualisation of cardiac structures. *J. Am. Soc. Echocardiogr.* **11**, 693–701.

Kuznetsov, V. P. (1971). Equations of nonlinear acoustics. *Sov. Phys. Acoust*. **16**, 467–470.

Labat, V., Remenieras, J. P., Bou Matar, O., Ouahabi, A., and Patat, F. (2000). Harmonic propagation of pulsed finite amplitude sound beams: Experimental determination of the nonlinearity parameter B/A. *Ultrasonics* **38**, 292–296.

Landsberger, B. J. and Hamilton, M. F. (2000). Second-harmonic generation in sound beams reflected from, and transmitted through, immersed elastic solids. *J. Acoust. Soc. Am*. **108**, 906–917.

Law, W. K., Frizzell, L. A., and Dunn, F. (1981). Ultrasonic determination of the nonlinearity parameter B/A for biological media. *J. Acoust. Soc. Am*. **69**, 1210–1212.

Law, W. K., Frizzell, L. A., and Dunn, F. (1985). Determination of the nonlinearity parameter B/A of biological media. *Ultrasound in Med. & Biol*. **11**, 307–318.

Lee, Y. S. and Hamilton, M. F. (1995). Time-domain modeling of pulsed finite-amplitude sound beams. *J. Acoust. Soc. Am*. **97**, 906–917.

Li, Y. and Zagzebski, J. A. (2000). Computer model for harmonic ultrasound imaging. *IEEE Trans. Ultrason. Ferroelec. Freq. Control* **47**, 1259–1272.

Liu, D. L. D., von Behren, P., and Kim, J. (2001). Single transmit imaging. *IEEE Ultrason. Symp. Proc*., 1481–1484.

Makin, I. R. S., Averkiou, M. A., and Hamilton, M. F. (2000). Second-harmonic generation in a sound beam reflected and transmitted at a curved interface. *J. Acoust. Soc. Am.* **108**, 1505–1513.

McDonald, B. E. and Kuperman, W. A. (1987). Time domain formulation for pulse propagation including nonlinear behavior in a caustic. *J. Acoust. Soc. Am.* **81**, 1406–1417.

Mor-Avi, V., Caiani, E. G., Collins, K. A., Korcarz, C. E., Bednarz, J. E., and Lang, R. M. (2001). Combined assessment of myocardial perfusion and regional left ventricular function by analysis of contrast-enhanced power modulation images. *Circulation* **104**, 352–357.

Muir, T. O. (1980). Nonlinear effects in acoustic imaging. *Acoust. Imaging*. Plenum Press, New York, 93–109.

Muir, T. G., and Carstensen E. L. (1980). Prediction of nonlinear acoustic effects at biomedical frequencies and intensities. *Ultrasound in Med. & Biol.* **6**, 345–357.

Nachef, S., Cathignol, D., Naze Tjotta, J., Berg, A. M., and Tjotta, S. (1995). Investigation of a high intensity sound beam from a plane transducer: Experimental and theoretical results. *J. Acoust. Soc. Am.* **98**, 2303–2323.

Naugol'nykh, K. A. and Romanenko, E. V. (1959). Amplification factor of a focusing system as a function of sound intensity. *Sov. Phys. Acoust*. **5**, 191–195.

Naze Tjotta, J., and Tjotta, S. (1981). Nonlinear equations of acoustics, with applications to parametric arrays. *J. Acoust. Soc. Am.* **69**, 1644–1652.

Nowicki, A., Kowalewski, T., Secomski, W., and Wojcik, J. (1998). Estimation of acoustical streaming: Theoretical model, Doppler measurements and optical visualization. *European J. Ultrasound* **7**, 73–81.

Nyborg, W. L. (1998). *Nonlinear Acoustics*, Chapt. 7. M. F. Hamilton and D. T. Blackstock (eds.). Academic Press, San Diego.

Parker, K. J. and Friets, E. M. (1987). On the measurement of shock waves. *IEEE Trans. Ultrason. Ferroelec. Freq. Control* **34**, 454–460.

Pestorious, F. M. (1973). *Propagation of Plane Acoustic Noise of Finite Amplitude*, Technical Report ARL-TR-73–23. Applied Research Laboratories, University of Texas, Austin.

Remenieras, J. P., Bou Matar, O., Labat, V., and Patat, F. (2000). Time-domain modeling of nonlinear distortion of pulsed finite amplitude sound beams. *Ultrasonics* **38**, 305–311.

Sahin, A., and Baker, A. C. (1993). Nonlinear propagation in the pressure fields of plane and focused rectangular apertures. *Advances in Nonlinear Acoustics*. H. Hobaek (ed.). Elsevier, London, pp. 303–308.

Sempsrott, J. M. and O'Brien Jr., W. D. (1999). Experimental verification of acoustic saturation. *IEEE Ultrason. Symp. Proc*., 1287–1290.

Shi, W. T. and Forsberg, F. (2000). Ultrasonic characterization of the nonlinear properties of contrast microbubbles. *Ultrasound in Med. & Biol.* **26**, 93–104.

Simpson, D. H., Chin, C. T., and Burns, P. N. (1999). Pulse inversion Doppler: A new method for detecting nonlinear echoes from microbubble contrast agents. *IEEE Trans. Ultrason. Ferroelec. Freq. Control* **46**, 372–382.

Spencer, K. T., Bernarz, J., Rafter, P. G., Korcarz, C., and Lang, R. M. (1998). Use of harmonic imaging without echocardiographic contrast to improve two-dimensional image quality. *Am. J. Cardiol.* **82**, 794–799.

Starritt, H. C., Perkins, M. A., Duck, F. A., and Humphrey, V. F. (1985). Evidence for ultrasonic finite-amplitude distortion in muscle using medical equipment. *J. Acoust. Soc. Am.* **77**, 302–306.

Starritt, H. C., Duck, F. A., Hawkins, A. I., and Humphrey, V. F. (1986). The development of harmonic distortion in pulsed finite-amplitude ultrasound passing through liver. *Phys. Med. Biol*. **31**, 1401–1409.

Szabo, T. L. (1993). Time domain nonlinear wave equations for lossy media. In *Advances in Nonlinear Acoustics: Proceedings of 13th ISNA*. H. Hobaek (ed.). World Scientific, Singapore, pp. 89–94.

Szabo, T. L., Clougherty, F., and Grossman, C. (1999). Effects of nonlinearity on the estimation of in situ values of acoustic output parameters. *J. Ultrasound in Med*. **18**, 33–42.

Takeuchi. (1996). Coded excitation for harmonics imaging. *IEEE Ultrason. Symp. Proc., 1433–1436*.

Tavakkoli, J., Cathignol, D., Souchon, R., and Sapozhnikov, O. A. (1998). Modeling of pulsed finite-amplitude focused sound beams in time domain. *J. Acoust. Soc. Am*. **104**, 2061–2072.

Ten Cate, F. J. (1993). An experimental investigation of the nonlinear pressure field produced by a plane circular piston. *J. Acoust. Soc. Am*. **94**, 1084–1089.

Tjotta, S. (2000). On some nonlinear effects in ultrasonic fields. *Ultrasonics* **38**, 278–283.

Too, G. P. J. and Ginsberg, J. H. (1992). Nonlinear progressive wave equation model for transient and steady-state sound beams. *J. Acoust. Soc. Am*. **92**, 59–68.

Tranquart, F., Grenier, N., Eder, V., and Pourcelot, L. (1999). Clinical use of ultrasound tissue harmonic imaging. *Ultrasound in Med. & Biol*. **25**, 889–894.

van Wijk, M. C., and Thijjsen, J. M. (2002). Performance testing of medical ultrasound equipment: Fundamental vs. harmonic mode. *Ultrasonics* **40**, 585–591.

Wallace, K. D., Holland, M. R., and Miller, J. G. (2001). Improved description of shock wave evolution in media with frequency power law dependent attenuation. *J. Acoust. Soc. Am*. **109**, 2263–2265.

Ward, B., Baker, A. C., and Humphrey, V. F. (1996). Nonlinear propagation applied to the improvement of lateral resolution in medical ultrasound scanners. *Proceedings of 1995 World Congress on Ultrasonics*, 965–968.

Ward, B., Baker, A. C., and Humphrey, V. F. (1997). Nonlinear propagation applied to the improvement of resolution in diagnostic medical ultrasound equipment. *J. Acoust. Soc. Am*. **10**, 143–154.

Watson, A. J., Humphrey, V. F., Baker, A. C., and Duck, F. A. (1990). Nonlinear propagation of focused ultrasound in tissue-like media. *Frontiers of Nonlinear Acoustics, Proceedings of the 12th ISNA, Austin, TX*, Elsevier, London, pp. 445–450.

Westervelt, P. J. (1963). Parametric acoustic array. *J. Acoust. Soc. Am*. **35**, 535–537.

Wojcik, G., Mould Jr., J., Ayter, S., and Carcione, L. M. (1998). A study of second harmonic generation by focused medical transdcuer pulses. *IEEE Ultrason. Symp. Proc.*, pp. 1583–1588.

Wojcik, G. L., Mould Jr., J. C., and Carcione, L. M. (1999a). Combined transducer and nonlinear tissue propagation. *Proc. Intr. Mech. Engr. Congress & Exposition*.

Wojcik, G. L., Szabo, T., Mould, J., Carcione, L., and Clougherty, F. (1999b). Nonlinear pulse calculations & data in water and a tissue mimic. *IEEE Ultrason. Symp. Proc*., 1521–1526.

Wu, J. and Tong, J. (1994). Measurements of nonlinearity parameter B/A of contrast agents. *Ultrasound in Med. & Biol*. **20**, 195–201.

Yongchen, S., Yanwu, D., Jie, T., and Zhensheng, T. (1986). Ultrasonic propagation parameters in human tissues. *IEEE Ultrason. Symp. Proc*., 905–908.

Zhang, J. and Dunn, F. (1991). A small volume thermodynamic system for B/A measurement. *J. Acoust. Soc. Am*. **89**, 73–79.

Zhang, J., Kuhlenschmidt, and Dunn, F. (1991). Influences of structural factors of biological media on the acoustic nonlinearity parameter B/A. *J. Acoust. Soc. Am*. **89**, 80–91.

This page intentionally left blank

13 ULTRASONIC EXPOSIMETRY AND ACOUSTIC MEASUREMENTS

Chapter Contents

13.1 INTRODUCTION TO MEASUREMENTS

Measurements related to ultrasound imaging are performed at several levels. First, the acoustical, mechanical, and chemical properties of materials used in transducer construction are determined. Second, various properties of arrays, both acoustical and electrical, are measured either as a whole or element-by-element. Thirdly, extensive acoustic output measurements are conducted on the imaging system and each transducer in different modes. Fourth, performance tests are used to evaluate the imaging capabilities of an imaging system and transducer combination.

13.2 MATERIALS CHARACTERIZATION

13.2.1 Transducer Materials

Determining the acoustic properties of materials with ultrasound is an ongoing process for many industries; however, a particular emphasis for imaging equipment is the evaluation of materials for transducers. Especially, as higher performance, wider bandwidth arrays are designed, materials with low losses and specific acoustic properties are required. Key parameters of a material are its sound speed, density, and acoustic characteristic impedance, loss, and phase velocity dispersion as a function of frequency. Auxiliary information may also be needed, such as chemical compatibility, thermal and mechanical properties, and strength when bonded to other materials. For accurate finite element modeling of transducer arrays, both longitudinal and shear wave parameters are required (Powell *et al*., 1997).

Earlier methods employed discrete single-frequency measurements using tone bursts. Selfridge (1985) measured many materials at a single frequency in a simple reflection arrangement. To increase the frequency range, several transducers were often used to obtain data. For the key parameters, broadband spectroscopy using ultrasound provides a precise and direct methodology. Zeqiri (1988) demonstrated that equivalent results could be obtained by using broadband methods. Also known as the through transmission substitution method, this approach usually involves two broadband nonfocusing transducers aligned in a water tank (shown in Figure 13.1). PVDF transducers (see Section 5.8.5) provide superior bandwidth for this application. An impulse excitation is applied to the transmitting transducer, and the signal received by the second transducer is digitized. Next a sample material, with parallel sides and a known thickness and diameter larger than the extent of the beam, is inserted between the transducers and aligned. With the sample in place, the signal is once again recorded on a digital sampling scope. Calculations based on the ratio of the absolute spectra can determine the attenuation through the sample over a wide bandwidth. The sound speed dispersion can be found from the phase of the ratio of spectra. An independent determination of material density, a coarse determination of the midband sound speed, and appropriate corrections for reflections and transmissions through the sample boundaries are also usually required. More complete details can be found in Zeqiri (1988), Wu (1996), He (1999), and Waters *et al*. (2000). This method can be extended

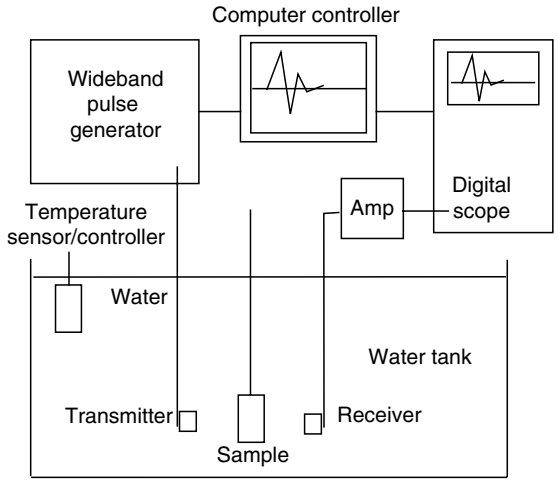

Figure 13.1 Experimental configuration for broadband through transmission substitution method for determination of acoustic material properties.

to shear waves (Wu, 1996) through the use of a critical angle conversion without the need for shear wave transducers. These measurements agree well with the theory presented in Chapter 4 (see Figures 4.6–4.7) so that the dispersion can be determined reliably from material absorption alone. Another variation of the method is a pulse-echo version with a single transducer and a known reflector behind the sample; this approach involves a double pass through the material (Wu, 2001).

13.2.2 Tissue Measurements

Most of the measurements made on tissue have been made using procedures similar to those in Section 13.2.1. The handling of tissue, safety precautions, and temperature control are additional considerations. The tissue itself is often sealed in a chamber with acoustically transparent windows on either side. The sealed chamber then can be treated as a sample in the description outlined in the last section.

Whereas most of the materials in the previous chapter are homogeneous, tissues are not and more elaborate procedures are needed to capture their complexity. Bamber (1986, 1992) provides reviews of measurement methods. One characteristic is the heterogeneous nature of tissue, or its spatial variation point to point. Large area scans can be time consuming, so faster methods of through transmission measurements have been devised (Hinkelman *et al*., 1994, 1997), as was described in Section 9.3. Related studies of the heterogeneties of the breast have been done by Freiburger *et al*. (1992) and Zhu and Steinberg (1992). At the University of Rochester, more recent work involves studies using two-dimensional arrays and circumferential ring arrays (Jansson *et al*., 1998; Liu and Waag, 1998). Another characteristic of tissue is angular scattering, which is a component of attenuation. In this case, a fixed

transmitter is used along with a receiver that can be rotated in angle (Nassiri and Hill, 1986). The measurement of another characteristic, anisotropy, also utilizes a similar angular positioning capability (Mottley and Miller, 1988), as discussed in Section 9.4.

13.2.3 Measurement Considerations

In these measurements, other factors are involved that can invalidate results or cause errors. Because of variations along the beam, diffraction can introduce a loss and dispersion of its own (described as diffraction loss in Chapter 6). In the substitution method, the signal spectrum with the sample inserted is divided by that without the sample. A hidden goal in this measurement is to make the ratio of diffraction losses for the two cases equal to one or be negligible for the measurement. If the S parameter for water path without a sample for identical circular nonfocusing transducers separated by z is

$$S_w = \frac{z\lambda_w}{a^2} \tag{13.1}$$

where a is the transducer radius and λ_w is the wavelength in water, then the sample S parameter of thickness Δz can be expressed (Szabo, 1993) as

$$S_s = S_w\left[1 + \frac{\Delta z}{z}\left(\frac{v_s}{v_w} - 1\right)\right] \tag{13.2}$$

where v_s is the sample sound speed and v_w is the water sound speed. For diffraction to be close in the two cases, the second factor in brackets in Eq. (13.2) must be small. Bamber (1986) discusses diffraction correction for angular backscatter measurements.

Nonlinearity of the water used in the tanks for these experiments can cause excess attenuation and significant distortion. To keep measurements in the linear range, the nonlinearity parameter (σ), Eq. (12.4c), should be small, less than 0.1 (Szabo, 1993; Wu, 1996).

13.3 TRANSDUCERS

13.3.1 Impedance

Recall from Chapter 5 that a transducer can be regarded as a three-port device. Typically a backing material (port 2) is used in the construction of the transducer, so that the electrical port (port 3) and the business end (acoustic port 1) are of interest. The measurement of the electrical impedance as a function of frequency can be an important diagnostic quality check during various stages of manufacture. Impedance measurements of each element in an array also can be valuable in determining the element-to-element variability across the array. In a manufacturing environment involving large numbers of arrays, automated, computer-controlled data gathering and evaluation are necessary (Fisher, 1983).

For an impedance measurement, a network analyzer of the appropriate frequency range is attached to the array through a switch that allows connection to each element

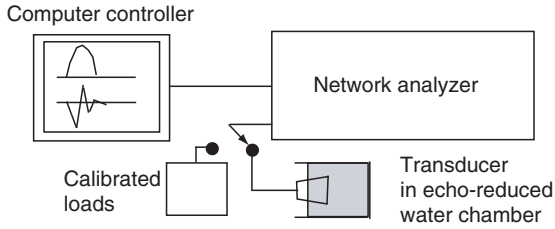

Figure 13.2 Impedance measurement with a network analyzer (impedance plot).

in turn (Figure 13.2). Because of the three-port nature of the transducer, the impedance is affected by acoustic port loading, which must be controlled. Usually, the business end (port 1) of the transducer is placed in a water chamber with absorbing sides. Before the transducer can be measured, the analyzer is calibrated with the fixture used to connect to the transducer. Output display choices are magnitude and phase, admittance and phase, and real and imaginary parts. The latter pair is preferred because the real part is related directly to the radiation resistance; however, magnitude and phase are more common in the literature (Davidsen and Smith, 1993; Ritter *et al*., 2002). Data can be compared to simulations from transducer models (described in Chapter 5) in order to check the realization of a design (as in Figure 13.3).

Considerable information can be derived from impedance measurements made at different stages of manufacture. A step-by-step walk-through of this process with data compared to finite element modeling at each stage under different loading conditions can be found in Powell *et al*. (1997). These types of measurements for crystals of different geometries can be used to characterize piezoelectric materials (Selfridge *et al*., 1980; Szabo, 1982; *IEEE*, 1987; Powell *et al*., 1997; Ritter *et al*., 2000).

13.3.2 Pulse-Echo Testing

Electrical measurements, useful as they are, still provide only an indirect measure of acoustic performance. A standard measure of transducer acoustic performance is a pulse-echo test, in which a transducer element is excited by a prescribed waveform (often an impulse) and the round-trip signal from an aligned flat target is obtained (as illustrated by Figure 13.4). The received signal is digitized, and a fast Fourier transform (FFT) and Hilbert transform (described in Appendix A) are used to obtain the spectrum and pulse envelope, an example of which is given by Figure 13.5. Features can be extracted from the data automatically and compared element to element. Typical features may be overall pulse-echo sensitivity or insertion loss, pulse-envelope length at various decibel levels from the peak, and various measures of bandwidth, such as the −6-dB absolute or fractional bandwidth.

For this measurement, it is preferable to place the flat plate in a focal plane. Recall that at the focal point of a circularly symmetric transducer, the spatial impulse response is a delta function, so the pulse is a scaled replica of the source excitation (as pointed out in Chapter 7). If a one-dimensional array element is measured, then

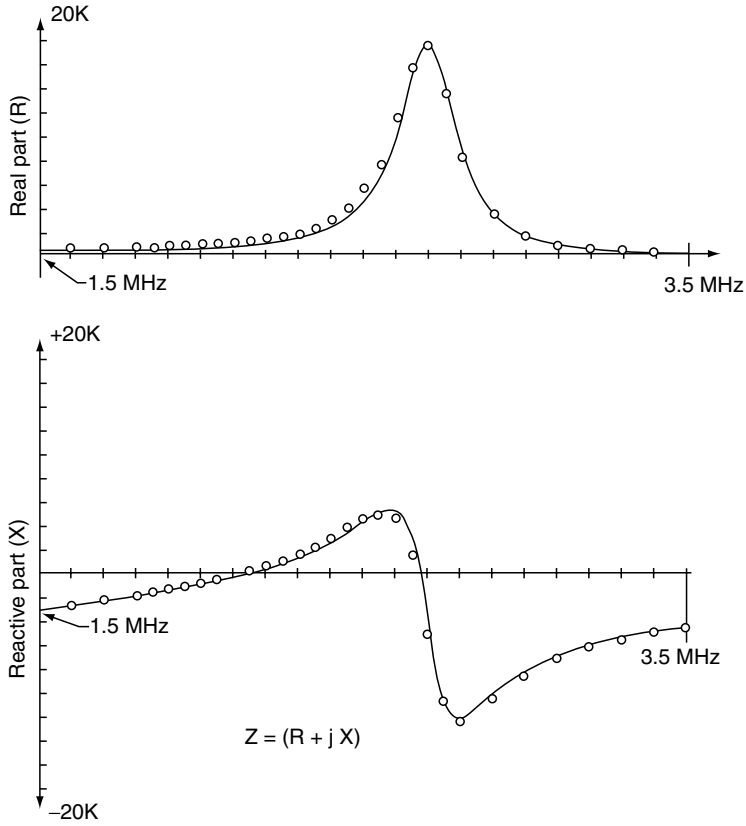

Figure 13.3 Impedance measurements for a PZT-5H resonator with an epoxy backing and $w/d = 0.0.371$; real (top) and imaginary (bottom) compared to model (from Selfridge *et al.*, 1980).

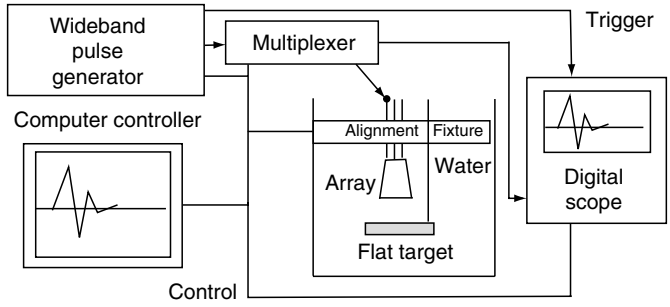

Figure 13.4 Pulse-echo testing of array elements.

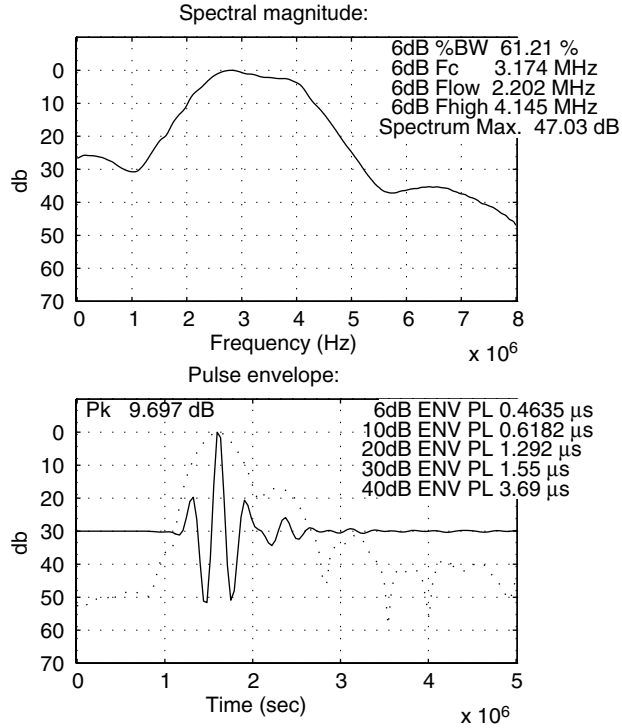

Figure 13.5 A typical pulse and spectrum data plot showing pulse and spectrum widths.

the elevation focal plane is appropriate because in the azimuth plane, the element will appear to be in the far field so that the original source function is recovered. Of course, a diffraction loss will be incurred (as discussed in Sections 6.8 and 8.3).

Another alternative for a target is a steel ball, which has simpler alignment requirements. In this case, only a small part of the surface of the ball acts as a reflector back to the transducer. In general, echoes from flat plates correlate better with transducer model simulations. An example of an automated measurement for a 30-MHz array is shown in Figure 13.6. If an imaging system is used to drive a number of elements, a flat plate can be used; however, a more sensitive test with this kind of excitation is a beamplot measurement.

13.3.3 Beamplots

A measure of how well an array operates with an imaging system is the beamplot test (Bamber and Phelps, 1977). This measurement is conducted in a water tank with fixturing that can align and translate either the transducer assembly or a needlelike or ball target along and near the acoustic axis of the beam. Provisions for alignment include *xyz* translation and rotational capabilities.

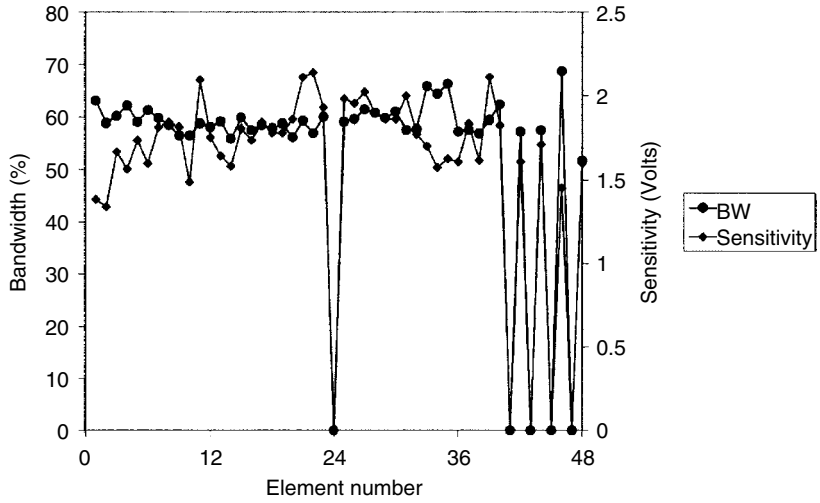

Figure 13.6 Automated sensitivity and bandwidth for a 30 MHz array. Element 24 and four elements on the end are open electrically (from Ritter *et al.*, 2002, IEEE).

Usually a selected feature of the waveform, such as peak-to-peak voltage, is determined and plotted versus the automatically stepped translation axis (Figure 13.7). It is common to normalize the beamplot to the largest value measured on-axis at the depth selected. Of particular interest are beam widths at different levels. Most commonly used levels are the −6-dB level, which is also known as full width half maximum (FWHM), and the −20- and −40-dB levels. The FWHM values are associated with resolution; the lower ones that are less than or equal to -40 dB, with contrast resolution. Beam data gathered in a plane are most often presented as a contour map with the contours representing decibel levels (as discussed in Chapter 6).

An imaging system can be used to focus and steer a beam along a chosen direction for measurement. Through the translation of the target (or transducer), a lateral beamplot can be acquired. The entire pulse-echo field can be mapped out by translating along the beam axis as well. However, this measurement can be time consuming. An alternate method to driving the transducer with an imaging system is to synthesize the appropriate delayed signals needed for focusing and steering with a programmable waveform generator, with appropriate switching to each element, and with the receive beamforming done in software; however, this can also be lengthy.

Another type of beamplot of interest for arrays is an element beamplot. As discussed in Chapter 7, individual elements have a wide directivity and govern off-axis sensitivity. Related to this directivity is cross-talk among elements (Larson, 1981). Examples of these measurements can be found in Ritter *et al.* (2002) and Davidsen and Smith (1993).

Beamplotting can be combined with other tests in an integrated automatic test station such as that described by Fisher (1983) in Figure 13.8. Although the equipment described is now out-of-date, the principles still hold. In this case, the beam-

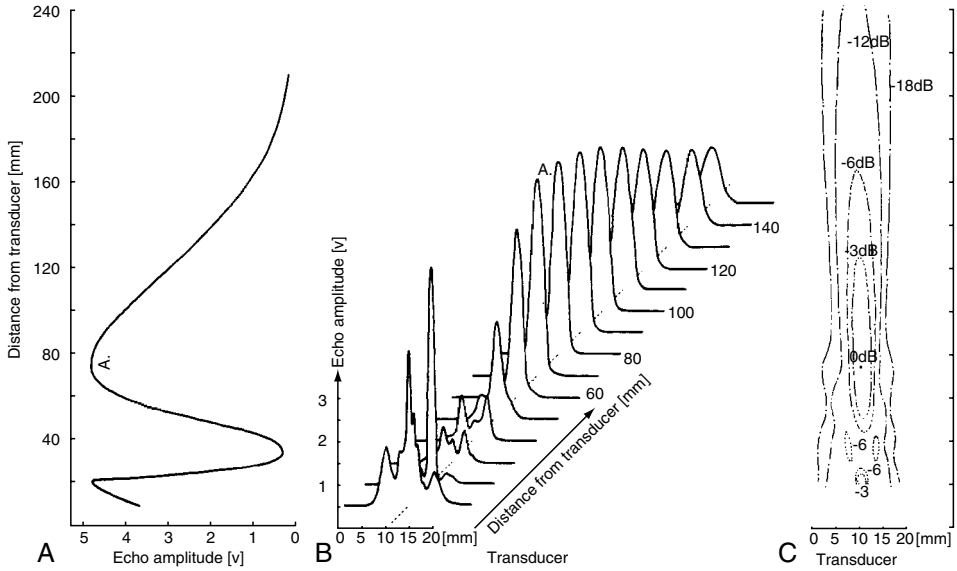

Figure 13.7 Acoustic field of a 1.5-MHz nonfocusing circular transducer as measured in beamplot tank. (A) Axial amplitude. (B) Lateral beamplots as function of depth. (C) Contour plot of field (reprinted from Bamber and Phelps, 1977, with permission from Elsevier).

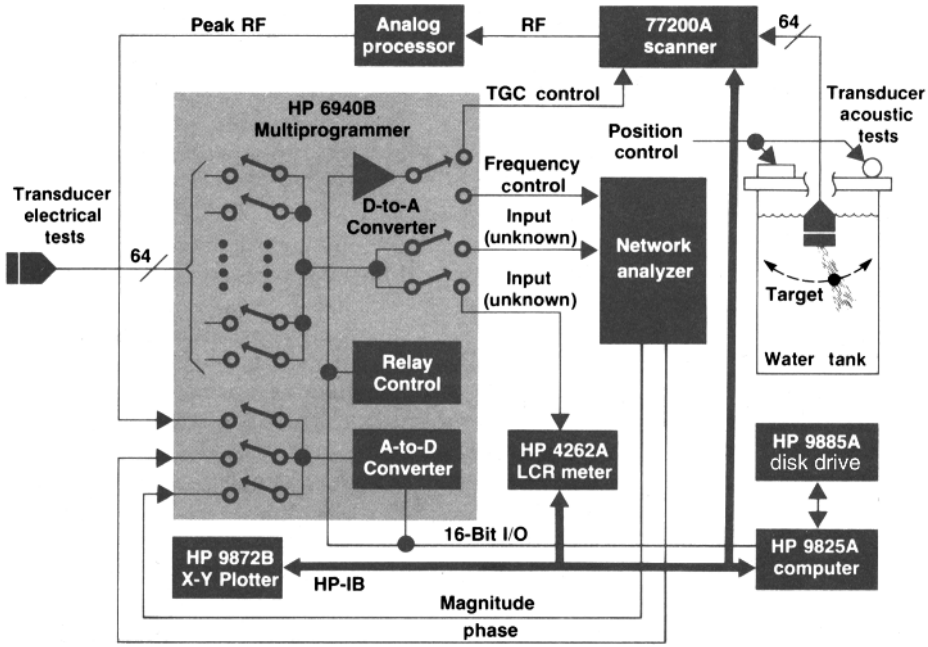

Figure 13.8 Automated transducer test station (from Fisher, 1983, reprinted by permission of Hewlett Packard).

forming capabilities of an imaging system can be evaluated for various modes and system settings.

For one-way beamplotting, a hydrophone can be used instead of a target. The spot size of the hydrophone must be much smaller than the beamwidth to be measured (Lum *et al*., 1996), as discussed in Section 13.4.2. A robust alignment method can be found in IEC 61828 (2001).

There is a much faster way of measuring beams from imaging systems. Beams can be evaluated in real time using a Schlieren system. Systems designed for this type of measurement include rapid scanning and a means of beam visualization (Hanafy *et al*., 1991). This method derives data from the deflections of laser light scattered by perturbations of the refractive index of water by the sound beam. In this case, the depiction of the beam at each point is a result of light passing perpendicularly through the beam, so an integrated value for the beam results. The Schlieren system can be synchronized with an imaging system so that continuous wave (CW) or pulsed wavefronts can be tracked in time along any selected vector direction (LeDet and Zanelli, 1999). Examples of Schlieren measurements are a CW visualization of a complete beam (shown in Figure 13.9) and a pulsed wavefront of a focused beam (shown in Figure 13.10).

13.4 ACOUSTIC OUTPUT MEASUREMENTS

13.4.1 Introduction

Measurements related to ultrasound-induced bioeffects have evolved into a branch of science with its own name: ''ultrasonic exposimetry.'' Three major types of measurements in this area are absolute pressure by hydrophones, absolute acoustic power by radiation force balances, and temperature rise by thermal sensing devices. All of these measurements are required for imaging systems in the United States, and there are limits on acoustic output regulated by the U.S. Food and Drug Administration (FDA). Additional measurements are described by various standards of International Electrotechnical Commission Technical Committees 62b and 87. Certain countries, such as Japan, have their own requirements. The rationale behind these measurements and regulations are discussed in more detail in Chapter 15 on bioeffects. Here we concern ourselves only with the measurements themselves.

There are many resources for these measurements; therefore, details and methodology can be found in the references and standards. A collection of topics can be found in Ziskin and Lewin (2000), a special issue of *IEEE Transactions on Ultrasonics, Ferroelectrics, and Frequency Control* (1988), and the *IEEE Guide for Medical Ultrasound Field Parameter Measurements* (1990). Measurement protocol and methods can be found in two American Institute of Ultrasound in Medicine/National Electrical Manufacturers Association documents (1998a, 1998b). In addition, Harris discusses the basic measurements (1985) and presents a more recent overview (1999). An overview of the equipment used for these measurements can be found in Ide and Ohdaira (1988).

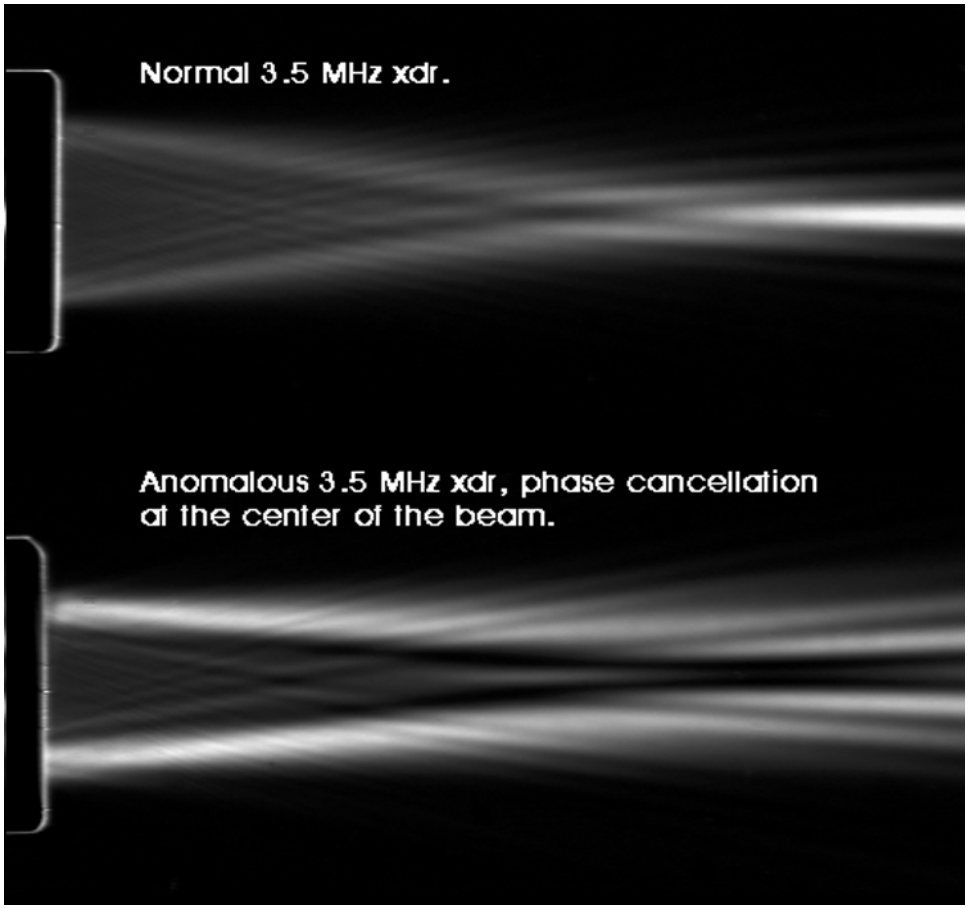

Figure 13.9 Measurements of CW beams with and without defects by an Onda Schlieren system (courtesy of C. I. Zanelli, Onda Corporation).

13.4.2 Hydrophone Characteristics

Hydrophones are a unique type of transducer intended to make nonperturbing, absolute measurements of pressure waves over an extremely wide bandwidth at an infinitesimally small spatial point. They are designed, in other words, to be as close as possible to ideal spatial point and time samplers in a water tank. The two most popular styles of hydrophones in use are the membrane and the needle (shown in Figure 13.11).

The membrane type consists of a thin sheet of the piezoelectric material PVDF stretched across a hoop a few centimeters in diameter and poled in its center to be piezoelectrically active in a small circular region, typically 0.2–1 mm in diameter. The membrane is so thin that it is practically transparent to waves in the normal imaging frequency range. Hydrophone transducers have a half-wave resonance

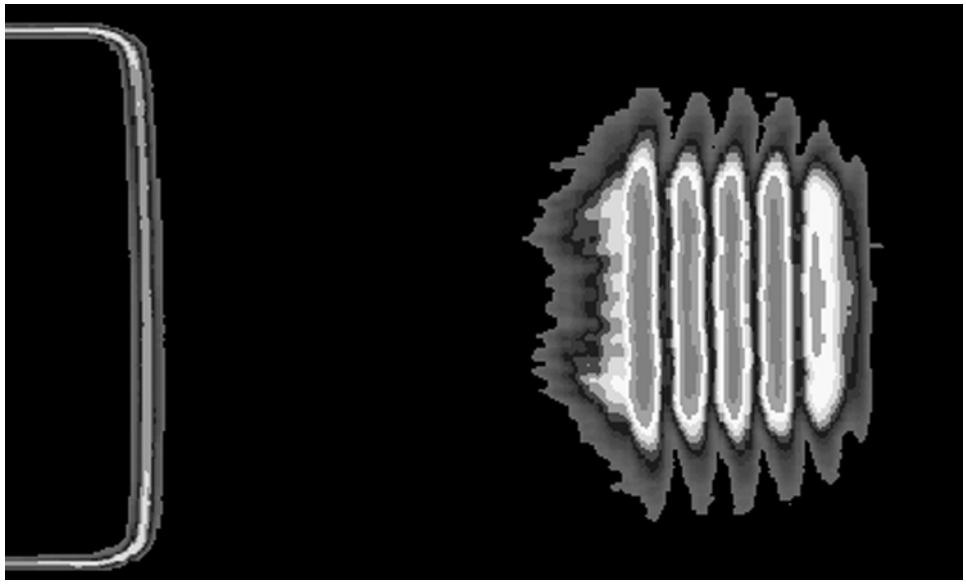

Figure 13.10 Measurement of a pulsed wavefront of a focused beam by an Onda Schlieren system (courtesy of C. I. Zanelli, Onda Corporation) (see also color insert).

frequency between 20 and 40 MHz, depending on their thickness (described in Chapter 5). Note that the speed of sound for PVDF is about 2 mm/μs, so for a 25-μm thick hydrophone, the center frequency is about 67 MHz. For the bilaminar design, which is immune to water conduction and radio frequency (RF) interference effects, two layers are used so that the center frequency is half that of one layer, or about 33 MHz. This resonance corresponds approximately to the one-way (receiver) frequency response shown in Figure 13.12 for 15-μm-thick bilaminar hydrophones. Note that with a matched compensated external amplifier, the overall hyrophone-amplifier response can be made flat over a nearly 30-MHz range.

The needle hydrophone (Lewin, 1981) is a compact broad-bandwidth device on the order of 1 mm in diameter with good directivity. This transducer is also a half-wave resonator.

While the low-frequency response is flat (between 1 and 10 MHz in the range for most diagnostic imaging transducers), the low-frequency response, which depends on the diameter of the hydrophone, it is not smooth. The needle hydrophone has an advantage over the membrane-style hydrophone in that it can be used for *in situ* exposure measurements in the body and in many other applications where limited accessibility is a problem. Although needle hydrophones have become primary hydrophones in many laboratories, membrane hydrophones have become more prevalent for acoustic output measurements because of their reliability and relatively flat frequency response over the range necessary for imaging transducers.

In order to qualify as absolute pressure sensors, hydrophones must be kept in calibration. This is usually done at a national standards laboratory or similar service.

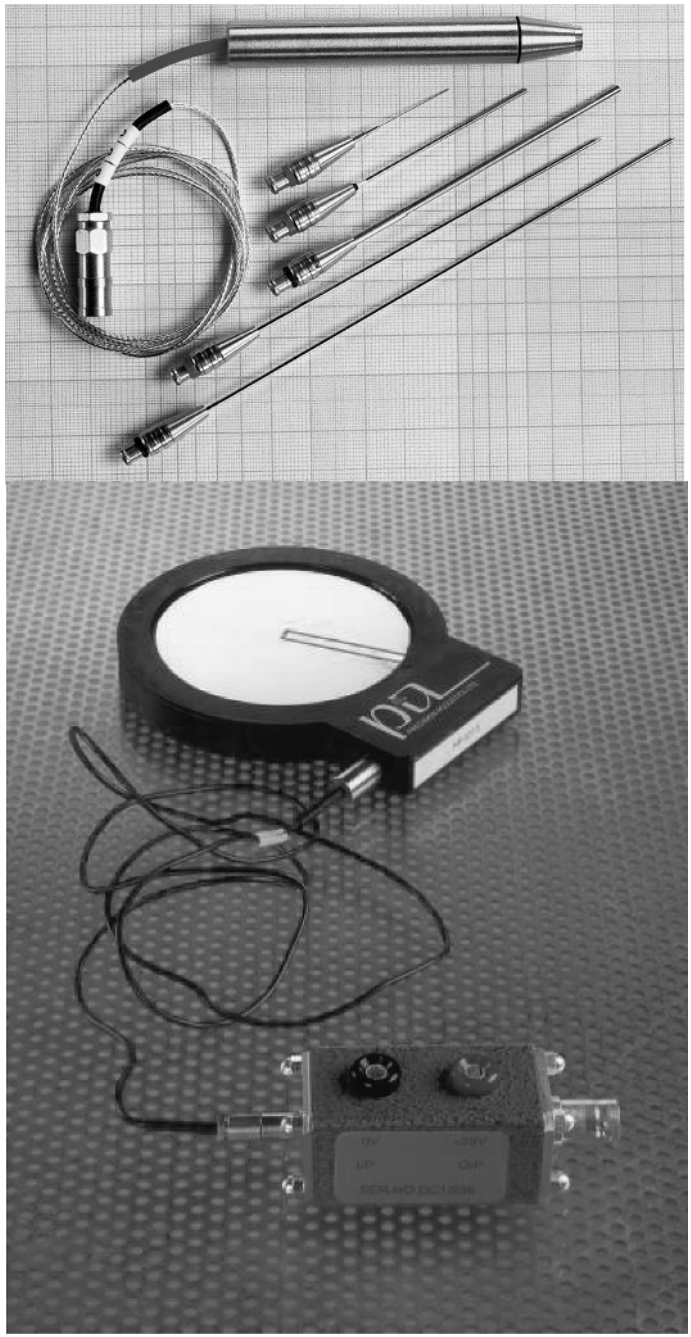

Figure 13.11 (Top) Needle hydrophone. (Bottom) Bilaminar membrane hydrophone and external amplifier (courtesy of D. Bell, Precision Acoustics Ltd.).

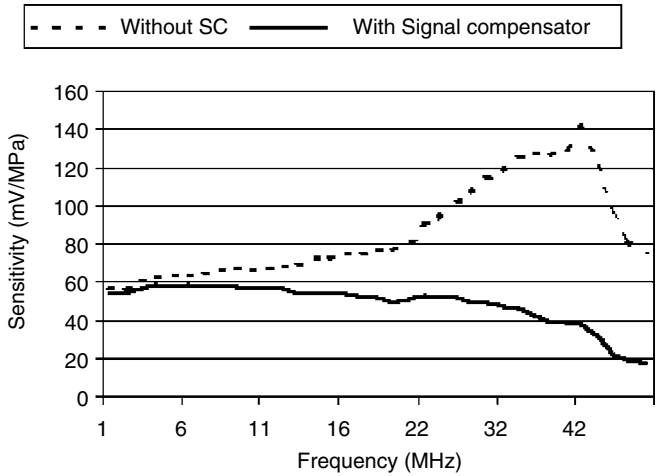

Figure 13.12 Sensitivity curves for bilaminar membrane hydrophones with and without compensating external amplifiers (courtesy of D. Bell, Precision Acoustics Ltd.).

Hydrophone sensitivity (one-way response) is often expressed as the end of cable sensitivity, M_L (volts/megaPascal), which includes the hydrophone, an associated amplifier, and a cable specified for a load impedance (usually 50 ohms). Sensitivity is also given in terms of decibels are 1 $\mu v/Pa$ from the relation,

$$G = 20 \log_{10} (M_L/M_{REF}) \tag{13.3}$$

where $M_{REF} = 1\mu v/Pa$ and *Pa* stands for Pascal, a unit of pressure.

Another important aspect of a hydrophone is its directional characteristics. Typically, the directivity of a hydrophone is similar to that of a piston source, which varies with frequency (as described in Chapter 6) and is imbedded in a hard baffle (see Section 7.7). One goal of hydrophone measurement is to adequately sample the acoustic field of an imaging transducer with enough spatial resolution. The International Electrotechnical Commission Technical Committee 87 criterion for ''enough resolution'' is for the maximum effective hydrophone radius ($b_{\max}$) to be

$$b_{\max} = \frac{\lambda}{4}\left[(l/2a)^2 + 0.25\right]^{1/2} \tag{13.4}$$

in which a is the transducer radius or equivalent dimension, λ is wavelength in water, and l is the axial distance between the transducer and hydrophone. In other words, the higher the center frequency of the transducer, the smaller the spot size has to be. As an example, consider a 20-MHz transducer with a diameter of 6.35 mm ($2a$) and a focal length of 19 mm (l); this case gives a value of $b_{\max} = 57\,\mu$m. In order to show the effect of not having a small enough spot size, the field of this 20 MHz focusing transducer was measured in its geometric focal plane by a hydrophone with a 500-μm spot diameter and another with a spot size on the order of 40 μm (Lum *et al.*,

1996). Data are compared to the theoretically expected beam-shape (a sinc function from Chapter 6) in Figure 13.13. Note that for this extreme case, the hydrophone with the spot size that is larger than the previous requirement averages over the beam. Note that the smaller hydrophone captures the beam well and meets the criteria of Eq. (13.4) (compared to theory).

The wide bandwidth of hydrophones is necessary to capture the harmonics associated with beam propagation through water, which is highly nonlinear (as discussed in Chapter 12). Waveforms and spectra for the two hydrophones are shown in Figure 13.14. The first hydprohone in this comparison is bilaminar and has a resonance of 33 MHz; the second hydrophone, an experimental research hydrophone made at a Hewlett Packard research laboratory with a single film thickness of 4 μm, has a bandwidth approaching 200 MHz, and is not commercially available (Lum *et al*., 1996). The wider bandwidth device shows almost 40 harmonics.

13.4.3 Hydrophone Measurements of Absolute Pressure and Derived Parameters

A tank setup for making hydrophone measurements is illustrated in Figure 13.15 (Lewin and Schafer, 1988). Either the transducer under test or the hydrophone is held fixed, the other is aligned along the acoustic axis, and the separation between the two along the axis is varied. These adjustments require x, y, and z translation, as well as rotation.

Measurements are most often made along the acoustic propagation axis z in order to extract waveform features. These features are derived or calculated from the pressure waveform, $p(t)$, in water as transmitted by the imaging system and its transducer operating in a particular mode. Note that it is really the hydrophone voltage, $v(t)$, that is measured and converted to a pressure waveform by dividing it by the appropriate sensitivity constant corresponding to the acoustic working frequency, f_{awf}, of the spectrum of the voltage waveform, $p = v/M_L$.

To meet U.S. regulations and the international standard IEC Standard 60601-2-37, a number of parameters are derived from the original pressure waveform data by imaging system manufacturers. Measurement details can be found in Harris (1985) and AIUM/NEMA (1998a). The data are reported to the FDA and are also measured and tabulated according to standards issued by the IEC. Acoustic output data are also used by algorithms within imaging systems to calculate output display indices, as prescribed by the output display standard (AIUM/NEMA, 1998b) and the international standard IEC Standard 60601-2–37 (2002) (both described in Chapter 15). To find maximum values of the derived parameters for the many different modes of an imaging system can be a challenging task (Szabo *et al*., 1988), as described in Chapter 15.

The major derived features are the following:

pulse pressure squared integral,

$$PPI(z) = \int_0^T p^2(t, z)dt = \int_0^T v^2(t, z)/M_L^2 dt \tag{13.5}$$

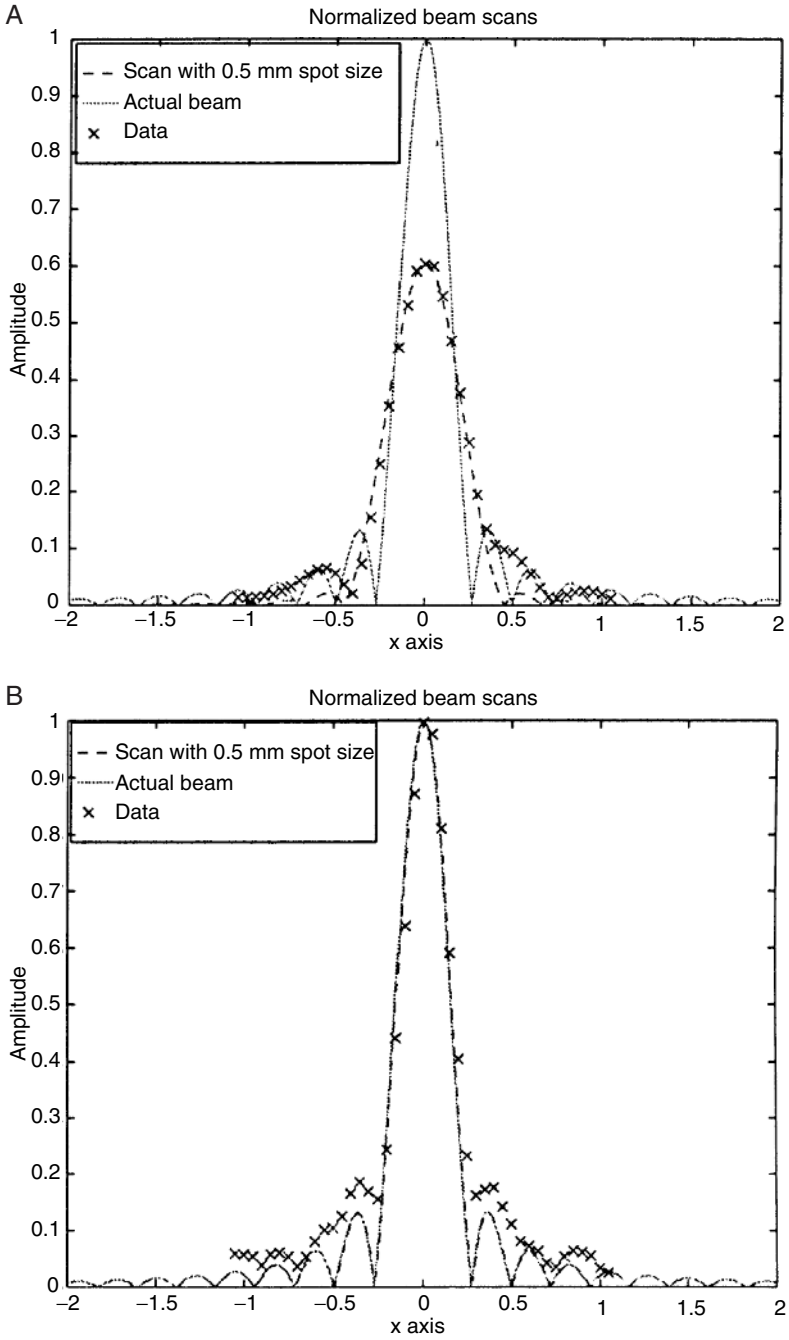

Figure 13.13 Linear scans of a 20-MHz focusing transducer with two membrane hydrophones. (A) 500-μm diameter. Each data point is shown by an x, and dashed lines connect them; dotted lines give the actual ideal beam-plot. (B) 37-μm diameter (from Lum *et al.*, 1996, *IEEE*).

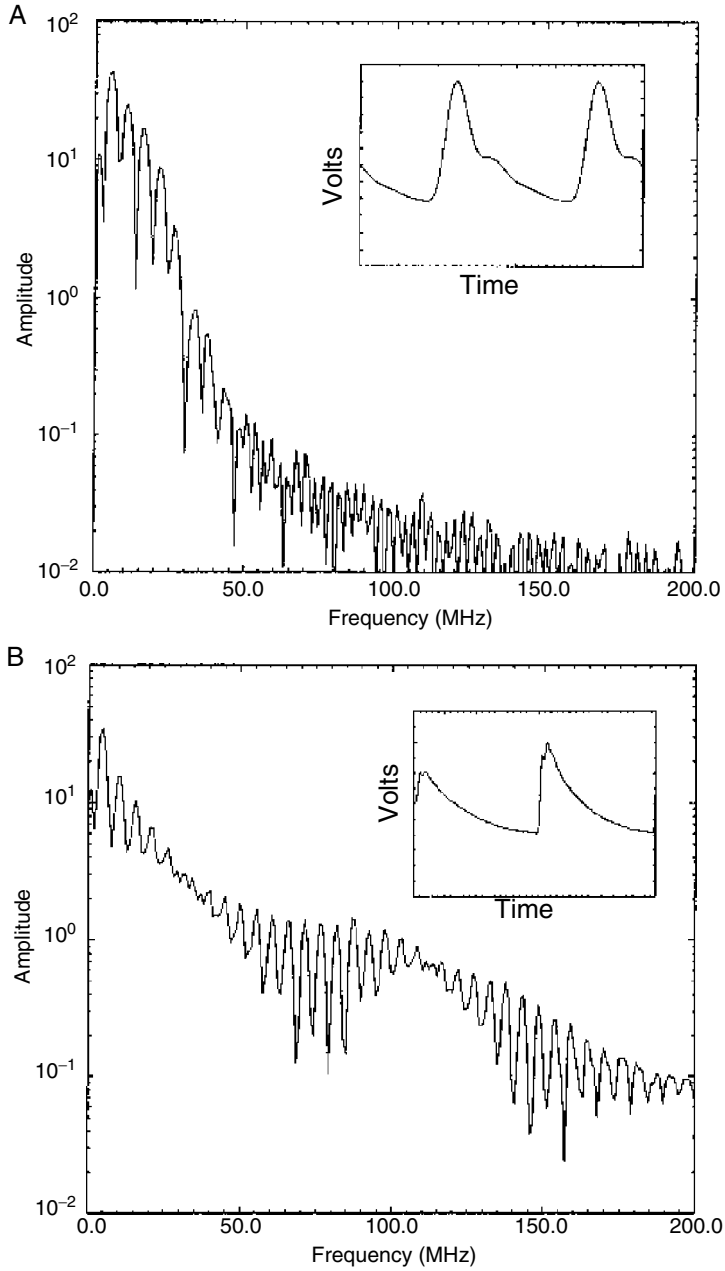

Figure 13.14 Waveforms (insets) and spectra for a 5-MHz fundamental source as measured by two membrane hydrophones. (A) 500-μm diameter. (B) 37-μm diameter (from Lum *et al.*, 1996, *IEEE*).

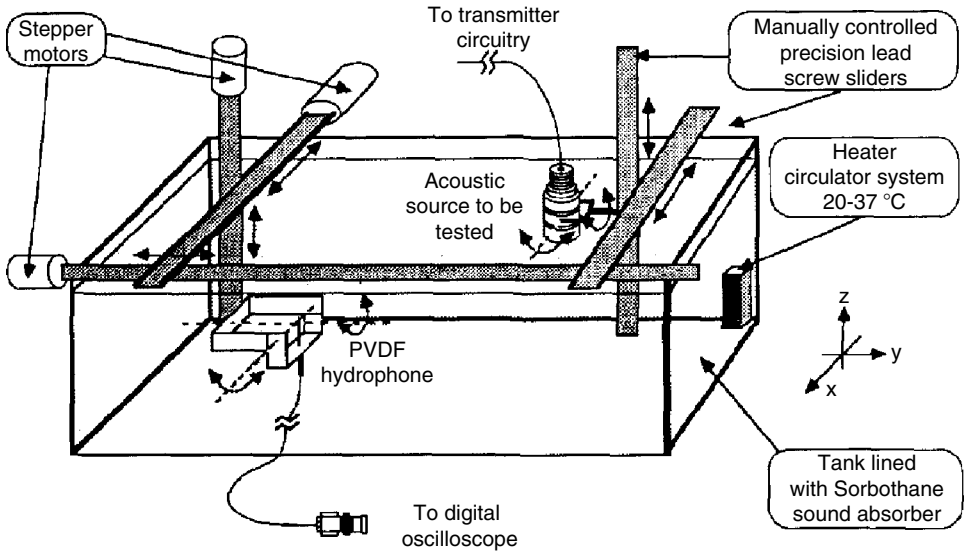

Figure 13.15 Water tank for hydrophone measurements (from Lewin and Schafer, 1988, *IEEE*).

pulse intensity integral

$$PII = PPI/(\rho c) \tag{13.6}$$

where ρ is the density of water, c is the speed of sound in water, and the pressure and particle velocity are assumed to be in phase;

spatial peak temporal average intensity,

$$I_{SPTA} = MAX\left[\int_0^{T_{PRF}} v^2(t, z)dt/(M_L^2 \rho c T_{PRF})\right] = MAX[PII(z)/T_{PRF}] \tag{13.7}$$

measured at the location of the maximum or highest value of intensity on acoustic axis z, and T_{PRF} is the time interval between pulses;

peak rarefactional pressure,

$$p_r = v_-/M_L \tag{13.8}$$

where v_- is the minimum negative peak voltage in a waveform corresponding to rarefactional pressure (see Chapter 12 for more on nonlinear waveform distortion). The spatial peak spatial average intensity (I_{SPPA}) is defined as the spatial peak instantaneous intensity averaged over the 10–90% intensity pulse duration; however, this parameter is no longer used.

All these water values have derated counterparts denoted by the subscript "0.3." The concept of *in situ* or derated values was introduced as a conservative estimate of the overall effects of average soft tissue absorption; it was not intended to be a realistic

description of any particular type of tissue. The derating is a 0.3-dB/MHz-cm factor applied to intensities, corresponding to a linear factor of exp $(-0.069 f_c z)$, in which z is the on-axis distance from the transducer in centimeters, and f_c is the transducer center frequency in MHz. More recently, acoustic working frequency, the −3-dB mean frequency, is used instead of center frequency. Values of pressure measured in water are converted into intensity (related to pressure squared) and are derated by *in situ* exponential derating factors, which are exp $(-0.069 f_c z)$ for intensity

$$I_{SPTA.3}(z) = MAX[I_{SPTA}(z) \exp(-0.069 f_c z)] \tag{13.9}$$

As an example, I_{SPTA} and $I_{SPTA.3}$ are plotted along the z axis for a 2.5-MHz center frequency transducer in Figure 13.16. In the top of Figure 13.16, the I_{SPTA} water value curves in dB are shown for a rectangular array for coincident and noncoincident foci. Also shown on a dB scale is the derating factor. When the derating factor line is subtracted (in dB) from these curves (the equivalent of linear multiplication), the derated values of I_{SPTA} result as shown in the bottom of the figure. Note that for the noncoincident case, the derating process moves the peak closer to the transducer. For pressure, the derating is exp $(-0.0345 f_c z)$; a plot of derated pressure is given in Figure 14.6.

13.4.4 Force Balance Measurements of Absolute Power

A force balance is a sensitive instrument for measuring the acoustic radiation force exerted by an acoustic field (as described in Chapter 12). This force is a result of energy transfer to an ideal absorbing target. The relation is

$$W = gF \tag{13.10}$$

Where F is the radiation force on an ideal absorber, W is time average acoustic power, and g is a constant determined by calibration. In general, for an angle θ between the beam axis and the normal of the reflecting surface,

$$W = gF/2 \cos^2 \theta \tag{13.11}$$

The most common types of force balances are shown in Figure 13.17. The most popular type is on the left, and it consists of an absorbing target suspended from a microbalance. A thin membrane is usually used to separate the water enclosing the target from the face of the transducer. Ultrasound is directed upward, and the radiation force displaces the absorbing target. Because the target is delicately balanced, its movement is sensed by a microbalance that provides a digital reading. This reading is translated into time average power from Eq. (13.10) above. The constant g in this equation is determined through calibration methods as a function of frequency by using sources with known power outputs.

13.4.5 Measurements of Temperature Rise

The primary thermal measurement carried out for safety is determining the surface temperature of transducers in air or tissue-mimicking material. When a transducer is

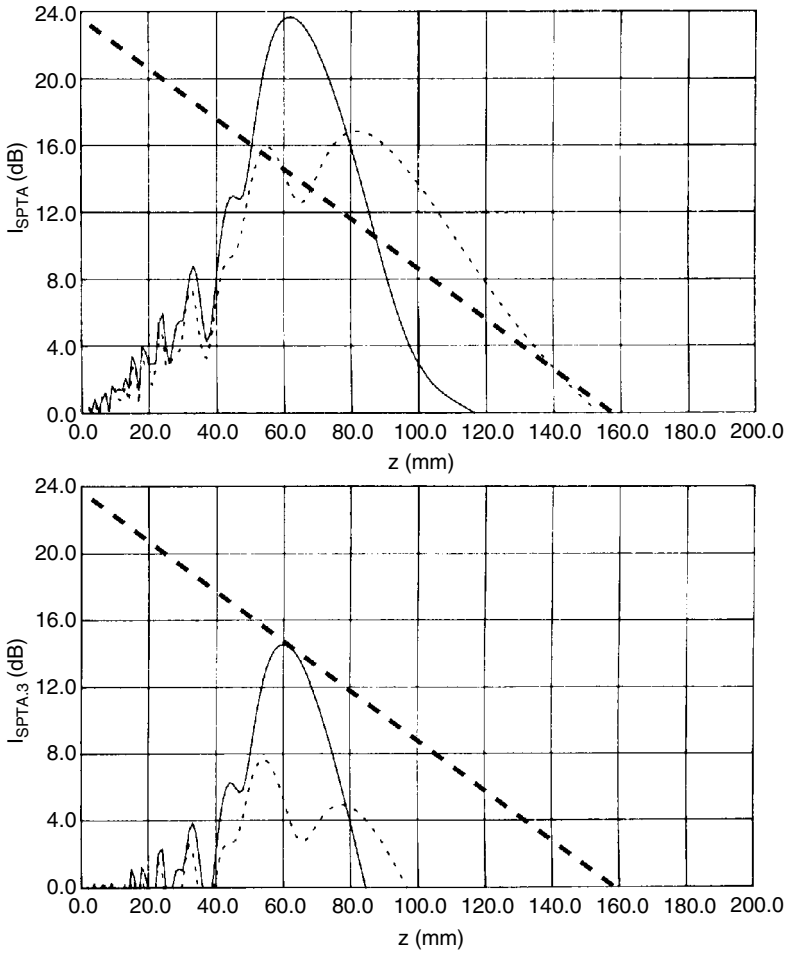

Figure 13.16 (Top) I_{SPTA} curves in water versus acoustic axis *z* for a rectangular array with a coincident azimuth and elevation (peaked curve) and a noncoincident case along with *in situ* derating factor (shown as dashed line). (Bottom) Derated I_{SPTA} curves along with derating factor (dashed line).

not in contact with the body, most of its acoustic power is reflected at the elevation lens—air interface; consequently, its acoustic output is turned inward, which results in an effect called self-heating. The net outcome is that the outer surface of a transducer heats up slightly. This temperature rise is measured with a thermocouple for different operating modes, as described in IEC Standard 60601-2-37 (2002), to ensure that the rise does not exceed a prescribed limit. Certain probes that are inserted in the body have a smaller allowable rise and often have a cutoff mechanism should the internal temperature rise exceed this limit (Ziskin and Szabo, 1993).

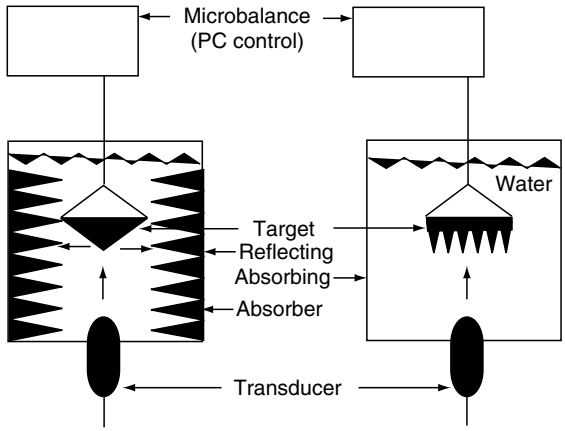

Figure 13.17 Types of radiation force balances: (A) reflecting absorbing target, (B) direct absorbing target.

Temperature rises are also associated with an acoustic beam propagating in an absorbing medium. For a transducer producing an acoustic field with a local time average intensity, $I(x, y, z)$, the local heat of a wave in this field in an absorbing medium with an absorption coefficient α is

$$q = 2\alpha I \tag{13.12}$$

where q is the time rate of heat production per unit volume. The temperature rise is most often measured by a thermocouple. Except for initial viscous thermocouple effects, the temperature rise (τ) is

$$\frac{d\tau}{dt} = \frac{q}{C_H} = \frac{2\alpha I}{C_H} \tag{13.13}$$

where C_H is the heat capacity per unit volume. Thermocouples are embedded in an absorbing medium, often a tissue-mimicking phantom, for this type of measurement. Special layered phantoms have been made to simulate the thermal properties of different parts of the human body (Wu *et al.*, 1995; Shaw *et al.*, 1999). Effects of blood perfusion and cooling, as well as acoustic streaming, are not usually included in these phantoms, but they will be discussed in Chapter 15.

13.5 PERFORMANCE MEASUREMENTS

There are several primitive ways in which the performance of an imaging system can be tested. The modes most often evaluated are B-mode imaging, Doppler, and color flow imaging (CFI) by the use of special purpose phantoms.

The most common imaging objects are tissue-mimicking phantoms with various targets embedded in them. An example of an imaging phantom was displayed in

Figures 8.1 and 8.2. Note that resolution can be determined from the filament point targets, cyst fill-in by the circular scatter-free objects, and contrast by the column of circular objects filled with varying densities of small scatterers. Related forms of imaging phantoms are the Cardiff step phantom and contrast phantoms consisting of objects that have different densities of scatterers relative to a host matrix material. Other forms of imaging phantoms, such as a breast phantom, provide a more realistic imaging object. Imaging performance measurements on a more universal basis (system to system) can be quite involved because the entire image processing chain (described in Chapter 10) has to be accounted for, calibrated, or compensated for in the process of image evaluation. Methodology can be found in standards (IEC; AIUM, 1990) and guidelines.

Phantoms designed for Doppler and CFI testing are called "flow phantoms." They consist of tubing and a pump through which a scattering fluid is circulated at user variable rates. A less expensive method is a "string" phantom in which a cord is moved at controlled rates. The velocity of the flow of fluid or the string is independently known and can be compared to the values produced by the imaging system.

13.6 THOUGHT EXPERIMENTS

The function of different types of measurements changes through the design cycle of system improvement or a new device such as a transducer. First, many measurements are made during the design phase to explore the effect of new materials and design prototypes. Second, the design is refined and tested for clinical efficacy and robustness from manufacturing, environmental, and safety perspectives. Finally, a number of devices of the final design are made in a production environment to evaluate the consistency of the manufacturing process and acoustic output with statistics.

Along the way, accurate simulation programs can be applied to the initial design, device diagnosis, and design refinement (finding causes of unwanted second-order effects and then reducing them). Simulation programs guide the design process and provide sanity checks and reference points with which measurements can be compared; they can also speed up the process by predicting and eliminating designs that are unsuitable and never built. Modeling programs range from first-order transducer design, finite element modeling, beamforming, signal processing and filtering, system level performance, and nonlinear acoustic output prediction.

BIBLIOGRAPHY

Larson, J. D. (1981). Non-ideal radiators in phased array transducers. *IEEE Ultrason. Symp. Proc.*, 673–683.

Schafer, M. E. and Lewin, P. A. (1988). A computerized system for measuring the acoustic output from diagnostic ultrasound equipment. *IEEE Trans. Ultrason. Ferroelec. Freq. Control* **35**, 102–109.

Wu, J. (1996). Determination of velocity and attenuation of shear waves using ultrasonic spectroscopy. *J. Acoust. Soc. Am.* **99**, 2871–2875.

References

American Institute of Ultrasound in Medicine. (July 13, 1990). *Standard Methods for Measuring Performance of Pulse-Echo Ultrasound Imaging Equipment*. AIUM Publications, Laurel, MD.

American Institute of Ultrasound in Medicine/National Electrical Manufacturers Association (AIUM/NEMA). (1998a). *Acoustic Output Measurement Standard for Diagnostic Ultrasound Equipment*. AIUM Publications, Laurel, MD.

AIUM/NEMA. (1998b). *Standard for Real-Time Display of Thermal and Mechanical Acoustic Output Indices on Diagnostic Ultrasound Equipment*. Revision 1. AIUM Publications, Laurel, MD.

Bamber, J. C. (1986). *Physical Principles of Medical Ultrasonics*. C. R. Hill, (ed.). John Wiley & Sons, Chichester, UK, pp. 118–199.

Bamber, J. C. (1998). Ultrasonic properties of tissue. In *Ultrasound in Medicine*. F. A. Duck, A. C. Baker, and H. C. Starritt (eds.). Institute of Physics Publishing, Bristol, UK.

Bamber, J. C. and Phelps, (1977) The effective directivity characteristic of a pulsed ultrasound transducer and its measurement by semi-automatic means, *Ultrasonics* **15**, 169–174.

Davidsen, R. E. and Smith, S. W. (1993). Sparse geometries for two-dimensional array transducers in volumetric imaging. *IEEE Ultrason. Symp. Proc*., 1091–1094.

Fisher, G. A. (1983). Transducer test system design. *Hewlett Packard J*. **34**, 24–25.

Freiburger, P. D., Sullivan, D. C., LeBlanc, B. H., Smith, S. W., and Trahey, G. E. (1992). Two dimensional ultrasonic beam distortion in the breast: In vivo measurements and effects. *Ultrason. Imag*. **14**, 398–414.

Hanafy, A., Zanelli, C. I., and McAvoy, B. R. (1991). Quantitative real-time pulsed Schlieren imaging of ultrasonic waves. *IEEE Ultrason. Symp. Proc*., 1223–1227.

Harris, G. R. (1985). A discussion of procedures for ultrasonic intensity and power calculations from miniature hydrophone measurements. *Ultrasound in Med. & Biol*. **11**, 803–817.

Harris, G. R. (1999). Medical ultrasound exposure measurements: Update on devices, methods, and problems. *IEEE Ultrason. Symp. Proc*. 1341–1352.

He, P. (1999). Experimental verification of models for determining dispersion from attenuation. *IEEE Trans. Ultrason. Ferroelec. Freq. Control* **46**, 706–714.

Hinkelman, L. M., Liu, D.-L., Metlay, L. A., and Waag, R. C. (1994). Measurements of ultrasonic pulse arrival time and energy level variations produced by propagation through abdominal wall. *J. Acoust. Soc. Am*. **95**, 530–541.

Hinkelman, L. M., Szabo, T. L., and Waag, R. C. (1997). Measurements of ultrasonic pulse distortion produced by human chest wall. *J. Acoust. Soc. Am*. **101**, 2365–2373.

Ide, M. and Ohdaira, E. (1988). Measurement of diagnostic electronic linear arrays by miniature hydrophone scanning. *IEEE Trans. Ultrason. Ferrolec. Freq. Control* **35**, 214–219.

IEC Standard 61828. (2001). *Ultrasonics: Focusing Transducers Definitions and Measurement Methods for the Transmitted Fields*. International Electrotechnical Commission, Geneva, Switzerland.

IEC Standard 60601-2-37 (2002). *Medical Electrical Equipment, Part 2: Particular Requirements for the Safety of Ultrasonic Medical Diagnostic and Monitoring Equipment*. International Electrotechnical Commission, Geneva, Switzerland.

IEEE Guide for Medical Ultrasound Field Parameter Measurements. (June 29, 1990). IEEE Standard 790–1989.

IEEE Trans. Ultrason. Ferroelec. Freq. Control 35, (March 1988). Special issue on ultrasonic exposimetry.

IEEE Standard on 176–1987 Piezoelectricity. (Jan. 1, 1987).

Jansson, T. T., Mast, T. D., and Waag, R. C. (1998). Measurements of differential scattering cross section using a ring transducer. *J. Acoust. Soc. Am.* **103**, 3169–3179.

LeDet, E. G. and Zanelli, C. I. (1999). A novel, rapid method to measure the effective aperture of array elements. *IEEE Ultrason. Symp. Proc.*, 1077–1080.

Lewin, P. A. (1981). Miniature piezoelectric polymer ultrasonic hydrophone probes. *Ultrasonics*, 213–216.

Lewin, P. A. and Schafer, M. R., (1988). A computerized system for measuring the acoustinc output from diagnostic ultrasound equipment. *IEEE Trans. Ultrason. Ferro Freq Contr* **35**, 102–109.

Liu, D.-L. and Waag, R. C. (1998). Estimation and correction of ultrasonic wavefront distortion using pulse-echo data received in a two-dimensional aperture. *IEEE Trans. Ultrason. Ferroelec Freq. Control* **45**, 473–490.

Lum, P., Greenstein, M., Grossman, C., and Szabo, T. L. (1996). High frequency membrane hydrophone. *IEEE Trans. Ultrason. Ferroelec. Freq. Control* **43**, 536–543.

Mottley, J. G. and Miller, J. G. (1988). Anisotropy of the ultrasonic backscatter of myocardial tissue, Part I: Theory and measurements in vitro. *J. Acoust. Soc. Am.* **85**, 755–761.

Nassiri, D. K. and Hill, C. R. (1986). The use of angular acoustic scattering measurements to estimate structural parameters of human and animal tissues. *J. Acoust. Soc. Am.* **79**, 2048–2054.

Powell, D. J., Wojcik, G. L., Desilets, C. S., Gururaja, T. R., Guggenberger, K., Sherrit, S., and Mukherjee, B. K. (1997). Incremental "model-build-test" validation exercise for a 1-D biomedical ultrasonic imaging array. *IEEE Ultrason. Symp. Proc.* 1669–1674.

Ritter, T., Geng, X., Shung, K. K., Lopath, P. D., Park, S.-E., and Shrout, T. R. (2000). Single crystal PZN/PT-polymer composites for ultrasound transducer applications. *IEEE Trans. Ultrason. Ferroelec. Freq. Control* **47**, 792–800.

Ritter, T. A., Shrout, T. R., Tutwiler, R., and Shung, K. K. (2002). A 30-MHz piezo-composite ultrasound array for medical imaging applications. *IEEE Trans. Ultrason. Ferroelec. Freq. Control* **49**, 217–230.

Selfridge, A. R. (1985). Approximate material properties in isotropic materials. *IEEE Trans. Sonics Ultrason.* **SU-32**, 381–394.

Selfridge, A. R., Kino, G. S., and Khuri-Yakub, R. (1980). Fundamental concepts in acoustic transducer array design. *IEEE Ultrason. Symp. Proc.*, 989–993.

Shaw, A., Pay, N., Preston, R. C., and Bond, A. (1999). A proposed standard thermal test object for medical ultrasound. *Ultrasound in Med. & Biol.* **25**, 121–132.

Szabo, T. L. (1982). Miniature phased-array transducer modeling and design. *IEEE Ultrason. Symp. Proc.*, 810–814.

Szabo, T. L. (1993). *Linear and Nonlinear Acoustic Propagation in Lossy Media*, Ph. D. thesis. University of Bath, Bath, UK.

Szabo, T. L., Melton Jr., H. E., and Hempstead, P. S. (1988). Ultrasonic output measurements of multiple mode diagnostic ultrasound systems. *IEEE Trans. Ultrason. Ferroelec. Freq. Control* **35**, 220–231.

Waters, K. R., Hughes, M. S., Mobley, J., Brandenburger, G. H., and Miller, J. G. (2000). On the applicability of Kramers-Kronig relations for ultrasonic attenuation obeying a frequency power law. *J. Acoust. Soc. Am.* **108**, 556–563.

Wu, J. (1996). Effects of nonlinear interaction on measurements of frequency dependent attenuation coefficients. *J. Acoust. Soc. Am.* **99**, 3380–3384.

Wu, J. (2001). Tofu as a tissue-mimicking material. *Ultrasound in Med. & Biol*. **27**, 1297–1300.

Wu, J., Cubberley, F., Gormley, G., and Szabo, T. L. (1995). Temperature rise generated by diagnostic ultrasound in a transcranial phantom. *Ultrasound in Med. & Biol*. **21**, 561–568.

Zeqiri, B. (1988). An intercomparison of discrete-frequency and broad-band techniques for the determination of ultrasonic attenuation. In *Physics in Medical Ultrasound*. D. H. Evans and K. Martin, (eds.). IPSM, London, pp. 27–35.

Zhu, Q. and Steinberg, B. D. (1992). Large-transducer measurements of wave-front distortion in the female breast. *Ultrason. Imag*. **14**, 276–299.

Ziskin, M. C. and Lewin, P. A. (eds.) (2000). *Ultrasonic Exposimetry.* CRC Press, Inc., Boca Rotan, FL.

Ziskin, M. C. and Szabo, T. L. (1993). Impact of safety considerations on ultrasound equipment and design and use, Chap. 12. In *Advances in Ultrasound Techniques and Instrumentation*. P. N. T. Wells (ed.). Churchill Livingstone, New York.

This page intentionally left blank

14 ULTRASOUND CONTRAST AGENTS

Chapter Contents

14.1 INTRODUCTION

Many of us are already familiar with the concept of contrast agents. For example, you may have heard about or experienced a test in which mildly radioactive liquids are

ingested or injected to light up the digestive tract or blood vessels on x-rays or computed tomography (CT) scans.

The application of contrast agents to ultrasound is comparatively recent and is still under development. The first reported use of contrast agents by Gramiak and Shah (1968) led to the conclusion that increased reflectivity was caused by microbubbles of gas. Early pioneers in this area (Feigenbaum *et al*., 1970; Goldberg, 1971; Ziskin *et al*., 1972) helped establish techniques useful for cardiac irregularities such as shunts, leaky valves, and visualization of larger vessels and chambers. These methods were limited by the large size and short life of bubbles that could be produced (Meltzer *et al*., 1980). In the 1980s, research on deliberately designed contrast agents (Ophir and Parker, 1989; Goldberg, 1993) began to show promise.

By the early 1990s, contrast agents were being manufactured and tested in early laboratory tests and clinical trials. Miller (1981) described an experiment for detecting the second harmonic of bubbles. Tucker and Wesby (1968) and Eatock (1985) proposed the nonlinear detection of nitrogen bubbles for decompression applications. Imaging contrast agents at the second harmonic was thought to improve contrast between agents and surrounding tissue that was believed to behave linearly at diagnostic pressure levels. Imaging system manufacturers and independent research led to the discovery of tissue harmonic imaging (THI), as described in Chapter 12. The nonlinear properties of contrast agents led not only to imaging at the second harmonic, but also to a number of other useful applications and advantages (to be discussed later).

Most present contrast agents are gas-filled, encapsulated microbubbles that are injected into the venous system to act as red blood cell tracers. By increasing reflectivity, contrast agents enhance echo amplitudes to improve sensitivity in deep absorbing tissues or in otherwise invisible small vessels. These bubbles have unusual properties in the presence of an ultrasound field. They are nonlinear resonators that, under certain conditions, can change size, cavitate, fragment, or be moved.

Sections 14.2 and 14.3 explain these physical characteristics of microbubbles in a sound field. Conditions for bubble destruction and cavitation are discussed in Section 14.4. The structure and properties of typical contrast agents are compared. Unusual characteristics of contrast agents (described in Section 14.5) have led to several new imaging methods (explained in Section 14.6) and signal processing methods. Well beyond their original intended applications, contrast agents also have potential in therapy, drug delivery, and the location of targeted sites (as explained in Section 14.7). Information about safety issues about contrast agents is treated in more depth in Chapter 15. Finally, equations of motion appropriate for bubble simulation will be presented in Section 14.8.

14.2 MICROBUBBLE AS LINEAR RESONATOR

The kinds of bubbles of interest are very small (with diameters on the order of μm) and are filled with gas. From the scattering theory of Chapter 8, to first

approximation, the scattering properties are those of a small sphere. Since wavelengths for diagnostic ultrasound range, 1−0.1 mm (1.5−15 MHz), are much larger than a bubble radius (a), and $ka \ll 1$, one might conclude that the bubble behaves like a Rayleigh scatterer. Using the Born approximation, Eq. (8.9a), de Jong (1993) compared the scattering cross section of an air bubble to an iron sphere. Both were in water and each had a radius of 1μm, and de Jong found that the air bubble had a cross section 100 million times greater than that of the iron sphere. The main contribution is not through the density term, but through the significantly different compressibility of the gas bubble. This equation also shows that the scattering cross section depends on the fourth power of frequency and the sixth power of the radius.

An air bubble, unlike the iron sphere, has a fragile, flexible boundary with enclosing fluid (water or blood). When insonified, the bubble expands and contracts with the rhythm of the compressional and rarefactional half cycles of the sound wave (as illustrated by Figure 14.1). Mechanically, the response of the bubble is controlled by the springlike stiffness of the entrapped gas and the inertia of the fluid pushing on the surface of the bubble. The balance between these competing factors can result in a resonant frequency,

$$f_r = \frac{1}{2\pi a}\sqrt{\frac{3\gamma_C P_0}{\rho}} \tag{14.1}$$

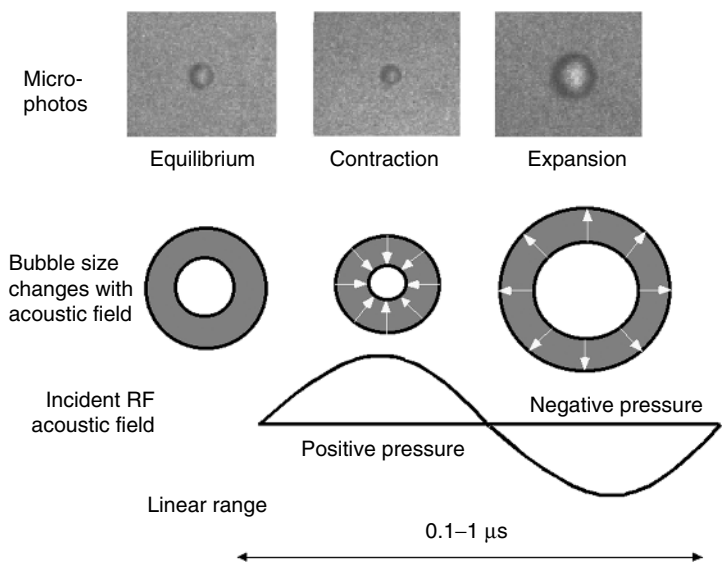

Figure 14.1 (Bottom) Symmetrical pacing of bubble expansion and compression with the compressional and rarefactional half cycles of an ultrasound wave. (Top) Measurement of this effect (adapted from P.G. Rafter, Philips Medical Systems; images from Dayton *et al.*, 1999a *IEEE*).

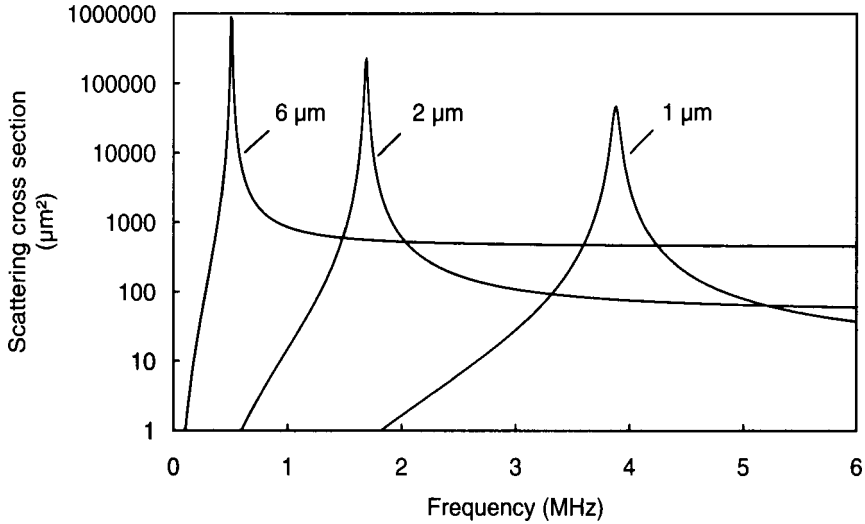

Figure 14.2 Scattering cross sections of ideal gas bubbles in lossless water as a function of frequency for three diameters: 1, 2, and 6 μm (from de Jong, 1993).

where a is the equilibrium bubble radius, $\gamma_C = C_p/C_v$ (ratio of heat capacities at constant pressure and constant volume), ρ is the density of the surrounding medium, and P_0 is the static pressure at the bubble surface. For small pressures (less than one atmosphere) on an air bubble in water (Leighton, 1994), $f_r(Hz) \approx 3/a(m)$. For example, for $a = 2\,\mu m$, $f_r = 1.5$ MHz.

The simple linear model of a bubble in a fluid is that of a damped harmonic oscillator. This resonator can be modeled by a series LC equivalent circuit (Blackstock, 2000) with an inductance representing acoustic mass, $L = \rho/(4\pi a)$, and a capacitance representing stiffness, $C = 4\pi a^3/(3\gamma_C P_0)$. The model can be refined by adding surface tension as well as a resistance for viscous and thermal losses (Anderson and Hampton, 1980; Leighton, 1994).

Calculations for an ideal gas bubble without losses (de Jong, 1993) are shown in Figure 14.2. Typical characteristics are a Rayleigh (f^4) frequency dependence below resonance and a nearly constant value equal to the physical cross section at frequencies much greater than resonance. At-resonance values for the cross section can be 1000 times greater than values predicted by the Born approximation.

14.3 MICROBUBBLE AS NONLINEAR RESONATOR

The previous analysis only holds for small forced vibrations. As pressure amplitude is increased, the bubble cannot keep up. For larger-amplitude sound fields, a bubble can expand with the sound field, but it cannot contract without limit because the volume of entrapped gas can only be compressed so far (as depicted in Figure 14.3). As a result of these differences, the pressure response of the bubble as a function of time becomes

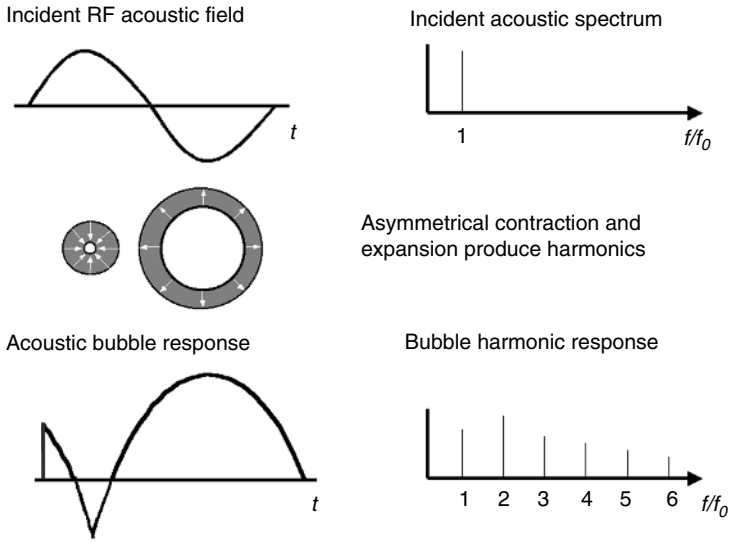

Figure 14.3 In higher-pressure incident sound fields, the microbubble response becomes nonlinear because compression is limited and shortened compared to expansion, leading to asymmetry and harmonics (courtesy of P. G. Rafter, Philips Medical Systems).

asymmetric. The corresponding harmonic response of an ideal bubble can be computed by a modified Rayleigh–Plesset equation (given in Section 14.8). Calculations for three bubble sizes and a 50-kPa pressure amplitude are shown in Figure 14.4; the asymmetric expansion and contraction of bubble size versus time is given on the left with the resulting harmonics on the right. Note that the frequency response is a function of both bubble size and the insonifying pressure amplitude.

14.4 CAVITATION AND BUBBLE DESTRUCTION

14.4.1 Rectified Diffusion

By itself, an air bubble will dissolve in a liquid; but under ultrasound insonification, it can resonate and grow under certain conditions. Since there is usually dissolved gas in a liquid outside a bubble, certain circumstances can cause this gas to be pumped into a bubble with help from a sound beam. Consider the bubble under compression depicted in Figure 14.3, where the pressure is high but the net surface area for gas to enter is small. During the expansion phase, the pressure is very low and creates a pressure gradient that draws outer dissolved gas into the bubble. Also, a large surface area is available for gas infusion. As the bubble grows, its minimum radius also grows. This process, called the ''area effect,'' tends to grow the bubble rapidly. A comparison of the shell thicknesses in the same figure indicates that the shell thickens on

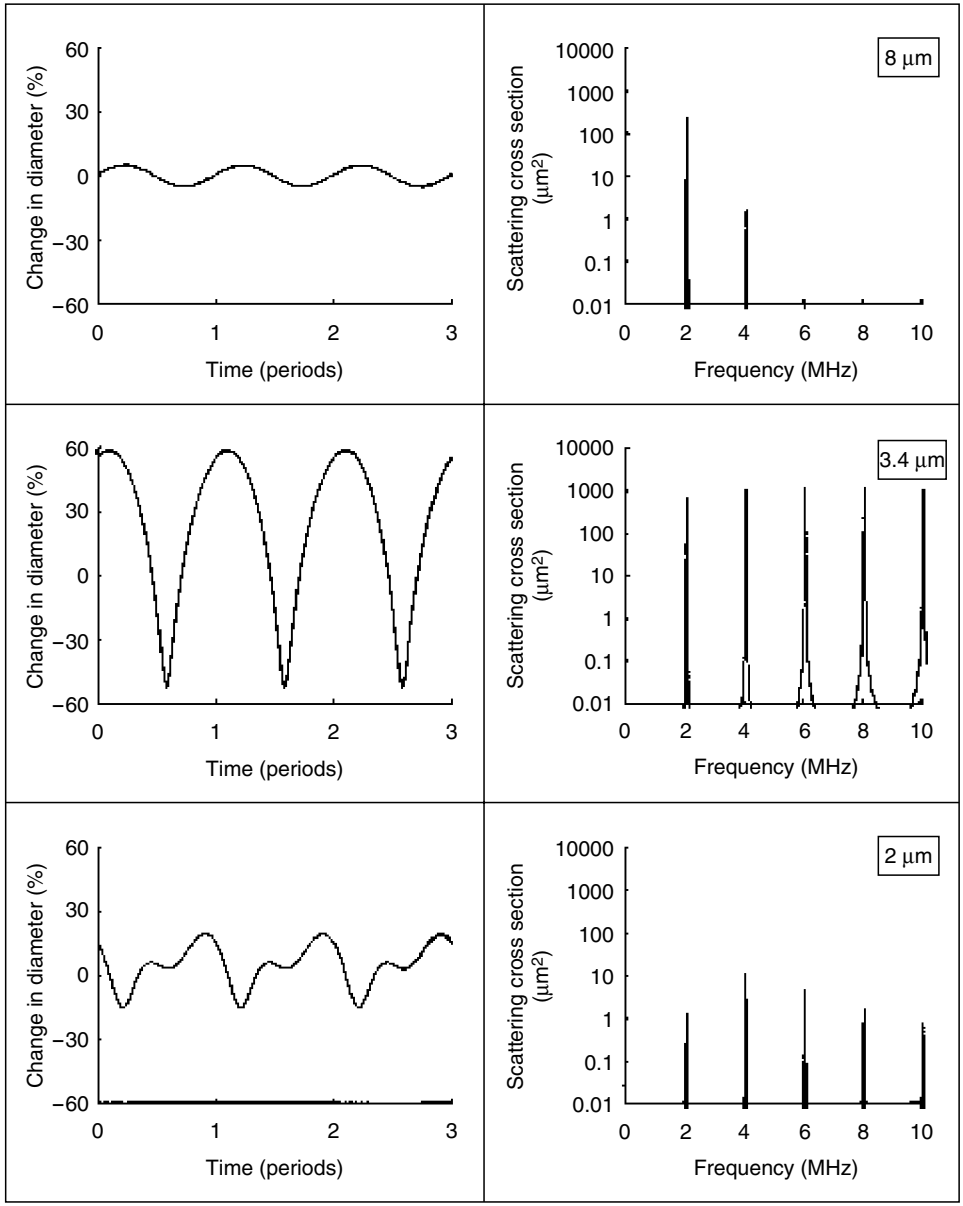

Figure 14.4 (Left panels) Simulated relative change in diameter of an ideal gas bubble in water for a sinusoidal excitation of 2 MHz and a pressure amplitude of 50 kPa for three bubble diameters: 6 μm (above resonance), 3.4 μm (resonance) and 2 μm (below resonance). (Right panels) Corresponding spectral responses (from de Jong, 1993).

compression and thins on expansion. These changes also enable more gases to enter the bubble and work in the same direction as the area effect to increase the bubble size rapidly. The overall process (Eller and Flynn, 1965; Crum, 1984; Leighton, 1994) is called "rectified diffusion."

14.4.2 Cavitation

A general term for the modification of preexisting bubbles or the formation of new bubbles or a group of bubbles by applied sound is called "acoustic cavitation" (Apfel, 1984; Leighton, 1994). Neppiras (1984) qualifies this definition by adding that both expansion and contraction of the gas body must be involved. "Stable cavitation" is a term (Flynn, 1964) that refers to the sustainable, periodic nonlinear expansion or contraction of a gas body or bubble. Unstable or "transient cavitation" (Flynn, 1964) refers to the rapid growth and violent collapse of a bubble. For years, this collapse was viewed as a singular catastrophic event (Leighton, 1998) producing fragmentation, temperatures in excess of 5000°K, the generation of free radicals, shock waves, and a light emission called "sonoluminescence." Detection of this light has been used as evidence that transient cavitation occurred. Gaitan and Crum (1990) were able to measure sonoluminescence of a single bubble in a water glycerine mixture at 22 kHz over thousands of cycles. Currently, "inertial cavitation" is a more appropriate descriptor of these events rather than transient cavitation (Leighton, 1998). The mechanisms for sonoluminescence are still being discussed, and the necessary conditions for populations of bubbles are believed to be different than those for a single bubble.

Inertial cavitation is a threshold event. Apfel and Holland (1991) calculated the conditions for this threshold by assuming a temperature maximum of 5000°K as a necessary condition for cavitation to occur. The conditions are appropriate for short pulses less than 10 cycles and low-duty cycles, like those in diagnostic ultrasound. Their computations are plotted in Figure 14.5. Here the thresholds are shown as curves for pulses of three different center frequencies. Each curve has a pressure minimum called P_{opt} at a radius equal to R_{opt}, the condition for lowest pressure threshold for a specified frequency. For example, at 5 MHz, these values are 0.58 MPa and 0.3 μm, respectively. Note that for a higher pressure P', as shown on the graph, a wider range of radii, 0.1−0.6 μm, will fall under the threshold. Notice also that at 10 MHz, these threshold minimum values are 0.85 MPa and 0.2 μm, respectively. The trend is that the threshold increases with frequency. The limiting values to the left of the minimum of each curve are governed by surface tension, and those on the right are controlled by a condition in which the ratio of the maximum radius to the equilibrium radius value exceeds a critical value. From their calculations, they estimated P_{opt} for an air bubble in water as a function of frequency as

$$p_{opt} \approx 0.245\sqrt{f_c} \tag{14.2}$$

where the center frequency is in MHz and the values are slightly conservative compared to the minima of the curves.

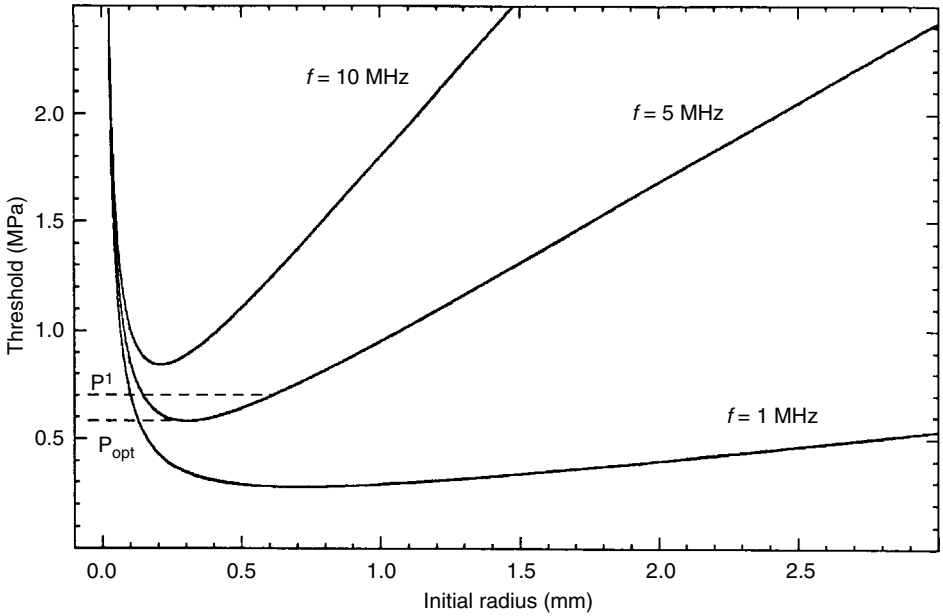

Figure 14.5 Peak rarefaction pressure threshold as a function of bubble radius for three frequencies of insonification: 1, 5, and 10 MHz. These curves represent inertial cavitation pressure amplitude thresholds (from Apfel and Holland, 1991, reprinted with permission from the World Federation of Ultrasound in Medicine and Biology).

14.4.3 Mechanical Index

This threshold equation led to the definition of a mechanical index (MI) (AIUM/NEMA, 1998) to estimate the likelihood of inertial cavitation with an intervening tissue path,

$$MI = \frac{P_{r.3}}{\sqrt{f_c}} \tag{14.3}$$

where $P_{r.3}$ is the maximum axial value of rarefactional pressure measured in water, $p_r(z)$, and derated along the beam axis, z, by an *in situ* exponential factor,

$$P_{r.3} = maximum[p_r(z) \exp(-0.0345 f_c z)] \tag{14.4}$$

More information about the rationale behind the MI can be found in Abbott (1999). A plot of this calculation for a 3.5-MHz center frequency is given by the top half of Figure 14.6. Curves are shown for the exponential derating factor, as well as $p_r(z)$, their product, and locations of maxima. When used by itself, p_r refers to the maximum peak rarefactional pressure in water. Note that the *in situ* derating factor, taken as a conservative average value for tissue, will not be the same as a specific tissue path in a diagnostic exam. The peak water value for p_r is usually located at a distance less than the geometric focal length, and it is dependent on nonlinear effects in water (discussed in Chapter 12). The location of the derated value is closer to the transducer. MI, the

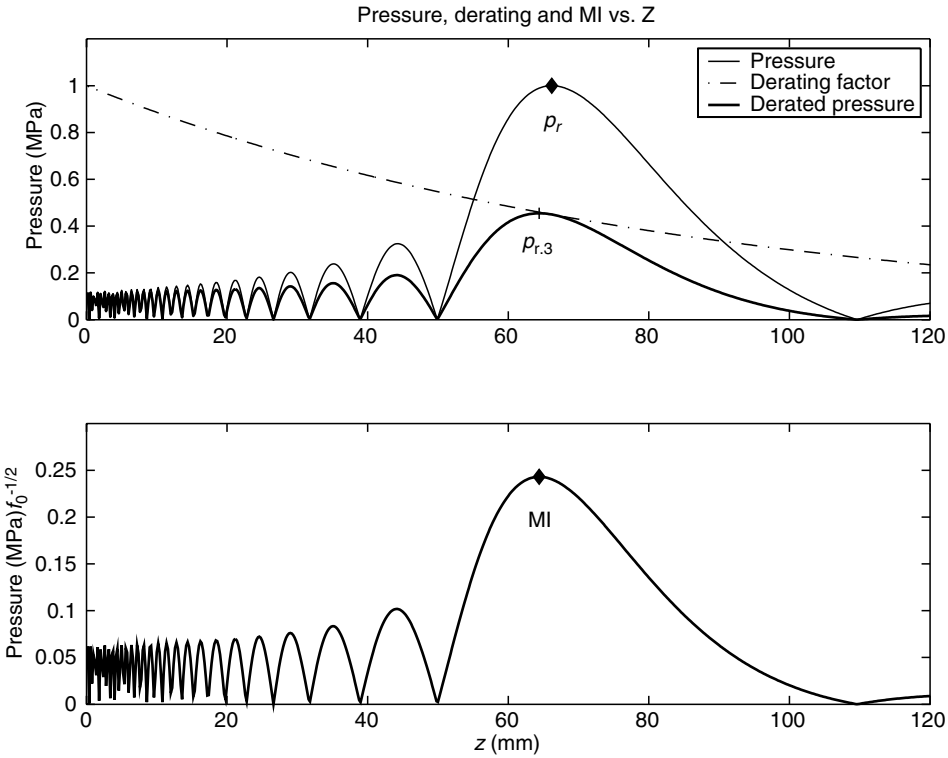

Figure 14.6 (Top) (Thin solid line) Rarefactional pressure amplitude measured in water as a function of distance from the transducer. (Dashed line) Exponential derating factor. (Thick solid line) Derated pressure is the product of rarefactional pressure amplitude and exponential departing factor. (Bottom) Derated pressure divided by $\sqrt{f_c}$. Maximum of this curve is MI.

peak value of Eq. (14.3) and shown in the bottom half of Figure 14.6, is a value that is proportional to the rarefactional pressure level measured, so a higher MI indicates a greater pressure level. A display of MI (discussed in Chapter 13) is available in real time on all systems marketed in the United States (AIUM/NEMA, 1998) and is discussed further in Chapter 15. In the United States, the recommended maximum for MI is 1.9. Note that the MI display gives a relative measure of maximum pressure amplitude but not its location, and the location may not coincide with the region of interest.

14.5 ULTRASOUND CONTRAST AGENTS

14.5.1 Basic Physical Characteristics of Ultrasound Contrast Agents

A contrast agent is a designer bubble. The structure of a contrast agent is typically a sphere containing perfluorocarbon gas or air about 1–10 μm in diameter with a thin elastic shell approximately 10–200 nm thick. There may be no shell but a surfactant,

or a shell with one layer or several. The small size of contrast agents is a deliberate attempt to mimic the size of red blood cells so that the agents can move into capillaries and pass through the pulmonary circulation system. For the purposes of measuring perfusion in the heart, these microspheres need to be inert to alter neither hemodynamics nor coronary blood flow, but instead to act as blood tracers with high echogenecity (de Jong, 1993). In a typical application, the agent is administered as a bolus or by infusion intravenously, and it passes through the pulmonary system and emerges in the left ventricle. An important design goal is for the microbubbles to persist and to not dissolve quickly.

After injection, the original distribution of microspheres of different diameters is altered by three factors (de Jong, 1993). The lung capillaries act as a filter (as shown by Figure 14.7). In addition, the original concentration of agent is diluted in the circulatory system and is affected by pressure gradients. A measured distribution after lung passage of Albunex, a first-generation agent with an air bubble covered by a sonicated albumin shell, is presented in Figure 14.8. From this information, it is evident that smaller bubbles with diameters in the 2–6 μm range are to be preferred for cardiac applications.

One major difference between air bubbles and contrast agents is the effect of the shell, which constrains the expansion and raises the resonant frequency. The overall effect on resonance can be expressed by (de Jong *et al.*, 1992),

$$f_{re}^2 = f_r^2 + \frac{S_p}{4\pi^2 m} \tag{14.5}$$

where S_p is the stiffness of the shell, m is the effective mass of the system, and f_r is the free gas bubble resonance given earlier. Calculations for several agents and an air bubble in water (de Jong *et al.*, 2000) are shown in Figure 14.9. These agents range

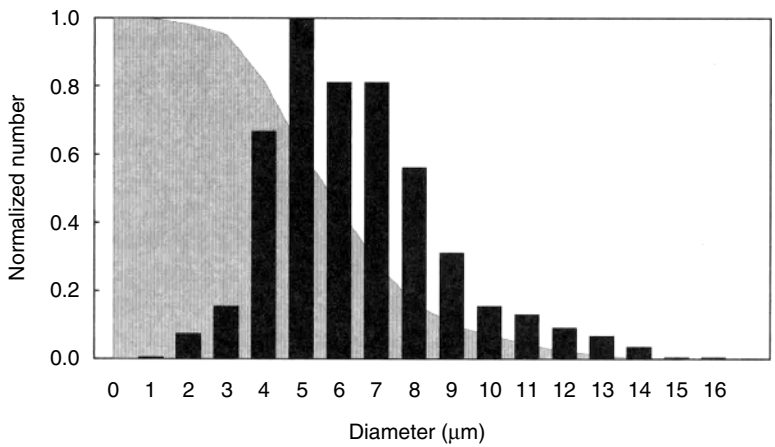

Figure 14.7 Bars represent normalized size distribution of lung capillaries, and the shaded area shows the probability that a microsphere of a particular size will pass through the capillaries (from de Jong, 1993).

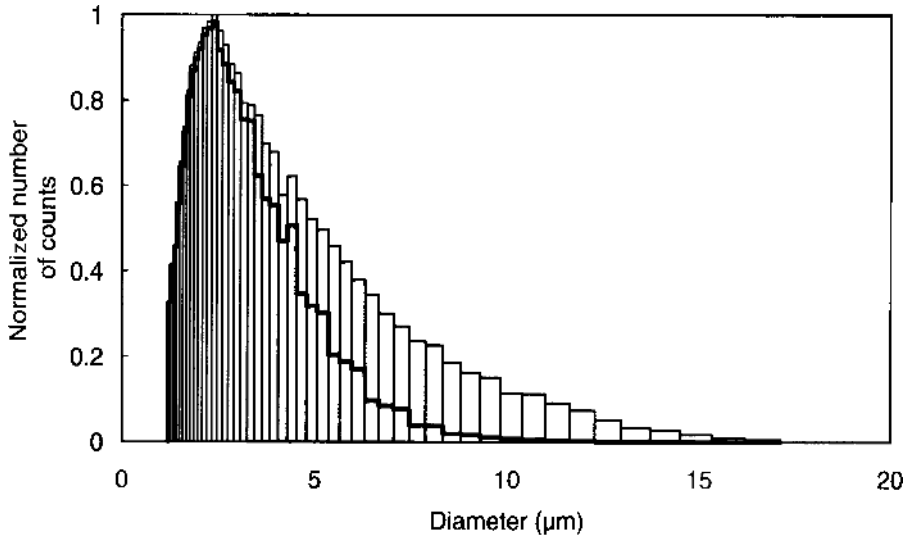

Figure 14.8 Microbubble measurements by a Coulter counter shown as normalized size distributions of Albunex (thin curve) compared with calculated size distribution (thick curve) after lung passage based on the probability curve from Figure 14.7 (from de Jong, 1993).

from a thick rigid shell to a very flexible shell in the following order: Quantison, Albunex, and Sonovue, with an air bubble being the most flexible. Consequently, for a given bubble size, air has the lowest resonant frequency and Quantison has the highest.

Current contrast agents are listed in Table 14.1. The majority of these gases are perfluorocarbon-like gases or air, and the shells vary from human serum albumin (administered in different ways) to surfactants. All materials were tested to be biocompatible and to be absorbed into the circulatory system. The amount of gas in a typical bolus injection is on the order of 20–100 μl (Cosgrove, 1998). What happens to gases from contrast agents after they diffuse out? They are carried along by blood and released when passing through the lungs.

14.5.2 Acoustic Excitation of Ultrasound Contrast Agents

The behavior of these agents under acoustic excitation fall into three classes (Frinking *et al*., 1999), depending on the structure of the microbubble and the level of the insonifying pressure amplitude and frequency: stable linear (also known as low MI), stable nonlinear scattering (medium MI), and transient nonlinear scattering (high MI). There is a fourth class, called super MI, with levels above those used in diagnostic imaging (to be discussed in Chapter 15). Characteristics of a bubble as a linear resonator have been discussed in the last section. In Figure 14.10, properties of Albunex are shown for microbubbles of three diameters as an example of the stable nonlinear regime. Compared to Figure 14.4 for an air bubble, the changes are more

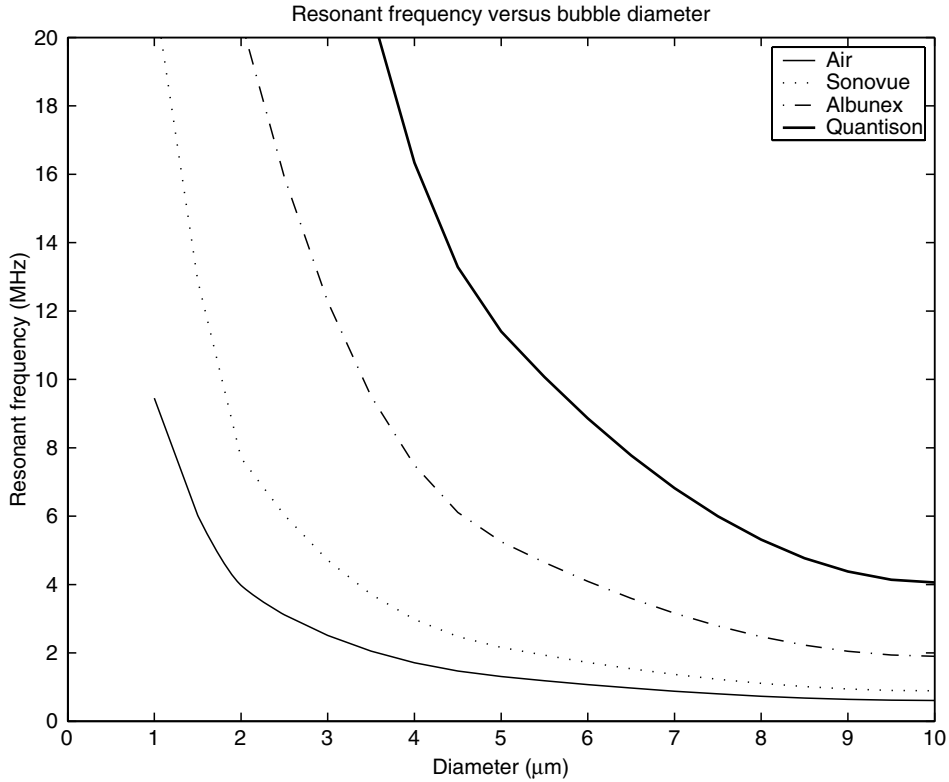

Figure 14.9 Resonant frequency versus bubble diameter for air, Sonovue, Albunex, and Quantison (based on calculations from de Jong *et al.*, 2000).

muted, with the largest ones occurring when the 2-MHz excitation is close to resonance (9.6 μm diameter).

Under high levels of pressure (but still within the limits for MI recommended by the FDA), contrast agents demonstrated unexpected behavior. Clinicians discovered that some agents disappeared from view when insonified or were destroyed (Porter and Xie, 1995), whereas others reported brighter regions in an image. These conflicting observations were resolved by Frinking *et al.*'s study (1999) of Quantison microspheres. Figure 14.11a shows scattered power from these microspheres as a function of frequency for a low acoustic pressure insonification level. At low frequencies, the scattering is linear. In their experiment, a destructive acoustic pulse with a center frequency of 0.5 Mhz and a 1.6-MPa pressure was turned on, and the power was remeasured 0.6 ms later. As evident from the graph in Figure 14.11b, the scattering increased by 20 dB and has a resonance peak at 3 MHz in the upper curve, which corresponds to that of a free gas in good agreement with the prediction. The scattering response for a similar experiment but with an insonifying frequency of 1 MHz is shown in Figure 14.11c, and it has a resonance at 1.3 MHz. These resonances corresponded to

Table 14.1 Ultrasound Contrast Agents

Manufacturer	Name	Gas	Shell
Acusphere	AI-700	Decafluorobutane	Polymer
Alliance/Photogen	Imagent	Perfluorohexane	Surfactant
Bracco	Sonovue	Sulfurhexafluoride	Phospholipid
Bracco	BR14	Perfluorocarbon	Phospholipid
Byk-Gulden	BY963	Air	Lipid
BMS	Definity	Octafluoropropane	Liposome
Mallinckrodt	Albunex	Air	Albumin
Amersham	Optison	Octafluoropropane	Albumin
Amersham	Sonazoid	Perfluorocarbon	Lipid
Point Biomedical	CardioSphere	Air	Polymer bilayer
Porter	PESDA	Perfluorocarbon	Albumin
Quadrant	Quantison	Air	Albumin
Schering	Echovist	Air	No
Schering	Levovist	Air	Fatty acid
Schering	Sonavist	Air	Polymer
Sonus (withdrawn)	Echogen	Dodecafluoropentane	Surfactant

mean diameters of 2 and 1.2 μm and a release of only 1% of the available population. After release, the free gas bubbles dissolved within 10 and 20 ms (in accordance with theory for these sizes). In summary, the sequence of steps is as follows: Figure 14.11a depicts the initial states, as well as responses, for stable linear and stable nonlinear insonification levels; Figures 14.11b and 14.11c illustrate the higher scattering levels after a high pressure signal, at the transient nonlinear level, caused by the mechanical failure and fragmentation of the shell, as well as the release of the gas from the shell. Frinking *et al*. (1999) called this large increase in scattered power ''power-enhanced scattering.'' For thick-shelled Quantison (see Figure 14.9) , internal gas is air, which takes 1–5 ms before dissolving and disappearing from view.

14.5.3 Mechanisms of Destruction of Ultrasound Contrast Agents

Is this destructive process cavitation? By the definitions presented earlier, yes. Is it inertial cavitation with sonoluminescence? Most likely it is not, but rather, it is a mechanical failure of the shell. In the destructive process just described, there are different types of cavitations corresponding to the pressure amplitude level of insonification and insonifying frequency. The growing number of contrast agents, their unique structures and materials, and their distribution of sizes suggest that there may be other types of cavitation that remain to be characterized.

Other windows into the destruction of contrast agents involve acoustical and optical detectors (Holland *et al*., 1992; Dayton *et al*., 1997; Morgan *et al*., 1998; Wu and Tong, 1998; Dayton *et al*., 1999; Chomas *et al*., 2000, 2001; Chen *et al*., 2002; Deng and Lizzi, 2002). From some of these studies, a fourth category of bubble destruction at extremely high levels of pressure (super MI),

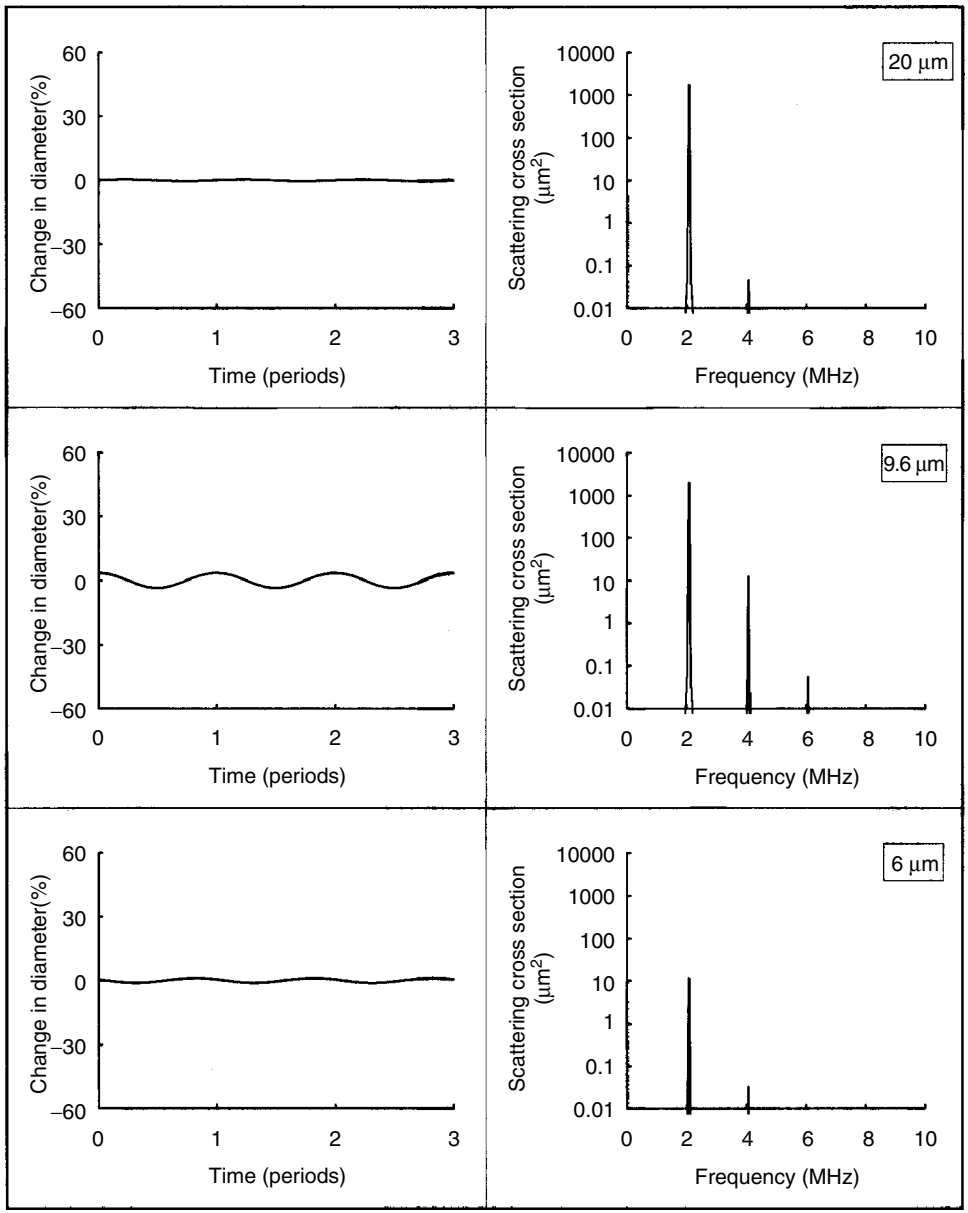

Figure 14.10 (Left panels) Simulated relative change in diameter of an Albunex bubble in water for a sinusoidal excitation of 2 MHz and a pressure amplitude of 50 kPa for three bubble diameters: 20 μm (above resonance), 9.6 μm (resonance), and 6 μm (half resonance). (Right panels) Corresponding spectral responses (from de Jong, 1993).

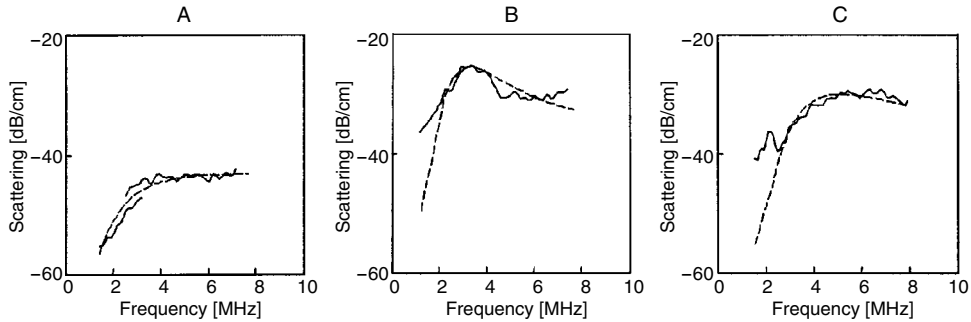

Figure 14.11 (A) Scattering versus frequency of a dilution of 1:4500 of Quantison measured without the high-amplitude ultrasound burst (solid line is measured scattering, and dashed line is theoretical spectrum using measured size distribution). (B) Solid line is measured scattering 0.6 ms after the transmission of the 0.5-MHz high-amplitude ultrasound burst at the same region, and dashed line is theoretical spectrum. (C) The same as in (B) but now using the 1.0-MHz transducer for generating the high-amplitude burst (solid line is measurement and dashed line is theoretical spectrum) (from Frinking *et al.*, 1999, Acoustical Society of America).

corresponding to those applied in high-intensity focused ultrasound (HIFU) or lithotripsy, has revealed new phenomena and bioeffects (to be described separately in Chapter 15). In this section, emphasis is on contrast agent changes that occur at normal diagnostic pressure levels.

Chomas *et al.* (2000) has produced remarkable measurements, both optical and acoustical, of microbubble destruction. In Figure 14.12, the demise of an experimental contrast agent, M1950, insonified with a 2.4-MHz, three-cycle-long pulse with $p_r = -1.2$ MPa, is captured with a high-speed framing camera and streak camera capable of 10 ps resolution. This experimental agent made by Mallinckrodt, Inc. is made of a gas decafluorobutane (C_4F_{10}) encapsulated in a phospholipid shell. A continuous streak image bubble diameter in Figure 14.12h shows the temporal evolution of the breakup, which is detailed in cross-sectional snapshots at different time intervals over an observation time from (b) to (f) of 80 ns. This type of destruction has been identified as fragmentation (Chomas *et al.*, 2001), a type of rapid destruction on a microsecond scale in which excessive expansion and contraction ($R_{max}/R_{min} > 10$) of the microbubble causes instability, and there is an irreversible fragmentation into smaller bubbles that dissolve.

Two other mechanisms for bubble destruction are forms of diffusion (Chomas *et al.*, 2001). Both involve the diffusion of gas out of a microbubble. Just as helium diffuses out of a toy balloon gradually and the balloon loses its buoyancy, there is a similar effect called "static diffusion" for microbubbles. No sound is involved. Typical times for this process for a 2-μm diameter bubble filled with gases are the following: air (25 ms), C_3F_5 (400 ms), and C_4F_{10} (4000 ms). The second mechanism is acoustically driven diffusion. Factors involved are the gradient of gas across the shell into the surrounding fluid, the initial radius, and the dynamic modal shapes of microbubbles that contribute to a convective effect. Because a contrast agent has a shell, and often a

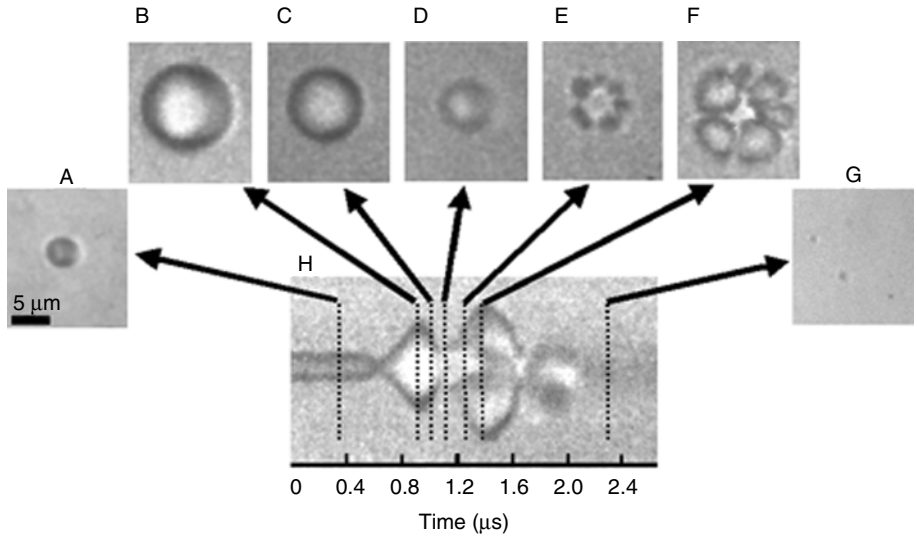

Figure 14.12 Optical frame images and streak image corresponding to the oscillation and fragmentation of a contrast agent microbubble, where fragmentation occurs during compression. The bubble has an initial diameter of 3 μm, shown in (A). The streak image in (H) shows the diameter of the bubble as a function of time, and dashed lines indicate the times at which the two-dimensional cross-sectional frame images in (A)–(G) were acquired relative to the streak image (from Chomas *et al.*, 2000, American Institute of Physics).

heavier gas, the balance between compressional and rarefactional phases is different than that for a free air bubble; so unlike rectified diffusion, gas is moved out of the bubble and the diameter shrinks over time. Instead of being pumped up, as in rectified diffusion, encapsulated microbubbles are pumped down. From their numerous experiments, Chomas *et al*. (2001) have observed that a single ultrasound pulse is enough to set the acoustically driven diffusion process in motion.

To summarize what seems to be a complicated set of interactions involving the applied pressure field characteristics, as well as contrast agent structure and size, it is helpful to view the microbubble as a fragile viscoelastic resonator. Just as there are different responses for solid elastic materials, encapsulated microbubbles also have linear and nonlinear ranges, as well as irreversible plastic and inelastic limits to increasing amounts of pressure. In addition, as resonators, they ring depending on their size and the amount of damping of their viscoelastic shells. As the frequency content of the exciting pulse approaches the resonant frequencies of the contrast agent, the effects of excitation become magnified and lead to larger displacements or a larger ratio of maximum-to-minimum microbubble diameters. Either acoustically accelerated diffusion can occur or, for large maximum-to-minimum diameter ratios, the shell can fragment. Freed gas can cause short-lived, elevated levels of backscatter and then dissolve. Chen *et al*. (2002) have observed that contrast agents behave differently once the shell is fragmented. They found multiple resonance peaks after

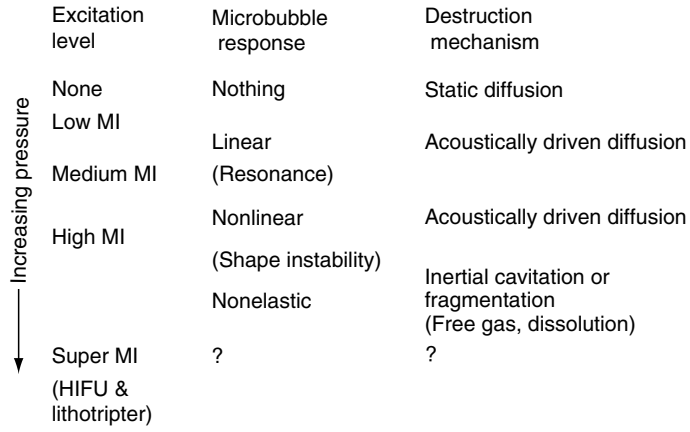

Figure 14.13 Diagram of causes of ultrasound contrast agent destruction.

insonification of the remains of the air-filled agent that they believed corresponded to resonances from a distribution of bubbles and inertial cavitation events. They concluded that a second agent, filled with a heavier gas, fragmented into tiny subresonant bubbles (< 0.3 μm) with no inertial cavitation events.

These factors are diagrammed in Figure 14.13. On the left is a scale of increasing incident pressure levels from zero to extremely high levels used for lithotripsy (kidney stone fragmentation) or HIFU for surgery; these are matched up to a series of mechanical factor thresholds and their destructive consequences. The way these thresholds align with absolute pressure levels depends on the encapsulated microbubble structure, or in other words, the mechanical response scale is flexible and unique to the agent type. A practical consequence of this matchup is that imaging system manufacturers are implementing individual protocols tailored to different types of agents. For example, a particular destructive effect such as fragmentation may occur at different pressure thresholds for each agent. With different excitation pulses and timing intervals, a range of effects can occur (as described in the next section on ultrasound contrast agent imaging). Deliberate destruction of contrast agents for targeted drug delivery is discussed in Section 14.7.

14.5.4 Secondary Physical Characteristics of Ultrasound Contrast Agents

Characterization of ultrasound contrast agents can be complicated because of interrelated factors: the structure and concentration of agent, both spatially and in dilution; and the spatial distribution and harmonic content of the insonifying field, as well as its timing sequence. Ways of identifying the unique properties of each agent, as well as the optimum matching of the acoustics and signal processing, are still under development. A number of associated effects have received less attention and will be discussed here for completeness.

In addition to backscattering, contrast agents can attenuate the sound field enough to block the signal from reaching deeper depths and to cause shadowing. The intersection of the beam with the agent is called the scattering cross section, $\sum_{TS}(f)$, whereas the attenuation is called the extinction cross section, $\sum_{TE}(f)$. Bouakaz *et al*. (1998) have proposed a standard measure of the effectiveness of an agent, the scattering-to-attenuation ratio (STAR). A perfect agent would have a high scattering and low attenuation, or a high value of STAR. A definition of STAR suited to measurement is

$$STAR(f) = \frac{\sum_{TS}(f)}{\sum_{TE}(f)} = \frac{1}{1 + \sum_{TA}(f)/\sum_{TS}(f)} \tag{14.6}$$

where $\sum_{TA}(f)$ is the total absorption cross section. Another important parameter is the contrast-to-tissue ratio (CTR) (de Jong *et al*., 2002), which is the relative amplitude of backscatter from a contrast agent to the backscatter from tissue and is often considered at a frequency such as the second harmonic (see Figure 14.11 as an example). This topic is addressed in Section 14.6. In addition, there are many other characteristics of contrast agents that can be measured as a function of incident pressure and time and frequency (Bleeker *et al*., 1990; Shi and Forsberg, 2000), as well as the nonlinearity parameter, B/A (Wu and Tong, 1997), which is two to three orders of magnitude larger than those of tissues.

Several nonlinear-related physical effects, which are more difficult to measure, also occur with contrast agents in fluids. The first is that delicate microbubbles (Wu, 1991) can be pushed around by radiation forces, like the ones described in Chapter 13. Dayton *et al*. (1997) have identified two major types of forces (Leighton, 1994): a primary radiation force caused by a pressure gradient that displaces microbubbles (as shown in Figure 14.14b), and a secondary force (illustrated by Figure 4.14c). These secondary, or Bjerknes, forces are caused by pressures reradiated by microbubbles, and

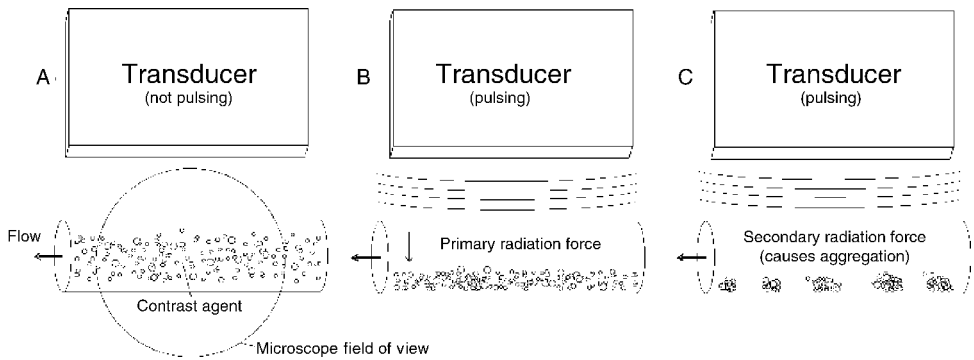

Figure 14.14 Configuration of ultrasound transducer above a tube containing contrast agents flowing to the left, shown as a microscope view. (A) No sound. (B) Primary radiation force pushes the contrast agent away from the transducer during pulsing. (C) Microspheres, which are pushed into closer proximity by primary radiation force under transducer pulsing, aggregate due to secondary radiation force (from Dayton *et al*., 1997, *IEEE).*

they often result in mutual bubble attraction and the formation of aggregates, or bubble clusters.

Another nonlinear effect associated with the inevitable pressure gradients is microstreaming (described in Chapter 12). This version of microstreaming is smaller in scale and occurs near boundaries (Wu, 2002) and around bubbles (Leighton, 1994), and it has been observed near contrast agents. Under certain conditions, another phenomenon related to microstreaming is reparable sonoporation, which is the reversible process of opening and resealing cells in a suspension containing contrast agents in an insonifying field (Wu, 2002).

Finally, much of the analysis for predicting the response of contrast agents to acoustic fields has been based on linear amplitude-modulated sinusoidal excitation or short pulses. Because of the travel path of the beam to the site of the contrast agent, the beam and waveforms undergo nonlinear distortion and absorption (as described in Chapter 12). Initial research by Ayme (Ayme *et al.*, 1986; Ayme and Carstensen, 1989) showed that the response of microbubbles is greater for an amplitude-modulated sinusoid rather than a nonlinearly distorted pressure wave of the same amplitude. Recent studies indicate that when a nonlinearly distorted wave meets a nonlinear encapsulated microbubble, the response of the bubble is not as exciting as if it had met a linear waveform (Hansen *et al.*, 2001). The simultaneous excitation of the microsphere by a range of frequencies (fundamental and harmonic) creates different vibrational modes and scattered frequencies, and, in general, a more muted response (de Jong *et al.*, 2002). This work provides insight into contrast agent response under more realistic circumstances.

14.6 IMAGING WITH ULTRASOUND CONTRAST AGENTS

Ultrasound contrast agents were designed with several objectives, other than applications as blood tracers, that enhance sensitivity in small vessels and at deeper penetration depths (Reid *et al.*, 1983). One goal is opacification, which is the visualization or brightening of a blood pool volume. A primary example is the application of this effect to the left ventricle of the heart, or "left ventricular opacification" (LVO). An apical four-chamber view of the heart in Figure 14.15 aids visualization of the problems encountered. In this view, the transducer would be positioned at the top of the diagram, or at the apex of the heart, and it shines downward. When an ultrasound beam is parallel to a surface of the heart, there is little backscatter (dropout near the apex), and anisotropic effects from the muscle fibers (discussed in Chapter 9), in combination with poor sensitivity caused by body wall effects, make visualization of the entire chamber difficult, especially through a cardiac cycle. Yet it is important to track this volume of blood to determine the ejection fraction (a measure of the heart acting as a pump) or to identify irregular local wall motions of the endocardium (inner surface of the heart) under stress testing.

Refer to the left diagram of Figure 14.15 to review the cardiac cycle. The heart cycle involves the return of venous blood to the right atrium, which, when filled, flows into the right ventricle, which pumps blood into the lungs. After oxygenation, blood

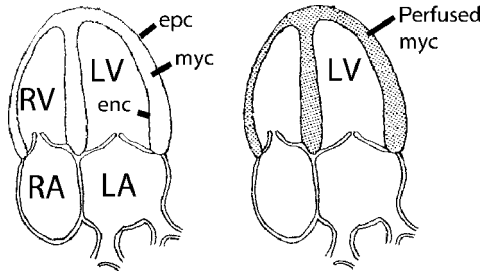

Figure 14.15 (Left) Diagram of a standard ultrasound apical four-chamber view of the heart. The transducer would be at the top or apex. Key: LV = left ventricle, LA = left atrium, RA = right atrium, RV = right ventricle, enc = endocardium, myc = myocardium, and epc = epicardium (Right) Myocardium perfused with blood shown with shading surrounding the left ventricle.

from the lungs fills the left atrium, where the mitral valve releases it to be pumped out by the strong left ventricle, after which the heart relaxes. The instant of maximum left ventricle pumping is called ''systole,'' and the relaxation phase is called ''diastole.'' The main heart muscle, called the myocardium, is sandwiched between the endocardium and epicardium, the outer surface of the heart.

A second primary application for these agents is determining and visualizing regions of blood perfusion or the amount of blood delivered into a local volume of tissue (small vessels or capillaries) per unit of time. Abnormalities in the ability of the blood to soak into tissue can be very revealing for diagnosis. In Figure 14.15, the normally perfused myocardium depicted at the left is invisible in terms of ultrasound visualization. Over several heart cycles, a contrast agent enters the circulatory system, and eventually the myocardium, so that this region is made visible to ultrasound imaging (as depicted as a shaded area on the right in Figure 14.15). For cardiac applications, measuring perfusion is termed ''myocardial echocardiography'' (MCE). Regions where blood cannot reach may indicate ischemia (local lack of blood in a region or a regional circulation problem) or an infarct (tissue death). This information is vital for determining the extent of injury from a heart attack and for diagnosing appropriate therapy. Perfusion is also important in other tissues to indicate abnormalities such as angiogenesis or increased vascularization in tumors and the location of lesions.

In order to fulfill these major objectives, the strange and unexpected interactions of ultrasound with contrast agents began to be understood, and ingenious methods ways of harnessing these characteristics were invented. The application of encapsulated microbubble contrast agents evolved as the physical interactions of ultrasound became better known, the design of agents was improved, and imaging systems and signal processing methods were adapted and tuned to the unique characteristics of each agent. The elusive ''hide-and-seek'' game with ultrasound that these agents have played can be interpreted in terms of the mechanisms of encapsulated microbubble destruction (just discussed and diagrammed in Figure 14.13).

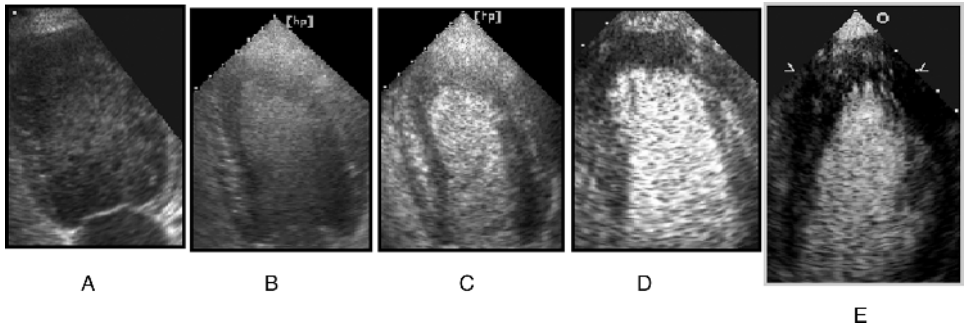

Figure 14.16 Evolution of ultrasound contrast agent imaging. (A) Imaging with first-generation agent at the fundamental frequency. (B) Imaging with second-generation agent at the fundamental. (C) Imaging with second-generation at the second harmonic. (D) Imaging with improved transducer field at the second harmonic. (E) Imaging with tissue-subtracting signal processing (power modulation) (courtesy of P. G. Rafter, Philips Medical Systems).

In order to review some of these developments as applied to LVO imaging, refer to Figure 14.16, which is a series of views of the left ventricle in the imaging plane that were presented by Figure 14.15. To compare images, note the degree of contrast between the myocardium, visible as an upside-down ''U'' shape, with the interior of the left ventricle. The first generation of encapsulated agents were short lived for LVO applications (Figure 14.16a). First, the gas used (air) dissolved quickly, so microbubbles underwent destruction by static diffusion without any help. Second, under the usual pressure levels used for B-mode imaging, agents were rapidly destroyed by fragmentation. These observations led to a triggered method in which the transmit pulses were spaced out over longer time intervals so that the contrast agent had time to be replenished before being destroyed again (Porter and Xie, 1995). As seen in Figure 14.16b, even with the next generation of agents, contrast between the agents and the surrounding tissue, though slightly improved, was not dramatic. Work on second harmonic imaging, based on the higher B/A nonlinearity of the microbubbles compared to tissue, did improve contrast at the second harmonic frequency (Schrope *et al*., 1992; Schrope and Newhouse, 1993) (as shown by Figure 14.16c). Unfortunately, the degree of contrast was not as great as expected because of the nonlinearity of tissues. Advances in transducer technology, a lower fundamental frequency, a smoother transmitted field pattern, and newer contrast agents led to an improved image (Rafter *et al*., 2002), as depicted in Figure 14.16d.

Finally, application of a tissue-minimizing signal processing method, here power modulation (Brock-Fisher *et al*., 1996) in conjunction with power Doppler imaging (Burns *et al*., 1994) and system settings matched to the particular contrast agent in terms of frequency, transmit level, and pulse interval, has resulted in a long-persisting strong contrast effect with good endocardial border definition (depicted in Figure 14.16d). Here a low pressure or MI level is applied to avoid fragmentation so that the main physical effect is acoustically driven diffusion.

For the second major application, MCE, a different strategy is needed to detect low concentrations of agent in the myocardium. One real-time approach is to let the contrast agent enter the left ventricle and eventually the myocardium at a low transmit pressure (MI) level with a signal processing method, such as power modulation or pulse inversion, to enhance the low levels of agent flowing into the myocardium. The time sequence of power Doppler images at the bottom of Figure 14.17 shows the progressive increase of agent in the myocardium from dark (none) to bright (saturation). The myocardium can be mapped into a number of contiguous segments, each corresponding to a zone mainly supplied by a particular coronary artery. By measuring the acoustic intensity at a region of interest (ROI, shown in lower left of Figure 14.17) in a particular segment as a function of time, a time intensity curve can be drawn (as depicted in the top of Figure 14.17). This curve has the form,

$$I = I_0[1 - \exp(-bt)] \tag{14.7}$$

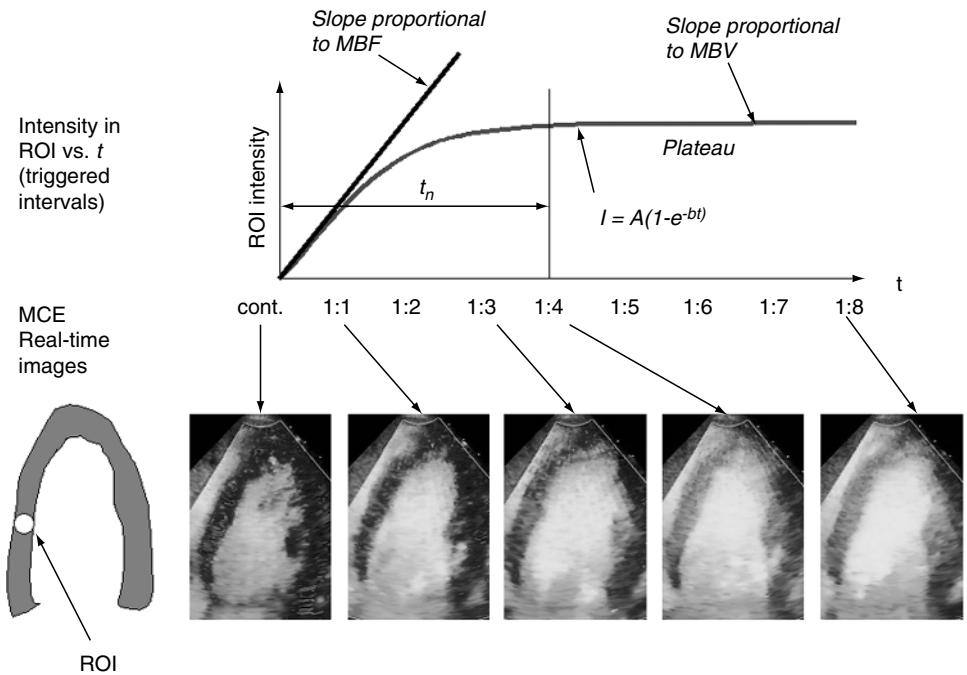

Figure 14.17 Low pressure (MI), real-time myocardial perfusion imaging method. (Top) Graph of region of interest intensity versus time perfusion filling curve, showing initial slope proportional to myocardial blood flow (MBF), a plateau region with a slope proportional to myocardial blood volume (MBV), and a time (t_n) to reach the plateau. Time is in triggered-interval ratios such as 1:8, meaning an interval 8 times the basic unit with reference to initial administration of contrast depicted as ''cont.'' (Bottom left) Insert highlights region of interest (ROI) for intensity measurement. (Bottom right) Time sequence series of left ventricle views depicting perfusion of the myocardium and beginning with contrast agent entering the left ventricle (courtesy of P. G. Rafter, Philips Medical Systems) (see also color insert).

where b is a constant to be determined empirically. Wei *et al*. (1998) have shown that the initial slope of this curve is myocardial blood flow (MBF), and the plateau region is proportional to the myocardial blood volume (MBV); these are important characteristics of perfusion. The constant b can be found from the time required to reach the plateau region. Analysis of video contrast data over time is called "videodensitometry."

Power Doppler provides an apparent sensitivity gain for these applications over color flow imaging (CFI) because objectionable low signal levels are mapped to low intensities (as described in Section 11.7.4). Harmonic power Doppler has an additional benefit: a contrast-to-tissue ratio improvement over B-mode harmonic imaging, since a harmonic tissue signal is suppressed with a wall filter. Changes in microbubble scattering or movement are detected through correlation, pulse to pulse (as described in Chapter 11), especially during shell fragmentation and agent replenishment. Tissue movement is displayed also, so careful triggering and pulse timing are needed to minimize these effects.

An alternative triggered, but not real-time, method is to deliberately destroy the contrast agent microbubbles at a high pressure (MI) level so that fragmentation occurs (Wei *et al*., 1998). With new agents, an elevated echogenicity occurs briefly as free gas is exposed after fragmentation (as described in Section 14.5.2). After the remaining free gas dissolves, the return of fresh microbubbles at the second harmonic can be measured as a function of time at a position in the myocardium. In this method, the transmit frames are triggered by the electrocardiograph (ECG) waveform with a pair of pulses, one for destruction and the next for imaging, that are separated by several heartbeats. Because bubble destruction takes place, sufficient time is needed between imaging frames to let these effects settle; these long-time intervals are why this is not a real-time approach. Because the triggering interval must be changed in this method, the overall time is approximately three times longer than the real-time approach.

Another method called "release burst imaging" (Frinking *et al*., 2000) uses destructive pulses alternated with imaging pulses. This method provides independent control of the two types of pulses, with the release pulse causing fragmentation and enhanced scattering (as described in Section 14.5.2).

Other approaches take advantage of differences in the spectral responses of microbubbles and tissue. Unlike linear responses, spectra for waves in or reflected by nonlinear media change shape with the pressure amplitude level. Therefore, at any given frequency, there is a difference in amplitude between a contrast agent and a tissue that is a function of the pressure-drive level. An example of exploiting this effect is to lower the pressure level until the tissue harmonic signals are barely detectable but the scattering from the more nonlinear contrast agent microbubbles are still visible; therefore, agent-to-tissue contrast is increased over what it was at a higher pressure level (Powers *et al*., 2000). This reduction in pressure also minimizes bubble destruction. Operating at low pressures has another advantage: Microbubbles remain nonlinear, but tissue falls into a linear region so that tissue removal signal processing, such as pulse inversion or power modulation, can be applied.

Contrast also improves in regions above the second harmonic (Rafter *et al*., 2002; Bouakaz *et al*., 2002). As shown in Figure 14.18, bandpass receive filters can be

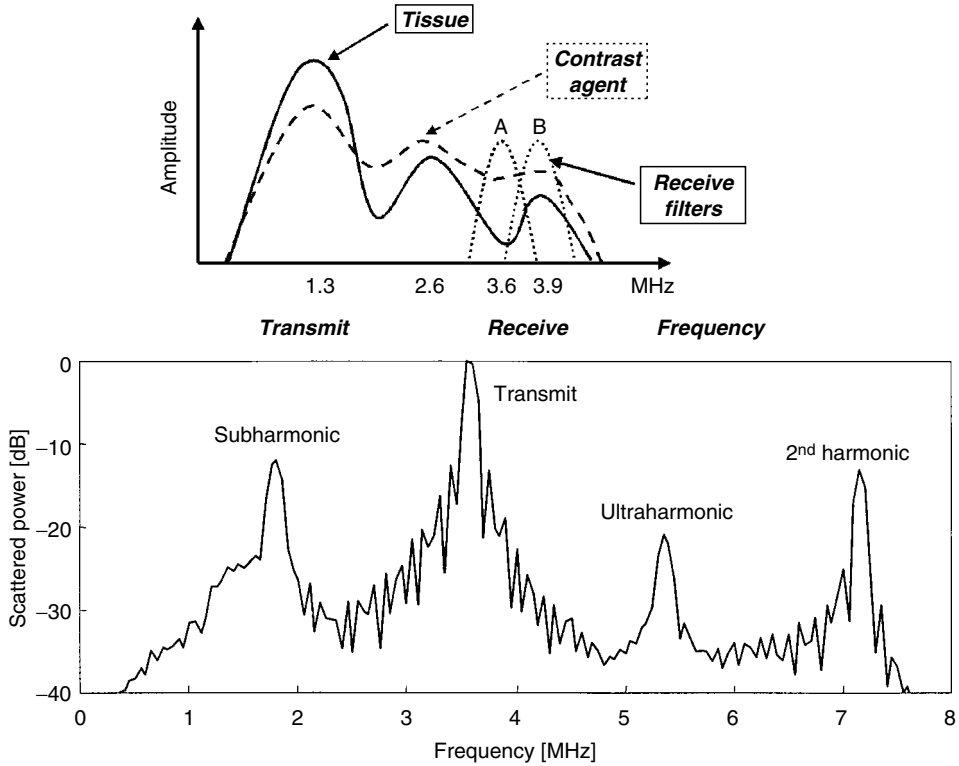

Figure 14.18 (Top) Pulse-echo spectral responses for contrast agent and tissue. Transmit at 1.3 MHz, second harmonic at 2.6 MHz, and third harmonic at 3.9 MHz. Receive filters placed at (A) null between second and third harmonic or (B) at the third harmonic (courtesy of P. G. Rafter, Philips Medical Systems). (Bottom) Scatter spectral response of contrast agent SonoVue showing subharmonics, ultraharmonics, and harmonics. The transmitted waveform was a 40-cycle long toneburst at 3.5 MHz at a peak negative pressure of 75 kPa (from Frinking *et al.*, 2000, reprinted with permission of the World Federation of Ultrasound in Medicine and Biology).

placed, for example, at either of two regions with larger contrast. Capturing these regions requires a transducer with either an extremely wide bandwidth or special construction. Another way of improving contrast is to utilize subharmonics and ultraharmonics (noninteger multiples or submultiples of the fundamental), which are generated by certain agents (Shankar *et al.*, 1998; Frinking *et al.*, 2000; Shi *et al.*, 2002) and not by tissue (as illustrated in the bottom of Figure 14.18).

Different methods can be combined. For example (Powers *et al.*, 2000), a high-pressure transmit pulse is followed by low-pressure transmit pulses for stable real-time imaging of the contrast agent replenishment combined with pulse inversion signal processing. Here the initial pulse in a sequence causes bubble fragmentation, and low pressure in subsequent pulses enhances the contrast between scattering from the contrast agent and surrounding tissue and also provides a means for real-time perfusion studies.

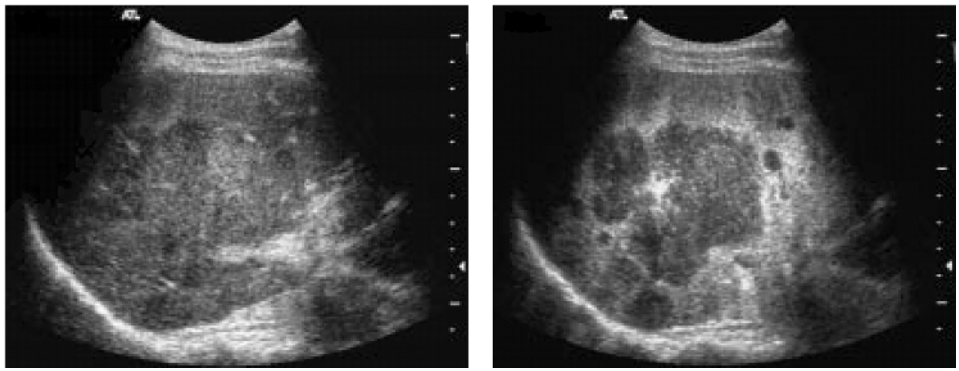

Figure 14.19 (Left) Liver imaged with the conventional fundamental method does not show any focal lesions in a 63-year-old man. (Right) Same liver with contrast agent, pulse inversion harmonic imaging, and late phase method reveals a large metastasis (large dark region with well-defined border) and several lesions (reproduced with permission from Powers *et al.*, 2000, Philips Medical Systems).

Measurement of perfusion is not limited to cardiac applications, but can be extended to other organs (Kono *et al*., 1997; Forsberg *et al*., 2000; Powers *et al*., 2000; Mor-Avi *et al*., 2001) such as the liver (the effects of a similar methodology are illustrated in Figure 14.19). Here tumors do not absorb contrast agents as well as surrounding tissue, and a large metastasis is obvious as a dark region with smaller lesions.

14.7 THERAPEUTIC ULTRASOUND CONTRAST AGENTS: SMART BUBBLES

Who would have anticipated that after the first generation of gas-filled contrast agents was fragmented by ultrasound that encapsulated microbubbles would eventually be designed deliberately for destruction? A new breed of contrast agents (if this name is still appropriate) is under development to carry drugs to targeted sites where medication can be released by ultrasound-induced fragmentation. Most forms of medication administered orally or intravenously have a systemic effect throughout the body; consequently, larger amounts than necessary must be administered for the intended region to compensate for dilution and waste. Unwanted side effects are often the result. There is also the possibility that the medication will not reach the intended site. Therapeutic ultrasound contrast agents may be able to deliver precisely the needed amount of medication to the intended site. This prospect would be an exciting breakthrough to which ultrasound could contribute.

Lindner (2001) and Hughes *et al*. (2003) review strategies for targeting therapeutic microbubble agents to desired sites. Some of these methodologies are depicted in Figure 14.20. Two approaches to guide encapsulated microbubbles to target cells are electric field attraction and conduction (Wong *et al*., 1994), shown in Figure 14.20a, and acoustic radiation forces (Dayton *et al*., 1999b), shown in Figure 14.20b. Depicted in Figure 14.20c, target cells have an affinity for the shell material (such as

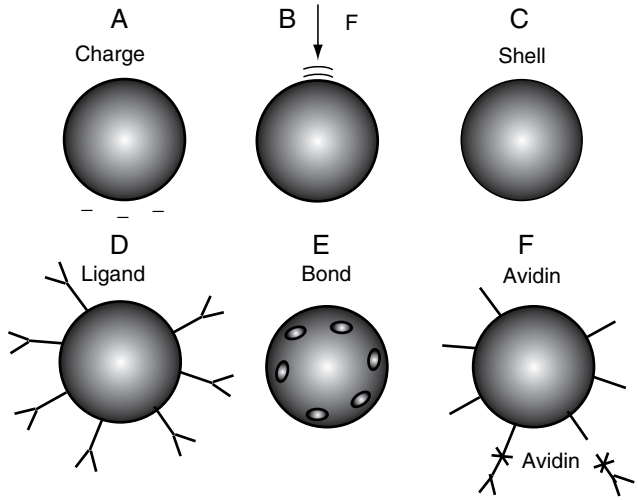

Figure 14.20 Methods for delivering therapeutic contrast agents. (A) Electrical field attraction. (B) Acoustic radiation force. (C) Delicious or attractive shell material. (D) Ligands tethered to agent surface seek bioconjugation with target receptors. (E) Active material covalently bonded to agent surface. (F) Bonding by biotin avidin linking.

albumin or a lipid). Strong covalent bonds can be created between ligands anchored to the agent membrane surface and target receptors. Ligands, shown in Figure 14.20d, are seeker molecules (atoms, ions, or radicals) that have the potential of forming a complex with the right material. Ligands (Hughes *et al*., 2003) include drugs, antibodies, proteins, and viruses. An important application of the antibody ligand is to seek out and neutralize specific disease invaders or antigens. Material, such as DNA, can be covalently bonded onto the surface of the agent (Unger *et al*, 2003), as illustrated by Figure 14.20d. Finally, the agent can be linked to fibrin (in a thrombus) through an avidin biotin connection (Lindner, 2001). In this method (see Figure 14.20f) a biotin antibody is released to attach to the target cell such as fibrin, followed by avidin and an agent with a biotinylated phospholipid encapsulation.

Although these microbubbles may be designed primarily for drug delivery, a secondary function might be to aid in the identification of the release areas. Smart bubbles could be prepared to recognize specific antigens and to reveal locations and extent of disease, as well as to deliver appropriate therapy. Drugs (Unger *et al*., 2003) can be hidden inside the agent, be contained in the outer membrane or in multiple layers, be bonded covalently, or be dangling on the ends of tethers.

Many diseases are introduced and maintained by the vascular system. The research of Dayton *et al*. (2001) has shown that it is possible to distinguish between the acoustic characteristics of freely circulating contrast agents and those ingested or phagocytosed by white blood cells (leukocytes) that have been activated to attack

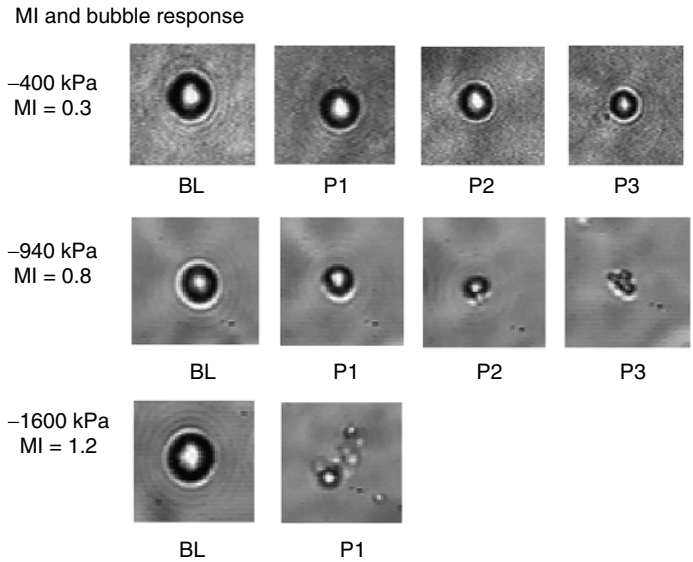

Figure 14.21 Time sequences of phagocytosed microbubbles at three pressure levels of insonification (one cycle at 2.25 MHz) corresponding to MI = 0.3 (top row), MI = 0.8 (middle row), and MI = 1.2 (bottom row). BL is baseline image; P1 represents each bubble snapshot with a time sequence increasing left to right 1 = 1, 2, 3) (from Lindner, 2001, *IEEE).*

inflammation. Their method used pulse inversion and frequency shifts to discriminate between free and phagocytosed bubbles. These results indicate that it may be possible to find the extent and degree of inflammation. Figure 14.21 shows that phagocytosed contrast agent microbubbles (those ingested by white blood cells in response to invaders, the agents) follow a trend similar to free microbubbles even though they are encased in a higher-viscosity medium. Allen *et al*. (2002) have found that therapeutic contrast agents with thick shells (500 nm) need longer pulses (not just one cycle) to reach a fragmentation threshold.

Thrombi and vulnerable plaque are cited as causes for heart attacks, stroke, and death. Other early work shows that targeted agents can find and bind with blood clots (Lindner, 2001). The potential is there for developing agents that not only can locate the thrombi, but also can deliver a therapeutic payload upon fragmentation. Another interesting application is agents that deliver cytotoxic drugs to regions of angiogenesis (growth of new blood vessels) that feed tumor growth (Lindner, 2001; Unger *et al*., 2003; Hughes *et al*., 2003).

Even though the emphasis here has been on encapsulated microbubbles, there are other types of therapeutic contrast agents. These include nongaseous acoustically reflective liposomes and perfluorocarbon emulsion nanoparticles (Hughes *et al*., 2003).

14.8 EQUATIONS OF MOTION FOR CONTRAST AGENTS

Models for contrast agent microbubble characteristics tend to fall into three groups of nonlinear equations that must be solved numerically. The theoretical basis for oscillating gas bubbles began with Lord Rayleigh (1917), who first derived an equation describing their behavior. Since then, the original equation has been improved on and some believe it should be called the Rayleigh–Plesset–Nolting–Nepiras–Poritsky equation for those who have contributed to its evolution (Leighton, 1994). The abbreviated name for this nonlinear equation of motion is the Rayleigh–Plesset equation. The next group consists of modifications to this basic equation to account for shell and other damping effects as well as shell forces. While not derived from first principles, this type of model, in which the shell is assumed to be extremely thin, often depends on experimentally derived parameters and is quite useful. The last group is the type of model that accounts for the finite thickness of the shell and forces, as well as the elastic nature of the shell in a more formal way.

The key variables for the Rayleigh–Plesset equation are a spherical bubble of radius R_0, filled with gas, floating in an incompressible fluid with a hydrostatic pressure, p_0, acted on by a time-varying input pressure field, $P(t)$. The internal pressure is a combination of the gas pressure, p_g, and the liquid vapor pressure, p_v,

$$p_i = p_g + p_v = 2\sigma/R_0 + p_v \tag{14.8}$$

where the inwardly directed surface tension pressure is $p_\sigma = 2\sigma/R_0$. The internal pressure is subject to the gas law so that the pressure just beyond the bubble wall (Leighton, 1994) is

$$p_L = (p_0 + 2\sigma/R_0 - p_v)\left(\frac{R_0}{R}\right)^{3\kappa} + p_v - 2\sigma/R \tag{14.9}$$

where $R = R(t)$ is the dynamic radius of the bubble to be found, and κ is the polytropic gas index. The overall equation is

$$\ddot{R}R + \frac{3\dot{R}^2}{2} = \frac{1}{\rho}\left(p_L - \frac{4\eta\dot{R}}{R} - P(t)\right) \tag{14.10a}$$

where each dot represents a derivative, ρ is the liquid density, and the forcing function, P(t), and a damping term for the shear viscosity of the fluid, η, have been added. Substituting Eq. (14.9) into Eq. (14.10a) provides a more familiar form of the Rayleigh–Plesset equation (Eatock, 1985),

$$R\ddot{R} + \frac{3\dot{R}^2}{2} = \frac{1}{\rho}\left((p_0 + 2\sigma/R_0 - p_v)\left(\frac{R_0}{R}\right)^{3\kappa} + p_v - p_0 - 2\sigma/R - \frac{4\eta\dot{R}}{R} - P(t)\right) \tag{14.10b}$$

The first, second, and next-to-the-last terms are nonlinear. Leighton (1994) discusses the limitations of this equation, which is applicable to a spherically symmetrical free gas bubble in an incompressible fluid and other alternative equations. The major shortcoming of this approach for applications to contrast agents is the missing shell.

The shell has the effect of increasing the overall mechanical stiffness of the contrast agent, and shell viscosity increases sound damping. Two primary modifications of Eq. (14.10b) can be added to account for the extra damping of the shell and the restoring force of the shell (de Jong, 1993; de Jong and Hoff, 1993). The damping from the viscosity damping of the fluid is supplemented by other sources of damping (de Jong *et al*., 1992; de Jong, 1993) to give a total damping parameter,

$$\delta_t = \delta_{vis} + \delta_{rad} + \delta_{th} + \delta_f \tag{14.11a}$$

where δ_{visc} is the viscous damping, δ_{rad} is reradiation damping, δ_{th} is thermal conduction damping, and δ_f is damping due to friction within the shell. Finally, another term for a shell-restoring force includes a shell elastic parameter, (S_p). The modified equation of motion is

$$\rho R\ddot{R} + \rho\frac{3\dot{R}^2}{2} = p_{g0}\left(\frac{R_0}{R}\right)^{3\kappa} + p_v - p_0 - 2\sigma/R - S_p\left(\frac{1}{R_0} - \frac{1}{R}\right) - \delta_t\omega_0\rho R\dot{R} - P(t) \tag{14.11b}$$

where p_{g0} is the initial pressure inside the bubble and ω_0 is the center frequency of the excitation pressure waveform. In this semiempirical approach, both S_p and δ_f are determined by measurement (de Jong and Hoff, 1993). The effect of the shell stiffness on resonance frequency was discussed in Section 14.5.1. Several figures, including Figures 14.2, 14.4, 14.10, and 14.11, were generated by this model.

A more accurate description of the effects of the shell have been presented by Hoff *et al*. (2000) based on Church (1995), who introduced a model in a more formal way to account for shell effects. The shell thickness can be modeled as a viscoelastic layer that changes thickness in proportion to the stretching of the dynamic radius. Two shell parameters, the shear modulus (G_s) and the shear viscosity (μ_s), can be determined from measurements.

For therapeutic contrast agents, a different approach is required for their thicker fluid shells. Allen *et al*. (2002) have generalized the Rayleigh–Plesset equation for a liquid shell of arbitrary thickness, viscosity, and density. Here more accurate descriptions of spherical oscillations and the dynamic changes of shell thickness are required for predictions of bubble instability and estimates of fragmentation thresholds.

14.9 CONCLUSION

From their accidental discovery to commercial realization, ultrasound contrast agents have proved to be a difficult technology to implement. Realization of clinically successful applications have been hard won through control of microbubble physics and new agent materials, adaptive signal processing techniques, and harmonic imaging. Working through the vascular system, contrast agents have opened new windows for diagnosis, revealing anomalies in circulation and disease states. They have also improved sensitivity and made possible clinically useful images for a portion

of the population previously written off as too difficult to image by conventional techniques. Ultrasound contrast imaging is still under development and growth as the uniqueness of each agent, its optimal ultrasound excitation, appropriate signal processing for different applications, and clinical efficacy, safety, and suitability are explored.

The potential applications of therapeutic contrast agents promise to create even higher challenges. Multiple uses for these agents will require even greater understanding of the physics of their behavior in order to position and deliver payloads in appropriate targeting sites and to provide adequate imaging sensitivity to reveal locations of different types of disease. The relatively low cost, portability, and general accessibility of ultrasound are key advantages in this new field of molecular imaging.

BIBLIOGRAPHY

Frinking, P. J. A., Bouakaz, A., Kirkhorn, J., Ten Cate, F. J., and de Jong, N. (2000). Ultrasound contrast imaging: Current and new potential methods. *Ultrasound in Med. & Biol*. **26**, 965–975. An overall review article on contrast imaging.

Goldberg, B. B., Raichlen, J. S., and Forsberg, F. (2001). *Ultrasound Contrast Agents: Basic Principles and Clinical Applications*, 2nd ed., Martin Dunitz Ltd., London. Information about the clinical application of contrast agents.

Hughes, M. S. Lanza, G. M., Marsh, J. N., and Wickline, S. A. (2003). Targeted ultrasonic contrast agents for molecular imaging and therapy: A brief review. *Medica Mundi*. **47**, 66–73. An introduction to therapeutic contrast agents. Also available on the web, which is a good way to keep up with this fast-changing field.

Leighton, T. G. (1994). *The Acoustic Bubble*. Academic Press, New York. A detailed and lucid source of knowledge about microbubbles.

Lindner, J. R. (2001). Targeted ultrasound contrast agents: Diagnostic and therapeutic potential. *IEEE Ultrason. Symp. Proc*., 1695–1703. An introduction to therapeutic contrast agents

Lord Rayleigh. (1917). On the pressure developed in a liquid during the collapse of a spherical cavity. *Philos. Mag*. **34**, 94–98.

Neppiras, E. A. (1984). Acoustic cavitation: An introduction. *Ultrasonics* **22**, 25–28.

Powers, J., Porter, T. R., Wilson, S., Averkiou, M., Skyba, D., and Bruce, M. (2000). Ultrasound contrast imaging research. *Medica Mundi* **44**, 28–36. An overall review article on ultrasound contrast imaging.

Reid, C. L., Rawanishi, D. T., and McRay, C. R. (1983). Accuracy of evaluation of the presence and severity of aortic and mitral regurgitation by contrast 2-dimensional echocardiography. *Am. Cardio*. **52**, 519.

Schrope, B. A., and Newhouse, V. L. (1993). Second harmonic ultrasound blood perfusion measurement. *Ultrasound in Med. & Biol*. **19**, 567–579.

Schrope, B., Newhouse, V. L., and Uhlendorf, V. (1992). Simulated capillary blood flow measurement using a non-linear ultrasonic contrast agent. *Ultrason. Imag*. **14**, 134–158.

Unger, E., Matsunga, T. O. Schermann, P. A., and Zutshi, R. (2003). Microbattles in molecular imaging and therapy. *Medica Mundi* **47**, 58–65. An introduction to therapeutic contrast agents. Also available on the web.

References

Abbot, J. G. (1999). Rationale and derivation of MI and TI: A review. *Ultrasound in Med. & Biol*. **25**, 431–441.

Allen, J., May, D. J., and Ferrara, K. W. (2002). Dynamics of therapeutic ultrasound contrast agents. *Ultrasound in Med. & Biol*. **28**, 805–816.

American Institute of Ultrasound in Medicine/National Electrical Manufacturers Association (AIUM/NEMA). (1998). *Standard for Real-Time Display of Thermal and Mechanical Acoustic Indices on Diagnostic Ultrasound Equipment*. AIUM Publications, Laurel, MD.

Anderson, A. L. and Hampton, L. D. (1980). Acoustics of gas-bearing sediments 1, background. *J. Acoust. Soc. Am*. **67**, 1865–1889.

Apfel, R. E. (1984). Acoustic cavitation inception. *Ultrasonics* **22**, 167–173.

Apfel, R. E., and Holland C. K. (1991). Gauging the likelihood of cavitation from short-pulse, low duty cycle diagnostic ultrasound. *Ultrasound in Med. & Biol*. **17**, 179–185.

Ayme, E. J., and Carstensen, E. L. (1989). Cavitation induced by asymmetric distorted pulses of ultrasound: Theoretical predictions. *IEEE Trans. Ultrason. Ferroelec. Freq. Control* **36**, 32–40.

Ayme, E. J., Carstensen, E. L., Parker, K. J., and Flynn, H. G. (1986). Microbubble response to finite amplitude waveforms. *IEEE Ultrason. Symp. Proc.,* 985–988.

Blackstock, D. T. (2000). *Fundamentals of Physical Acoustics*. John Wiley & Sons, New York.

Bleeker, H. J., Shung, K. K., and Barnhart, J. L. (1990). Ultrasonic characterizationof Albunex, a new contrast agent. *J. Acoust. Soc. Am*. **87**, 1792–1797.

Bouakaz, A., de Jong, N., and Cachard, C. (1998). Standard properties of ultrasound contrast agents. *Ultrasound in Med. & Biol*. **24**, 469–472.

Bouakaz, A., Frigstad, S., Ten Cate, F. J., and de Jong, N. (2002). Super harmonic imaging: A new imaging technique for improved contrast detection. *Ultrasound in Med. & Biol*. **28**, 59–68.

Brock-Fisher, G. A., Poland, M. D., and Rafter, P. G. (Nov. 26, 1996). *Means for Increasing Sensitivity in Non-Linear Ultrasound Imaging Systems*. US patent 5,577,505.

Burns, P. N., Powers, J. E., Simpson, D. H., Brezina, A., Kolin, A., Chin, C. T., Uhlendorf, V., and Fritzch, T. (1994). Harmonic power mode Doppler using microbubble contrast agents: An improved method for small vessel flow imaging. *IEEE Ultrason. Symp. Proc*., 1547–1550.

Chen, W.-S., Matula, T. J., and Crum, L. A. (2002). The disappearance of ultrasound contrast bubbles: Observations of bubble dissolution and cavitation nucleation. *Ultrasound in Med. & Biol*. **28**, 793–803.

Chomas, J., Dayton, P., Allen, J., Morgan, K., and Ferrara, K. (2000). High speed optical observation of contrast agent collapse. *Appl. Phys. Lett*. **77**, 1056–1058.

Chomas, J., Dayton, P., Allen, J., Morgan, K., and Ferrara, K. W. (2001). Mechanisms of contrast agent destruction. *IEEE Trans. Ultrason. Ferroelec. Freq. Control* **48**, 232–248.

Church, C. C. (1995). The effects of an elastic solid surface layer on the radial pulsations of gas bubbles. *J. Acoust. Soc. Am*. **97**, 1510–1521.

Cosgrove, D. O. (1998). Echo-enhancing (ultrasound contrast) agents, Chapt. 12. In *Ultrasound in Medicine*, Medical Science Series. F. A. Duck, A. C. Baker, and H. C. Starritt (eds.). Institute of Physics Publishing, Bristol, UK.

Crum, L. A. (1984). Rectified diffusion. *Ultrasonics* **22**, 215–223.

Dayton, P. A., Morgan, K. E., Klibanov, A. L., Brandenburger, G., Nightingale, K. R., and Ferrara, W. K. (1997). An preliminary evaluation of the effects of primary and secondary

radiation forces on acoustic contrast agents. *IEEE Trans. Ultrason. Ferroelec. Freq. Control* **44**, 1264–1277.

Dayton, P., Morgan, K., Klibanov, S., Brandenburger, G., and Ferrara, K. (1999a). Optical and acoustical observation of ultrasound contrast agents. *IEEE Trans. Ultrason. Ferroelec. Freq. Control*. **46**, 220–232.

Dayton, P. A., Morgan, K., Klibanov, S., Brandcriologer, G., and Ferrara, K. (1990b). Acoustic radiation force in vivo: Av mechanism to assist targeting of microbubbles. *Ultrasound in Med. & Biol*. **25**, 1195–1201.

Dayton, P. A., Chomas, J. E., Lum, A., Allen, J., Lindner, J. R., Simon, S. I., and Ferrara, K. W. (2001). Optical and acoustical dynamics of microbubble contrast agents inside neutrophils. *Biophys. J*. **80**, 1547–1556.

de Jong, N. (1993). *Acoustic Properties of Ultrasound Contrast Agents*, Ph.D. thesis. Erasmus University, Rotterdam, Netherlands.

de Jong, N., and Hoff, L. (1993). Ultrasound scattering properties of Albunex microspheres. *Ultrasonics* **31**, 175–181.

de Jong, N., Hoff, L., Skotland, T., and Bom, N. (1992). Absorption and scatter of encapsulated gas filled microspheres: Theoretical considerations and some measurements. *Ultrasonics* **30**, 95–103.

de Jong, N., Bouakaz, A., and Frinking, P. (2000). Harmonic imaging for ultrasound contrast agents. *IEEE Ultrason. Symp. Proc*., 1725–1728.

de Jong, N., Bouakaz, A., and Ten Cate, F. J. (2002). Contrast harmonic imaging. *Ultrasonics* **40**, 567–573.

Deng, C. X., and Lizzi, F. L. (2002). A review of physical phenomena associated with ultrasonic contrast agents and illustrative clinical applications. *Ultrasound in Med. & Biol*. **28**, 277–286.

Eatock, E. A. (1985). Numerical studies of the spectrum of low intensity ultrasound scattered by bubbles. *J. Acoust. Soc. Am*. **77**, 1692–1701.

Eller, A. I. and Flynn, H. G. (1965). Rectified diffusion through nonlinear pulsations of cavitation bubbles. *J. Acoust. Soc. Am*. **37**, 493–503.

Feigenbaum, H., Stone, J., and Lee, D. (1970). Identification of ultrasound echoes from the left ventricle by use of intracardiac injections of indocine green. *Circulation* **41**, 615.

Flynn, H. G. (1964). Physics of acoustic cavitation in liquids. In *Physical Acoustics*, Vol. 1, Part B. W. P. Mason (ed.). Academic Press, New York, pp. 57–172.

Forsberg, F., Liu, J. B., Chiou, H. J., Rawool, N. M., Parker, L., and Goldberg, B. B. (2000). Comparison of fundamental and wideband harmonic contrast imaging of liver tumors. *Ultrasonics* **38**, 110–113.

Frinking, P. J. A., Bouakaz, A., Kirkhorn, J., Ten Cate, F. J., and de Jong, N. (2000). Ultrasound contrast imaging: Current and new potential methods. *Ultrasound in Med. & Biol*. **26**, 965–975.

Frinking, P. J. A., de Jong, N., and Cespedes, E. I. (1999). Scattering properties of encapsulated gas bubbles at high pressures. *J. Acoust. Soc. Am*. **105**, 1989–1996.

Gaitan, D. F. and Crum, L. A. (1990). Observation of sonoluminescence from a single cavitation bubble in a water/glycerine mixture. *Frontiers of Nonlinear Acoustics*. M. F. Hamilton and D. T. Blackstock (eds.). Elsevier, London, pp. 191–196.

Goldberg, B. B. (1971). Ultrasonic measurement of the aortic arch, right pulmonary artery, and left atrium. *Radiology* **101**, 383.

Goldberg, B., Contrast Agents, Chapt. 3, In *Advances in Ultrasound Techniques and Instrumentation*, P. N. T. Wells, ed. Churchill Livingstone, New York.

Gramiak, R. and Shah, P. (1968). Echocardiography of the aortic root. *Invest. Radiol*. **3**, 356–388.

Hansen, R., Angelsen, B. A. J., and Johansen, T. F. (2001). Reduction of nonlinear contrast agent scattering due to nonlinear wave propagation. *IEEE Ultrason. Symp. Proc.*, 1725–1728.

Hoff, L., Sontum, P. C., and Hovem, J. M. (2000). Oscillations of polymeric microbubbles: Effect of the encapsulating shell. *J. Acoust. Soc. Am.* **107**, 2272–2280.

Holland, C. K., Roy, R. A., Apfel, R. E., and Crum, L. A. (1992). In vitro detection of cavitation induced by a diagnostic ultrasound system. *IEEE Trans. Ultrason. Ferroelec. Freq. Control* **39**, 95–101.

Kono, Y., Moriyasu, F., Nada, T., Suginoshita, Y., Matsumura, T., Kobayashi, K., Nakamura, T., and Chiba, T. (1997). Gray scale second harmonic imaging of the liver: A preliminary animal study. *Ultrasound in Med. & Biol.* **23**, 719–726.

Leighton, T. G. (1994). *The Acoustic Bubble*. Academic Press, New York.

Leighton, T. G. (1998). An introduction to acoustic cavitation, Chap. 11. In *Ultrasound in Medicine*, Medical Science Series, F. A. Duck, A. C. Baker, and H. C. Starritt (eds.). Institute of Physics Publishing, Bristol, UK.

Lindner, J. R. (2001). Targeted ultrasound contrast agents: Diagnostic and therapeutic potential. *IEEE Ultrason. Symp. Proc.*, 1695–1703.

Lord Rayleigh. (1917). On the pressure developed in a liquid during the collapse of a spherical cavity. *Philos. Mag.* **34**, 94–98.

Meltzer, R. S., Tickner, G., Salines, T. P., and Popp, R. L. (1980). The source of ultrasound contrast effect. *J. Clin. Ultrasound* **8**, 121–127.

Miller, D. (1981). Ultrasonic detection of resonant cavitation bubbles in a flow tube by their second harmonic emissions. *Ultrasonics* **22**, 217–224.

Mor-Avi, V., Caiani, E. G., Collins, K. A., Korcarz, C. E., Bednarz, J. E., and Lang, R. M. (2001). Combined assessment of myocardial perfusion and regional left ventricular function by analysis of contrast-enhanced power modulation images. *Circulation* **104**, 352–357.

Morgan, K., Kruse, D., Dayton, P., and Ferrara, K. (1998). Changes in the echoes from ultrasonic contrast agents with imaging parameters. *IEEE Trans. Ultrason. Ferroelec. Freq. Control* **45**, 1537–1548.

Ophir, J. and Parker, K. J. (1989). Contrast agents in diagnostic ultrasound. *Ultrasound in Med & Biol.* **15**, 319–333.

Porter, T. R., and Xie, F. (1995). Transient myocardial contrast after initial exposure to diagnostic ultrasound pressures with minute doses of intravenously injected microbubbles: Demonstration and potential mechanisms. *Circulation* **92**, 2391–2395.

Powers, J., Porter, T. R., Wilson, S., Averkiou, M., Skyba, D., and Bruce, M. (2000). Ultrasound contrast imaging research. *Medica Mundi* **44**, 28–36.

Rafter, P. G., Perry, J. L. T., and Chen, J. (July 30, 2002). *Wideband Phased-Array Transducer for Uniform Harmonic Imaging, Contrast Agent Detection, and Destruction. US patent 6,425,869.*

Shankar, P. M., Krishna, P. D., and Newhouse, V. L. (1998). Advantages of subharmonic over second harmonic backscatter for contrast-to-tissue echo enhancement. *Ultrasound in Med. & Biol.* **24**, 395.

Shi, W. T. and Forsberg, F. (2000). Ultrasonic characterization of the nonlinear properties of contrast microbubbles. *Ultrasound in Med. & Biol.* **26**, 93–104.

Shi, W. T., Hoff, L., and Forsberg, F. (2002). Subharmonic performance of contrast microbubbles: An experimental and numerical investigation. *IEEE Ultrason. Symp. Proc.*, 1908–1911.

Tucker, D. G. and Wesby, V. G. (1968). *Lancet* **1**, 1253.

Wei, K., Jayaweera, A. R., Firoozan, S., Linka, A., Skyba, D. M., and Kaul, S. (1998). Quantification of myocardial blood flow with ultrasound-induced destruction of microbubbles administered as a constant venous infusion. *Circulation* **97**, 473–483.

Wong, J. Y., Langer, R., and Ingber, D. E. (1994). Electrically conducting polymers can noninvasively control the shape and growth of mammalian cells. *Proc. Natl. Acad. Sci. USA* **91**, 3201–3204.

Wu, J. (1991). Acoustical tweezers. *J. Acoust. Soc. Am.* **89**, 2140–2143.

Wu, J. (2002). Theoretical study on shear stress generated by microstreaming surrounding contrast agents attached to living cells. *Ultrasound in Med. & Biol.* **28**, 125–129.

Wu, J. and Tong, J. (1997). Measurements of the nonlinearity parameter B/A of contrast agents. *Ultrasound in Med. & Biol.* **24**, 153–159.

Wu, J. and Tong, J. (1998). Experimental study of stability of contrast agents. *Ultrasound in Med. & Biol.* **24**, 257–265.

Ziskin, M. C., Bonakdapour, A., Weinstein, D. P., and Lynch, P. R. (1972). Contrast agents for diagnostic ultrasound. *Invest. Radiol.* **6**, 500.

15 ULTRASOUND-INDUCED BIOEFFECTS

Chapter Contents

15.1 INTRODUCTION

Safety is the focus of the last chapter, but it is first in importance. In order to convey this topic adequately, knowledge of acoustic focused fields, absorption, imaging systems, imaging modes, nonlinear effects, contrast agents, and measurements from previous chapters will be applied to our understanding of utrasound-induced bioeffects.

It is well known that too much sunlight can be harmful. Are there conditions under which the medical application of ultrasound also becomes destructive? Because of the thermal and mechanical interaction of ultrasound with tissue, the answers are a bit more complicated than they are for sunlight or x-ray exposures. Ultrasound-induced bioeffects depend on the intended outcome, as well as the clinical circumstance.

To examine intended outcome, we can classify the widespread use of medical ultrasound into five major categories: diagnostic imaging, therapy, hyperthermia, lithotripsy, and surgery. Diagnostic imaging includes scanned beams operating from 1–50 MHz (up to intravascular imaging and high-frequency applications). Physical therapists use low frequency (0.75–3 MHz) to apply ultrasound to promote healing, loosen muscles and joints, relieve pain, and increase blood flow to stimulate natural body defenses. Hyperthermia is the deliberate heating of a region of the body with ultrasound to selectively arrest the reproduction of cancerous tissues or tumors. Lithotripsy is the extracorporeal or percutaneous application of ultrasonic shock waves to selectively disintegrate kidney stones (or gallstones, etc.) *in vivo* without surgery. High-intensity focused ultrasound (HIFU) is the application of ultrasound to perform surgery within the body, specifically to produce highly localized lesions. There are other applications, such as dental descalers and ultrasonic scapels, which will not be covered in this discussion.

Most of the primary effects are based on the following three parameters (defined in measurements in Chapter 13): time-averaged source acoustic power (W), peak rarefactional pressure (p_r), and spatial peak temporal average intensity (I_{SPTA}). Diagnostic ultrasound will be compared to the other medical ultrasound applications introduced above. Typical parameters for these applications are summarized in Table 15.1, to which we shall refer as we compare the different modalities in detail in Section 15.6. An historical overview of ultrasound-induced bioeffects and safety issues begins this chapter (Section 15.2). The three primary parameters are then related to two significant ultrasound-induced bioeffects: temperature elevation (Section 15.3 and equations in Section 15.8) and mechanical effects (Section 15.4 and Chapter 14). The

TABLE 15.1 Comparison of Water Values for Medical Ultrasound Modalities (Mean values in parentheses)

Modality	f_c (MHz)	Power (W)	P_r (Mpa)	I_{SPTA} (W/cm^2)
B-mode	1–15	0.0003–0.285 (0.075)	0.45–5.54 (2.3)	0.0003–0.991 (0.34)
PW Doppler	1–10	0.01–0.44 (0.1)	0.67–5.3 (2.04)	0.173–9.08 (1.18)
U. therapy	0.75–3.4	1–15	0.3	3
Hyperthermia	0.5–5.0		0.6–6.0	1–10
HIFU	1–10			1000–10,000 (peak)
Lithotripsy	0.5–10		5–15	

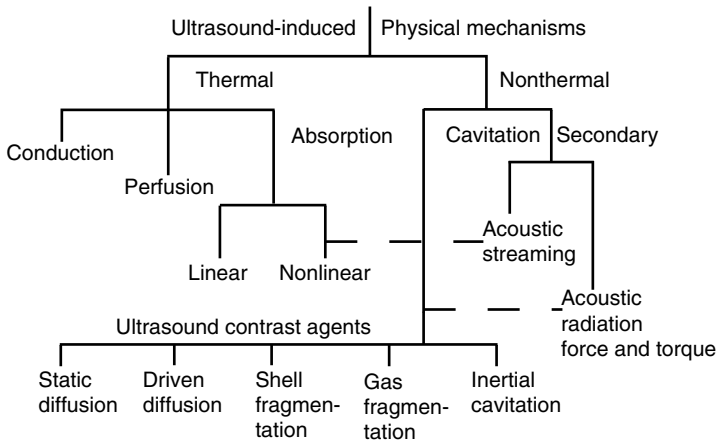

Figure 15.1 Relationships of ultrasound-induced bioeffects for diagnostic ultrasound.

output display standard (ODS) is explained briefly in Section 15.5. Secondary bioeffects, such as radiation force and streaming and their causes, are discussed in Section 15.7. A chart relating the bioeffects covered in this chapter is provided by Figure 15.1, to which we refer throughout the rest of the chapter.

15.2 ULTRASOUND-INDUCED BIOEFFECTS: OBSERVATION TO REGULATION

Clinical uses of ultrasound are known to have the potential to create two major types of bioeffects: heating and cavitation. Knowledge and understanding of these effects began from observations and evolved into their application, control, and regulation. O'Brien (1998) provides a comprehensive review of these events. More information can be found in Nyborg and Ziskin (1985) and NCRP (2002).

In the first practical realization of pulse-echo ranging in 1917 (discussed in Chapter 1), Paul Langevin developed large quartz transducers resonating at 150 kHz and connected to vacuum tube amplifiers. With an application of 2.5 kilovolts, he was able to produce one kilowatt of peak ultrasonic power. He noticed that fish were killed in a water tank when the source was turned on; if he put his hand in the water, he felt a painful sensation. This effect was later identified as cavitation, or the collapsing and resonating of gas bubbles by ultrasound.

During the 1930s and 1940s, ultrasound-induced heating of tissue was widely applied. As described earlier for physical therapy, ultrasound can have beneficial healing effects. Unfortunately at this time, because the mechanisms of and the amount of heat generated by ultrasound were not well understood or controlled, accidents occurred. Even though intensities of less than 10 watts/cm^2 were used, in some cases, ultrasound was found to accelerate cancer growth. These results led to the Erlangen conference, which put a hold on the therapeutic application of ultrasound. Research also indicated that ultrasound could form lesions at high enough intensities, and in 1942, ultrasound surgery was proposed.

Research on bioeffects continued as diagnostic imaging methods developed in the 1950s and 1960s. By the 1970s, enough clinical imaging equipment was in use to perform millions of exams. Professional, trade, and standards organizations such as the American Institute of Ultrasound in Medicine (AIUM), the National Electronics Manufacturers Association (NEMA), the International Electrotechnical Commission (IEC), and the World Federation for Ultrasound in Medicine and Biology (WFUMB), as well as the National Institutes of Health (NIH) and the National Council on Radiation Protection and Measurements (NCRP), began to formulate standard methods for ultrasound output measurement and imaging system use in the late 1970s and early 1980s. The first U. S. ultrasound safety standard appeared in 1983. Accurate measurements of acoustic output were made possible by the then-recent development of polyvinylidene-difluoride (PVDF) hydrophones.

In 1985, the Food and Drug Administration (FDA) of the United States was empowered by Congress to regulate the acoustic output of medical devices, including diagnostic ultrasound imaging systems. The limiting values selected were based on the output levels of imaging equipment that existed on or before May 26,1976, the date of the passage of the Medical Device Amendment to the Food, Drug, and Cosmetic Act. In the 1970s, ultrasound imaging equipment consisted mainly of static B-scanners with articulated arms and a few real-time mechanical scanners (see Chapter 1). By the mid-1980s, ultrasound equipment became dominated by real-time phased array and linear array imaging systems. The FDA limits were revised in 1987 and 1992, and the latest revision is listed in Table 15.2. The process for approving ultrasound imaging systems is called the 510 (*k*) procedure (FDA, 1993; 1997). The revision of 1992 introduced the output display standard (ODS)(AIUM/NEMA, 1998a), a revolutionary concept of providing users information on the two primary bioeffects, as described in Section 15.5 and explained in a document (AIUM, 2002).

To ensure a consistent means of measuring acoustic output values, measurement standards were developed by three organizations. A joint AIUM, NEMA, and FDA effort produced the first version in 1983, a second version in 1989, and a third version

TABLE 15.2 Track 3 FDA Limits on Acoustic Output

	Pre-ODS	Pre-ODS	Post-ODS	Post-ODS
Application	$I_{SPTA.3}(mW/cm^2)$	$I_{SPPA.3}(W/cm^2)$	$I_{SPTA.3}(mW/cm^2)$	MI
Fetal imaging	94	190	720	1.9
Cardiac	430	190	720	1.9
Peripheral vascular	720	190	720	1.9
Opthalmic	17	28	50	0.23

Revised in 1998. MI=Mechanical index

in 1998 (AIUM/NEMA, 1998b). These standards detailed not only how the measurements were to be carried out, but also the characteristics of the equipment needed for a particular measurement, as well as the maintenance and calibration of measurement equipment. During this same time period, the IEC Technical Committee 87 issued several standards governing acoustic output measurement and devices. At the present time, aside from regulations developed internally within individual countries, the IEC, including Technical Committee 62, has become the main international group for developing standards for ultrasound medical devices of all types. A slightly modified version of the ODS was incorporated into international standard IEC 60601-2-37 (IEC, 2002).

The organizations listed earlier continue actively to refine and develop the understanding of ultrasound-induced bioeffects. Fairly detailed discussions and reviews of the latest findings on bioeffects are disseminated in professional meetings and are published. The most active organizations are the AIUM and WFUMB Symposia on safety and standardization in medical ultrasound. In 2002, the NCRP published a most authoritative and thorough compendium on bioeffects. Ultrasound federations such as the Australasian Society for Ultrasound in Medicine (ASUM) and the European Federation of Societies for Ultrasound in Medicine and Biology (EFSUMB) have also published guidelines, recently summarized by Barnett *et al*. (2000). Individual societies also are involved in these issues. As examples, the American Society of Echocardiographers (ASE) published guidelines for the use of contrast agents, and the EFSUMB reviewed recent bioeffects publications (Duck, 2000).

Safety encompasses not only bioeffects, but also the application of ultrasound, including the training and qualification of the clinicians and sonographers. Some of these topics and a more complete listing of societies involved with ultrasound are given in Section 15.9.

15.3 THERMAL EFFECTS

15.3.1 Introduction

The concern over temperature rise induced by ultrasound in the body is based on observed changes in cellular activity as a function of temperature. In general, for

TABLE 15.3 Temperature Effects

Temperature Range (Degrees Centigrade)	Effect
37–39	No harmful effects for extended periods
39–43	Detrimental effects for long enough times
>41	Threshold for fetal problems for extended periods
44–46	Coagulation of protein
>45	Enzymes become denatured
>41.8	Cancer cells die (fail to reproduce)
	Often taken as damage threshold—except eye

From Miller and Ziskin, 1989.

healthy activity of enzymes, the enzymic activity doubles for every 10°C rise. The human body is able to tolerate hot drinks and fevers for a certain period of time. A fever of $+2°C$ is not a problem, where 37°C is taken as an average core body temperature. Table 15.3 identifies stages of temperature effects.

Data can be combined to determine the shortest duration for any temperature reported for a detrimental effect; it is possible to develop an empiric relation for times below, for which there have been no observed adverse effects (Miller and Ziskin, 1989),

$$t = 4^{43-T}(minutes) \tag{15.1}$$

where T is temperature in degrees Centigrade. Even though the validity of this equation is discussed in more detail, including pregnant women in hot tubs and pigs in heated chambers (NCRP, 2002), this equation is still a reasonable guide to the effects of heating and exposure. Times from this equation are plotted in Figure 15.2. For example, an elevation of 2°C gives a time of 256 min, and a 6°C rise gives a time of 1 min. This equation implies that by shortening the time of the exam, the detrimental effects of higher temperature rises can be minimized.

What are the mechanisms by which ultrasound can heat tissues? During propagation, energy is lost to absorption; that energy is converted to heat. The direct contact of the transducer creates the direct transfer of heat by conduction. These mechanisms are diagrammed in Figure 15.1.

15.3.2 Heat Conduction Effects

The transducer itself can be a source of heat by direct contact with the body. A transducer that is left unused and selected may have acoustic power flowing to the outer absorbing lens, where it encounters air, is reflected back, and causes self-heating (Duck *et al.*, 1989). Since the study of this effect, surface temperature rises of transducers in air or an air–gel mixture are controlled not to exceed a few degrees by IEC Standard 60601-2-37 (IEC, 2002).

Once the transducer is placed on the body and is acoustically loaded, the energy is released to propagate into the body and not the transducer, and the normal mecha-

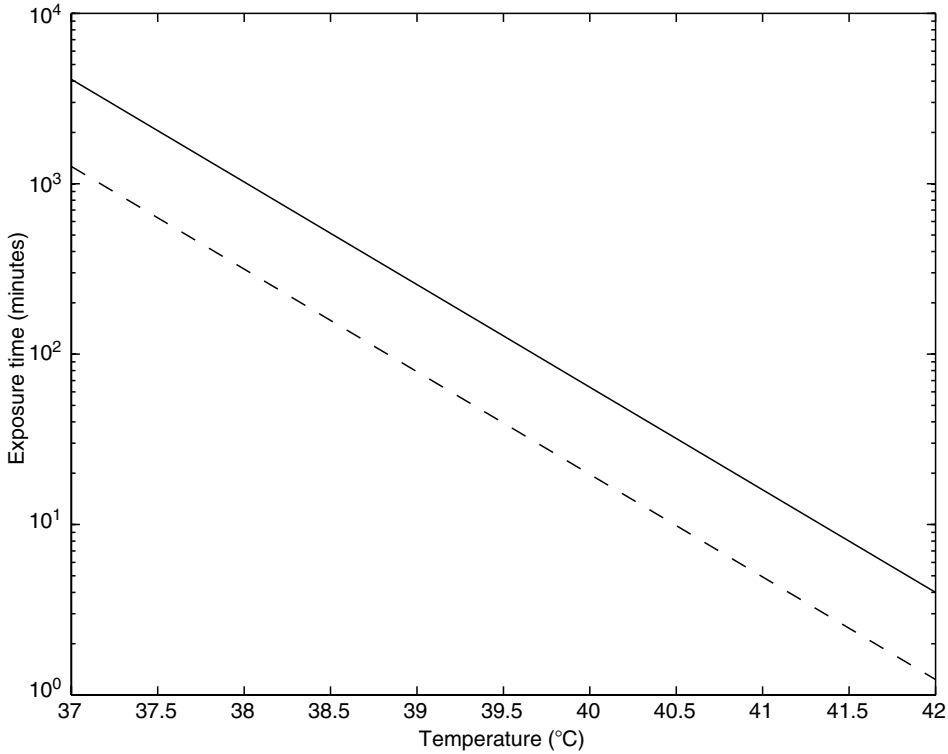

Figure 15.2 Curves relating temperature elevation to duration of exposure at which there have been no observed adverse effects. Curve A corresponds to Eq. (15.1); dashed line corresponds to Eq. (15.5).

nisms of body cooling through perfusion reduce the heating considerably. For most healthy people, the skin can detect small changes in temperature; however, the communication of this sensation may not be possible for the ill and very young. In addition, for intracavity transducers such as transophageal probes, built-in safety sensors detect excessive temperature rises, alert the user, and cut off the electric power to the transducer (Ziskin and Szabo, 1993). Because the temperature contribution is very localized to the surface and smaller than the absorption contribution, it is often neglected in temperature elevation estimates.

15.3.3 Absorption Effects

The pattern of heating initially is related to the distribution of intensity in the absorbed beam. The volume rate of heat generation, q_v, due to absorption can be modeled as proportional to the acoustic intensity, $I(x,y,z)$, and absorption α at a single frequency,

$$q_v = 2\alpha I \tag{15.2}$$

The highest temperatures along the beam axis are not that sensitive to beam details and can be determined from an integral of q_v times the temperature response of a small source in the medium. For circularly symmetric transducers, the temperature rise can be calculated by a heated disk model (referred to in Section 15.8). After initial propagation, the heat diffuses slowly into the tissue (a process that expands, smoothes out, and diminishes the original pattern). At higher pressure levels, additional heating is caused by nonlinear effects (as explained in Chapter 12).

15.3.4 Perfusion Effects

The cooling effects of blood perfusion in tissue must also be included in an estimation of temperature elevation. Whereas the full computation requires the bioheat equation (also described in Section 15.8), Nyborg (1988) has shown that for a long enough time, the temperature from a small source has a spatial falloff that is exponential,

$$T = (2C/r)\exp(-r/L) \tag{15.3a}$$

where L is a perfusion length and

$$C = \frac{q_v dv}{8\pi c_v \kappa} \tag{15.3b}$$

in which dv is the volume of the source, c_v is the volume-specific heat for tissue, and κ is thermal diffusivity. Perfusion lengths for different tissues range from 1 to 20 (as given by Table 15.4). From this table, the heart, which is very active and perfused with blood, has a low value of 3.2 mm, and fat has a large perfusion length of 19.5 mm. The latter contributes to the high thermal insulation properties of fat. Nyborg (1988) also showed that once a uniform temperature distribution is established and the heat source is turned off, temperature decays exponentially as

$$T = T_0 \exp(-t/\tau) \tag{15.4}$$

where τ is the perfusion time constant (values of which are found in Table 15.4). Note that for the heart, decay is fast or 1.15 minutes to the *1/e* value compared to 66.7 minutes for fat.

TABLE 15.4 Perfusion Parameters

Tissue	Perfusion Time Constant τ seconds	Thermal Diffusivity κ mm^2/s	Perfusion Length L mm
Kidney	14.7	0.13	1.4
Heart	69	0.15	3.2
Liver	98	0.15	3.8
Brain	109	0.13	3.8
Muscle	2140	0.15	18
Fat	4000	0.095	19.5

From NCRP (1992) and AIUM (1998).

15.3.5 Combined Contributions to Temperature Elevation

A computation for the thermal rise at the interface between a transducer and the body of a patient, including perfusion and absorption, is given by Figure 15.3. For this case, the transducer was turned on at $t = 0$ and off at $t = 180$ sec. The direct heat conduction contribution can be seen to be small. More details and a more exact description of the temperature-generating process are given in Section 15.8.

For a stationary mode such as Doppler or M-mode, the beams in one direction are important. In a scanned mode, such as B-mode sector scan, a number of beams are sent in different directions into the body, so the determination of the resulting temperature distribution must account for the arrangement of the beams. Different simple models for estimating the temperature rise for different scanned and non-scanned situations will be presented in Section 15.5.2.

15.3.6 Biologically Sensitive Sites

In addition to soft tissue, there are several sites that are regarded as more sensitive to temperature. One is the fetus, which undergoes considerable change in the first trimester. As the fetal bone develops and ossifies, it can absorb higher temperature elevation than the surrounding soft tissue under insonification. When transducers are placed directly on the neonatal and adult skull, a concern is that the elevated

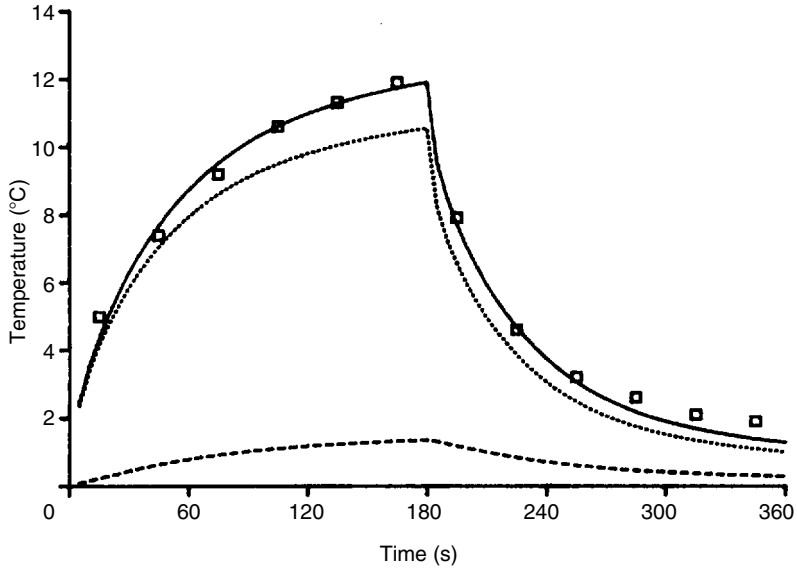

Figure 15.3 Computed temperature for the interface between a 5-MHz circular transducer and a patient. (Solid line) Total temperature rise; dots are data from Williams *et al.*, 1987. (Dotted line) Temperature contribution from absorption. (Dashed line) Temperature contribution from surface conduction. $I_0 = 140\,\text{mW/cm}^2$, L = 4.6 mm, and $\alpha = 50\,\text{Np}^{-1}\,\text{m}$ (from Nyborg, 1988).

temperature of the bone may alter the temperature of brain tissue. Another sensitive site is the eye, which is well perfused except for the lens and is therefore somewhat limited in its ability to dissipate externally applied heat. These sites are discussed by Rott (1999a).

Recommendations from WFUMB (1998) in regard to ultrasound-induced temperature elevation are the following:

1. A diagnostic ultrasound exposure that produces a maximum *in situ* temperature rise of no more than 1.5°C above normal physiological levels (37°C) may be used clinically without reservation on thermal grounds.
2. A diagnostic ultrasound exposure that elevates embryonic and fetal *in situ* temperature above 41°C (4°C above normal temperature) for 5 min or more should be considered potentially hazardous.
3. The risk of adverse effects is increased with the duration of exposure.

One can see that points two and three correspond to a more conservative exposure duration law than Eq. (15.1), or

$$t = 4^{42.15-T} \tag{15.5}$$

Here a rise of 1.5°C corresponds to a duration of 158 min; a rise of 4°C corresponds to 5 min (see Figure 15.2). These calculations assume that the transducer is held exactly at the same place for the whole time (a long dwell time); in reality, there is considerable movement in a typical exam and the hand is not steady for extended periods of time. The main problem for users of ultrasound was how to apply this information and to find out what temperature rises were generated by the imaging system.

15.4 MECHANICAL EFFECTS

Major ultrasound-induced mechanical effects have been covered in great detail in Chapter 14. These effects are summarized in Figure 15.1. As discussed in Section 15.5.3, the focus of attention in this area is shifting from naturally occurring nucleation sites in the body to ultrasound contrast agents. These encapsulated agents vary considerably in their response to ultrasound, depending on the gas and shell materials.

15.5 THE OUTPUT DISPLAY STANDARD

15.5.1 Origins of the Output Display Standard

Until 1992, ultrasound imaging systems were regulated by measuring highest values of derated acoustic output parameters in various modes (B-mode, Doppler, etc.). The two primary ultrasound-induced bioeffects had been known for a number of years, but the relationship between these effects and the acoustic output had not been thoroughly examined. Furthermore, questions remained as to which output

parameters were most relevant. Were there other parameters connected to bioeffects equally worthy of being measured? Where were the locations of the highest temperature elevations, and how could they be estimated? Was there a way of relating cavitation to parameters of an imaging system? These questions and many more confronted a team formed from AIUM, NEMA, and the FDA to develop a revolutionary step in acoustic output control. Their goal was to come up with real-time algorithms for predicting relative temperature rises and the potential for inertial cavitation events. The output of these algorithms were to become the thermal indices (TIs) and mechanical index (MI) that would be displayed in real time on imaging systems for the particular mode and settings used at the time. The result of several years of work (1988–1992) by these experts was the output display standard (ODS) (AIUM/NEMA, 1998a).

The indices are relative indicators—not predictors—of absolute values. An example of a thermal index is

$$TI = \frac{W_0}{W_{deg}} \tag{15.6}$$

where W_0 is the time-averaged acoustic power of the source (or another power parameter) and W_{deg} is the power necessary to raise the target tissue 1°C based on specific tissue and thermal models. A conservative perfusion length of 10 mm was used in the TI derivations. With this kind of a definition, the temperature-predicting algorithms are linked to an actual acoustic output parameter (in this case, W_0) that is calibrated to the system output through extensive acoustic output measurements. Because internal acoustic output control algorithms (Szabo *et al.*, 1988) limit the acoustic output as a function of system settings and the applied voltage levels to the transducer for the mode selected, this information is available for the real-time calculations of the thermal and mechanical indices.

The MI, already introduced in Chapter 14, is

$$MI = p_{r.3}(z_{sp})/\sqrt{f_c} \tag{15.7}$$

where the derated pressure (*MPa*) is at the location of the derated pulse intensity integral, $PII_{.3}$ (see Chapter 13) maximum, and f_c is the center frequency (or more recently, the acoustic working frequency) in MHz. To make MI unitless, it is multiplied by a units factor $\sqrt{1\,MHz}/1\,MPa$. Again, the value of pressure is a known and system-controlled acoustic output parameter in a predictive formula.

The detailed formulas for the indices are not discussed here; the reader is referred to the standards themselves: AIUM/NEMA (1998a), Standard 60601-2-37 62 (IEC, 2002), and an explanation of their derivation by Abbott (1999).

15.5.2 Thermal Indices

Where are the hottest spots located? On which parameters do the temperature rises depend? Three main TI categories are soft tissue (TIS), bone (bone at focus) thermal index (TIB), and cranial-bone (bone at surface) thermal index (TIC). The main results are summarized in Figure 15.4.

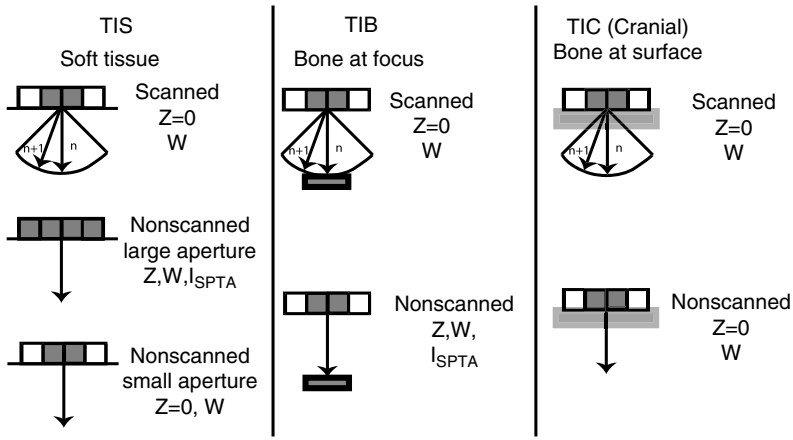

Figure 15.4 Thermal indices (TIs) from the ODS for different modes and configurations. Shaded regions represent active apertures.

On the left side of this figure are the soft tissue indices. On the top left is a scanned mode where, because of the overlap of beams, the hottest spot is at the surface and is proportional to power (W_0). Below are two nonscanned modes for large apertures (active area $> 1\,\text{cm}^2$) and small apertures (active area $\leq 1\,\text{cm}^2$). The large aperture, depending on the strength of focusing, can have a hot spot related to I_{SPTA} at some depth or at the surface related to power.

The two indices associated with bone are the TIB and TIC (in the next columns of Figure 15.4). The motivation for the TIB (middle column) is the sensitive case of a fetal bone located at the focal depth. Two cases include one that is scanned, where the location of maximum heating is at the surface and related to power, and another that is the nonscanned case of bone at the focal depth and related to intensity. Bone absorbs at a higher rate than soft tissue (Carstensen *et al.*, 1990), so for the nonscanned case, the prediction is related to the -6-dB beamwidth at the depth where intensity is the highest. Finally, for the cranial TIC in the right column of Figure 15.4, the hot spot is related to power at the surface for both the scanned and nonscanned cases.

As an example of a TI calculation, the TIS of the scanned mode at the surface will be used. For this case, a typical power is 78 mW and if the center frequency is 5 MHz,

$$\text{TIS} = \frac{W_0(\text{mW})}{210/f_c(MHz)} = \frac{78}{210/5} = 1.94 \tag{15.8}$$

In summary, in five out of seven cases (as shown in Figure 15.4), TI is related to power and is located at the skin surface.

15.5.3 Mechanical Index

The rationale for MI was explained in Section 14.4. The formula is based on the assumption that a nucleation site of just the right resonant size is available for inertial

cavitation. Holland *et al*. (1992) demonstrated that cavitation could occur when an imaging system insonified water full of bubbles of different sizes. When the experiment was repeated with degassed water, no cavitation events were observed. At the time that ODS was developed, there were three reasons for including an MI. The first was that cavitation was observed to occur with lithotripters, although at much lower frequencies and higher pressure levels. Second, *in vitro* experiments with lower organisms showed that cavitation might occur at pulse levels similar to those used in diagnostic imaging. Third, lung and intestinal hemorrhages occurred in adult (but not fetal) mice at diagnostic levels. Now, a decade later, these reasons and the original data have been reviewed by the original researchers. Their conclusions (Carstensen *et al*., 2000) indicate that there may not be any natural nucleation sites within the human body of any consequence for mechanical effects to occur. In addition, the fetus does not provide any nucleation sites for cavitation (Rott, 1999b). More on this topic can be found in Sections 15.5.4 and 15.7. The FDA has limited the maximum value of MI to 1.9 (as in Table 15.2), except for special cases. Finally, the widespread use of ultrasound contrast agents has opened up the possibilities of other kinds of mechanical effects (these are also discussed in Section 15.7).

15.5.4 The ODS Revisited

Even though the original intention of the architects of the ODS was not to develop exact predictions of temperature rises, but rather to develop relative indications of temperature effects, that has not stopped people from using TIs as absolute temperature estimators. In order to provide reasonably simple algorithms for real-time ODS calculations, some compromises on the conservative side were made (Curly, 1993; AIUM, 1998a; Abbott, 1999). Research showed that many of the temperature elevations were dependent on acoustic power (a parameter relatively insensitive to details of beam structure). In a recent survey of different imaging systems (as discussed in Section 15.6.6), total acoustic power in water is typically only 125 mW with a maximum value of about 440 mW (Henderson *et al*., 1995). O'Brien and Ellis (1999) calculated the source time-averaged power needed to achieve a derated upper limit of $I_{SPTA.3} = 720\ \text{mw/cm}^2$.

Shaw *et al*. (1997, 1999) and Duck (2000), using a more comprehensive temperature prediction program, found that the TI formulas gave values that were equal to or greater than their computations, sometimes by a factor of two. By using manufacturer's data for pulsed Doppler, they predicted nonscanned TI values in excess of 1.5 for a number of cases. Shaw *et al*. (1998) also compared actual temperature rises measured in thermal test objects for 19 system transducer combinations to the corresponding calculated on-screen TI values. There is reasonable agreement between the calculated TI and the measured temperature rise under attenuated conditions. Exceptions were for cases without overlying absorption such as the cranial TI, TIC. These results were in agreement with the earlier findings of Wu *et al*. (1995), who also compared TIC predictions from an imaging system to thermocouple measurements on bone and a tissue-mimicking material (TMM) phantom. They demonstrated that the temperature rise caused by the absorption was well predicted and deviations in data could be attributed to transducer self-heating not included in the prediction. Heating and cooling mechanisms are diagrammed in Figure 15.1.

Ellis and O'Brien (1996) compared maximum temperature predictions from their monopole source model to the nonscanned TIS formula based on the heated disk model. They found that the TIS agreed with their more accurate results for the majority of cases that cover most of the combinations of apertures and frequencies in commercial imaging systems. Specifically, they demonstrated that for F numbers (F#s) of less than 2, the TIS underestimated temperature rise but the TIS values were less than 0.4 and need not be displayed. They found that the unscanned TIS model underestimated the temperature rise predicted by their model for larger apertures and higher frequencies; however, these exceptional cases, $F > 3$, are most likely not combinations that occur clinically (an aperture of 2 cm at 12 MHz and apertures of 4 cm at 7 MHz and above).

Researchers from the NCRP (2002) have reviewed a number of temperature predictions compared with tissue-mimicking material TMM phantoms and animal experiments. They have concluded that the ODS algorithms are often higher than those that would occur clinically. They identified three areas where underestimates could occur: (1) where a significant low-absorption path in tissues is involved, (2) when transducer self-heating provides a significant contribution, and (3) when measurements made for ODS are influenced by nonlinear propagation saturation effects.

Cavitation effects have been extensively discussed in reports (AIUM, 2000; NCRP, 2002). The reviews by Rott (1999b) and Carstensen *et al*. (2000) indicate the likelihood that cavitation may occur in the human body, is smaller, and its consequences may not be as clinically significant as originally thought when the MI was conceived.

The introduction of contrast agents, however, presents an different potential for cavitation (as discussed in Chapter 14 and shown in Figure 15.1). Different types of ultrasound contrast agents vary greatly in their response to the same insonifying field. After fragmentation of the shell of an agent, free gas can either diffuse or cavitate, depending on the type of gas and the incident pressure field. Until better methods are devised, MI serves as a threshold indicator for this situation.

15.6 COMPARISON OF MEDICAL ULTRASOUND MODALITIES

15.6.1 Introduction

Bioeffects involved with diagnostic ultrasound imaging can be compared to those associated with other medical ultrasound modalities. Ultrasound-induced bioeffects form a continuum of effects when all major modalities are examined. To put these modalities in perspective, some of the primary parameters for these modalities are listed in Table 15.1. More information on each modality is available in the following sections.

15.6.2 Ultrasound Therapy

Ultrasound therapy has been in wide use for more than 40 years (Stewart, 1982; Lehmann, 1990). In the 1950s and 1960s, most medical ultrasound conference papers

were about therapy—not imaging. Main applications that have been reported to be of clinical value include reduction of muscular spasms; treatment of contractures; relief and healing of sports-related injuries; relief of pain; increased extensibility and treatment of contractures for collagen tissue (scar tissue) and connective tissues; heating of joint structures; treatment to improve limited joint motion, decrease in joint stiffness, arthritis, periarthritis, and bursitisis; wound healing (Dyson *et al*., 1970); and the healing of varicose ulcers. Ultrasound therapy includes many other applications from cosmetic and postcosmetic surgery treatment, including sonopheresis to improve the penetration of products to muscle treatment for racehorse injuries. Not all ultrasound therapy claims for efficacy in new applications have been substantiated clinically.

Ultrasound is mainly applied by physical therapists who are trained to place the transducer using a coupling oil or gel over a muscular area with a moving rotary motion to minimize dwell time. The output is limited typically to a maximum of 3 watts/cm^2. A continuous wave or pulsed mode is usually available, and a timer up to 10 min is usually required. In normal application, ultrasound can be applied near bones where additional heating can occur, including shear wave conversion, so the therapist remains vigilant, keeps the transducer moving, and asks if the patient feels excessive heat. The author has had a number of ultrasound therapy sessions for muscular injuries and can attest to their beneficial effects. During ultrasound application, he felt a warm sensation in the applied area.

From Table 15.1, a key acoustic output parameter is the spatial average temporal average intensity (I_{SATA}) at the face of the transducer, which is the power divided by the effective radiating area. A typical maximum value for this intensity is 3 watts/cm^2.

In conclusion, the heating mechanism in ultrasound therapy is a much higher I_{SATA} and a combination of higher acoustic power applied over a large surface area than that used for diagnostic applications. Ultrasound therapy is applied routinely, most likely, in far greater numbers than those of diagnostic ultrasound and for a longer overall period of commercial application. The ultrasound in this modality is known to interact with tissue, injuries, and wounds.

15.6.3 Hyperthermia

Table 15.3 lists temperatures in excess of 41.8°C as a critical temperature above which cancer cells have difficulty reproducing and surviving. Hyperthermia with ultrasound is a means for insonifying cancerous tissues typically in a range of 41–45°C to stop their growth, often in conjunction with other therapies such as chemotherapy (Hand, 1998; Hynynen, 1998). Hyperthermia systems (Diederich and Hynynen, 1999) consisting of arrays of planar piston transducers have been built to cover large surface areas for superficial cancer growth. For deep-seated tumors, strongly focused transducers, often in an overlapping arrangement, have an advantage over other nonultrasound hyperthermia methods in directing heat selectively to an interior region of the body. Phased linear, two-dimensional, and annular arrays have been investigated (Ebbini and Cain, 1989). Intracavitary devices for hyperthermia are primarly transrectal for application to the prostate.

For conventional applications, the temperature of cancerous tissue is elevated to 42–43°C for an extended period of 30–120 min. In accordance with an exposure law, equivalent doses can be administered at higher temperatures and shorter durations. Considerable attention must be directed to account for the cooling effects of perfusion from both large and small vessels and to avoid bones in the acoustic path (Lele, 1972; Newman and Lele, 1985).

In terms of acoustic output for hyperthermia, I_{SATA} ranges from 2 to 10 W/cm^2 for superficial application, and low duty cycle, high peak intensities up to 1 kWw/cm^2 are used for deeper, pulsed applications (Hynynen, 1987). Transducers are not scanned but held still. The heating mechanism is proportional to acoustic intensity delivered to the target site.

15.6.4 High-Intensity Focused Ultrasound (HIFU)

Surgery with ultrasound can be achieved by focusing high-intensity ultrasound (several hundred kW/cm^2) on a tissue region to produce a lesion (Fry, 1979; ter Haar, 1995, 1998). Exposure is typically 5–10 sec, and temperatures of 60–100° C are achieved (Chen *et al*., 1997). The ellipsoidal shape of the lesion corresponds roughly to the −6-dB contour of the beam near the focal point. The heating is very selective and confined to a small region in the order of 1–10 mm. When done well, the lesion is ''trackless,'' or there is no tissue damage between the skin entry point and the lesion itself. A series of lesions, with time intervals in between for cooling, can be created in a pattern to cover a larger area. The advantage of ultrasound surgery is that no incisions are required; it is precise, and, if done properly, there is little extra trauma to the patient.

To first order, assumptions in modeling the heating are no perfusion and the same heating mechanism based on absorption (described earlier). The heating is very rapid so that the heating process is very nonlinear. Ultrasound surgery creates instantaneous coagulative necrosis, since temperatures in excess of 60°C are used (see Table 15.3). At very high temperatures, tissue can be boiled and vaporized, and the resulting gases can block the penetration of ultrasound and cavitate (Sanghvi *et al*., 1995; Chen *et al*., 1997). These events can cause uncontrollable results and are to be avoided (Meaning *et al*., 2000). However, bubbles can be alternatively considered as enhancers to the heating process (Holt and Roy, 2001). The effects in this range of exposure are collectively called ''super MI effects'' in Chapter 14.

Commercial HIFU systems are available in several countries, including the United States. A number of HIFU systems are being used in China, where tens of thousands of people have undergone HIFU surgery, mainly for tumors. Work is continuing to refine the methodology.

In terms of acoustic output, pulses on the order of 0.1–10 sec long are used for each lesion and are repeated about every 10 seconds for other locations. Like the other modalities, the primary mechanism in HIFU is heating, but unlike them, the heat is produced rapidly with much higher peak intensities, I_{SATA}, in the range of 1–10 kW/cm^2 averaged over the −6-dB contour in the focal plane.

15.6.5 Lithotripsy

Extracorporeal shock wave lithotripters (ESWLs), introduced in 1984, are noninvasive devices designed to disintegrate kidney stones and other types of stones without surgery (Halliwell, 1998, Delius, 2000). The patient is placed in a water tank or coupled through a water bag, and a high-amplitude, high focal gain transducer/reflector is focused on the kidney. Stones are fragmented and pulverized by the repeated action of lithotripter pulses and are naturally passed out of the patient. The hard stones absorb most of the pressure so that the surrounding tissue is relatively unaffected. The mechanisms of destruction are believed to be a combination of cavitation (Coleman and Saunders, 1993) and cyclic mechanical stressing. Types of lithotripters include spark discharge (electrohydraulic), piezoelectric, electromagnetic magnetostrictive, and chemical (explosive charges). Many models are in widespread use because 5–15% of the population is afflicted with kidney stones.

The acoustic output of lithotripters proved to be difficult to measure as hydrophones were destroyed in the process. Eventually this problem was solved, and lithotripter waveforms in water typically have a high positive p_c part with a peak in the 30–120 MPa (Coleman and Saunders, 1989) range followed by a shallower negative p_r part in the -5 to -15 MPa range (Delius, 2000). The shape of the waveform (in particular, the extremely large positive-to-negative change in pressure within the waveform) is believed to play a role in the fragmentation process. The waveform starts with an extremely steep rise time (nanoseconds), the p_c/p_r ratio is typically 4–8 (Harris, 1992), and the overall pulse duration is on the order of a few microseconds. A key difference between diagnostic imaging and lithotripsy is that the center frequency of lithotripter pulses is about 100–600 kHz (Delius, 2000) and the transient portions (nanoseconds rise time) of the waveform extend over a broader bandwidth. Another difference is a low-duty cycle (typically on the order of a pulse a second); consequently, the I_{SPTA} is extremely small. For measurement purposes, PVDF hydrophones are used (Lewin *et al*., 1990; Halliwell, 1998).

15.6.6 Diagnostic Ultrasound Imaging

Even though derated values are usually considered for the acoustic output of diagnostic ultrasound imaging, water values will be used for discussion to be consistent with the water values for other medical ultrasound modalities in Table 15.1 for comparison purposes only. Diagnostic values in Table 15.1 were taken from a survey of 82 imaging systems by Henderson *et al*., (1995). For each parameter, a range of water values is given, as well as the median (most frequently occurring) value in parentheses. These table values represent an increase over those obtained by Duck and Martin in 1991, just before the ODS was introduced with revised FDA values (see Table 15.2).

In order to put these water values into meaningful contexts, clinical applications need to be considered. For almost every medical ultrasound modality considered that has a bioeffect, absorption plays a dominant role. For example, consider the water values of I_{SPTA} that varied over a considerable range of values. From the survey of acoustic output by Henderson *et al*. (1995), 90% of the values fell below 3 W/cm^2, and the highest value, 9.08 W/cm^2, had a corresponding power of only 130 mW. If

the manufacturers complied with the FDA requirements, which is highly likely, then the highest derated intensity corresponding to the measured values listed in Table 15.2 is $I_{SPTA.3} = 720\,\text{mW/cm}^2$. Derating is the product of the water intensity as a function of depth multiplied by an exponential derating factor as a function of depth. The net result is a shifting of the position of the peak value as well as a reduction in value (as illustrated by Figure 13.15). The same effect results if another value of absorption, more appropriate to a given clinical situation, is used. A single peak water value is insufficient information to apply derating appropriate to a clinical situation.

Ideally, the user would have full knowledge of all the tissues and their size along the acoustic path and be able to calculate the absorption to the target region of interest while performing the exam. Smith *et al*. (1985) have shown through measurements of a cadaver that reasonable estimates of acoustic intensity can be made from a detailed knowledge of the acoustic properties for the individual layers, including power law absorption, impedance and sound speed, and layer thickness. To improve on a layered model would be more involved. From the discussions of aberration and scattering of real tissue in Chapter 9 as well as of the beam simulations in Chapter 12 for beams passing through abdominal walls, the use of homogeneous layers may overestimate the coherency of a beam and its ability to focus through realistic body walls. The homogeneous layer approach can serve to estimate the most coherent propagation possible, equivalent to the worst case for safety purposes.

At this stage in the evolution of ultrasound imaging, however, the system user does not have the detailed information on loss along the acoustic path but does recognize the clinical application and target site. The user may decide to accept an average conservative value such as the derating factor applied to the calculation of output display indices with the realization that in certain circumstances, the losses may be underestimated. One possible underestimated situation often debated is the path to the fetus. This topic is extensively reviewed in Section 9.3.4 of the NCRP report (2002). The present derating factor, NCRP researchers concluded, is reasonable for second and third trimester exams but not conservative enough to cover all obstetric cases, and they provided options. For these exceptional cases, with a long fluid path, the user can use the output display indices to lower the transmit level to the minimum level necessary to obtain an image. This strategy is consistent with the ALARA principle, which is to adjust acoustic output to a level "as low as reasonably achievable" (Ziskin and Szabo, 1993).

How do the acoustic output levels of diagnostic ultrasound compare with other medical ultrasound modalities? From Table 15.1, a principal difference is that for most diagnostic applications, I_{SPTA} is, on the average, less than a W/cm^2, whereas ultrasound therapy and hyperthermia typically have 3–10 W/cm^2. While an I_{SPTA} value in an imaging plane may cover a region of 1 to a few mm^2, ultrasound therapy and superficial hyperthermia are applied directly over areas typically larger than $10\,\text{cm}^2$ with much higher intensities. For these two modalities, the intended outcomes are to raise the temperature of tissue by several degrees Centigrade. For diagnostic imaging, TI formulas of the ODS with derated values or alternative methods (NCRP, 2002) can be used to estimate temperature elevation and ALARA can be used to minimize exposure time.

Both HIFU and lithotripsy employ very high-amplitude pressure pulses that can cause cavitation. Unlike the three diagnostic pressure levels of resonance and cavitation described for contrast agents in Section 14.5.2, these extremely high pressures for lithotripsy and HIFU can operate at a super or fourth level, at which tissues and materials can break down, causing biochemical effects that produce gas nuclei for cavitation. These effects are not yet understood but have been observed. For these two latter applications, pulse shapes and pressure amplitudes are quite different from those used for diagnostic ultrasound: compressional pressures in water typically in excess of 75 MPa followed by −15MPa of rarefactional pressure in repeating pulses microseconds long for lithotripters, and extremely high-intensity insonifications of several seconds duration for HIFU.

In summary, in terms of bioeffects, these modalities have intended outcomes that distinguish them from diagnostic imaging. The acoustic output level, pulse shape, frequency range, and/or region of application (summarized in Table 15.1) are substantially different than those used in diagnostic imaging.

15.7 PRIMARY AND SECONDARY ULTRASOUND-INDUCED BIOEFFECTS

One of the primary ultrasound-induced mechanisms (diagrammed in Figure 15.1) is heating. The comparison of the five major medical ultrasound modalities indicate that several mechanisms affect heating mechanism. Absorption is the major heating mechanism. As pressure amplitude increases, nonlinear propagation converts more of the spectrum of the pressure waveform into higher harmonics, which are absorbed at a higher rate (as described in Chapter 12). This higher rate of absorption causes increased heating over what would be expected under linear circumstances (Hynynen, 1987). At the HIFU intensity levels, ultrasound interaction goes beyond elastic limits and involves other mechanisms. Except at these high levels, the effects of heating and their consequences are better understood (NCRP, 2002), as summarized in Table 15.3, and can be controlled by limiting heating and the duration of exposure.

The nonlinear nature of tissues, including fluids, creates several other secondary effects that have been described in Chapter 12. Acoustic streaming and microstreaming (patterns of circulatory flow) cause a gentle movement of fluids and possible aggregation and agglutination, may alter transport across biologic membranes, and can have cooling effects (Wu *et al*., 1998). Acoustic radiation forces and torques are also by-products of nonlinear properties of tissues (Duck, 1998). Radiation forces occur only during an acoustic pulse, and they are much smaller than the tensile strength of tissue (Starritt, 2000). When applied as pulses to the ear or skin, they can evoke auditory or tactile responses (Dalecki *et al*., 1995). These secondary effects are small and are being investigated. They can also be beneficial, for example, in the transport of drugs in a vessel or for use in discriminating between fluid-filled and solid cysts in the breast (Nightingale *et al*., 1995).

The second primary effect is cavitation. The MI and an earlier guiding strategy for dealing with inertial cavitation are based on the possible existence of free gas bubbles of a size that could resonate at the insonifying frequency. In a recent review of work on

cavitation studies conducted on animals, insects, and plants, Carstensen *et al*. (2000) argued that, with the exception of the intestines, there may be no naturally occurring nucleation sites for inertial cavitation of consequence in the human body.

The introduction of bubbles or ultrasound contrast into the blood stream can interact with ultrasound at diagnostic levels. As discussed in Chapter 14, static diffusion, acoustically driven diffusion, fragmentation, and inertial cavitation are possible mechanisms for agent destruction. Clearly, the thresholds for ultrasound interaction with ultrasound contrast agents fall within the diagnostic range, and more work is necessary to understand the different responses of each agent to various pressure waveforms and amplitudes. At the present time, one perspective is that once the shell of an agent is ruptured by ultrasound, MI can be applied to the remaining freed gas. As described in Chapter 14, responses for an encapsulated agent with air or a heavy gas can be very different. Even though no meaningful health risks have been reported in connection with ultrasound contrast agents in the United States, premature ventricular contractions have been observed elsewhere in conjunction with the ultrasound and contrast agents (van Der Wouw *et al*., 2000; Zachary *et al*., 2001, 2002).

15.8 EQUATIONS FOR PREDICTING TEMPERATURE RISE

The highest temperatures along the beam axis are not that sensitive to beam details, and for circularly symmetric transducers, they can be calculated by a heated disk model (Thomenius, 1990; NCRP, 1992) in which the diameter of the disk is given by a −6-dB beamwidth at each axial distance z (Figure 15.5). Here the volume rate of heat generation due to absorption can be modeled as proportional to the acoustic intensity (I) and absorption at a single frequency,

$$q_v = 2\alpha I = 2\alpha I_0 \exp(-2\alpha z) \tag{15.9}$$

For a tissue with an absorption α, the heat generated at a time-averaged rate per unit volume is given locally by q_v,

$$q_v = 2\alpha I_i(t, r) \tag{15.10}$$

where I_i is the instantaneous intensity based on the assumption that the pressure and particle velocity are in phase. The value for I_i is often based on the focused field of the transducer. The volume rate of heat generation (q_v) due to absorption can be modeled as proportional to the acoustic intensity, $I(x,y,z)$, and absorption α at a single frequency,

$$q_v = 2\alpha I \tag{15.11}$$

For a more realistic estimate of heat generation in tissue, the Pennes bioheat transfer equation is used often,

$$\frac{1}{\kappa}\frac{\partial T}{\partial t} + \Delta T/L - \nabla^2 T = q_v/K \tag{15.12}$$

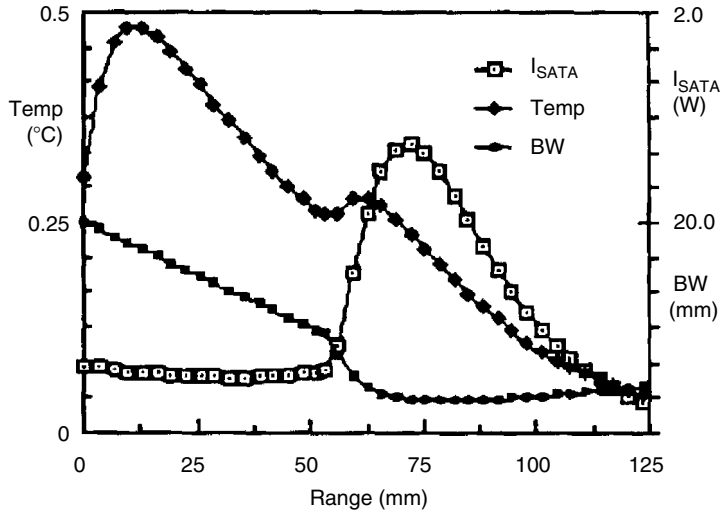

Figure 15.5 Axial profiles calculated from the heated disk model for a 3 MHz transducer with a diameter of 20 mm and a spherical focus of 100 mm. Thermal indices (TIs) from the ODS for different modes and configurations. Shown are spatial average temporal average intensity (I_{SATA}), (W/cm^2), temperature rise (Temp), and −6-dB beamwidth (BW) (from Thomenius, 1990, *IEEE*).

where:

T_a is ambient temperature
T is temperature
$\Delta T = T - T_a$
q_v = heat source function
κ = thermal diffusivity
K = thermal conductivity
τ = perfusion time constant

A perfusion length L, which defines the region of influence of a heat source, is given by

$$L = \sqrt{\kappa\tau} \tag{15.13}$$

Other useful quantities are summarized in Table 15.4. The terms in the bioheat equation on the left-hand side are for heat diffusion, heat loss from blood perfusion, and heat conduction; the term on the right-hand side is the heat source from the acoustic beam, Eq. (15.11). More information and solutions for the bioheat equation can be found in Nyborg (1988) and Thomenius (1990).

O'Brien (1996) introduced a monopole source model that is in general agreement with the heated disk model and which shows that for rectangular apertures, heating is less than that predicted for circular apertures.

15.9 CONCLUSIONS

As new applications of diagnostic ultrasound outpace the complete understanding of the underlying physical mechanisms, the need for continuing research and debate continues. Considerable effort has been focused on bioeffects. Many important experiments on smaller animals have been conducted; however, the interpretation of results is not always straightforward to apply to humans. While they point to possible effects and trends, care must be taken in interpretation to account for differences in structure among species (O'Brien and Zachary, 1996, 1997), the relative size of structures relative to the insonifying wavelengths and beam, and dilution ratios of contrast agents, for example.

Even though there is not enough space here to do justice to the many animal studies on bioeffects, the reader is referred to reports by societies such as the NCRP, AIUM, and WFUMB. The most comprehensive compilation of animal studies, recommendations, and guidelines for the safe use of ultrasound can be found in the NCRP report (2002). A shorter and slightly different viewpoint can be found in Barnett *et al*. (2000).

These reports emphasize those situations in which caution is recommended. These cases are sometimes referred to as *potential ris*ks. Rott (1999a) explains that this term states that there is no known real risk that could be quantified in numerical values, but because of an insufficient scientific data base, there remains the possibility of damage in worst case situations.

Balancing this point of view is the risk versus benefit trade-off. This decision involves "a real expectation of obtaining diagnostic data that would have a beneficial effect on the continuing medical management of the patient" (Barnett *et al*., 2000). The risk aspects not covered in the reports above are the clinical consequences of not doing an ultrasound exam. In other words, will the lack of diagnostic information from the proposed ultrasound imaging pose a greater risk to the health of the patient than the potential risk of doing the exam? This aspect of the risk/benefit equation is not as well documented in an organized manner; however, the benefits affecting the well-being and medical management of the patient are the primary concerns in ultrasound examinations on a daily basis.

Ultrasound organizations are in general agreement that ultrasound imaging is generally a very safe procedure (AIUM, 1998; 2002) (see Section 15.3.6). The debate centers on certain restricted cases in which some groups advocate more caution and a commonsense ALARA approach. Education about safety issues is important to increase individual responsibility and awareness of ultrasound practitioners.

In fact, many societies and groups are involved in a worldwide effort to understand the safety issues connected with diagnostic ultrasound, including defining appropriate applications of ultrasound, as well as the adequate training and education of those using imaging equipment. A partial list of these groups, many of them part of WFUMB, are listed in Appendix D along with professional societies that frequently publish relevant articles. Some of these groups focus on a clinical application of ultrasound, publish guidelines and standards, sponsor continuing education pro-

grams, and serve as a forum for advancing ultrasound clinical application and research.

As diagnostic ultrasound has recently past the 50-year mark of active use, it has done so with a remarkable safety record. Unlike computed tomography (CT) and especially multidetector CT, diagnostic ultrasound does not have an identified major safety concern like ionizing radiation (Ward, 2003). From the graph of the number of imaging exams given annually worldwide in Figure 1.14, one comes to the conclusion that the total number of ultrasound exams given must number in the billions! In the United States, an estimated 75% of infants have been exposed to ultrasound before birth. In some countries, such as Germany, Norway, Iceland, and Austria, all pregnant women are screened with ultrasound.

Even though so many ultrasound exams have been given, this does not mean there is absolutely no risk involved. Most exams are done under different conditions and without long-term follow-up. There are few systematic studies of ultrasound on large populations over long periods of time. Some of these studies are reviewed in the NCRP report (2002). Under these circumstances, some vigilance is necessary in identifying the applications of ultrasound where risk is higher. As the science of ultrasound advances, some of the remaining questions will be answered as new questions take their place. Some questions may never be answered satisfactorily because of the complexity, adaptability, and variety of responses of the human body. Fortunately, experts from professional organizations are actively engaged in finding answers and developing guidelines.

As diagnostic ultrasound widens its horizons, the way sonography is conducted will be redefined. As new methodologies emerge with far greater diagnostic benefit potential, such as therapeutic contrast agents, they may also carry a different risk than those considered now. For each case, the risk–benefit decision may become less straightforward than it is presently.

Out of many topics at the growing edge of ultrasound, two are highlighted here. The portability, accessibility, low cost, and good image quality of small ultrasound imaging systems is challenging where and how diagnostic imaging can be practiced. Consider two large-scale applications of ultrasound in which small systems provide a benefit in terms of the economies of scale: screening and surveillance. In several countries, pregnant women are part of a screening process as a preventive measure to identify possible fetal abnormalities that can be addressed during pregnancy. The U. S.-based Occupational Safety and Health Administration (OSHA, 2004) defines screening as "a method for detecting disease or body dysfunction before an individual would normally seek medical care. Screening tests are usually administered to individuals without current symptoms, but who may be at high risk for certain adverse health outcomes." OSHA (2004) defines surveillance as "the analysis of health information to look for problems that may be occurring in the workplace that require targeted prevention, and thus serves as a feedback loop to the employer."

Is the use of diagnostic ultrasound limited to cases in which it is medically indicated? What are the ethical implications when it is not? Portable systems with high image quality provide alternatives for many places that cannot afford fully loaded systems. What training would be required for these applications? Under

these circumstances, how can high quality ultrasound exams and care be maintained? Certainly, these alternatives provide many new opportunities for the growth of diagnostic ultrasound if the challenges can be met.

Two editorials (Filly, 2003; Greenbaum, 2003) discuss some of the serious issues concerning portable systems. They also consider replacing the term "handheld sonography" by "sonoscopes." Sonoscopes, they argue, could be regarded as a twenty-first century equivalent of the stethoscope. Filly (2003) points out that the cost of these systems is still rather expensive for each medical student to own one. Most of the smaller ultrasound systems that produce images of very good quality can not yet be considered to be handheld but rather "hand-carried." While the present cost of these imaging systems is beyond the budget of a medical student, a low-cost handheld ultrasound system may not be that far away. With the invisible wind of enabling technology providing the technological means for new advances, a solution in the form of a prototype pocket ultrasound was recently described by Saijo *et al*. (2003). This imaging device consists of a mechanical transducer plugged into the USB port of a handheld PC. Robert Hooke, who envisioned the use of sound for diagnosis and anticipated the stethoscope more than 300 years ago (see Chapter 1), might be amused by these recent developments if he were alive today to hear *and* see "the internal parts of bodies . . . by the sound they make."

Bibliography

AIUM. (1998). *Bioeffects and Safety of Diagnostic Ultrasound.* AIUM Publications, Laurel, MD. An overview of ultrasound-induced bioeffect and safety considerations.

NCRP. (Dec. 2002). *Exposure Criteria for Medial Diagnostic Ultrasound, Part II. Criteria Based on All Known Mechanisms.* Report **140**, NCRP, Bethesda, MD. An authoritative reference for ultrasound-induced bioeffects.

Nyborg, W. L. and Ziskin, M. C. (eds.). (1985). Biological effects of ultrasound. In *Clinics in Diagnostic Ultrasound*, Vol. 16. Churchill Livingstone, New York, pp. 135–155.

WFUMB Symposium on Safety of Ultrasound in Medicine: Conclusions and Recommendations for Thermal and Non-Thermal Mechanisms of Biological Effects of Ultrasound. (1998). S. B. Branett (ed.). *Ultrasound in Med. & Biol.* **244**, 1–55.

References

Abbott, J. G. (1999). Rationale and derivation of MI and TI: A review. *Ultrasound in Med. & Biol*. **25**, 431–441.

American Institute of Ultrasound in Medicine (AIUM). (1993). *Bioeffects and Safety of Diagnostic Ultrasound*. AIUM Publications, Laurel, MD.

AIUM. (1998). *Bioeffects and Safety of Diagnostic Ultrasound*. AIUM Publications, Laurel, MD.

AIUM. (2000). *Mechanical Bioeffects from Diagnostic Ultrasound: AIUM Consensus Statements*. AIUM Publications, Rockville, MD.

AIUM. (2002). *Medical Ultrasound Safety.* AIUM Publications, Rockville, MD.

American Institute of Ultrasound in Medicine/National Electrical Manufacturers Association (AIUM/NEMA). (1998a). *Standard for Real-Time Display of Thermal and Mechanical Acoustic Output Indices on Diagnostic Ultrasound Equipment*, Revision 1. AIUM Publications, Laurel, MD.

AIUM/NEMA. (1998b). *Acoustic Output Measurement Standard for Diagnostic Ultrasound Equipment*. AIUM Publications, Laurel, MD.

Barnett, S. B., ter Haar, G. R., Ziskin, M. C., Rott, H.-D., Duck, F. A., and Meda, K. (2000). International recommendations and guidelines for the safe use of diagnostic ultrasound in medicine. *Ultrasound in Med. & Biol*. **26**, 355–366.

Carstensen, E. L., Child, S. Z., Norton, S., and Nyborg, W. (1990). Ultrasonic heating of the skull. *J. Acoust. Soc. Am*. **87**, 1310–1317.

Carstensen, E. L., Gracewski, S., and Dalecki, D. (2000). The search for cavitation *in vivo*. *Ultrasound in Med. & Biol*. **26**, 1377–1385.

Chen, L., ter Haar, G. R., and Hill, C. R. (1997). Influence of ablated tissue on the formation of high-intensity focused ultrasound lesions. *Ultrasound in Med. & Biol*. **23**, 921–931.

Curly, M. G. (1993). Soft tissue temperature rise caused by scanned, diagnostic ultrasound. *IEEE Trans. Ultrason. Ferroelec. Freq. Control*. **40**, 59–66.

Coleman, A. J. and Saunders, J. E. (1989). A survey of the acoustic output of commerical extracorporeal shock wave lithotripters. *Ultrasound in Med. & Biol*. **15**, 213–227.

Coleman, A. J. and Saunders, J. E. (1993). A review of the physical effects of the high amplitude acoustic fields used in extracorporeal lithotripsy. *Ultrasonics* **31**, 75–89.

Dalecki, D., Child, S. Z., Raeman, C. H., Carstensen, E. L. (1995). Tactile perception of ultrasound. *J. Acoust. Soc. Am*. **97**, 3165–3170.

Delius, M. (2000). Lithotripsy. *Ultrasound in Med. & Biol*. **26**, Sup. 1, S55–S58.

Diederich, C. J., and Hynynen, K. (1999). Ultrasound technology for hyperthermia. *Ultrasound in Med. & Biol*. **25**, 871–887.

Duck, F. A. (1998). Radiation pressure and streaming, Chapt. 3, *Ultrasound in Medicine*, Medical Science series, F. A., Duck, A. C. Baker and H. C. Starritt, (eds.). Institute of Physics Publishing, Bristol, UK. 1998.

Duck, F. A. (2000). EFSUMB reviews of recent safety literature, European Committee for Medical Ultrasound Safety (ECMUS). *European J. Ultrasound* **11**, 151–154.

Duck, F. A. and Martin, K. (1991). Trends in diagnostic ultrasound exposure. *Phys. Med. Biol*. **36**, 1423–1432.

Duck, F. A., Starritt, H. C., ter Haar, G. R., and Lunt, M. J. (1989). Surface heating of diagnostic ultrasound transducers. *Br. J. Radiol*. **67**, 1005–1013.

Dyson, M., Pond, J. B., Joseph, J., and Warwick, R. (1970). Stimulation of tissue regeneration by pulsed plane-wave ultrasound. *IEEE Trans. Sonics Ultrason*. **SU-17**, 133–139.

Ebbini, E. S. and Cain, C. A. (1989). Multiple-focus ultrasound phased-array pattern synthesis: Optimal driving-signal conditions for hyperthermia. *IEEE Trans. Ultrason. Ferroelec. Freq. Control* **36**, 540–548.

Ellis, D. S. and O'Brien Jr., W. D. (1996). The monopole-source solution for estimating tissue temperature increases for focused ultrasound fields, *IEEE Trans. Ultrason. Ferroelec. Freq. Control* **43**, 88–97.

Food and Drug Administration (FDA). (1993). *Revised 510(k) Diagnostic Ultrasound Guidance for 1993*. Center for Devices and Radiological Health, U. S. FDA, Rockville, MD.

FDA. (1997). *Information for Manufacturers Seeking Marketing Clearance of Diagnostic Ultrasound Systems and Transducers*. Center for Devices and Radiological Health, U. S. FDA, Rockville, MD.

Filly, R. A. (2003). Is it time for the Sonoscope? If so, then let's do it right. *J. Ultrasound Med.* **22**, 323–325.

Fry, F. J. (1979). Biological effects of ultrasound: A review. *Proc. IEEE* **67**, 604–619.

Greenbaum, L. D. (2003). Is it time for the Sonoscope? *J. Ultrasound Med.* **22**, 321–322.

Halliwell, M. (1998). Acoustic wave lithotripsy, Chap. 10. In *Ultrasound in Medicine*, Medical Science Series, F. A. Duck, A. C. Baker, and H. C. Starritt (eds.). Institute of Physics Publishing, Bristol, UK.

Hand, J. F. (1998). Ultrasound hyperthermia and the prediction of heating, Chap. 8. In *Ultrasound in Medicine*, Medical Science Series, F. A. Duck, A. C. Baker, and H. C. Starritt (eds.). Institute of Physics Publishing, Bristol, UK.

Harris, G. R. (1992). Lithotripsy pulse measurement errors due to nonideal hydrophone and amplifier frequency responses. *IEEE Trans. Ultrason. Ferroelec. Freq. Control* **39**, 256–261.

Henderson, J., Willson, K., Jago, J. R., and Whittingham, T. A. (1995). A survey of the acoustic outputs of diagnostic ultrasound equipment in current clinical use. *Ultrasound in Med. & Biol.* **217**, 699–705.

Holland, C. K., Roy, R. A., Apfel, R. E., and Crum, L. A. (1992). In vitro detection of cavitation induced by a diagnostic ultrasound system. *IEEE Trans. Ultrason. Ferroelec. Freq. Control* **39**, 95–101.

Holt, R. G. and Roy, R. A. (2001). Measurements of bubble-enhancing heating from focused MHz frequency ultrasound in a tissue-mimicking material. *Ultrasound in Med. & Biol.* **27**, 1399–1412.

Hynynen, K. (1987). Demonstration of enhanced temperature elevation due to nonlinear propagation of focused ultrasound in a dog's thigh in vivo. *Ultrasound in Med. & Biol.* **13**, 85–91.

Hynynen, K. (1998). Present status of ultrasound hyperthermia. *IEEE Ultrason. Symp. Proc.*, 941–946.

International Electrotechnical Commission (IEC). Standard 61828 (2001). *Ultrasonics: Focusing Transducers. Definitions and Measurement Methods for the Transmitted Fields*. IEC, Geneva, Switzerland.

IEC Standard 60601-2-37 (2002). *Medical Electrical Equipment, Part 2: Particular Requirements for the Safety of Ultrasonic Medical Diagnostic and Monitoring Equipment*. IEC, Geneva, Switzerland.

Lehmann, J. F. (1990). *Therapeutic Heat and Cold (Rehabilitation Medicine Library)*, 4th ed. Lippincott, Williams & Wilkins, Philadelphia.

Lele, P. P. (1972). Local hyperthermia by ultrasound for cancer therapy. In *Ultrasound Therapy Workshop: Proceedings on the Interaction of Ultrasound and Biological Tissues*, Lehman, J. F., and Guy, A. W. (eds.). Lehman, J.F., and Guy, A.W. (eds.). HEW Publication (FDA) 73–8008, pp. 141–152.

Lewin, P. A., Chapelon, J.-Y., Mestas, J.-L., Birer, A., and Cathignol, D. (1990). A novel method to control p+/p−ratio of the shock wave pulses used in the extracorporeal piezoelectric lithotripsy (EPL). *Ultrasound in Med. & Biol.* **16**, 473–488.

Meaning, P. M., Cahill, M. D., and ter Haar, G. R. (2000). The intensity dependence of lesion position shift during focused ultrasound surgery. *Ultrasound in Med. & Biol.* **26**, 441–450.

Miller, M. W. and Ziskin, M. C. (1989). Biological consequences of hyperthermia. *Ultrasound in Med. & Biol.* **15**, 707.

National Council on Radiation Protection and Measurements (NCRP). (June 1, 1992). *Exposure Criteria for Medical Diagnostic Ultrasound, Part I: Criteria Based on Thermal Mechanisms*. NCRP, Bethesda, MD.

NCRP. (Dec. 2002). *Exposure Criteria for Medical Diagnostic Ultrasound, Part II. Criteria Based on All Known Mechanisms*. Report **140**, NCRP, Bethesda, MD.

Nightingale, K. R., Kornguth, P. J., Walker, W. F., McDermott, and Trahey, G. E. (1995). A novel ultrasonic technique for differentiating cysts from solid lesions: Preliminary results in the breast. *Ultrasound in Med. & Biol*. **21**, 745–751.

Newman, W. H. and Lele, P. P. (1985). Measurement of thermal properties of perfused biological tissue by transient heating with focused ultrasound, *IEEE Ultarson. Symp. Proc*., 913–916.

Nyborg, W. L. (1988). Solutions of the bio-heat transfer equation. *Phys. Med. Biol*., **33**, 785–792.

O'Brien Jr., W. D. (1998). Assessing the risks for modern diagnostic ultrasound imaging. *Japanese J. of Applied Phys*. **37**, 2781–2788.

O'Brien Jr., W. D. and Ellis, D. S. (1999). Evaluation of the unscanned soft-tissue thermal index. *IEEE Trans. Ultrason. Ferroelec. Freq. Control* **46**, 1459–1476.

O'Brien Jr., W. D. and Zachary, J. F. (1996). Rabbit and pig lung damage comparison from exposure to continuous wave 30-kHz ultrasound. *Ultrasound in Med. & Biol*. **22**, 345–353.

O'Brien Jr., W. D. and Zachary, J. F. (1997). Lung damage assessment from exposure to pulsed-wave ultrasound in the rabbit, mouse, and pig. *IEEE Trans. Ultrason. Ferroelec. Freq. Control* **44**, 473–485.

Occupational Safety and Health Administration (2004). Website, www.osha.gov.

Rott, H.-D. (1999a). EFSUMB: Tutorial thermal teratology, European Committee for Medical Ultrasound Safety (ECMUS). *European J. Ultrasound* **9**, 281–283.

Rott, H.-D. (1999b). EFSUMB: Acoustic cavitation and capillary bleeding, European Committee for Medical Ultrasound Safety (ECMUS). *European J. Ultrasound* **9**, 277–280.

Saijo, Y., Kobayashi, K., Arai, H., Nemoto, Y., and Nitta, S. (2003). Pocket-size echo connectable to a personal computer. *Ultrasound in Med. & Biol*. **29(5S)**, S54.

Sanghvi, N. T., Fry, F. J., Bihrle, R., Foster, R. S., Phillips, M. H., Syrus, J., Zaitsev, A. and Hennige, C. (1995). Microbubbles during tissue treatment using high intensity focused ultrasound. *IEEE Ultrason. Symp. Proc*., 1249–1253.

Shaw, A., Preston, R. C., and Bond, A. D. (1997). *Assessment of the Likely Thermal Index Values for Pulsed Doppler Ultrasonic Equipment*, Stage I: Calculation based on manufacturers' data, NPL Report CIRA(EXT)018, National Physical Laboratory, Teddington, UK.

Shaw, A., Pay, N. M., and Preston, R. C. (1998). *Assessment of the Likely Thermal Index Values for Pulsed Doppler Ultrasonic Equipment*, Stages II and III: Experimental assessment of scanner-transducer combinations, NPL Report CMAM 12. National Physical Laboratory, Teddington, UK.

Shaw, A., Pay, N., Preston, R. C., and Bond, A. (1999). A proposed standard thermal test object for medical ultrasound. *Ultrasound in Med. & Biol*. **25**, 121–132.

Smith, S. W., Stewart, H. F., and Jenkins, D. P. (1985). A plane layered model to estimate in situ ultrasound exposures. *Ultrasonics* **23**, 31–40.

Starritt, H. (2000). 61–64 EFSUMB: Safety tutorial radiation stress and its bio-effects, European Committee for Medical Ultrasound Safety (ECMUS). *European J. Ultrasound* **11**, 61–64.

Stewart, H. F. (1982). Ultrasound therapy, Chapt. 6. In *Essentials of Medical Ultrasound*. Humana Press, Clifton, NJ.

Szabo, T. L., Melton Jr., H. E., and Hempstead, P. S. (1988). Ultrasonic output measurements of multiple mode diagnostic ultrasound systems. *IEEE Trans. Ultrason. Ferroelec. Freq. Control*. **35**, 220–231.

ter Haar, G. R. (1995). Ultrasound focal beam surgery. *Ultrasound in Med. & Biol*. **21**, 1089–1100.

ter Haar, G. R. (1998). Focused ultrasound surgery, Chapt. 9. In *Ultrasound in Medicine*, Medical Science Series, F. A. Duck, A. C. Baker, and H. C. Starritt (eds.). Institute of Physics Publishing, Bristol, UK.

Thomenius, K. E. (1990). Thermal dosimetry models for diagnostic ultrasound. *IEEE Ultrason. Symp. Proc*., 1249–1253.

van Der Wouw, P. A., Brauns, A. C., Bailey, S. E., Powers, J. E., and Wilde, A. A. (2000). Premature ventricular contractions during triggered imaging with ultrasound contrast. *J. Am. Soc. Echocardiogr.* **13**, 288–294.

Ward, P. (2003). Failure to minimize radiation dose risks public outcry, legal claims. *Diag. Imag. Europe* **19**, 5.

WFUMB Symposium on Safety of Ultrasound in Medicine: Conclusions and Recommendations on Thermal and Non-Thermal Mechanisms for Biological Effects of Ultrasound. (1998). S. B. Barnett (ed.). *Ultrasound in Med. & Biol*. **244**, 1–55.

Williams, A. R., McHale, J., Bowditch, M., Miller, D. L., and Reed, B. (1987). *Ultrasound in Med. & Biol*. **13**, 249–258.

Wu, J., Cubberley, F., Gormley, G., and Szabo, T. L. (1995). Temperature rise generated by diagnostic ultrasound in a transcranial phantom. *Ultrasound in Med. & Biol*., **21**, 561–568.

Wu, J., Winkler, A. J., and O'Neill, T. P. (1998). Effect of acoustic streaming on ultrasonic heating. *Ultrasound in Med. & Biol*. **24**, 153–159.

Zachary, J. F., Hartleben, S. A., Frizzell, L. A., and O'Brien Jr., W. D. (2001). Contrast agent-induced cardiac arrhythmias in rats. *IEEE Ultrason. Symp. Proc*., 1709–1712.

Zachary, J. F., Hartleben, S. A., Frizzell, L. A., and O'Brien Jr., W. D. (2002). Arrhythmias in rat hearts exposed to pulsed ultrasound after intravenous injection of contrast agent. *J. of Ultrasound in Med*. **21**, 1347–1356.

Ziskin, M. C., and Szabo, T. L. (1993). Impact of safety considerations on ultrasound equipment and design and use, Chapt. 12. In *Advances in Ultrasound Techniques and Instrumentation*, P. N. T. Wells (ed.). Churchill Livingstone, New York.

APPENDIX A

Chapter Contents

A.1 INTRODUCTION

The Fourier transform, besides being an elegant and useful mathematical tool, also has an intuitive interpretation that extends to many physical processes. The Fourier transform is applied extensively in electrical engineering, signal processing, optics, acoustics, and the solution of partial differential equations.

For example, consider an acoustic wave received by a transducer and converted to an electrical pulse. This electrical pulse-echo signal can be seen on the screen of a digital sampling scope as a function of time. The same signal, when connected to a spectrum analyzer, can be observed as a spectrum. The Fourier transform is the relation between the pulse and its spectrum. On many scopes, a spectrum calculated directly by a fast Fourier transform (FFT) can also be displayed simultaneously with the time trace.

This appendix briefly reviews some of the useful and intriguing properties of the Fourier transform and its near relative, the Hilbert transform. In addition, it gives an explanation of the digital Fourier transform and its application. For more details, derivations, and applications, the reader is referred to the sources listed in the Bibliography.

A.2 THE FOURIER TRANSFORM

A.2.1 Definitions

The minus *i* Fourier transform, also known as the Fourier integral, is defined as

$$G(s) = \Im_{-i}[g(u)] = \int_{-\infty}^{\infty} g(u)e^{-i2\pi us}dt \tag{A.1}$$

in which $G(s)$ is the minus *i* Fourier transform of $h(u)$, i is $\sqrt{-1}$, and $\Im$ symbolizes the Fourier transform operator. Where possible, capital letters will represent transformed variables, and lower-cased letters will represent the untransformed function. Another operation, the ''inverse'' minus *i* Fourier transform, can be used to determine $g(u)$ from $G(s)$,

$$g(u) = \Im_{-i}^{-1}[G(s)] = \int_{-\infty}^{\infty} G(s)e^{i2\pi us}df \tag{A.2}$$

in which $\Im^{-1}$ is the symbol for the inverse Fourier transform. Also there is a plus *i* Fourier transform,

$$G(s) = \Im_{i}[g(u)] = \int_{-\infty}^{\infty} g(u)e^{i2\pi us}dt \tag{A.3}$$

as well as a plus *i* inverse transform

$$g(u) = \Im_{i}^{-1}[G(s)] = \int_{-\infty}^{\infty} G(s)e^{-i2\pi us}df \tag{A.4}$$

How are the minus *i* and plus *i* transforms related? Both Eqs. (A.1) and (A.4) have the same form, as well as Eqs. (A.2) and (A.3). If in Eq. (A.1) we replace s with $-s$, then $G(-s)$ results, as well as a transform that looks like that of Eq. (A.3). This result can be generalized as follows: If the minus *i* transform of $g(u)$ is known as $G(s)$, then the plus *i* transform of $g(u)$ is $G(-s)$. In this book, the most frequently used Fourier transform operation is a minus *i* Fourier transform, $\Im_{-i}$, so the $-i$ designation will be understood, $\Im = \Im_{-i}$, unless the operator is specifically denoted as $\Im_i$ for a plus *i* transform.

For a Fourier transform to exist, several conditions must be met in general. The function $g(u)$ to be transformed must be absolutely integrable, $|g(u)|$ under infinite

limits. Also, $g(u)$ can only have finite discontinuities. The function cannot have an infinite number of maximum and minima, though some experts disagree on this point. As a commonsense rule, if physical processes are described by a Fourier transform, they usually exist because they must obey physical laws like the conservation of energy. We shall also find it convenient to use functions that are infinite in amplitude like the impulse function, which, strictly speaking, can only be considered to exist in a limiting sense. These functions are called generalized functions that have special properties in the limit.

A.2.2 Fourier Transform Pairs

Many Fourier transforms of functions have been determined analytically; a short list of frequently used functions and their transforms is given in Table A.1. Others are available in transform tables of the references. From the principle of linearity, superposition can be used to combine transform pairs to create more complicated functions. Shorthand symbols and names for these functions follow those that can be found in Bracewell (2000).

Before these functions are introduced, the scaling theorem will be found to be most useful,

$$\Im_{-i}[g(at)] = \frac{1}{|a|} G(f/a) \tag{A.5}$$

TABLE A.1 Theorems for Fourier Transforms

Theorem	$f(x)$	$F(s) = \Im_{-i}[f(x)]$	$\Im_{+i}[f(x)]$
Definitions	$f(x)$	$F(s)$	$F(-s)$
Similarity	$f(ax)$	$(1/\|a\|)F(s/a)$	$(1/\|a\|)F(-s/a)$
Addition	$f(x) + g(x)$	$F(s) + G(s)$	$F(-s) + G(-s)$
Shift	$f(x-a)$	$\exp(-i2\pi as)F(s)$	$\exp(i2\pi as)F(s)$
Combined	$f[b(x-a)]$	$\exp(-i2\pi as)F(s/b)$	$\exp(i2\pi as)(1/\|b\|)F(-s/b)$
Modulation	$f(x)cos(2\pi s_0 x)$	$\frac{1}{2}[F(s-s_0) + F(s+s_0)]$	$\frac{1}{2}[F(-s-s_0) + F(-s+s_0)]$
Convolution	$f(x)^* g(x)$	$F(s)G(s)$	$F(-s)G(-s)$
Autocorrelation	$F(x)^* f^*(-x)$	$\|F(s)\|^2$	$\|F(-s)\|^2$
Derivatives	$f'(x)$	$i2\pi sF(s)$	$-i2\pi sF(-s)$
Derivatives	$-i2\pi xf(x)$	$F'(s)$	$F'(-s)$
Derivative of convolution	$\frac{d}{dx}[f(x)^* g(x)]$ $= f'(x)^* g(x)$ $= f(x)^* g'(x)$	$i2\pi sF(s)G(s)$	$-i2\pi sF(-s)G-(s)$
Rayleigh	$\int_{-\infty}^{\infty} \|f(x)\|^2 dx$	$\int_{-\infty}^{\infty} \|F(s)\|^2 ds$	$\int_{-\infty}^{\infty} \|F(-s)\|^2 ds$
Power	$\int_{-\infty}^{\infty} f(x)g^*(x)dx$	$\int_{-\infty}^{\infty} F(s)G^*(s)ds$	$\int_{-\infty}^{\infty} F(-s)G^*(-s)ds$

Modified from Bracewell, 2000.

The impulse function, already mentioned in Chapter 2, is a generalized function that has the unusual property that it samples the integrand:

$$\int_{-\infty}^{\infty} \delta(t - t_0)g(t)dt = g(t_0) \tag{A.6a}$$

When the transform of the impulse function is taken, the result is an exponential

$$H(f) = \int_{-\infty}^{\infty} \delta(t - t_0)e^{-i2\pi ft}dt = e^{-i2\pi ft_0} \tag{A.6b}$$

which shows that a delay in time is equivalent to a multiplicative exponential delay factor in the frequency domain. When the impulse has no delay or $t_0 = 0$, $H(f) = 1.0$, a constant.

Because the *sine* and *cosine* are defined in terms of the difference and sum of two exponentials, they become impulse functions in the transform domain (as indicated in Table A.2).

A delay can be added to the scaling theorem to make it even more useful,

$$\Im_{-i}[g(a(t - b))] = \frac{e^{-i2\pi bf}}{|a|} G(f/a) \tag{A.7}$$

An important unique property of the impulse function is

$$\delta(at) = \frac{1}{|a|}\delta(t) \tag{A.8}$$

Now consider an infinite sequence of impulses, each spaced an interval $a = t_0$ apart from each other. This series of impulse functions also has a special name, "shah" $III(t/a)$, and has an unusual property: The shah function is its own transform,

$$G(f) = \int_{-\infty}^{\infty} III(t/t_0)e^{-i2\pi ft}dt = \int_{-\infty}^{\infty} \sum_{-\infty}^{\infty} \delta(t - nt_0)e^{-i2\pi ft}dt = t_0 III(ft_0) = t_0 \sum_{-\infty}^{\infty} \delta(f - n/t_0) \tag{A.9}$$

as shown in Table A.1. Note that the transform of the shah function is another series of impulses spaced at "$1/a$" and with a weight of "a" rather than one.

Besides its sampling capability in time, the shah function is also called a replicating function because when it is convolved in the transform domain with another function, it replicates the function at all its impulse locations. These features will be described in more detail in Section A.2.5.

Another function that is its own transform is the Gaussian; this is for a=b=c=1 for the Gaussian in Table A.2. The Gaussian has the useful properties of smoothness and differentiability. It also appears in statistics, limiting cases, and the solutions to many physical problems.

Another useful function is the Heaviside unit step function, defined as

TABLE A.2 Minus i Fourier Transform Pairs

Function	$g(t)$	$G(f) = \Im_{-i}[g(t)]$
Delayed impulse or Dirac delta	$a_0\delta(t-a)$	$a_0 \exp(-i2\pi af)$
Rect or rectangle (base c, delay a)	$b\Pi\left(\frac{t-a}{c}\right)$	$bc \exp(-i2\pi af) sinc(cf)$
Delayed Gaussian	$b \exp\left[-\pi\left(\frac{t-a}{c}\right)^2\right]$	$bc \exp[-\pi c^2 f^2] \cdot \exp(-i2\pi af)$
Shah (interval a)	$III(t/a)$	$aIII(fa)$
Triangle (base c, delay a)	$b\Lambda\left(\frac{t-a}{c}\right)$	$bcexp(-i2\pi af) sinc^2(cf)$
Sign or signum at $t = 0$	$\text{sgn}(t)$	$-i/\pi f$
Cosine	$\cos(\omega_0 t)$	$\frac{1}{2}[\delta(f-\omega_0/2\pi) + \delta(f+\omega_0/2\pi)]$
Sine	$\sin(\omega_0 t)$	$-i/2[\delta(f-\omega_0/2\pi) - \delta(f+\omega_0/2\pi)]$

$$H(t) = \begin{matrix} 0 & t<0 \\ 1/2 & t=0 \\ 1 & t>0 \end{matrix} \tag{A.10}$$

it can be combined with weighted and delayed versions of itself to create the rect or rectangle and sign or signum functions of Table A.2. The Fourier transform of the rect function is the *sinc* function, both of which appeared in Chapter 2. The *sinc* is defined as

$$sinc(t) = \frac{sin(\pi t)}{\pi t} \tag{A.11}$$

Finally, the triangle function has a transform that is a $\text{sinc}^2(f)$.

A.2.3 Fundamental Fourier Transform Operations

As indicated in Chapter 2, functions in the transform domain (usually functions of f or k) can be multiplied either to obtain an overall transfer function from a sequence of individual transfer functions or to construct a transform for a complicated function from simpler ones,

$$\Im_{-i}[g(t) *_t h(t)] = G(f)H(f) \tag{A.12}$$

This expression shows that if the time (or space) counterparts of these functions are convolved, an equivalent result will be obtained. The convolution operation for two functions (g and h) is defined below.

$$e(t) = \int_{-\infty}^{\infty} g(\tau)h(t-\tau)d\tau = g(t) *_t h(t) \tag{A.13}$$

The product of the integrand can be visualized as two functions, $g(\tau)$ and another function $h(\tau - t)$, which is h flipped right to left and slid across g for different numerical values of the constant t. For each particular value of t, there is an overlap of the two functions, the area of which corresponds to the amplitude of $e(t)$ there. This process

is continued until the flipped h function has slid completely across function g. Two notable general characteristics of convolution are its smoothing effect and elongation (the resulting signal usually has a length greater than either individual signal).

Correlation is an operation like convolution except the shifted function is **not** flipped but remains in its original orientation; therefore, correlation can be expressed as a special case of convolution,

$$g \otimes h = \int_{-\infty}^{\infty} g(\tau - t)h(\tau)d\tau = g(t)^* h(-t) \tag{A.14}$$

This operation serves two useful purposes: It can be a measure of the similarity between two waveforms, and the location of the peak of the correlation serves as a measure of relative delay between waveforms.

Autocorrelation is a special case of correlation in which the shift function is the same as the other function and a star is its shorthand symbol,

$$g \star g = \int_{-\infty}^{\infty} g(\tau)g(\tau - t)d\tau = g(t)^* g^*(-t) \tag{A.15}$$

in which g^* is the complex conjugate of g.

These key relations and others are listed in Table A.2. Certain general principles can be applied to functions to extend their usefulness. The scaling principle, Eq. (A.5), already encountered in Chapter 2 for both the time-frequency and space-wavenumber Fourier transforms, appears with other principles in Table A.2. The shift-delay theorem, mentioned as Eqs. (A.5) and (A.6b) can be combined with the scaling theorem to give Eq. (A.8).

The Power and Rayleigh theorems are handy for estimating energy content and limiting values. For example, the power of a plane acoustic wave propagating in a lossless medium would be expected to satisfy the power theorem in each plane.

$$\int_{-\infty}^{\infty} g(u)h^*(u)du = \int_{-\infty}^{\infty} G(s)H^*(s)ds \tag{A.16}$$

The Rayleigh theorem can be applied to a known signal or spectrum as a bound on its value in the other domain.

$$\int_{-\infty}^{\infty} |g(u)|^2 du = \int_{-\infty}^{\infty} |G(s)|^2 ds \tag{A.17}$$

Derivatives have a Fourier transform equivalent in the other domain, an important feature that can be applied to the solution of differential equations.

$$\mathfrak{I}_{-i}\left(\frac{\partial^n g}{\partial u^n}\right) = (i2\pi s)^n G(s) \tag{A.18a}$$

$$\mathfrak{I}_{i}\left(\frac{\partial^n g}{\partial u^n}\right) = (-i2\pi s)^n G(s) \tag{A.18b}$$

A.2.4 The Sampled Waveform

In many cases, physical signals or data cannot be represented simply by a tidy closed form or analytical expressions. Often only a series of discrete numbers and an associated index representing an independent variable such as time or distance are available. These numbers may represent a continuous waveform sampled at regular intervals or data.

What happens when sampling occurs? In Figure A.1a, a single continuous waveform in time, $g(t)$, is sampled at intervals of Δt. The total length of the time record is T seconds long. This sampling process can be described by the shah function,

$$s(t) = g(t)III(t/\Delta t) = \sum_{n=-\infty}^{\infty} g(n\Delta t)\delta(t - n\Delta t) \tag{A.19}$$

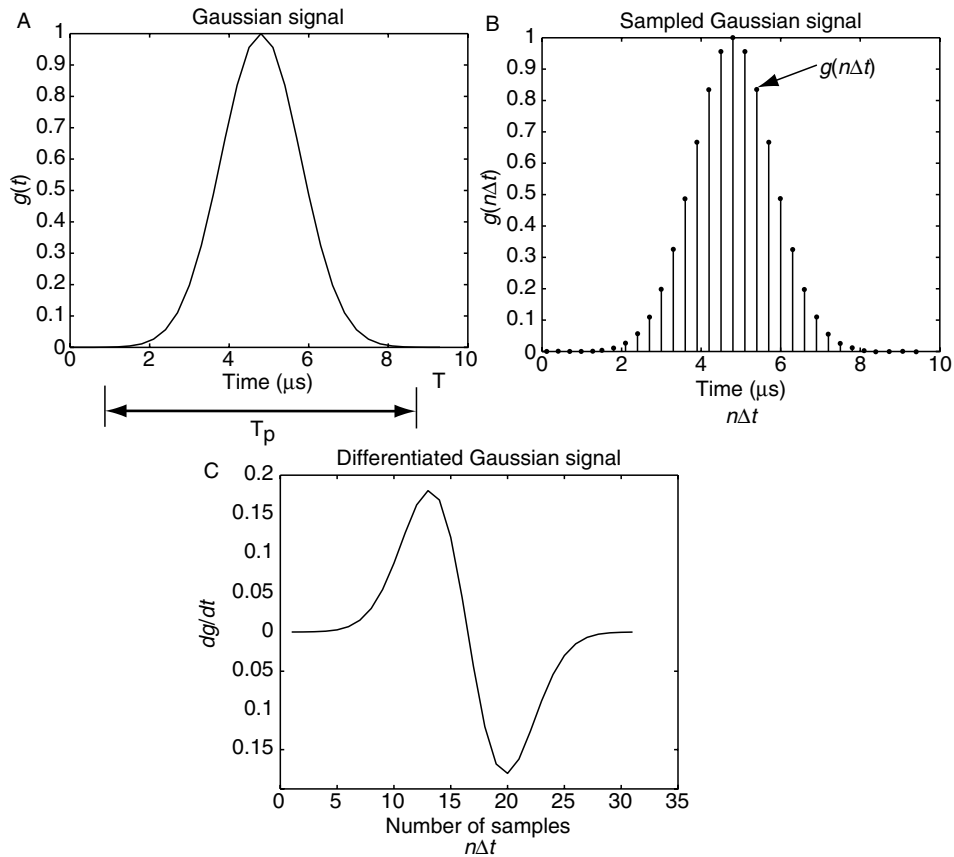

Figure A.1 (A) Time waveform delayed to fit into a positive time interval. (B) Delayed waveform sampled at intervals of Δt. (C) Sampled waveform numerically differentiated with respect to time.

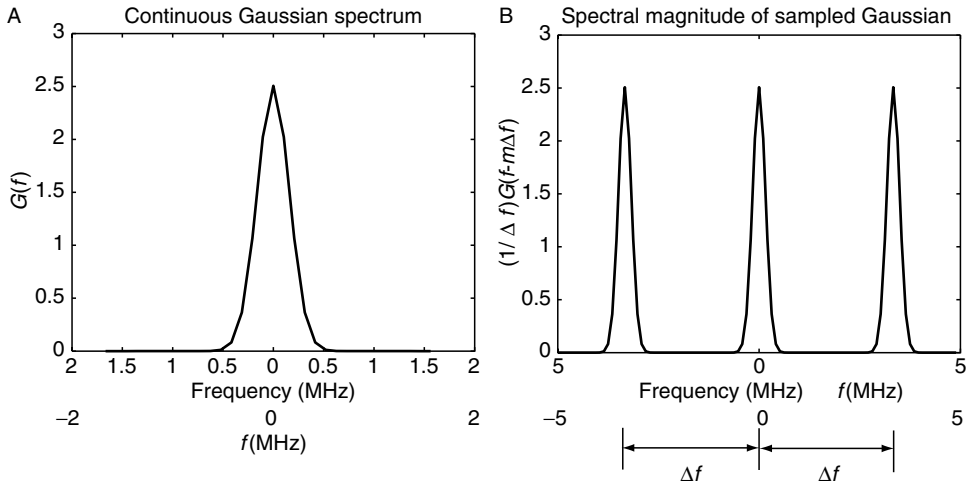

Figure A.2 (A) Fourier transform of a continuous waveform from Figure A.1a. (B) Fourier transform of a sampled waveform from Figure A.1b.

and is shown in Figure A.1b. The Fourier transform of this sampled time function is given by the following, in which $G(f)$ is the continuous $-i$ Fourier transform of $g(t)$, (shown in Figure A.2a):

$$S(f) = G(f)^*[(1/\Delta f)III(f/\Delta f)] = (1/\Delta f)\sum_{m=-\infty}^{\infty} G(f - m\Delta f) \tag{A.20}$$

with $\Delta f = 1/\Delta t$ (the result is illustrated by Figure A.2b). Note that the separation between the sequence of replicated spectra is equal to Δf. Each spectrum is like $G(f)$ in shape, but the magnitude (which here and elsewhere in the book represents the full complex spectrum) is multiplied in amplitude by a factor of Δt.

Overall, there is a basic problem. While the time waveform is sampled, its spectrum is not! Furthermore, there are many repeated continuous spectra—not just one—thanks to the replicating property of the shah function. To be truly digital, each individual spectrum must also be represented by a series of samples.

This problem can be solved by a mathematical trick. Represent the time waveform as a series of identically sampled waveforms, each reoccurring at a time period T consisting of N samples (as displayed in Figure A.3a) This series is described by

$$s(t) = g(t)III(t/\Delta t) * \frac{1}{T}III(t/T) = \frac{1}{T}\sum_{p=-\infty}^{\infty}\sum_{m=-\infty}^{\infty} g(m\Delta t)\delta(t - m\Delta t - pT) \tag{A.21}$$

which has the $-i$ Fourier transform,

$$S(f) = G(f)III(fT)^*[III(f\Delta t)\Delta t] = \Delta t\sum_{m=-\infty}^{\infty}\sum_{p=-\infty}^{\infty} G(\frac{p}{T})\delta(f - p/T - m/\Delta t) \tag{A.22}$$

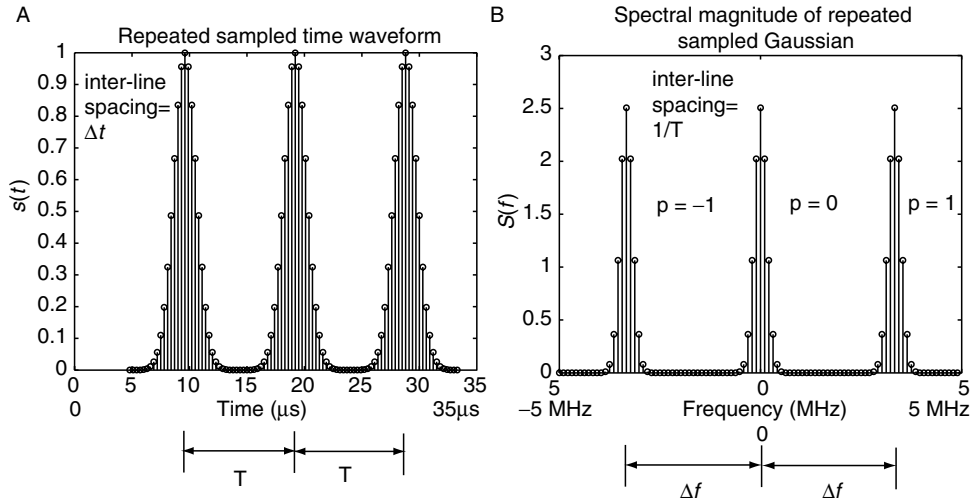

Figure A.3 (A) Repeated sampled waveform. (B) Fourier transform of a repeated sampled waveform.

The key point here is that the spectrum is not only recurring as a series, but each individual spectrum is sampled finely at a rate 1/T (as obvious from Figure A.3b), and it is repeated at a frequency of $\Delta f = 1/\Delta t$.

Sampling rates are explained most simply by restricting each spectrum to be bounded by a certain bandwidth (BW). The selection of the sample rate Δt appears arbitrary, but if the sampling is done at least at the Nyquist rate, $\Delta t \leq 1/\mathrm{BW}$, the continuous waveform, $g(t)$, can be recovered. More generally, the Nyquist rate is stated as $\Delta t = \frac{1}{2} f_{\max}$ where the bandwidth of interest is $\mathrm{BW} = 2\mathrm{f}_{\max}$ centered at f_c (note in the example shown in the figures, $f_c = 0$).

To illustrate the recovery process (Figure A.4), a rect function window of width BW is centered on the spectrum of interest and multiplied by $1/\Delta f$,

$$S(f) = G(f)III(fT)^*[III(f\Delta t)\Delta t][\frac{1}{2f_{\max}}\prod(f/2f_{\max})] \tag{A.23}$$

Here the inverse $-i$ Fourier transform of the above is taken,

$$s(t) = g(t)III(t/\Delta t) * \frac{1}{T}III(t/T) * sinc(2f_{\max}t) \tag{A.24}$$

in which the first term is the sampled function $g(t)$, which is convolved by the replicating shah function (second term) and convolved by an interpolating *sinc* function that restores the sampled $g(t)$ to its original form of Figure A.1a. This last windowing step is often tacitly understood because the waveform and spectrum corresponding to the series term $p = 0$ is the focus of interest. Most graphics routines connect the dots between the numerical sample values and display the inverse

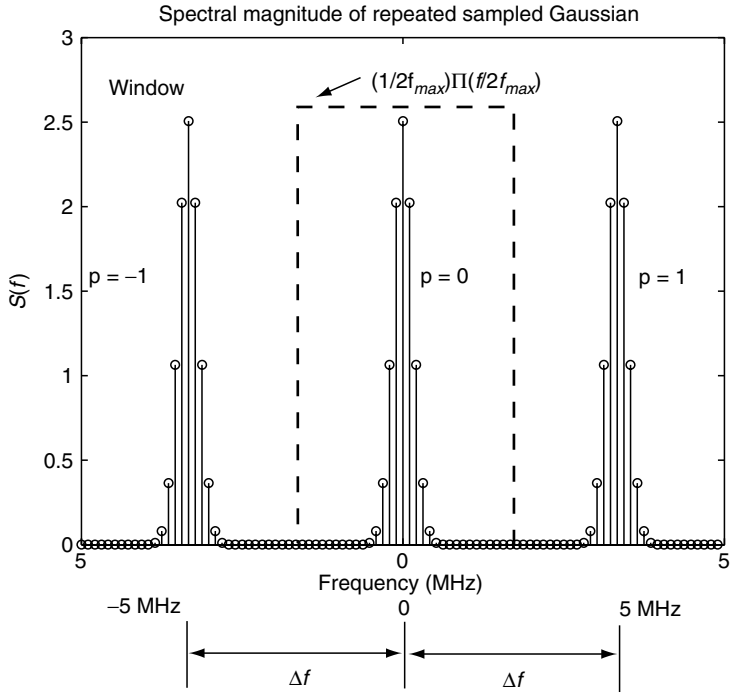

Figure A.4 Windowing of the fundamental spectrum from Figure A.3b.

transform of Eq. (A.22), windowed by the time interval T to the original time segment of interest, as a continuous function. Note that an adequate sampling rate still must be met for these conditions to hold.

A.2.5 The Digital Fourier Transform

From the previous sampling discussion, a mathematical form of both a periodic time waveform and a periodic spectrum were needed to achieve sampling in both domains. In practice, the focus is on only one period in each domain; therefore, the approach can be applied to a single waveform and spectrum at a time. For a finite number of samples (N), another way of achieving equivalent results is through the use of the digital Fourier transform (DFT), which also has periodic properties.

Recall that waveform or data series is represented by a sequence of numbers such as $g(n)$ based on an index $n = 0, 1 \ldots N - 1$. The number sequence is associated with a sampled physical quantity such as voltage, $g(n\Delta t)$. The index of the sequence is associated with an independent variable such as time (t), as well as a sampling interval such as Δt so that the variable extends from 0, Δt, $2\Delta t, \ldots$ to $(N - 1)\Delta t$ and constitutes a finite interval, $T = N\Delta t$.

In the usual bare bones formulation of the DFT, the user has to keep track of all the associations between the sample points and the independent variable, for there are just a sequence of numbers (the function) and integer indices. The minus i DFT of the sequence $g(n)$ is defined as

$$G(m) = DFT_{-i}[g(n)] = \sum_{n=0}^{N-1} g(n)e^{-i2\pi mn/N} \tag{A.25}$$

Note that the transformed sequence, $G(m)$, has an index m; therefore, each value of $G(m)$ corresponds to a sum of a weighted sequence of exponentials over N. If the index n exceeds $N-1$, the transformed sequence repeats itself because the exponential has a period N (a property essential for the periodic nature of the sampling process described in the last section). Once again, the focus is on the first N points. The inverse minus i DFT is

$$g(n) = DFT_{-i}^{-1}[G(m)] = \frac{1}{N}\sum_{m=0}^{N-1} G(m)e^{i2\pi mn/N} \tag{A.26}$$

Similar general principles and transform pairs hold for DFTs, but because a finite number of samples are involved, extra care must be taken in their application.

The FFT (Cooley and Tukey, 1965) is an efficient algorithm for calculating a DFT. Standard FFT algorithms are available, such as those in MATLAB. The next section will provide the detailed steps needed for the application of DFTs to Fourier transform calculations, as well as a MATLAB program for carrying them out. A final section has extra advice on sampling and practical applications.

A.2.6 Calculating a Fourier Transform with an FFT

Since more is involved in obtaining a Fourier transform of a function than just applying an FFT, the steps are described here. We begin with a continuous function of time, $g(t)$, that is similar to the one in Figure A.1. Much of the discussion follows the reasoning of Section A.2.4. A key difference between a continuous Fourier transform and a digital Fourier transform can be found by comparing Eq. (A.1), the definition of a Fourier transform, Eq. (A.22), the Fourier transform of a repeated sampled waveform, and the definition of a DFT, Eq. (A.25). This difference is that the DFT is simply a sum. To approximate a continuous integral, a sampling interval is required, as well as a sum, as evident from Eq. (A.22). The missing ingredient is Δt. In order to estimate a continuous Fourier transform by a numerical approach, the sampled waveform (a series of points) must be multiplied by Δt before performing the FFT.

An example is calculated by the MATLAB program, gausdemo.m, which compares a continuous Fourier transform of a Gaussian with that calculated by an FFT. The function for this example is $\exp(-at^2)$. Since the function extends into negative time, we shift it forward by a delay (b) so that it is centered in an interval 0 to T as shown in Figure A.5.

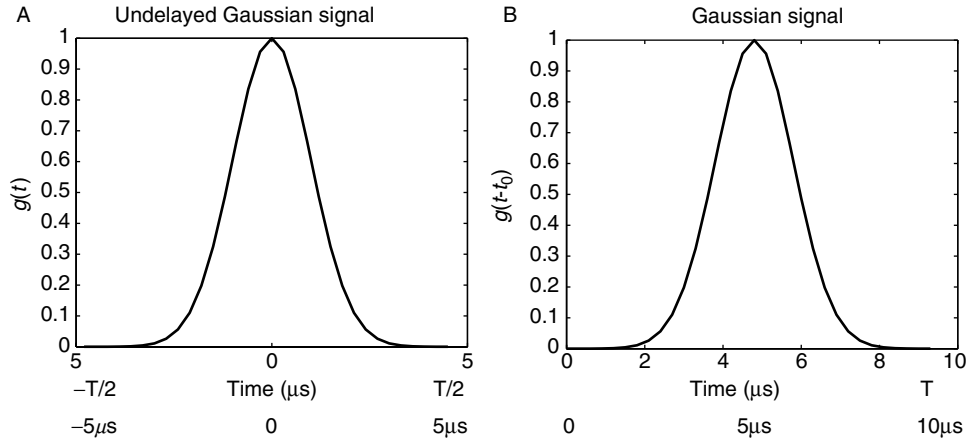

Figure A.5 (A) Gaussian waveform centered at origin. (B) Delayed Gaussian waveform.

$$h(t) = g(t - b) \tag{A.27}$$

For this example, the sampled function is a Gaussian symmetric about $t = 0.0$, with $a = 0.5$, and is defined over an interval of 9.6 μs so $b = 4.8$ μs and

$$h(t) = \exp[-a(t-b)^2] = \exp[-0.5(t-4.8)^2] \tag{A.28}$$

Note that within this interval, this shifted time function drops close to zero at the ends (as illustrated by Figure A.5a).

This shifted waveform is to be sampled at a regular interval Δt, but how is Δt selected? The usual advice is sample at the Nyquist rate or at

$$\Delta t = 1/2f_{\max} \tag{A.29a}$$

where $f_{\max}$ is the highest frequency in a band-limited spectrum. Unfortunately, we most likely do not know what $f_{\max}$ is or what the spectrum looks like or we would not be calculating the spectrum in the first place. If $f_{\max}$ is known, a conservative estimate is to use the sampling rate of

$$\Delta t_c = 1/10f_{\max} \tag{A.29b}$$

given by Weaver (1989). The determination of $f_{\max}$ must be done carefully: If a filter or beam profile is to be calculated by a transform and viewed on a decibel (logarithmic) scale (the usual case), then this frequency should be based on the scale to be used to avoid overlap or aliasing.

Most often a waveform is not a simple amplitude-modulated *sine* wave, and it may contain higher-frequency cycles or transients. Another approach is to look for the steepest transition slope in the waveform and to choose the shortest time interval containing the transition, δt. Then $f_{high} \approx 1/\delta t$ or

$$\Delta t = \delta t/2 = 1/2f_{high} \tag{A.29c}$$

In practice, this sampling rate may fall between the Nyquist rate and Weaver's recommendation.

To explore the differences in sampling rates, the Gaussian (a well-behaved function compared to the wide variety of functions that occur in practice) will be used. To find the locations where the maximum slopes occur, we differentiate the function with respect to time either analytically (if possible) or numerically. The result of a numerical differentiation by a MATLAB function *diff.m* is shown in Figure A.1c and indicates two time locations where slope is maximum. To find these times analytically, the usual min-max procedure is to differentiate the function and set the result equal to zero. In this case, the solution of setting the slope to zero is for t=b, where the slope is zero. For this particular problem, the function is differentiated a second time and the result set to zero, so the solutions for the locations of the maximum slopes are

$$t = t_0 \pm 1/\sqrt{2a} \tag{A.30a}$$

The slope can be estimated numerically as

$$\frac{\mathrm{dh}}{\mathrm{dt}} \approx \frac{\Delta \mathrm{h}}{\Delta \mathrm{t}} = \frac{\mathrm{h}[(\mathrm{n}+1)\Delta \mathrm{t}] - \mathrm{h}(\mathrm{n}\Delta \mathrm{t})}{\Delta \mathrm{t}} \tag{A.30b}$$

where the closest sample points to the location of the maximum slope are implied (Figure A.1b). For this example, the maximum slope is $dh/dt = 0.06065$ at $t = t_0 \pm 1$. Sampling can be regarded as an exercise in a numerical approximation of this slope as $\Delta h/\Delta t$. For $\Delta t = 0.30\,\mu$s, the approximate slope is 0.06; for $\Delta t = 0.15\,\mu$s, it is 0.0605, which is recommended. The numerically determined slope approaches the ideal value asymptotically as the sampling interval is decreased. From Figure A.2a, $f_{\max}$ appears to be about 1 MHz on a linear scale when seen at a larger magnification. The standard Nyquist sampling rate gives the sampling interval as $\Delta t = 0.50\,\mu$s. Weaver's sampling criteria yields $\Delta t = 0.10\,\mu$s. In summary, the standard Nyquist sampling approach can underestimate the sampling required for a nonsinusoidal waveform. The Weaver criterion provides a more conservative estimate, and the numerical approximation of the maximum slope (the transient approach) gives reasonable estimate based on the properties of the waveform under consideration without prior knowledge of $f_{\max}$.

Next the number of samples (N) needs to be chosen. Weaver (1989) suggests this number to be at least

$$N = 10(T_p/2 + b)/\Delta t \tag{A.31}$$

Again, this is a conservative number; the minimum needed is $\frac{1}{10}$ this value for a well-behaved waveform like the one in our example for which the waveform drops so rapidly that there is not much left at the ends of the interval chosen. The importance of N is evident from Figure A.3b, which shows the frequency sampling interval as $1/T = 1/(N\Delta t)$.

For our example, the recommended sampling from the transient criteria is $\Delta t_c = 0.15\,\mu$s, and $T_p \approx 7\,\mu$s, so if $b = 3.5\,\mu$s, therefore $N = 467$. To be a bit safer and round up to the nearest power of 2 (the usual choice for an FFT), let $N = 512$ so that $T = 76.8\,\mu$s. For most FFT routines, it is desirable to have N be a power of 2.

Note that this time sequence is to be associated with the running index, 0, 1, 2, ... 511, 512, just as the sampled waveform, $h(n\Delta t)$, is associated with the shown sequence, $h(n)$. Note that adding a significant number of zeros may change the resulting spectrum. Because of the good behavior of the waveform in this example, we can use the criteria above divided by 10. For the Nyquist criteria, this approach (rounded up to the nearest power of 2) gives $N = 16$; for the Weaver sampling, $N = 128$, and by the transient method, $N = 64$. For the purposes of demonstrating the calculation process with adequate graphical clarity, the figures in this appendix were calculated with $\Delta t = 0.30\,\mu s$ and $N = 32$, which are better than the values obtained by the Nyquist sampling criteria but less than the recommended values. Through the MATLAB program gausdemo.m, which compares an analytically determined spectrum of a Gaussian with that determined by the FFT process described here, the reader can experiment with the effects of changing the sampling interval and number of points.

Again, it is important in general that, if possible, the signal be very small or close to zero at the ends of this interval, which is true for this function. This requirement makes sense because of the periodic nature of the DFT; a jump at the ends of this cyclic progression would result in an artificial transient discontinuity that could introduce artifacts into the calculation. A window function such as a Hamming or Hanning function is often multiplied by the function to be transformed to reduce the signal to small values at the ends of the time interval; there are trade-offs in selecting these functions (Kino, 1987). The final delayed sampled waveform appears in Figure A.1b.

In order to perform these calculations, we use MATLAB command "fft." This command calculates a DFT according to Eq. (A.25) except that an internal computational index runs from 1 to N, which makes no difference in the outcome. Take the FFT (equal to the minus i DFT) of $h(n)$ and multiply it by Δt, similar to the operation in Eq. (A.22),

$$H(m) = \Delta t\{\mathrm{DFT}_{-i}[h(n)]\} \tag{A.32}$$

and the result is Figure A.6a. The multiplication by Δt is analogous to the dt in the integrand of the continuous Fourier transform. Note this operation is similar to Eq. (A.22) and Figure A.3b.

Usually a spectrum is displayed with a frequency range extending from negative to positive frequencies. The real and imaginary parts of the DFT calculation in Figure A.6a, however, correspond to an unshifted frequency row vector of two contiguous segments, 0 to $N/2 - 1$ and then $N/2$ to $N - 1$, both multiplied by Δf. This sequence of numbers will be called "$f_{unshift}(m)$" with indices 0 to $N - 1$, as illustrated by the abscissa in Figure A.6a. First, however, if shifting by a delay b was necessary, then the complex spectrum must be corrected for this by

$$G(f) = H(f)\exp(i2\pi bf) \tag{A.33a}$$

which in digital terms is equivalent to

$$G(m) = H(m)\exp\left(i2\pi bf_{unshift}(m)\right) \tag{A.33b}$$

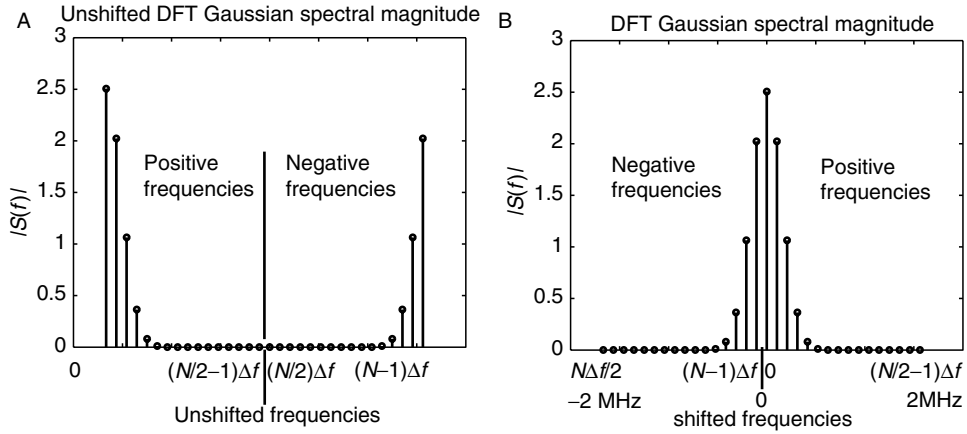

Figure A.6 (A) Magnitude of the FFT of the sampled delayed Gaussian waveform plotted against the unshifted sample indices. (B) Spectral magnitude versus shifted frequencies after (A) has undergone a shift operation.

Next, the real and imaginary parts of the DFT calculation shown in Figure A.6a need to be reshuffled to correspond to the standard frequency convention for a more convenient display of results. There is a DFT theorem that can be applied to this problem,

$$H(-m) = H(N-m) \tag{A.34}$$

so that the transformed sequence can be remapped from the unshifted vector, $f_{unshift}(m)$, to a new arrangement based on a new vector, $f_{shift}(m)$, as given by Figure A.6b. This new mapping corresponds to frequencies running from $N\Delta f/2 \ldots (N-1)\Delta f$, 0, $\Delta f \ldots (N/2-1)\Delta f$. Note that adding a point corresponding to a frequency index $N\Delta f/2$ (not shown) on the right end would repeat the leftmost value at $N\Delta f/2$. This reshuffling operation can be executed by MATLAB function "fftshift.m."

A continuous function $H(f)$ can be recovered from $H(m)$ by the interpolation formula or by fitting a smooth curve to the points where the final result is shown in Figure A.6b. Usually a plot routine connects the sample points automatically so no extra step is necessary for interpolation.

The program gausdemo.m compares the calculated digital spectrum just explained to an analytically determined spectrum and shows that the magnitudes correspond exactly. From theory, a constant phase of zero radians is expected. The spectrum of the digitally determined phase, calculated by MATLAB functions "angle.m" and "unwrap.m," show that the expected phase is recovered only over those frequencies where the spectral Gaussian function is numerically defined, roughly between −1 and 1 MHz, and outside this range, numerical noise results.

In summary, the recommended steps in finding are the following:

1. Determine sampling interval Δt, number of points N, and sampling period T.
2. Shift the waveform to center of T, if necessary.
3. Multiply the waveform by Δt and take its fft.
4. Correct for inserted delay by multiplying the complex spectrum by corresponding phase factor, if necessary.
5. Shift the spectrum points to correspond to the negative-to-positive frequency convention.
6. Plot the spectrum (or interpolate points).

A.2.7 Calculating an Inverse Fourier Transform and a Hilbert Transform with an FFT

Often a complex spectrum is given and the corresponding pulse is required. In many cases, it is desirable to calculate the envelope of the pulse and/or its quadrature signal. All of these pulse characteristics can be obtained in a single calculation. The quadrature signal of a *cosine* is a *sine*, for example. The quadrature signal has the interesting property that it is minimum where the real signal is maximum, and it is usually 90° out of phase from the real signal. The overall time signal that consists of the real and imaginary quadrature signals is called the "analytic signal."

Two methods for determining the quadrature waveform will now be given, and the previous Gaussian example will be used. Consider the spectrum that has already been determined by the process described in the last section. In this example, the spectrum is real; in general, it is complex.

Given the original complex spectrum before shifting, set the values for the negative frequencies equal to zero (points corresponding to $N/2$ to $N-1$).

Now the inverse FFT (corresponding to an inverse $-i$ DFT) is taken and multiplied by $2/(\Delta t)$,

$$h(n) = [2/\Delta t]\{\mathrm{DFT}_{-i}^{-1}[H(m)]\} \tag{A.35}$$

and the real and imaginary parts of $h(n)$ are illustrated by Figure A.7. Note that multiplying by $1/(\Delta t)$ and the factor $(1/N)$ implicit in the definition of the inverse DFT, Eq. (A.26), is equivalent to multiplying by $1/T$, the fine frequency sampling interval. The multiplication by a factor of two compensates for the missing half of the spectrum. The real waveform corresponds to the original waveform. The process of dropping the negative frequencies is the equivalent of taking a Hilbert transform, so that an imaginary or quadrature signal is obtained simultaneously with the real part (more on the Hilbert transform can be found in Chapter 5).The pulse magnitude or envelope can be found by calculating

$$\mathrm{ENV}[h(n)] = \sqrt{\{REAL[h(n)]\}^2 + \{IMAG[h(n)]\}^2} \tag{A.36}$$

and its usual display is given in Figure A.7 simultaneously with the real part. A more conventional presentation is with the envelope on a dB scale and the spectral magnitude shown simultaneously, also on a dB scale (as given in Figure 13.5). Note that the

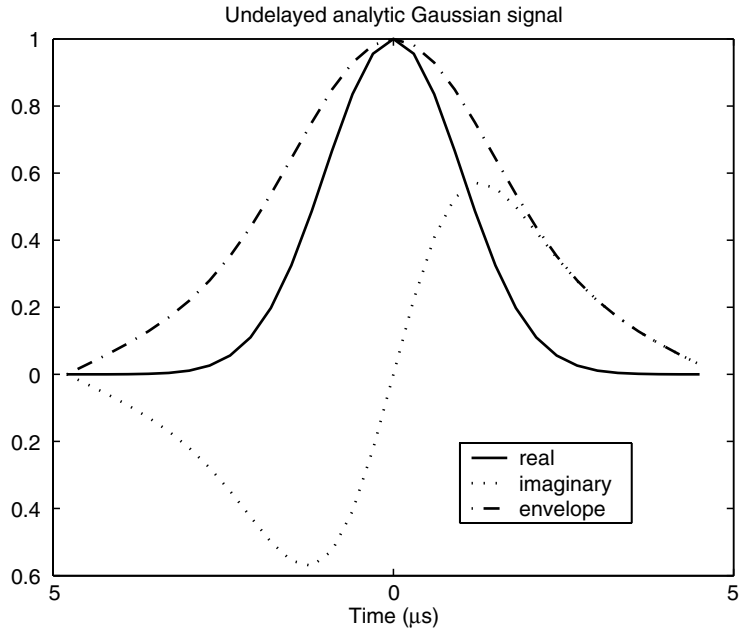

Figure A.7 The real and quadrature waveforms and envelope of an analytic signal versus time.

overall time range with an sampling interval, $\Delta t = 1/(N\Delta f)$, can be adjusted (advanced or delayed) by extracting the desired points or windowing to enhance the presentation of the pulse, and uninteresting points can be dropped to expand the view of the pulse.

An alternative and more convenient way of obtaining the analytic signal is to use the MATLAB function "hilbert.m" on the original real waveform. This operation results in the simultaneous creation of the real and imaginary (quadrature) signals. The envelope can be obtained by applying the MATLAB command "abs" on the complex time signal. The mathematical operations that generated the figures (and more) in this appendix can be found in a program written in MATLAB. This program, Appendix A.m provides many examples of FFT operations and compares an analytically determined spectrum of a Gaussian to that calculated by the steps in this appendix.

A.2.8 Calculating a Two-Dimensional Fourier Transform with FFTs

In order to calculate a two-dimensional Fourier transform with FFTs, a little extra work is needed. In this case, the data are described by a matrix (X). If the dimensions of the matrix are not powers of 2, then the two-dimensional FFT MATLAB function "fft2.m" adds zeros so the lengths conform and returns these new lengths as variables mrows (number of rows) and ncols (number of columns). For a two-dimensional FFT,

quadrants of data need to be moved to bring the arrangement of the calculations into a conventional pattern; fortunately, this operation can be accomplished by the "fftshift" MATLAB fuction "fftshift.m." Discrete Fourier transforms of multiple dimensions of higher order "ND" can be computed through the MATLAB function "fftn.m."

Bibliography

Bateman, H. (1954). *Tables of Integral Transforms*, Vol. 1, Bateman manuscript project A. Erde'lyi (ed.). McGraw Hill, New York.

Bracewell, R. (2000). *The Fourier Transform and Its Applications*. McGraw-Hill, New York.

Campbell, G. A. and Foster, R. M. (1948). *Fourier Integrals for Practical Applications*. D. van Nostrand (ed.). New York.

Goodman, J. W. (1968). *Introduction to Fourier Optics*. McGraw Hill, New York.

Rabiner, L. R., and Gold, R. B. (1975). *Theory and Application of Digital Signal Processing*. Prentice-Hall, Englewood Cliffs, NJ.

Weaver, H. J. (1989). *Theory of Discrete and Continuous Fourier Analysis*. John Wiley & Sons, New York.

References

Bracewell, R. (2000). *The Fourier Transform and Its Applications*. McGraw-Hill, New York.

Cooley, J. W., and Tukey, J. W. (1965). An algorithm for the machine computation of complex Fourier series. *Math. Comp.*, 297–301.

Kino, G. S. (1987). *Acoustic Waves: Devices, Imaging, and Analog Signal Processing*. Prentice-Hall, Englewood Cliffs, NJ, Sec. 4.5.3.

Weaver, H. J. (1989). *Theory of Discrete and Continuous Fourier Analysis*. John Wiley & Sons, New York.

APPENDIX B

TABLE B.1 Properties of Tissues

Tissue	C	α	y	ρ	Z	B/A
(units)	M/s	dB/MHz^y–cm		Kg/m^3	megaRayls	
Blood	1584	0.14	1.21	1060	1.679	6
Bone	3198	3.54	0.9[b]	1990	6.364	—
Brain	1562	0.58	1.3	1035	1.617	6.55
Breast	1510	0.75	1.5	1020	1.540	9.63
Fat	1430	0.6	1*	928	1.327	10.3
Heart	1554	0.52	1*	1060	1.647	5.8
Kidney	1560	10	2[b]	1050	1.638	8.98
Liver	1578	0.45	1.05	1050	1.657	6.75
Muscle	1580	0.57	1*	1041	1.645	7.43
Spleen	1567	0.4	1.3	1054	1.652	7.8
Milk	1553c	0.5	1	1030	1.600	—
Honey	2030[s]	—	—	1420[s]	2.89[s]	—
Water @ 20°C	1482.3	2.17e-3	2	1.00	1.482	4.96

REFERENCES

Bamber, J. C. (1998). Ultrasonic properties of tissue. In *Ultrasound in Medicine*. F. A. Duck, A. C. Baker, and H. C. Starritt (eds.). Institute of Physics Publishing, Bristol, UK.

Duck, F. A. (1990). *Physical Properties of Tissue: A Comprehensive Review.* Academic Press, London.

Selfridge, A. R. (1985). Approximate material properties in isotropic materials. *IEEE Trans. Sonics Ultrason.* **SU-32**, 381–394.

TABLE B.2 Properties of Piezoelectric Transducer Materials

Material	ρ	$\epsilon^s_{33}/\epsilon_0$	k_T	c_{TL} km/s	Z_L MR	k'_{33}	c'_{33L} km/s	Z'_{33} MR	k_{33}	c_{33L} km/s	Z_{33} MR
PZT-5A	7.75	830	0.49	4.350	33.71	0.66	3227	25.01	0.705	3693	28.62
PZT-5H	7.50	1470	0.50	4.560	34.31	0.70	3800	29	0.75		
$BaTiO_3$	5.7	1260	0.38	5.47	31.18	0.47			0.50		
$LiNbO_3$	4.64	39	0.49	7.36	34.2						
Quartz	2.65	4.5	0.093	5.0	13.3						
PVDF	1.78	12	0.11	2.2	3.92						
PMN-PT	8.06	680	0.64	4.646	37.45	0.9066	3.057	24.64	0.94	3.343	26.94
PZN-PT	8.31	1000	0.5	4.03	33.49	0.878	2.624	21.81	0.91	2.417	20.09
Comp A	6.01	376	0.80	3.0	18.03						
Comp B	4.37	622	0.66	3.79	16.58						
Navy VI	7.5	1470	0.5	4.575	34.31	0.698	3986	29.9	0.75	3.851	28.88

Note: Comp A is a 1–3 composite 69% PZN-PT and 31% D-80 filler.
Comp B is a 1–3 composite with 51% Navy type VI (equivalent to PZT-5H) and 49% D-80 filler.
Also in the table, density ρ is in units of 10^3 kg/m^3 and MR is megaRayls. The subscript L is for longitudinal wave; therefore, c_{TL} represents the thickness mode longitudinal sound speed.
Sources for the last five materials are Park and Shrout (1997) and Ritter *et al.* (2000).

REFERENCES

Kino, G. S. (1987). *Acoustic Waves: Devices, Imaging, and Analog Signal Processing*. Prentice-Hall, Englewood Cliffs, NJ.

Park, S.-E. and Shrout, T. R. (1997). Characteristics of relaxor-based piezoelectric single crystals for ultrasonic transducers. *IEEE Trans. Ultrason. Ferroelec. Freq. Control* **44**, 1140–1147.

Ritter, T., Geng, X., Shung, K. K., Lopatin, P. D., Park, S.-E., and Shrout, T. R. (2000). Single crystal PZN/PT-polymer composites for ultrasound transducer applications. *IEEE Trans. Ultrason. Ferroelec. Freq. Control* **47**, 792–800.

APPENDIX C

Chapter Contents

C.1 DEVELOPMENT OF ONE-DIMENSIONAL KLM MODEL BASED ON ABCD MATRICES

As shown in Figure C.1, the Krimholtz–Leedom–Matthaei (KLM) model (Leedom *et al.*, 1978) provides a separation of the electrical and acoustical parts of the transduction process. This partitioning will allow us to analyze these parts individually to improve the design of the transducer. Note there are three ports: electrical (#3) and two acoustical (#1 and #2). Port 1 will be used for the transmission of acoustic energy into the body or water, and acoustic port 2 radiates into a transducer backing material. The equivalent loads for port 1 on the right (R) and port 2 on the left (L) will be called $Z_R = Z_W$ (water) and $Z_L = Z_B$ (backing). For a derivation of the KLM model, the reader is referred to Leedom *et al.* (1978) or Kino (1987).

Armed only with simple 2 x 2 ABCD matrices from Chapter 3, we shall construct a numerical equivalent circuit model (van Kervel and Thijssen, 1983) that will tell us a great deal about how a piezoelectric transducer works. A simplified version of Figure C.1 is shown in Figure 5.8, which represents a nodal numbering scheme to identify points along the signal path. Beginning at port 3, we attach a voltage source V_g with a source resistance R_g to port 3 through a general tuning network with its own ABCD matrix. A particular tuning network implemented in this program is shown in Figure 5.10, which consists of an inductor and an inductive loss resistor and has a series impedance, $Z_S = R_S + i\omega L_S$. The product E of the first matrices 1 and 2 is

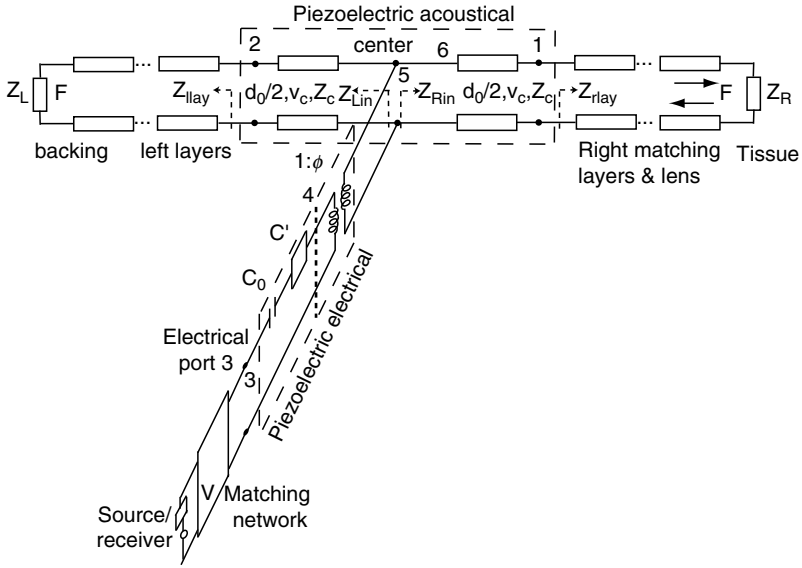

Figure C.1 KLM equivalent circuit model with acoustic layers and loads and electrical matching.

$$[E] = \begin{pmatrix} 1 & Z_S + R_g \\ 0 & 1 \end{pmatrix} = \begin{pmatrix} 1 & R_g \\ 0 & 1 \end{pmatrix} \begin{pmatrix} 1 & Z_s \\ 0 & 1 \end{pmatrix} \tag{C.1}$$

Inside port 3 are two capacitive elements between nodes 3 and 4. The first term is C_0 with a reactance $iX_0 = -i/\omega C_0$. The second term represents the current contribution to the acoustic output where $iX' = -i/\omega C'$ and

$$C' = -C_0/\left[k_t^2 sinc(\omega/\omega_0)\right] \tag{C.2}$$

where X' is related to the minus i Fourier transform of the rectangular shape of the electric field between the electrodes of the piezoelectric. Here the piezoelectric coupling constant k_t for the thickness expander mode is used. Multiplying the matrices of the series elements X_0 and X' results in overall matrix C,

$$[C] = \begin{pmatrix} 1 & iX_0 \\ 0 & 1 \end{pmatrix} \begin{pmatrix} 1 & iX' \\ 0 & 1 \end{pmatrix} = \begin{pmatrix} 1 & (C_0 + C')/(i\omega C_0 C') \\ 0 & 1 \end{pmatrix} \tag{C.3}$$

To complete the electrical part of the model, the transformer between nodes 4 and 5 that converts electrical signals to acoustic waves and vice versa is needed. Here the turns ratio of the transformer is

$$\phi = k_t \left(\frac{\pi}{\omega_0 C_0 Z_C}\right)^{1/2} sinc[\omega/(2\omega_0)] \tag{C.4}$$

where Z_C is the normalized impedance of the crystal,

$$Z_C = AZ_0 = A\left(C^D/\rho_c\right)^{1/2}\rho_c = A\left(C^D\rho_c\right)^{1/2} \tag{C.5}$$

where the crystal has a thickness d_0, an area A, a density ρ_C, and an elastic constant C^D. All the acoustic impedances in this model are normalized by area because one of the acoustic output variables is force (not pressure). For the transformer, the matrix is

$$[T] = \begin{pmatrix} \phi & 0 \\ 0 & 1/\phi \end{pmatrix} \tag{C.6}$$

At node 5, the acoustic center of the model shown in Figure C.1, a right turn needs to be made toward the desired load (Z_R). The blocks to the right are symbols for transmission lines representing each of the layers along the way. In this model, this center is placed in the center of the crystal so that the first layer between nodes 6 and 1 is half of the crystal with a thickness $d_0/2$; the other layers between nodes 1 and Z_R are usually matching layers, bond layers, a lens, and so forth. In the left direction, since this is a politically correct symmetric model, there is another half-thickness crystal layer as well as other possible layers along the way to the left load, which is the backing, $Z_L = AZ_B$. Let the impedance looking to the left of center be Z_{LIN} and that looking to the right be Z_{RIN}. Then, at the center, these two impedances appear to be in parallel (as shown in Figure C.1). For the right path, Z_{LIN} acts as a parallel shunt impedance element with a matrix,

$$[Z] = \begin{pmatrix} 1 & 0 \\ 1/Z_{LIN} & 1 \end{pmatrix} \tag{C.7}$$

The path to the right can be described by the matrix chain $[E][C][T][Z]$.

What are Z_{LIN} and Z_{RIN}? So far, the description of the model has moved from electrical port 3 to acoustic port 1 in the same manner as the transducer would be excited, but in fact, the matrix calculations actually start at Z_R because matrices are multiplied right to left. In Figure C.2, the computation starts with the nth right layer and load Z_R. Each transmission line layer has thickness d_{nR}, a sound speed c_{nR}, a normalized impedance Z_{nR}, and a wavenumber γ_{nR} (note for lossless transmission lines, $\gamma_{nR} = i\omega/c_{nR}$). An overall ABCD matrix can be obtained from the product of the layer matrices from the one closest to the load to the half-crystal layer. A more

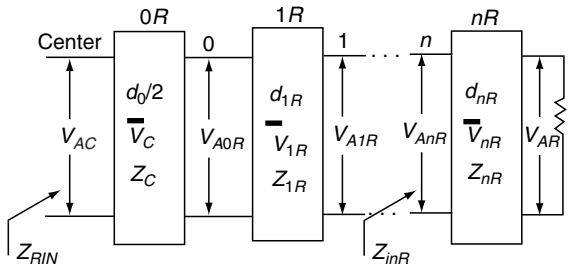

Figure C.2 Numbering scheme for right path acoustic layers.

numerically stable result is obtained by calculating the two important variables, input impedance and acoustic voltage ratios, in a sequential manner from right to left. For example, the computation would start with

$$Z_{inR} = \frac{A_{nR}Z_R + B_{nR}}{C_{nR}Z_R + D_{nR}} \tag{C.8a}$$

where $Z_R = AZ_W$ and continue with

$$Z_{i(n-1)R} = \frac{A_{(n-1)R}Z_{inR} + B_{(n-1)R}}{C_{(n-1)R}Z_{inR} + D_{(n-1)R}} \tag{C.8b}$$

until Z_{RIN} is determined. Therefore, the impedance of a layer is used to feed the calculation of the layer to its left. In a similar manner, the acoustic voltage transfer ratio (equivalent to acoustic force) is found layer by layer. For example, for layer nR, it is

$$\frac{V_{AR}}{V_{AnR}} = \frac{Z_R}{A_{nR}Z_R + B_{nR}} \tag{C.8c}$$

This process ends up in an overall transfer function for all the right layers,

$$\frac{V_{AR}}{V_{AC}} = \frac{V_{A0R}}{V_{AC}}\frac{V_{A1R}}{V_{A0R}}\cdots\frac{V_{AR}}{V_{AnR}} \tag{C.8d}$$

Similar calculations result in V_{AL}/V_{AC} and Z_{LIN} on the left side; however, usually the only layer involved is the half-crystal layer with a backing load. The final transfer ratio, V_{AR}/V_G, is the product of the individual ratios for each matrix all the way back to the source at V_G.

References

Kino, G. S. (1987). *Acoustic Waves: Devices, Imaging, and Analog Signal Processing*. Prentice-Hall, Englewood Cliffs, NJ.

Leedom, D. A., Krimholtz, R., and Matthaei, G. L. (1978). Equivalent circuits for transducers having arbitrary even- or odd-symmetry piezoelectric excitation. *IEEE Trans. Sonics Ultrason.* **SU-25**, 115–125.

van Kervel, S. H. and Thijssen, J. M. (1983). A calculation scheme for the optimum design of ultrasonic transducers. *Ultrasonics*, 134–140.

APPENDIX D

List of groups interested in diagnostic ultrasound:

Acoustical Society of America (ASA)
American Society of Echocardiography (ASE)
American Endosonography Club (AEC)
American Institute of Physics (AIP)
American Institute of Ultrasound in Medicine (AIUM)
The American Registry of Diagnostic Medical Sonographers (ARDMS)
Applications in Radiology (SCAR)
Arizona Society of Echocardiography (ArSE)
Austrian Society of Ultrasound in Medicine and Biology (OGUM)
Australian Society for Ultrasound in Medicine (ASUM)
Australian Sonographers Association (ASA)
Belgium Society of Ultrasound in Medicine and Biology
British Medical Ultrasound Society (BMUS)
Bulgarian Ultrasound Association in Medicine and Biology
Canadian College of Physicists in Medicine (CCPM)
Canadian Organization of Medical Physicists (COMP)
Canadian Society of Diagnostic Medical Sonographers (CSDMS)
Croatian Society for Ultrasound in Medicine and Biology
Cyber 3D-Ultrasound Society
Czech Society for Ultrasound
The Danish Society of Diagnostic Ultrasound
European Society of Cardiology (ESC)
Finnish Society for Ultrasound in Medicine and Biology
Foundation for Ultrasound in Medicine and Biology (Netherlands)
French Society of Ultrasound in Medicine and Biology
German Society of Ultrasound in Medicine and Biology
Hellenic Society of Ultrasound in Medicine and Biology

Hungarian Society of Ultrasound in Medicine and Biology
International Electrotechnical Commission (IEC)
IEEE Ultrasonics Ferroelectrics and Frequency Control (IEEE UFFC)
Israeli Society of Ultrasound in Medicine
Italian Society of Ultrasound in Medicine and Biology
Musculoskeletal Ultrasound Society (MUSoc)
(American) National Board of Echocardiography (NBE)
Norwegian Society for Diagnostic Ultrasound in Medicine (NFUD)
Polish Ultrasound Society for Ultrasound in Medicine (PUS)
Portuguese Ultrasound Society for Ultrasound in Medicine (GRUPUGE)
Radiological Society of America (RSNA)
Romanian Society for Ultrasonography in Medicine and Biology (SRUMB)
Russian Society of Diagnostic Ultrasound in Medicine Society for Computer
Slovakia Society for Ultrasound in Medicine (SSUM, Slovakia)
Slovene Society for Ultrasonics
Society of Diagnostic Medical Sonographers (SDMS)
Society of Radiologists in Ultrasound (SRU)
Society of Vascular Technology (SVT)
Spanish Ultrasound Society (SEECO)
Swedish Society for Ultrasound in Medicine (SSMU)
Swiss Ultrasound Society in Medicine and Biology (SGUMB)
Ultrasound Training Center Cluj-Napoca (CFU)

INDEX